University of Kent

Kent Academic Repository

Alesbrook, Luke Stephen (2019) *The Analysis of Two Unique Micrometeorite Collections, and the Effect of Atmospheric Entry on Extra-Terrestrial Particles.* Doctor of Philosophy (PhD) thesis, University of Kent.

Downloaded from

https://kar.kent.ac.uk/84235/ The University of Kent's Academic Repository KAR

The version of record is available from

This document version

Author's Accepted Manuscript

DOI for this version

Licence for this version

CC BY-NC (Attribution-NonCommercial)

Additional information

Versions of research works

Versions of Record

If this version is the version of record, it is the same as the published version available on the publisher's web site. Cite as the published version.

Author Accepted Manuscripts

If this document is identified as the Author Accepted Manuscript it is the version after peer review but before type setting, copy editing or publisher branding. Cite as Surname, Initial. (Year) 'Title of article'. To be published in ***Title of Journal*** , Volume and issue numbers [peer-reviewed accepted version]. Available at: DOI or URL (Accessed: date).

Enquiries

If you have questions about this document contact ResearchSupport@kent.ac.uk. Please include the URL of the record in KAR. If you believe that your, or a third party's rights have been compromised through this document please see our Take Down policy (available from https://www.kent.ac.uk/guides/kar-the-kent-academic-repository#policies).

The Analysis of Two Unique Micrometeorite Collections, and the Effect of Atmospheric Entry on Extra-Terrestrial Particles.

A thesis submitted for the degree of
Doctor of Philosophy

by

Luke Stephen Alesbrook

School of Physical Sciences

University of Kent
Canterbury
U.K

Declaration

This thesis has been composed by the author and has not been submitted as an exercise for a degree at any other higher educational institute.
All data used in this thesis is the authors own unless stated otherwise

Acknowledgements

Firstly I would like to thank my supervisor *Dr Penny Wozniakiewicz* for all of her help, guidance, the many cakes, cookies and cups of tea over the course of the past four years. Thank you also to my second supervisor *Prof Mark Burchell* who despite an exceptionally busy schedule, always had time to provide help, ideas and very useful references when they were needed. I would also like to thank *Mike Cole* for his help in discussing problems that arose, and for his immense patience in allowing me to be under his feet, asking questions during shots. My thanks also go to *Dr Mark Price* and *Dr Kathryn Harriss* for all their help, guidance, and letting me steal their keys to break into Penny's office when she was off on maternity.

Special thanks also goes to *Dr Tim Kinnear* for generally being awesome and without whom, writing and debugging code would have taken 50 times longer. Thanks also to *Ricky, and Jamie* for their help, DnD games nights and pointing out which ideas were just dumb at the start of this process. Thanks also to *Sam, Justyn, and Callum* for the trips to the pub and making SEPNET conferences all the more interesting. To everyone in 104, especially the chemists, I am very grateful that problems on the board would gather a group and get solved, it was massively helpful.

There is no way this thesis would have been completed if it was not for the help and support of my wife *Lucy*. Thank you for all your help, patience, love, support and nagging (well that one could maybe have been toned down a little). Last but not least I would like to thank my family for all their support and guidance, without whom I might have ended up as a florist as the careers people suggested.

Abstract

Each year 40,000 tons of extra-terrestrial material reaches the Earth's surface as micrometeorites. These small (sub 1 mm) grains of material supply the majority of the extra-terrestrial flux reaching Earth. Unfortunately due to their small size they are often completely altered by their atmospheric passage and hence no-longer accurately reflect the mineralogy of their precursor grain. Despite the trauma of atmospheric entry, some dust grains remain intact through entry as a result of their trajectory and these may provide pristine samples of early solar system material, or material from a larger extra-terrestrial body. As such, micrometeorites provide an important vector for the analysis of the solar system's evolution and planetary science. This thesis examines the results of two novel micrometeorite collections, and the effects that atmospheric entry has on incoming micrometeorites.

The two examined collections took place on the Kwajalein atoll in the mid-pacific and from the Halley VI research station in the Antarctic. Results recovered from these collections showed limited numbers of extra-terrestrial particles were recovered for further analysis from the Kwajalein survey, with none found on the Antarctic filters. Work was carried out to aid in the separation of extra-terrestrial material from the terrestrial debris often encountered in micrometeorite collections. Results from this work demonstrated the feasibility of, not only separating out material, but also provides possible links to micrometeorites and other meteoritic samples. This thesis also discusses the eight new extra-terrestrial candidates found upon the Kwajalein filters.

The effects of atmospheric entry was investigated using specially designed equipment to allow passage through air for Light Gas Gun projectiles. Olivine projectile passage, through atmosphere, at hyper-velocity speeds was successfully carried out with the projectiles being recovered intact at speeds upto $2\,\mathrm{km\,s^{-1}}$. At speeds exceeding $2\,\mathrm{km\,s^{-1}}$, the force at launch was sufficient to disrupt the projectile prior to its passage through the atmospheric target. Results for these experiments show a trend of increasing surface damage at higher velocities and provides avenues for increasing projectile temperature at slower launch velocities.

Contents

Declaration i

Acknowledgements ii

Abstract iii

List of Tables xiii

List of Figures xvi

I Introduction and Methods 1

1 Introduction 2

1.1 What are Micrometeorites? 2

1.2 The Classification of Micrometeorites 4

1.2.1 Melted Micrometeorites 5

1.2.1.1 S-Type Spherules 6

1.2.1.2 G-Type Spherules 8

1.2.1.3 I-Type Spherules 8

1.2.2 Scoriaceous Micrometeorites 8

1.2.3 Unmelted Micrometeorites 9

1.2.3.1 Fine-Grained Micrometeorites 9

1.2.3.2 Coarse-Grained Micrometeorites 9

1.2.3.3 Refractory Micrometeorites 10
1.2.3.4 UltraCarbonaceous Micrometeorites 10
1.2.3.5 Chondritic Porous Micrometeorites 10
1.3 Micrometeorite Collection Methods 11
1.3.1 Introduction: 11
1.3.2 Non-Antarctic Collections 12
1.3.2.1 Deep Sea Sediment Collections 12
1.3.2.2 Greenland Lake Collections 14
1.3.2.3 Sedimentary Rock Collections 15
1.3.2.4 Sedimentary rocks: Salt Deposits 16
1.3.2.5 Urban Collections 17
1.3.3 Antarctic Collections 17
1.3.3.1 South Pole Water Well: 18
1.3.3.2 Concordia Collection 20
1.3.3.3 Antarctic Blue Ice Collection 21
1.3.3.4 Dome Fuji Station Collection 23
1.3.3.5 Transantarctic Mountains 24
1.3.3.6 Larkman Nunatak 25
1.3.4 Micrometeoroid Collection 26
1.3.4.1 Low Earth Orbit Collections: 26
1.3.5 Summary 30
1.4 Alteration of Micrometeorites 30
1.4.1 Atmospheric Alteration 30
1.4.1.1 Morphological Changes 30
1.4.1.2 Chemical Changes 33
1.4.2 Terrestrial Weathering 34
1.4.2.1 Loss of Glass 35

1.4.2.2 Preferential Loss of Elements 35
1.5 Aim of Thesis 35

2 Methodologies **37**

2.1 Scanning Electron Microscope 37
2.1.1 SEM Design 38
2.1.2 SEM Detectors 41
2.1.3 SEM Imaging Complications 43
2.1.4 EDX Complications 44
2.1.5 Summary 46
2.2 Optical Microscopy 46
2.2.1 History 46
2.2.2 Lenses 46
2.2.3 Limitations to Optical Microscopy 47
2.2.4 Summary 48
2.3 Light Gas Gun 49
2.3.1 Operating Principles 49
2.3.2 The Kent LGG Design 50
2.3.3 Gun Firing Procedure and Shot Analysis 54
2.3.4 Summary 56
2.4 Other Analytical Techniques Used in this PhD 56
2.4.1 Raman Spectroscopy 56
2.4.1.1 Operating Principles 56
2.4.1.2 Summary 58
2.4.2 Focused Ion Beam 58
2.4.3 TEM 60
2.4.4 Summary 61

II Results Part A: Studies of Micrometeorites from Collections 62

3 Collection of Micrometeorites from Kwajalein and the British Antarctic Survey 63

3.1 Collection of Particles 63

3.1.1 The Collector 64

3.1.2 Kwajalein Collections Overview 65

3.1.3 BAS Collection 66

3.2 Sample Preparation and Analysis 68

3.2.1 Preparation of the Filters 68

3.2.2 Surveying Filters 70

3.2.3 Picking and Preparing Candidate Micrometeorites 73

3.3 Terrestrial Particles on Filters 76

3.3.1 Fly Ash 76

3.3.2 Volcanic Ash 78

3.3.3 Other Terrestrial Spheres 78

3.3.4 The Kwajalein Collection 79

3.3.4.1 Non-Spherical Contamination 79

3.3.4.2 Spherical Contamination 84

3.3.5 British Antarctic Survey Collection 87

3.3.5.1 Non-Spherical Contamination 87

3.3.5.2 Spherical Contamination 91

3.3.6 Summary 92

4 Establishing Criteria to Identify Micrometeorites 94

4.1 Introduction 94

4.2 Method 95

4.3 Results 96

4.3.1 Composition of Micrometeorites 96
4.3.2 Micrometeorites vs Chondrites 98
4.3.2.1 Chondrite Subtypes 98
4.3.2.2 Micrometeorites vs Bulk Chondritic Composition 101
4.3.2.3 Micrometeorites vs Chondritic Component Mineral Compositions 104
4.3.2.4 Summary 106
4.3.3 Micrometeorites vs Non-Chondrites 106
4.3.3.1 Non-Chondrite Subtypes 106
4.3.3.2 Micrometeorites vs Non-Chondrite Compositions 110
4.3.4 Micrometeorites vs Terrestrial Debris 112
4.3.4.1 Fly Ash 112
4.3.4.2 Volcanic Ash Composition 113
4.4 Summary 115

5 Analysis of Candidate Micrometeorites 118

5.1 Collected Extra-Terrestrial Particles 118
5.1.1 Spherical Particle Flux 118
5.2 Collected Particles 121
5.2.1 Extra-Terrestrial Candidates 121
5.2.2 Plotted Spheres 122
5.2.3 Detailed Analyses of Micrometeorite Candidates 133
5.2.3.1 Candidate 8-4-2 133
5.2.3.2 Candidate 9-9-7 136
5.2.3.3 Candidate 11-5-29 138
5.2.3.4 Candidate 11-8-16 140
5.2.3.5 Candidate 11-9-40 142
5.2.3.6 Candidate 12-1-56 144

5.2.3.7 Candidate 12-2-10 147
5.2.3.8 Candidate 12-7-25 149
5.2.3.9 Candidate 12-8-24 151
5.3 Discussion 152
5.3.1 Collector Performance 152
5.3.2 Collection Bias and Flux 153
5.3.3 Collection Events 156
5.4 Summary 157

III Atmospheric Flight 159

6 Atmospheric Flight 1: Preliminary Experimentation 160
6.1 Design of the Environment Tube 160
6.1.1 EVT Components 161
6.2 Shot Programme 1 164
6.2.1 Preliminary Pressure Testing 164
6.2.2 Preliminary Shots into the Environment Tube 167
6.2.2.1 Test Shot Setup 167
6.2.2.2 Results 168
6.3 Shot Programme 2: Determining the Parameter Space for Micrometeorite Analogues using the LGG and the EVT 169
6.3.1 Micrometeorite Analogue Projectiles 170
6.3.2 Initial Shots 175
6.3.2.1 Shot 1: Conditions 176
6.3.2.2 Shot 1: Results 177
6.3.3 Defining the Experimental Limitations 178
6.3.3.1 Disruption on Impact with the Capture Media 179
6.3.3.2 Avoiding Breakup Upon Impact with EVT Foils 179

6.3.3.3 Confirming the Survivability of the Micrometeorite Analogue Using the New Limits . . . 183

6.4 Summary . . . 184

7 Atmospheric Flight 2: Theoretical Calculations 186

7.1 Atmospheric Flight . . . 186

7.1.1 Atmospheric flight Background . . . 186

7.1.1.1 Overview . . . 186

7.1.1.2 Flow Regimes . . . 187

7.1.2 Derivation of Mass Change . . . 189

7.1.3 Derivation of the Impact Velocity . . . 190

7.1.4 Derivation of Atmospheric Heating . . . 192

7.2 Impact into the Projectile Stopping Medium . . . 194

7.2.1 Hypervelocity Impacts Background . . . 194

7.2.2 Derivation of u_t and v_i . . . 196

7.2.2.1 Derivation of u_t . . . 196

7.2.2.2 Calculation of Peak Impact Pressure . . . 198

7.2.3 Temperature Change During Impact . . . 200

7.3 Summary . . . 202

8 Atmospheric Flight 3: Thermal Alteration of Projectiles Passing Through Atmosphere 203

8.1 Building on Theoretical Results . . . 203

8.1.1 Overview of Theoretical Results . . . 203

8.1.2 EVT Design Improvement: Increasing Atmospheric Pressure . . . 203

8.1.2.1 Adaptations to the Environment Tube Design to Increase Contained Pressure . . . 204

8.1.3 EVT Design Improvement: Reducing Foil Induced Shock . . . 207

8.1.3.1 Adaptations to the Environment Tube Design to Reduce Foil Impact Shock . . . 207
8.1.4 Summary of Changes Carried Forward . . . 213
8.2 Shot Program 3 . . . 213
8.2.1 Aims . . . 213
8.2.2 Results . . . 214
8.2.2.1 Surface Morphology . . . 216
8.2.2.2 Chemical Composition . . . 220
8.2.2.3 Raman Peak Locations and Structure . . . 222
8.2.2.4 Line-Scans . . . 224
8.2.2.5 FIB-TEM . . . 227
8.3 Comparison with Previous Experiments . . . 229
8.4 Summary . . . 230

Final Conclusions and Future Work **232**

Bibliography **xxvi**

Appendices **xlviii**

A Resin Tests **xlix**

B Spherical Contamination **liii**

C Achondrite Meteorite subtypes **lvii**

D Raw Compositional Data **lxi**

E Ternary diagrams **cxxviii**

E.1 Titanium Oxide . . . cxxix
E.2 Compositional ternary diagrams . . . cxxx

E.2.1 Terrestrial Spheres cxxx
E.2.1.1 Fly Ash cxxx
E.2.1.2 Volcanic Ash cxxxii
E.2.2 Chondrites cxxxiv
E.2.2.1 Bulk cxxxiv
E.2.2.2 Chondritic areas cxxxvi
E.2.3 Achondrites cxxxviii
E.2.3.1 Bulk cxxxviii
E.2.3.2 Achondrite subtypes cxl
E.3 Volcanic ash composition versus Micrometeorite composition cxlii
E.3.1 Volcanic Ash cxlii
E.4 Terrestrial Debris versus CAIs cxlv
E.5 Chondrite Minerals versus Terrestrial Debris and MMs cxlvii
E.6 Achondrite Plots cxlix
E.7 Candidate MMs versus Achondrites cli

F Picked Particle details **cliii**
F.1 Analysed Spheres cliii
F.2 SEM Conditions for Picked Particle Analysis cliii

G Diagrams **clv**
G.1 Collector Casing Schematic clv
G.2 Environment Tube diagrams clvii

H Derivations **clxii**
H.1 Impact Velocity clxii
H.2 Atmospheric Heating clxiii
H.3 Derivation of Equation 7.18 clxiv
H.4 Derivation of 7.26 clxvi

I Peridot data **clxix**

J Shot Program **clxxiii**

J.1 Shot Program 1 clxxiii

J.2 Shot Program 2 clxxiv

J.3 foil rig setups clxxvi

List of Tables

2.1 Comparison of electron gun statistics 40

3.1 List of examined filters 72

3.2 Coal compositions 77

4.1 Comparative abundance of oxides in collated spheres 96

4.2 Carbonaceous chondrite subtypes 101

5.1 Kwajalein atoll sphere compositions 119

6.1 Peridot details 176

6.2 Summary of shots 1-6 184

7.1 a and b values for the target and projectile 199

8.1 Foil thickness pressure test results 206

8.2 Shot program 3 results 214

8.3 Peak positions of peridots 224

A.1 Results of embedding techniques experiments l

A.1 Table A.1 continued. li

A.1 Table A.1 continued. lii

B.1 Collected Spheres liv

B.2 Breakdown of Iron rich spherules lv

B.3 Breakdown of Aluminium rich spherules lvi

C.1 Achondite Subtypes lviii
C.1 Achondite Subtypes lix
C.1 Achondite Subtypes lx

D.1 Micrometeorite raw data lxii
D.1 Micrometeorite raw data lxiii
D.1 Micrometeorite raw data lxiv
D.1 Micrometeorite raw data lxv
D.1 Micrometeorite raw data lxvi
D.1 Micrometeorite raw data lxvii
D.1 Micrometeorite raw data lxviii
D.2 Raw data for fly ash lxix
D.2 Raw data for fly ash lxx
D.2 Raw data for fly ash lxxi
D.2 Raw data for fly ash lxxii
D.2 Raw data for fly ash lxxiii
D.2 Raw data for fly ash lxxiv
D.2 Raw data for fly ash lxxv
D.2 Raw data for fly ash lxxvi
D.3 Raw data for volcanic ash lxxvii
D.3 Raw data for volcanic ash lxxviii
D.3 Raw data for volcanic ash lxxix
D.3 Raw data for volcanic ash lxxx
D.3 Raw data for volcanic ash lxxxi
D.3 Raw data for volcanic ash lxxxii
D.3 Raw data for volcanic ash lxxxiii

D.3 Raw data for volcanic ash lxxxiv

F.1 Extra-terrestrial Candidates cliii

F.2 SEM Conditions for Picked Particles Analysis cliv

I.1 Peridot Preliminary Analysis Data clxix

I.1 Peridot Preliminary Analysis Data clxx

I.1 Peridot Preliminary Analysis Data clxxi

I.1 Peridot Preliminary Analysis Data clxxii

J.3 Foil Rig Setups clxxvi

List of Figures

1.1 Poyniting Robertson effect 3

1.2 Location of Antarctic MM collections 18

1.3 SPWW Schematic 19

1.4 LDEF's orbit 27

1.5 Kinetically altered particles 33

2.1 Three lens SEM column 38

2.2 Backscatter electrons vs secondary electrons 41

2.3 Production of EDX X-ray 42

2.4 Spherical aberration 43

2.5 SEM interaction volume 45

2.6 Optical lenses 47

2.7 Depth of focus of lenses 48

2.8 Kent LGG layout 51

2.9 Burst disc examples 53

2.10 Breech block diagram 54

2.11 Blast tank flight paths 54

2.12 Kent LGG target chamber 55

2.13 Rayleigh and Raman scattering 57

2.14 FIB processing images 59

2.15 FIB attachment images 60

3.1 Kwajalein micrometeorite collector 64
3.2 Kwajalein and BAS collection filter assembly 67
3.3 Filter washing set up 69
3.4 Filter attached to SEM stub 69
3.5 Whole filter map 74
3.6 Picked micrometeorites on double-sided tape 75
3.7 Irregularly shaped particles from the Kwajalein atoll 80
3.8 Volcanic ash spherule from the Kwajalein atoll 85
3.9 Iron-titanium spherule from the Kwajalein atoll 86
3.10 Kwajalein FeCr sphere contaminate sphere 87
3.11 Area of high abundance of FeCr spheres 88
3.12 Irregularly shaped particles from the BAS micrometeorite collection . . . 89
3.12 Irregularly shaped particles from the BAS micrometeorite collection . . . 90
3.13 Example contaminant spheres from BAS collections 93

4.1 Abundances of Ca Mg and Al in micrometeorites 97
4.2 102
4.3 Comparison of Al, Ca and Mg oxide abundances in micrometeorites with bulk chondritic compositions 102
4.4 MgO,CaO and Al(2) O(3) ratios of each chondrite components 103
4.5 Terrestrial debris and CAI compositions 104
4.6 Mineral compositions of chondrites 105
4.7 Bulk achondrite Al-Mg-Ca ratios 111
4.8 Bulk achondrite Al-Mg-Ca ratios 112
4.9 Al Fe and Mg abundances in micrometeorites and fly ash 113
4.10 Composition of various volcanic ash particles 114
4.11 MgO,Al(2) O(3) and CaO ternary of volcanic ash vs micrometeorites . . 115
4.12 Compositional zones of micrometeorites and terrestrial debris 116

5.1 Flux of particles 120

5.2 Elemental ratios of micrometeorite candidates vs other micrometeorites, fly ash and volcanic ash 122

5.3 Terrestrial debris and CAI compositions 124

5.3 Terrestrial debris and CAI compositions 125

5.3 Terrestrial debris and CAI compositions 126

5.4 Elemental ratios of spheres from the Kwajalein atoll collection and chondritic components 127

5.4 Elemental ratios of spheres from the Kwajalein atoll collection and chondritic components 128

5.4 Elemental ratios of spheres from the Kwajalein atoll collection and chondritic components 129

5.5 Candidate micrometeorites versus achondrites subtypes 130

5.5 Candidate micrometeorite versus achondrites subtypes 131

5.5 Candidate micrometeorite versus achondrites subtypes 132

5.6 Candidate 8-4-2 133

5.7 Comparison of spectra from the two areas of candidate 8-4-2 134

5.8 Sphere 8-4-2 composition plot 135

5.9 Candidate 9-9-7 136

5.10 Comparison of dendritic crystal compositions with the matrix of candidate 9-9-7 136

5.11 Candidate 9-9-7 composition plot 137

5.12 Candidate 11-5-29 138

5.13 Candidate 11-5-29 composition plot 139

5.14 Candidate 11-8-16 140

5.15 Candidate 11-8-16 following second polishing 141

5.16 Candidate 11-8-16 composition plot 141

5.17 Candidate 11-9-40 142

5.18 Candidate 11-9-40 composition plot 143

5.19 Candidate 12-1-56 144
5.20 Spectra of different regions of sphere 12-1-56 145
5.21 Candidate 12-1-56 composition plot 146
5.22 Candidate 12-2-10 147
5.23 Candidate 10-2-10 region comparison 148
5.24 Candidate 12-2-10 composition plot 148
5.25 Candidate 12-7-25 149
5.26 Candidate 12-7-25 composition plot 150
5.27 Candidate 12-8-24 151
5.28 Candidate 12-8-24 composition plot 152
5.29 Effective collection radius for the Kwajalein collector 154

6.1 Capture mechanism cartridge 163
6.2 EVT design and prototype 165
6.3 EVT intial pressure test result 166
6.4 EVT test shot light flash 169
6.5 EVT test shot projectile capture 169
6.6 Gem facet diagram 170
6.7 Peridot initial inclusion and fractures 172
6.8 Peridot gemstone used projectile in atmospheric alteration simulations . 173
6.9 Pre shooting EDX spectra of the peridot gemstones 174
6.10 Peridot Raman spectrum compared to standard 175
6.11 Olivine projectile seated in the sabot 176
6.12 Shot 1 chamber impact 178
6.13 Shot 2 olivine capture 179
6.14 Setup for Mylar foil tests 180
6.15 Setup for Mylar foil tests 181
6.16 Foils from shot 4 and 5 182

6.17 Cracks in the EVT following ethanol wash 184

7.1 Calculated mass loss from atmospheric flight 190
7.2 Impact speed of the projectile vs its launch speed 191
7.3 Atmospheric heating in the environment tube 193
7.4 Projectile a and b plots 198
7.5 Impact pressure for firing velocities 199
7.6 Change in temperature of the olivine projectile during impact 200
7.7 Change in temperature of the aerogel block during impact 201

8.1 Pressure and velocity conditions to heat olivine to 2000 °C 204
8.2 Design of breech block changes following preliminary testing 205
8.3 Buckshot and 3mm peridot 209
8.4 Foil setup for use to test the buck shot method (Shot 8b) 209
8.5 Shot 10b results 211
8.6 ToF trace showing buckshot and olivine projectile 212
8.7 Postshot BSE Peridot Images 215
8.8 Preshot polishing marks on the surface of the peridots 217
8.9 Post-shot polishing marks changes on the surface of the peridots 219
8.10 Before and after shooting composition trend 221
8.11 Before and after shooting composition changes 222
8.12 Raman spectra prior to shooting 223
8.13 Example line-scan data acquisition area 225
8.14 Example line-scan data fit 225
8.15 Steepness graph for Mg, Si,and Fe line-scan data 226
8.16 Map and image of iron beads contained inside of peridot 21 228
8.17 TEM Image of peridot 21 post-shot 230

E.1 Titanium Oxide Ternary Graphs cxxix

E.2 Ternary Diagrams showing FA Composition cxxx
E.2 Ternary Diagrams showing FA Composition cxxxi
E.3 Ternary Diagrams showing VA Composition cxxxii
E.3 Ternary Diagrams showing VA Composition cxxxiii
E.4 Ternary Diagrams showing chondrite Composition cxxxiv
E.4 Ternary Diagrams showing chondrite Composition cxxxv
E.5 Ternary Diagrams showing chondritic component composition cxxxvi
E.5 Ternary Diagrams showing chondritic component composition cxxxvii
E.6 Ternary Diagrams showing chondritic component composition cxxxviii
E.6 Ternary Diagrams showing chondritic component composition cxxxix
E.7 Ternary Diagrams showing chondritic component composition cxl
E.7 Ternary Diagrams showing chondritic component composition cxli
E.8 Ternary Diagrams showing Micrometeorite composition Versus Volcanic Ash Composition cxlii
E.8 Ternary Diagrams showing Micrometeorite composition Versus Volcanic Ash Composition cxliii
E.9 Terrestrial debris and CAI Compositions cxlv
E.9 Terrestrial debris and CAI Compositions cxlvi
E.10 Terrestrial debris, MMs and chondrite point spectra mineral data cxlvii
E.11 Terrestrial debris, MMs and chondrite point spectra mineral data cxlviii
E.12 Terrestrial debris, MMs and chondrite point spectra mineral data cl
E.13 Candidate MMs vs achondrite subtypes cli
E.14 Candidate MMs vs achondrite subtypes clii

G.1 Kwajalein Collector Casing clvi
G.2 Schematics of other plates used in the EVT clvii
G.3 Schematics of the breech block clviii
G.4 Schematics of the breech block cover plate clix

G.5 Schematics of the entry aperture central plate clx

G.6 Second Breech Block clxi

Acronyms

AMM Antarctic Micrometeorites
AOAS Amoeboid Olivine Aggregates
BAS British Antarctic Survey
BSE Backscatter Electrons
CAIS Calcium Aluminium Inclusions
CAT Calcium, Aluminium, Titanium Rich
CCD Charged Coupled Device
CGMMS Coarse-Grained Micrometeorites
CPIPDS Chondritic Porous Interplantary Dust Particles
CS Cosmic Spherules
DOF Depth-of-Field
DSS Deep Sea Spherule
EDX Energy Dispersive X-ray
EH 'High Iron Enstatite Chondrite'
EL 'Low Iron Enstatite Chondrite'
EM Electro-Magnetic
ET Extra-terrestrial
EVT Environment Tube
FA Fly Ash
FGMMS Fine-grained Micrometeorites
FIB Focused Ion Beam
GEMS Glass With Embedded Metal And Sulfides
H 'High Iron Content'
HED Howardite, Eucrite, Diogenite
HPLC High Performance Liquid Chromatography
IDPS Interplanetary Dust Particles
K Kakangari
L 'Low Iron Iron Content'
LDEF Long Duration Exposure Facility
LEO Low Earth Orbit
LGG Light Gas Gun
LL 'Very Low Iron Content'
MFP Mean Free Path
MM Micrometeorites
NEE Near Earth Environment
OC Ordinary Chondrite
PCTE Poly Carbonate Track Etched
PETE Polyethylene Terephthalate
PVDF Polyvinylidene Difluroride
R Rumurti
SCMM Scoriaceous Micrometeorite
SE Secondary Electrons
SEM Scanning Electron Microscope
SNC Shergottite, Nakhlite, Chassignite
SPWW South Pole Water Well
STST Stainless Steel
TEM Transmission Electron Microscope
TOF Time Of Flight
TOF Time-of-Flight
UCMMS Ultra Carbonaceous Micrometeorties
UMMS Unmelted Micrometeorites
US-SMDC United States Space And Missile Defence Command
VA Volcanic Ash

VP Varible Pressure

Part I

Introduction and Methods

Chapter 1
Introduction

1.1 What are Micrometeorites?

Each year the Earth is bombarded by billions of particles of dust and debris *(Love and Brownlee 1993).* Some of these particles are man-made (e.g. debris from satellites and rocket exhaust). These predominately exist in the near-Earth environment, being limited to areas where human space flight has occurred. Others however, originate from within our solar system, from comets and asteroids, planets and moons *(Messenger 2002).* These Extra-terrestrial (ET) particles are referred to as Micrometeoroids and Interplanetary dust particles (IDPs) whilst travelling through space and the Earth's atmosphere, and Micrometeorites (MM) upon reaching the Earth's surface.

Whilst MMs contain less mass than their larger meteorite cousins, they are far more common with 40,000 $\pm$ 20,000 tonnes arriving at the Earth each year *(Love and Brownlee 1993)* and are thought to be the predominate method of transport of extra-terrestrial material to the Earth *(Zolensky, Pieters, et al. 2000).* Upon reaching the Earth these small bodies pass through the atmosphere and are subjected to extreme heating, causing a number of changes including loss of volatiles and changes in morphology*(Greshake, KLöCK, et al. 1998).* Due to their small size and low mass, the heating experienced by these bodies occurs at a much higher altitude and for a reduced period when compared with larger bodies, resulting in an increased chance of survival *(Love and Brownlee 1991).* Depending on the entry trajectory and velocity of the particles, it is therefore possible for small amounts of the incoming particles to pass through the atmosphere along entry corridors which results in little or no melting *(Flynn 1989; Messenger 2002).*

Micrometeorites are thought to mainly originate from asteroidal parent bodies as a result of collisions *(Genge, Grady, and Hutchison 1997).* However modelling work

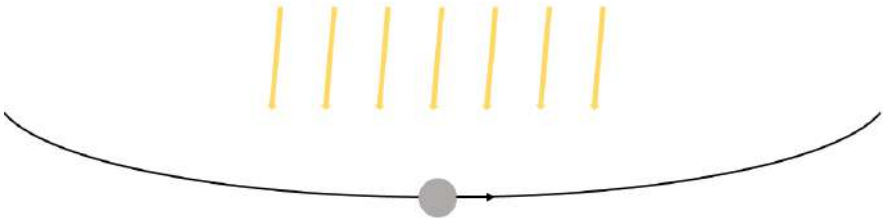


Figure 1.1: Showing the Poynting-Robertson effect as viewed with the stationary frame positioned with the particle. The particle is moving right with respect to the star, as such from the particle reference frame the photons from the star have an x component, which acts to slow the particle down.

suggests that in Low Earth Orbit (LEO) most particles are cometary, given off as the comet heats up and melts during its approach into the inner solar system *(Carrillo-Sánchez, Nesvorný, et al. 2016)*. Recent work has shown that it is likely that most cometary and asteroid dust reach the earth with a similar geocentric velocity *(Carrillo-Sánchez, Plane, et al. 2015)*. Transport of the interplanetary dust grains from the asteroidal or comet parent body is commonly accomplished via the Poynting-Robertson effect; radiation pressure from the Sun slows the particle down in its orbit, allowing the particle to fall in towards the Sun (see Figure 1.1). In this way particles from bodies in Copernican, circular orbits that don't intersect the Earth's orbit can still pass through the Earth's orbit and be caught in the Earth's gravitational well. In the case of some cometary dust, it is possible that its orbit is already overlapping the orbit of the Earth. It is unlikely that many cometary grains will survive atmospheric entry due to their high entry angle. The high entry angles of most cometary dust grains arise from the orbital trajectory of their parent body. Some grains however will reach the Earth's surface, passing safely through the atmosphere either due to the orbital path of their parent, or later perturbations putting them into a safe entry corridor *(Messenger 2002)*. MMs are likely created during collisions between bodies in the asteroid belt, in an impact which has sufficient energy to disrupt the surface, fragment the parent body and release the dust particles from the gravity well of their parent *(Genge, Grady, and Hutchison 1997)*.

MMs provide us with a method to investigate the processes that have occurred on their parent bodies without the need for space missions. Like meteorites, they provide a much larger sample set, both in terms of mass and number of bodies that can be studied. MMs are thought to come from a wider range of locations than larger meteorites as evidenced by the wider range of characteristics that do not fit with current meteorite classifications (e.g. ultra carbonaceous MMs from *Duprat, Dobrică, et al. 2010*) and as such can provide additional complementary information to that which can be found

during the study of meteorites. As it is likely that some MM progenitors are comets (e.g. ultra carbonaceous and chondritic porous MMs *(Duprat, Dobrică, et al. 2010; Noguchi et al. 2015)*), whilst other are likely to asteroidal in origin *(Genge, Gileski, and Grady 2005)*. The composition of MMs can give insight into both the inner (primitive asteroids) and outer (comets) early solar system's composition and processes. These factors combine to make MMs an important source of information for processes which have occurred, and are occurring in our solar system.

MMs also have an economic impact: due to their high relative velocities, these particles pose a significant threat to both spacecraft in the near Earth environment and those operating further away (e.g ESA's Olympus Satellite suffered life-ending damage from small dust impacts *(Caswell, McBride, and Taylor 1995)*). Understanding how many of these particles a spacecraft is likely to encounter, at what relative velocities, and the trajectories the particles will be travelling, will allow for future craft to have shielding better designed for such challenges. This will ultimately cut down cost by increasing the lifetime of the craft.

1.2 The Classification of Micrometeorites

Early attempts to categorise MMs such as those by *Brownlee, Olszewski, and Wheelock 1982* divided them into two main groups according to their bulk chemistry: chondritic and non-chondritic. These two groups were further subdivided according to their dominant mineralogy and/or particle structure (e.g. shape, porosity etc) into the chondritic porous, chondritic filled, chondritic smooth or metal mound silicates for the chondritic MMs and iron-sulphur-nickel, iron-nickel, mafic, carbonate, phosphate or Ca-Al silicates for the non-chondritic MMs. However the number and condition of MMs available for these early studies were limited; the study focused on 1200 highly weathered spheres which were from deep sea sediments collected via magnetic separation *(Brownlee, Pilachowski, and Hodge 1979)* as opposed to the 5700 non-magnetically separated, mostly unweathered, spheres examined more recently by *Taylor, Alexander, and Wengert 2008*. This means that the samples were biased towards less porous metallic particles (see Section 2). Improvements in collection methods have enabled more complete collections which are less biased by terrestrial environments, resulting in changes to these original classification schemes. As a result, the most widely used classification scheme is currently that of *Genge, Engrand, et al. 2008*. This incorporates work done on IDPs collected from the stratosphere, as well as MMs collected from a variety of surfaces on the Earth. This classification system will be used for the remainder of this

thesis.

Genge, Engrand, et al. 2008 proposed that the primary classes of MMs are divided into three groups based on the degree of alteration experienced during atmospheric entry. Those that experience little to no heating are known as the unmelted MMs, and although they often exhibit melt rims, they remain unaltered inside. Those that experience complete melting during entry form spherules and are referred to as melted MMs or Cosmic Spherules (CS) *(Talyor, Matrajt, and Guan 2012).* In between these two classes are the Scoriaceous Micrometeorite (ScMM) which have experienced heavy melting similar to CSs, but contain relict grains representing surviving mineralogy *(Genge, Engrand, et al. 2008; Greshake, KLöCK, et al. 1998).* MMs exhibit a wide range of properties depending upon both the degree of heating experienced and their precursor mineralogy, resulting in the definition of several subtypes *(Talyor, Matrajt, and Guan 2012).* These primary classes of MMs are further explored below.

1.2.1 Melted Micrometeorites

Melted MMs, or cosmic spheres (CSs), were the first type of micrometeorite to be identified on Earth in deep sea sediments *(Murray and Renard 1891).* This was partly due to their characteristic spherical shape making them easy to separate out from the angular terrestrial matter that was also collected. It is this ease to separate that may be responsible for the propensity of melted MMs amongst those particles being identified and studied to date. Unfortunately most CSs retain little information about their parent bodies composition and evolution, due to the alteration of much of their original mineralogy and petrology following the significant heating, experienced during atmospheric entry *(Greshake, KLöCK, et al. 1998; Genge 2006).* However, work carried out in the Antarctic suggests that Fe/Mn and Fe/Mg ratios can be used to identify possible origins (e.g. see) *Taylor, Herzog, and Delaney 2007, Ginneken, Gattacceca, et al. 2017.*

It is possible to further sub categorise CSs according to their structure into stony (S-type), magnetite within silicate glass (G-type), and Iron (I-type) *(Genge, Engrand, et al. 2008).* The S type CSs can further be subdivided into six additional subtypes: CAT (containing Ca,Ti and Al), glass (mostly composed of glass), cryptocrystalline (containing large quantities of sub-micron crystals), barred olivine (dominated by barred olivine), porphyritic olivine (dominated by equant and skeletal olivine) and coarse-grained spheres (containing large relict grains) *(Genge, Engrand, et al. 2008).* These

subtypes are explained in detail in the following section.

1.2.1.1 S-Type Spherules

S-type spherules are amongst the most abundant spherules, accounting for ≈ 97% of the micrometeorite flux based on studies of the South Pole Water Well (SPWW) collections *(Taylor, Lever, and Harvey 2000).* S-type spherules are categorised by their high Si content, with roughly chondritic compositions. The S-type subcategories are thought to reflect the peak temperature reached by the particles as they pass through the atmosphere *(Taylor and Brownlee 1991),* however, recent work has also suggested that these subtypes are also likely linked to the original chemistry, and morphology, of the parent body *(Ginneken, Gattacceca, et al. 2017).*

CAT: Accounting for 1% of the total CS ET flux reaching Earth, Calcium, Aluminium, Titanium rich (CAT) spherules are those S-type spherules which have experienced the highest peak temperatures during atmospheric entry *(Taylor, Lever, and Harvey 2000; Genge, Engrand, et al. 2008).* Temperatures in the range 1800-2200^oC are estimated to be required for the observed enrichment in refractory elements, and the loss of volatiles. Consequently CAT spherules have higher abundances of refractory Ca, Al and Ti than would be expected in a chondritic body *(Brownlee, Bates, and Beauchamp 1983).* CAT spherules suffer high degradation and weathering once in terrestrial environments, more than is experienced by other CS types *(Taylor, Lever, and Harvey 2000).*

Glassy Spherules: Glassy spherules at the SPWW made up 17% of the recovered ET particles *(Taylor, Lever, and Harvey 2000).* They are formed under the next highest peak temperatures, yet show far more uniformity in composition and morphology and have lost greater amounts of volatiles during atmospheric passage than are observed in CAT spherules. Glassy spgherules are likely produced by the complete melting of grains during atmospheric entry, followed by a subsquent rapid cooling. Due to the higher temperatures need to melt all nuclei within the parent grain, glassy spheres are thought to be formed from amongst the largest originators *(Ginneken, Gattacceca, et al. 2017).* While generally highly uniform, glassy spherules containing vesicles and Fe-Ni grains have been identified *(Genge, Engrand, et al. 2008).* Glassy spherules appear to have a maximum entry size with few particles being recovered exceeding 400 µm, suggesting particles exceeding this size fragment during entry *(Prasad, Rudraswami, and Panda 2013).* Glassy spherules are significantly less prone to weathering when compared to CAT spherules and are amongst the hardiest of the S-type spherules *(Prasad,*

Rudraswami, and Panda 2013).

Cryptocrystalline: Cryptocrystalline spherules are identifiable by their characteristic sub-micron crystallites. The crystals are often olivine or pyroxene, however cryptocrystalline spherules may also contain large amounts of magnetite *(Genge, Engrand, et al. 2008).* These spherules have experienced melting but have retained a nucleus from which these crystallites could form. Cryptocrystalline spherules therefore have experienced lower entry temperatures than glassy or CAT spherules.

Barred Olivine: Barred-olivine spherules are, contrary to their name, often ovoid. The olivine crystals they contain grow in parallel to each other along the ovoids minor axis and are substantially longer than those within cryptocrystalline spherules *(Genge, Engrand, et al. 2008).* The increased crystal lengths imply that barred-olivine spherules are heated for longer and yet are formed at a lower temperature than cryptocrystalline spherules, however at a higher temperature than the porphyritic spherules described below *(Taylor, Lever, and Harvey 2000).* Barred-olivine spherules occasionally contain Fe-Ni metal beads which are thought to have 'solidified' out of the silicate melt as the particle is heated *(Genge, Engrand, et al. 2008).* Recent work has shown links between many barred olivine CSs and the matrices of carbonaceous chondrites *(Ginneken, Gattacceca, et al. 2017).*

Porphyritic: Porphyritic spherules show a wide range of textures, crystals and compositions. Porphyritic particles retain large amounts of their interior structure and as such are thought to be the least heated of the S-type spheres *(Genge, Engrand, et al. 2008).* Due to the limited heating and low temperatures reached, the crystals they contain are the most structured of those in any melted sphere, varying greatly in size, and making these spherules a likely source of relict grains *(Taylor, Lever, and Harvey 2000).* Both of these features indicate a lengthened heating period (at a slower rate) and cooling times and, as such, porphyritic spheres bridge the gap between S-type spheres and those which have undergone partial melting such as scoriaceous particles.

Coarse-Grained Coarse-grained spherules are those particles which can clearly be seen to result from the melting of coarse-grained precursors *(Genge, Engrand, et al. 2008).* Coarse-grained spherules contain the most relict grains and as such do not display a bulk chondritic composition like the other S-type spheres.

1.2.1.2 G-Type Spherules

G-type spherules 'fill the gap' between silicon dominated S-type spherules, and iron dominated I-type spherules. G-type spherules tend to exhibit magnetite dendrites contained within interstitial silicate glass. They often exhibit a wide range of compositions and morphologies; they may contain metal beads, relict grains and voids*(Genge, Engrand, et al. 2008).* Based on SPWW collections G-type spherules are believed to account for $< 1\%$ of CSs, the least of any CS type to the overall ET flux budget *(Taylor, Lever, and Harvey 2000).*

1.2.1.3 I-Type Spherules

I-type spherules are some of the earliest types of MMs discovered *(Murray and Renard 1891).* Due to their high iron and nickel content they are highly magnetic and hence are easily separated out from the most terrestrial contaminates, which are predominately non-magnetic. I-type spherules often dominate collections whose spherules have undergone high levels of weathering, such as deep sea sediment collections and collections from salt deposits or rocks (see sections 1.3.2.4). In collections believed to exhibit low levels of weathering (e.g. SPWW) I-type spherules make up only $\approx 2\%$ of the total CS flux *(Taylor, Lever, and Harvey 2000).* This discrepancy in I-type flux is likely due to the weathering and loss of the generally more abundant, less resistant S-types.

1.2.2 Scoriaceous Micrometeorites

Scoriaceous Micrometeorite (ScMM) experience less heating than CSs *(Genge, Engrand, et al. 2008),* and, as such, still contain grains which bear some resemblance to the precursor micrometeoroid *(Genge, Grady, and Hutchison 1997).* These particles are often vesicular in nature, contain relict grains and, due to the lesser amount of atmospheric heating experienced, may retain some of their previous shape. It should be noted, that as mentioned above, relict grains and vesicles can occur in CSs along with vesicles in unmelted MMs and therefore these cannot be used to solely identify ScMMs *(Genge, Engrand, et al. 2008).* A major difference between CSs and ScMMs is the presence of magnetite rims on the ScMMs *(Toppani et al. 2001).* Due to the small population of examples available for study and the wide ranging attributes of the ScMMs group, unlike CSs and the unmelted MMs (UMMs) discussed in section 1.2.3, they are unable to be accurately broken into smaller subsections for easier categorisation. Due to the loss of large crystals during passage through the atmosphere, the mineralogy of ScMMs is dominated by the occurrence of glasses, quenched olivines and pyroxenes with few

larger remaining features *(Kurat et al. 1994).*

1.2.3 Unmelted Micrometeorites

Unmelted Micrometeorites (UMMs) experience the least heating, their shape is highly irregular and chemically they are the most primitive of all the MMs *(Genge, Engrand, et al. 2008).* Similar to CSs the UMMs can be further divided into several subtypes: fine-grained (FgMMs), coarse-grained (CgMMs), refractory (RMMs), ultra-carbonaceous (UcAMMs) and chondritic porous (CpMMs) *(Genge, Engrand, et al. 2008; Genge, Gileski, and Grady 2005; Noguchi et al. 2015).*

1.2.3.1 Fine-Grained Micrometeorites

Fine-grained Micrometeorites (FgMMs) range from chemically homogeneous type C1 which, rarely, incorporate large anhydrous silicates, through to the chemically heterogeneous type C3 which are often highly porous and contain multiple anhydrous silicate particles within *(Genge and Grady 2002).* C3 FgMMs can also resemble ScMMs as they can also include an igneous rim formed via surface melting during atmospheric entry *(Genge, Engrand, et al. 2008; Toppani et al. 2001).* Roughly 28% of FgMMs have an igneous rim *(Genge 2006).* The compositions of the igneous rims which form suggest that they originated directly from the melting of the fine grained matrix *(Genge 2006).* FgMMs are also similar in composition to that of the matrix of CM2 and CR2 meteorites, which are thought to sample asteroids *(Genge, Gileski, and Grady 2005),* however it has also been argued that FgMMs are in fact fragments of cometary bodies *(Klöck and Stadermann 1994).* CU3 FgMMs therefore potentially provide a unique insight in the processes and composition of comets. Unfortunately due to a back freeze in the South Pole water well, where the water in the system refroze following a system failure, it is believed that most FgMMs in this location, would have been destroyed *(Taylor, Lever, and Harvey 2000).* This failure removes one of the more unbiased and largest collection methods from providing information about this MM type.

1.2.3.2 Coarse-Grained Micrometeorites

The chemical composition and petrographic descriptions of Coarse-Grained Micrometeorites (CgMMs) varies greatly and, as such, it is standard for CgMMs to be split into several subtypes according to their dominate mineralogy: porphyritic olivine/pyroxene, granular olivine/pyroxene, barred olivine, radiate pyroxene, type 1 (containing fayalite (Fa) and/or fosterite (Fs) $< 10 mol\%$) and type 2 (containing Fa and or Fs $> 10 mol\%$)

(Genge, Engrand, et al. 2008). CgMMs are similar in composition to type 1(b) and 2(ab) chondrules in composition and structure, however, it should be noted that there is a lack of barred olivine when compared with said chondrules *(Taylor, Lever, and Harvey 1998; Genge, Gileski, and Grady 2005).* As with FgMMs, CgMMs can also show an igneous rim, however these are rare *(Genge 2006).* Where identified, these rims also show a similar composition to those formed on the FgMMs which suggests they may be composite MMs made of both Fg and Cg components *(Genge 2006).* CgMMs are inherently more durable than FgMMs and are more likely to survive weathering whilst exposed to the Earth's environment *(Taylor, Lever, and Harvey 2000).* Their greater survivability gives rise to a bias in amounts found when compared with FgMMs which must be taken in account when determining flux rates.

1.2.3.3 Refractory Micrometeorites

Refractory MMs are dominated by refractory minerals and can be further subdivided into porous, compact and hydrated types *(Genge, Engrand, et al. 2008).* However, only three have been found so far, one for each type (*Greshake, Bischoff, and Hoppe 1996, Engrand, Maurette, et al. 1995, Genge, Engrand, et al. 2008*). One of the particles, KWP3F5, contained melted silicates which is indicative of high levels of atmospheric heating, however, this is not the case for all refractory MMs as a similar particle contained abundances of presolar silicates suggesting little to no heating during its passage through the atmosphere *(Genge, Engrand, et al. 2008; Taylor, Lever, and Govoni 2001).*

1.2.3.4 UltraCarbonaceous Micrometeorites

Ultra Carbonaceous Micrometeorties (UcMMs) contain unusually high quantities of carbon (>50%). The carbon content within the UcAMMs is greater than that of the Chondritic Porous Interplantary Dust Particles (CpIPDs) which are thought to sample comets *(Duprat, Engrand, et al. 2007; Dobrica. et al. 2009).* The chemical composition of the UcMMs is also similar to that of comets and as such many of the UcMMs are thought to be cometary in origin (based on Stardust analyses) *(Duprat, Engrand, et al. 2007; Dobrica. et al. 2009).*

1.2.3.5 Chondritic Porous Micrometeorites

Chondritic Porous Interplantary Dust Particles (CpIPDs), contain Glass with Embedded Metal and Sulfides (GEMS) and enstatite whiskers structures thought to be indicative of vapour phase condensation in the pre-solar molecular cloud, and therefore

consistent with current ideas of a primitive cometary origin *(Noguchi et al. 2015)*. They share a similar composition to those particles recovered from comet 81P/Wild *(Noguchi et al. 2015)*. At the point of writing, 40 such particles have been found in Antarctic snows and ices.

1.3 Micrometeorite Collection Methods

1.3.1 Introduction:

MMs are currently identified in a number of ways: firstly CS's can be identified by their characteristic shape, which is unlike most naturally occurring terrestrial dust (spherical vs angular terrestrial dust). Secondly, identifying grains which have bulk chondritic compositions which can be used to separate them out from terrestrial debris. However it is unlikely that all ET spherules will have bulk chondritic compositions, with some possibly being achondritic or being made of chondritic fragments such as Calcium Aluminium inclusions (CAIs) (e.g. basaltic CSs recovered from the SPWW *(Taylor, Herzog, and Delaney 2007)*). Unequilibrated compositions are also a good indicator of extra-terrestrial origin as most terrestrial material has been processed and thus equilibrated. Finally isotope analysis can be used to isolate those particles which have not been present on the Earth's surface via changes in isotope ratios. All of these methods however are time consuming and, due to the high number of terrestrial dust grains, it is not possible to analyse every grain, as such collections take place in areas of low background dust or employ separation methods to reduce the number of particles requiring analysis.

Separating ET dust from background anthropogenic and natural terrestrial dust is a significant challenge in MM collections. Much of the anthropogenic dust is generated by combustion (mostly in power generation and incineration plants). Whilst, in most power plants a large percentage of this is captured inside of the stacks via electrostatic collectors, it has been estimated that 0.2% of the fly ash produced is still released *(Goodarzi 2006)*. As 600,000,000 tonnes of fly ash was estimated to have been produced worldwide in 2010, a minimum of 1,200,000 tonnes of ash was released into the Earth's atmosphere*(Ahmaruzzaman 2010)*. Additionally, not all plants are fitted with these collectors for the removal of fly ash from the stack with some emitting more than 6 000 000 tonnes yr^{-1} of ash per year into the environment *(Blaha et al. 2008)*. It is clear that in such cases, the total extra-terrestrial flux of particles is completely dominated by a single plant; making identifying any ET particles in their vicinity unfeasible. In

addition to fly ash, human activity such as mining and welding account for a significant further production of terrestrial dust. This has led to many collection attempts being performed away from areas of high human habitation.

In addition to separation problems due to their compositions, MMs are often highly susceptible to terrestrial weathering, either through the leeching of elements or the destruction of fragile components via mechanical or thermal mechanisms. Reducing the amount of time a particle is in contact with the Earth's environment is therefore an important consideration in their collection.

Over the years a number of different techniques to collect MMs have been developed including: collections from sediments at the bottom of the oceans (so called Deep Sea Spherule (DSS) collections) *(Brownlee, Bates, and Schramm 1997),* collections from Antarctic locations e.g. melt water from the South Pole Water Well (SPWW) *(Taylor, Lever, and Harvey 1998),* collections from the frontier mountains *(Rochette et al. 2008)* and Greenland's snow and ices *(Taylor, Lever, and Harvey 2000),* and collections from within salt deposits and within rocks such as limestone and chalk *(Davidson et al. 2007; Suttle and Genge 2017).* Additionally, extra-terrestrial collections have been performed directly from the atmosphere by stratospheric flights *(Brownlee, Bates, and Schramm 1997),* and even collections from low Earth orbit from platforms such as the long duration exposure facility (LDEF) *(Love and Brownlee 1993).* These collections can be broadly broken into Antarctic and non-Antarctic collections, and each method has advantages and disadvantages based on the differing levels of weathering, collection and exposure times and levels of contamination *(Taylor, Lever, and Harvey 1998).* These aspects will be discussed in detail in the following section.

1.3.2 Non-Antarctic Collections

1.3.2.1 Deep Sea Sediment Collections

The earliest successful collection of MMs was performed in 1891 where they were contained amongst the collection of sediments taken from the deep sea bed *(Murray and Renard 1891).* Since then such Deep Sea Spherule (DSS) collections have been performed by a number of authors yielding several notable collections (e.g. *Brownlee, Pilachowski, and Hodge 1979; T Jan 1983; Peng and Lui 1989*).

In order to collect the particles from the sea bed, a magnetic rake is dragged across the sea floor, gathering up the magnetic particles *(Brownlee, Pilachowski, and Hodge 1979; Suavet, Gattacceca, et al. 2009).* As many MMs are magnetic, whilst most terrestrial particle are not, MMs are preferentially collected by the rake. Once the designated area has been raked, the device is removed from the water and the particles are removed from the rake. The particles can then be subdivided and examined. This method however results in the collection of only those particles which are magnetic and due to the ease of identification, most authors have focussed on spherules. DSS are also able to be hand picked from collected sediment, however at a much slower rate and with a smaller area coverage (e.g. see *Prasad 2013*)

Deep Sea Spherule collections produce some of the oldest (earliest settled) MMs collected, with average ages greater than 10,000 yrs, with only those particles collected from rocks and salts being older ($>$ 1 GYr,*(Maurette, Hammer, Brownlee, et al. 1986)*). Due to the age and size of the oceans, deep sea sediment has possibly the largest accumulation of particles due to its greater exposure time and area.

One of the major draw backs of the deep sea collection method is the requirement for the particles to be ferromagnetic in order to be picked up by the magnetic rake in large quantities. This limits the number of collectable spheres, with those collected forming two groups, containing either iron or manganese *(Millard and Finkelman 1970).* Consequently it is incapable of calculating the total flux of extra-terrestrial particles, as some of the spheres (e.g. CAT , glassy etc) simply cannot be collected.

An additional issue with DSS collections is that many of the falling particles do not survive due to being exposed to extreme conditions for long period of time (e.g. salty, alkaline water, high pressures and variable temperatures) and cannot be examined. As such, as well as the bias for magnetic material, DSS collections are also affected by terrestrial weathering, with many of the surviving spheres exhibiting evidence of weathering (e.g. the preferential leeching of the glasses from the particles in the collections) *(Taylor, Lever, and Harvey 2000).* Similarly the collections show a preferential loss of small stony particles *(Maurette, Hammer, Brownlee, et al. 1986),* however, the mechanism for this process is less clear.

The heavily biased nature of the collections reduces the accuracy of any generalisable comments based solely upon the results of the DSS samples. The loss of non magnetic spherule types and the preferential etching of glass and ultimate destruction of glassy

particles means that for DSS collections, the total number of particles and the ratios of the types of particles are not representative.

1.3.2.2 Greenland Lake Collections

The melt water of Greenland's seasonal lakes provides another location for the collection of MMs. These are formed in the summer months by melting glaciers which releases samples of MMs and other sediment that have collected on their surface during the winter months. The sediment sinks to the bottom of the lake forming bacteria rich, cryoconite. At the end of the summer the lakes refreeze and the process repeats. *Maurette, Hammer, Harvey, et al. 1994* sampled the cryoconite during the summer months and discovered the presence of MMs. The collection made use of pumps to 'vacuum up' cryoconite from the lake beds, allowing for particles of sizes greater than 50 µm to be collected and examined. Due to the method of collection from the melt water, any particle smaller than 50 µm could not be sampled, due to difficulty in separating it from other debris.

As the method for the creation of the cyroconite is periodic, based on the life cycle of the bacteria, it is possible to calculate the maximum ages of the particles in the lakes, yielding theoretical maximum accumulation age of the site, of around 50,000 years *(Maurette, Hammer, Harvey, et al. 1994),* however, unlike other collections, the samples are not representative of a continuous flux, instead, particles melt out of the ice in which they have been entombed. This should suggest that more MMs could be found in the Greenland lakes than the South Pole Water Well (SPWW) (see section 1.3.3.1), purely due to the increased surface area collected from. The age of the lake makes the likelihood of rare particles appearing in the collections substantially higher. Unfortunately, the long exposure time also makes identifying the age of the particles difficult, thus hindering calculations of flux for these rare particles.

The constant thawing and refreezing of the lakes in which the MMs are encased also biases the collection towards more mechanically risistant particles; more delicate MMs are destroyed by the freeze-thaw process *(Maurette, Hammer, Harvey, et al. 1994).* The collection shows a marked depletion in the number of iron rich particles when compared to other collections, specifically the DSS collections. The most likely cause of which is the loss of denser particles from the sampled lake deposits through some mechanism.

Further to the physical processes undertaken during the life cycle of the lakes, the MMs embedded into the cyroconite are also subjected to biological processes from bacteria that reside there. These biological processes produce numerous compounds which can effect particles contained within the ice (e.g. colloidal iron oxide) *(Maurette, Hammer, Harvey, et al. 1994).* Colloidal compounds are well known for acting as chemical transport vectors *(Frimmel 2007)* and will therefore incorporate trace elements from the melt water, to themselves, prior to bonding with the MMs, further contaminating them. It was suggested that ices further north with shorter summers will reduce these biological effects as the amount of bacteria able to survive will be greatly reduced *(Maurette, Hammer, Harvey, et al. 1994).*

Both the freeze-thaw bias and contamination limit the use of the Greenland lakes collections in discussions of characteristic chemistry and comparative flux rates. However, the Greenland lakes and ices allow the collection of particles which may not be found in other locations *(Maurette, Hammer, Brownlee, et al. 1986).* For example, glassy spheres are uncommon in many other collections, either due to the short exposure periods the collections cover (e.g. stratospheric flights) or the high amount of weathering (e.g. DSS collections).

1.3.2.3 Sedimentary Rock Collections

In recent years several collections have taken place identifying fossilised MMs in sedimentary rocks including limestone and chalk (e.g. see *Parnell, Salter, and West 2016; Suttle and Genge 2017*). Due to the significant ages of these samples they can provide detailed information on the geological ET flux.

This has enabled these collections to identify changes in the ET record and highlight possible date ranges for the formation events which led to the creation of these particles (e.g. the formation of L type chondrites following the disruption of the precursor object *(Schmitz, Tassinari, and Peucker-Ehrenbrink 2001)*)

Recovered fossilised MMs have also provided information on the atmospheric conditions early in the Earth's evolution. For example analysis of the shape and chemistry of the collected cosmic spherules recovered from Australian limestone by *Tomkins et al. 2016* showed interlocking crystals of magnetite, which implies the presence of oxygen during the CS's atmospheric entry and would not occur in a CO_2 environment.Based on the age of the limestone deposit, Archaean upper atmosphere likely contained significant

levels of O_2.

Sedimentary rock collections however remain biased towards more mechanically resistant particles. Due to the harsh condition that the fossilised CS's have encountered, many of the more fragile particles are likely lost and the surviving particles are heavily weathered and in most cases suffer severe chemical alteration as a result of their terrestrial habitation *(Taylor and Brownlee 1991).*

1.3.2.4 Sedimentary rocks: Salt Deposits

Most current collection methods span a geologically short time period for the age of the particles recovered. Due to the significant age of most salt deposits they provide considerably older samples (≈250 Myr for salt deposits against ≈140 Myr for other collections), providing an opportunity to examine the ET flux which occurred during another phase of the Earth's life cycle *(Davidson et al. 2007).*

A recent collection by Davidson et al (2007) was performed by dissolving 4 kg of halite collected from Meadowbank mine in Cheshire, UK, in distilled water and extracting the non-soluble particulate residue for examination. Extraction was carried out via magnetic separation from the remaining solid mass *(Davidson et al. 2007).* Similarly to the DS collections, the collection steps involved in collecting particle from the salt deposits mean that only ferrous particles can be examined.

Salt deposits have a well constrained age (to within ≈ 3 Myr), allowing numerous deposits to accurately cover a wide range of years. Evaluation of multiple salt deposits can therefore potentially allow the assessment of ET flux across a significantly wider time period than other methods *(Davidson et al. 2007),* and can allow the flux change of MMs over a geological time-scale to be seen. Analysis of MMs contained within salt deposits will hence allow identification of the changes which occurred to the ET flux over the geological record.

A significant problem which affects salt deposits as a source of MMs is the corrosive environment which the particles have to survive in for a prolonged period. Consequently the collected particles are heavily weathered e.g. having lost silica and have undergone significant alteration from terrestrial processes *(Davidson et al. 2007).* The conditions result in only the most robust particles being able to survive containment within the salt. It is highly likely therefore that the number of particles collected is a small fraction

of those which were originally present in the material. Flux estimates calculated from the particles found in the precipitate are 97.5% lower than the currently accepted values *(Davidson et al. 2007),* showing a significant proportion of the MMs have been lost.

1.3.2.5 Urban Collections

Collections have also been carried out in urban locations. The ease of access and short setup time allows these collections to be carried out on a small budget and with minimal training, allowing for members of the public to assist in the particle collection and for larger areas to be examined.

Urban collections allow particles which have only a short terrestrial residence time to be collected *(Genge, Larsen, et al. 2017),* and, as such, the particles collected have a have been exposed to weathering influences on the Earths surface for significantly shorter periods than MMs collected from other collections making urban collections, a good source of large, unweathered CS's .

Unfortunately however these collections suffer from their close proximity to human activity and thus have high levels of anthropogenic debris included. As such it often not possible to separate out small or irregularly shaped particles, resulting in only the largest spheres being identified *(Genge, Larsen, et al. 2017).*

1.3.3 Antarctic Collections

The lack of human activity in the Antarctic make it ideal for the collections of MMs. There is a lack of man-made debris and contaminants which often plague collections closer to anthropogenic activities, and, due to the relatively consistent snow-rate, ages of particles can be estimated and extra-terrestrial flux calculated *(Duprat, Engrand, et al. 2007).* To date, a number of collections have taken place in the Antarctic, sampling from the ices and snows including collections such as: the SPWW collection *(Taylor, Lever, Harvey, and Govoni 1997),* the Concordia station snows collection *(Duprat, Engrand, et al. 2007; Dobrica. et al. 2009),* the Antarctic blue ices collection *(Maurette, Olinger, et al. 1991)* and the Dome Fuji Stations collection *(Nakamura et al. 1999).*

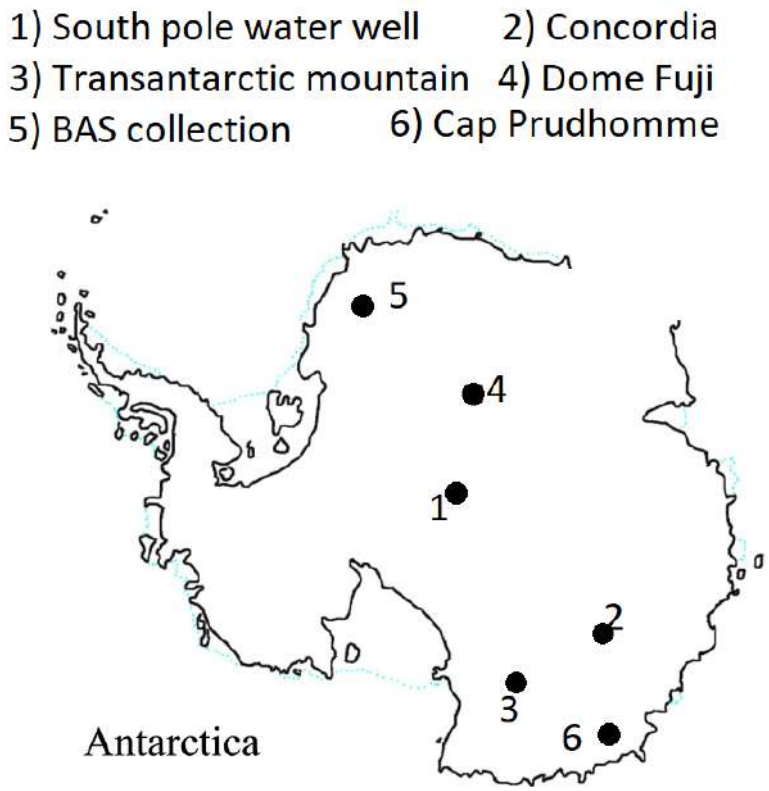


Figure 1.2: The location of major Antarctic micrometeorite collections.

1.3.3.1 South Pole Water Well:

The South Pole Water Well (SPWW) is based at the Scott-Amundson station (see Figure 1.2) in Antarctica *(Taylor, Lever, and Harvey 1998)*. The collection method makes use of the station's water supply, which is generated via the heating of the Antarctic ice.

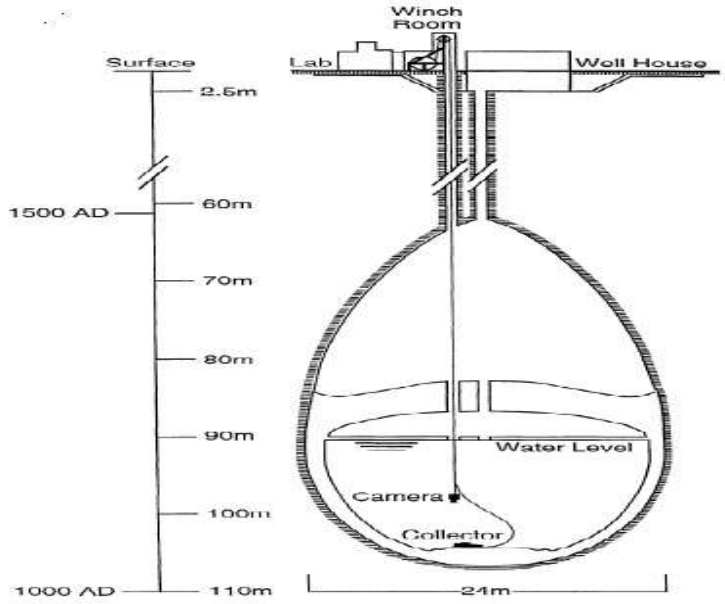


Figure 1.3: Schematic of the south pole water well with the MM collector *(Taylor, Lever, and Harvey 2000)*

MMs land on the snow, which over a number of years form layers of ice with the MMs contained within. As the station melts the ice to produce water, the MMs it contains are released and fall to the bottom of the SPWW *(Taylor, Lever, and Harvey 1998).* They are then collected using suction via a robot at the bottom of the well. The suctioned water is passed through different sized filters *(Taylor, Lever, and Harvey 1998),* with the smallest size particles collected being 50 µm *(Taylor, Lever, and Harvey 1998; Taylor, Lever, and Harvey 2000).* The collections take place in two regions: a central plateau, and pockets which line the walls of the chamber (see Figure 1.3).

The suction pump used to collect the MMs from within the SPWW operates at between 2.5 and 6 times the pressure required to collect iron/stony spherules four times the size of the largest included in the survey and was designed to remove all MMs regardless of morphology, and chemistry *(Taylor, Lever, and Harvey 1998).* Because of this, it exceeded 99% efficiency during lab tests. Due to the method of collection there is no bias towards magnetic particles, or particles of certain sizes.

Despite this, the SPWW collections cannot be said to be representative of the infalling particle flux for two reasons; firstly contamination and loss of particles in the pool, and secondly weathering of the surviving particles by the acidic ice water. The loss of the particles in the pool occurred due to the re-freezing of a section of the SPWW

after a power failure of the pump which led to the loss of the more porous FgMMs *(Taylor, Lever, and Harvey 2000).* The failure of the pump also added large amounts of contaminants to the system in the form of iron oxide grains *(Taylor, Lever, and Harvey 2000)* making it difficult to separate out non-melted particles. As such the study, to date, has focused on CSs. Additional forms of contamination are also present in the SPWW following other repairs to the system. These range from soft 'glue-balls' to pieces of copper wiring *(Taylor, Lever, and Harvey 2000),* however, these are far more easily separated out.

The main source of weathering for the SPWW spherules comes from their residence in PH 4.6 water for $\approx$ 4 years before collection *(Taylor, Lever, and Harvey 2000).* The water preferentially dissolves the nickel and glass in the particles. Despite this, when compared to the DSS samples, the SPWW particles appears to have endured far less weathering, with SPWW MMs showing greatly reduced etching and a much higher proportion of interstitial glass *(Taylor, Lever, and Harvey 2000).* Therefore while the SPWW is systematically biased towards the more mechanically resistant types of MMs (cosmic spherules, ScMM and CgMMs), the bias is significantly reduced when compared to previous collections methods, likely as a result of both the conditions and the reduced age of the particles.

The extra-terrestrial flux at the Earth's surface as calculated via the SPWW collections gives 2,700 tonnes per year for particle of sizes 20 µm $< r <$ 400 µm *(Taylor, Lever, and Harvey 2000).*

1.3.3.2 Concordia Collection

Collections of snow and ices at the Concordia Station (see Figure 1.2) started in 2000 with a second collection in 2002. Snow was collected in trenches at a depth that dated back to the mid-seventies to avoid contamination from the human habitation of the station which began in 1996. The collection area was upwind of the station and collections were made using sledges so that there was no engine pollutants created at the collection site *(Duprat, Engrand, et al. 2007).* The collected snow was placed in tins and taken back via sledge to the Concordia station where it was melted and filtered through a 30 µm mesh *(Dobrica, et al. 2011).*

The lack of mechanical pumping in the collection of the particles for the Concordia samples means that a significant difficulty faced by the SPWW, namely contamination

(Taylor, Lever, and Harvey 2000) is removed. This gives the Concordia collection a smaller systematic bias than previous Antarctic collections, in addition to making it possible to more easily separate out the spheres *(Gounelle, Engrand, et al. 2005).* By collecting the particles while still frozen, and thawing and draining the particles at the station, as opposed to melting and separating from the environment in situ as was the case from the previously mentioned collections *(Taylor, Lever, and Harvey 1998),* the particles were extracted in a clean environment.

As the collections were stored in the snow and filtered out during the melting phase, the length of time exposed to the melt water is considerably reduced ($\approx$ 1-20 hrs *(Duprat, Engrand, et al. 2007)*) compared to both the SPWW and Greenland collections. This leads to the amount of aqueous alteration being significantly reduced *(Duprat, Engrand, et al. 2007),* with Concordia sample, showing reduced levels of depletion of sulphides and calcites.

An interesting find made by the Concordia collection was the discovery of Ultra Carbonaceous Antarctic Micro-Meteorites (UcMMs) which are characterised by a high concentration of disordered carbon nano structures *(Dobrică et al. 2012)* (see Section 1.2.3.4). These UcMMs are similar to collections of CP IDPs from the stratosphere and particles collected from comet 81P/Wild 2 by NASA's Stardust mission. While every precaution was taken to remove contaminations from the collection site, inevitably there was still trace amounts found. However, in most cases the debris was easily noticeable and separable *(Duprat, Engrand, et al. 2007),* meaning that it had only a limited effect on the samples collected. The cleanliness of the collection site meant that the focus was not only the easily separated spherules, and thus enabled these UcMMs to be discovered. It is therefore possible that these particles exist in other collections but have been missed due to the selection criteria.

1.3.3.3 Antarctic Blue Ice Collection

Antarctic blue ice collections originally aimed to build upon the earlier successes of the Greenland ice lakes sample, by removing much of the destructive cyroconite and refreezing, aspects *(Maurette, Hammer, Harvey, et al. 1994).* In order to achieve this, the sample fields were moved south into colder regions of Antarctica where the ice remains frozen throughout the year (see Figure 1.2).

The collection used high power steam jets to melt pockets of ice (roughly 3 m^3 in size) at Cap Prod'homme*(Maurette, Hammer, Harvey, et al. 1994).* Prior to the addition of the hot water, bore holes were drilled into the ice. This process of drilling down allowed for the ice from which the samples were taken to have formed prior to the industrial revolution, thus greatly reducing the number of terrestrial components which could contaminate the samples. The melt water was then filtered via pumps though meshes of 50 µm, 100 µm, and 400 µm meshes onto which the particles were collected *(Maurette, Olinger, et al. 1991).*

These collections show a strong correlation with both DSS collections and the Greenland lake collections in the ratios of abundances of particles of different sizes found *(Maurette, Olinger, et al. 1991).* This shows that the unmelted particles follow a similar size distribution pattern to that of the melted particles.

One of the major advantages of the blue ice collections is the exceptional purity of the samples; the age of the ice means that the samples pre-date any human activity or serious contamination by fly ash *(Maurette, Hammer, Harvey, et al. 1994).* This allows for smaller MMs to be examined, with later collections including the use of 25 µm filters, from which ET particles were collected and studied.

A limitation of the collection method is the reduction in soluble elements (sulphur and calcium) found in the MMs *(Maurette, Hammer, Harvey, et al. 1994)* when compared with particles collected via stratospheric flights *(Flynn 1994).* This loss could be explained via the exposure of the particles to the heated water, and is similar to that experienced by other collections methods (e.g. SPWW, Greenland Collections) where the particles have been exposed to water for a significant period of time. The increased loss is likely due to the high temperature of water being applied increasing the rate of reaction.

Data from the Greenland lakes collection and Antarctic blue ice collections were combined to allow a calculation of the flux rate of MMs on Earth's surface, with the ratios of particle types collected from the Antarctic blue ices used to extrapolate the numbers of particles which would have been found from the Greenland survey, if the local weathering conditions had not been present. This gave an estimated flux of 20,000 tonnes per year *(Maurette, Olinger, et al. 1991)* in agreement with values derived from LEO (40,000 $\pm$ 20,000 tonnes per year *(Brownlee and Love 1993)*).

1.3.3.4 Dome Fuji Station Collection

The Dome Fuji Station collections (see Figure 1.2) were taken from sub-surface snows at a depth of 2 to 5 meters. Due to the constant snow fall rate in the region, this makes their ages between 50 and 70 years old *(Nakamura et al. 1999),* and consequently before the first human activities in the region. In order to extract the particles, the snows were melted inside of a steel tank; the precipitate was then pumped out from the bottom of the container and left in the open to dry where upon it was frozen and stored for transport to Japan for analysis.

Once the sample had been returned to Japan the collected sediment was thawed and separated. This was done firstly by density as compared with pure water, with the floating particles siphoned off and removed. Secondly magnetic particles were removed from the leftover sediment. Finally, left over sediment was separated by filtration after being left to stand for 10 hrs, with filter sizes 100 µm, 190 µm and 95 µm and 6 µm *(Nakamura et al. 1999).*

Analysis of the collected samples showed that the magnetic fraction contained the majority of the extra-terrestrial particles and therefore much of the following evaluations were based on these samples. However it is likely that MMs do exist in the other sediments, but in much lower concentrations *(Nakamura et al. 1999).*

A number of results about the chemical composition of MMs were found. Firstly, that the interior composition of the MMs is often significantly different to that of the outside surface, which also leads to a substantial change in surface colour *(Nakamura et al. 1999).* A number of possible reasons for this were put forward, mainly that a magnetite rim formed around the particle during its passage through the atmosphere, indicating that a temperature exceeding 1100^{o}C was reached *(Brownlee, Blanchard, et al. 1975; Toppani et al. 2001)* (see Section 1.4). However, it is also possible that the colour change on the surface of the particle could be due to weathering which occurred while the particle was on the surface, yet this does not explain the relative increase in iron found on the surface of the particles.

A significant result from the Dome Fuji collections was the discovery of CpIDP-like MMs *(Noguchi et al. 2015).* Prior to this all IDPs which had been collected were from stratospheric flights and thus had suffered significant disruption and, due to their highly porous nature, were badly contaminated with the silicone oil. Both of these

factors were either substantially, or completely removed during this collection *(Noguchi et al. 2015).* This also showed that it is possible for particles of likely cometary origin to survive passage through the atmosphere and survive surface terrestrial weathering prior to collection.

Despite the shorter time spent in the snow, the CpIDP-like MMS appear to have experienced leeching of magnesium during their time in the Antarctic snow *(Noguchi et al. 2015).* Due to their extremely porous nature it is highly likely that the weathering they underwent was significantly increased compared with more impermeable common MMs. The susceptibility of CpIDP-like MMs to terrestrial weathering likely results in the breakup of the particles and therefore is also probable in other collections, which focus on particles < 50 µm, these IDP-like particles were not found amongst the samples.

In spite of high levels of weathering observed on CpIDP-like MMs, limited chemical changes were observed in other MMs *(Nakamura et al. 1999).* The composition of particles collected from the Dome Fuji Station show similarities to both strongly, and mildly, heated CM Chondrites from various sources, making it likely that the composition of the particles collected is mostly unaltered by terrestrial weathering.

Contamination of the samples was widespread, including hairs, fibres, paint and wood *(Nakamura et al. 1999).* The large quantities of contaminants within the sample played a large part in the reduction of the recovery rate of particles from the sample (recovery rates were found to be $\approx 45\%$). Recovery rates were calculated based on the expected yield of MMs from the sample compared with what was actually recovered. Contaminants required that the selection criteria be narrowed (including discarding fractions of sediment after brief analysis) so as to avoid interference from terrestrial debris meaning that many possible particles would have been overlooked.

1.3.3.5 Transantarctic Mountains

These collections take place in the Frontier mountains (see Figure 1.2), where weathering has resulted in the formation of numerous gullies and crevices. These act as natural wind breaks which collect wind blown debris *(Suavet, Rochette, et al. 2009).* These samples are on average over 1 Myr old *(Rochette et al. 2008).* Samples were collected from these rocky outcrops, by hand using trowels and returned to the station where they were separated out via vacuum pumping and then dry filtered through 100 µm, 200 µm, 400 µm and 800 µm meshes. After separation, the CSs were manually extracted using

an optical microscope; any spheres found in the >400 µm segments were then placed in epoxy and further examined using SEM-EDS, a large fraction of the 200-400 µm range was also examined in this fashion *(Rochette et al. 2008)*.

A significant result of this collection method was the high concentration of large (>400 µm) MMs, probably due to the long exposure times of the collection site, combined with the preferential removal of smaller and lighter particles by the wind *(Rochette et al. 2008)*. This occurs as smaller particles deposited on top of the debris can be subsequently removed by the reduced wind in the crevices, however heavier particles will not be moved when sheltered. The samples were found to contain over 3300 particles with sizes greater than 400 µm, well above the 106 found in the SPWW collection (the next largest single sample in this size range) *(Rochette et al. 2008)*.

Some of the MMs recovered using this method showed signs of weathering; including etched and damaged faces, in-filled cavities, and replaced silicates and metals *(Ginneken, Genge, et al. 2016)*. However, the collection method has preserved a number of less mechanically resistant particles (e.g. large numbers of pure glassy spherules) which are absent in other collections (e.g. SPWW and DSS). The low weathered conditions of many of the particles allows more delicate, non-spherical particles to survive, and a study of these particles led to the discovery of a CV-type MM, the first such found in this size range *(Van Ginneken et al. 2012)*. the discovery of this particle shows that it is possible for this type of MM to survive atmospheric entry, and habitation on the Earths surface.

The large sample size collected and the unaltered nature of the particles allows for discussion on the origin of the particles in further detail than the more altered DSS collections. As such it is possible to predict the origin of the particles in the collection both from their compositions, and from the oxygen isotopes present. From these details it was found that a significant proportion of the particles collected were asteroidal and comparable to larger meteorite types. Of the eight unmelted particles larger than 400 µm which were examined, five were OC-like MMs and the other three were singularly CM, CV and CI type particles *(Van Ginneken et al. 2012)*.

1.3.3.6 Larkman Nunatak

The Larkman nunatak collection utilised a moraine found at the base of the nunatak. Moraines are formed at the sides and terminus of glaciers, by material which left behind

by movement of the glacier. Material left behind by the glacier can be collected and examined for micrometeorites *(Genge, Ginneken, et al. 2018).* Due to the amount of material collected by the glacier and subsequently deposited in the moraine large amounts of material are available for analysis with 634 MMs recovered from 3kg of material *(Genge, Ginneken, et al. 2018).*

Also recovered from the moraine were a number of micro-tektites and impact spherules which can be used to date the age of the material recovered, with an accumulation age of the samples being between 780 to 580 ka *(Genge, Ginneken, et al. 2018),* giving a sample of E.T. material from a duration significantly longer than that offered by most other collections, offering the possibility of large number of particles being collected.

Unfortunately biases do exist in the collection method. whilst moraines do act as good vectors for the recovery of MMs small and low density particles are lost, both by wind transport away from the collection location and due to the loss of mechanically less-resistant particles inside of the ice *(Genge, Ginneken, et al. 2018; Harvey and Maurette 1991).* Additionally due to the exposure of the particles to ice for prolonged periods and exposure to water during the period at the glaciers edge, many particles show signs of weathering including etching, metal and glass replacement and the embedding of terrestrial material in cavities. The particle collected from the nunatak are roughly in similar proportion to the previously described Transantarctic Mountains collection *(Genge, Ginneken, et al. 2018),* with the majority of particle being collection being mechanically resistant CSs (92%).

1.3.4 Micrometeoroid Collection

1.3.4.1 Low Earth Orbit Collections:

Low Earth Orbit (LEO) collections of cosmic dust work on the premise of incoming dust impacting onto a surface prior to entry in the Earth's atmosphere. A variety of dedicated and non-dedicated surfaces exposed to LEO dust flux have been surveyed for impact features since the dawn of the space age (e.g. NASA space debris sensor (Kapton, acoustic sensor and resistive grids) *(Hamilton et al. 2017),* Hubble Space Telescope solar array panels (solar array) *(Berthoud and Paul 1996),* Mir Environment Effects Package (Aerogel)) *(Hoerz et al. 1999)* . These particles often leave behind fragments or residues (depending on the impact speeds and capture media) that can provide details of chemistry and size. A notable example of LEO collection was performed by Long

Duration Exposure Facility (LDEF).

LDEF was a 12 sided, bus-sized, prism shaped satellite launched in April 1984 by the space shuttle Challenger. It was positioned in a stable near Earth orbit (mean altitude: 458 km, orbital velocity: 7.64 kms^{-1}, orbital inclination: 28.5^{o} *(McDonnell 1991)*) with one end continually facing outwards from the Earth and the other facing inwards. Originally intended to be in orbit around the Earth for a period of 11 months before retrieval, the Challenger disaster resulted in the grounding of the space shuttle fleet and LDEF was eventually collected from orbit by the Columbia in January 1990 giving a total exposure time of 5 years and 9 months. LDEF carried 57 experiments into orbit, including materials for testing in the harsh LEO environment (e.g. exposure to atomic oxygen), as well as a variety of passive surfaces for the collection of LEO dust.

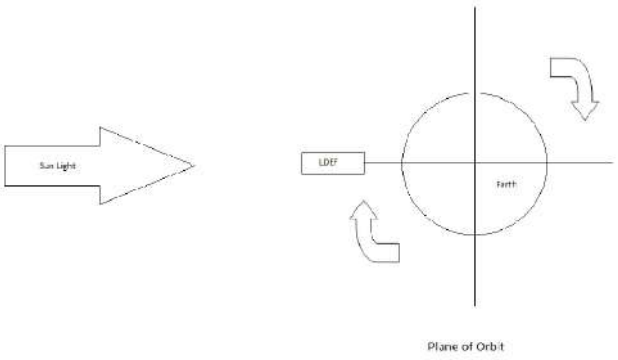


Figure 1.4: LDEF's orbit around the Earth

Upon return, impact features were surveyed and investigated by several groups (e.g. *McDonnell et al. 1991; Hörz et al. 1991*). As the first possible impact on LDEF would have occur no earlier than its launch date, it is possible to calculate the flux of impactors onto LDEF, yielding a total flux of 4x 10^4 $\pm$ 2x 10^4 tonnesyr^{-1} *(Brownlee and Love 1993).* This is close, still within uncertainty, but slightly lower than the value calculated via observed and numerical calculations (e.g 5.38x 10^4tonne yr^{-1} from *Zolensky, Bland, et al. 2006*). A possible reason for the lower value of flux as calculated from LDEF is due to the satellite missing meteor showers and storms due to its relative small size and capture area.

In addition to flux data, the impacts on LDEF surfaces allow an examination of the chemical compositions of the impactors *(McDonnell 1991).* However due to LDEF not having a mechanism to enable the capture and gradual deceleration of the impactor, any analysis of their chemical structure must come from the shocked, leftover residues as the particles themselves do not survive the impact *(Barrett, Zolensky, and Bernhard 1993).* An unfortunate side effect of this, is the mixing and evaporation which occurs as a result of the impact. Examination of the residue, gives an interpretation of the chemical make up of the impactors prior to the longer thermal alteration and oxidation that they experience passing through the atmosphere. The ability to examine the chemical compositions of particles which may not survive atmospheric passage therefore comes at the cost of the shocked and mixed chemistry and an inability to examine their structure of morphology.

Whilst being in space does remove much of the human contamination that is found in samples on Earth, the Near Earth Environment (NEE) still contains multiple terrestrial debris types (e.g. NAK droplets, SRM ejecta, paint flakes) from rocket launches. These too will have impacted on LDEF.*(Murr and Kinard 1993).* A way to discriminate between the terrestrial particles from the meteoroids was required to allow flux data to be calculated. Due to the limit on post-impact particle analysis, an experiment (Interplanetary Dust Experiment, IDE) was launched on-board LDEF to attempt to discern the difference of these two impact types through their mass, velocity, trajectory and time-of-impact *(Oliver et al. 1994).* The results from IDE, in conjunction with SEM analysis of particle residues, allows for the removal of most orbital debris contaminates from the flux data received from LDEF *(Oliver et al. 1994).*

Stratospheric flights: Stratospheric collections of MMs first began in the early 1970's with collections of extra-terrestrial particles, firstly via balloons and then high altitude fixed wing aircraft *(Brownlee, Ferry, and Tomandl 1976).* In both methods the particles are caught on silicone oils, either via having air blown onto them, as is the case with the balloon launches, or having collided with the plate pushed through the air by the aircraft *(Brownlee, Tomandl, and Olszewski 1977).* The silicone oil is used as method for capture due to difficulties in finding materials which would remain viscous and ductile at the low temperatures experienced at the collection heights. The collected particles can then be returned to Earth for further analysis.

This method of capturing the MMs allows smaller particles, which would be unlikely to settle on the Earth's surface due to their small size, to be examined. Due to the particles small size, the are decelerated at very high altitudes ($\approx$ 100 km), at low pressures,

and therefore have experienced lower levels of thermal alteration. The reduced thermal alteration is exhibited by the lack of melting which they have undergone than Earth based methods of collection *(Brownlee, Tomandl, and Olszewski 1977).* In addition to this, the gradual slow down of the particle which occurs in the higher atmosphere allows for a 'soft capture' resulting in significantly less damage to the particle than was experienced upon LDEF. These two points together allow stratospheric flights to collect the most unaltered MMs of any of the previously discussed collection types with a minimum size of collected particle far less than that otherwise found (2 µm minimum size) *(Brownlee, Ferry, and Tomandl 1976).*

In addition to the reduced level of heating experienced, the collection of the particles in the stratosphere greatly reduces the chance of the particles interacting with aerosols or solvents, thereby greatly reducing the weathering of the collected particles. Stratospheric flights are therefore (currently) the most successful method (by number collected) of collecting unweathered particles *(Brownlee 2001).*

Due to the unaltered state of the collected particle, stratospheric flights have provided large numbers of IDPs across all collections, and therefore provide a large part of our current samples of comets *(Messenger 2002).* While in recent times IDP-like CpMMs have been collected from terrestrial samples in the Antarctic *(Noguchi et al. 2015)* currently only 40 have been found. This leaves stratospheric flights as our main source of IDP and IDP-like particles.

A significant drawback of this method for the collection of MMs was the silicone oil. Almost all extra-terrestrial particles contain silicon, often in the form of silicon oxide *(Genge, Engrand, et al. 2008),* hence separating out the contaminant oil from the particle's naturally occur chemistry is difficult, often leading to a much higher silicon compositions than would be expected. Additionally the process of removing the particles from the silicone oil, can result in significant disruption to any porous brittle particles, such as IDPs, which have been captured. The oil contamination leads to an inability to carry out analysis of major elements and oxides in the particle, meaning stratospheric collections can only show the ratios between the elements contained within a captured particle only if the oil contamination is well constrained *(Brownlee, Ferry, and Tomandl 1976).* Recently major breakthroughs in stratospheric collections have been made replacing silicone oil with polyurethane foam, which allows a fully quantitative analysis of the particle's chemical composition. Replacement of silicone oils by polyeurathene foams eliminates a major source of contamination, completely removing

silicon and other major constituent elements of ET particles from the capture method *(Messenger et al. 2015).*

Stratospheric collections occur over a short time span, limited by the air time of the craft on which the collectors are carried, which currently lasts around 8 hrs *(Messenger et al. 2015).* The short sampling time along with the mobile nature of the collections makes using stratospheric data for flux calculations otiose. This means that currently we do not have an accurate method for collecting flux data on IDPs or similar particles.

1.3.5 Summary

We can see that over the past 30 years the collection methods for finding MMs have considerably improved; going from highly weathered collections with significant biases or contaminations, such as DSS collection or stratospheric flight collections, to cleaner and less weathered, such as the Dome Fuji station collection, Antarctic Blue Ice collections and Transantarctic mountains collections, in little over 100 years. However there is still room for improvement; reducing terrestrial residence time will further reduce weathering, increasing the time resolution will allow the ET flux to be calculated more accurately and allow the effects of cometary passes to be analysed. Finally, running multiple collections in different locations will allow the effects of global position (and thus possible effects of orbit inclination) on the ET flux be observed.

1.4 Alteration of Micrometeorites

Particles which fall to Earth are rarely unchanged by the processes they encounter during atmospheric entry and after settling on the Earth's surface. The high temperatures reached during their passage through the atmosphere can melt and chemically change the particle, while exposure to water on the Earth's surface can hydrate minerals and leach elements.

1.4.1 Atmospheric Alteration

1.4.1.1 Morphological Changes

Atmospheric alteration of particles is dominated by the extreme heating experienced by particles as they are decelerated. Particles are melted, change shape and lose struc-

tural information as their component structures thermally degrade.

The heating particles experience during passage through the Earth's atmosphere is closely related to its size, its entry velocity and the angle of entry. Particles which enter the atmosphere at shallow angles experience reduced heating when compared to those particles which enter the atmosphere at steeper angles. Whilst low entry angles produce less heating, entry angles $> 80° - 85°$ result in the particle 'bouncing of the atmosphere' instead of penetrating through it *(Love and Brownlee 1993).* Additionally, smaller particles experience less heating effects during entry, due to their smaller cross section area and thus appear less changed from the processes. Particles whose entry diameter is smaller than 50 µm experience significantly less heating and appear to be mostly unchanged by their passage assuming an asteroidal origin *(Love and Brownlee 1993).*

It was formerly thought that the entry angle of a particle and its entry velocity are also closely related to the body which formed the particle. For asteroids which exist in a near circular orbit along the orbital plane, the entry angles tend to be large and velocities tend to be low. For particles formed from cometary bodies, it was thought that the entry velocities be much higher due to the highly eccentric nature of their orbits. Additionally, many comets do not orbit in the same plane as the planets and asteroids, meaning that it is likely that any particle descending from a comet will enter the Earth's atmosphere at an angle lower than that needed for a safe passage. As such it was believed that is highly unlikely that any collectable or analysable fragment fo cometary dust would survive atmospheric passage unmelted even with 'low' entry angles *(Love and Brownlee 1991).* However, as evidenced by the identification of CpIDPs on the Earths surface, some cometary particle are able to pass through the Earth's atmosphere unscathed.

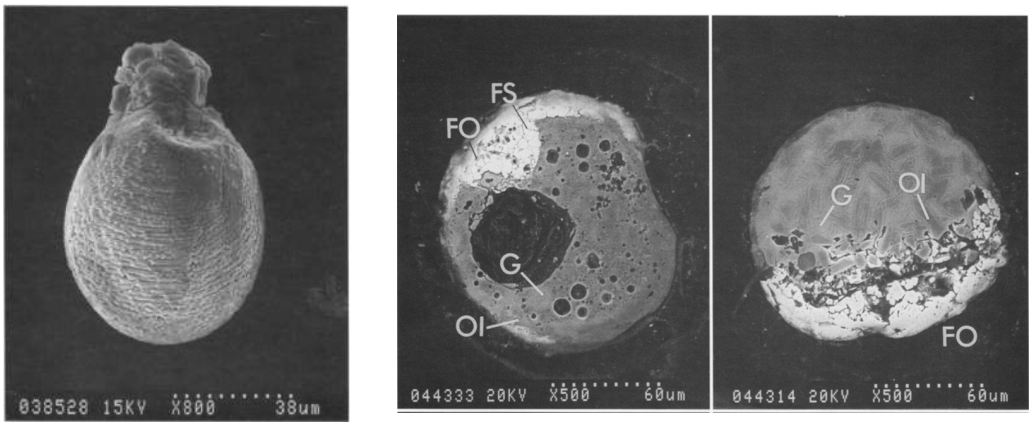
More recent research has however shown that the entry angle and speed of an incoming particles is not necessarily linked to it parent body. Work by *Nesvorný et al. 2010* has shown that much of the dust formed by Jupiter-Family-Comets is likely to be perturbed by the gravitational field of Jupiter and approach earth at a similar velocity and angle to asteroidal dust, and as such will have a similar likelihood of passing through the atmosphere. Research carried out by *Carrillo-Sánchez, Nesvorný, et al. 2016* has shown that cometary dust is responsible for 80% of the cosmic dust accreted by the Earth's atmosphere; an almost complete reversal of the previously described model. These results can explain the discrepancy between the ratio of recovered MMs to that of recovered meteorites (carbonaceous-like MMs to ordinary-chondrite-like MMs have a ratio of $\approx 6:1$ whilst meteorites are dominated by ordinary chondrites *(Nesvorný et al.*

2010)) with cometary dust dominating the small particle flux, but larger meteorites being asteroidal due to the difficulty in perturbing larger cometary fragments.

Most of the highest temperatures experienced by a particle during its atmospheric passage occurs at heights of 80-85 km. The heating the particle receives is also dependant on each particle's physical characteristics in addition to its entry details. In this way a larger denser particle will experience a greater peak temperature than a similar sized less dense or smaller particle *(Love and Brownlee 1993; Rudraswami et al. 2016).* Due to the increased heating larger particles are exposed to, many are lost or are reduced in size by a factor of 1.5 to 2 with a mass change of between 3 - 10 times *(Love and Brownlee 1993).* Most of the mass lost during atmospheric entry is down to a mixture of fragmentation and evaporation. Heated particles will loss material via evaporation of volatiles in their chemistry and particles may fragment either along the lines of structural weakness in the particle (i.e. along matrix lines between mechanically stronger igneous grains), or due to the creation of dehydration cracks formed during entry heating *(Genge 2008).* As the peak temperature and deceleration occur at too high altitude with too low air pressure, it is unlikely that the pressure during the descent will be able to fracture most structures before they are melted *(Love and Brownlee 1993).*

The heating of particles during atmospheric entry also results in many particles losing mass. This mass loss is due to combination of the evaporation of volatiles contained within the particle and the evaporation of material from the particle's surface. Evaporation of the particle occurs at between 70 km- 90 km *(Rudraswami et al. 2016),* during and following the peak temperatures reached. Evaporation occurs during the period in which the particle is molten, starting as the surface heats and melts and lasting until the particle has slowed, or lost enough material, to be small enough to solidify.

The degree of thermal alteration a particle has experienced during its descent through the atmosphere can most easily be seen by the morphological change the particle has undergone; the most thermally altered particles are nearly perfectly spherical, while lightly altered particles maintain their irregular shapes. These changes in morphology are caused by the melting and rotation of the particle as it passes through the Earth's atmosphere. If the particles rotation is not random, this change in morphology can result in a more elongated shape, commonly referred to as a flight morphology (see figure 1.5).



(a) (b)

Figure 1.5: Two particles demonstrating the main forms of kinetic alteration of a particle passing through the atmosphere: a) Change in morphology. b) Movement of heavy elements. Both figures are taken from *Genge and Grady 1998.*

Vesicles Vesicles are also often formed during heating; they are small cavities formed inside heated particles as volatiles degas from within. Direct dissolution of the gas into melt is too slow to explain the size of the vesicles seen in MMs, as such it is likely that gas is trapped within the particle as a result of a surface melt layer which impedes gas loss into the atmosphere *(Genge 2017).* As such vesicles are only found in those particles which have undergone some level of melting and are not found in unmelted MMs *(Engrand and Maurette 1998).*

1.4.1.2 Chemical Changes

The heating experienced during atmospheric entry changes the chemical composition of the particle, as the temperatures reached can exceed the temperature of vaporisation of many compounds. It is therefore likely that many elements are lost, or reduced, via evaporation during the entry process *(Genge, Grady, and Hutchison 1997).* The particles that pass through the atmosphere and reach the surface therefore end up depleted in sulphides, chlorides and sodium. For sulphides (e.g. pyrrhotites) sulphur is lost and the remaining iron is oxidised transforming into magnetite *(Greshake, KLöCK, et al. 1998).* As the loss of sulphides starts at relatively low temperatures (≈ 300°C) the depletion of sulphur occurs in almost all MMs.

Decomposition of many carbonate phases also occurs. These processes all lead to a reduction in mass of the particle; at temperatures below 650°C, the mass loss of particles is dominated by the loss of H_2O and CH_4 *(Genge, Grady, and Hutchison*

1997). However, after 650°C the volatile loss becomes dominated by the loss of sulphur. In addition to the change in mass of the particle, this also leads to a significant difference in chemical make up between the collected sample, and the original mineralogy of the particle for even lightly heated particles.

Formation of Glass The super-heating of MMs during their passage through the atmosphere results in the breakdown of many or all of the complex crystal structures that were previously present. The cooling that the particle then experiences also occurs over a short time period, not giving the any remaining crystals time to reform, resulting in many cases in the complete loss of many of the large crystal structures. Particles which are not completely melted (ScMMs) also show similar signs of loss of crystal structure and the formation of glass. In cases where the heating is less intense, crystals inside of larger bodies may survive as a relict grain due to the low thermal conductivity of the particle combined with the surface heat loss due to the ablation of material from the edges of the particle *(Genge, Grady, and Hutchison 1997).*

Formation of Magnetite Rims The extreme heating which MMs experience also can also be used to explain the formation of magnetite rims of particles. Currently the formation of magnetite rims may be explained by one of two hypotheses; the first is that it occurs due to the melting and dissolution of iron within the in-falling particle during the micrometeorite's descent *(Toppani et al. 2001).* As a rotating particle is melted the iron rises to the surface and is oxidised as it solidifies. A second method for the formation of magnetite rims is the collection of Fe^{2+} ions from the atmospheric E band layer. Due to the column density of these ions, it is highly unlikely that this could form the required thickness that is often observed on collected particles *(Engrand and Maurette 1998).*

1.4.2 Terrestrial Weathering

The main cause of terrestrial weathering is the abundance of water in the air and in/on the ground. The water acts as both a method for morphological changes via erosion, and for chemical changes by acting as a solvent and by hydration. Due to the abundance of water on the Earth's surface most particles collected in any of the previously described surface based collection show some degree of morphological or chemical alteration from their exposure to the terrestrial environment.

1.4.2.1 Loss of Glass

Many of the particles collected from the Earth's surface show preferential loss of glass, due to the ease with which some glasses can be dissolved compared to that of crystals and solid metal grains. Particles which have been in contact with water for even short periods of time (<10's of years) show the loss of glassy phases particularly along the surface of particles *(Taylor, Lever, and Harvey 1998).* As well as changing the bulk composition of the particle, this loss of glass also has a significant effect on the morphology of the particle. In addition to the complete removal of glass, many particle, with remaining glassy regions find them to be 'poxed' after minimal exposure *(Ginneken, Genge, et al. 2016).*

1.4.2.2 Preferential Loss of Elements

Different elements are dissolved to different extents and form solutions in water with differing levels of ease. Exposure of MMs to water will hence show a preferential loss of the easier to dissolve elements. The amount of material lost in this way is strongly dependant on the length of time the particles are exposed to the conditions required to form a solute and how extreme the environment itself was (e.g. PH, concentration). Particles collected via DSS collections are therefore altered due to the alkali nature of the ocean and the lengthy residence (1000's of years) to a greater extent than those particles collected from areas of fresh water whose residence was only a few years (e.g. the SPWW) *(Brownlee, Pilachowski, and Hodge 1979; Taylor, Lever, and Harvey 2000).*

One of the elements most likely to be lost in this manner is Mg. Due to the high abundance of this element in MMs compared to terrestrial debris, it is often used to identify extra-terrestrial particles. An ideal collection method will therefore avoid exposure to water and thus the leaching of Mg into the environment.

1.5 Aim of Thesis

This thesis aims to provide insight into the composition and flux of micrometeorites via the analysis of two new and unique micrometeorite collections; one based on the Kwajalein atoll and the other at British Antarctic survey Halley VI station. These new collections build upon previous collections by removing the chance for terrestrial alteration to occur by directly sampling the particles from the air at ground level. These collections will be analysed independent of, and compared to, results taken from

previous micrometeorite collections.

In addition, this thesis also aims to provide information on common terrestrial contaminates based on data published in the literature. These data will be used to provide additional details for possible selection criteria based on the compositions of previously collected MMs, allowing for terrestrial contaminates to be more easily identified and removed from collections.

Finally, this thesis aims to build upon previous work carried out into the effects of atmospheric entry on micrometeorites. Previous work has focused on the chemical changes which occur in these particles, whilst the physical changes brought about by this process have only been simulated computationally, or using stationary pulse heating techniques (e.g. *Plane 2012; Toppani et al. 2001*). As such kinetic effects have not been reproduced in the laboratory. This thesis will aim to design and provide details for a new method for the reproduction of these kinetic effects using a two stage Light Gas Gun (LGG).

Chapter 2
Methodologies

This chapter will introduce and describe the main techniques used to analyse samples over the course of this PhD. These are Scanning Electron Microscopy and optical microscopy, which have both been used for the identification and analysis of micrometeorites and the analysis of the micrometeorite simulants in the atmospheric entry studies. This chapter also describes the Light Gas Gun facility used to accelerate MM simulants to a representative velocity in the atmospheric entry studies. Finally, brief descriptions of Transmission Electron Microscopy, Focused Ion Beam microscopy and Raman spectroscopy are also included; a more detailed discussion of these techniques is not given, as although used to analyse atmospheric entry simulants, the results were limited.

2.1 Scanning Electron Microscope

The Scanning Electron Microscope (SEM) uses a energetic electron beam to interact with the atoms of a sample. Interactions can occur via three ways: the collision between the incident beam electrons and bound elections in the sample results in the emission of an electron at low energies (these electrons are detected by Secondary Electrons (SE) imaging techniques); elastic scattering between the beam and the atom in the sample results in the emission of a high energy electron (used in Backscatter Electrons (BSE) imaging); and the excitation and subsequent de-excitation of bound electrons results in the release of X-rays (detected by an Energy Dispersive X-ray (EDX) detector).

Due to the De-Broglie wavelength of electrons being shorter than that of visible light, it is possible to resolve significantly smaller objects using SEM techniques than would be possible using optical microscopy. SEMs are therefore used extensively in the study of MMs where a high image magnification is required to be able to resolve features and surface textures. The SEM used in this thesis was a Hitachi S3400N, and details of the

setup used for analysis can be found in the respective chapters.

2.1.1 SEM Design

The SEM beam consists of highly localised energetic electrons. It is controlled within the SEM column via a series of electro-magnetic lenses (see Figure 2.1). The width of the beam, its shape and electron density all control image resolution and final image quality and as such many SEM components are given over to the control of these properties.

Modern SEM design consists of a number of common components; an electron gun which produces the electron beam and a column with various beam alignment components which direct the electron beam onto the sample which sits on a sample stage within a vacuum chamber. The column consists of single, or multiple, electro-magnetic condenser lenses and a focusing lens. In between the condenser lenses are a system of apertures used to remove (uncondensed) electrons preventing interference with the beam coherence. Between the final condenser lens and the focusing lens is a final changeable aperture and scanning coils used to control the beam spot size (see Figure 2.1) and deflect the beam, so that it can raster across the surface of the sample and produce an image *(Reed 2008)*

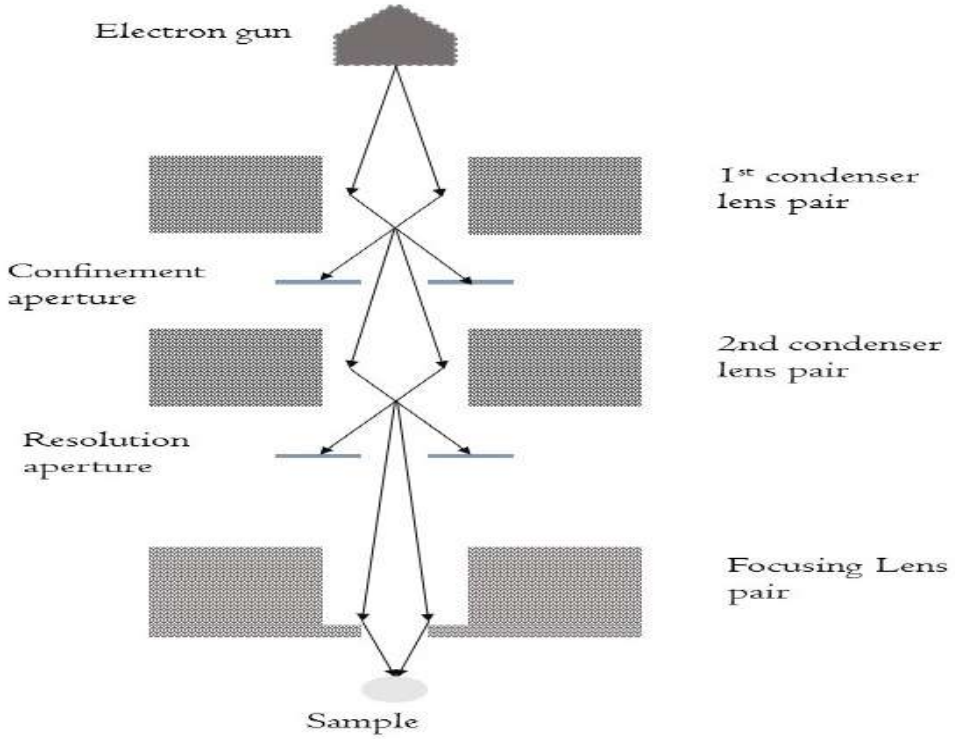


Figure 2.1: A schematic design of a three lens SEM column.

Electron Gun The electron beam of a SEM is produced via the electron gun. Currently two major types of electron gun are in production; thermionic guns and field emission guns (FEG). FEGs produce the electron beam via high potential gradients. The filament is made of a Tungsten crystal and is positioned in an area of high negative potential relative to a nearby electrode. The gradient is such that field emission occurs as the electrons are forcibly ripped from the atom *(Reed 2008).* The electrons exit the gun through an aperture and enter the column. Due to this method of electron production, the system itself must be under high vacuum to avoid the production of additional electrons from atmospheric atoms. This means that FEG-SEMs are unable to run in Variable Pressure mode which reduces the vacuum of the system. Due to the compositions of the particles we are examining (see Chapter 3), our inability to coat them, and their propensity for charging, we require the higher atmospheric pressures offered by Varible Pressure (VP) modes and as such are unable to use the FEG-SEM at the University of Kent for our analysis.

Due to the high vacuum requirements of FEGs, many SEMs including the S3400N, are instead equipped with thermionic guns. Thermionic guns use super heated filaments of metal (often tungsten) to produce the electron beam via ionisation. The electrons are energised by the filament and are given sufficient energy to overcome the potential that binds them to the nucleus *(Reed 2008).* As the electrons are produced via the direct heating of the tungsten filament, thermionic guns do not have the ionising effect upon contained atmosphere and hence do not have same vacuum requirements as FEGs. The reduction in vacuum requirement means that thermionic guns are often much cheaper to purchase and run than FEGs and can run VP modes.

In theory all of the electrons produced via a thermionic gun should originate at the filament's centre. However small aberrations in the filaments can cause fluctuations in its temperature gradient and, as such, the production of electrons from a thermionic gun does not often occur from a single point in practice *(Reed 2008).* This results in a larger minimum spot size than would otherwise be achieved. In contrast, FEG sources have a well constrained source on their tip for the production of electrons (usually $\approx 100nm$ *(*Scanning Electron Microscope: Training Module *2014)*) thus having a significantly reduced spot size. This makes FEG-SEMs preferable to thermionic SEMs for any work requiring high spatial resolutions and signal-to-noise ratios.

	Themionic		FE
Filament Type	Tungsten	LaB_6	Tungsten Crystal
Vacuum requirements (pa)	$\approx 10^{-2}$	$\approx 10^{-4}$	$\approx 10^{-7}$
Max. Resolution (m)	$\approx 10^{-4}$	$\approx 10^{-5}$	$\approx 10^{-9}$
Energy spread (ev)	1-5	0.5 - 3	0.2 - 0.3

Table 2.1: A comparison of generalised electron gun types requirements and outputs *(EM Resolutions LTD 2014)*

Lenses Due to the charged nature of electrons, SEM beam pathways can be significantly altered by the application of magnetic fields along the beam's route. As such SEM beams are focused via a series of electromagnetic lenses, which consist of coiled wiring enclosed within a ferrous shell. The wiring carries a high direct current which is used to generate the controlling magnetic field. Varying the current allows the magnetic field to be varied and the beam direction shifted or magnification changed. The beam confinement and direction is controlled by the condenser lenses which shifts in the beam angle and size caused by changes in the emission spot on the filament to be corrected. The final lens is the focusing objective lens which is used to control and remove aberrations in the beam and to control focus and the depth of the focus *(Reed 2008)*.

Apertures SEM apertures are used to confine the width of the electron beam and to remove spray electrons. The aperture prior to the final aperture are referred to as spray apertures *(Reed 2008)*, and are used to remove unconfined electrons from the edges of the beam. The removal of these electrons reduces the chance of beam electrons scattering on the lens or creating interference due to being badly confined. The final aperture is used to control the size of the beam, with larger beam sizes providing more current but at reduced resolution and depth-of-focus and smaller beam sizes providing much higher resolutions and depths-of-focus but often at far reduced currents. The current contained in the beam plays a large part in the single-to-noise ratio. The selection of the aperture therefore often depends highly upon the sample being studied.

Sample Stage The stage controls the position of the sample in the xy plane and in the z direction. By adjusting the stage the user can ensure that the region of the sample being examined is always within range of being in focus, regardless of the morphology of the sample surface. Automated stages also enable automated mapping of a sample to be performed, as was used in the filter analysis discribed in chapter 3.

2.1.2 SEM Detectors

Secondary Electron Imaging Secondary Electrons (SE) images are produced from secondary electrons which are produced when the incident beam electrons interact with atoms in the sample (see Figure 2.2). Due to the low energy of the secondary electrons, only electrons released from the surface of the sample can be detected as electrons from deeper within the sample are reabsorbed. The low energy of the electrons released also means that for SE imaging to take place, the sample chamber itself needs to be under a high vacuum to perform imaging, else the secondary electrons will be absorbed within the contained air *(Reed 2008)*. The angle between the interaction surface and the incoming electron beam changes the number of electrons released from the sample and, if the interaction surface is perpendicular to the angle of incidence then the number of electrons released is at the minimum. As the angle increases, the interaction volume also increase and the escape distance for the released electrons decreases, hence 'steeper' regions of the sample will appear brighter than those which are 'flat'. In this way SE images can provide topographical data with a single detector.

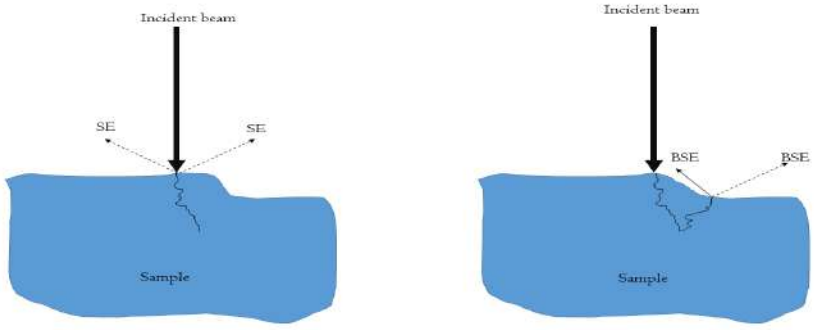


Figure 2.2: The production of secondary electrons and backscatter elections in a sample exposed to the electron beam.

Backscatter Electron Imaging Backscatter Electrons (BSE) are produced when the incident electrons are reflected back from the sample during a collision with an atom. These highly energetic electrons leave the sample and are collected via a split segment detector placed above the sample around the exit of the column. As an increase in density of the sample increases the chance of an electron being 'reflected', denser materials appear brighter than less dense materials in BSE images *(Reed 2008)*. BSE imaging is often used to provide information about the composition of a sample, including information such as homogeneity and purity, e.g. a pure homogenous sample will appear to have uniform brightness, whereas a more heterogeneous sample will show

variations in brightness. The detector is often torus-shaped, with the beam passing through the hole in the centre. BSE detectors are also often separated into multiple areas which can be activated individually, creating apparent shadows that allow the topography of the sample to be visualised. Some BSE detectors also provide a fifth segment for topographical imaging removed from the main torus. As the detector is not imaging straight down onto the sample, topographic features cause shadowing in the signal received.

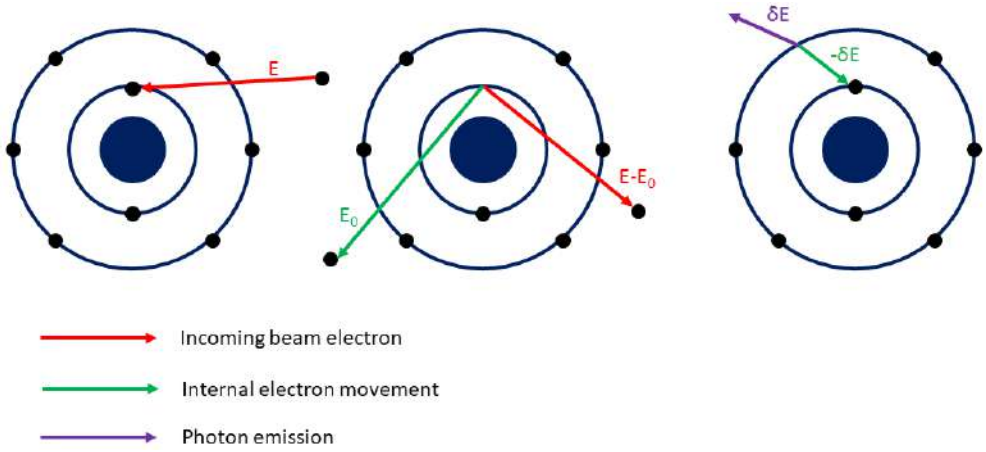


Figure 2.3: The production of an X-ray generated in an SEM for EDX analysis.

Energy Dispersive X-ray Spectrometer Energy dispersive X-ray spectrometry (EDX) uses the unique energy levels that electrons of a given element can be excited too, to identify the element. The interaction of electrons within the beam and electrons bound to atoms within the sample can ionise atoms. If the escaping electron leaves a lower energy shell of the atom it creates a 'hole' in the lower energy level. Electrons from higher energy shells will fall into and 'fill up the hole'. As they fall from higher energy states to 'fill in' lower energy shells, they release the change in energy as a photon (see Figure 2.3). Each element has distinct and unique energy levels and, as such, an element can be identified by the energy of the photon radiated by a 'falling' electron. When this energy is given off in the X-ray band, it can be detected by EDX sensors. In these, X-rays interact with a silicon drift sensor producing internal ionisation, which results in a current. This current is measured, allowing the energy of the interacting photon to be found, which then allows for the element in the sample to be identified. EDX examination provides a quick and non-destructive method for evaluating the composition of most samples, however to provide detailed quantitative analysis, samples must first be prepared so that the examined surface is flat.

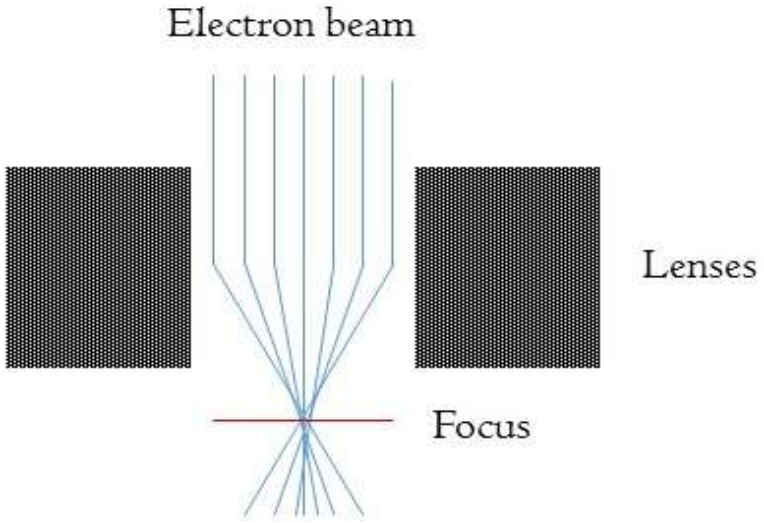


Figure 2.4: Diagram showing the effect of spherical aberration on a coherent electron beam passing through a magnetic lens.

2.1.3 SEM Imaging Complications

Spherical Aberrations Spherical aberration occurs due to the reduction in magnetic field strength with increasing distance, causing electrons towards the centre of the beam to be less well constrained by the magnetic lenses than those towards the edges *(Reed 2008)*. Due to the over-focus of the outer electrons, multiple focus points are created (see Figure 2.4), making it impossible to correctly focus the beam over the entire spot area, resulting in a blurred image. Spherical aberration can be overcome by the use of smaller apertures and working distance, however it remains a limiting factor on the maximum imaging zoom.

Astigmatism Astigmatism is caused by the electrons having different focusing distances in different planes due to the lenses focusing by different amounts in the perpendicular directions X and Y. As such an image in focus in the X direction will appear out of focus in the Y direction or vice versa. Correcting the B field in the two directions provides a method for reducing and eliminating astigmatisms *(Reed 2008)*.

Sample Charging Whilst most SEMs require a high vacuum to work, this often has the effect of reducing the charge from the beam to the sample being examined which can be dissipated. Due to the vacuum conditions the sample is exposed to, this charge can build up if the sample is not conductive. This increase in charge over the sample area increases the brightness of the region, and can cause loose samples to move when

exposed to the electron beam and fixed samples to interact with the beam causing beam shift.

In order to reduce the charging experienced by a non-conductive sample, two methods can be employed. The first is to apply a conductive material to the sample and attempt to earth it. Methods of attempting to earth a sample include the application of conductive tape (e.g. typically copper or aluminium tape), application of a coating to the sample (e.g. carbon coating) or via a conductive paint applied to the sample stub (e.g. silver dag). For this method to work the sample must be able to be earthed, which is not the case for all samples, such as cases where the sample is not a single solid piece. For samples where it is not practical to attempt to use an earthing tape, coating or paint (e.g. loose powders). A second method involving the introduction of air to the sample chamber can be used; this is often called Varible Pressure (VP) mode. The increase in interference due to the addition of atoms of air into the target chamber reduces the quality of the image captured due to an increase in background noise. To combat the additional noise, multiple images can be taken and averaged, to remove the random background interference. The addition of air to the chamber does mean that SE mode images cannot be obtained, as the electrons do not have the energy to pass through the air and reach the detector.

2.1.4 EDX Complications

Matrix Corrections Matrix corrections combines several significant problem EDX analysis into a single mathematical correction. The first difficulty is that a lighter element will attenuate the electron beam with a lower efficiency than a denser material and will thus emitted a lower number of photons. The second problem is that a fraction of the emitted photons will be reabsorbed by surrounding atoms and scattered and finally a fraction of the x-ray will be emitted as florescence as opposed to being initiated by the electron beam *(Newbury and Ritchie 2013)*. The matrix correction equation uses weighting factors for the fraction of x-rays lost or gained due to the above processes, to calculate a semi-quantitative abundances by calibrating the EDX spectra with that of a standard of a known composition.

Interaction Volume An additional problem faced when using EDX to analysis spectra is knowing the interaction volume of the electron beam. An electron inside of the beam will penetrate a depth of the sample (l). If the electron is elastically scattered, then it may experience a direction change and move away from the beam centre - giving

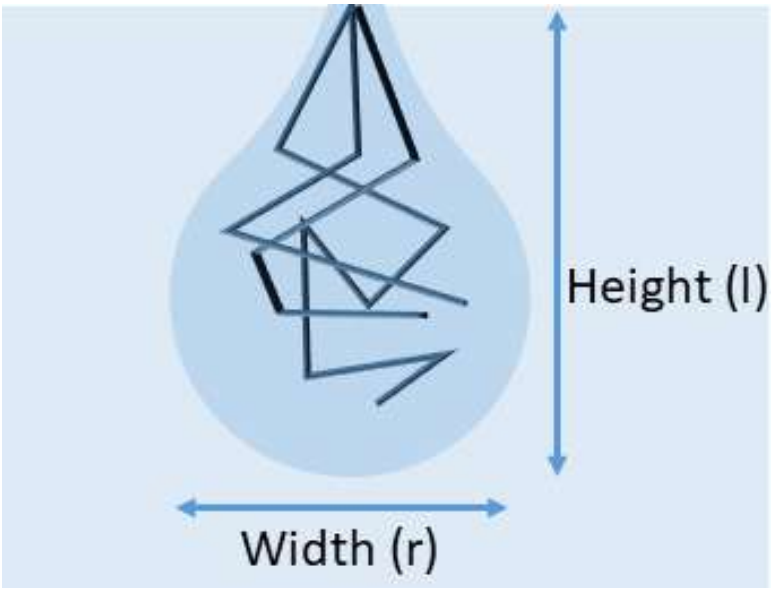


Figure 2.5: Simplified schematic showing the interaction volume of an electron beam penetrating a sample.

a depth (l) and a width (r) (see Figure 2.5). As such as opposed to a single point on the sample, a volume will instead be analysed and a spectra may contain information on surrounding material. The is of particular importance when taking spectra of small samples , such as micrometeorites, which may have an area smaller than that of the interaction volume, as contamination in the spectra from surrounding material will be included. Therefore in these situations, when preparing samples, it is necessary to have a good understanding/expectation of the chemistry of the surrounding material (i.e resin etc) and the sample, so that there is limited overlap allowing peaks obtained from the surrounding to be removed.

Analytical Uncertainties Finally analytical techniques used to gain data from the photons measured by the EDX detector can cause analytical errors to occur. Digital filtering (e.g. 'top hat' filtering, background modelling and peak smoothing) is carried out by post processing software to suppresses noise, deconvolve peak position and remove background gradients in the spectrum. As with any digital filtering, these processes can distort the spectra obtained, and obscure features. However correct calibration, using sample which are similar to those being examined provide a method for the reduction of these errors.

2.1.5 Summary

SEM techniques provide an effective method to gain insight into the surface and composition of micron-sized features. Whilst SEM techniques do experience difficulties in examining some samples due to charging, most samples can be examined provided suitable sample preparation is performed. For the analysis carried out in this thesis, details of the sample preparation is included in the relevant chapters, along with the working conditions of the SEM used.

2.2 Optical Microscopy

2.2.1 History

Optical microscopes first appeared in their current form as early as the 17th century and have undergone few structural changes since, other than to accommodate new technologies (e.g. computerisation). Modern compound microscopes consist of two main lens sets; the eyepiece and the objective lens, separated by the the microscope column. In addition to these lens, some microscopes are equipped with a third lens, often at a lower magnification at the end of column, providing an additional factor of magnification. The total magnification of the microscope is given by multiplication of the magnification of the eye piece, the objective and (if fitted) the aperture lens.

2.2.2 Lenses

Optical lenses are made of polished glass machined into concave and convex shapes. These lens are then positioned in series as shown in Figure 2.6. The objective is designed to allow a real image of the sample to be magnified and passed along the column to the eyepiece, which additionally magnifies the target passing on a virtual image via the converging lens *(Edmund Optics Worldwide 2018)*.

Each set of lenses, objective and eyepiece have different focal lengths. To ensure the image is in focus, the eyepiece focal length must be equal to the distance between the eyepiece and the objective. This is normally taken into account during the microscopes design and the eyepieces are fixed at this distance from the objective. The objective lens, however, requires focusing for each sample. A badly focused microscope will result in a blurred image with indistinct edges. Focusing is carried out by adjusting the distance between the objective lens and the sample to the objective lens' focal distance, either

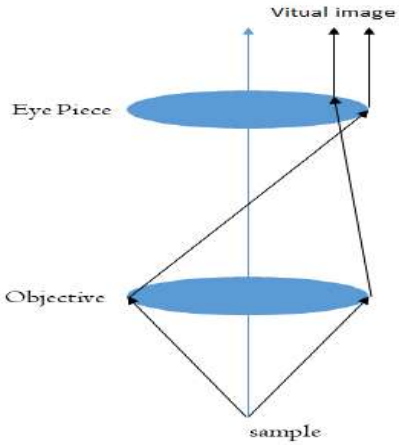


Figure 2.6: The standard positioning and light path of a transmission microscope showing the formation of a virtual image.

by raising and lowering the sample or lens assembly *(Watt 1997)*.

In addition to lateral focus, the Depth-of-Field (DoF) of a lens also plays an important part. This is the change in distance between the nearest and furthest point at which a sample can be resolved. As the focal length is a set distance from the objective lens, on irregular samples, areas above and below this distance will be unfocused. As a rule of thumb, a lens providing higher magnification will provide a lower DoF. Insufficient DoF in a system may be resolved by simply scanning the focus up and down the surface, allowing the focus to sit at each distance, however this presents a number of difficulties, not least in displaying the data comparatively. The DoF can also be altered by changing the lens aperture, with wider angles providing small depth of field than narrow angles (see Figure 2.7).

2.2.3 Limitations to Optical Microscopy

Optical microscopy has a number of limitations, that can broadly be split into two categories: those caused by aberrations in the lenses, and those caused by the diffraction of light. Aberration is caused by the improper shaping of the lens during manufacturing, resulting in light being incorrectly directed through the lens, resulting in multiple focal points. Diffraction effects become important when the sample features being analysed reach a size comparable to that of the wavelength of light. The minimum distance between two points in order to be able to resolved separately is given by:

$$l = 1.22\frac{l_{focal}\lambda}{D} \tag{2.1}$$

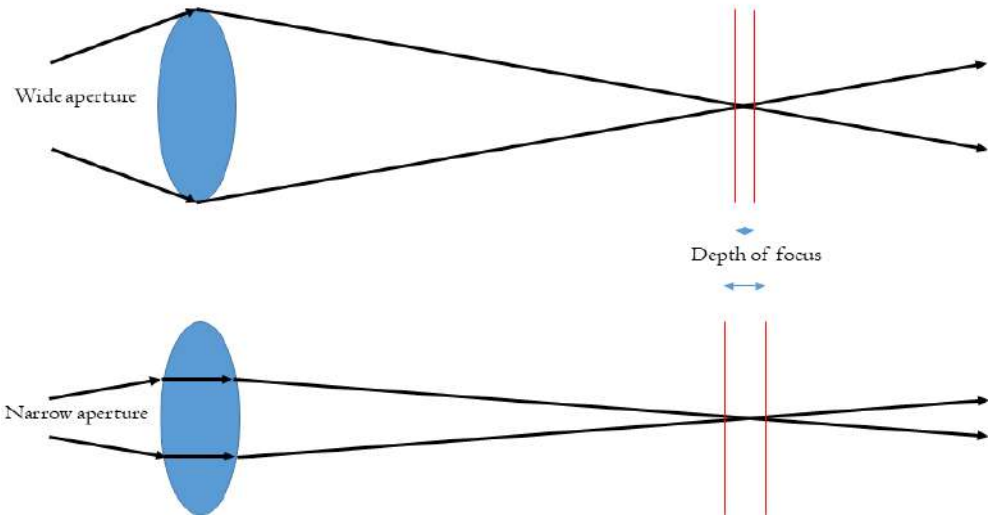


Figure 2.7: The change in depth-of-focus between a wide aperture and narrow aperture. The narrow aperture can be seen to provide a greater depth of focus.

where l is the spatial resolution of the system (m) or the minimum distance required, l_{focal} is the focal length of the lens (m), λ is the light's wavelength (m) and D is the diameter of the lens' aperture (m) *(Watt 1997)*. Equation 2.1 shows that a minimum size of around 1 µm can be reliably resolved by using bench top microscopes operating in visible part of the EM spectrum.

2.2.4 Summary

Whilst optical microscopes do not allow the same magnification as SEMs to be achieved, they hold a number of advantages over them. Firstly, they do not require vacuum conditions to operate, both allowing the examination of samples that cannot be exposed to an electron beam or vacuum conditions, whilst also allowing the manual articulation of a sample, including removing and manipulating parts of the sample in situ. Additionally, for transparent bodies, it is possible to position the lenses in such a way that changing the position of the focal point can allow an examination of the interior of the sample *(Watt 1997)*. These two features make optical microscopy a useful and complementary technique to SEM. Optical microscopy has been used in this thesis to aid in the picking of MMs as described in Chapter 3 and to aid in the selection of projectiles as described in Chapter 6.

2.3 Light Gas Gun

A number of methods for simulating hyper-velocity impact in the laboratory exist including Van de Graff accelerators *(Burchell et al. 1999),* flyer plate accelerators *(Hall et al. 2001),* Reddy shock tubes *(Reddy et al. 2015)* and laser experiments *(Dunne 2006).* However one of the most common methods for replicating hyper-velocity impacts in modern laboratories is the two stage Light Gas Gun (LGG) *(Rynearson and Rand 1972).* Using compressed gas to fire at speeds upto 7 $\mathrm{km\,s^{-1}}$, LGGs are capable of firing projectiles in the millimetre and centimetre size range. In recent years, three stage LGG's have also been proposed, enabling the maximum velocity achievable to be increased *(Piekutowski and Poormon 2006).* For the experimental program detailed in Chapter 6, shots were carried out on the Kent two stage LGG which is described below in section 2.3.2.

2.3.1 Operating Principles

LGGs operate by using a first stage of acceleration to compress gases behind the projectile and provide a second stage of acceleration directly to the projectile. In most LGGs, compression of a low density gas is provided via the ignition of a propellent and the subsequent acceleration of the piston into a chamber, where the pre-compressed propellent gas resides.

$$V_{max} = (\frac{2}{\gamma - 1})\sqrt{\gamma \frac{P}{\rho}} \tag{2.2}$$

From equation 2.2, where V_{max} is the maximum projectile velocity ($\mathrm{m\,s^{-1}}$), γ is the specific heat ratio of the gas, P is the gas pressure (Pa) and ρ is the gas density ($\mathrm{kg\,m^{-3}}$), it can be seen that low density gases compressed to high pressure will allow the highest projectile velocity to be achieved *(Doolan 2018).* For this reason most hyper-velocity shots use hydrogen and helium as the compressed initial gas to achieve shots at 7 $\mathrm{km\,s^{-1}}$. Higher density gases such as nitrogen may also be used in LGG operation for those shots requiring lower velocities.

Unlike other hyper-velocity acceleration methods mentioned, LGGs are capable of accelerating mm and cm sized projectiles of regular and (through the use of sabots) irregular morphology.

2.3.2 The Kent LGG Design

The Kent LGG is a two stage LGG, made up of 7 main parts: the Powder Chamber, the Pump Tube, the Central Breech, the Launch Tube, the Blast Tank and the Target Chamber (see Figure 2.8). Each of these sections is explained in more detail below.

Powder Chamber At the one of end of the gun sits the powder chamber (labelled '2' in Figure 2.8) in which is placed a powder cartridge. Upon firing, a pendulum is released which impacts the firing pin, igniting the priming powder; the initial firing process is similar to that used in the ignition of powder in handguns. The amount and type of powder added to the powder chamber varies depending on the shot characteristics required, with faster burning, more energetic powders providing more energy to the piston in a shorter time period, resulting in a greater piston velocity and therefore greater compression of the gas contained in the pump tube and, ultimately, greater acceleration of the projectile.

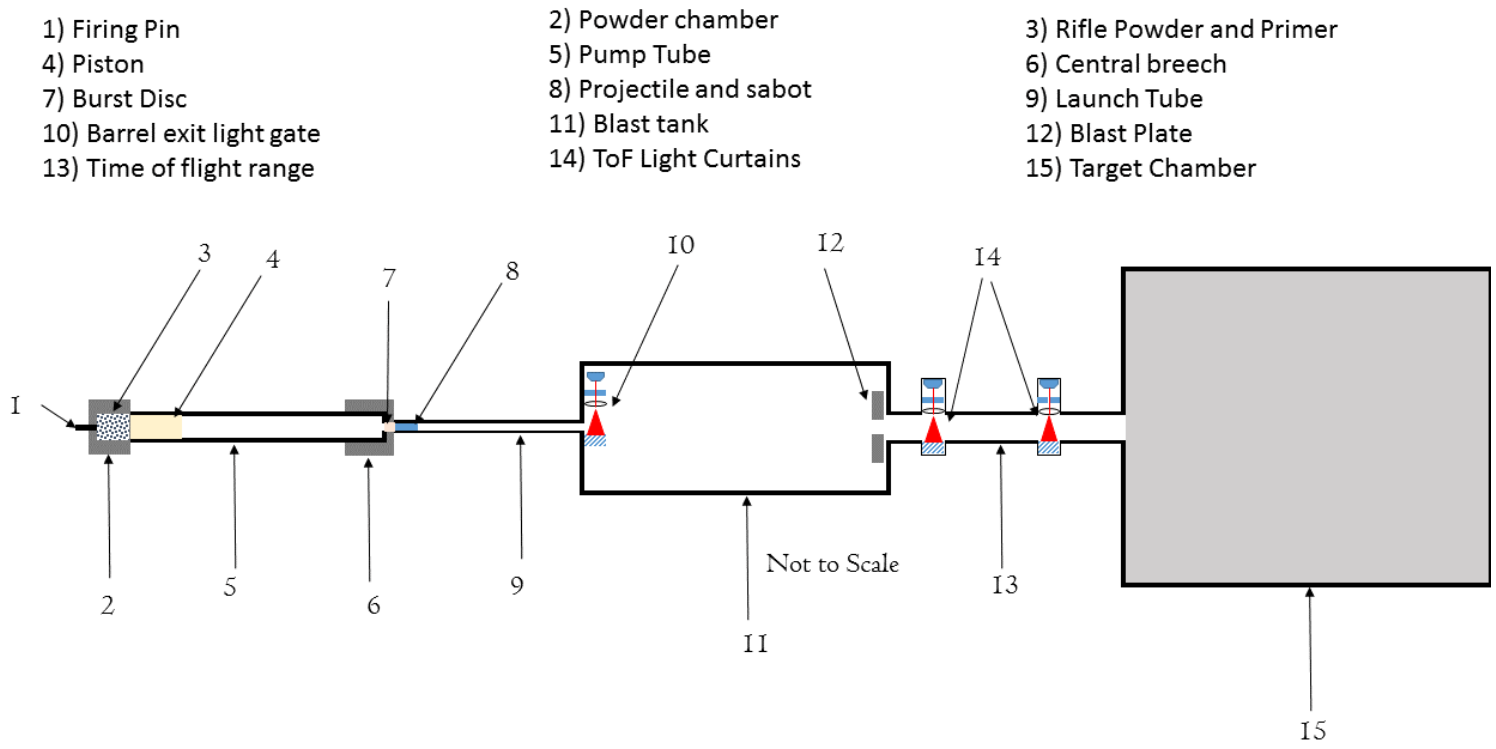


Figure 2.8: Showing the configuration of the main component parts of the Kent LGG prior to firing.

Pump Tube Connected to the powder chamber is the pump tube (labelled '5' in Figure 2.8). The pump tube is sealed at either end via a burst disc at the down-range end and the piston of the gun at the up-range end. For single stage operation, the accelerating gas is added until it reaches the required pressure to breech the burst disc and then accelerate the projectile. For two stage operation, the gas is added until it has reached the required operating pressure, however, the internal pressure is not high enough to break the burst disc and thus the additional pressure provided by the powder accelerated piston is required to burst the disc and fire the gun.

The burst discs are comprised of either metal or plastic, and are either scored or solid discs (plastic burst discs are unscored and for single stage shots only). Several burst discs are shown in Figure 2.9. They are cut to a thickness such that they are breeched when the propellent gas reaches a certain pressure. The thickness of a burst disc for a given pressure depends on the characteristics of the gun.

Central Breech The central breech consists of a 57 mm thick by 101.8 mm long stainless steel section used to join the pump tube and the launch tube via overlapping the ends of both (See Figure 2.10). The breech acts as a funnel, channelling the pressurised gas down the narrow launch tube from the wider pump tube. Due to the reduction of width of the barrel in the breech, the breech also captures the firing piston, preventing it from impacting onto the target. Due to the high pressure experienced by the breech during firing, it is covered with a collar serving the dual purpose of holding the three components together and, in the unlikely event of the breech experiencing catastrophic failure, containing debris.

Launch Tube and Blast Tank Down-range of the pump tube is the launch tube. It is connected to the pump tube via the central breech and connects the pump tube to the blast tank and target chamber. Prior to firing the projectile is positioned at the start of the launch tube in a sabot. The sabot ensures a 'snug' fit of the projectile within the launch tube, limiting the amount of gas escaping around the edges. Sabots used in the course of this thesis were quartered Isoplast 202EZ cylinders. The sides of the launch tube are rifled to impart a spin on the sabot, providing angular momentum to the projectile (the effects of which improve the accuracy of the projectile) and a method for the separation of the sabot from the projectile in the blast tank. Prior to firing, the launch tube and subsequent components further down range are evacuated of air.

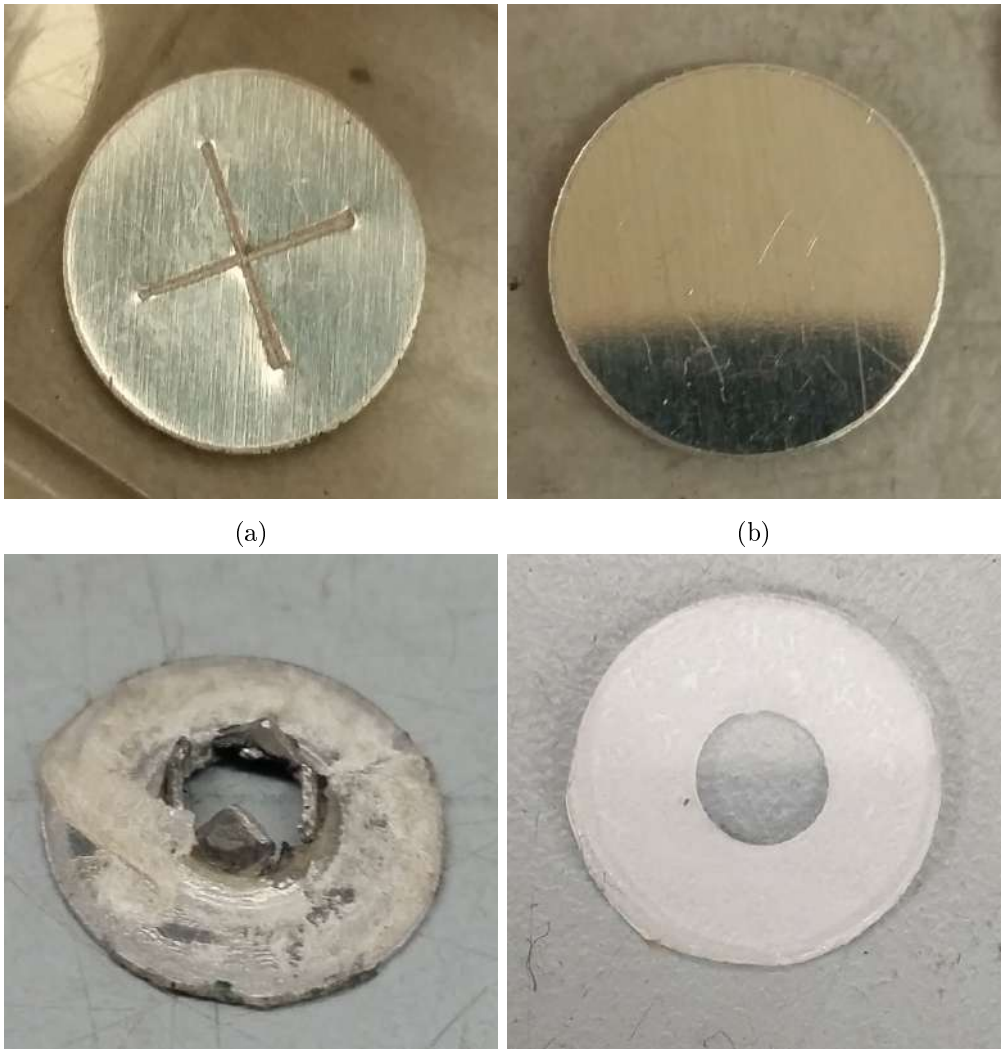


Figure 2.9: Showing a collections of burst discs a) a scored metal burst disc, b) a unscored burst c) a fired scored metal burst disc d) a clear plastic burst disc.

The blast tank consists of a flight area considerably wider than the launch tube. The aperture at the end is of a similar size to the launch tube, and is protected by a stop-plate. Due to the rotational energy given to the projectile from the rifling in the launch tube, the sabot pieces spin off-axis typically at about 6^o *(Burchell et al. 1999)* and impact the stop-plate situated over the blast tank exit aperture (see Figure 2.11), while the projectile itself continues and passes though the aperture into the Time-of-Flight (TOF) range and finally the target chamber.

Target Chamber The target chamber is a carbon steel chamber measuring $1.14 \times 1.14 \times 1.15$ m. The chamber is accessed via the rear door which measures 1.14×1.14 m,

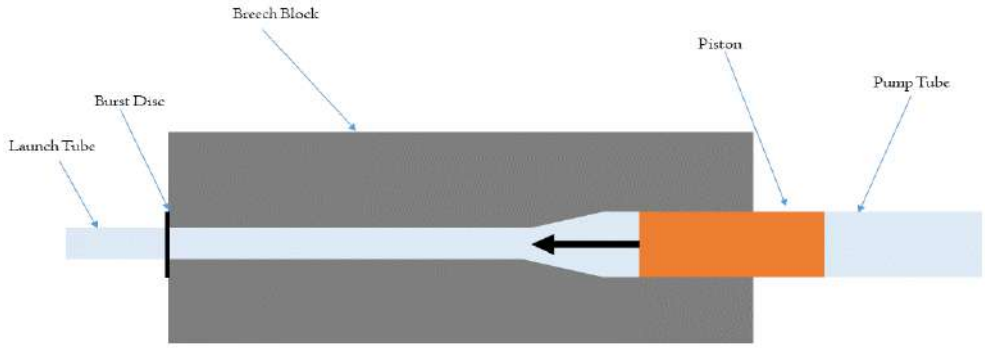


Figure 2.10: Showing the layout of the central breech used to connect the pump tube and the launch tube in the Kent LGG

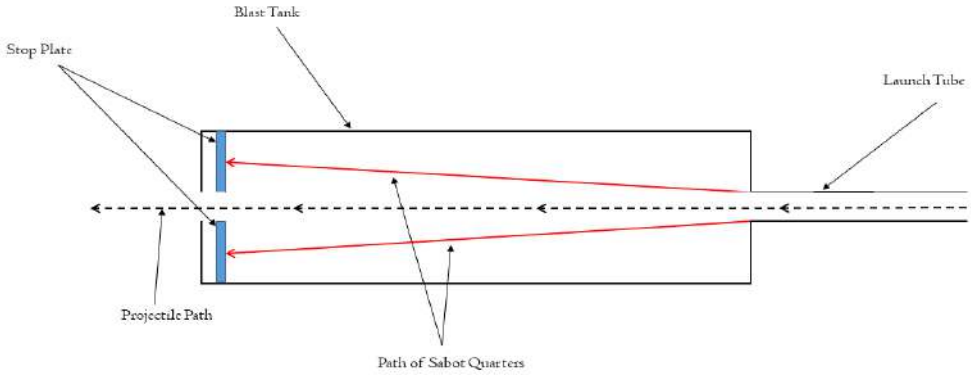


Figure 2.11: Showing the flight paths of the projectile and sabot parts inside of the blast tank at the end of the launch tube

allowing for precise alignment and positioning of the target (see Figure 2.12). Targets can either be fixed to the chamber door via a mounting plate in line with the barrel aperture, or positioned free standing in the centre of the chamber. The chamber has two viewing ports attached on the rear and left hand side of the chamber. Cameras can be aligned to these viewing ports to enable filming of the impact. Additional lighting inside of the chamber can be provided via torches or a halogen lamp powered through an auxiliary port. The target chamber is evacuated prior to firing down to a maximum pressure of 5000 Pa.

2.3.3 Gun Firing Procedure and Shot Analysis

Upon firing of the gun, the propellent in the cartridge is ignited, forcing the piston sealing the end of the pump tube to compress the pump tube's volume and thus increasing the pressure of the gas contained within. Once the gas reaches a critical pressure, the

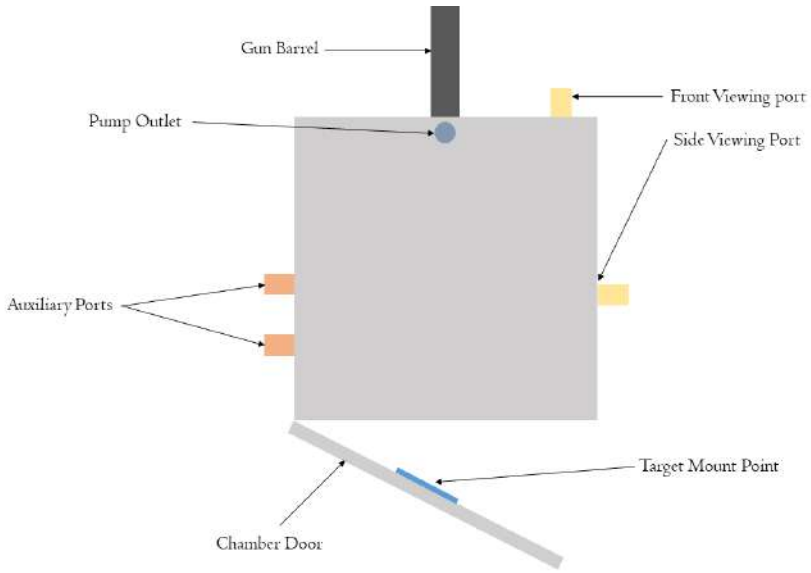


Figure 2.12: Showing the layout of main feature of the target chamber used with the Kent LGG.

burst disc sealing the down-range end of the pump tube ruptures, allowing the gas to escape down the launch tube, propelling the projectile in front of it. Upon reaching the end of the launch tube the barrel widens into the blast tank with the sabot falling away from the projectile at the centre of mass due to the centripetal forces imparted on it by the launch tube rifling.

Velocity Recording The passage of the projectile is recorded in four different places along the barrel of the gun: once by a light gate situated at the exit of the launch tube (the muzzle detector) and twice more by two light gates between the stop plate and the target chamber (the TOF range). The blast tanks stop plate is also equipped with a polyvinylidene difluroride (PVDF) sensor, which vibrates when the plate is impacted, the vibrations produce an electric current which is passed onto an oscilloscope. This allows the PVDF sensor to measure when the projectile has past from the vibrations created by the impact of the sabot segments.

The light gates on the TOF range consist of two 607 nm wavelength light curtains created via two 3 mW laser diodes *(Burchell et al. 1999)*. The light beam is focused through a barrel lens and passed through a subsequent slit to produce a thin light fan. The light fan is then passed through the TOF range and back onto another barrel fan which refocuses the light into a smaller beam and onto a photodiode. In this way the projectile passing through the beam results in a drop in light intensity which can be

measured via the output of the photodiode circuit, and displayed via an oscilloscope. The time between the two drops in light intensity, along with the known distance between them (49 cm) allows for the calculation of the projectile's velocity to within better than ±1%. The light gate situated on the TOF range gives a much better constrained projectile velocity than that given by the PVDF sensor and the muzzle detector, however for projectiles which impact off-axis the two earlier detectors (PVDF and muzzle) provide the only velocity measurement.

2.3.4 Summary

In this thesis the LGG will be used to attempt to simulate the entry velocity of extra-terrestrial particles entering the atmosphere. This involved using the LGG in both two stage and single stage firing configurations. The firing conditions for each shot, resultant velocities and results can be found in the relevant sections (Chapters 6, 8 and Appendix J).

2.4 Other Analytical Techniques Used in this PhD

2.4.1 Raman Spectroscopy

2.4.1.1 Operating Principles

Raman spectroscopy operates via the inelastic scattering of optical photons interacting with electrons in a sample. In normal Rayleigh scattering, photons interact with the molecule, raising electrons to higher virtual energy states. These states are unstable and short lived, with the excited electron dropping back to its stable state by the re-emittance of the photon resulting in photons being elasticity scattered.

In Raman scattering, however, it is the resultant nuclear motion inside of the molecule which is induced by the alteration of the electron cloud caused by the electron transition to a virtual state. As nucleons are significantly more massive than electrons, this rearrangement absorbs energy from the photon, meaning when the photon is re-emitted, as the electron falls back to its stable state, the final energy of the photon is less than it was originally *(Dent and Smith 2004),* this is called Stokes scattering. In cases where the electron was already in an excited vibrational state, it is possible for this reconfiguration to result in the electron falling back to its ground vibrational state, this results in the re-emitted photon having an energy above that which it had originally.

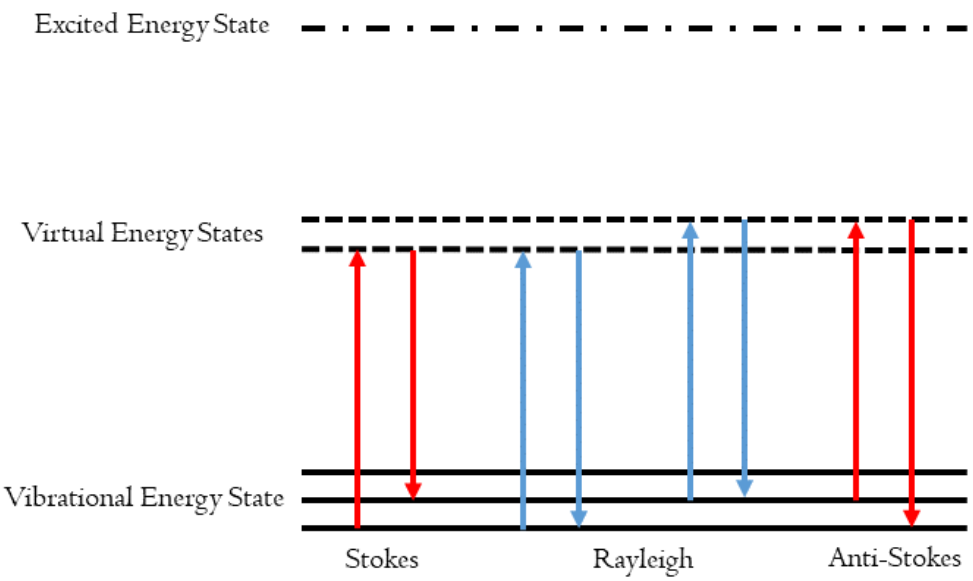


Figure 2.13: Rayleigh and Raman Stokes and anti-Stokes processes.

This is called anti-Atokes scattering (see figure 2.13). Raman scattering only occurs in $10^6 - 10^8$ interaction events and thus is far less common than Rayleigh scattering *(Larkin 2018)*.

The bonds between atoms inside of a structure all vibrate at a given frequency. This frequency is governed by the bond strength, and the mass of the bonded system. This can approximated to Hookes Law as shown in equation 2.3 *(Dent and Smith 2004)*.

$$f = \frac{1}{2\pi c}\sqrt{\frac{K}{\mu}} \tag{2.3}$$

Where f is the frequency of the vibration (Hz), c is the speed of light ($\mathrm{m\,s^{-1}}$), K is force constant of the bond (a measure of bond strength) and μ is the effective mass of the system (kg) and is given by equation 2.4.

$$\mu = \frac{M_1 M_2}{M_1 + M_2} \tag{2.4}$$

Where M_1 and M_2 are the masses of the bonded atoms (kg). Each bond environment therefore will vibrate at different energies which can be used to identify it. Combined, all the bond environments in a sample will give a characteristic spectra, which if the composition is well constrained, can be used to identify the bond structure.

Raman instrumentation relies on the use of monochromatic light to provide the photons needed to induce the excitation of electrons in the sample. After interacting with the sample, the emitted photons are collected via a Charged Coupled Device (CCD). As the energy of the photons are known before the interaction, any photons collected via the CCD with energy different to the excitation energy must have experienced Raman scattering. Due to the weakness of the Raman scattering, the scattering is often recorded over a large accumulation time. Any photons with energy the same as the initial energy (Rayleigh scattered photons, or reflected light from other sources) are filtered out. This is primarily achieved by the use of edge and notch filters which filter out radiation of the incident light and, in the case of edge filters, the anti-Stokes scattered photons *(Dent and Smith 2004; Semrock Inc 2019)*.

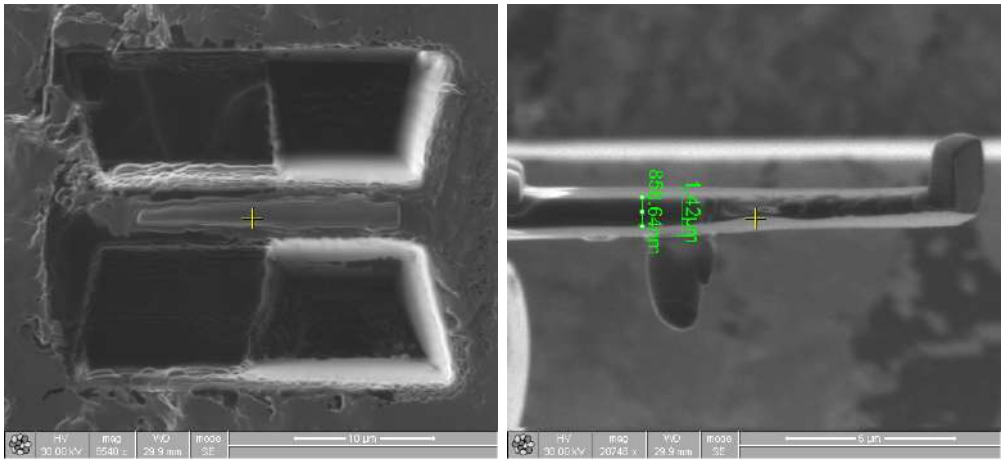
Raman spectrometers can also make use of mechanical stages to provide a mapping utility similar to that provided by the SEM. By rastering the beam position over the surface of the sample, large scale spectrograph maps of the sample can be recorded.

2.4.1.2 Summary

In summary Raman spectroscopy is a non-destructive method for gaining information on the bond structure of samples. Raman spectroscopy can be used to identify most changes which affect changes in the bonds of the sample, for example: phase changes in minerals, the heterogeneity of a sample, mineral compositions, changes in the crystallinity of a sample, and changes in composition. Raman spectroscopy provides a method for the examination of the atomic structure of a sample and provides complementary information to SEM evaluations of macroscopic structure.

2.4.2 Focused Ion Beam

This thesis has also made use of Focused Ion Beam (FIB) microscopy to image and mill samples for subsequent Transmission Electron Microscope (TEM) analysis. FIB operates on a similar principle to SEM, however, as opposed to using electrons to construct the beam, ions are used from relatively heavy atoms (often gallium) *(Volkert and Minor 2007)*. The interaction of the ions with the surface of the sample produces secondary electrons allowing imaging to occur. The much heaver ions produced are also able to strip atoms from the observation area in a process known as sputtering; as atoms are removed, the sample can be cut, or thinned on the sub-micron scale in a process referred to as milling. In addition to the removal of atoms from a sample, most FIBs



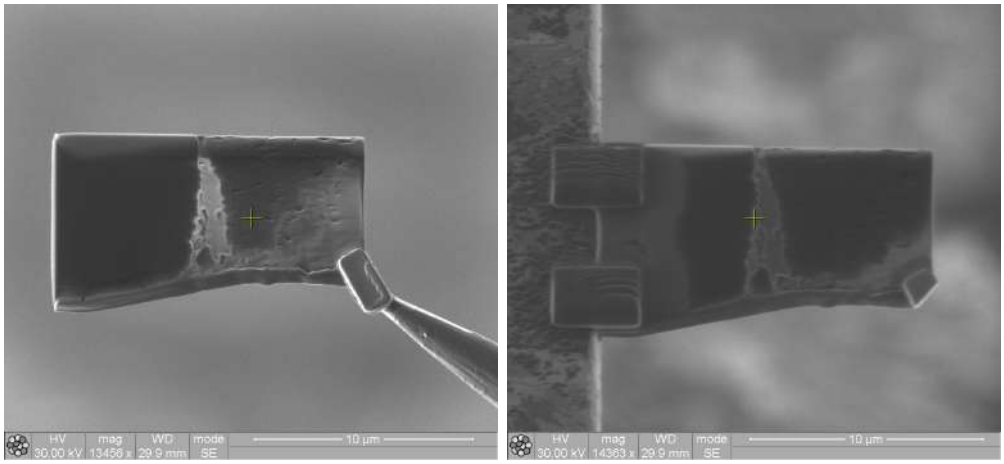
(a) (b)

Figure 2.14: Images showing the two main FIB cutting techniques used in this thesis a) cutting a thin sample out of large sample. b) milling a sample down to nano scale for TEM analysis.

are also capable of depositing atoms onto the surface of the sample (e.g. protective Pt coatings) *(Volkert and Minor 2007)*. The atoms are normally added to the chamber in a gaseous form and melded onto the surface of the sample in the beam interaction area.

To enable the removal of a thin section (lamella), the sample is milled step-wise on the left and right of a section resulting in a 10-50 µm thick pre-lamella. Prior to cutting a protective coating of platinum is added to top surface of the area to be cut away to protect it. Once the sample is cut to the correct thickness, the sample can then be tilted to a more extreme angle allowing additional material to be cut from the bottom and one edge of the sample, resulting in the section being held in place along a single edge. The sample is then attached to a micromanipulator via the depositing of atoms onto the sample and manipulator tip (the choice of deposited material is dependant on the sample). Once the sample is held by the manipulator, the final edge can be cut free. The sample is normally cut free whilst thicker than the final desired lamella, to reduce the chance of the sample breaking during the final cut and removal. The sample is then welded in place to a FIB/TEM grid where it can be thinned by removing additional material from the sides.

In summary FIB provides a method for imaging samples using produced secondary electrons in a similar process to SEM. FIB also allows the manipulation, cutting and attaching of samples on a nanometre scale, allowing for large to undergo TEM analysis.



(a) (b)

Figure 2.15: Images showing the a) the pre-lamella attached to a needle point Micromanipulator. A rectangular carbon atom deposition can be seen holding the lamella to the needle point b) a lamella attached to a TEM grid edge via two carbon atom depositions. The layers of the raster deposition can clearly be seen along with the remains of the deposition used to attach it to the micromanipulator.

2.4.3 TEM

The Transmission Electron Microscope (TEM) utilises an electron beam created in a similar fashion to those created for normal SEM usage. TEM, however, utilises much higher accelerating voltages, typically in the 100 kV - 300 kV range, providing a smaller electron wavelength *(Thermo Fisher Scientific 2019).* Unlike SEM, where the interaction with the sample surface is observed, TEM passes the electron beam through the sample with the transmitted electron being detected on a CCD underneath. Most TEM analysis consists of so called bright-field images. In these images areas of lower density appear brighter as a larger proportion of the beam is able to pass through. Conversely areas of higher density will appear darker as less electron were able to be transmitted. Bright field images are exceptionally dependant on the thickness of the sample, as an uneven sample will result in changes in the transparency of the lamella. TEMs are also able obtain the diffraction patterns of samples, this is performed by allowing the electron beam to be diffracted by the crystals inside the sample. Diffraction is able to be performed in both 2-D and 3-D.

2.4.4 Summary

FIB provides a accurate and consistent method for the preparation of samples for TEM analysis. Whilst FIB is itself able to perform analytical methods, these have not been discussed here, as they have not been used in this thesis. TEM provides a method for the analysis of the internal structures of samples, providing data on lattice lengths and crystallinity. Unfortunately this thesis has only briefly used the above methods for analysis, due to time constraints and equipment availability only selected sample were able to be analysed. This is described in more detail in the relevant sections.

Part II

Results Part A: Studies of Micrometeorites from Collections

Chapter 3
Collection of Micrometeorites from Kwajalein and the British Antarctic Survey

3.1 Collection of Particles

The samples of micrometeorites examined during the course of this PhD were collected from two locations; the Kwajalein atoll in the mid-pacific (8^{o}43'10.0"N 167^{o}43'35.1"E) ('Kwajalein collection') and the clean air Laboratory of the Halley VI Research Station (75^{o}34'02.4"S 25^{o}30'59.2"W) ('British Antarctic Survey (BAS) collection'). These locations were chosen due to their distance from regions of intense human activity and associated contamination: Kwajalein is over 1000 km from the nearest continent and for much of the year trade winds blow over the Kwajalein atoll providing a steady, unidirectional supply of clean ocean air. As an atoll it structure is mostly coral with soils produced from coralline sands and limited basaltic contributions *(Inc. 2010),* however additional building materials were flown in to construct the military base and surrounding housing. For the BAS collection, the collector was placed in a purpose built clean air sector laboratory, located 1 km up-wind of the research station. The position on the brunt ice shelf, ensures that it is upwind of any nunataks which could produce dust and positioned well away from locations of human habitation. In both cases, samples were collected from the air using high volume air samplers ensuring that the particles themselves were only exposed to a short, limited period of terrestrial weathering. Sampling duration was 1 week per filter with a flow rate of 1 $m^3\,min^{-1}$.



Figure 3.1: The Kwajalein micrometeorite collector in position on the Kwajalein atoll. The breeze blocks are to hold the collector in position.

3.1.1 The Collector

The collection mechanism works via a pressure differential across the filters and is created via a small pump housed inside of the collector casing. The casing consisted of a 0.6 metre high hollow box, attached to 0.5 metre legs. The pump was positioned within the housing so that the outlet was 1 metre above the ground (for structural diagrams of the housing see Appendix G.1). The air being sampled was sucked through the gap between the roofing of the housing and its main body, and drawn down into the casing, passing through a laser etched membrane filter which sifted the particles from the air. The roofing protected filters from direct accretion of very large particles and debris (e.g. leaves) and also provided protection for inclement weather conditions which could wash and blow away particles already situated on the filter (see Figure 3.1).

Due to the limited exposure of the the particles collected in this manner (they have zero residency on the surface being directly sampled during their descent) it is hoped that the weathering the particles experience should be significantly reduced. Unfortunately as the particles are collected after their atmospheric deceleration, they will still have experienced the significant heating effects and thus undergone morphological and chemical changes associated with entry.

3.1.2 Kwajalein Collections Overview

Collections of particles were carried out between October 2011 and January 2012 and again from May 2012 to August 2012 with the collector positioned at the airport on the Kwajalein atoll. The collection consisted of 42 filters Numbered 1-36 and a to g. Filters a, b and c remained in the UK/US as controls, filters e, f, g were shipped, but not used and thus used as shipping controls, with the remaining filters being exposed for 1 week intervals in the collector. Following completion of the collection all filters were shipped back to the UK and remained sealed until individual examination.

The Kwajalein collections used 5 µm laser etched PCTE filters for the duration of the collection. Each filter was 203 mm by 254 mm and positioned in an acrylic holder. During transport the holders were topped with two acrylic sheets held in place by bulldog clips in each corner as protection and vacuum sealed in an airtight bag.

The Kwajalein atoll is home to the United States Space and Missile Defence Command (US-SMDC) *(Office 2019c)* and is listed as a launch site for Pegasus rocket launches for equatorial orbit *(Office 2019b)*. As such, despite the lack of human habitation, it was expected that a number of particles would be collected as a result of these activities. A Pegasus rocket launch took place on June 13 2012 corresponding with the 2nd collection run, and taking place during the end of the week of Filter 13 with the week following being covered by Filter 3 *(Office 2019a)*.

Filters were found to contain significant levels of terrestrial contamination, the majority of which was irregularly shaped coral, mineral grains and soot particles (see Section 3.3). Unfortunately due to the propensity of the non-spherical contamination on the filters, it was only possible to examine spherical particles, meaning only CSs were identified. The main source of contamination with a spherical shape similar to that of the CS's was aluminium silicate-rich fly ash.

Additionally, the particles are also being captured in a harsh, tropical, coastal environment that is hot, humid and abundant in salty sea spray. Salty sea water and terrestrial particles are both suctioned through the filter and come into contact with any E.T. particles. Whilst the time in a damp environment is limited, particles may have become contained within the solid salt residues. The effects any such exposure will be considered when analysing the particles in Chapter 5.

In addition to the collection system installed for the University of Kent collection, an identical system installed by Lawrence Livermore National Laboratory survey for air quality control was also used between May 2012 and August 2012 to perform MM collections. Filters in both systems were opened, added and changed at the same time, resulting in two collectors running simultaneously. As such we have been able to analyse two filters covering the same period in some instances.

Due to the high concentration of salt in the air from sea around the Kwajalein atoll, collector efficiency degraded over the course of the collection period. The salt would precipitate on to the filter membrane blocking pores. This had the effect of reducing the flow rate, reducing the collector pressure at the head. As such it is likely that the capture area of the collector and the maximum size of captureable particles reduced over the course of each run. This salt had the effect of sticking the particles to the filter requiring additional preparation when condensing samples.

3.1.3 BAS Collection

Following on from the Kwajalein collections, the BAS collections occurred from the 14^{th} of January 2015 until the 12^{th} of July 2015. The Antarctic location was chosen to reduce the amount of non-spherical contamination present on the filter such as sand, coral and salt as well as a low temperature and low humidity environment. This should have enabled the evaluation of the non-spherical particles captured on the filter membrane. The collector was situated in CASLab, roughly 1 km upwind of the Halley VI Research Station, avoiding particulates created from the station's day-to-day activities (diesel generators, clothing fibre, visiting aircraft etc.) This means that, unlike the collections that took place on the Kwajalein atoll, the BAS returned filters were examined for UMMs and other irregularly shaped extra-terrestrial particles.

In addition, due to the changes in the location, modifications of the collection system were required. The collector used was an existing system used by BAS to perform aerosol analysis and was situated indoors to control the system temperature and facilitate the changing of the filter irrespective of weather conditions. Therefore, unlike the collection at Kwajalein where the collector sucked air directly onto the filter, an inlet was extended to pass outside of the collection building via an aluminium pipe and funnel. This likely had the effect of reducing the head of the system due to skin friction which can be

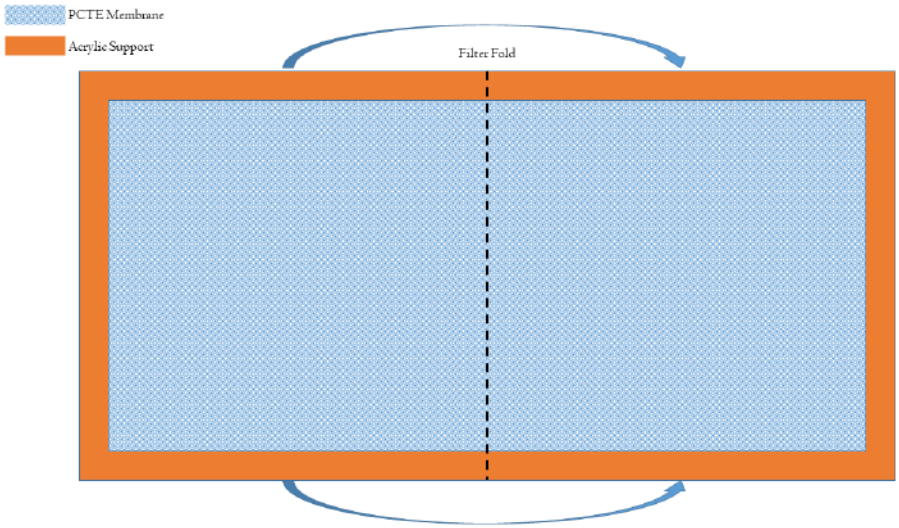


Figure 3.2: The filter assembly for the BAS micrometeorite collections.

calculated via the Darcy-Weisbach equation as shown in 3.1

$$\Delta p = \frac{f_d \cdot \rho}{2D} \cdot (\frac{Q}{A})^2 \cdot L \tag{3.1}$$

where Δp is the total loss of pressure at the head (Pa), f_d is the flow coefficient, ρ is the fluid density ($\mathrm{kg\,m^{-3}}$), D is the internal diameter or hydraulic diameter of the pipe (m), Q is the volumetric flow rate ($\mathrm{m\,s^{-1}}$), A is the cross sectional area of the pipe ($\mathrm{m^2}$) and L is the pipe length (m). Therefore any increase in the length of the air inlet will reduce the inlet pressure, reducing the number and size of particles collected. The condition of the piping is also unknown with a number of aluminium fragments being recovered on the filters, likely originating from the setup.

Due to the lack of salt clogging the filter pores, BAS collections did not suffer the same degradation in flow rate as the Kwajalein filters and ran at a near constant rate throughout the entire collection. As such these BAS filters sampled higher volumes of air than the Kwajalein filters. It was also envisaged that the reduction in salt would result in loose particles on the filter surface and a number of changes where carried out to the filter assembly to ensure no particle loss. Firstly some of the BAS filters were made of 5 µm PETE as opposed to PCTE as was used for the Kwajalein collections. This allowed the washed filters to settle onto the carbon tape on the SEM stubs in a more regular way due to the material's higher resistance to stretching. Stretching was a factor during the Kwajalein collections, with the filters becoming misshapen under the suction pressure during washing (see Section 3.2.1). The change in filter material had no

effect on the collector's efficiency or storage of the filters. The filters were again stored on an acrylic frame, however as the reduction in salt would likely result in particles being able to freely move over the filter surface, for storage the filters were folded with the collection surface contained on the inside (see Figure 3.2) as opposed to between to acrylic sheets as had been the case with the Kwajalein samples.

3.2 Sample Preparation and Analysis

3.2.1 Preparation of the Filters

Following the return of the filters to the UK, the samples were kept in their sealed containers. Initial examination of the filters from Kwajalein showed them to be coated in salt; precipitated out from captured sea spray and had solidified into a solid coating 'glueing' down any other collected particles. Therefore, prior to examination, the filters where washed to remove the salt from the surface and to condense the particles into a smaller, easier to examine area (a circular region roughly 20 mm in diameter). The washing procedure was carried out in a clean environment: inside a laminar flow cabinet cleaned with acetone soaked, lint-free cloths. The washing procedure consisted of raising the filters with exposed side up and applying 3 litres of room temperature High Performance Liquid Chromatography (HPLC) grade water to dissolve the salt. A suction cup was positioned on the underside (non collecting side) in the centre of the filter. Suction was applied to create a depression in the filter into which the water could flow (bringing with it any captured particles) and also to pull the salt water through the membrane, as the the filter was not porous enough to allow the water to flow through naturally (see Figure 3.3).

The washing procedure unfortunately resulted in a number of negative effects. The first of which was the stretching of the PCTE filter membranes caused by the suction applied to the small central area. For the BAS filters, which were stored folded in half, this central area already contained a significant crease, thus the additional suction applied here resulted in the the membrane stretching, exacerbating the deformation. When the filter was allowed to settle, these creases often appeared in the settled sample as a ripple along the surface of the sample (see figure 3.4). As such the final sample was not flat which made mapping surveys problematic due to the changing focus. Additionally the edges of the suction cup sometimes created ridges in the filter during washing, as such it caused a build of particles along these edges resulting in a 'tide mark' of high particle density.

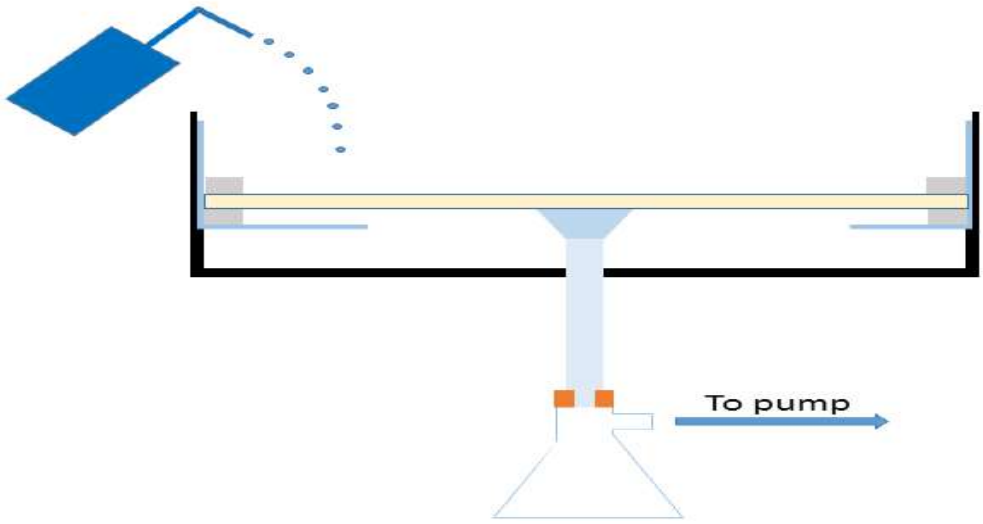


Figure 3.3: Showing the setup for the washing procedure for filters collected in Kwajalien and Antarctica. Filters collected in Kwajalien used a smaller sized suction cup than the one shown in the image.

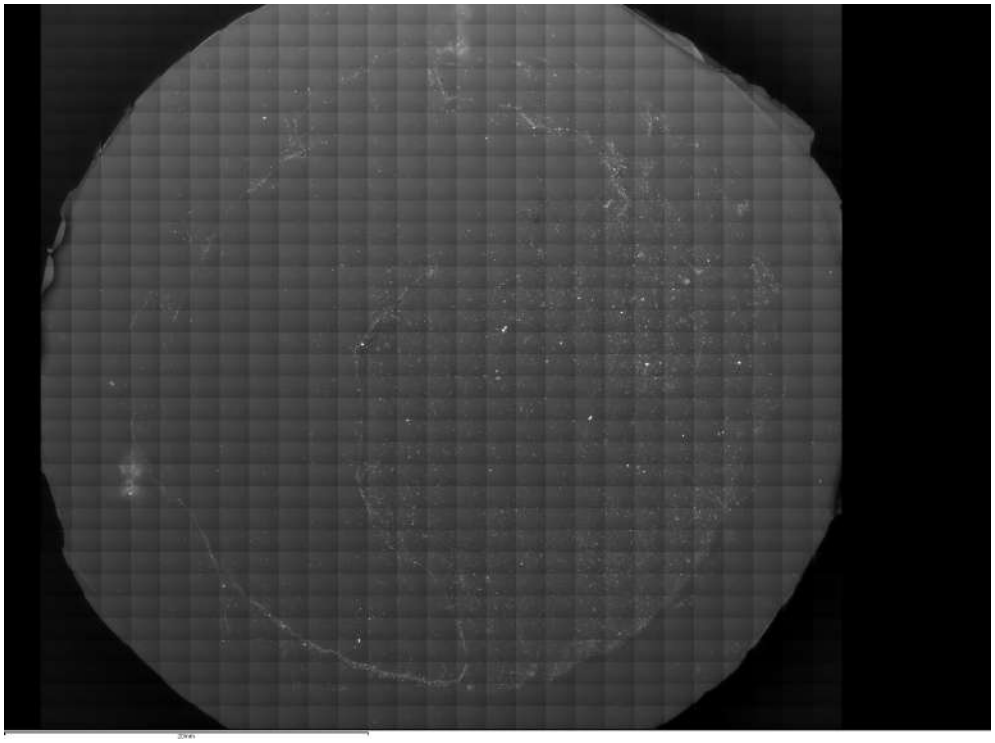


Figure 3.4: Kwajalein Filter 8 attached to an SEM stub. The tide mark caused by the washing procedure can clearly be seen, along with the ripple caused by filter stretching produced by the suction cup.

Following washing, the filters were positioned above a 52 mm diameter aluminium SEM stub so that the condensed region of particles was central to the stub and allowed to settle onto it while drying overnight, with desiccant cartridges placed in the flow cabinet to speed up the drying process. The 52 mm stub was significantly wider than the condensed area on the filter, ensuring all collected particles remained. To prevent the filters from shifting they were attached to the stub via double sided carbon tape. The filters were cut around the edges of the stub, with the remaining 'cleaned' filter being placed back into the sealed bag in which it was transported. The SEM stub with the attached filter section was placed inside a cleaned sample box and then placed inside a desiccator cabinet.

Due to the large number of total filters exposed, and the large area of each (despite condensing), in both the Kwajalein and BAS collections, we were unable to examine every filter, as such we chose to examine four filters from the Kwajalein atoll in conjunction with five previously examined filters to give a roughly two month overview of particle flux. We also chose to examine four filters from the BAS collections which correspond to the same time of year the Kwajalein filters were exposed, or to unusual solar system events such as cometary passes. The details of these filters and the dates ran are given in Table 3.1.

3.2.2 Surveying Filters

Once prepared, candidate MMs were identified on the condensed filters by collecting automated image maps which were searched frame by frame for particles of interest. Filters were analysed using a Hitachi SN-3400N SEM using automated BackScatter SEM imaging at 75x magnification ('zoomed out'), providing an overview of the particles of interest's locations over the entire filter (see Figure 3.5). During mapping and subsequent analysis of the filters, to reduce the charging of the particles on the filter, the VP-SEM conditions were set at 150 pascal. Due to the small size of the particles and high vacuum pressures, the voltage was set to 20 kV with a working distance of 10 mm(which is the EDX detector's optimal working distance). Mapping of the filters was carried out using Oxford Instruments Inca and Aztec software.

In order to ensure that all particles down to a size of roughly 5 µm were identified, a magnification of 500x with a frame size of 1024 by 768 pixels was adopted ('zoomed in'). At this magnification, manageable file sizes limited the mapping areas and in order to cover each filter from centre to tide mark, more than 30 individual overnight maps

would be required. Consequently, in order to speed up the process and have sufficient equipment time to analyse multiple filters, only a quarter of each filter was mapped, for each filter studied. The maps were all located in the top right quadrant of the filter with roughly nine 'zoomed in' maps taken per filter (due to the increased maximum maps size allowed by Oxford Instruments Aztec, only eight maps were collected for filters exclusively analysed by Aztec). Large terrestrial particles identified in the 'zoomed out' maps were used as locations for the anchoring of the 'zoomed in' maps. These maps were made of between 400 and 1200 frames, with each frame overlapping by ten pixels and consisting of 3 images averaged together to increase the signal-to-noise ratio. Following the completion of each map the frames were montaged together, with frame alignment carried out by eye.

Following the completion of a map, each frame was examined for any spherical or partly spherical particles. Abnormally shaped particles, and particles of differing contrasts (reflecting density) from common background contaminants were also identified as possible IDP or FgMM-like particles. This process was carried out manually, via visual inspection of the frames of the map. The use of coded solutions was not practical due to the high amount of terrestrial contamination, which would have resulted in either a large number of false-negatives, with multiple partially spherical, or partially covered or contained particles being missed, or a large number of false positives with many contaminants being included. The location of particles identified in the process were recorded for future examination. Whilst it was not possible to use absolute coordinate systems for the location, it was possible to use the relative locations to other objects to re-identify these particles at a later date. To ensure that particle identification was consistent across filters (which had been mapped by different researcher: Dr Wozniakiewicz and the author), two maps were analysed independently by the author and Dr Wozniakiewicz and results showed that no additional extra-terrestrial candidates were identified by either researcher.

Table 3.1: The location filter material and examiner of the the filters from the BAS and Kwajalein MM collections.

Filter Number	location	examiner	filter type	Start Date	End Date	Notes
K04	Kwajalein	Previous work	PCTE	17/05/2012	24/05/2012	
K09	Kwajalien	This Thesis	PCTE	24/05/2012	31/05/2012	
K08	Kwajalien	This Thesis	PCTE	31/05/2012	07/06/2012	
K13	Kwajalien	Previous work	PCTE	07/06/2012	14/06/2012	NuStar launch on 13/06/2012
K03	Kwajalien	Previous work	PCTE	14/06/2012	21/06/2012	Week Following NuStar launch
K10	Kwajalien	Previous work	PCTE	21/06/2012	28/06/2012	
K11	Kwajalien	This Thesis	PCTE	21/06/2012	28/06/2012	
K12	Kwajalien	This Thesis	PCTE	06/07/2012	14/07/2012	c-Andromedids
K06	Kwajalien	Previous work	PCTE	14/07/2012	21/07/2012	
K05	Kwajalien	Previous work	PCTE	03/12/2011	09/12/2011	
K07	Kwajalien	Previous work	PCTE	19/07/2012	26/07/2012	
B14	Antarctica	This Thesis	PETE	14/04/2015	20/04/2015	
B15	Antarctica	This Thesis	PETE	01/06/2015	08/06/2015	
B16	Antarctica	This Thesis	PETE	15/06/2015	22/06/2015	
B17	Antarctica	This Thesis	PETE	07/07/2015	14/07/2015	

Once candidates were identified, the sample was placed back into the SEM, and additional analyses (higher resolution images and EDX) of the particles was performed. As the filters were not always perfectly flat, any particles which appeared out of focus, but were potentially spherical on the original automated map frames, were also checked. The particles were imaged at a higher magnification allowing details of their surface to be observed. Any spherical particles, or particles which showed evidence of non-terrestrial morphology (e.g. apparent fusion crust) were imaged with EDX spectra taken, and were noted, for picking and future SEM analysis. Details of the picked particles along with their additional analysis images can been seen in Chapter 5.

Testing of the washing procedure on clean unused filters had shown no spherical contamination during the washing process. Similarly analysis of the control filters also showed little, to no, sign of contamination for preparation. In both cases any contamination was limited to fibres clearly not of E.T. origin and far larger than the expected sizes of the particles on the collection filters.

3.2.3 Picking and Preparing Candidate Micrometeorites

Candidate MMs identified for future analysis required picking, embedding in resin, and polishing such that flat surfaces were produced to facilitate quantitative EDX analysis. A number of particles were identified for further study on each of the filters, and these were picked from the filter using a superfine eyelash brush, coated in a small amount of glue. The glue was taken from a small piece of adhesive tape by carefully swiping the hair across its surface until a small coating was positioned at its tip. The picked particles were placed on a sheet of the identical adhesive tape stuck on one side to a clear plastic plate. The double side tape also had 4 pieces of pure copper wire positioned on it in the form of a set of cross hairs, to aid in locating the particle during polishing and analysis (the particle was placed in the centre of the copper cross hairs, see Figure 3.6).

The use of double sided tape, as the adhesive method for the picked particles, had been previously selected following a series of experiments. These experiments aimed to identify the best method for the preparation of the picked particle in a resin block, and, as such, focused on how well the adhesive held the particle in place, reacted with the resin (e.g. produced bubbles, did not remain stuck), and released the particle after it had been embedded. This aimed to reduce the amount of bubbles observed in the resin post-setting, and making the removal of the resin block from the adhesive easier and

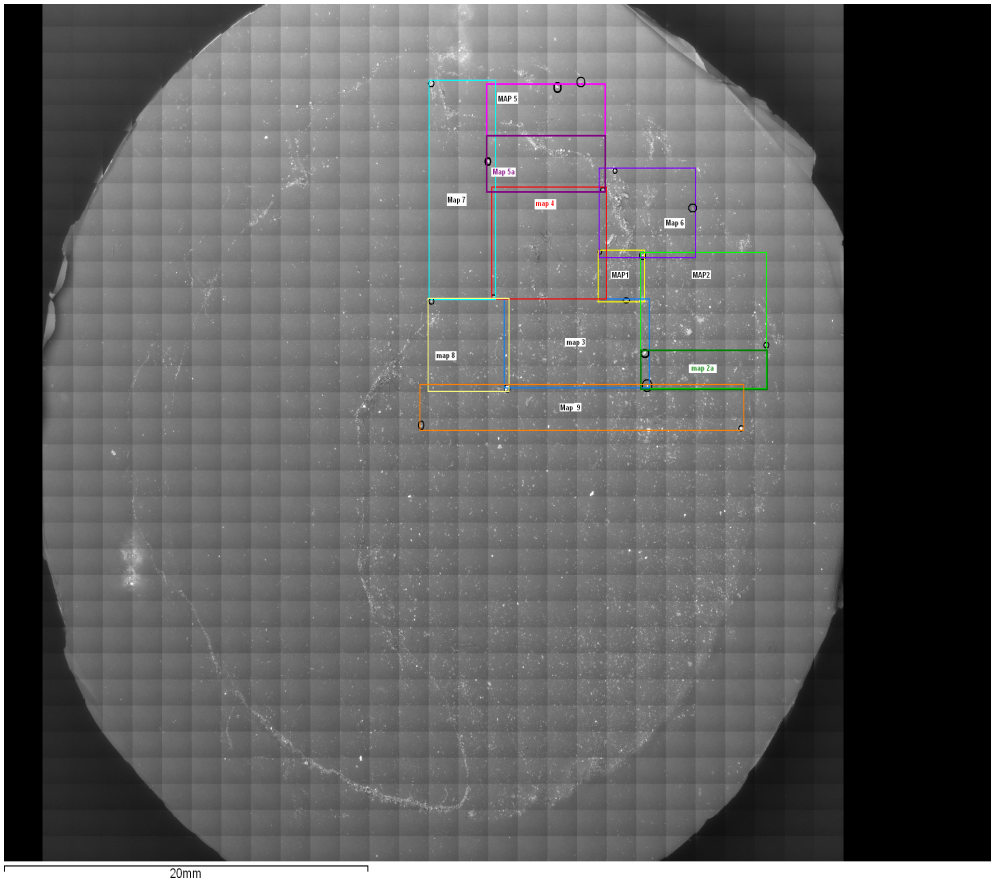


Figure 3.5: Showing the location of 500x magnification, 'zoom in', maps on the 75x magnification, 'zoom out', map of filter 8.

without leaving the particle behind (e.g. plucking from the resin).

These tests consisted of two different resin types (1: Buehler 'epo thin' and Struers 'specifix 20'), three different methods for sticking particles down (1: carbon tape (CT) which had been previously used, 2: double sided tape (DST), and 3: a layered method of CT and DST) along with several curing methods (1: baking the DST prior to embedding to remove bubble-producing volatiles that may be given off during heating and 2: setting the resin under vacuum conditions in order to try and pull the bubbles out of the solution) and two resin application methods (1: applied normally and 2: a small application over the particle which was allowed to set before the remaining resin was applied). The results of these test were that Struers 'Specifix 20' applied onto untreated DST with normal application produced the best result. The full results can be seen Appendix A. Following its positioning on the double sided tape the picked candidate was embedded in resin. The resin block was made by filling a mould sealed at one end by

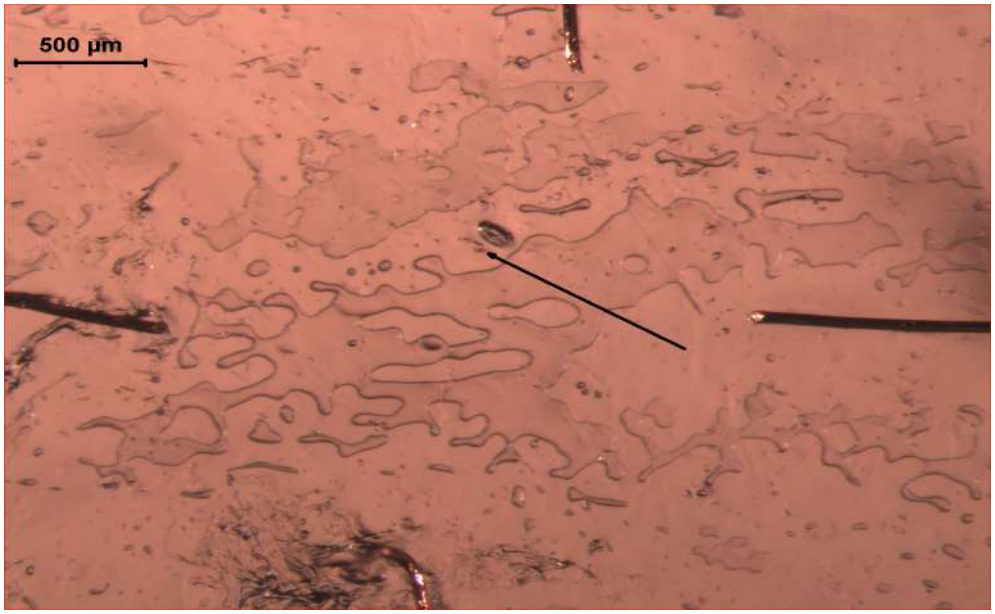


Figure 3.6: A picked MM taken from F8-M7 shown in position on the double sided tape between the copper wire cross hairs.

the clear plastic plate. This seal was created by applying Blu-tac to the joint between the mould and the stub around the outer wall of the mould which was held in place by the DST layer. Prior to it being sealed to the SEM stub, the inner wall of the resin mould was coated in a silicone oil release agent to allow the removal of the resin block without damaging it. The resulting resin block was prepared for SEM analysis via the removal of excess, uneven material from the back of the block by diamond saw and polishing of the resin block's surface via diamond paste. Polishing was carried out by progressing from 3 µm to $\frac{1}{4}$ µm diamond paste to reveal the mm's interior (continuing until approximately $\frac{2}{5}$ of the way through the MM). As the samples were so small, only a few minutes of polishing at each grade was required to expose the particle's interior.

The cut and polished embedded particles were then attached to aluminium SEM stubs using carbon tabs, before carbon coating and applying conductive copper tape to reduce charging (as quantitative EDX was required, VP mode could no longer be used as charge control on the samples). These were then studied by SEM for a second time obtaining higher resolution images of the interior of the particles (setup: high vacuum with a 10 mm + 0.2 mm working distance at 20 Kv accelerating voltage). The exact SEM conditions including beam current used to quantitatively analyse each of polished MMs are given in Appendix F.

3.3 Terrestrial Particles on Filters

It had been envisaged the location of the collections on Kwajalein atoll and in Antarctica would minimise much of the contamination caused by human activity. Whilst the collector filters (particularity the BAS filters) showed reduced levels of contamination, all filters showed signs of contamination from a variety of sources.

3.3.1 Fly Ash

Fly Ash (FA) is made up of small particles produced during combustion. Originally named for those particles which 'fly' up the stack in power plants (as opposed to bottom ash which remained in place), the name has been extended in general use to include the majority of small exhaust particles, such as those produced by oil and diesel combustion. The majority of FA, however, is produced by the coal burning process. As such the phrase 'fly ash' has come to have two meanings, in this thesis the acronym FA will be used to describe any anthropogenic produced dust as it is commonly used in most parlance, while *fly ash* will be used when describing particles only emitted from powerplant stacks in-line with the term's original definition.

In general coal burning power plants, *fly ash* makes up to 75% of the total ash produced *(Blaha et al. 2008)*. Fortunately, not all of this is released into the environment, with the majority of the particles being collected in the stack via electrostatic precipitators or other methods (e.g. baghouses, dust cyclones) *(Goodarzi 2006)*. Electrostatic precipitators are capable of high levels of efficiency, exceeding 99% *(Blaha et al. 2008)* thus reducing the contamination from equipped power stations. However, not all power plants use particulate control devices and from unequipped power plants, the rate of *fly ash* released into the atmosphere may extend in to 10's of tons per day, with five power plants in Singrauli area of India, producing roughly 6 million tons of uncollected *fly ash* per year *(Blaha et al. 2008)*. Many of the particles remain airborne for prolonged periods, are capable of travelling large distances (>1000 km), and are capable of contaminating collections far from the source of their origin *(Inoue et al. 2014)*.

The chemical composition of *fly ash* particles are strongly dependant on the type of coal burnt in the production of the particles and the fuel's composition. For the major element composition of *fly ash* produced via different coal types see Table 3.2. Coal is split into 3 major rankings based on carbon content and geological age, lignite, bituminous and subbituminous. As the geological age of coal increases, the carbon

Table 3.2: Showing the oxides present in the fly ash formed from three different type of coal commonly used in commercial coal fed power plants. Data taken from *Ahmaruzzaman 2010.*

Component	Bituminous	Subbituminous	Lignite
SiO2 (%wt)	20-60	40-60	15-45
Al2O3 (%wt)	5-35	20-30	20-25
Fe2O3 (%wt)	10-40	4-10	4-15
CaO (%wt)	1-12	5-30	15-40
LOI* (%wt)	0-15	0-3	0-5

*Amount lost on ignition

content of the coal also increases, with lignite being the youngest coal type having 60-75%wt carbon and the oldest commercially used bituminous containing 85-92%wt carbon. Higher carbon contents reduce the number of volatiles contained within the coal, resulting in higher grade coal producing less volatile containing *fly ash.*Unfortunately the high cost and scarcity of bituminous coals means that in many locations lower grade, higher polluting coals are used as the primary fuel source.

Fly ash is therefore enriched in the elements found in the coal combusted, however, due to the temperature reached during the burning, *fly ash* is depleted in volatile elements (e.g. Hg) *(Goodarzi 2006).* This results in a composition typically dominated by aluminium silicate glasses, these can exhibit iron-rich crystalline phases and may contain unburnt carbon from the original coal *(Ward and French 2006).* These particles can form spherules as they melt, however, not all particles will be emitted as spherules; some ($\approx 10\%$) will be emitted as irregular shapes *(Goodarzi 2006).*

FA is a combination of *fly ash* and other anthropogenic dust sources. Due to the selection criteria of many micrometeorite collections, generally only spherical FA was of interest. The formation of spherical dust grains could be a result of two main methods: the weathering of grains, or the melting and re-solidifying of droplets in areas where their surface tension is able to form spherules. As such, spherical FA particles can come from a wide range of locations including car exhausts, rocket exhausts, metal working (e.g. soldering and welding), and chemical production. As such this broader definition has a much wider range of compositions, from pure metallic welding spherules *(Langway and Marvin 1965),* to the silicate rich *fly ash* . Despite the additional possible origins, the vast majority of fly ash still originates from production of power from fossil fuels.

The FA data used in creating the database was collected primarily by two methods; firstly directly from the electrostatic collectors installed on the examined power plant.

This was the main collection method for research into different FA potential for use in Portland cement (e.g. see *Blaha et al. 2008*). The second method involved direct collection from the region surrounding the power plant. This was the primary collection method for research into environmental factors, or for those power plants without electrostatic collectors (e.g. see *Sarkar et al. 2006*). All of the ash was analysed via EDX and a full breakdown of the analysis method for the ash can be seen in the corresponding papers listed in Appendix D.

3.3.2 Volcanic Ash

Volcanic Ash (VA) is produced via volcanic eruptions, but unlike FA, where the particles size tends to be small due to the filtration of larger particles by stack collectors, VA exist in a large range of sizes.

The shape of the VA particles is dependant on the composition of the magma from which particles emitted. Low density magma will result in the most spherically shaped, ash droplets, with the shape being governed by the surface density of the particle *(Heiken 1972).* Whilst the original ash will have the same composition as the magma, following interactions in the plume, the resultant sphere exhibits a range of compositions from basaltic to almost pure SiO_2 *(Meeker and Hinkley 1993).* Non-spherical particles can be easily removed from collections focusing on solely CSs, but must be considered if attempting to identify unmelted MMs.

The VA data discussed here are from papers where particles were collected in multiple ways, with the two primary methods being collection directly from the air using samplers, or later collection from settled dust on the ground. For older samples VA was collected from rocky ash deposits. Almost all of the dust was analysed via SEM-EDX however some methods used electron microprobe techniques. As the data used in this thesis was taken from literature and detailed methods for the collection and analysis of the dust grains can be seen in the corresponding papers listed in Appendix D. The most abundant types of each contaminate for each collection, including non-spherical particles are discussed in more detail below.

3.3.3 Other Terrestrial Spheres

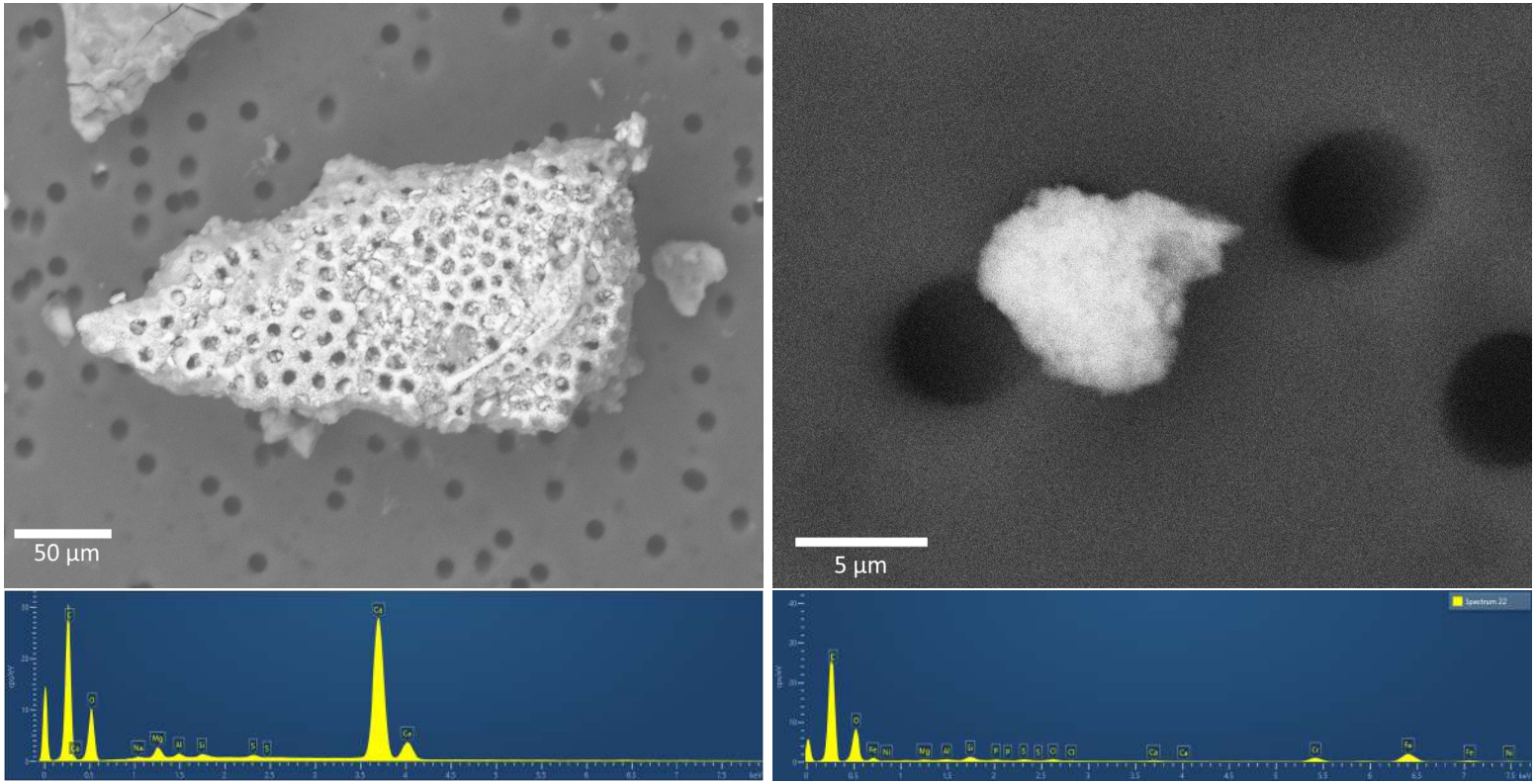
Whilst FA and VA make up the majority of spheres found on the filters, a number of other sources for spherical particles exist in the terrestrial environment. Spheri-

cal particles can be produced by fireworks (which may contain exotic metals used for colouring) *(Larson 2017),* from tars (used as tarmac, roofing and glues) *(Crozier 1960),* from desert sand (e.g. rounded mineral grains produced by weathering and Iberulites formed from sahara grains transported to the troposphere) *(Díaz-Hernández and Párraga 2008).* The abundance of these particle types are however far lower than FA and VA and are unlikely to be present on the filter to a significant degree.

3.3.4 The Kwajalein Collection

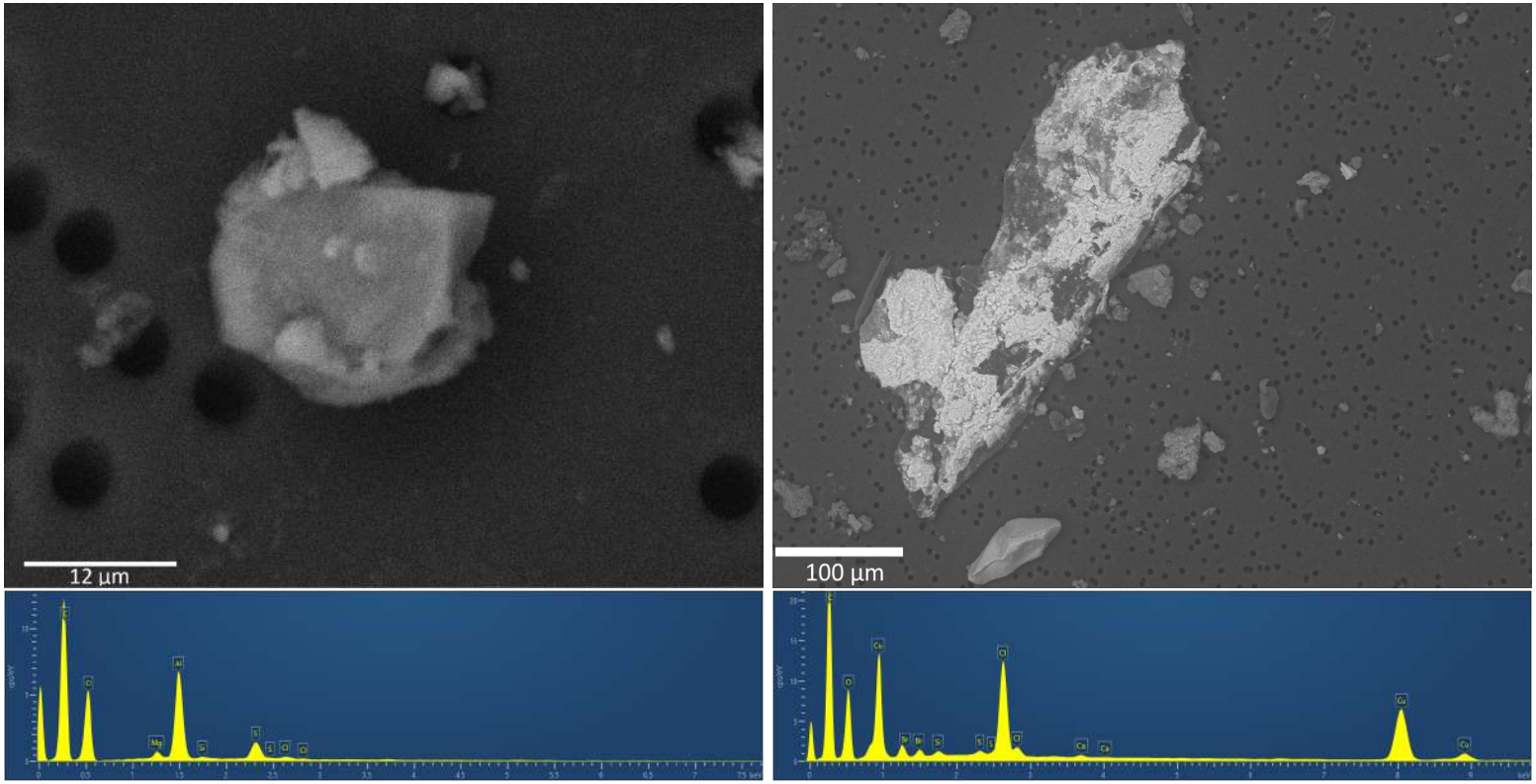
3.3.4.1 Non-Spherical Contamination

Salt The close vicinity of the collector to the sea exposed the collector to humid air and large amounts of salt spray. The particulates were sucked up by the collector and deposited on the filter membrane. As the filter dried, the salt precipitated out and remained on the filter surface, forming a crust on the top of the other collected material, effectively glueing it down onto the filter. As the salt deposits are soluble, most of this contamination was removed during the washing procedure, however, occasional salt crystals with characteristic dipyramid shapes were observed on the washed filters.



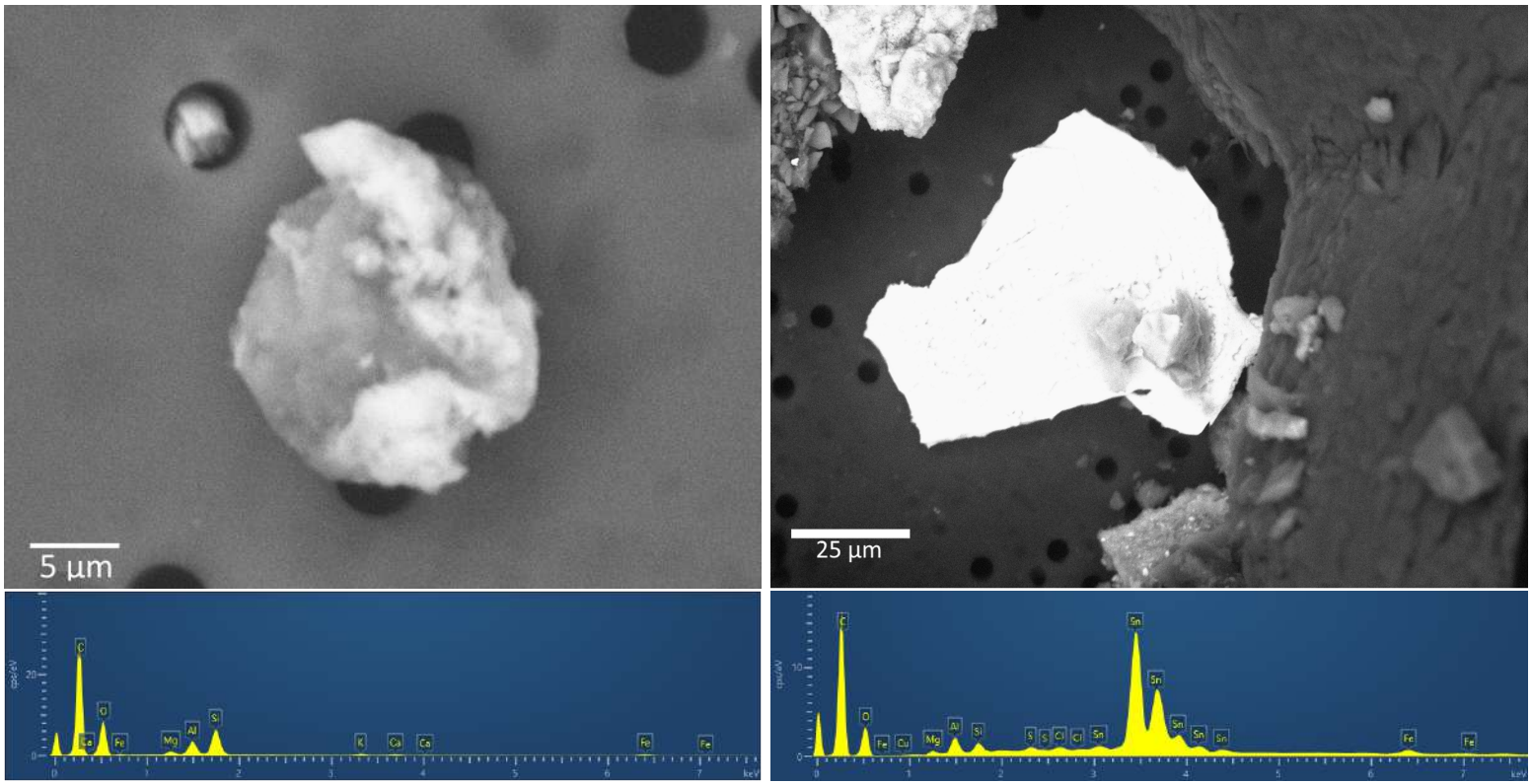
(a) (b)

Figure 3.7: BSE images of some irregularly shaped contaminates from the Kwajalein MM collection with associated spectra. a) A piece of biological debris from filter 8 of the Kwajalein MM collection, b) An Fe-Cr rich particle collected on filter 11 of the Kwajalein collection, c) An Al-rich particle collected on filter 8 of the Kwajalein MM collection, d) A Cu-Cl rich particle from filter 8 of the Kwajalein MM collection, e) A Mg-Al-S mineral grain collected on filter 8 of the Kwajalein MM collection, believed to be the result of casing erosion, f) A Sn-rich particle collected on filter 8 of the Kwajalein MM collection.



(c) (d)

Figure 3.7: BSE images of some irregularly shaped contaminates from the Kwajalein MM collection with associated spectra. a) A piece of biological debris from filter 8 of the Kwajalein MM collection, b) An Fe-Cr rich particle collected on filter 11 of the Kwajalein collection, c) An Al-rich particle collected on filter 8 of the Kwajalein MM collection, d) A Cu-Cl rich particle from filter 8 of the Kwajalein MM collection, e) A Mg-Al-S mineral grain collected on filter 8 of the Kwajalein MM collection, believed to be the result of casing erosion, f) A Sn-rich particle collected on filter 8 of the Kwajalein MM collection.



(e) (f)

Figure 3.7: BSE images of some irregularly shaped contaminates from the Kwajalein MM collection with associated spectra. a) A piece of biological debris from filter 8 of the Kwajalein MM collection, b) An Fe-Cr rich particle collected on filter 11 of the Kwajalein collection, c) An Al-rich particle collected on filter 8 of the Kwajalein MM collection, d) A Cu-Cl rich particle from filter 8 of the Kwajalein MM collection, e) A Mg-Al-S mineral grain collected on filter 8 of the Kwajalein MM collection, believed to be the result of casing erosion, f) A Sn-rich particle collected on filter 8 of the Kwajalein MM collection.

Biological Contamination Due to the mid-Pacific location of the collector, fragments of diatoms and coral were often observed (e.g see Figure 3.7a). A number of larger objects, including pieces of insect, spores, and fibres likely from local vegetation were also observed. Due to their characteristic shapes, and compositions (Ca+C+O or C+O), these were easily identified on the filter surface, and as such were not examined. Together these biological contaminates comprised a significant fraction of the large irregularly shaped particles found on the filter.

Fe-rich Particles These grains often were often alloys and contained a number of minor metals components, such as chromium, zinc, titanium and manganese. These particles were often fluffy or plated in nature and conglomerated, as opposed to appearing to be a single grain (e.g. see Figure 3.7b).

Al-Rich Particles Similarly to iron, aluminium is a material which is extensively used in many anthropogenic situations, and is liable to to be produced as the result of most human activity. Individual Al-rich particles often appear to be a single grain and homogenous in nature, however there was significant variation between particles varying from fluffy to smooth with varying amounts of Si, Mg, Cl and S (e.g. see Figure 3.7c). These particles are likely to be forms of fly ash, or products of sampler erosion (see Section 3.3.1).

Cu-Cl Rich Particles These particles were often small, rarely exceeding 25 µm in size, however, with occasional massive grains exceeding 100 µm (e.g. see Figure 3.7d). Due to their composition, these particles appeared brightest in BSE images and blue optically, so are likely copper (II) chloride. These particles are likely the result of weathering of electrical systems and plumbing on the island. As copper in these systems readily reacts, it can easily form a number of salts, including copper chloride.

Mineral Grains These particles varied significantly in size, and morphology, and included grains of olivine, feldspar, pyroxene, but were dominated by quartz (e.g. see Figure 3.7e). These minerals are likely the product of natural weathering, and possibly volcanic eruptions and were likely collected by the wind from the atolls few volcanic outcrops.

Sn-Rich Particles A number of Sn-rich particles were also found. They varied in shape and morphology, from almost spherical, to angular, and appear bright in BSE

images (e.g. see Figure 3.7f). Similarly to Fe and Al, Sn is commonly used in anthropogenic processes, often in the form of solder. This is the likely source for these particles.

Due to the large amount of unanticipated non-spherical contamination recovered on the filters, it became apparent that more vigorous selection criteria were required and hence it was decided to only analyse them for spherical particles. Based on preliminary analysis of Map 1 of Filter 8 it was also shown to be impossible to cover a representative number of filters in a reasonable time due to the large number of false positives from the non-spherical particles, therefore only 25% of the filter was analysed.

3.3.4.2 Spherical Contamination

Despite significantly reducing the number of contamination particles analysed by removing non-spheres from the search, there remained a number of spherical terrestrial contamination particles. As additional analysis on particles was carried out based almost solely on spherical morphology, quantitative data on the distribution and numbers of these extra spherules has been obtained, and can been seen with its BAS survey counterpart in Appendix B. The most common forms of terrestrial spheres are described in more detail below.

Volcanic Spheres The Kwajalein filters also contained a large number of particles which are volcanic in origin. These particles are likely to have been sourced via offshore eruptions and carried to the atoll by winds. Spherical particles can also be formed outside of the plume by lightning strikes, which super heat and melt the non-spherical ash *(Genareau et al. 2015)*. For this reason, both spherical and non-spherical particle data has therefore been included. These particles also tend to display a number of vesicles, and surface pockmarks (see Figure 3.8). These spheres were collected in addition to the MMs, as they are difficult to separate out from extra-terrestrial particles based solely on visual observations, and can remain difficult to separate out until internal structures are analysed.

Fe-rich Spheres A number of different iron rich spheres were observed on the filters (FeTi, FeCr) (see Figure 3.9). Iron-titanium-rich spheres increased in abundance following the NuStar launch on 13/06/2012 (see table 5.1) and are likely directly produced by the rocket launch. Fortunately, due to the presence of titanium in these spherules, they were easily separated from the extra-terrestrial candidates. However, due to their

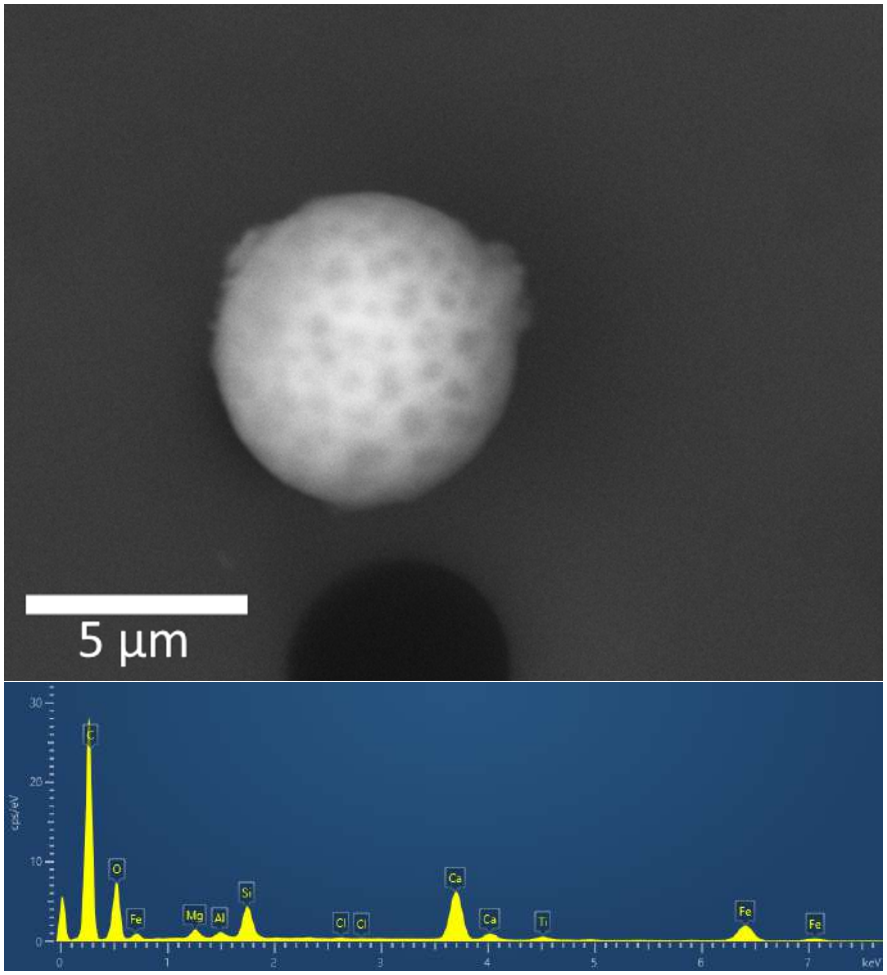


Figure 3.8: A possible volcanic ash spherule from the Kwajalein atoll MM collection. Image taken in BSE at 150 Pa at 20 kV. EDX spectra was taken at a working distance of 10 mm.

shape and morphology, it was not possible to separate them out based solely on visual observation, and as such, iron-titanium spheres were often selected for further analysis during the initial sphere selection based on the 75x zoom-out maps.

Iron Chromium spheres showed significant changes in brightness across their surface, with the bright areas showing increased levels of iron (see Figure 3.10). These spheres were also primarily found on filter 11, directly after the NuStar launch, in several areas of high abundance as shown in Figure 3.11. Due to the high abundance of these spheres each sphere was not individually analysed. Instead an EDX spectra was taken of a sample of 10-15 spheres off each map. The abundance of spheres was counted from the 500x magnification images taken for the section maps.

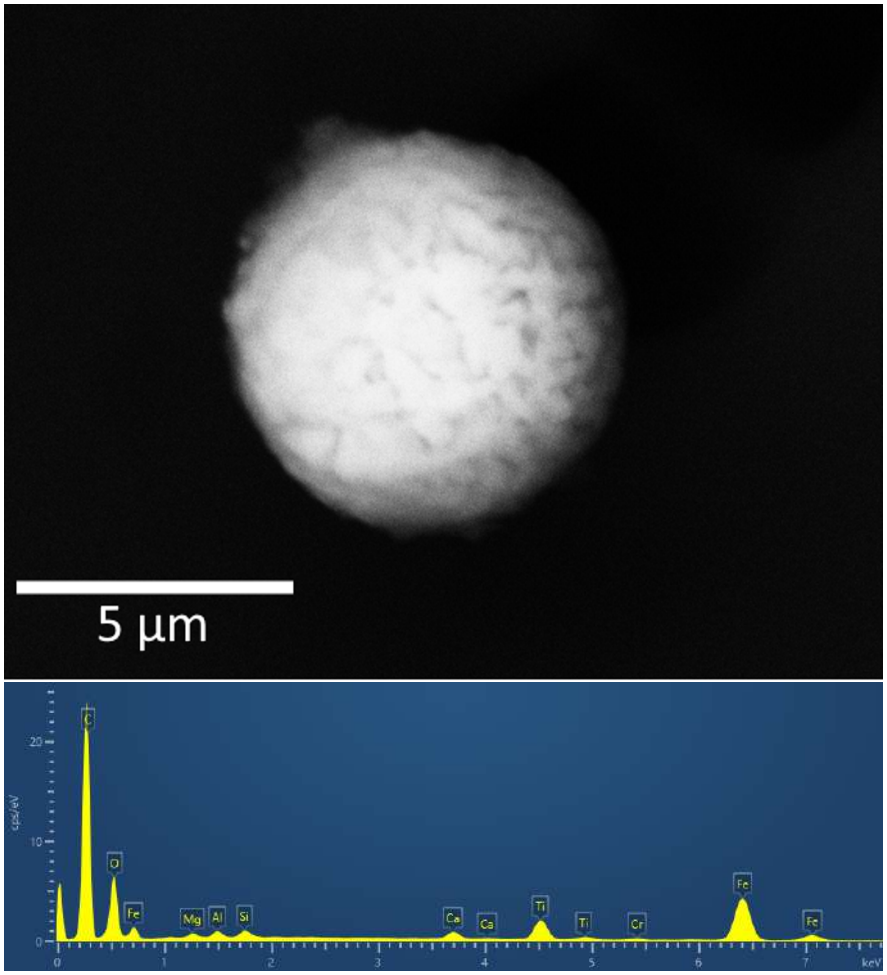


Figure 3.9: An iron-titanium spherule collected from the Kwajalein atoll following the NuStar rocket launch. Image taken in BSE at 150 Pa at 20 kV. EDX spectra was taken at a working distance of 10 mm.

The origin of these spheres is unknown, as features similar to these are not seen on any other filters. The collection of the sphere into discrete locations on the filter surface would imply that they have an origin in the preparation of the filter. There are two main methods for the deposition of these spheres; a bias towards them collecting on this filter due to a manufacturing difference in the filter membrane (although measurements of the laser etched pores show sizes within the ranges of the other frames). If the laser etching resulted in areas of reduced pore size, this could result in these spheres being able to accumulate in pockets on the filter, in the same way that large particles can be seen to have conglomerated along the filter creases. The second method is the washing procedure adding them to the surface. If these spheres were added to the filter via the washing procedure, it could be expected to see these spheres on other filters which have been washed in an identical method with water from the same source in each instance.

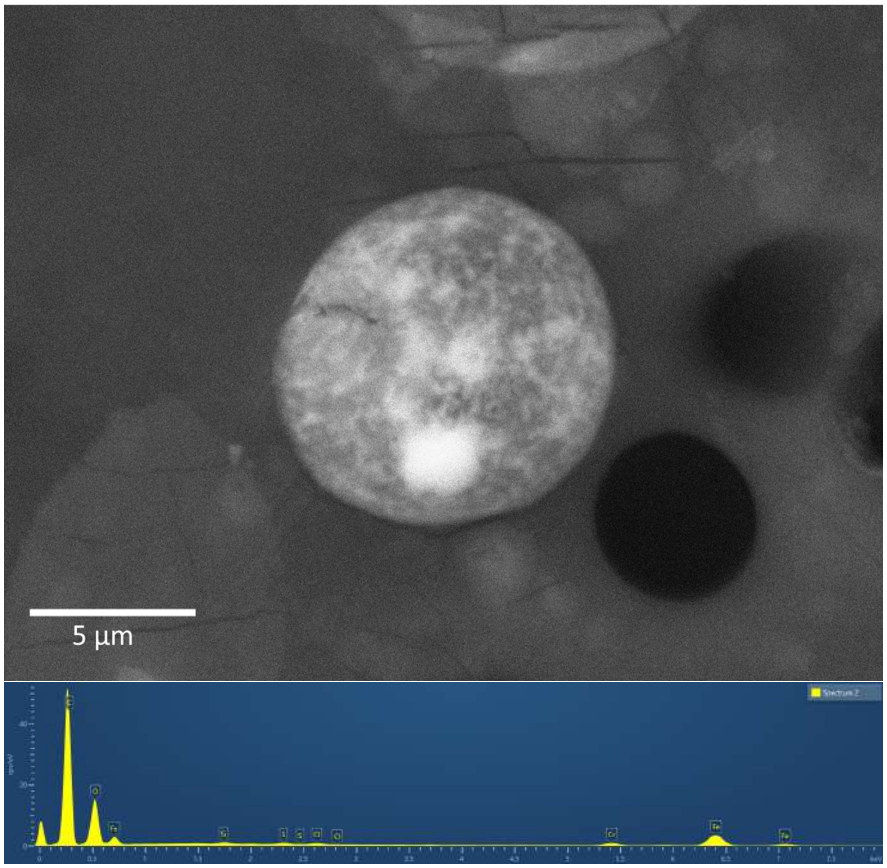


Figure 3.10: A BSE image of a FeCr contaminate sphere collected on the Kwajalein atoll. Image taken at 150 Pa with a 20 kV accelerating voltage.

It is also possible that these spheres formed as a result of the NuStar launch, however, this does not explain the formation of high density regions on the filter, which occurred post washing.

3.3.5 British Antarctic Survey Collection

3.3.5.1 Non-Spherical Contamination

The BAS collections did show significantly lower levels of contamination than those recovered from Kwajalein, enabling the analysis of all collected particles. The BAS collections however did still include a number of irregularly shaped terrestrial contaminates similar to those on the Kwajalein filters. Previous research has shown that it is possible for transiting dust from other locations to be deposited in the Antarctic regions, with confirmed terrestrial dust transits from Patagonia and other southern hemisphere regions, and this is the likely source of much of the contamination *(Gasso et al. 2010;*

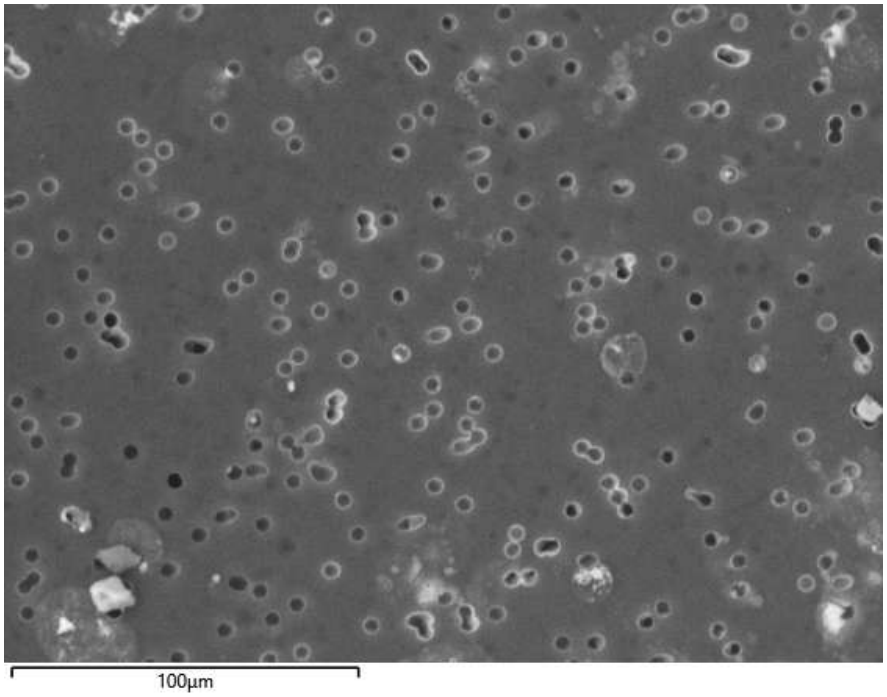


Figure 3.11: An area of high FeCr sphere density.

Neff and Bertler 2015). These contaminants include iron particles, copper chlorides and aluminium rich particulates. A selection of common non-spherical contaminates can be seen in Figure 3.12.

(a) (b)

Figure 3.12: BSE images of examples of irregularly shaped contaminants from the MM collection based at the BAS Halley VI research station. a) An Antimony particle collected on filter 16 of the Kwajalein collection b) A piece of Cr-S-rich debris from filter 14 of the BAS MM collection, c) An iron silicate particle from filter 14 of the BAS MM collection, d) A Mn-rich particle collected on filter 13 of the BAS collection

(c) (d)

Figure 3.12: BSE images of examples of irregularly shaped contaminants from the MM collection based at the BAS Halley VI research station. a) An Antimony particle collected on filter 16 of the Kwajalein collection b) A piece of Cr-S-rich debris from filter 14 of the BAS MM collection, c) An iron silicate particle from filter 14 of the BAS MM collection, d) A Mn-rich particle collected on filter 13 of the BAS collection

Sb-Rich Particles Several small fragments of antimony were found on the filters following collection. The shape of these particles was regular and hexagonal in appearance. As such it is likely that this are crystal grains of antimony, and natural in occurrence. Antinomy naturally forms crystals of a trigonal-hexagonal Scalenohedra, which would fit the shape of these fragments *(Mindat.org 2019).* It is also highly unlikely that metallic fragments which had been used in anthropogenic processes would display such regular patterns as antimony is mostly used in alloy production and hence is melted, making the likely origin of these particles to be natural.

Cr-Rich Particles Many chromium-rich particulates were also found on the filter surface. Unlike the antimony particles, these fragments showed a wide variation in both shape and composition, with particles being found containing sulphur and iron. As chromium is often used as a surface coating to reduce corrosion and wear on many surfaces, and is used to increase steel strength when alloying, these fragments are likely to be man-made, originating either from the collector itself, or the Halley VI station.

Many other metal rich particles such as iron silicates, metal salts and manganese rich particulates were also found on the collection. These are thought to be a mix of both anthropogenic and natural particles, many of which also occurred on the Kwajalein collection.

Kwajalein-like Particles Similarly to the Kwajalein collections, both Fe-rich and Al-rich particles were also recovered from the filter at a variety of sizes and with varying morphologies.

3.3.5.2 Spherical Contamination

In addition to irregularly shaped contamination, a number of clearly terrestrial particles were found which were spherical. These spherical contaminates are discussed below.

Si-Al BAS collections showed a large number of spheres dominated by an aluminium silicate composition (as shown in Figure 3.13). The number of these spheres found vastly outnumbered the MM candidates. These particles exhibit similar sizes to those found during stratospheric flight, rarely exceeding 10 µm in size with particle counts increasing with decreasing sizes, *(Brownlee, Ferry, and Tomandl 1976).* However, unlike those previously identified particles, ours are not pure $Al\,Si\,O_2$, instead, showing a range

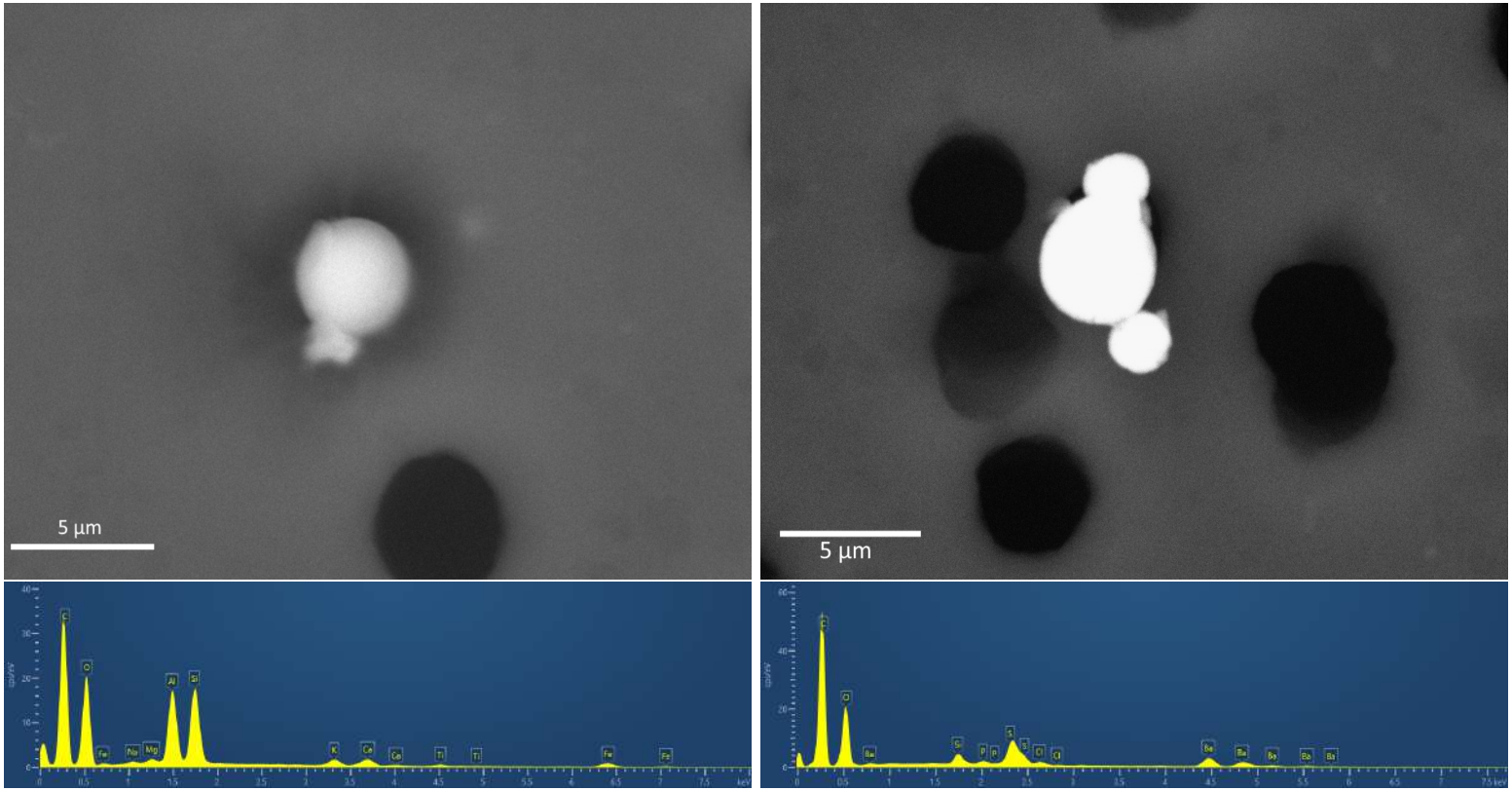
of additional elements in their composition, the most common of which are Ca, Mg, Fe and Ti.

Ba-Rich Particles BAS collections also contained large numbers of Ba-S-rich spherules. These spheres are often found in groups and are likely to be anthropogenic in origin as Ba S has been commonly used as a component of white pigment in paint for over 100 years *(O'Brien 1915)*. These spherules were not found on the Kwajalein collection and are found in lower quantities than other spherical contaminates.

FeTi Particles The BAS collection also contained numerous spherules whose chemistry is dominated by Fe and Ti. The majority of these particles are under 10 µm, but occasionally larger spheres were observed. The smaller spheres appear in much lower abundances than the AlSi spheres. The larger spheres were much rarer and had abundances more similar to that of MMs despite their terrestrial origin.

3.3.6 Summary

Two collection were analysed to identify E.T. particles, one on Kwajalein atoll and the other in Antarctica. A number of E.T. candidates were identified along with multiple recurring terrestrial contamination types. Despite envisaging that the filter locations would eliminate terrestrial contamination, both collections showed significant amount of terrestrial debris. Whilst transferring the collection from Kwajalein reduced the effects of the contamination, allowing the study of all particles, the number recovered still proved excessive for the study of the entirety of each filter. As such only 25% of each filter was studied, and new methods were required for the identification of extra-terrestrial particles from amongst large numbers of terrestrial particles.



(a) (b)

Figure 3.13: Examples of contaminant spheres taken from the BAS collections at the Haley VI research station with corresponding spectra. a) Al-Si-rich sphere from filter 14. b) Ba-S-rich sphere from filter 15.

Chapter 4
Establishing Criteria to Identify Micrometeorites

4.1 Introduction

The number of MMs found in recent years has increased significantly, and, as such, we now have a large database of previously found particles for comparison. As noted previously, identification of MMs has primarily relied upon the assumption that they share a bulk chondritic chemical make-up, as similar chemistries are not found in terrestrial material *(Genge, Engrand, et al. 2008)*. However, not all MMs share a bulk chondritic composition (e.g. some have been shown to have achondritic compositions *(Gounelle, Chaussidon, et al. 2009)*). Assuming the MMs sample the same parent bodies as meteorites, it could be assumed that at $\approx 10\%$ of falls will have non-chondritic compositions *(Bischoff and Geiger 1995)*. Furthermore, the small size of the spheres recovered in the collections makes it likely that they would be a sample of a single meteorite component (e.g. a piece of chondrule or matrix) as opposed to a melt of multiple regions, skewing their compositions away from the bulk chondritic composition and replacing it with the component specific composition. In addition, many spheres will have undergone significant thermal alteration likely removing volatiles from their 'bulk chondritic' chemistry. Unfortunately identifying differentiated compositions is difficult due to their similarity to many terrestrial contaminates (which have also undergone differentiation), and thus have been discarded. Therefore, many previous collections, are incomplete having only focused on a subset of possible compositions. We have therefore evaluated the compositions of spherules from over 200 studies of Fly Ash (FA), Volcanic Ash (VA), MMs from previous collections, and from larger chondritic and achondritic meteorites (both bulk and component) to highlight possible compositions which can be firmly identified as extra-terrestrial.

4.2 Method

In an effort to identify the likely range of composition that are exculsive to E.T. materials, we collated the compositional data for chondrites, achondrites, and the two main sources of background spherules (VA and FA) from over 200 sources.

Data for major elements (%wt oxides) for MMs, meteorites, FA and VA were collected from a number of sources. The MM data are mostly individual CS compositional data, however several unmelted MMs are also included the dataset. Full details of the MMs used can be seen in Appendix D.

Following the collation, the data were processed using Python, with results being displayed on ternary diagrams. Using the data displayed in Table 4.1 those oxides were identified which could be used to separate extra-terrestrial particles from those produced on the Earth. Only oxides, in which data for two thirds of the particles previously recovered exists were used for analysis. Additionally it was required that there was at least 50 percent data coverage for any given particle type. The oxides identified by this process were SiO_2, Al_2O_3, FeO, CaO, MgO and TiO_2. Titanium Oxide has not been included in the following work due to its low relative content compared to the other elements, however several ternary diagrams plotted can been seen in Appendix E.1. The ratio between an ET particle and an average terrestrial particle is shown in column 9; high ratios indicate a large difference between the terrestrial and ET sphere. It should be noted that difficulties arose with regards to how the valency of iron was calculated between different sources with some quoting all FeO other all Fe_2O_3. This thesis has assumed all iron oxides are of the form FeO when discussing MMs and data given in terms of Fe_2O_3 has been converted using equation 4.1 to allow comparisons. The data and references used in the production of this analysis can be seen Appendix D.

$$FeO = 0.8998 Fe_2O_3 \tag{4.1}$$

By plotting various element combinations on ternary diagrams, those elements which showed the clearest segregation of MMs/meteorite versus terrestrial sample were identified. Commonly used oxide tracers for extra-terrestrial identification include magnesium oxide (typically found in high abundance in extra-terrestrial bodies), and aluminium oxide (due to the high levels of aluminium present in the Earth's crust, as well as aluminium use in many man-made objects). Trace elements commonly found in both extra-terrestrial and terrestrial ash were also included in the dataset.

Table 4.1: Showing the average abundances of different oxides in the collated sphere origin groups. The ratio between the average terrestrial and micrometeorite abundance is shown as a normalised ratio in the ratio column.

Oxide	Fly Ash		Micrometeorite		Volcanic Ash		terrestrial	Ratio	
-	*wt%*	n	*wt%*	n	*wt%*	n	Average	-	n
SiO_2	48.08	241	44.68	228	57.55	241	52.82	1.18	710
Al_2O_3	24.29	241	2.95	228	14.03	241	19.16	6.5	710
FeO	9.36	241	16.95	228	8.40	241	8.88	1.91	710
CaO	7.13	241	2.19	228	6.56	241	6.85	3.13	710
MgO	2.16	240	28.66	228	5.62	224	3.88	7.38	692
SO_3	1.27	216	0.54	13	0.35	80	0.81	1.49	309
K_2O	1.87	233	0.55	51	2.05	241	1.96	3.56	525
Na_2O	0.91	233	0.7	51	2.94	241	1.93	2.74	525
TiO_2	1.08	226	0.14	221	1.56	238	1.32	9.57	685
P_2O_5	0.64	188	0.18	13	0.33	177	0.49	2.73	378
NiO	0.306	3	0.11	221	NED	0	NED	1.36	224
MnO	0.12	112	0.35	221	0.13	135	2.72	3.00	468
Cr_2O_3	0.03	4	0.23	224	NED	0	NED	18.08	225
BaO	0.38	19	NED	0	NED	0	NED	NED	19
SrO	0.33	11	NED	0	NED	0	NED	NED	11
V_2O_5	0.03	3	NED	0	NED	0	NED	NED	3
LOI	4.3	137	N/A	N/A	5.83	24	5.07	N/A	161
Total	98.9	241	99.54	228	99.29	241	N/A	N/A	710

NED: Not Enough Data

By comparing the average composition of the collated data, it was aimed to be able to identify the three elements with the highest change between terrestrial and extra-terrestrial spheres (see Table 4.1), as a starting point for this process.

4.3 Results

4.3.1 Composition of Micrometeorites

The MM plots shown in Figure 4.1 include a range of differing MM types, including CSs, Basaltic MMs and FgMMs. Most MM compositions appear to be well constrained into a single region, however the basaltic MMs can be seen separate from the other due to their much higher aluminium content.

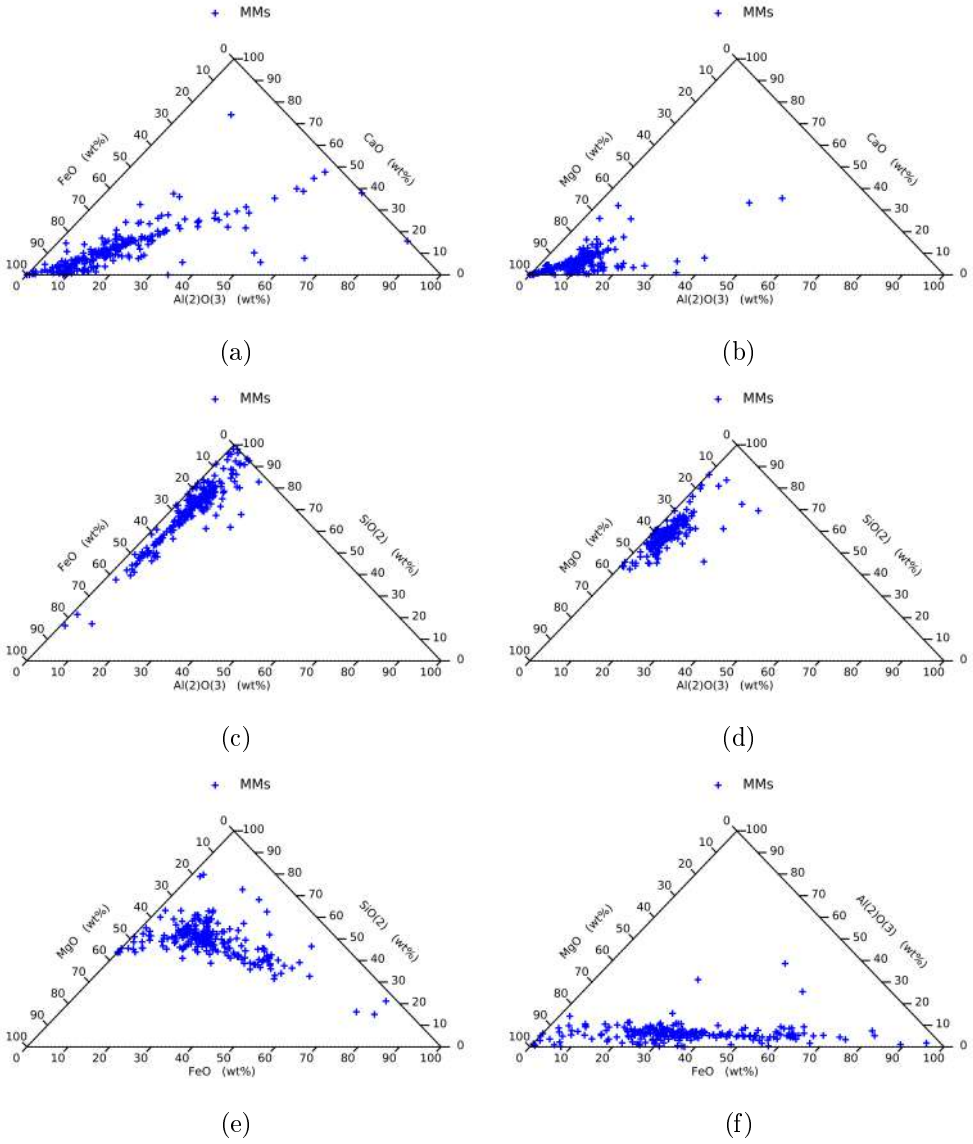


Figure 4.1: Showing the ratio of oxide abundances contained in previously collected micrometeorites from a variety of sources (see Appendix D.)

Figure 4.1 illustrates that the majority of MMs show high levels of Mg relative to the terrestrial tracers of aluminium and calcium. In addition to the collection of MMs with a $>60wt\%$ magnesium content, a selection of particles exist with 30-40$wt\%$ calcium oxide, a far higher percentage than occurs in the majority of MMs. A collection of identical plots for each terrestrial particle type, and for meteorites, can be found in Appendix E.2.

4.3.2 Micrometeorites vs Chondrites

Fragments of extra-terrestrial bodies larger than a few millimetres reaching the Earth's surface are known as meteorites and provide most of the remaining extra-terrestrial flux reaching the Earth's surface. Despite significantly more MMs arriving at the Earth's surface than larger meteorites *(Zolensky, Bland, et al. 2006),* meteorites have been known and examined for far longer, due to their larger size and relative ease to detect in desert locations with meteoritic material being used as early as 3200 BC *(Rehren et al. 2013).* Original identification was based solely on morphology and hue. As the number of samples increased and difference between samples became apparent a number of different methods for the identification of meteorites were proposed. For the remainder of this thesis the method outlined in *Weisberg, McCoy, and Krot 2006* shall be used.

Based on their bulk compositions and textures meteorites can be divided into chondrites and non-chondrites. Chondrites are thought to be primitive *(Weisberg, McCoy, and Krot 2006),* although in most cases they have undergone some thermal or aqueous alteration, whereas non-chondrites are believed to have undergone higher levels of processing, including melting and differentiation. Currently chondrites comprise the bulk of meteorites found in collections with only 14.6% of material being non-chondritic in origin. These meteorite types and their subtypes are discussed in more detail in the following Sections (4.3.2.1 and 4.3.3).

4.3.2.1 Chondrite Subtypes

Chondrites account for 86% of modern falls (those collected after being observed passing through the atmosphere) and Antarctic finds (those meteorites found in the Antarctic without an observed fall and hence no timeline of terrestrial interaction) being chondritic *(Zolensky, Bland, et al. 2006).* Having formed in the early solar system, chondritic meteorites contain some of the most primitive material in the solar system; which suggests that they were formed by direct accretion out of the protoplanetary disc early in the solar system's history and have since suffered little modification. Due to the early formation of the bodies, many share similarities in composition with the non-volatile composition of the Sun, with the most primitive CI type meteorites being the most closely matched *(Weisberg, McCoy, and Krot 2006).* Most chondrites have high levels of iron-nickel metal spread throughout their body, and substantial amounts of olivine and pyroxenes, both of which demonstrate limited exposure to heating and thermal metamorphism.

The bulk of most chondritic meteorites is comprised of matrix, refractory inclusions, FeNi metal and chondrules *(Weisberg, McCoy, and Krot 2006),* although some chondrites (CIs) do not contain chondrules. The matrix is the fine grained material enclosing inclusions and chondrules. This contains the bulk of the composition of any chondritic meteorite. The defining feature of many chondritic meteorites is the presence of chondrules. These are small (sub-mm to 10s of mm) spherical 'grains' of primitive material held suspended in the matrix of the meteorite. The process for the formation of chondrules is still not well understood *(Pape et al. 2019).* Chondrules are formed of pieces of material, thought to be pre-planetary dust grains from the solar nebula, which have been flash heated above melting $\approx 1800K$ and formed spherical droplets before quenching and accreting into the large body. However, chondrules are thought to directly sample the early solar system's proto-planetary disc *(Pape et al. 2019),* and they can have significantly different compositions to the matrix and additionally have iron metal rims formed around them.

In addition to chondrules, many meteorites also contain refractory inclusions including Calcium Aluminium inclusions (CAIs) and Amoeboid Olivine Aggregates (AOAs). CAIs are thought to be older than chondrules, having formed in the solar nebula, and are taken to have ages similar to that of the solar system, as well having compositions which are entirely made of refractory elements which precipitated out of the nebula early into its development *(MacPherson et al. 2005).* AOAs are the most common type of refractory inclusion in carbonaceous chondrites. They are irregularly shaped and are mostly made of fosterite, Ca-rich pyroxene, Fe metal, Ni metal *(Weisberg, Connolly, and Ebel 2004).* It is believed that they are unmelted and may provide the link between chondrules and CAIs having chemical similarities with both groups *(Krot et al. 2004).*

Most chondrites exhibit unequilibrated compositions, minerals and structures that would not naturally form next to one another and would homogenise if melted. This suggests that the individual grains of chondrites formed separately and then accreted together after formation and have undergone little to no alteration since their formation *(Weisberg, McCoy, and Krot 2006).* Some chondrites however are equilibrated, and this likely after formation during impact events.

Chondrites can be subdivided into five additional groups based on their compositions and levels of alteration. These features are thought to be indicative of their origin and, as such, meteorites placed in the same group can be thought of as likely sharing a parent body. The five subgroups are Ordinary Chondrite (OC), Carbonaceous Chondrites, Enstatite Chondrites, Kakangari (K) Chondrites, and Rumurti (R) Chondrites.

Ordinary Chondrites Ordinary Chondrite (OC)s are the most common type of meteorite find accounting for $79.5 - 80\%$ of all finds *(Zolensky, Bland, et al. 2006; The Natural History Museum 2002).* All OCs show varying degrees of thermal alteration and are split into three further subgroups based on the amount of iron contained within the meteorite and its metal to oxide ratio: 'High iron content' (H) with high iron content in a high metal to oxide ratio, L with a lower iron content and lower metal-to-oxide ratio, and LL with very low iron, almost all of which exists as an oxide in the silicate *(Vernazza et al. 2015).* It is likely that these three subtypes indicate three separate parent bodies and, due to the similarity in composition between the subtypes, it is likely that the parent bodies are in the same family of asteroid (e.g *Pedersen et al. 2019; Haack, Keil, et al. 1996; Yin et al. 2014*).

Carbonaceous Chondrites Carbonaceous chondrites, unlike ordinary chondrites, show very little evidence of thermal alteration, instead often showing evidence of aqueous alteration, in the form of hydrated minerals such as serpentine that can only be produced in the prolonged presence of liquid water *(Velbel, Tonui, and Zolensky 2012).* Carbonaceous chondrites vary greatly in composition, number of chondrules and petrological type, resulting in a number of subclasses of carbonaceous chondrites. The breakdown of these subtypes is shown in Table 4.2.

Enstatite Chondrites Enstatite Chondrites only account for 1.6% of modern recorded falls *(Zolensky, Bland, et al. 2006).* As implied in their name, the pyroxene in these meteorites is Fe-poor, Mg-rich enstatite. The iron which is found in enstatite meteorites is almost completely found as iron sulphide or iron metal implying that the meteorites are formed in a region depleted in oxygen probably within the orbit of mercury *(Kallemeyn and Wasson 1986).* Enstatite chondrites can be further subdivided into two subclasses, EH and EL, where the EH subgroups contains higher levels of iron than the EL group.

Rumuruti Chondrites Rumurti (R) chondrites are a rare chondrite type of which only 31 finds have been catalogued *(The Natural History Museum 2002),* they appear metamorphosed and are brecciated *(Weisberg, McCoy, and Krot 2006).* R chondrites are amongst the most heavily oxidised meteorites currently known, with most of the metals contained being oxidised *(Rout, Keil, and Bischoff 2010).* The high levels of oxidisation in R type chondrites manifests itself in a number of ways including an abundance of sulphides, low levels of metallic Fe and Ni and high ^{17}O. They contain NiO bearing FeO rich olivine and show a relative lack of chondrules *(Weisberg, McCoy, and Krot*

Table 4.2: Table showing the Subtypes of Carbonaceous chondrites along with their main properties

Subtype	Description	Petrological types
CI	High water content. Fine grained.	1
CM	Small chondrules ≈ 3mm with 20vol% abundance. Matrix mostly Phyliosillicates. High iron content 20-22%.	1-2
CV	1mm diameter chondrules 35 to 45 vol%, grey fusion crust contains CAIs upto 10 vol%, matrix dominated byμm size olivine.	2-3
CO	Contains small CAI's up to 15 % of matrix, matrix dominated byμm size olivine, small free metal Fe and Ni inclusions small chondrules of less 1 mm.	3
CK	Shows signs of silicate darkening. 1 mm sized chondrules roughly 45 vol%.	3-6
CR	Small chondrules about 0.7 mm with 50 vol% abundance high metal content.	1-2
CB	High metal content with cm sized chondrules, Signs of melting, may originate from 2 Pallas.	3
CH	Very high metal content up to 70 %, Similar to CB but with fewer CAI's.	3

2006). In addition, in comparison to other chondrites, R chondrites have large amounts of aluminium containing beads and inclusions.

Kakangari Chondrites Kakangari (K) chondrites are another rare group with only 4 known specimens. The matrix makes up a large portion of their total volume and they contain high amounts of iron metal (similar to the of H group OCs). Unlike most other chondrites the matrix is enstatite rich and often contains higher levels of Mg than the surrounding chondrules *(Weisberg, Prinz, et al. 1996).* It is currently thought the precursors to the matrix were similar to that seen in IDPs which underwent thermal processing prior to accretion *(Brearley 1989).*

4.3.2.2 Micrometeorites vs Bulk Chondritic Composition

The compositions of MMs compared with the bulk composition of different chondrites subtypes are shown in Figure 4.3. As would be expected based on the selection criteria of previous work, almost all the previously collected micrometeorites inhabit the same

region as the bulk chemistry. It can be noted from Figure 4.3 that a single subtype remains separate from the main region. This is the R chondrites which display chemistry significantly different from that of most chondrites. Several MMs can also be seen separated from the main group, in both cases with a corresponding increase in the aluminium oxide content. It is important to note that the whilst the bulk chemistry of chondrites is well constrained, there is significant difference when the measurements focus on a single point.

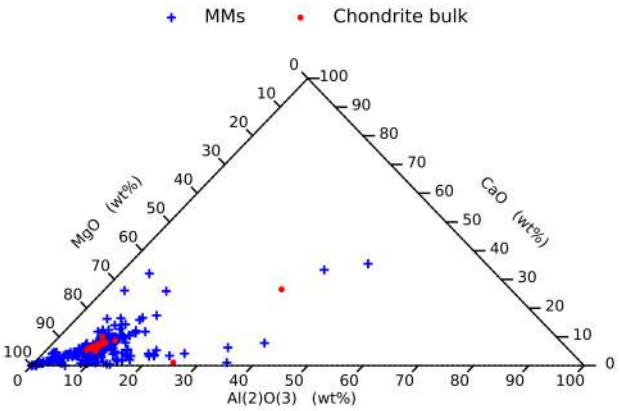


Figure 4.2

Figure 4.3: Showing the relative wt % abundances of aluminium, calcium and magnesium oxides in micrometeorites from historic collections, compared with the bulk composition of chondrites: a) MM composition vs bulk chondritic compositions. The raw data with corresponding papers can be seen in Appendix D.

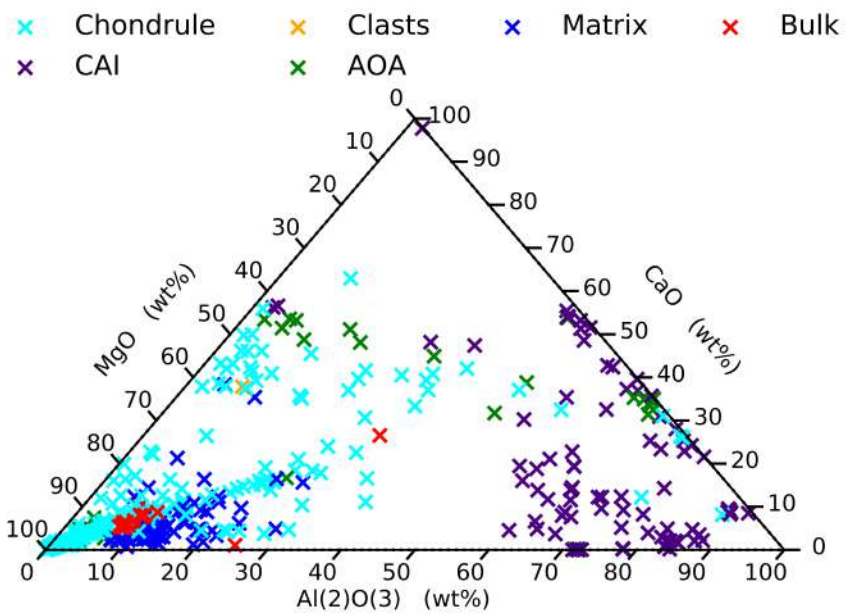
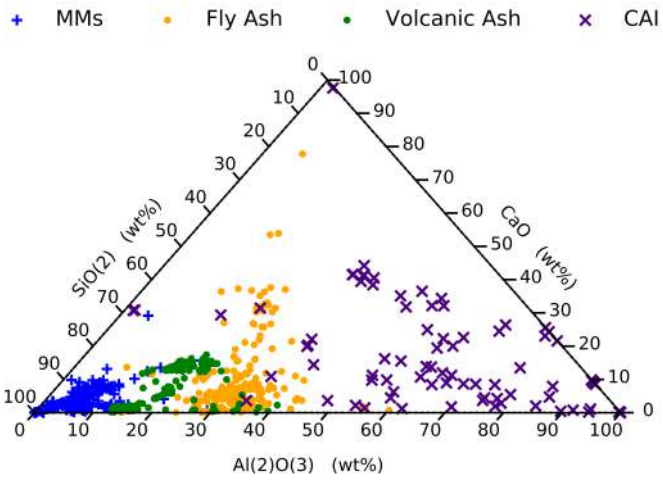


Figure 4.4: The MgO,CaO and Al(2) O(3) ratios of different chondrite components taken from a range of chondrite types. The abundances are given in wt%.

Micrometeorites vs Chondrite Component Compositions Comparing the composition of the different components which make up chondrites on the ternary as shown in Figure 4.4 shows a much larger scatter of composition than would be implied by bulk chemistry alone (see Figure 4.3a). Whilst components can be seen to group together, significant spread is observed. The matrix (commonly Mg-rich olivine or pyroxene) and bulk compositions have compositions abundant in Mg similar to previously collected MMs. The chondrules however, have a much wider range of compositions than any of the other component features, spreading from little to no aluminium and calcium, to little to no magnesium. As such MMs, derived from chondrules, could be expected to share these compositions, and thus be missed if sampling is restricted to those with bulk chondritic compositions. CAIs also inhabit the high Aluminium-Calcium areas of the plot and, if sampling a CAI, it could again be anticipated that such MMs would be missed in such bulk chondritic searches.



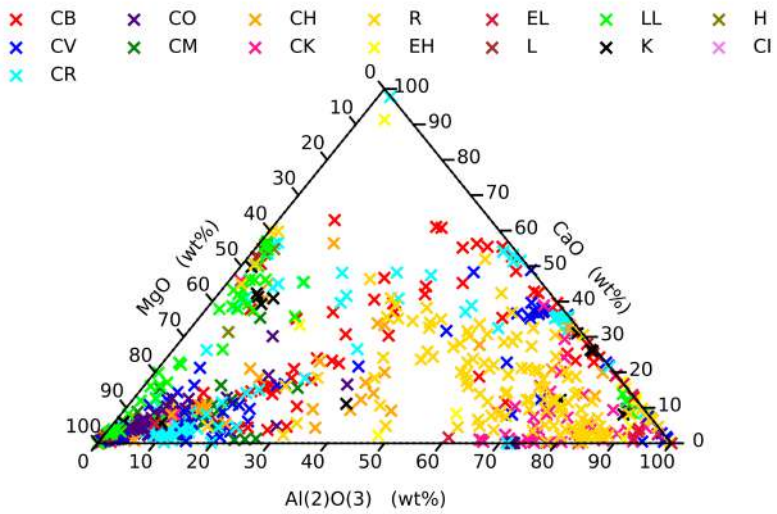
(a)

Figure 4.5: A number of different element ratios used in an attempt to separate out the extra-terrestrial CAIs whose Ca-Al-Mg ratios are similar to terrestrial materials. Abundances are shown in wt%.

In most cases the silicon ratio is enough to separate out the low silicon CAIs from the terrestrial debris, where the silicon is retained at the temperatures where most of these spheres are produced. In Figure 4.5, it can be seen that it is possible to successfully separate out both previously collected MMs, terrestrial debris, and CAIs into separate locations on the plot (due to the lower abundance of silicon), and thus, it is also possible to identify any sphere occupying the CAI region of the plot as a likely extra-terrestrial candidate which does not have a bulk Chondritic composition. Other compared element ratio plots can be seen in Appendix E.4.

4.3.2.3 Micrometeorites vs Chondritic Component Mineral Compositions

Comparisons with non-bulk measurements show a much wider spread of chemistries than their bulk measurement counterparts (Figure 4.6). This is to be expected, as different minerals are constructed of different elements.



(a)

Figure 4.6: Ratios of aluminium calcium and magnesium oxides in different chondrites when measurements are not averaged over the entire body. a) Location of different chondrite types based on single point analysis. All ratios are in wt%.

In Figure 4.6 (a), where the analysis is split by the analysed chondrite type, no clear groups appear. It is therefore important to note, that whilst MMs may be collected based on bulk chondritic composition, chondrites themselves do not display this homogeneity, with individual components local compositions, being mineral and not parent meteorite dependant. The variation of mineral compositions which form each chondrite component raises questions about using bulk chondritic compositions as a sole selection criterion (e.g. see *(Genge, Grady, and Hutchison 1997; Kurat et al. 1994)*). As such it is possible that MMs may have been discarded as not being bulk chondritic despite having originated from a chondritic parent body.

Comparisons of local chemistry show significant overlap, with olivine and pyroxene showing characteristics that match bulk chondritic, due to the high abundance of these minerals in most chondrites. Other, less frequent, minerals however often do not display this relationship, as they do not dominate the mineralogy of their meteorite. Unfortunately particles made up of these 'lesser occurring' minerals are likely to be missed, as their chemistry is often similar to that of terrestrial particles. See Appendix E.5 for plots comparing mineral data to terrestrial debris and previously collected MMs.

4.3.2.4 Summary

Overall, identifying chondritic minerals from terrestrial material is not easily done based solely on composition and as such cannot be used to identify MMs. However the compositions of matrix, CAIs and chondrules can be separated from common terrestrial spherules and therefore could, potentially, be used as an identifier of E.T. origin.

4.3.3 Micrometeorites vs Non-Chondrites

Achondrites are meteorites lacking in chondrules, which have undergone partial or complete melting and differentiation. They make up 14.6% of recorded falls (8.3% are stony achondrites, 1.2% are stony iron and 5.2% are irons) *(Zolensky, Bland, et al. 2006).* Unlike chondrites, which have experienced limited heating preserving primitive material, many achondrites are thought to have experienced high levels of prolonged heating. The extent of this heating results in a much more processed body than chondrites. Similarly to the chondrites, non-chondrites can be broken into major subgroups: Primitives, Asteroidal or Basaltic, Martian and Lunar, (known as stony achondrites), as well as Stony-Irons and Irons *(Weisberg, McCoy, and Krot 2006),* which will be discussed in more detail below and in Appendix C.

Due to the amount of heating experienced by most non-chondrites, it is likely that they formed in larger bodies which possess the internal pressures and radioactive nuclei to sufficiently heat the parent body to temperatures able to melt the primitive materials *(Mittlefehldt, McCoy, and Goodrich 1998).* Due to the temperatures achieved, these bodies are also able to undergo planetary differentiation, resulting in distinct boundaries between materials and layers, as density separation occurs. Stony achondrites are likely formed in the crust of these differentiated bodies, and thus they contain less metals than the chondrites and rarely, if at all, contain Fe-Ni. The stony irons by comparison are thought to have formed in the boundary region between the silicate rich crust and the metal rich core and show major differences to the other achondrites types, including high levels of iron, and other metals (e.g. nickel) *(Mittlefehldt, McCoy, and Goodrich 1998).* Finally, it is thought that the irons are direct samples of the core itself *(Mittlefehldt, McCoy, and Goodrich 1998).*

4.3.3.1 Non-Chondrite Subtypes

Primitive Achondrites Primitive achondrites appear to occupy the middle ground between chondrites and achondrites; they appear achondritic in texture, however, with

chondritic chemistry and are thought to be the least heated and altered of the achondrites *(Mittlefehldt, McCoy, and Goodrich 1998).* It is currently thought that these meteorites show an intermediate stage of differentiation, with chondrites being undifferentiated, primitive achondrites being partially differentiated and achondrites being differentiated *(McSween 1987).* The primitive achondrites can be split further into: Acapulcoites, Lodranites, Winonites, Ureilites and Brachinites.

Acapulcoites and Lodranites share similar chemistries, however, morphologically both are distinct (Acapulcoites are fine-grained and Lodranites are course-grained). Acapulcoites are thought to have experienced temperatures of approximately 950^{o}C as they show signs of iron nickel melting and loss of iron sulphide minerals (e.g. troilite) *(Weisberg, McCoy, and Krot 2006).* Lodranites are thought to have experienced higher temperatures in the region of 1050-1200 ^{o}C. The melting of iron nickel would be complete in this range and hence Lodranites show depletion in these metals. Similarly, plagioclase would also be melted at these temperatures and hence Lodranites also are lacking plagioclase minerals *(Weisberg, McCoy, and Krot 2006).*

The Brachinites are ultra-mafic (high in Mg and Fe and very low in Si) meteorites which are primarily comprised of olivines. They appear unbrecciated, and made up of large coarse grains *(Keil 2014).* Winonites are finer grained with compositions similar to enstatite chondrites. They contain partial melts of chondritic material and have been found to contain relict chondrules *(Weisberg, McCoy, and Krot 2006).* Finally, Ureilites are thought to be the most highly heated of the primitive achondrites *(Goodrich et al. 2001)* and are mostly comprised of olivine and pigeonite *(Warren 2011).* Ureilites have a wide range of oxygen isotope ratios and contain relatively large amounts of carbon ($\approx$ 3 wt%) both of which are similar to carbonaceous chondrites *(McSween 1987).*

Martian Achondrites The Martian achondrites show a common oxygen isotope fractionation, different from other subtypes. They also show relatively young crystallisation ages, only 1.3 Gyr, significantly less than that of most other recovered meteorites. The very young crystallisation ages (roughly 1.3 Gyr vs 4.5 Gyr for chondrites), implies that igneous activity continued for a prolonged period of time, extending far past the period seen in smaller protoplanet and asteroids *(Weisberg, McCoy, and Krot 2006).* Abundances of trapped gases show significant similarities to the Martian atmosphere which, as far as is currently known, are unique to Mars and allows the origin of the meteorites to be well constrained *(McSween 1987).* Most Martian meteorites fall into 3 separate groups the Shergottites, the Nakhlites and the Chassignites collectively known as SNC meteorites. There are also several unique meteorites referred to as ungrouped Martian

meteorites such as ALH 84001 which show distinct morphologies but are clearly linked to Mars by chemistry.

Shergottites are the most abundant of the Martian meteorites and range from volcanic in texture, such as basaltic Shergottites, to slowly cooled, coarse-grained igneous (plutonic), including Iherzolitic and olivine-phyric Shergottites *(Weisberg, McCoy, and Krot 2006).* Their crystal size and arrangement is dependant on the origin, with basaltic Shergottites having smaller, more aligned crystals than their plutonic cousins*(McSween 1987).* All Shergottites show signs of significant shocking, with plagioclase being often found in the form of maskelynite, a shock-formed glass, requiring shock pressures of ≈30 GPa *(McSween 1987).*

Nakhlites mostly consist of Ca rich pyroxenes with lesser amounts of olivine. Whereas chassignites are mostly dominated by olivines with lesser amounts of pyroxenes. Both Chassignites and Nakhlites show little, or no, evidence for the extensive shock metamorphism seen in the Shergottites.

Lunar Achondrites Lunar achondrites are those meteorites that have originated from the moon. Unlike most other meteorites these are the only samples for which a direct comparison (against lunar material collected during the Apollo missions) currently exists. Lunar meteorites are split into sub-types dependant on the likely source of origin on the moon: impact breccia or mare basalts.

Mare basalts are mostly basaltic (mafic) in composition. Impact Breccias are samples of the lunar surface which have been superheated and shocked as a result of impacts onto the lunar surface. They can contain basaltic material similar to mare basalts as clasts. Most of the brecciated meteorites recovered have been dominated by feldspars, however, a few have been basaltic *(Korotev 2005).*

Asteroidal Achondrites Asteroidal meteorites make up the remainder of the stony achondrites and are the most abundant of the achondrites *(McSween 1987).* The asteroidal achondrites are subdivided into smaller related groups: Howardites, Eucrites, Diogenites, Aubrites and Angrites, as well as several ungrouped examples.

The Howardites, Eucrites and Diogenites (HEDs) are often referred to as a single subgroup, or removed from the asteroidal group and positioned as their own subtype.

HED meteorites make up the largest fraction of achondrites, and show a common oxygen fraction line indicating that they all originate from the same area of the solar system - thought to be Vesta *(McSween 1987).* Eucrites are basaltic in nature and tend to be formed of either monomict (of one rock type) or polymict (of many rock types) breccias *(Mittlefehldt and Lindstrom 2003).* They contain calcium-rich plagioclase and reduced iron, features not normally found in terrestrial basalts *(McSween 1987).* Eucrites are believed to sample the upper crust of Vesta. Diogenites are pyroxene-rich meteorites that are commonly brecciated *(Beck and McSween Jr. 2010).* Unlike Eucrites, Diogenites have pyroxenes which tend to have higher magnesium contents and they contain limited plagioclase *(McSween 1987)* and appear to be plutonic, and therefore Diogenites are thought to sample deeper into Vesta's crust than Eucrites. Howardites appear to be mixes of brecciated Eucrites and Diogenites *(McSween 1987)* as well as having a number of impact features, including glasses and impact melts *(Singerling, McSween, and Taylor 2013).* Due to their mix of compositions, they are thought to sample Vesta's surface regolith.

Aubrites are closely related to enstatite chondrites and are thought to have formed out of an enstatite chondrite-like precursor object *(Keil et al. 2011).* As such, they contain very little iron in their mineralogy; almost all of the enstatite and diopside is FeO free, with most of the iron content being found in heavily reduced iron beads *(Weisberg, McCoy, and Krot 2006).* The Aubrite chemistry indicates a heavily reducing environment with no water, and, similarly to HED meteorites, they also are brecciated *(McSween 1987).*

Angrites are mafic rocks with a severely depleted alkali content *(Keil 2012).* They appear unshocked, and contrary to other asteroidal achondrites, they are not brecciated, nor do they appear to have undergone the same levels of metamorphism *(Mittlefehldt, Killgore, and Lee 2002).* They vary in composition, but are generally rich in Ti, Ca and Al bearing pyroxenes, olivine and plagioclase *(McSween 1987).*

Stony-Iron Achondrites Unlike achondrites, stony irons have substantially more iron in their bulk composition. They are thought to have formed in the boundary layer between the silicate-rich crust and the metal-rich core in differentiated bodies and may represent a different sampling depth *(Haack and McCoy 1998).* The stony irons can be split into two main groups, the Pallasites and the Mesosiderites.

Pallasites are the most abundant of the stony-irons and can be easily identified by their characteristic appearance, being comprised of large olivine grains in a metal matrix *(McSween 1987)*. Most Pallasites are comprised of magnesium-rich ($\approx Fo88$) olivine embedded in a roughly equal amount of iron-nickel metal, although there are five finds which currently do not fit with this. Three, the Eagle Station finds, have olivines which exhibit a higher Fe content ($\approx Fo80$) and a higher nickel metal content than the main group *(Haack and McCoy 1998)*. The remaining two finds are known as pyroxene Pallasites, for their pyroxene content (0.7 -3.0 % vol *Weisberg, McCoy, and Krot 2006*), however, they share no similarities with other Pallasites and as such are likely from two separate bodies.

Mesosiderites are breccias consisting of equal amounts of silicates embedded in a iron-rich matrix. Unlike Pallasites, where it is thought molten metal surrounded the silicates and previously solidified metals, the metals in the matrix are almost uniform in composition, implying that all the metal was completely molten when mixed with the silicates *(Haack and McCoy 1998)*. Mesosiderites also show a far higher proportion of pyroxenes in their silicates, with the silicates appearing basaltic, lacking in olivines and similar to HED achondrites. This implies that the silicates in Mesosiderites are from the crust of the parent body and Mesosiderites must therefore be a mix of crust and core material, likely the result of impacts *(McSween 1987)*.

Irons Iron achondrites consist almost solely of iron-nickel metal with a small amount of germanium and gallium. They represent a significant mass fraction of recovered E.T. material. They often have nickel ratios in the regions of 5-20 %, although this fraction can sometimes exceed 50% *(Mittlefehldt, McCoy, and Goodrich 1998)*. Many iron achondrites show signs of widmanstatten patterns, made up of long interlacing iron nickel crystals (kamacite and taenite). The formation of these patterns requires extremely long cooling periods of at least Myr scale. Iron achondrites can be split into subgroups based on their gallium, germanium, iridium and nickel ratios which are thought to sample multiple parent bodies.

4.3.3.2 Micrometeorites vs Non-Chondrite Compositions

As achondrites have undergone differentiation, one would expect their bulk global chemistries to be more representative of their chemistry at a local level, although surviving mineral grains will still have compositions determined by their crystal chemistry. The Mg-Ca-Al bulk chemistry of achondrites is shown in Figure 4.7.

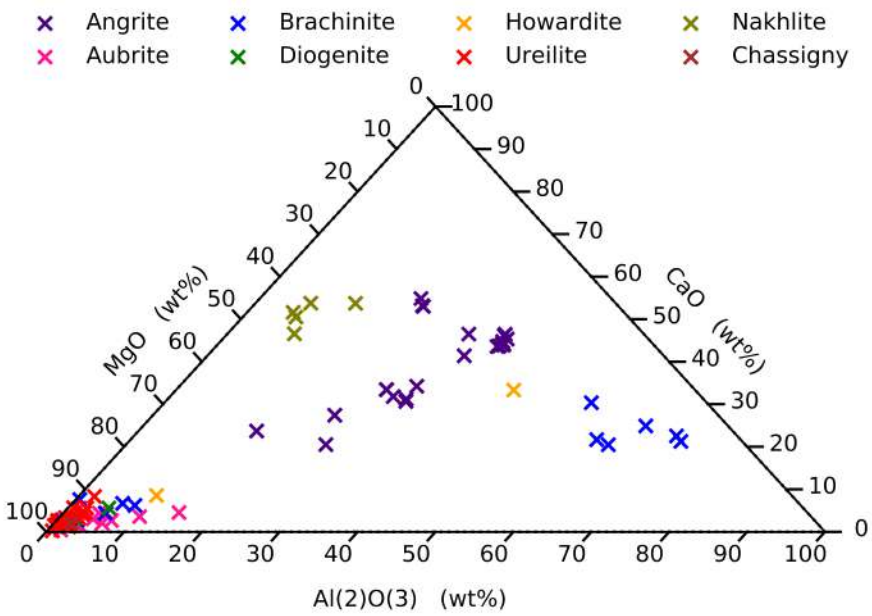


Figure 4.7: The ratio of Al, Mg and Ca in the bulk spectra of achondrite subtypes. Abundances are shown in wt%.

Most of the achondrite types are contained in the same region as the bulk chondritic chemistry. Angrites, Brachinites and Nakhlites, show significant differences which can be explained by their higher calcium content than most chondrites. Comparing the ratios of achondrites with the ratio of commonly found spherules, shows that for Nakhlites, the aluminium ratio is low enough when compared to magnesium and calcium to enable the separation of any Nakhlite produced spherule from those of the common terrestrial spherules (see Figure 4.8). This agrees with previous research which has shown that it is possible to identify achondritic particles on the basis of their Fe to Mg and Ca to Al ratios in situation with limited background particle flux *(Taylor, Herzog, and Delaney 2007)*.

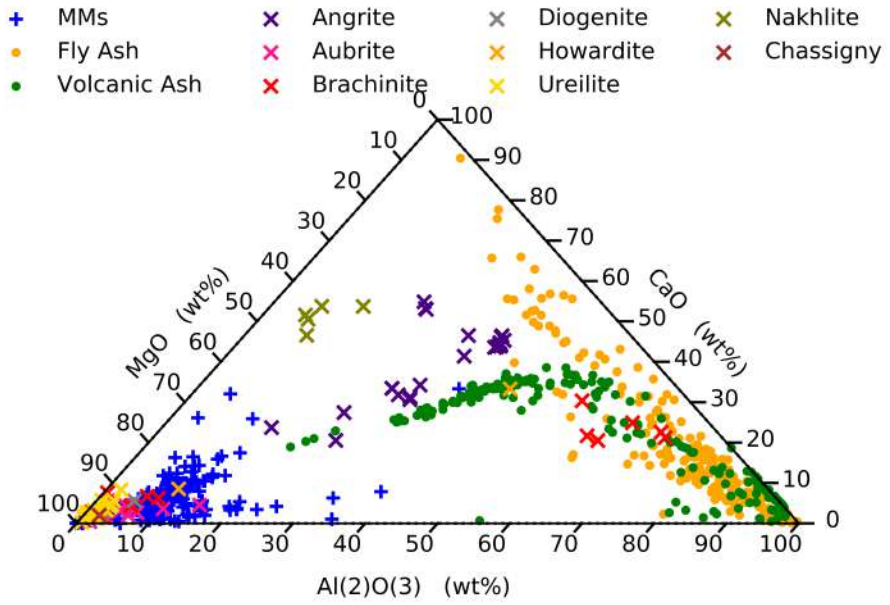


Figure 4.8: The ratio of Al, Mg and Ca in the bulk spectra of achondrite subtypes. Abundances are shown in wt%.

Unfortunately it is not possible to distinguish (from terrestrial contaminants) the other two subgroups based solely on their compositional ratios in the same way (for details see plots in Appendix E.6) and, as such, it may not be possible to separate out spheres derived for these achondrites from terrestrial contamination in this manner. The Brachinites and Angrites, although sharing no direct chemical link to the terrestrial particles also follow similar trends to the volcanic ash, likely due to the crystal fractionation of magma on the parent body, making a quick separation from these particles difficult.

4.3.4 Micrometeorites vs Terrestrial Debris

The aim of comparing MMs to terrestrial debris is to highlight possible compositional components which can be used to accurately identify E.T. particles. Descriptions of fly ash and volcanic ash particles can be seen in Section 3.3.1 and Section 3.3.2 respectively.

4.3.4.1 Fly Ash

Due to the high levels of aluminium in the majority of fly ash sources, separating out MMs from fly ash particles should be easily accomplished using the magnesium to

aluminium to iron ratios as shown in figure 4.9.

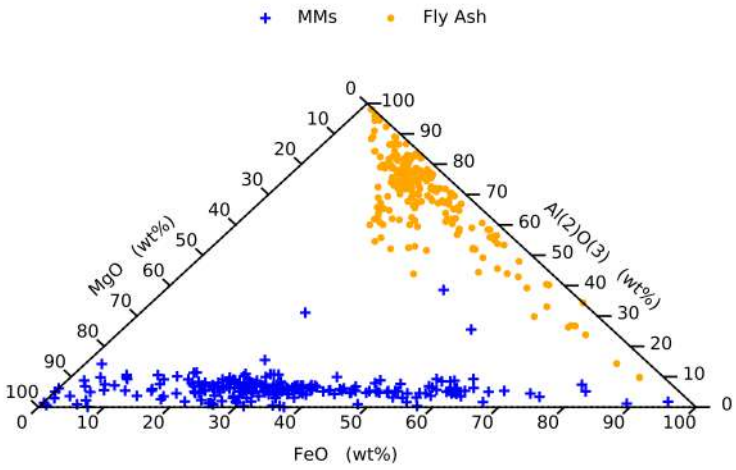


Figure 4.9: Showing the MgO, FeO and Al(2) O(3) abundances of MMs and fly ash. MMs were collected via historical collections, with MM and FA data being taken from sources shown in Appendix D.

The MMs are shown to be magnesium rich, and aluminium poor when compared alongside to iron content, with over 75% of the MMs previously collected containing greater than 50% (wt) (Mg:Al:Fe) magnesium. FA shows considerable depletion of magnesium, with fewer than 8% of the collected fly ash particles containing greater than 10% (wt) abundance. Similarly, MMs are shown to be depleted in aluminium relative to the abundance of the other elements, with less than 5% having greater than 15% (wt) aluminium (Al:Mg:Fe), whilst FA is shown to have increased relative aluminium abundance with more than 90% of FA spheres having above 50% (wt) aluminium (Al:Mg:Fe). This makes separating out MMs from the majority of anthropogenic spherules a simple case of comparing aluminium abundances, and those particles whose chemistry is aluminium dominated are unlikely to extra-terrestrial in origin. MMs derived of CAIs or those containing aluminium-rich corundum however would likely be missed and as such any particle with MM-like texture but high aluminium should also have it (Si:Ca:Al) ratio compared as shown in figure 4.5.

4.3.4.2 Volcanic Ash Composition

Analysis of the volcanic ash is described in Appendix E.2. Using the tracer elements commonly used to identify E.T. objects, compositional trends based on the location of the collected particles (see figure 4.10) could be seen.

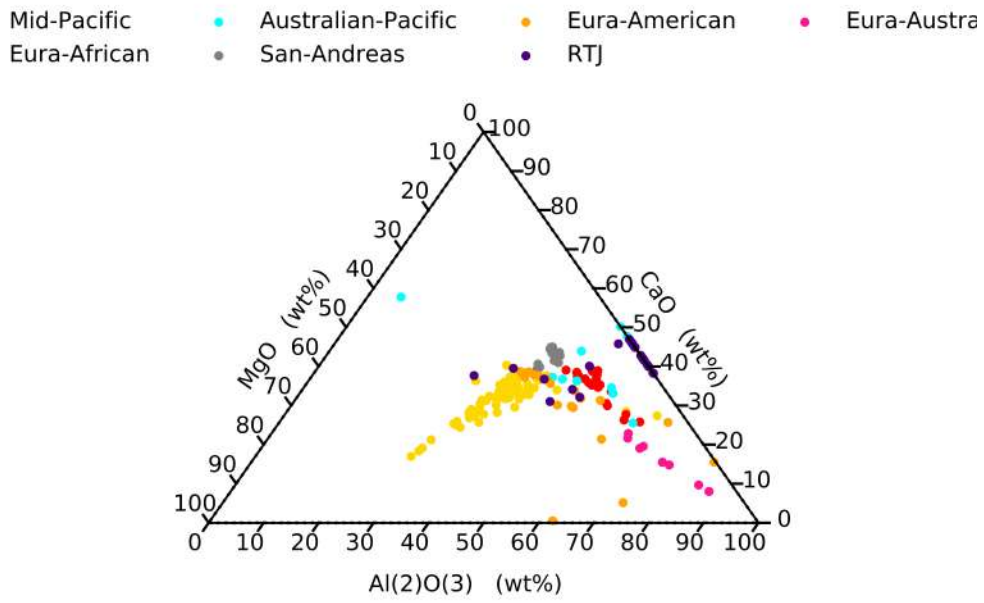


Figure 4.10: Showing how the composition of volcanic ash varies with the location of its production. Data has been taken from a number of sources which can be seen in D.

From Figure 4.10 we can see that compositional changes in the VA released during eruption varies considerably with location. Whilst not all are low viscosity lava normally associated with volcanic spherules, lightning strikes have been shown to produce spheres independent of viscosity *(Genareau et al. 2015)*. Ash formed in the mid-Pacific hotspots shows a larger MgO component than that of ash formed in all other locations. This makes separating out extra-terrestrial dust from Mid Pacific VA, such as the type most likely found on the Kwajalein atoll, which as described previously is basaltic in composition, a more complex proposition than other terrestrial debris, as can be seen in Figure 4.11.

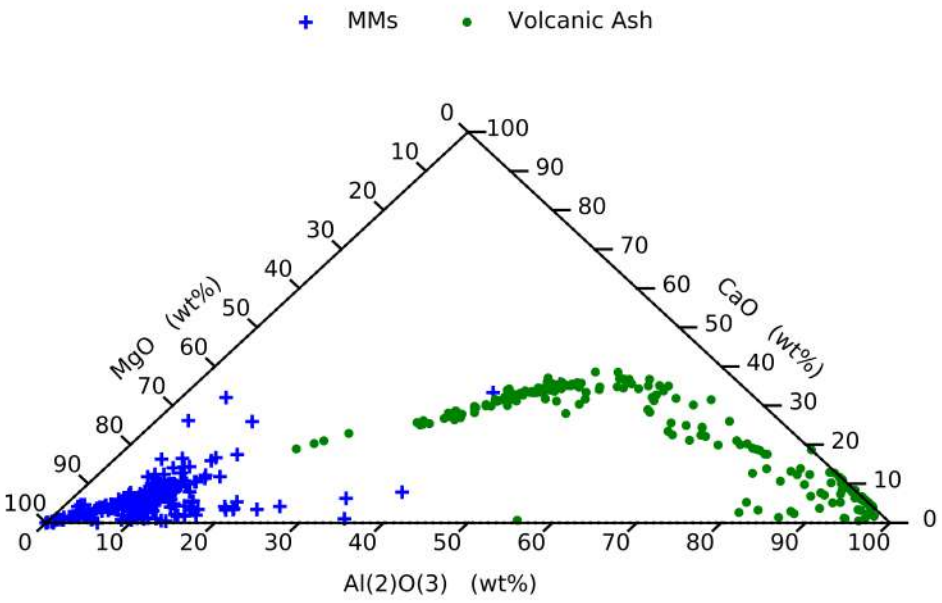


Figure 4.11: Ternary diagram of MgO, Al(2) O(3) and CaO ratios of VA and MM spheres. Data are taken from previous collections with data and references shown in Appendix D.

The higher magnesium content can be seen driving the VA from the mid-Pacific low-Mg high-Al region into the low-Al high-Mg region occupied by the MMs. This creates the possibility for particles to be falsely categorised on the basis of these element ratios. Attempting to find a suitable collection of elements using the list of common elements to remove the overlap was not possible, with it continuing in some form in each repetition (see Appendix E.3.1). However, it can also be seen that the overlap area does change, with differing number of particles in each overlap. As such comparing multiple element ratios should be able to distinguish between particles of the two types.

4.4 Summary

Previous collections have based the initial identification of MMs on their bulk chondritic compositions. This chapter has shown that not all extra-terrestrial bodies, or even compositions across a single chondrite sample, show a bulk chondritic composition. It is impossible to say whether this close relation between the bulk chemistry of the chondrites and MMs is as a result of: the selection criteria used in their collection; a true relationship of the chemistry of chondrites and MMs; or a number bias in the amount of MMs which are produced, or survive, atmospheric entry.

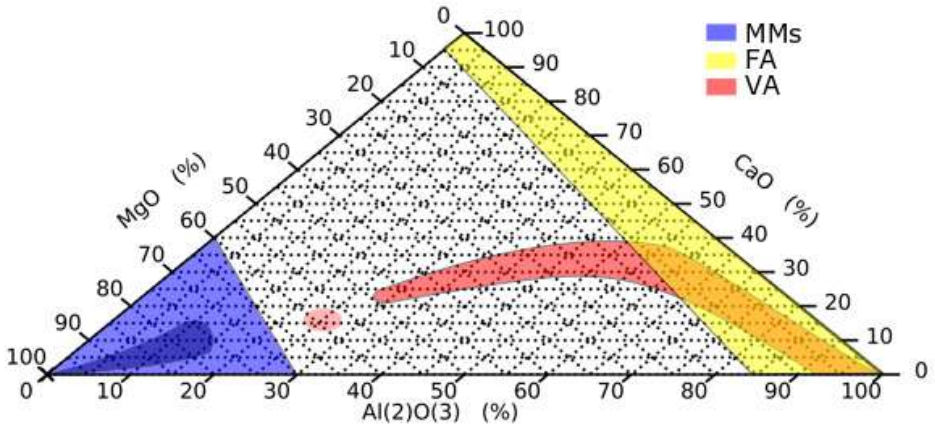


Figure 4.12: The compositional zone inhabited by MMs and common forms of terrestrial debris. Note the dark blue areas highlights the region with high MM particle density.

It has been demonstrated that in collections with large numbers of particles using bulk chondritic compositions to separate out extra-terrestrial spheres from terrestrial contamination is an effective method, however the number of false negatives is unknown. In most cases it is possible to separate out CSs from terrestrial spheres on the basis of Al, Ca and Mg ratios and still collect all the bulk chondritic particles, and a minimum Mg ratio of 10% wt is sufficient to remove the bulk of anthropogenic and natural dust from a collection.

Overall it has been possible to highlight compositional 'zones' likely to be terrestrial in origin and 'zones' which indicate possible extra-terrestrial origin. A break down of these three major regions can be seen in Figure 4.12, where MMs almost solely inhabit the bottom left of the plot. Particles in-between these regions would require further analysis to clearly identify the particles' origin.

This chapter has also shown that it is possible to identify candidate CAI derived MMs by comparing the magnesium, aluminium and silicon ratios. However this method would not be helpful in finding MMs made up of solely lesser minerals from larger chondrites due to the difficulty in separating out these fragments from terrestrial material. It has also shown that in many cases the matrix of chondrites and some chondrules do share similar chemistries to the bulk measurements and, as such, many previously collected MMs may be fragments of material which share similar origins.

As the particles analysed from these collections are small, it is likely that they are formed of only a single component (i.e. a piece of chondrule or fragment of matrix). This chapter has shown that it is possible to produce compositional 'Zones' associated with such individual components and thus, the precursor grains to the collected MMs may be identified.

Chapter 5
Analysis of Candidate Micrometeorites

5.1 Collected Extra-Terrestrial Particles

Overview Analysis of the four Kwajalein filters showed a collection of particles which demonstrated extra-terrestrial compositions. As particles had not been polished to a flat surface, the initial analysis is qualitative. As such every particle with a Si-Mg-rich composition (roughly greater than 10% wt) was regarded as possibly extra-terrestrial, and particles with a diameter above above 10 µm were selected for picking. The 10 µm diameter limit was used as it was deemed the size threshold for picking by hand. However, particles with diameters below the picking threshold have been included as extra-terrestrial in the flux estimates based solely on their SiMg rich composition. The number of particles with each composition are shown in Table 5.1.

Unfortunately, it was not possible to consider FeO rich spherules as E.T. due to the number of terrestrial sources for the production of these particles. As such, all FeO rich spheres have been classed as terrestrial contamination for this analysis.

5.1.1 Spherical Particle Flux

Table 5.1: The number of spherical particles (including particles less than the 10 µm picking limit) collected from the eight analysed filters, showing the dominant chemical signatures from the SEM-EDX data performed in situ on the filters. Si-Mg-rich silicates and Fe(Ni) spherules are regarded as possibly extra-terrestrial in origin and are included in the total extra-terrestrial count. All other particles are classed as terrestrial contamination and are included in the total terrestrial count.

	Kwajalein				BAS			
	Filter 9 24/05/2012	Filter 8 31/05/2012	Filter 11 21/06/2012	Filter 12 06/07/2012	Filter 14 14/04/2015	Filter 13 01/06/2015	Filter 16 15/06/2015	Filter 26 07/07/2015
SiMg	**4**	**3**	**24**	**5**	**3**	**5**	**7**	**6**
Fe(Ni)	**0**	**0**	**4**	**1**	**4**	**4**	**11**	**8**
Fe(O,Cr,Ti,Ca,S)	**20**	**12**	**581**	**21**	**7**	**9**	**16**	**14**
Fe(O)	*15*	*4*	*24*	*8*	*4*	*4*	*11*	*8*
Fe(Cr)	*1*	*0*	*549*	*0*	*1*	*0*	*2*	*3*
Fe(Ti)	*3*	*8*	*7*	*3*	*1*	*2*	*1*	*1*
Fe(S)	*1*	*0*	*4*	*0*	*0*	*0*	*0*	*0*
Fe(Ca)	*0*	*0*	*1*	*2*	*0*	*2*	*0*	*1*
Fe(Si)	*0*	*0*	*0*	*0*	*1*	*1*	*2*	*1*
SiAl(Fe,Ca,Mg,Sb/Ba)	**71**	**43**	**33**	**16**	**184**	**125**	**105**	**105**
SiAl	*44*	*16*	*21*	*10*	*142*	*79*	*89*	*87*
SiAl(Fe)	*15*	*7*	*0*	*2*	*7*	*4*	*1*	*2*
SiAl(Ca)	*5*	*14*	*12*	*3*	*9*	*39*	*9*	*11*
SiAl(Ti)	*0*	*0*	*0*	*0*	*4*	*3*	*4*	*4*
SiAl(Mg)	*7*	*6*	*0*	*1*	*10*	*0*	*1*	*1*
SiAl(CaMg)	*0*	*0*	*0*	*0*	*9*	*0*	*0*	*0*
SiAl(Ba/Sb)	*0*	*0*	*0*	*0*	*3*	*0*	*1*	*0*
Al	**0**	**0**	**7**	**18**	**1**	**5**	**2**	**1**
Other	**14**	**6**	**8**	**2**	**15**	**10**	**4**	**9**
Total E.T.	19	7	50	12	7	9	18	14
Total Terrestrial	90	57	63	38	203	145	116	121
Total	109	64	113	50	210	154	134	135

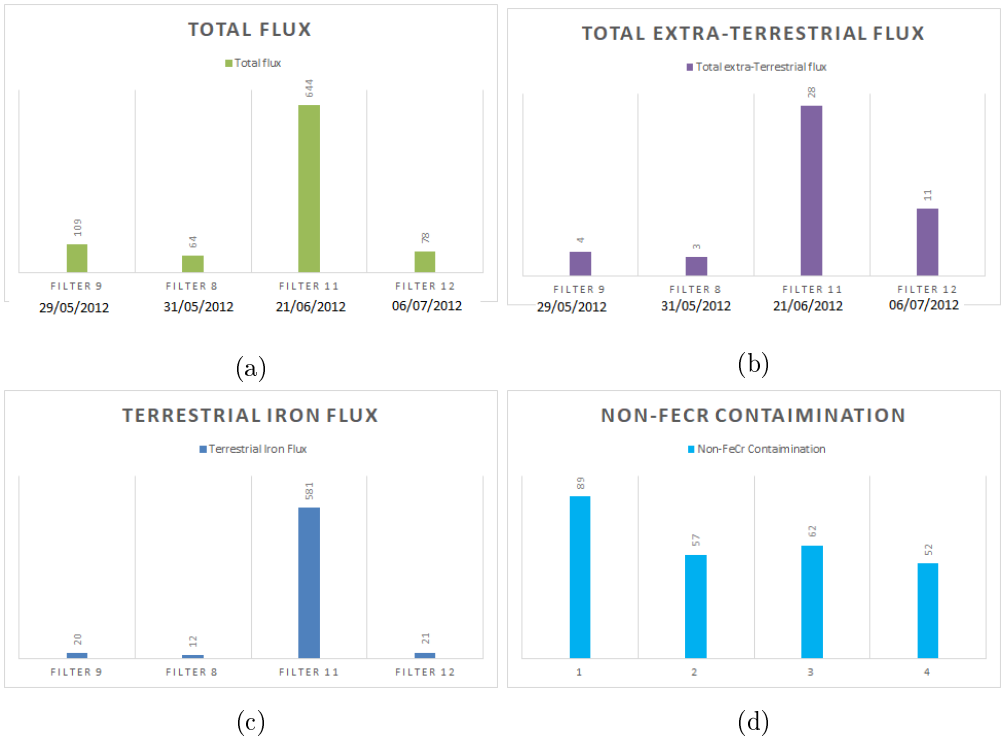


Figure 5.1: Bar charts showing the flux of different particle types from the four filters analysed from the Kwajalein atoll. The start date for each filter exposure is shown below the filter number. a) All spherical particles collected for each of the four Kwajalein filters analysed b) All extra-terrestrial candidate spheres c) Iron spheres thought to be terrestrial in origin d) Terrestrial spheres minus the flux of iron-chrome rich spheres.

Comparing the particles collected from the Kwajalein atoll we can see a clear correlation to the number of particles collected in the terrestrial spheres categories in the weeks following the NuStar launch on the 13th of June 2012 (K11 and K12). Filter K11 and K12 show a much higher abundance of Fe-rich particles than Filters K8 and K9, which were collected in the weeks preceding the launch. In particular, this increase is almost solely the result of to the increase in Iron-Chromium spheres found, with the remainder of the terrestrial flux showing a much smaller increase of around 100% (Figure 5.1 d). The week starting the 28th June, the collector experienced a power cut and as such were unable to operate for a significant time period, and therefore, we are unable to obtain data regarding the number of particles which fell during this week.

It is likely that the increase in Fe-rich particles is directly connected to the launch of the NuStar. Pegasus rockets are propelled via the use of solid rocket motors *(Office 2019b)*, and as such is a likely cause of these particles with both Iron and Chromium being used in both construction of the casing and often included as burn rate modifiers

in the fuel *(Anderson 1983).*

From Figure 5.1 d, a 100% increase in the amount of other terrestrial spherules can be seen following the NuStar launch (e.g. Al-rich). The significant drop off as seen for the total number of Fe-rich particles is not repeated here however. This would imply that either the Non-Fe-Cr-rich particle increase is not due to the launch, or that the particles in the remaining categories fell over a wider time span than the Fe-Cr particles. Analysis was also performed on filters K10 (21st to 28th June) and K03 (14th to 21st June) which took place over the same time period as K11 and the week following the NuStar launch respectively. Filter K10 showed a marked increase in terrestrial contaminants while filter K03 showed the highest abundance of E.T. candidates with a lower increase in terrestrial contaminants *(P.J.Wozniakiewicz Per. Comm).*

The increase in number of E.T. candidates in K11, along with the increase in terrestrial particles, does suggest that many of the E.T. candidates are likely a product of the rocket launch, and that, despite their apparent E.T. composition, many of these particle are not E.T. in origin. However due to their small size, most were unable to be picked and as such, their origins cannot be confirmed. These data do indicate the flaw in pure compositional selection, when abnormal conditions are present and thus, rare particles exist in high quantities.

5.2 Collected Particles

5.2.1 Extra-Terrestrial Candidates

This section will discuss extra-terrestrial candidates collected from the Kwajalein atoll MM collection. The analysis setup for the spheres collected from the four Kwajalein filters is shown in Appendix F, and they are discussed in more detail in Section 5.2.3. A total of 10 E.T. candidates were picked and analysed further, with the remaining candidates too small for picking to be performed. This analysis was semi-quantitative in nature as, due to the small size, bulk EDX was performed, however it was not possible to analyse the particle edges without including resin inside the beam area. Additionally, due to the porous nature of some of the particles, it is likely that resin was absorbed into the particle. As such, a clear gap was left around the edges of the particles so as to

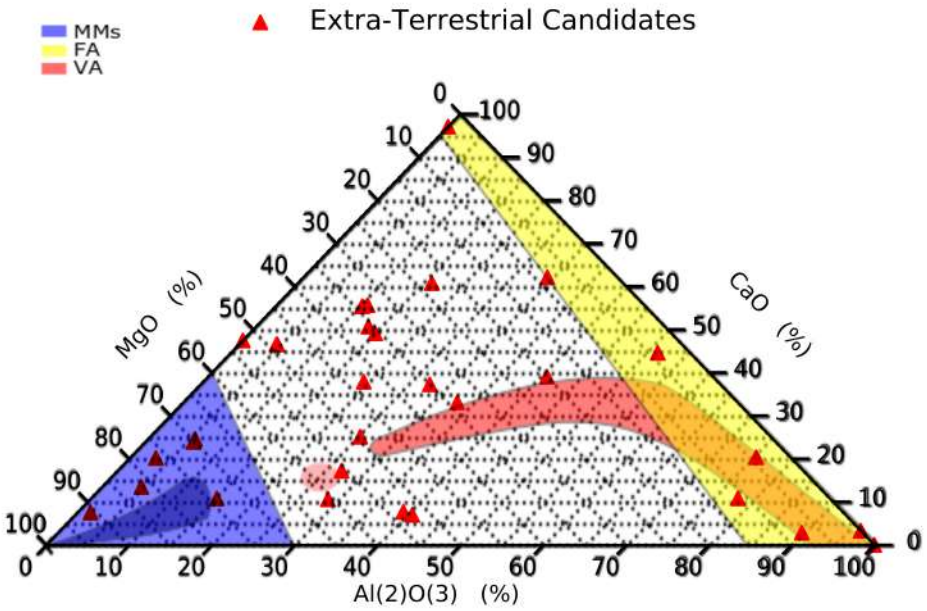


Figure 5.2: Semi quantitative ratios of MgO, Al(2) O(3) and CaO of the MM candidates from Kwajalein atoll plotted against the ratios of previously collected MMs and common terrestrial debris.

reduce any contamination of a spectrum by the resin, but it is unlikely that these steps completely removed all interference.

5.2.2 Plotted Spheres

Five particles have compositions within the range considered in most likely for E.T. particles in 4. A additional seven extra particles sit in a compositional region with a sufficiently high magnesium ratio to imply an extra-terrestrial origin, however, it can also be seen that there are a number of spheres which are most likely terrestrial in origin, exhibiting compositions which plot in regions occupied by terrestrial FA.

A number of spheres can be seen however which do not fit clearly into either groups, when the ratio of these elements are compared. Comparisons of other elemental ratios are shown in Figure 5.3. From these plots a similar pattern can be seen: five spheres sit consistently inside of the MM region of the plots, with a number of spheres moving between (likely to be) E.T. to terrestrial in origin. The largest number of potential E.T. spheres occurs when a comparison includes iron content as a factor, as can be seen in Figure 5.3 d and h. However many of these spheres appear distinctly terrestrial

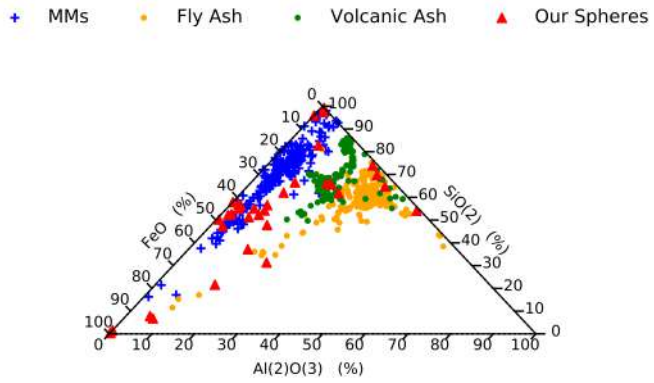
when their silicon, calcium and aluminium ratios are plotted in Figure 5.3 e. It is also important to note that in 5.3 it is the same 6 spheres which remain in the E.T. regions (spheres 7-2-10,3-7-30, 3-3-7, 11-9-40, 11-5-29 and 11-8-16).

A number of possible reasons for this change present themselves: firstly the MM dataset is incomplete and spheres of these compositions have either been discarded or were not present in previous collections. Secondly that these sphere are not E.T. in origin but are instead a form of terrestrial debris (e.g. FA or VA) which is particular to our collection location and as such has not been included in the terrestrial debris dataset. Therefore it cannot be completely ruled out that these particles are E.T. and as such it is important to expand both the terrestrial sphere and MMs datasets.

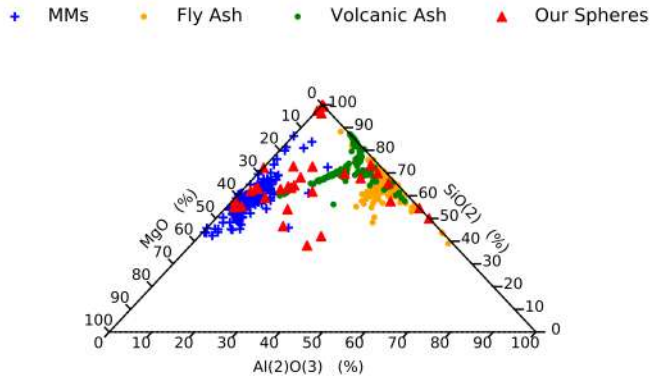
Whilst it was not possible to remove the possibility of a terrestrial origin from all spheres, comparisons with other meteorites were conducted to attempt to identify any possible E.T. origin. The ternarys in Figure 5.4 shows the relative ratio of abundances of elements in our spheres compared with chondritic components.

From Figure 5.4, it can be seen that many of the Kwajalein spheres share a composition similar to that bulk/matrix components with others falling in regions populated by AOAs and chondrules. It can also be seen that those particles which do not demonstrate a bulk chondritic composition tend to have higher ratios of calcium and lower iron content. None of the collected spheres show a calcium aluminium silicon composition similar to that of a CAI, however due to the small number of collected spheres this can not be taken as an indication of the population of these sphere types.

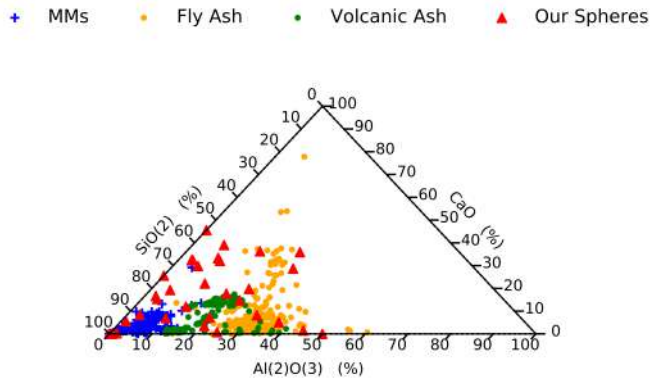
Finally ternarys comparing the compositions of the collected spheres with the compositions of achondrite types can be seen in Figure 5.5. A significant number of E.T. candidates have compositions similar to Urelite and Aubrites in graphs a and b, however graphs f, g and h show no particles have similar compositions to Urelite or Aubrite. On this basis it is also possible to rule any particles having a similar composition and hence origin to Diogentite, Howardite, or Chassignite. The particles which show similar compositions to Brachnite regions change from ternary to ternary, with no particles showing the a similar composition across all ratios. The position of individual candidates will be discussed in more detail in Section 5.2.3.



(a)

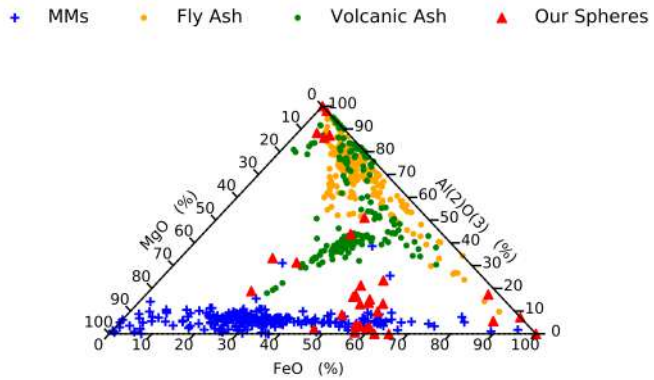


(b)

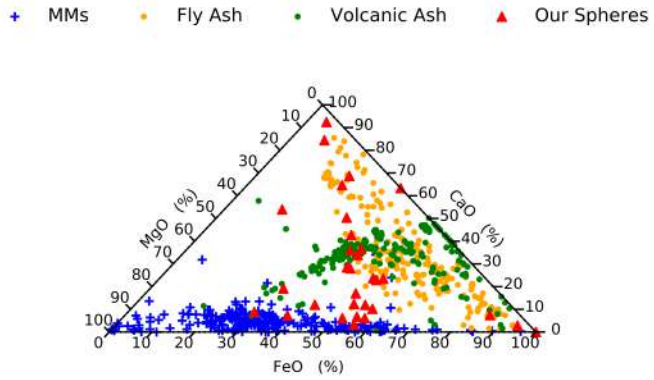


(c)

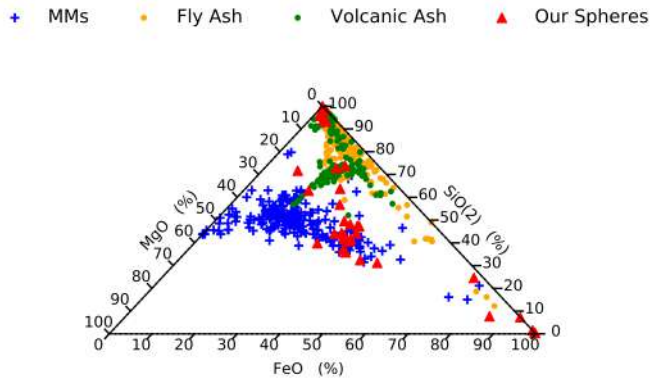
Figure 5.3: A number of different element ratios used in an attempt to separate out the extra-terrestrial CAIs whose Ca-Al-Mg ratios are similar to terrestrial materials. Abundances are shown in wt%.



(d)

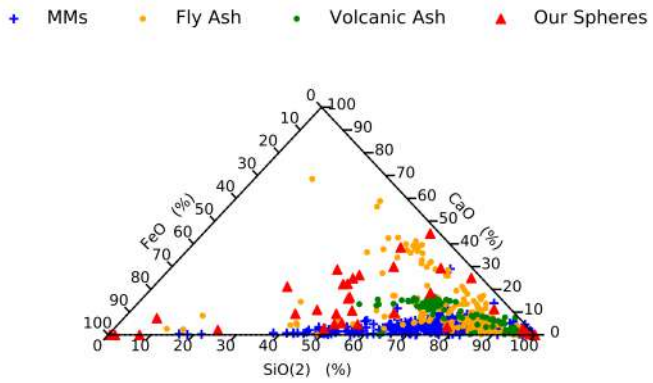


(e)

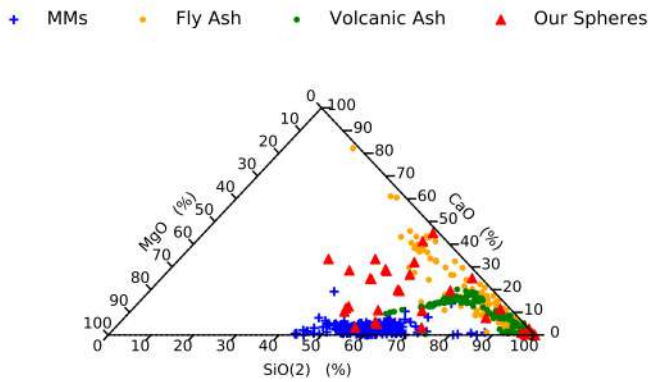


(f)

Figure 5.3: A number of different element ratios used in an attempt to separate out the extra-terrestrial CAIs whose Ca-Al-Mg ratios are similar to terrestrial materials. Abundances are shown in wt%.

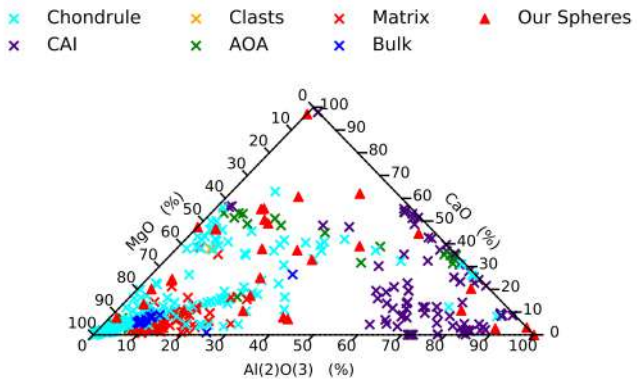


(g)

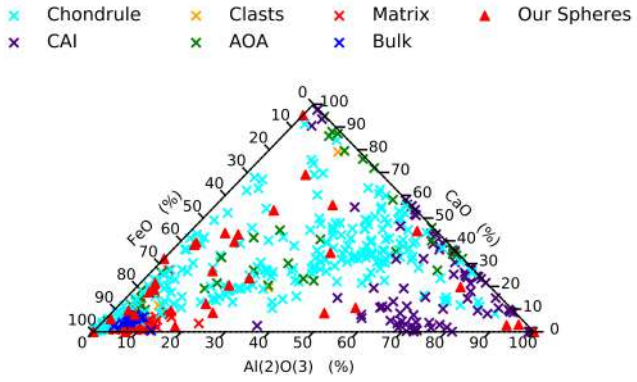


(h)

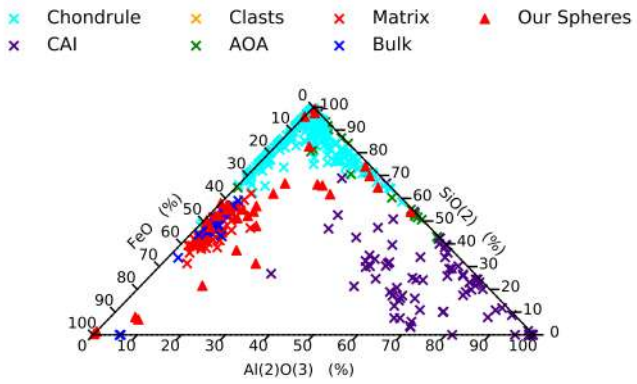
Figure 5.3: A number of different element ratios used in an attempt to separate out the extra-terrestrial CAIs whose Ca-Al-Mg ratios are similar to terrestrial materials. Abundances are shown in wt%.



(a)

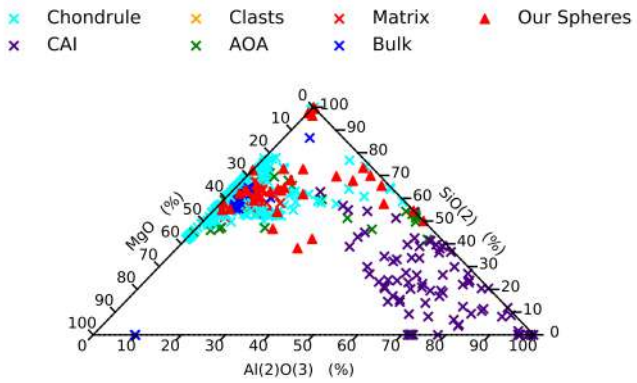


(b)

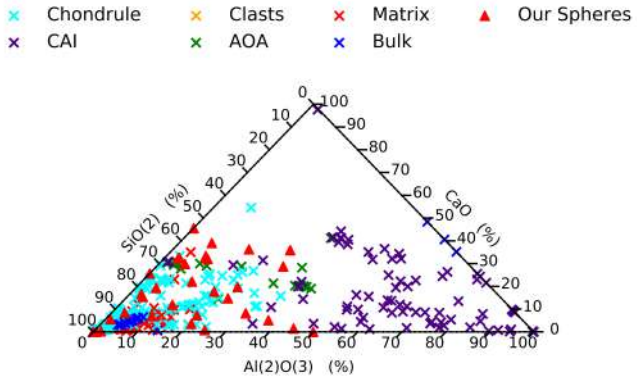


(c)

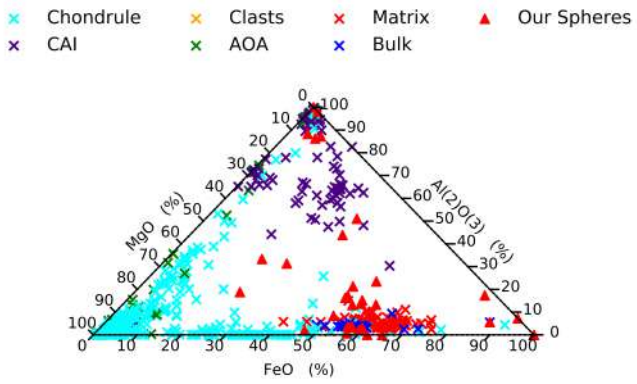
Figure 5.4: Ternarys plotting wt% data for various elements for spheres collected at Kwajalein atoll and common chondritic components.



(d)

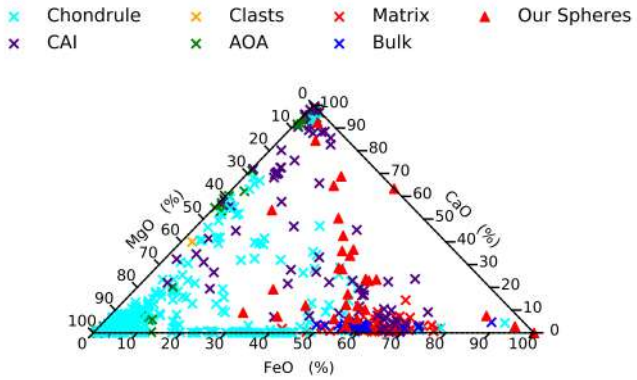


(e)

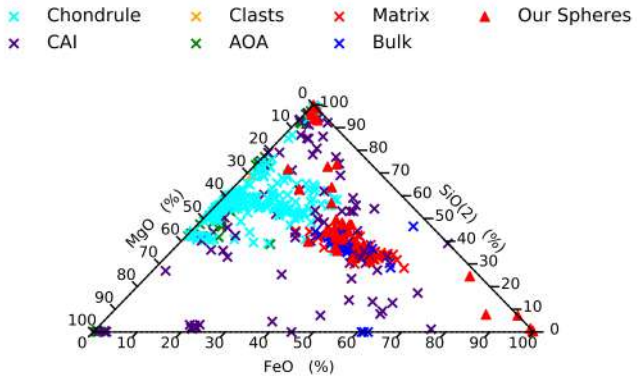


(f)

Figure 5.4: Ternarys plotting wt% data for various elements for spheres collected at Kwajalein atoll and common chondritic components.

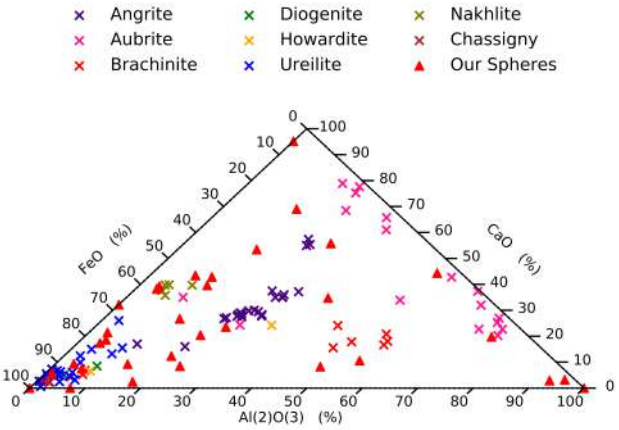


(g)

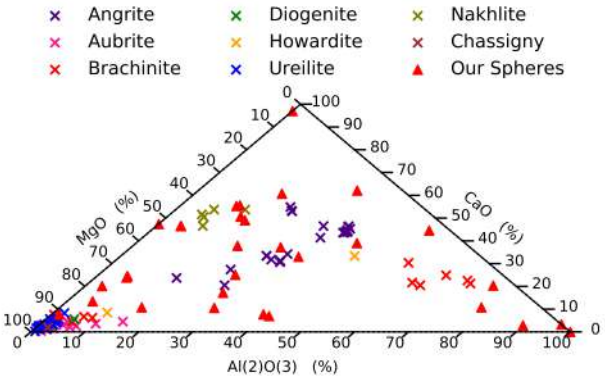


(h)

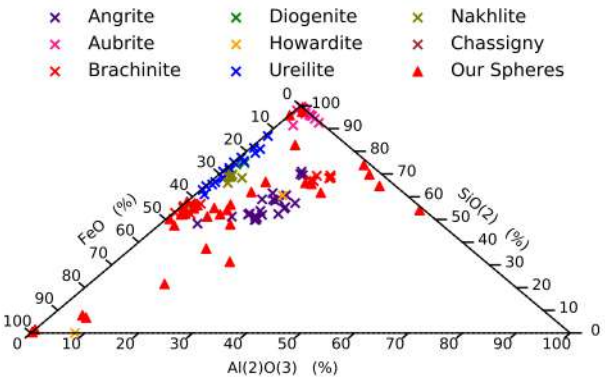
Figure 5.4: Ternarys plotting wt% data for various elements for spheres collected at Kwajalein atoll and common chondritic components.



(a)

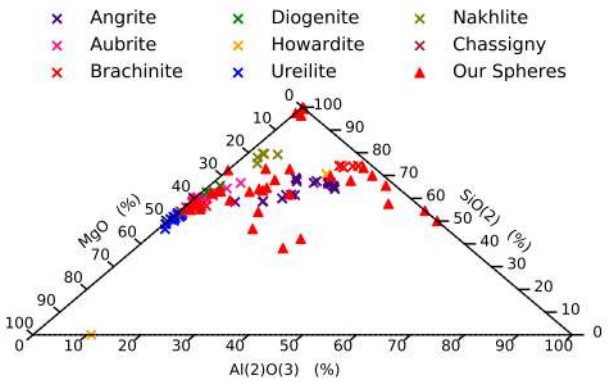


(b)

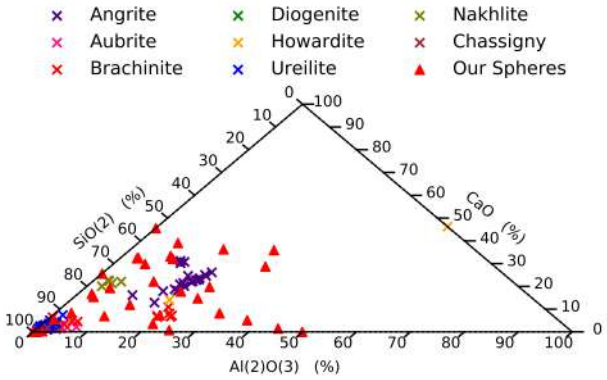


(c)

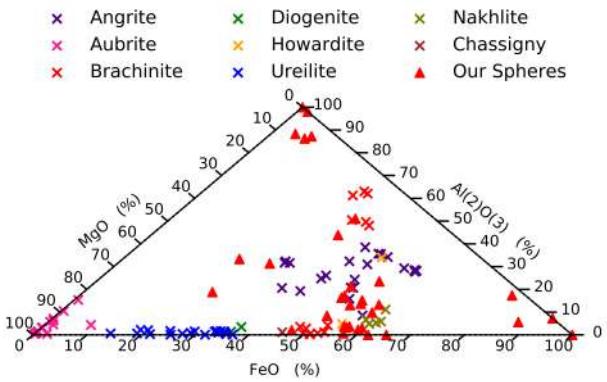
Figure 5.5: Showing the location of the candidate MMs compared to the compositional zones of bulk achondrite compositions. Abundances are shown in wt%



(d)

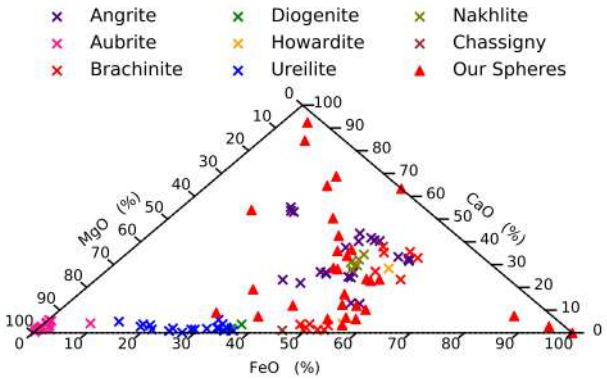


(e)

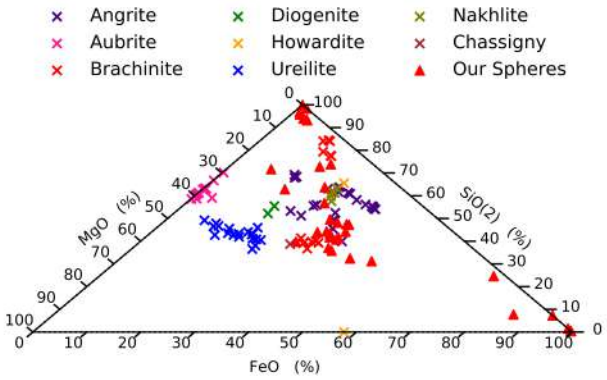


(f)

Figure 5.5: Showing the location of the candidate MMs compared to the compositional zones of bulk achondrite compositions. Abundances are shown in wt%



(g)



(h)

Figure 5.5: Showing the location of the candidate MMs compared to the compositional zones of bulk achondrite compositions. Abundances are shown in wt%

5.2.3 Detailed Analyses of Micrometeorite Candidates

5.2.3.1 Candidate 8-4-2

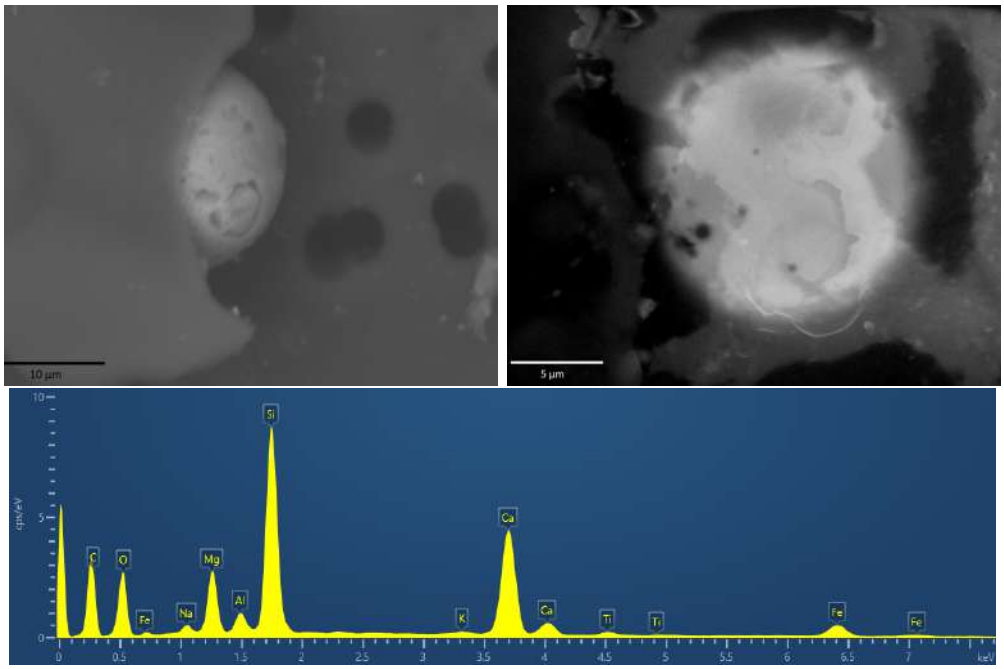


Figure 5.6: External (a) and internal (b) BSE images of candidate 8-4-2, along with the bulk spectrum obtained from the particle after preparation (c)

Candidate CS 8-4-2 appeared hidden under filter debris on initial inspection. The visible portion appeared spherical with a lightly etched and patterned surface (see Figure 5.6). Following polishing its interior showed two distinct BSE potentials, along with multiple dark vesicles.

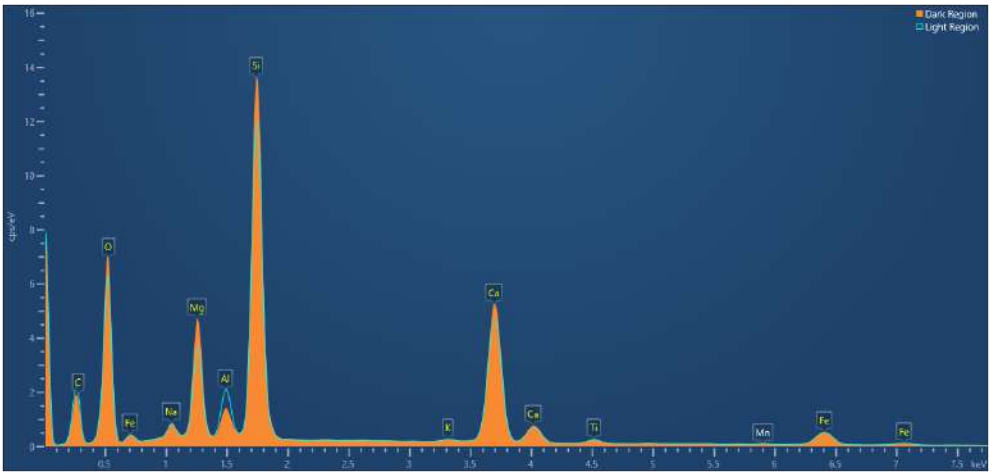


Figure 5.7: Comparisons of the spectra taken from the light and dark areas of candidate 8-4-2.

Comparisons of the spectra obtained from the light and dark regions suggest the lighter region is richer in aluminium and poorer in magnesium, silicon and calcium. From Figure 5.8 a, it can be seen that the composition of the sphere is unlike that of common terrestrial contaminant spherules (FA and VA). When compared to chondritic meteorite components the particle does not have a composition similar to single group on the ternary plot making any relationship unlikely. When plotted on ternary diagrams versus achondrites, it's composition consistently resembles Angrite compositions, however it can clearly be seen to be separate from the Angrites grouping on any plots involving aluminium. As such it is not possible to say that it is related to these achondrites. It is important to note however despite not fitting in with a certain achondrite group, the particle does remain in the achondrite populated regions of the ternary.

Combining the morphology of the sphere with its elemental abundance suggests that sphere 8-4-2 may be extra-terrestrial in origin with affinity to achondrites.

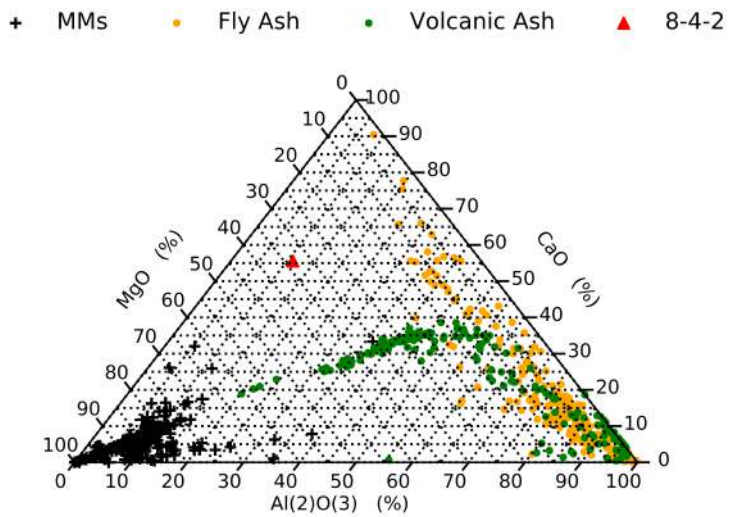


Figure 5.8: Showing the compositional ratios of sphere 8-4-2 from the Kwajalein atoll MM collection vs the locations of common terrestrial contamination and previously collected MMs

5.2.3.2 Candidate 9-9-7

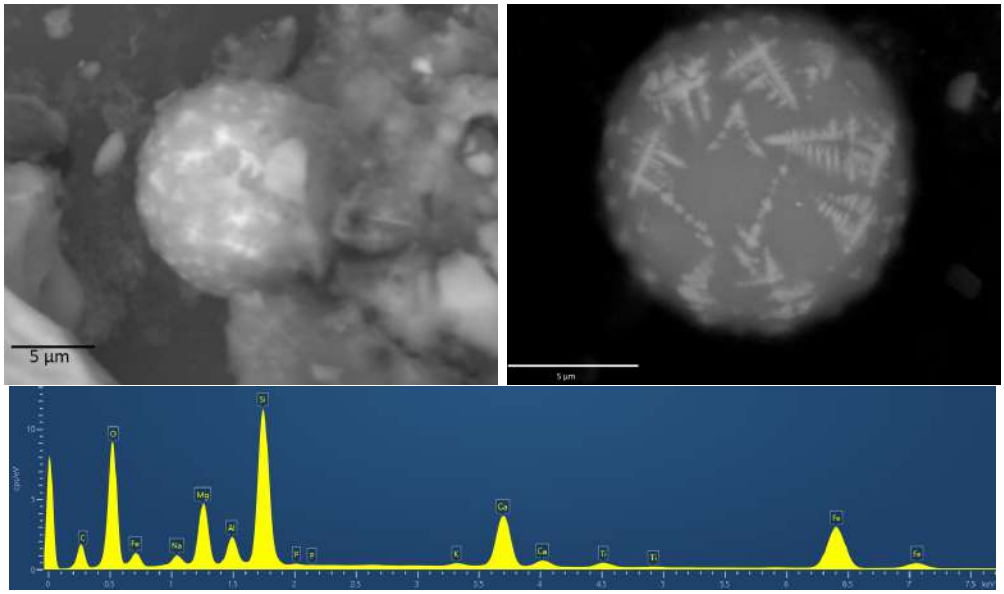


Figure 5.9: External (top left) and internal (top right) BSE images of candidate 9-9-7, along with the bulk spectra of the particle

Candidate 9-9-7 was partially embedded in debris on the filter. The particle's surface showed a number of bright regions high in iron set inside magnesium silicate. The interior of the particle exhibits a number of dendritic crystals evenly distributed throughout. Spectra obtained from this particle indicate that the brighter dendrites are iron oxides set in Mg rich glass/matrix (see Figure 5.10).

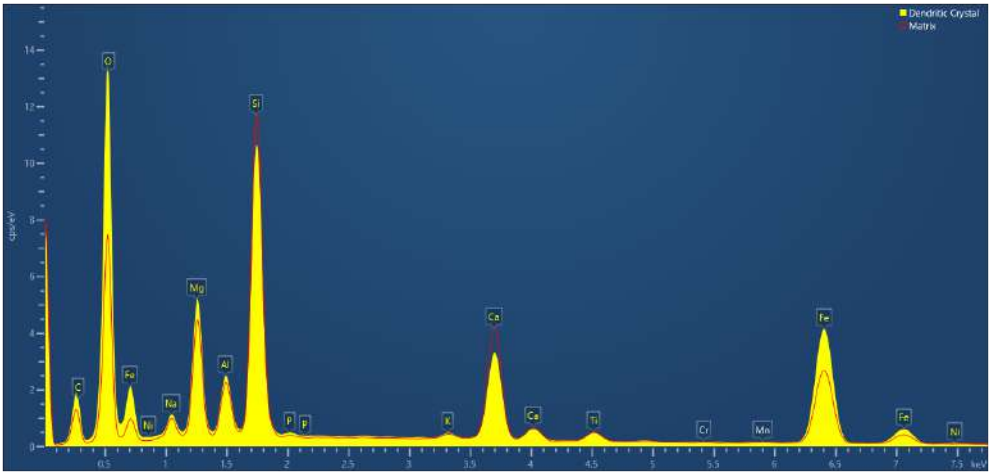
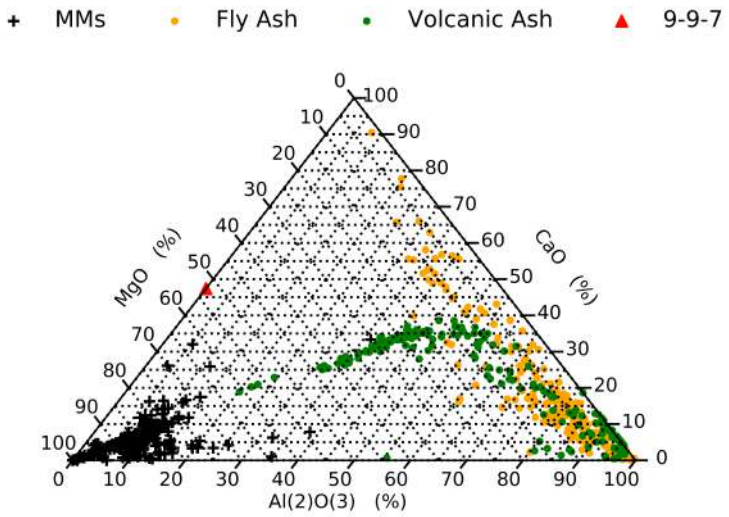


Figure 5.10: Direct comparison of the spectra of dendritic crystal in candidate 9-9-7 with a spectra of it matrix.



(a)

Figure 5.11: Showing the compositional ratios of candidate 9-9-7 from the Kwajalein atoll MM collection vs the locations of common terrestrial contamination and previously collected MMs

It can also be seen that the matrix of the sphere is higher in calcium than would be expected based on previously collected MMs, however the reason for the high abundance of calcium throughout the sphere is currently unknown. When compared to achondrites, the bulk chemistry of candidate 9-9-7 puts it amongst the angrites on every ternary diagram. Comparing its composition to the chondritic meteorite components shows that it does not sit in a single region dominated by a single component. The internal texture of candidate 9-9-7 is reminiscent of G-type and cryptocrystalline MMs and is contrary to the internal textures demonstrated by previously recovered achondritic MMs *(Taylor, Herzog, and Delaney 2007)*.

Candidate 9-9-7 has a chemistry that appears unrelated to common terrestrial spherules 5.11 but appears to be related to that of Angrite, achondritic meteorite. It has an internal structure similar to that of previously reported MMs. As such is likely E.T. in origin.

5.2.3.3 Candidate 11-5-29

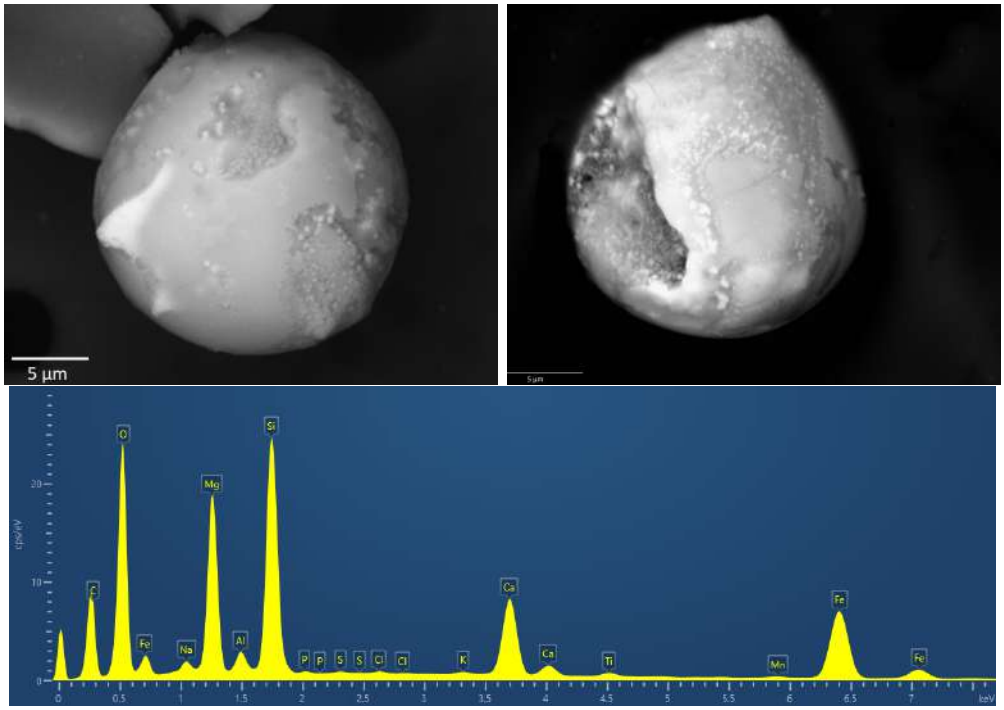


Figure 5.12: External (top left) and internal (top right) BSE images of candidate 11-5-29, along with the bulk spectra of the particle

Candidate 11-5-29 exhibits a complex surface with homogenous smooth regions, speckled regions containing large number of small calcium rich components and apparent bright features extruding. It's interior appears to be that of a porphyritic spherule, containing many small crystals, however it also contains regions which appear to be free of bright crystals. These regions are predominantly iron magnesium and silicon, with no calcium. The bulk spectra of the particle, however shows a significant calcium component. Analysis of the crystal and it's surroundings shows that these areas are calcium rich, providing the majority of the calcium in the bulk spectrum, whilst also having a higher iron content. These regions are therefore likely to be Fe-rich crystal in a Ca-rich matrix.

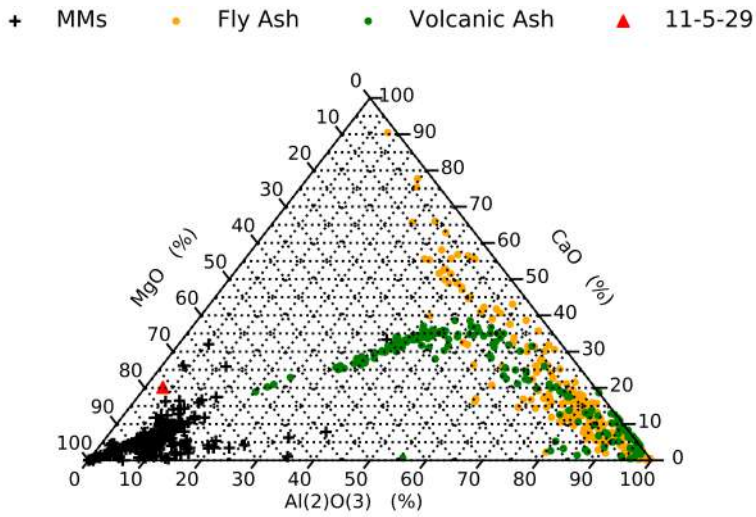


Figure 5.13: Showing the compositional ratios of candidate 11-5-29 from the Kwajalein atoll MM collection vs the locations of common terrestrial contamination and previously collected MMs

Candidate 11-5-29 has a composition similar to that of MMs and substantially different from terrestrial spheres on the Ca:Al:Mg plot (see Figure 5.13). When compared to chondritic meteorite components, candidate 11-5-29 sits near or inside the region of bulk chondritic compositions on all graphs and the inside the region dominated by chondrules in most, however its composition is significantly removed from that of CAIs when Fe:Si:Ca ratios are considered. It is important to note however that it is the particle's calcium content that provides the difference from the chondritic bulk composition. When compared to achondrite types the particle does not sit amongst any single group, and in many plots is completely separate from all achondrite dominated regions. Based on it's internal texture which is similar to previously collected porphyritic MMs, it's composition shadowing bulk chondritic compositions, and being unlike terrestrial spheres, it is likely that candidate 11-5-29 is E.T. in origin.

5.2.3.4 Candidate 11-8-16

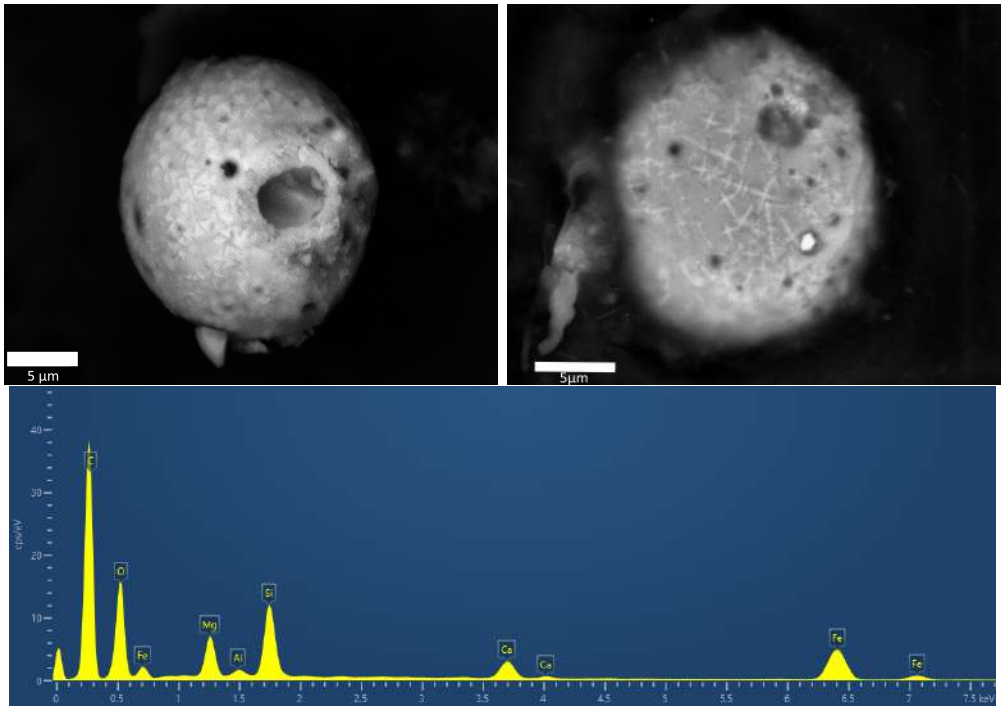


Figure 5.14: External (top left) and internal (twice prepared) (top right) BSE images of candidate 11-8-16, along with the bulk spectra of the particle

Candidate 11-8-16 exhibits bright triangular outcropping dendrites on its surface surrounded by a darker matrix. It has a single large vesicle surrounded with a number of smaller vesicles also outcrop on the surface dominated by a single large vesicles. These dendrites and vesicles are similar to those seen in sphere 9-9-7. Also outcropping is a single Cu-Fe-rich grain. A single Cu-rich grain has been previously reported inside a MM which had a Cu-Al-Fe-rich chemistry and has been linked to the Khatyrka meteorite *(Suttle, Twegar, et al. 2019)*. The Cu-rich grain in sphere 11-8-16 does not contain any aluminium and is likely to be pure copper or a Cu-Fe alloy. If confirmed this would be the second MM to be found containing a copper grain *(Suttle, Twegar, et al. 2019)* and would provide a unique chemistry to the literature. Due to the method of polishing it was possible to observe the grain emerge from within the particle and as such it is unlikely that this was added during preparation. This is further confirmed as no copper was used in the polishing or resin stages, the copper is also unlikely to have originated from the conductive tape. Finally to ensure that the grain was internal, the particle was re-prepared and imaged. Unfortunately to confirm the composition of the grain additional work is required; FIB and TEM analysis would enable the composition to be confirmed by ruling out any background contamination from other particle regions,

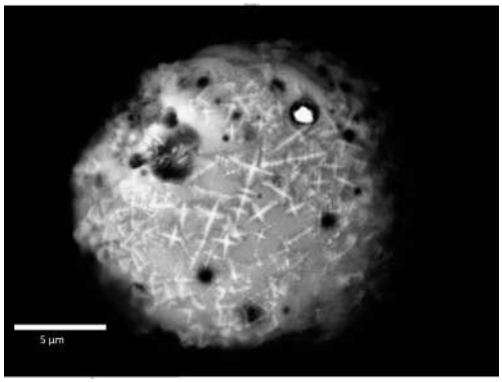


Figure 5.15: Image taken of candidate 11-8-16 following the second polishing. the copper nodule is still visible in the particle showing it not to be a fragment attached to the surface.

and would allow a better image of the grains structure to be obtained.

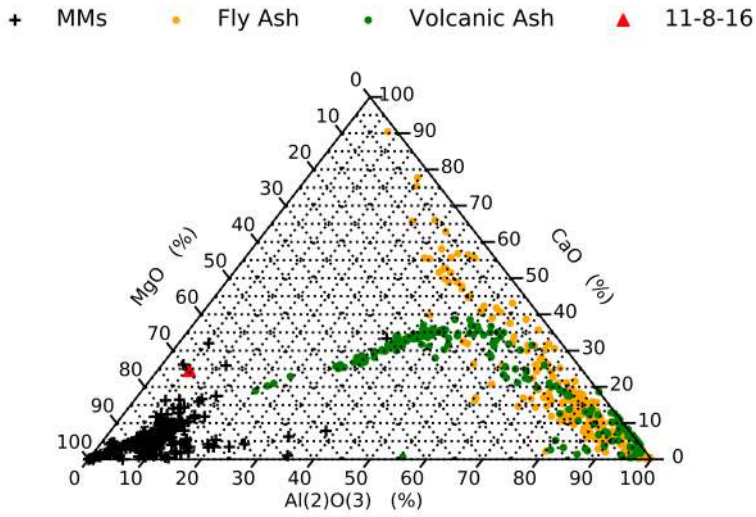


Figure 5.16: Showing the compositional ratios of candidate 11-8-16 from the Kwajalein atoll MM collection vs the locations of common terrestrial contamination and previously collected MMs

Figure 5.16 shows how the ratio of elements in candidate 11-8-16 are similar to those in previously collected MMs, and different from the terrestrial spheres. Comparing candidate 11-8-16 bulk composition with chondritic components shows that similarly to candidate 11-5-29, it sits in amongst the bulk chondritic compositions on plots not including Ca, and around the bulk chondritic region but its composition contains higher levels calcium. It composition is not similar to other E.T. body types and can been clearly seen to be separate from them on many plots. When it composition is compared against achondrite types, sphere 11-8-16 is clearly separate from each.

Based on candidates 11-8-16 internal structure and bulk composition, it is likely that it is extra-terrestrial in nature.

5.2.3.5 Candidate 11-9-40

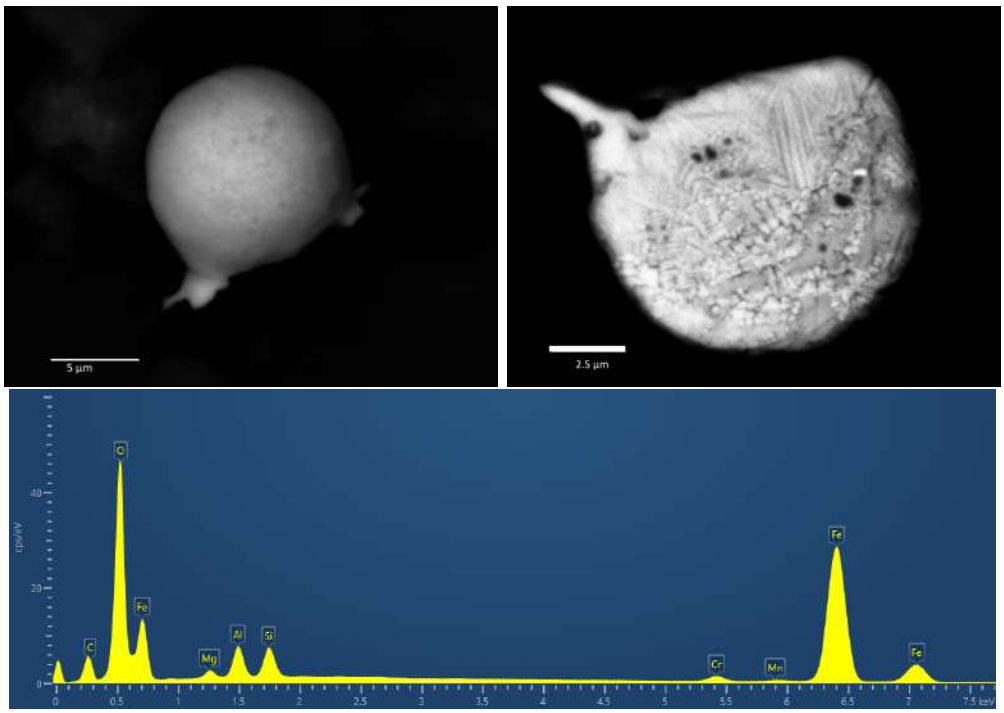
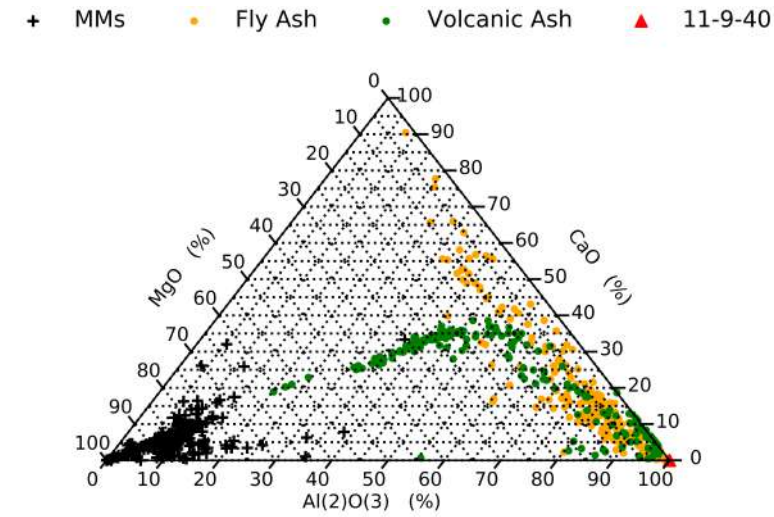
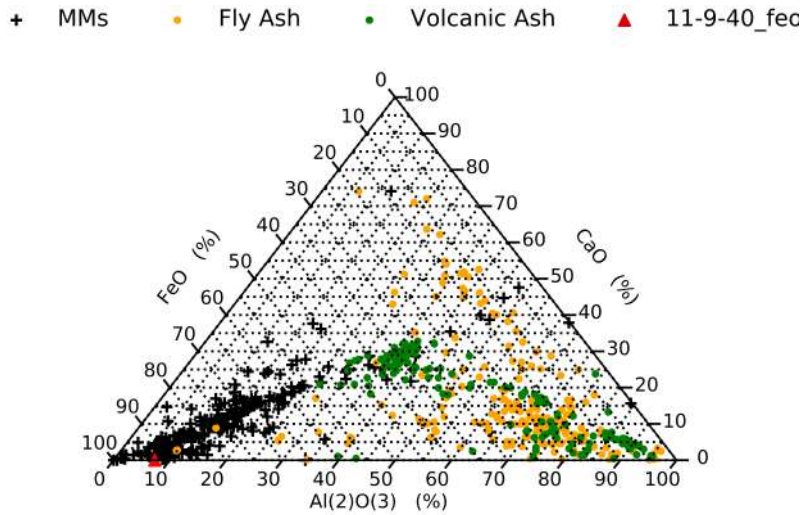


Figure 5.17: External (top left) and internal (top right) BSE images of candidate 11-9-40, along with the bulk spectra of the particle

Candidate 11-9-40 appeared to have a smooth slightly mottled surface, with no significant changes in brightness. It's shape was slightly elongated along a single axis, forming a teardrop shape. It's interior shows a distinct crystalline texture. The top half appears dominated by large parallel grain growth, whereas the lower half exhibits more equant crystals, which appear to show different brightnesses (perhaps indicative of different chemistries). Candidate 11-9-40 also exhibits a number of small vesicles which have outcropped from its surface. The candidate's chemistry is dominated by its iron content in both regions. This change in crystal size could therefore imply a cooling gradient across the spherule or are the result of size sorting during atmospheric entry *(Genge, Suttle, and Ginneken 2016)* .



(a)



(b)

Figure 5.18: Showing the compositional ratios of candidate 11-9-40 from the Kwajalein atoll MM collection vs the locations of common terrestrial contamination and previously collected MMs

Candidate 11-9-40 as plotted in figure 5.18 sits amongst the outliers of the MMs grouping, however its composition is sufficiently different to terrestrial spheres to likely belong to the MM group. However in Figure 5.18 b, it can be seen that replacing the magnesium with iron in the comparison makes the spherules composition more aligned with previously collected MMs. Its high iron content of sphere 11-9-40 would make it an I type candidate spherule, however due to the Cr contained within the particle, it

is more likely to be a G-type spherule. When plotted against chondrites types, sphere 11-9-40 sits separately from every component on a large number of the plots. Similarly when plotted against achondrite types, 11-9-40 does not sit amongst a single type group on many of plots and as such shows no affinity with either chondrite areas or achondrites

Despite it's apparently E.T. composition as shown in Figure 5.18 and it distinct texture, it is not possible to state that candidate 11-9-40 is E.T. in origin, due to the number and range of Fe-rich spherical contaminates collected on Kwajalein atoll, from which it is currently impossible to distinguish. Future work should include further analysis of this particle to obtain it's origin.

5.2.3.6 Candidate 12-1-56

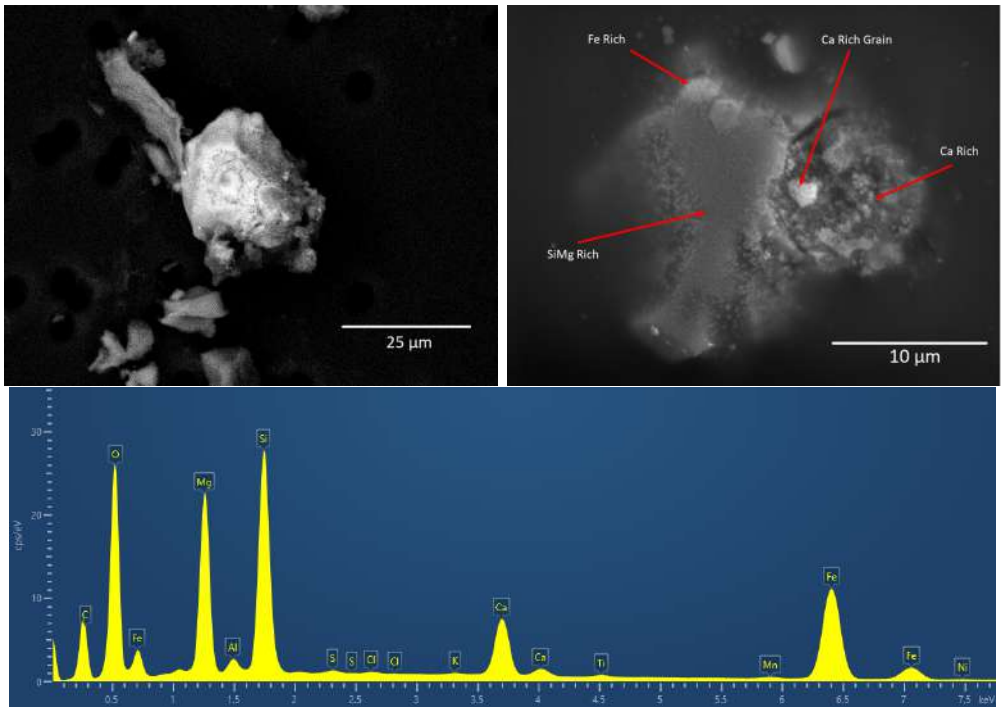


Figure 5.19: External (top left) and internal (top right) BSE images of candidate 12-1-56, along with the bulk spectra of the particle

Candidate 12-1-56 is a non-spherical grain which was identified from the Kwajalein filter based on its surface morphology and brightness which suggested that it may have magnetite coating. It is dominated by a smooth Mg-rich silicate phase which has small bright crystals at its edges which are Fe-rich. There also a few large Fe-rich crystals, and along the edge appears to be a porous region containing Ca-rich grains. The particle's

bulk chemistry is high in silicon, iron and magnesium indicating the probable presence of olivine. However analysis of the individual regions of the particle (see Figure 5.20), show a wide variety of chemistries; including Fe-rich and Ca-rich. The particle contains a large bright calcium rich inclusion on it right hand side, with the grain itself contained in larger darker Ca enriched region. Towards the top of the particle there is an iron rich grain embedded in the particle's top edge. The remainder of the particle consists of a SiMg rich area, which contains numerous small crystallites. These features combined together indicate a possible olivine grain attached to a fine grained matrix (*M. Genge per. comm.*).

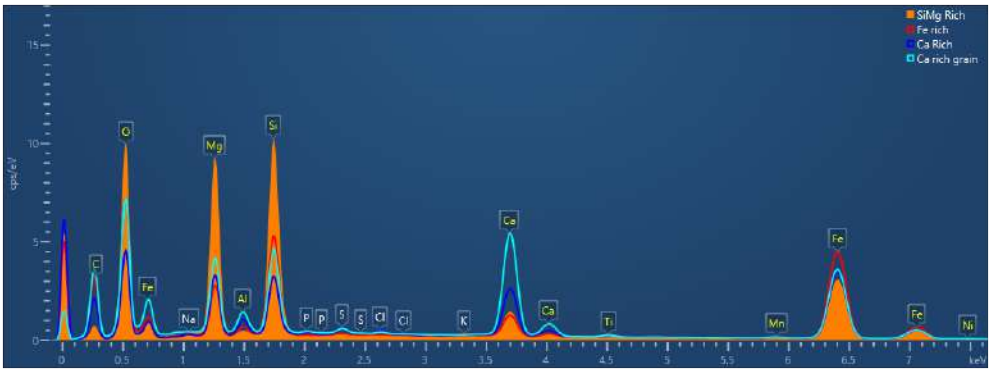
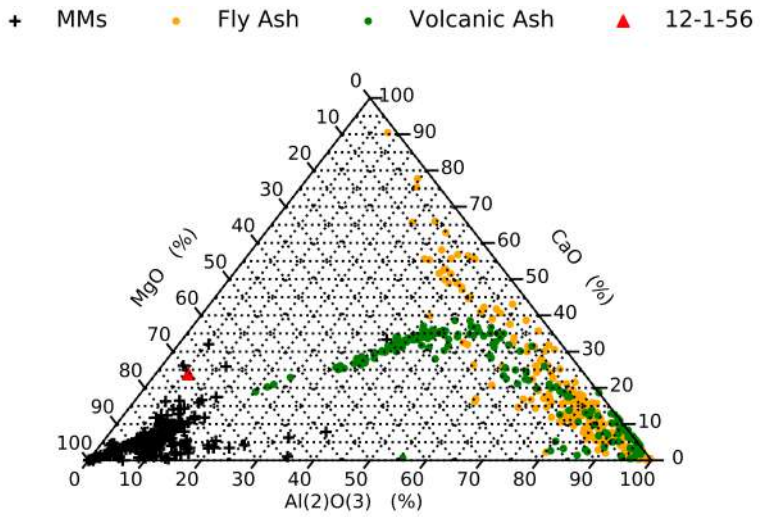
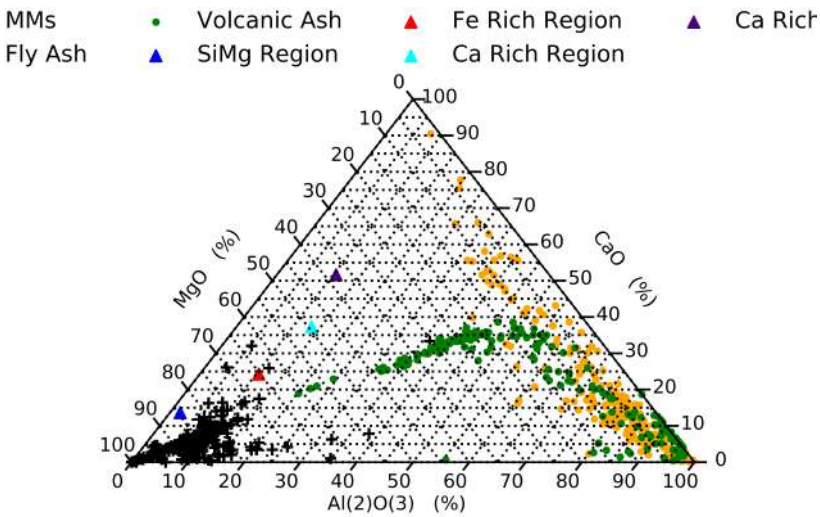


Figure 5.20: A comparison of the spectra taken in the 4 different regions of sphere 12-1-56 collected during the Kwajalein MM collection



(a)



(b)

Figure 5.21: Ratios of common terrestrial contamination and previously collected MMs vs a) the bulk compositional ratios and b)regional compositional ratios of candidate 12-1-56 from the Kwajalein atoll MM collection.

Comparing the particle's bulk chemistry to that of previously collected MMs and terrestrial debris shows that the particle is within the area occupied by MMs towards the richer in Ca grains. Comparing the particle with chondritic meteorite areas shows that the particle has a composition similar to the chondritic bulk dominated data when calcium is not included. On plots which do have calcium included, candidate 12-1-56 shows an increased calcium content compared to bulk chondritic. When compared with

the achondrite types candidate 12-1-56 does not appear to sit amongst any particular group consistently and as such is likely not related to any achondrite. Based on it's morphology showing a number of E.T. like components (small crystal growths, large metallic beads etc) and it's chondritic composition it is likely that candidate 12-1-56 is extra-terrestrial in origin.

5.2.3.7 Candidate 12-2-10

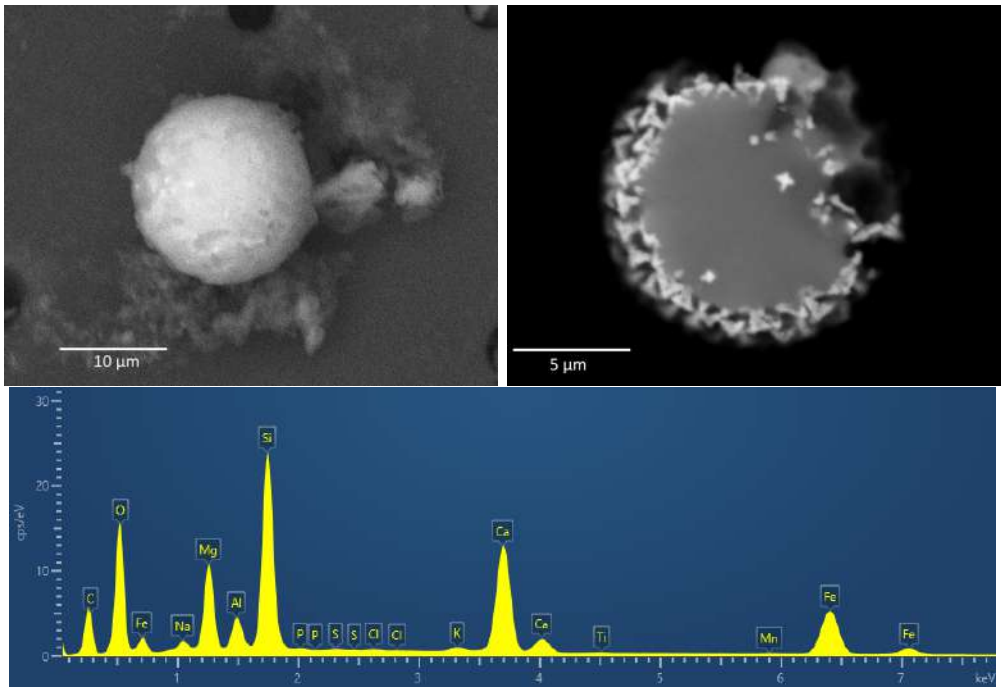


Figure 5.22: External (top left) and internal (top right) BSE images of candidate 12-2-10, along with the bulk spectra of the particle

Spherule 12-2-10 exhibited a lightly etched surface, with brighter grains embedded in the matrix. In a cross section its abnormal interior can be seen; it has a glassy inner region surrounded by a number of bright crystals. The interior of the sphere is rich in silicon, magnesium and calcium, with some iron and aluminium (see Figure 5.22), whilst the surrounding crystals show much higher levels of iron and oxygen, along with lower calcium and silicon values (see Figure 5.23).

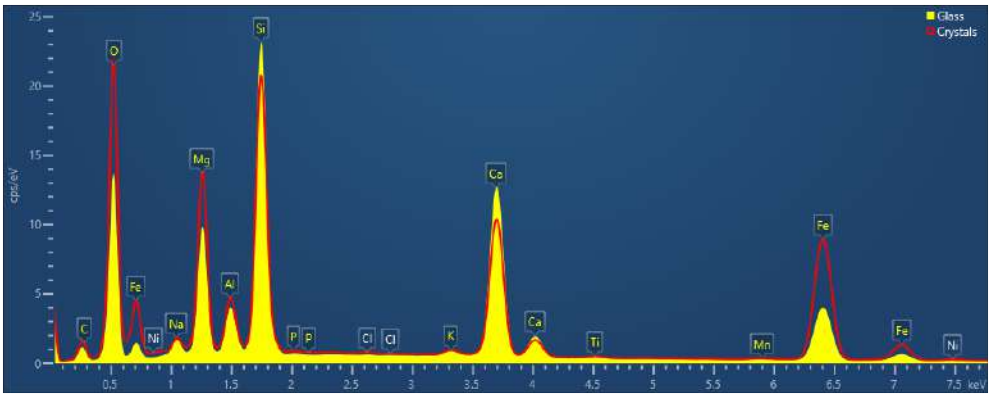


Figure 5.23: Comparison of EDX spectra obtained from the central glassy region and outer crystal layers of candidate 12-2-10

Despite the small size of the particle, the structure is reminiscent of the iron rich magnetite rims which can form on MMs, however the crystal size and depth of the iron rich area is far larger than would be expected in a magnetite rim *(Genge, Grady, and Hutchison 1997)* with each crystal exceeding 1 µm.

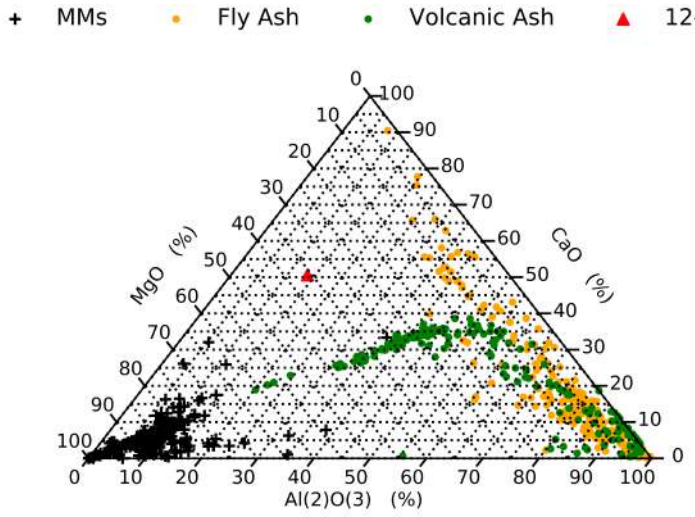


Figure 5.24: Showing the compositional ratios of candidate 12-2-10 from the Kwajalein atoll MM collection vs the locations of common terrestrial contamination and previously collected MMs

Candidate 12-2-10 sits in a region not occupied by either terrestrial or E.T. spheres (see Figure 5.24), due to its elevated Ca fraction. Comparisons with chondritic meteorite regions shows that it does not sit amongst or near any consistently, and appears to be independent of these groups. Similarly the particle's composition also appears to be

independent when compared to achondrite subtypes and does not sit in a single group.

Chemically, candidate 12-2-10 does not appear to be extra-terrestrial in nature. Its bulk composition is unlike that of previously recovered extra-terrestrial material. However the particle's composition is also unlike that of the most common terrestrial spheres, and as such it is not possible to chemically confirm either terrestrial or E.T. and as such it not currently possible to state either E.T. or terrestrial on the basis of its composition. It's structure is interesting, with a outer Fe-rich layer which is similar to a magnetite rims previously seen on MMs and as such candidate 12-2-10 warrants further analysis.

5.2.3.8 Candidate 12-7-25

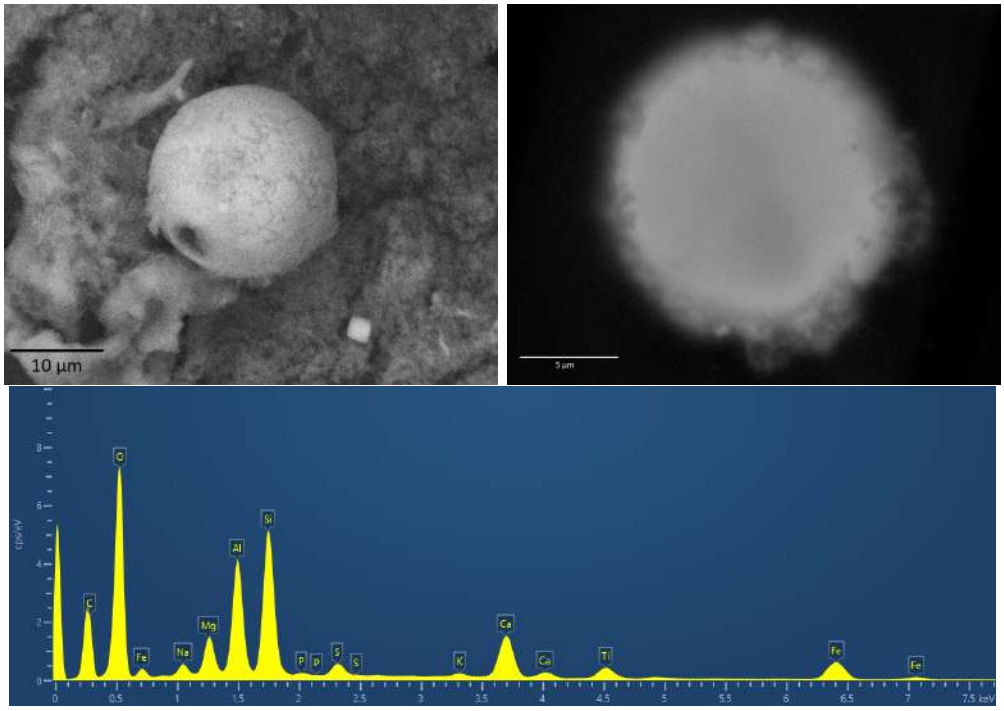
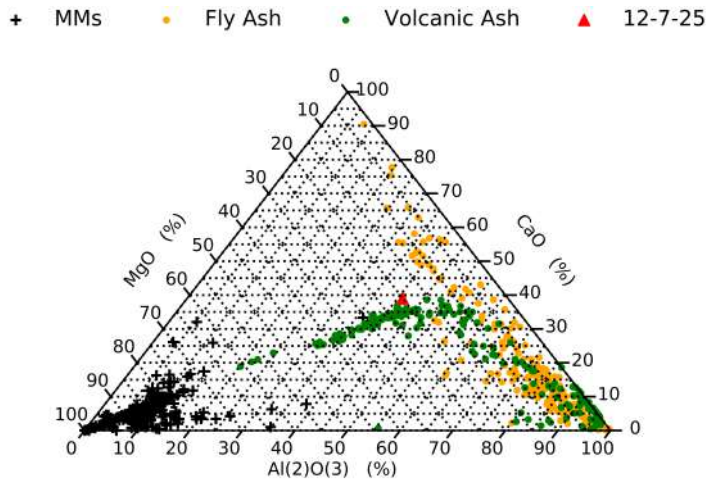
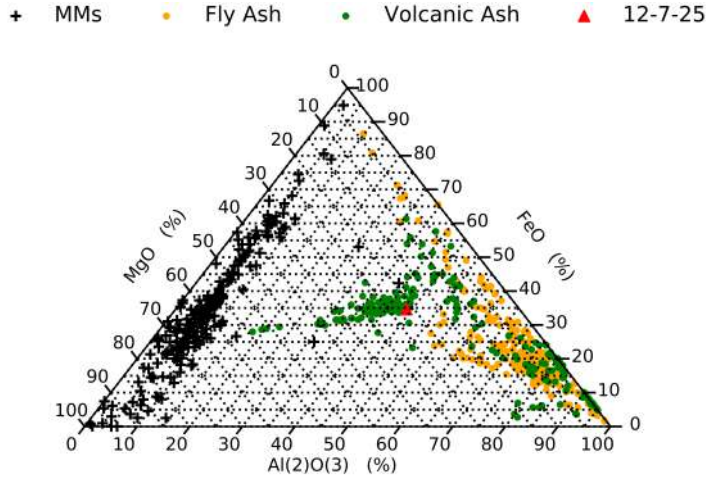


Figure 5.25: External (top left) and internal (top right) BSE images of candidate 12-7-25, along with the bulk spectra of the particle.

The outer surface of candidate 12-7-25 appears lightly etched however from it's interior it appears to be a smooth homogenous sphere. It is lacking in many of the identifying features which could be seen on many of the other collected spheres. It has a very high silicon content with high aluminium ratio compared to magnesium and iron.



(a)



(b)

Figure 5.26: Showing the compositional ratios of candidate 12-7-25 from the Kwajalein atoll MM collection vs the locations of common terrestrial contamination and previously collected MMs

The composition of sphere 12-7-25 does not match with the previously collected MMs when compared due to a much higher aluminium and calcium content. Unlike previous particles, the ratio of element following the removal of calcium still is not amongst the MMs but firmly in the region of terrestrial volcanic ash. As such, due to both it's morphology and chemistry not showing any signs of extra-terrestrial origin, it is highly likely that sphere 12-7-25 is a volcanic ash particle which had been collected during the experiment run.

5.2.3.9 Candidate 12-8-24

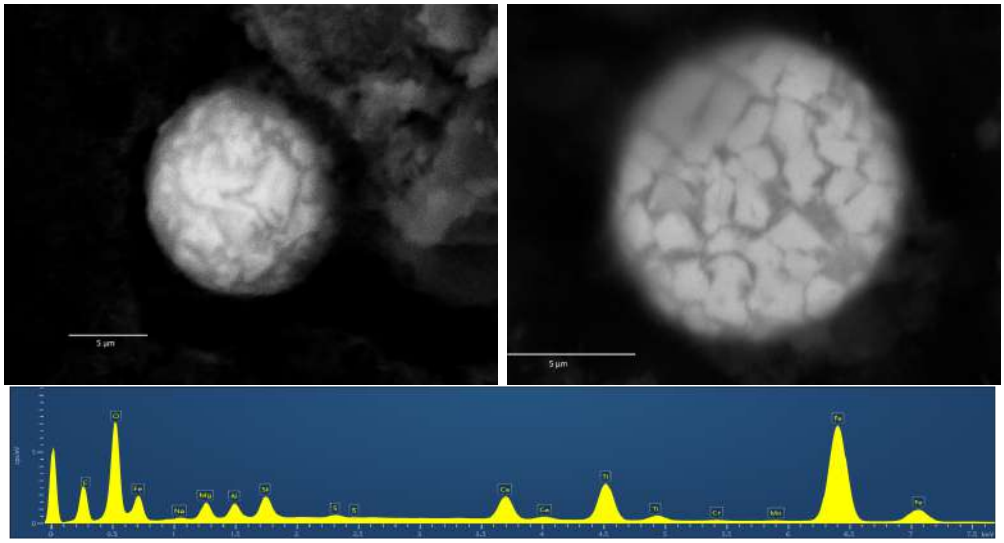


Figure 5.27: External (top left) and internal (top right) BSE images of candidate 12-8-24, along with the bulk spectra of the particle.

Candidate 12-8-24 appeared spherical with a large number of irregular iron rich grains on the surface. Its interior appears to to be constructed of a number of large crystals interlocked together. The crystals are rich in Fe and Ti and oxygen, all of which also dominate the bulk chemistry. The aluminium content is higher than that of the magnesium content, with small amount of chromium and manganese also being found.

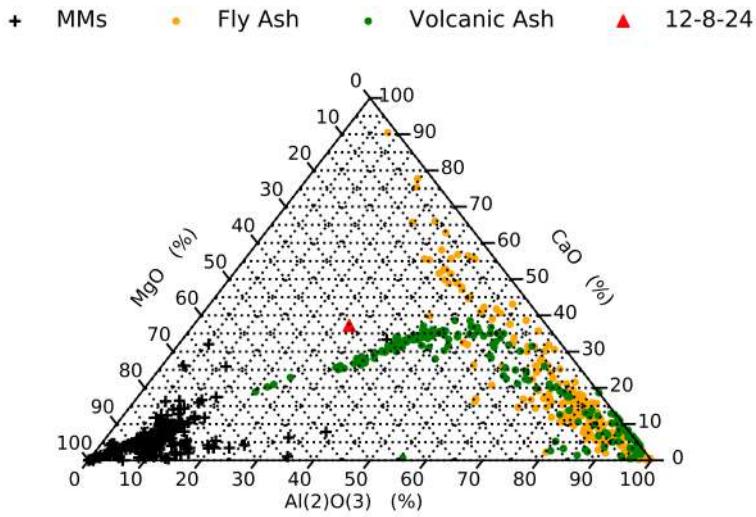


Figure 5.28: Showing the compositional ratios of candidate 12-8-24 from the Kwajalein atoll MM collection vs the locations of common terrestrial contamination and previously collected MMs

Plotting it's location on the same axis as the previous sphere we can see that it's chemistry matches it's morphology, and sits in a similar region to the other volcanic ash particles albeit with a raised calcium content. Comparison with chondritic components and achondrite subtypes shows no association. It is also unlikely that the particle is volcanic in origin, as it also does not show an association across multiple ternary graphs. As such it is likely that the particle is terrestrial in origin, and due to its high Ti content, artificial in origin.

5.3 Discussion

5.3.1 Collector Performance

Efficiency The performance of the collectors used in the two collections was below the level that which was originally planned. Filters collected from Kwajalein atoll showed a significant decrease in the flow rate over the collection period as a result of filter blockages caused by the formation of salt crusts. The formation of salt crusts led to a reduction in the flow rate over the collection period of around 15% - 40%. Despite this, large numbers of particles were recovered on the filter's surface in a large range of sizes (several millimetres to a few microns), demonstrating that the collector was working, albeit with a lower flow rate.

The collector in the Antarctic also performed below expectation, with a limited number of particles being collected despite a more consistent and higher average flow rate than was recorded at Kwajalein. The particle seen on the filters collected in the Antarctic are generally smaller, with no large E.T. candidates found. This is either due to the collector pressure not being sufficient to gather the particle in, or a lack of E.T. particles in the Antarctic environment, however large numbers of MMs have been recovered from other Antarctic collections (e.g. 3272 from the SPWW *(Taylor, Matrajt, et al. 2007)*).

The aim of situating the collector on the Kwajalein atoll was to reduce the amount of terrestrial contamination. The amount of contamination seen was below what would have been recovered in many locations with higher human activity, however the amount recovered was unfortunately still sufficient to remove the possibility of analysis of non-spherical particles.

The move of the collection location to the Antarctic significantly reduced the ratio of spherical to non-spherical particles. This was due to the almost complete removal of salt grains and large mineral grains from the filter surface. The BAS location proved to be the better location for a collection to take place, however it also highlighted the need for a bespoke collector. This collector would ideally run with a higher flow rate and not require the large pipe system that was used in the BAS collection.

Unfortunately calculations of efficiency and flux are difficult since the air flow was measured at the pump inlet; significantly removed from the filter. As such any air multiplication factors which arise due to the filter casing cannot be taken into account. The equipment used to perform these collections has since been removed and as such it is not possible to perform laboratory tests to ascertain the correct values. To improve any such calculation in future tests, air flow measurements should be taken at the casing inlet, not the pump inlet.

5.3.2 Collection Bias and Flux

Modelling the effective radius at which the collector would suction in particles shows a significant drop off in collection radius with increasing particle size (see Figure 5.29). The model used the force acting on the particle at a distance to calculate the acceleration at that distance. These values were then integrated twice over the the settling time of the particle, giving the total distance travelled by the particle in the direction of the pump. The maximum distance the particle a given size could travel in the free fall

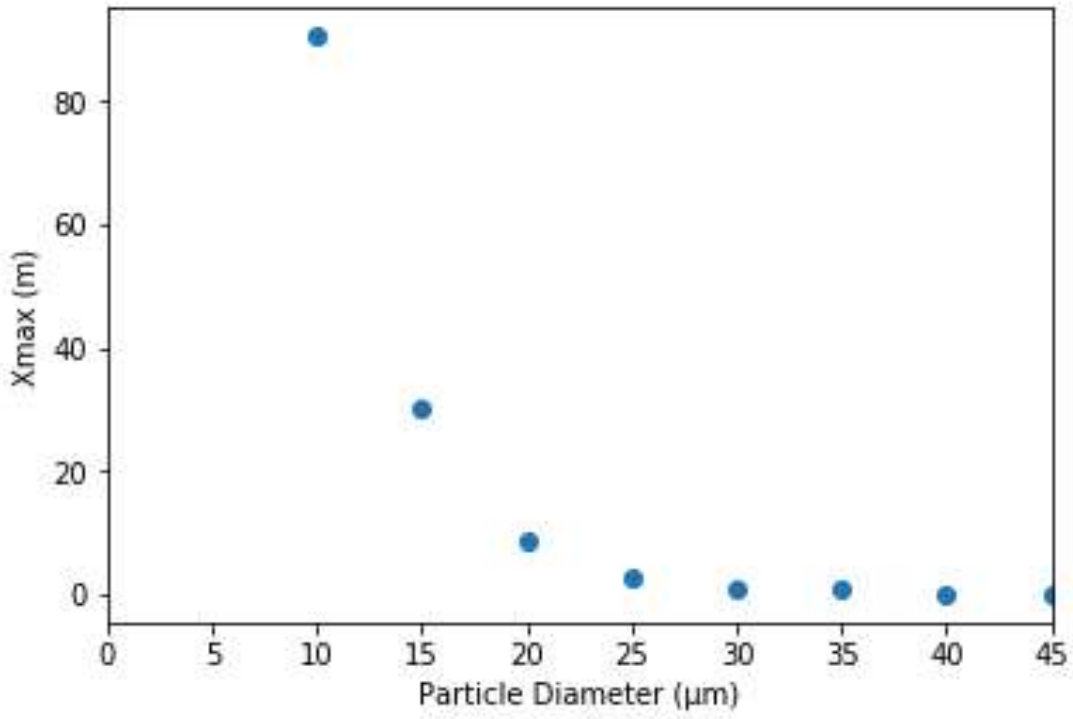


Figure 5.29: The effective radius of the Kwajalein MM collector for settling particles (made entirely of olivine) of a given size, starting at a height of 100m

time was assumed to be the collection limit of the pump for a particle of that size. This model assumes no wind or turbulence and provides a maximum value, the true collection volume is likely smaller than the model would suggest. From this it can bee seen that the smallest pickable particle (5-10 µm) will be able to be collected a substantial distance from the filter (assuming no wind or turbulence). The largest particles however (50-100 µm) would only be able to be collected if they settled directly down the side of the filter casing. As such the filters will be highly biased towards the smaller particles.

The small collection distance increases the effect of wind on the collections. The collectors effective radius is small enough that most collected larger particles will have been transported from outside the collector radius by the air currents onto the collector surface. As such it is likely that the wind direction facing surface collected the larger particles as the other surface directions would not be able to overcome the drag forces created by the wind. As such the inlet surface for particles over 50 µm is a quarter of that of the smaller spheres. Unfortunately weather data for the collection site is not available,and as such it is not possible to calculate accurately the effect of wind on the collection, however the site was chosen so that the wind direction would be of the sea, and not across the atoll limiting the effects of wind tunnels created by building and

ensuring that only 'fresh air' is sampled so as to reduce the contamination from the human habitation on the atoll.

Overall it is difficult to determine the effective radius of the collector without additional information on the air throughput of the casing inlet. Thus it has been simply modelled as a single inlet, with the entire mass flow passing through an area the size of the filter. It is however likely that the ambient conditions would reduce this effective radius and as such that this is probably a maximum value. The force acting on the particle is therefore the drag of the air passing towards the inlet and can be calculated as seen in 5.1

$$F_d = 3\pi\nu r\bar{V}_{ap} \tag{5.1}$$

where F_d is the force of drag at acting on the particle ν is the viscosity of air (Pa s), r is the particle radius (m), $\bar{V}_{ap}$ is the air speed at the particle ($\mathrm{m\,s^{-1}}$) and is given by:

$$\bar{V}_{ap} = \frac{\bar{V}_{ai}A}{A_a} \tag{5.2}$$

$\bar{V}_{ai}$ is the air velocity at the inlet ($\mathrm{m\,s^{-1}}$), A_a is the area of the sphere of radius X where X is the distance between the inlet (m^2) and the particle and A is the area of the inlet (m^2).

Based on the number of particles recovered from the SPWW, a particle larger than 50 µm would be expected to be found every other week *(Taylor, Lever, and Harvey 2000)*. Over the four weeks analysed in this thesis, no E.T. particle of this size has been identified. This filter bias provides a possible explanation for the reason no particles greater than 50 µm in diameter are seen in this collection; all the E.T. candidates are smaller than 20 µm. Conversely the lack of large particles may be due to seasonal variations and analysis of additional filters from the first collector run during winter should be undertaken to confirm if this is the case.

Calculating the flux of the of possible E.T. particles shown in Table 5.1 assumes that that the particles have an average density of 2800 $\mathrm{kg\,m^{-3}}$ for the SiMg-rich particles *(Plane 2012)* and density of 7000 $\mathrm{kg\,m^{-3}}$ for the FeNi-rich particles. The calculation also assumes that the effective radius of the filter is as given in Figure 5.29 and a total mass flux of 0.292 tonnes per year can be calculated from the collection results. This value is substantially lower than expected based on previous calculations *(Flynn 2002)* where particles in the 10 to 500 micron range are expected to provide the bulk of the micrometeorite flux. Comparisons of this flux rate with the SPWW also show

this value to be significantly lower than the 1,200 tonnes per year *(Taylor, Lever, and Harvey 1998)*. Flux calculation using the minimum collection distance of the filter edge gives an estimated flux of 95.4 tonnes per year. Again this value is significantly lower than would be expected and highlights the much lower efficiency of the collector than expected.

5.3.3 Collection Events

A number of filters were run in a time period which corresponded with terrestrial or E.T. events. It was possible to identify changes in the flux caused by the launch of NuStar. The results of which can be used to roughly identify settling times for particles of different sizes. Particles larger than 20 microns having increased and return to prelaunch conditions 3 weeks later. This change in particle flux is similar to that predicted based on previous work for the largest particles > 50 µm where they would be expected to settle out over the course of a week from 80km *(Kasten 1968)* . However differences occur between predicted and observed results for smaller particles, where a spike in flux can be seen two weeks later, despite previous work (e.g. see *(Messenger 2002; Flanagan and Tayler 1967; Kasten 1968)*) suggesting that it would be expected that 10-50 µm particles would not have reached the collector from the Pegasus rocket launch height (12,000 m) *(Office 2019b)* for several weeks due to their low settling velocity , and would likely have been mostly dispersed by air currents during the time taken to settle *(Tupper et al. 2004)*.

A number of possibilities for these discrepancies exist. Firstly, the settling rate assumes limited turbulence and abnormal air currents, both of which exist near to and in the region surrounding a rocket exhaust and that the particle remains in the hydrodynamic continuum regime. Secondly, weather patterns are also not included in these simulations and this will also influence the settling time of the particle significantly.

It was also intended that filters would correspond with the times of meteor showers (e.g. c-Andromedids for K12), however during those periods no change in flux on the filters was observed. Previous work has calculated 50-100 µm particle will have taken under a week, settling to ground level from 80 km (e.g. see *(Messenger 2002; Kasten 1968)*). As such, the filter corresponding to the week of the comet pass was analysed (K12). The filter did not show any increase in particle flux despite previous collections showing increase in flux during cometary passes *(Busemann et al. 2009)*. Two reasons present themselves as possible solutions to the lack of flux; firstly that the location for

the collection did not experience the flux increase due to local atmospheric conditions (e.g. rain, wind, no direct infall) or two; the particles were present but not collected due to the collection bias against larger particles.

5.4 Summary

Eight filters from the Kwajalein (K08, K09, K11, K12) and BAS (B14, B15, B16, B26) collections have been analysed. Filters collected from Kwajalein showed high level of contamination, which prevented analysis of non-spherical particles. Despite this a number of interesting particles were recovered and further analysed, resulting in eight extra-terrestrial candidates being identified. The filters collected from BAS filters showed a significant reduction in non-spherical contamination. Unfortunately they also also showed limited particles of interest. It is possible that the lack of particles is due to the reduction in flow rate caused by the indoor/outdoor setup of the filter required to allow maintenance in bad weather.

The Kwajalein MM collection allowed for a number of unweathered particles to be recovered. Unfortunately the number of particles which were collected per filter appears to be low, with fewer than 5 E.T. candidates appearing on the filters (K8:1, K9:1, K11:4, K12:4). It is possible that this could be rectified by increasing the air flow over the filter, allowing particles to be collected from a larger volume of air. Increasing the filter exposure time may also improve the number of particles collected per filter, however, this is likely to see diminishing returns as the salt build up on the filter surface increases.

The washing procedure used on the Kwajalein and BAS filters may also be improved, allowing for separation of particles and thus potentially removing large numbers of terrestrial particles, and enabling analysis of all particle types, not just CS's (e.g. by the addition of a magnetic ring around the suction cup, magnetic particles would form a ring around the remaining particles which are pulled into the centre). However, it is unlikely that any particles on the maps were missed as control sections were tested twice by two different operators, with no significant difference in the number of spherules identified, and as such it is unlikely to effect the number of CS's recovered.

By using the datasets compiled from previous particle collections, this thesis has been able to identify possible element ratios allowing terrestrial and E.T. particles to be distinguished chemically and thus highlighting regions outside bulk chondritic that may correspond to E.T. particles (e.g. CAI-like). The datasets have also been able to

identify E.T. CS candidates from particles in the Kwajalein atoll MM collection. The successful identification of particles can therefore confirm the utility of the database constructed Chapter 4.

Combining the datasets with SEM-EDX work has allowed us to identify particles as E.T. A number of these particles have exhibited a number of peculiarities, including Cu-rich grains, abnormal rims on glassy particles and increased Ca levels. These particle may represent new CS types found only at the sub 50µm size analysed in these collections, which had not previously been focused on. Unfortunately due to time constraints, it was not possible to perform more in-depth analysis of the spheres in question to confirm their E.T. origin (e.g. SIMS). The appearance of high Ca values in many of E.T. particles does raise an important question; is the calcium there, or is it a product of the washing or analysis procedure? To answer this, the particles would again require further analysis.

Given more time, this project would also benefit from the analysis of the remaining filters which were not able to be analysed in the allotted time frame. These would be able to provide a more in-depth analysis of the short term flux of MMs. Analysis of additional filters through multiple seasons would enable a comparison between the number of particles and particle types. A secondary test of the pump efficiency at the inlet following the additional tube would have helped the understanding of the low particle yield.

To summarise, the MM collection from the Kwajalein atoll and BAS collections both suffered from lower than expected particle yields. However the functionality of the collecting equipment premise has been proven. Work comparing the chemistry of collected spheres with other E.T. material and common terrestrial debris has enabled the identification of E.T. particles and highlighted additional non-chondritic chemistry which could reliably be E.T. in formation if found. Finally a number of E.T. particles have been recovered from the Kwajalein atoll MM collection, and imaged both externally and internally using SEM techniques, however further analysis would be require to reconcile the high Ca ratios within them with the bulk chondritic compositions or meteors and meteorites. Future work is needed to confirm the E.T. origin of the CS candidates. Future collections should focus on the design and construction of a custom collector, which would be able to be used in the same format at multiple locations at a higher flow rate now that the collector premise has been confirmed.

Part III

Atmospheric Flight

Chapter 6
Atmospheric Flight 1: Preliminary Experimentation

Previous experiments to investigate the effects of atmospheric entry on MMs have made use of stationary pulse heating techniques in addition to computational modelling to simulate the heating experienced (e.g. see *Toppani et al. 2001; Greshake, KLöCK, et al. 1998*). The experiments have been able to uncover a number of processes which occur during atmospheric entry and explain several features seen on collected MMs. For example computational work has shown the metal rich E band in the atmosphere was produced by MMs undergoing atmospheric entry *(Plane 2003)* and the formation of MM-like textures *(Toppani et al. 2001)*. However, these experiments do not reproduce all atmospheric effects, such as induced rotation and frictional break-up, therefore we aim to use the Light Gas Gun (LGG) at the University of Kent (see Section 2.3) to accelerate MM analogues though atmosphere at hyper-velocity speeds to simulate the effect of atmospheric entry on MMs. The standard operating conditions of the gun require that the target chamber be pumped down to below 0.5 mbar, therefore an Environment Tube (EVT) was designed to allow for the projectile to encounter atmosphere during its flight.

6.1 Design of the Environment Tube

Design Constraints The EVT design was limited by a number of primary and secondary constraints. Over the course of the design phase, logistical and morphological considerations were identified as the primary constraints, with operating and result collection considerations being the secondary constraints. Both primary and secondary constraints are summarised below:

- Primary constraints:

  - The length of the completed design cannot exceed the length of the target chamber (1 m).
  - The design must be able to withstand a peak pressure of 10 Atm and a constant pressure of 6 Atm, to fit with required safety regulations.
  - The design must able to retain $> 90\%$ of the enclosed atmosphere for a minimum of 30 minutes.
  - Any damage to the design should be observable prior to the evacuation of the target chamber.
  - The design should be able to be set-up and used by a single operator.
  - The projectile must be recoverable.

- Secondary constraints:
  - The projectile should be as large as possible to improve accuracy, and repeatability.
  - The projectile must be able to enter the chamber/atmosphere undamaged.
  - Passage through the atmosphere should be visible and recordable to allow the detection and investigation of atmospheric interactions.
  - The design should be easy to disassemble and clean.

6.1.1 EVT Components

The EVT is comprised of three parts: a flight tube, a breech block, and an entry aperture. The breech block acts as a seal to one end of the tube, as well as containing the stopping medium for decelerating and capturing the projectile. The stopping medium is a low density solid capable of slowing down and stopping the projectile over a short distance, whilst causing minimal damage to the projectile during its deceleration phase (to enable the identification of features formed from atmospheric passage). The flight tube consists of the range of the EVT, and is where the projectile interacts with the atmosphere. Finally, the entry aperture seals the tube prior to firing, whilst keeping atmosphere within the EVT as the target chamber is evacuated and allowing the projectile to enter the flight tube unscathed to interact with the contained atmosphere.

Flight Tube: In order to contain the air and allow for the recording of the projectile's passage through the chamber the flight tube was produced from clear acrylic (optically transparent for recording purposes). The flight tube has a circular cross section as opposed to a square cross section: circular cross section tubing being cheaper

and easier to produce than box section, making replacement parts easier to source. Additionally, in circular tubing the internal and peak pressures are equally applied over the entire surface area making the likelihood of part failure lower and thus increasing its lifespan. However the use of circular as opposed to square cross cross section, does introduce a visual aberration in viewing the tube interior, which requires compensation when placing, and setting up, any recording devices. The acrylic tube has a wall thickness of 10 mm allowing it to contain an air pressure exceeding 10 atm, future proofing the design to allow for increased air pressure to be investigated.

Breech Block In designing the breech block a number of additional considerations had to be included. Due to the projectile impacting the stopping medium, there is the possibility of the projectile's path being altered during its deceleration, and as such an increased probability of the projectile impacting the sides at the rear of the EVT. The breech block therefore has to be capable of capturing any debris which could be produced via the projectile colliding with the side of the tube. The breech block must also be able to seal to the flight tube and allow the positioning of the capture mechanism whilst not interfering with its ability to stop the projectile non-destructively.

The breech is made out of a 20 cm diameter aluminium block. The block consists of a 10 cm diameter, centred circular socket in which the flight tube is slotted. This provides a 5 cm aluminium wall around the edge of the flight tube in the impact area. The breech is sealed to the flight tube via the compression of an O-ring between the breech and the breech plate (see Appendix G.3, G.4). The compressed O-ring is pushed against the sides of the flight tube, providing a tight seal, while not resulting in over torsion and damage of the tube.

Several capture media were considered as the stopping mechanism (including silicone rubber, additional foils etc). As the prime requirement of the EVT was the intact recovery of the projectile with minimal alteration due to capture, this limited the options (e.g. as capturing via foils fragments the projectile). Initial shots used silicone rubber however, it was decided that for the main program aerogel would be used to decelerate and stop the projectile following its use on the NASA Stardust mission which had encountered and captured cometary particles during impacts of up to 6 $\mathrm{km\,s^{-1}}$ *(Brownlee, Tsou, et al. 2003).* The aerogel used for the capture of the projectiles was silica based and ranged in density from 112 $\mathrm{g\,cm^{-3}}$ to 167 $\mathrm{g\,cm^{-3}}$ and was provided by Makoto Tabata from the University of Chiba.



Figure 6.1: The loaded capture medium cartridge (Mylar walled) in the EVT.

Entry Aperture In order to seal the entry aperture, and yet allow the projectile to pass through unharmed, a cover for the aperture was needed that was structurally weak enough to allow the projectile to pierce through it without significant force being required, whilst also being impermeable to the air. A thin Mylar film was therefore chosen to seal the aperture. In order to ensure that the foil was not permeable to the air, it was coated in aluminium. For our initial work a foil of 15 µm thick aluminium coated Mylar was used.

Assembly Due to a manufacturing defect, there is a slight radius change between the two ends of the flight tube tubing, resulting in only one end fitting into the breech block. The capture mechanism is inserted into this end of the EVT flight tube. In order to insert the capture mechanism into the flight tube, it is first cut to size (using a scalpel to score and then snap the aerogel) with folded paper 'springs' positioned on to each sides creating a gentle vice to hold it in place when inserted into the flight tube. It is then inserted into a cylindrical paper cartridge (for later experiments 2 mm thick clear mylar film replaced the paper used in making the cartridge outer casing to enable visual observations) and slotted into the flight range. Once positioned, the wrapped paper/Mylar is released so the the folded paper can expand and hold the aerogel in position in the flight tube (see Figure 6.1).

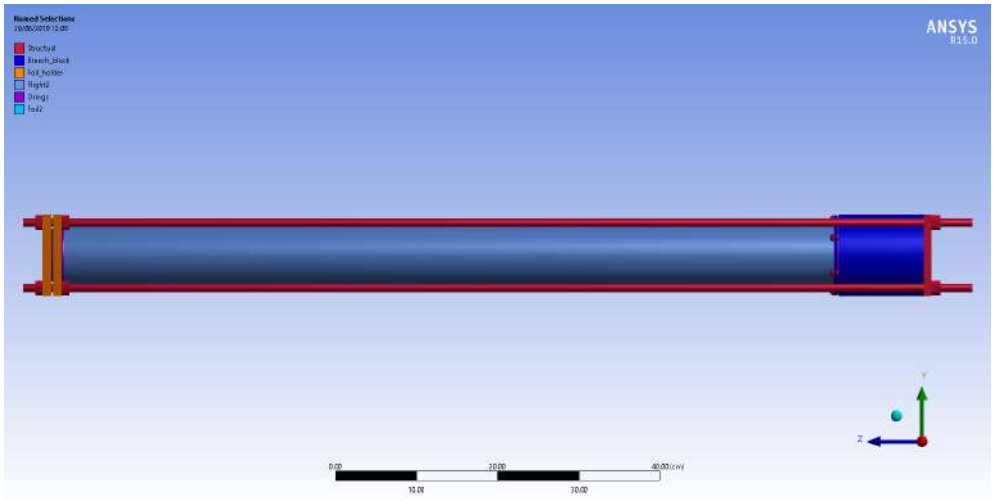
The breech topper is slid along the flight tube along with the breech O-ring and the flight tube is then slotted into the breech block. The topper is then screwed down into the breech block via six grub screws sealing the breech end of the chamber. The breech plate is then placed under the breech block. At the entry aperture, the O-rings are slotted into their grooves in the central plate and positioned so that the lower O-ring aligns the with flight tube walls. The foil was held in place between two square aluminium plates with 50 mm holes cut into through them in the center and four M8 holes in each corner 1 cm from the edge. The first plate (known as the central plate) is 8 mm thick and is sealed onto the end of the tube via an O-ring placed on the end of the tube, and around the edge of the hole in the plate (see Appendix G.5), with the foil positioned above the plate on another O-ring. The second plate is 1.5 mm thick and positioned above the foil and tightened to the first plate via four bolts in each corner side of the plates attached onto studding.

The studding runs down the length of the tube, and is attached to a final plate at the breech end of the tube. The bolts at the breech of the tube are tightened, compressing the O-rings between the central plate and the tube as well as between the entry aperture and central plates forming a seal. The rear plate acts to stop the breech block moving, should the rear O-ring be forgotten during the assembly, or the projectile miss the stopping mechanism and impact the breech block itself, in addition to spreading the load over the entire tube evenly. The studding is fed through the four corner holes in the plates with one nut per studding below the breech plate, between the breech plate and the central plate and one nut above the entry aperture plate. The studding is then tightened between the entry aperture and breech plates compressing the O-rings. The final nut between the plates is then tightened to the entry aperture ensuring a closed seal between the entry aperture plate and the central plate. See Figure 6.2 for the completed and assembled design.

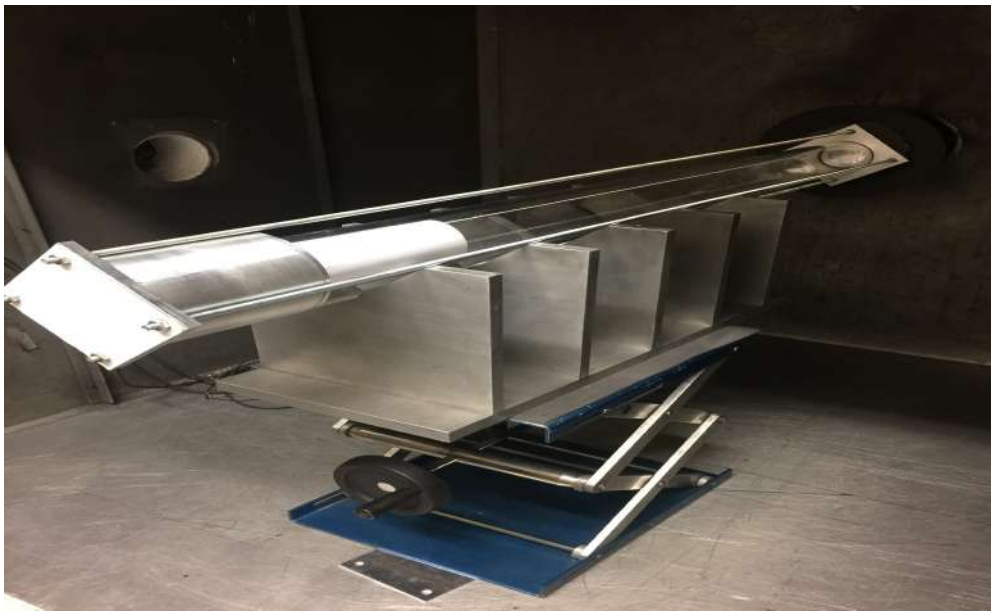
6.2 Shot Programme 1

6.2.1 Preliminary Pressure Testing

Prior to the tube being used for shots, the EVT was sealed and placed inside of the target chamber to undergo pressure testing to ensure that atmosphere could be retained when the target chamber was evacuated. For this test the projectile stopping mechanism was left out of the chamber and replaced with a partially inflated balloon with marked edges to allow for a visual check of the seal. If not sealed, the balloon would expand



(a) A scale 2 dimensional layout of the constituent parts of the EVT.



(b) Photo showing the assembled EVT

Figure 6.2: (a) The initial schematic of the EVT and (b) A photo of the constructed prototype.

as the target chamber was pumped-down. The EVT was positioned so that both the entry aperture and the target balloon were visible via the side and front ports on the target chamber respectively. The target chamber was then pumped-down to 100 mBar over a period of 10 minutes with the foil and balloon being checked approximately every minute for 5 minutes following the pump down.

The pressure inside the EVT was not measured in these early experiments, however, the pressure inside of the LGG target chamber is measured via a digital gauge situated

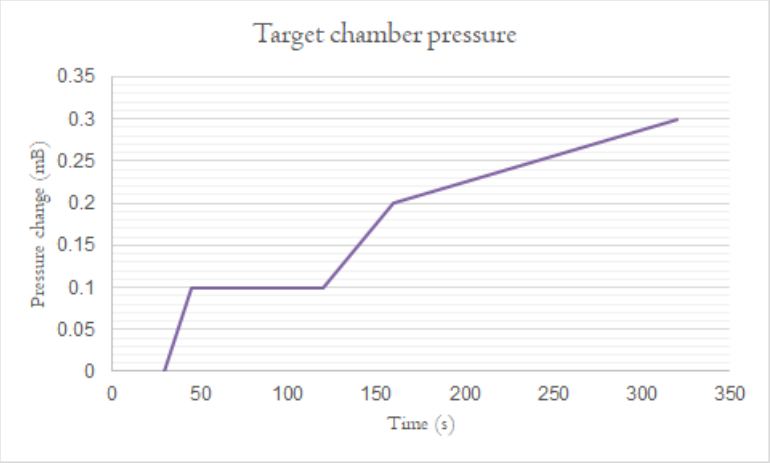


Figure 6.3: Plot of the increase in the pressure in target chamber containing the EVT as it varied over the course of 5 minutes following the conclusion of pump-down.

above the barrel inlet. From this gauge it could be seen that the pressure inside the target chamber showed a slight change over the course of the test (see Figure 6.3), however, visual observations of the balloon inside of the EVT also showed no change, with no deflation, or inflation, of the balloon.

Whilst it is likely that the chamber itself is not perfectly sealed, if it is assumed that the increase in pressure can only have occurred due to air leaking from the interior of the EVT, the maximum amount of air lost to the vacuum chamber by the EVT can be calculated. For a pressure change of ΔP the number of moles of air needed to enter the target chamber ($\eta_{\Delta P}$) is shown in equation 6.1

$$\eta_{\Delta P} = \frac{\Delta P_{tc} V_{tc}}{TR} \tag{6.1}$$

where $\eta_{\Delta P}$ is the number of moles required to change the pressure in the target chamber by amount ΔP_{tc} (Pa), V_{tc} is the volume of the target chamber (1 m^3), T is the temperature of the air (K) and R is the gas constant ($\mathrm{J\,mol^{-1}\,K}$). For the pressure change of 30 Pa observed in the target chamber, the amount of air added was 0.012 mol.

$$\eta_{ec} = \frac{P_{ec} V_{ec}}{TR} \tag{6.2}$$

The number of moles contained in the EVT at the beginning of the pump down can be calculated via Equation 6.2, where η is the number of moles contained in the EVT, P_{ec} is the pressure in the EVT (Pa), V_{ec} is the volume of the EVT ($\mathrm{m^3}$), T is the temperature (K)and R is the gas constant ($\mathrm{J\,mol^{-1}\,K}$). Using standard atmospheric conditions, the number of moles contained in the chamber at sealing was 0.159 mol. Therefore, the

EVT lost 7.5% of its total contained air over the ten minutes measured. As mentioned previously, this calculation assumes that the only source of air into the target chamber is via the EVT, however, it is likely that the seals along the gun barrel are also imperfect and a source of additional leaks, with previous tests showing that the target chamber can lose up to 25% of its vacuum over 60 hours resulting in an additional 0.16 mols of air entering the chamber every hour. This calculation also negates the volume of the balloon included inside of the EVT and assumes all air loss occurs after the pump down sequence, however due to the higher pressure on the outside of the EVT for a large period of the pump down, it was decided that this was unlikely to be a significant factor. However, should a shot not work as planned and a longer pump-down period was required (i.e. due to a misfire or an elongated pump down due to moisture etc), the target chamber required re-pressurising to ensure EVT pressure did not drop too low.

6.2.2 Preliminary Shots into the Environment Tube

Following the successful completion of the pressure test, the EVT was evaluated via a single shot test program. This aimed to identify any areas of weakness in the design to allow for alterations prior to the main shot program.

6.2.2.1 Test Shot Setup

Preliminary tests aimed to demonstrate the successful firing, atmospheric passage, and capture of a particle using the EVT. These tests used a 1 mm Stainless Steel (STST) ball bearing, loaded into a quartered sabot. The projectile was aimed to be fired at $\approx$3 $\mathrm{km\,s^{-1}}$ as a speed easily achievable, but slow enough so that the high density STST projectile would be captured in the silicon rubber. The STST ball bearing was known to be able to survive the impact with the front Mylar foil from previous experiments carried out at the University of Kent, and thus provided a method for identifying any issues with the recording of the interaction of the projectile with the contained gases. Additionally, due to the high density of the ball bearing, greatly above that of the projectiles to be used for the main experiment, the shot aimed to demonstrate that the EVT would be able to carry out multiple shots resulting in a projectile impact without failing due to the kinetic energy of the projectile.

The silicone projectile stopper media was included to test the ease of aligning the far end of the EVT with the end of the gun barrel. It was also included to test whether any path change would occur following the impact of the projectile with the stopping

mechanism. Given the high velocity and density of the projectile used in the test shot, a 5 cm thick cube of silicon rubber was used to ensure the projectile was stopped before reaching the rear of the breech block, as it is unlikely that aerogel would have been able to capture the projectile over the small distance to the breech.

The passage of the projectile through the air was filmed using a Panasonic HX-WA30 high speed camera in an attempt to view the light flash produced by the hyper-velocity interaction between the projectile and the contained atmosphere. This camera was chosen due to its long record time in high speed mode (20 s), as well as the camera's proven performance under low-light conditions. The camera was positioned at the side view port of the LGG target chamber and surrounded by black card to remove secondary illumination of the window.

The EVT was positioned in the centre of the LGG target chamber, winched to the correct height via a lab-jack and held in position by V-blocks placed on the lab-jack. The EVT was aligned with the firing line of the LGG using a red laser shone down the barrel of the launch tube; the laser is able penetrate the Mylar film and allows alignment of the projectile stopping mechanism inside of the chamber. Following alignment the target chamber was pumped down over the course of 15 minutes and the gun was fired immediately upon reaching the desired pressure of 5000 Pa (50 mBar).

6.2.2.2 Results

The passage of the projectile through the EVT was successfully captured by the camera. Analysis of the footage shows that a light streak could be observed in a single frame (see Figure 6.4). The position of the streak in the EVT confirms that air remains present in the chamber following pump-down, agreeing with the results of the pressure test (see Section 6.2.1).

Capture of the projectile in the silicone rubber was also accomplished without the projectile skewing off the front of the stopper and impacting the side of the flight tube or breech (see Figure 6.5). Further analysis of the projectile and the stopping mechanism was not carried out as the sample was lost. However, given the successful capture of the projectile and observation of a light flash, it was decided to continue with the experiment, moving onto more MM relevant analogues fired into aerogel.

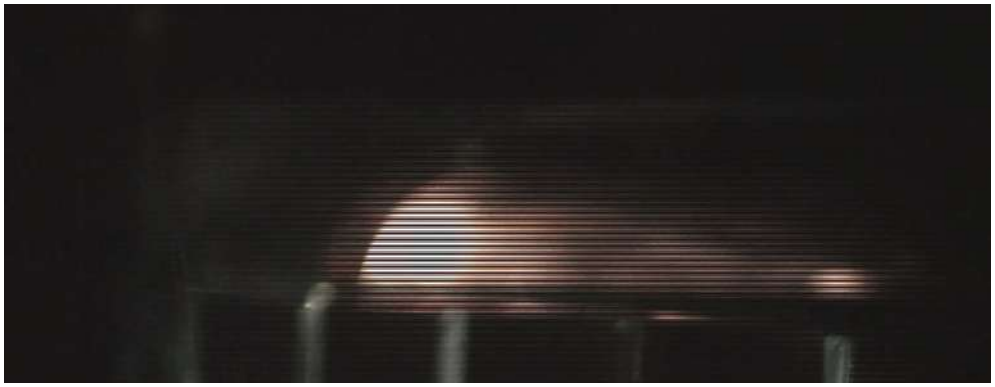


Figure 6.4: High speed camera frame showing the light flash recorded during the test shot of the EVT. The projectile is travelling from right to left.



Figure 6.5: The STST projectile having been captured in the silicone rubber. The projectile travelled straight into the target without any evidence of direction change, or impacts into the EVT itself.

6.3 Shot Programme 2: Determining the Parameter Space for Micrometeorite Analogues using the LGG and the EVT

Following the successful tests of the environment chamber's ability to contain air throughout the LGG pump-down period, and its ability to withstand the impact of

high density hypervelocity projectiles, a preliminary shot programme for the evaluation of the atmospheric effect on dust particles passing through atmosphere was carried out. The aim of the preliminary shots was to identify any issues arising from the use of a large olivine gem as the projectile (see below) (as they had not been well characterised for use in the LGG) prior to investigating the effects of atmospheric entry on more realistic MM analogues; specifically whether the method could reproduce the heating, melting and ablation processes experienced by incoming MMs.

6.3.1 Micrometeorite Analogue Projectiles

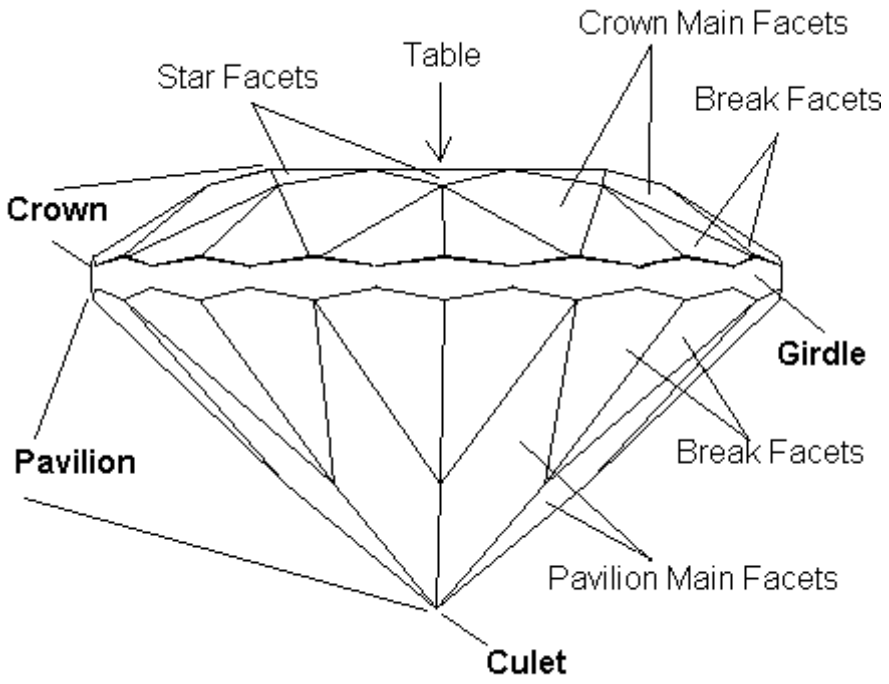
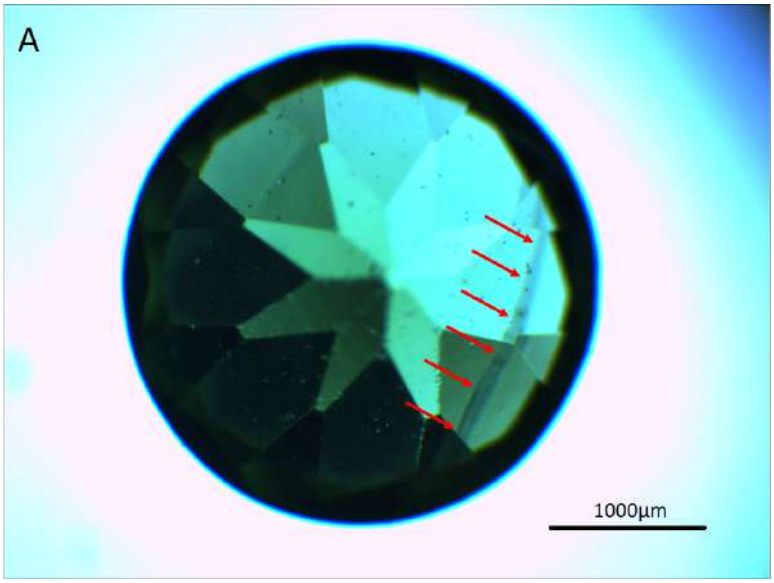


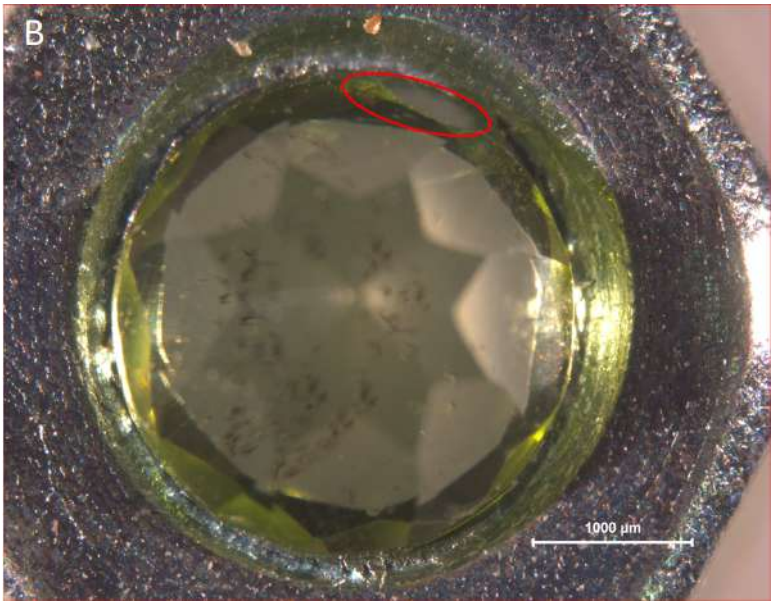
Figure 6.6: Illustration of the name and location of the facet of a brilliant cut gemstone *(Clark 2018)*.

For shot program 2, the projectiles used were changed from a 2 mm STST ball bearing, to a 3 mm (olivine) peridot gemstone cut in the brilliant fashion (see Figure 6.6). Whilst most MMs are composites of numerous minerals, olivine was chosen as the starting material due to its abundance in E.T. samples, and as a method to simplify the analysis of data by reducing the number of variables in each shot. A cut gemstone projectile was chosen so that changes in the shape could be easily observed and brilliant cut was chosen for its number of faces and edges at a variety of angles, whilst maintaining

its axial symmetry, improving its ability to be reproducibly fired in an identical manner. Prior to being fired, the gemstones were analysed with an optical microscope, to allow any internal fractures or inclusions to be identified (see Figure 6.7) and its morphology to be noted. A selection of images taken during this process are shown in Figure 6.8.

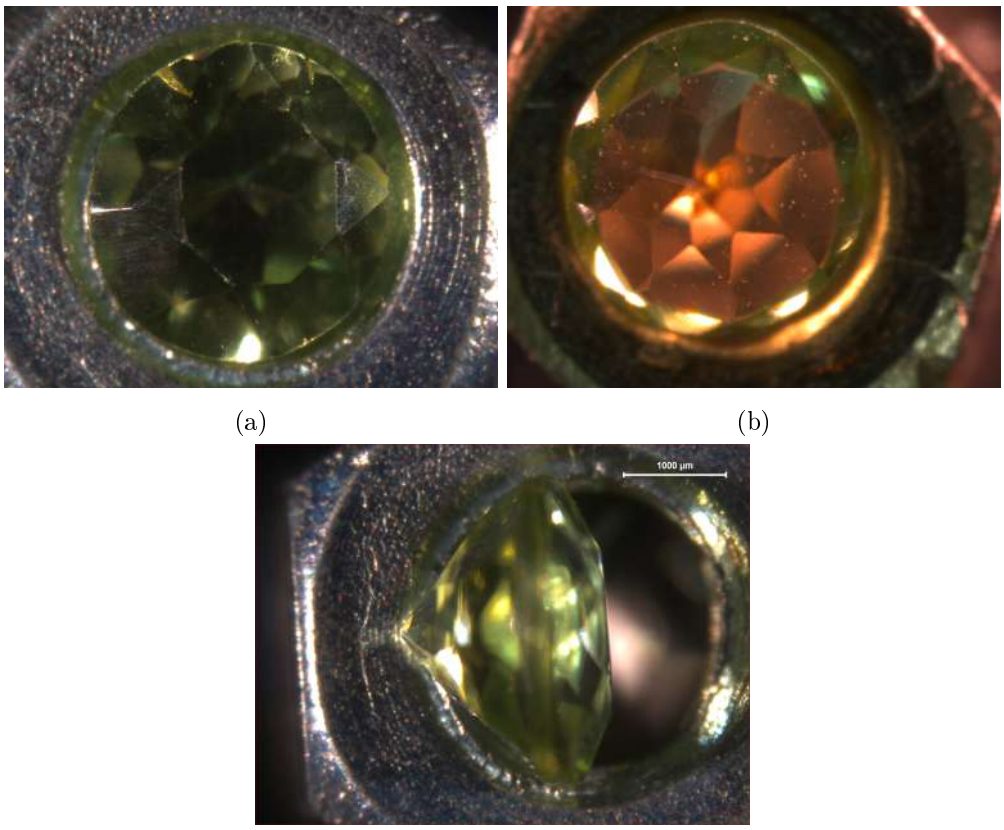


(a)



(b)

Figure 6.7: Showing peridots optically analysed prior to firing with flaws. a) A transmitted light optical image with red arrows highlighting a fracture in the interior of peridot 3. b) A reflected light optical image showing a large crack on the surface of peridot 5.



(a) (b)

(c)

Figure 6.8: One the peridot gemstones (peridot 1) used as a micrometeorite simulant in the atmospheric alteration experiments in three different orientations: a) Table up, b) Culet up, c) Side on.

In addition to optical images the gemstones were also analysed via SEM. Each gemstone was analysed in three orientations (table, side and culet up) as shown in Figure 6.9, to allow the whole surface and surface textures to be studied. In addition, EDX spectra were obtained (both 'point' and 'area' spectra) to confirm the olivine composition and the Mg/Fe ratio. Spectra were taken from horizontal regions to remove issues associated with topography. During this analysis a variety of surface contamination were observed.

Figure 6.9 illustrates the main type of contamination seen on the surface of the gemstones; unsymmetrical dark regions consisting of calcium containing smaller potassium and Cl-rich grains can be seen.

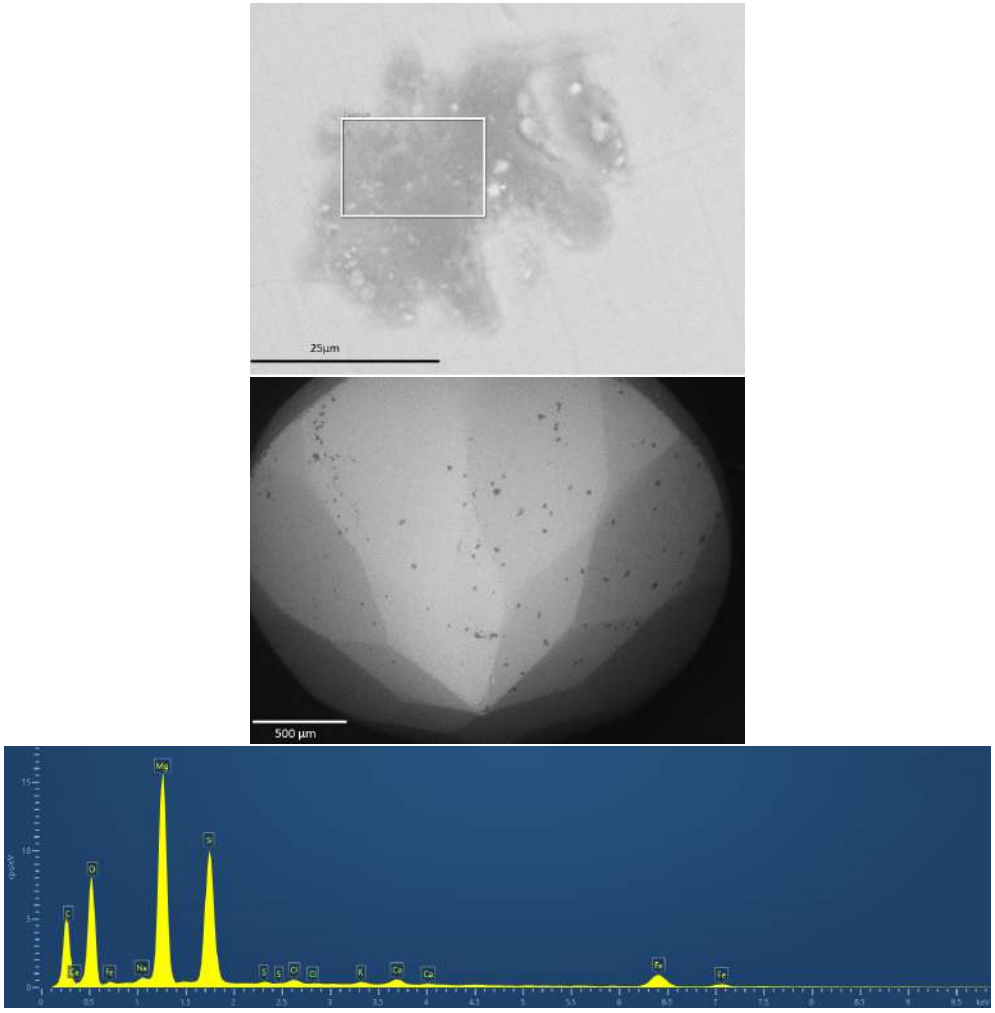


Figure 6.9: A) Large area spectrum of peridot 1 taken from the side. B) Zoomed image of peridot 1, with a spectrum taken on a single bright object on the surface. C) Spectrum taken on a single facet of peridot 1.

From the EDX spectra obtained it is possible to calculate the Fe/Mg ratio of the olivine. Assuming all Mg and Fe is contained uniformly within the olivine, rather than as discrete inclusions inside of the matrix (this would have been identified via optical microscopy described above) the composition of the projectiles is found to be approximately ($\pm 4\%$) ($Fo_{90}Fa_{10}$).

In addition to optical and SEM analyses, the gemstones were also analysed via Raman spectroscopy to confirm the olivine's crystal structure and composition. The gems were positioned on a M4 nut with their table horizontal as shown in Figure 6.8 A. The table was mapped using a 532 nm wavelength green laser using a 1800 line per mm grating. Figure 6.10 shows a typical olivine spectrum with peaks at around 850 and 815 cm^{-1}

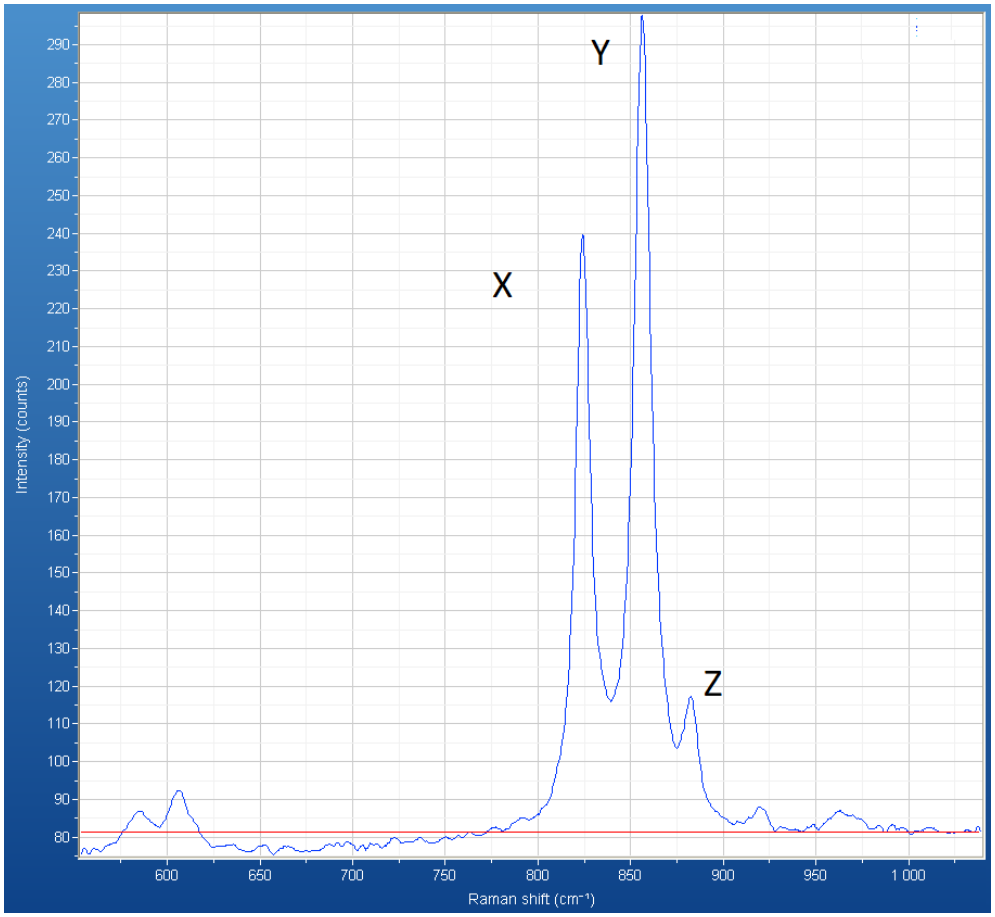


Figure 6.10: Example of a Raman spectrum obtained from a $Fo_{90}Fa_{10}$ unshot olivine gemstone, with the peaks X,Y,and Z labelled.

consistent with a ($Fo_{90}Fa_{10}$) olivine*(Mouri and Enami 2008)*.

Following characterisation of the peridots, any containing interior flaws or large exterior flaws were discarded. Table 6.1 shows the examined peridots, along with any features of interest and the corresponding shot the gemstone was used in. Those peridots used in test shots, or found to be flawed, were not characterised by Raman or SEM due to time constraints.

6.3.2 Initial Shots

The projectile stopper used in the preliminary shots was replaced with 122 $\mathrm{kg\,m^{-3}}$ aerogel cut to roughly 12 cm lengths with a 2.5 cm by 2.5 cm cross-section. The projectile stopper was positioned inside the chamber using the process described in

Table 6.1: A summary of the observational techniques and results for each peridot and the shot number the peridot was used for. Those peridots that were discarded due to inclusion or damage are also shown.

Peridot No.	Optical	SEM	Raman	Features	Usage
1	Y	Y	Y	N/A	Shot 1
2	Y	Y	Y	N/A	Shot 6
3	Y	Y	N	Interior fracture	Discarded
4	Y	N	N	N/A	Shot 2
5	Y	N	N	Large chip on girdle	Discarded
6	Y	N	N	N/A	Shot 3
7	Y	N	N	N/A	Shot 4
8	Y	N	N	N/A	Shot 5
9	Y	Y	Y	N/A	Shot 7
10	Y	N	N	Large fracture	Discarded

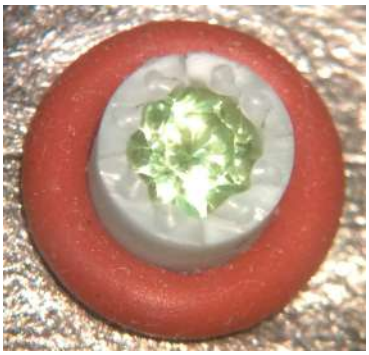


Figure 6.11: Photograph of the olivine projectile positioned inside of the quartered sabot prior to loading in the launch tube

Section 6.1. The firing speed of the projectile was reduced from 3 $\mathrm{km\,s^{-1}}$ to 2 $\mathrm{km\,s^{-1}}$.

6.3.2.1 Shot 1: Conditions

The shot was carried out after 20 minutes of pump-down time, with a pressure of ≈ 500 Pa recorded inside the target chamber immediately prior to firing the gun. The speed recorded for the shot was 2 ± 0.02 $\mathrm{km\,s^{-1}}$, with no sabot spray or other debris and only the projectile passing the entire distance to the target. For this shot peridot 1 was used as the projectile

Due to the irregular shape of the projectile, and the lack of any previous data on how the projectile would react to launch and impact, no camera was positioned to allow us to be able to view the chamber during the pump down, and identify any problems

prior to shooting. It also allowed for a quick visual inspection post-shot to ensure that the EVT had remained intact in the build-up to, and following, the shot.

6.3.2.2 Shot 1: Results

On inspection post-shot a single entry hole in the Mylar was observed along with fragments of aerogel spread along the interior of the EVT. However, no sign of the projectile or projectile fragments were found (see Figure 6.12). Analysis of the aerogel post-shot showed that the projectile had not survived the flight through the EVT and its subsequent capture. The single impact penetration hole through the Mylar (Figure 6.12a), implies that the projectile survived launch intact; a projectile that fractured during the acceleration phase would separate out due to the angular momentum imparted into the projectile, (in a similar manner to the sabot in the burst tank) and therefore, a fractured projectile would create multiple impact sites in the foil. Additionally the size of the penetration hole in the Mylar is too small for the projectile to have passed through in any orientation other than along the firing axis and it is therefore unlikely that the disruption is caused by any tumbling forces acting on the projectile. The absence of multiple impact sites and the size of the penetration hole in the Mylar foil imply that it was the interaction of the projectile with some, or all, components of the EVT which resulted in its catastrophic disruption.

The disruption of the aerogel at the far end of the EVT shows that the projectile (or projectile pieces) did impact onto the aerogel, however further analysis of the aerogel did not recover any projectile pieces. The complete disruption of the aerogel also removed any possibility of identifying any tracks in the medium, making the identification of the number of impacts in the aerogel impossible.

It is possible that the break-up of the projectile was a result of interactions with the atmosphere contained within the EVT. However, break-up of the projectile may also result from impacts into either the Mylar film covering the entry aperture of the EVT, or the aerogel used to slow the projectile down, as these were regions in which the highest shock to the projectile were likely to occur. The shock experienced at each interface will be determined by the impact parameters (e.g. velocity, pressure, material strength). As the experiment aims require that the projectile remains intact for study it was necessary to investigate these potential causes further to ultimately define the limitations of the setup.

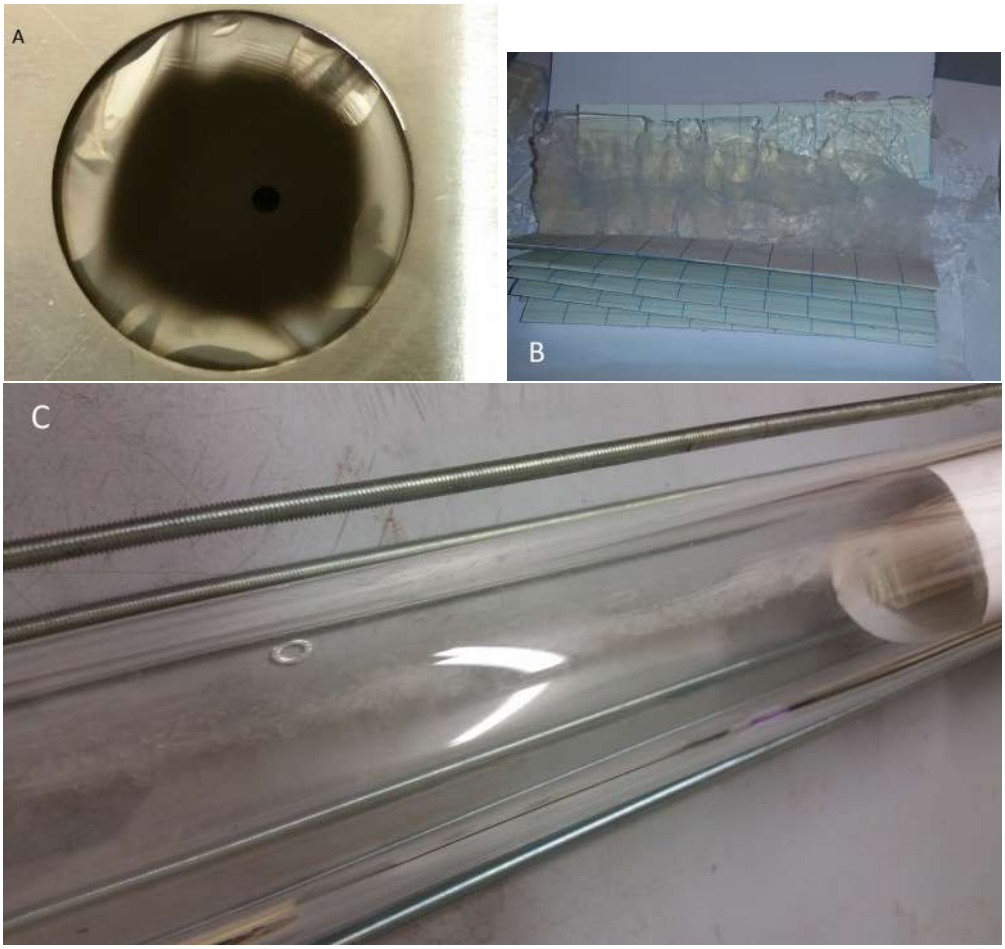


Figure 6.12: Photographs of A) The impacted Mylar foil, coated in gun debris and exhibiting a single, circular, penetration hole. B) The remains of the aerogel recovered from the end of the EVT in the packing used to load it. C) Aerogel debris ejected up the length of the chamber following the impact of the projectile or projectile pieces.

6.3.3 Defining the Experimental Limitations

In order to identify the cause of the damage to the projectile, additional test shots were carried out; firstly to determine how the foil covering the tube affects the projectile and, secondly, how the projectile stopping medium affects the projectile. The shots were designed to enable the effect of each component to be studied in isolation.

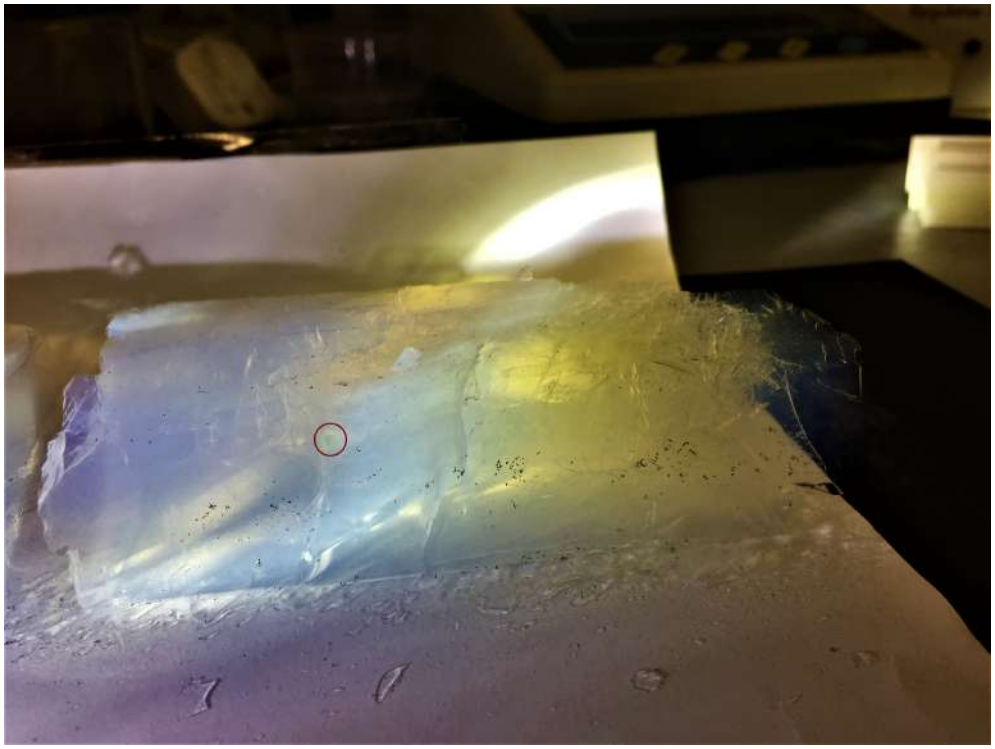


Figure 6.13: Photograph of the captured olivine projectile (Peridot 4) embedded in the aerogel projectile medium after impacting at 0.951 $\mathrm{km\,s^{-1}}$ during shot 2.

6.3.3.1 Disruption on Impact with the Capture Media

The survivability of the peridot impacting the aerogel was tested by reproducing the original shot conditions described in Section 6.3.2.1, but removing the use of the foil aperture cover and atmosphere such that the projectile impacts directly into the stopping medium.

Examination of the aerogel following the shot showed the projectile had generated a single track and remained intact at its end (Figure 6.13). Thus the impact into the aerogel capture media did not cause the original break-up of the projectile in shot 1.

6.3.3.2 Avoiding Breakup Upon Impact with EVT Foils

The program of shots performed to ascertain whether the Mylar entry aperture cover foil was disrupting the peridot involved firing the projectiles at a range of speeds into several Mylar foils. If the projectile was disrupted by the front foil, it will be observed as multiple fragments in the following foil. This allowed observations into whether the foils were responsible for the disruption to the projectile seen in shot 1, and, if so, at

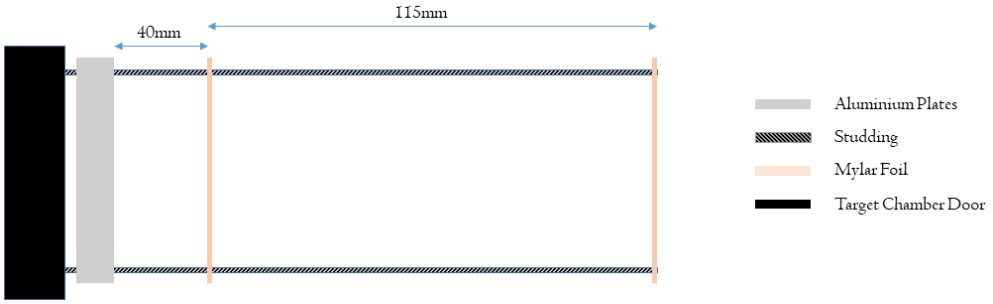


Figure 6.14: Schematic showing the set-up for the first foil test (shot 3) to study the effect of the Mylar foil on the peridot projectiles.

what velocity does the disruption begin to manifest.

The foils were held in an aluminium frame which were held together by small grub screws. The frames were positioned along studding via spacers to hold the frames a set distance apart. The studding was directly attached to the door of the chamber with the centre of the run along the firing axis of the gun. Before attaching the foil to the frames, the frame edges were smoothed to remove the chance of the foil splitting along a slit created by burrs. These were then placed sequentially along the studding, and were positioned at regular distances apart using spacers, with nothing in between the foils. In order to protect the target chamber door an aluminium stop plate (see Figure 6.14) was positioned as the last plate.

The projectile (peridot 6) was fired at 0.941 $\mathrm{km\,s^{-1}}$ (shot 3) using the single stage firing mechanism. Following firing the run was disassembled and the foils removed from the chamber and frames prior to any analysis.

The projectile was shown to have passed through both foils and impacted into the stopper plate. The first foil, again, had a single entry hole showing that the peridot was able to survive the acceleration stage in a single piece. Multiple penetration holes were observed, but it was realised that these may have resulted by secondary ejecta produced by the impact into the Al stopper plate.

Therefore this experiment was repeated with a 'paper backer' (comprised of 2 sheets of card folded twice resulting in 8 layers) in front of the aluminium stop plate. Furthermore, the number of foils was increased to three to provide additional shielding to the centre foil in case of projectile ejecta bouncing off the paper backing (see Figure

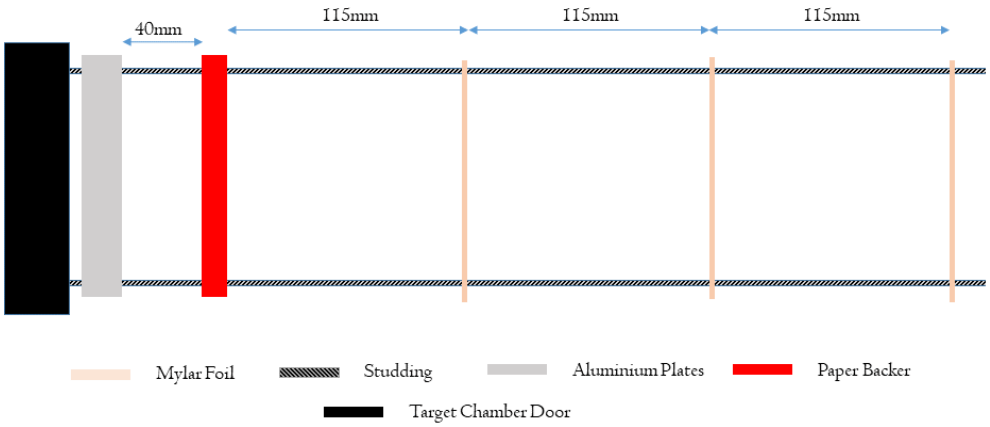


Figure 6.15: Showing the set-up for the second and third foil tests (Shot 4-5) to identify the effect of the Mylar foil on the peridot projectiles.

6.15). In this shot (shot 4) the projectile (peridot 7) was fired at 0.957 $\mathrm{km\,s^{-1}}$, using the single stage firing method. Once removed from the chamber the foils were analysed; all foils had a single entry and exit hole of a size similar to that of the original projectile (see Figure 6.16). The size of the holes and the lack of additional holes on each foil indicated the survival of the projectile following repeated impacts into the foils.

Shot 5 was a repeat of the shot 4 foil paper arrangement. Peridot 8 was shot with a velocity of 2.11 $\mathrm{km\,s^{-1}}$, attempting to match shot 1. Unlike in shots 3 and 4 there was a significant increase in hole diameter throughout consecutive foils, with the hole diameter growing to many times that of the projectiles diameter (see Figure 6.16).

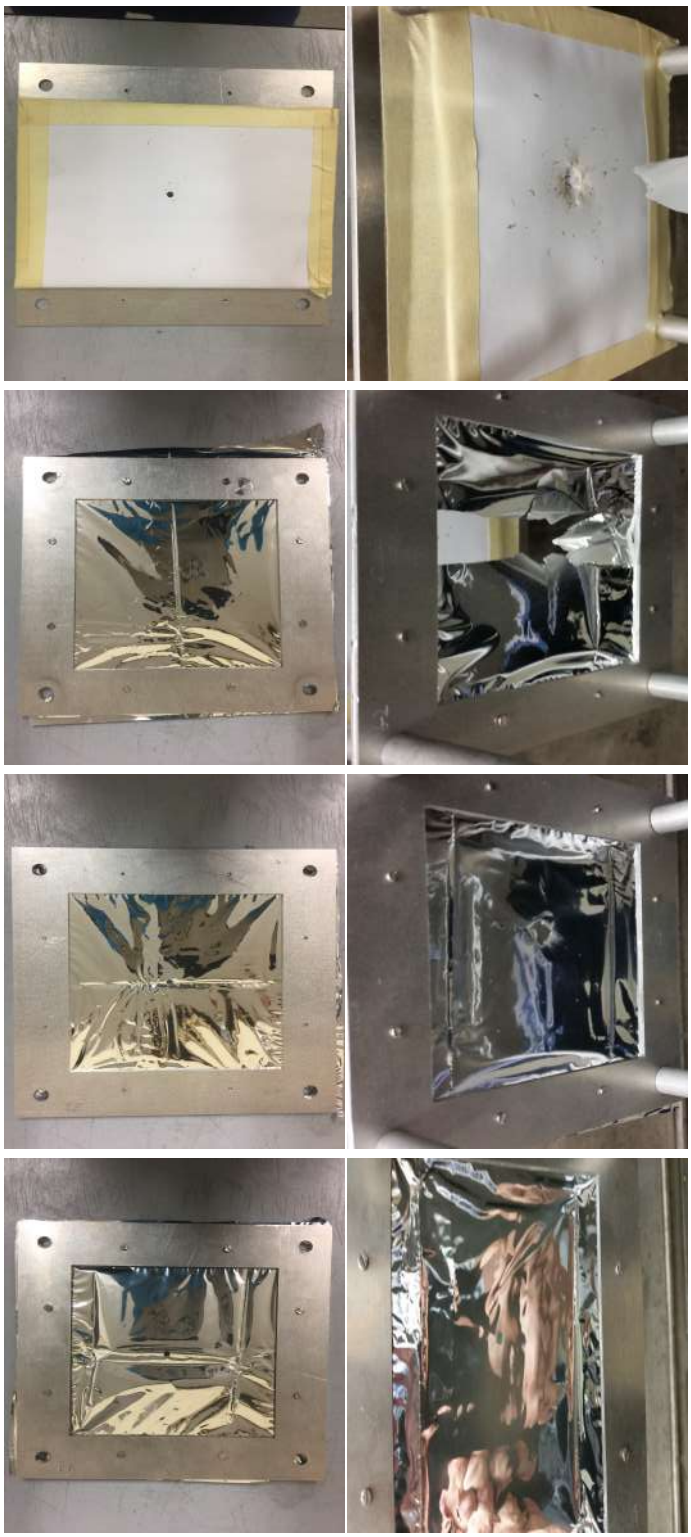


Figure 6.16: Photographs of the foils and paper stoppers after shooting in shots 4 (top row) and 5 (bottom row). Foils progress front to back from left to right. In shot 4 the holes in the foil do not increase in size, however in shot 5 the size rapidly increases. The small holes in both sets of foils are likely from impacts from ejecta from the previous foil.

It appears from shot 5 that the projectile is disrupted by its passage through the Mylar foils at speeds of 2 $\mathrm{km\,s^{-1}}$, with the projectile breaking up into numerous pieces and spreading over a wide area, thus creating the damage seen in the second and third foils, in a manner identical to that of Whipple shields *(Whipple 1947)*. From the results of shots 2 to 5 it can be seen that the likely cause of the catastrophic disruption of the projectile in shot 1 was the entry aperture Mylar foil cover.

6.3.3.3 Confirming the Survivability of the Micrometeorite Analogue Using the New Limits

Following the analysis of the limitations of the design, the EVT was reassembled with the projectile stopping medium consisting of aerogel of density 112 $\mathrm{g\,cm^{-3}}$, and the entry aperture covered with 15 µm thick aluminised Mylar foil. The projectile was fired at 1 $\mathrm{km\,s^{-1}}$.

Following the shot, the aerogel stopping medium was found to have remained in the breech and to be mostly intact, showing significantly less break-up and resulting powder spray up the EVT. Additionally, it preserved a clear single projectile track which culminated in the location of the intact projectile (see Figure 6.13).

Following the removal of the aerogel from the EVT, the tube and breech were washed with ethanol, and the O-rings were re-lubricated with vacuum grease. Unfortunately the ethanol wash reacted with the EVT, resulting in a number of small subsurface cracks appearing in the tube following the wash (see Figure 6.17). As such the shot was repeated to test the tube for any structural weaknesses caused by the wash and to rule out the shot process themselves as being responsible for the change. For the repeat shot, the integrity of the tube was watched during the entire pump-down sequence. Following the repeated shot, no growth in length of the cracks was recorded and as such the tube was declared safe for further testing.

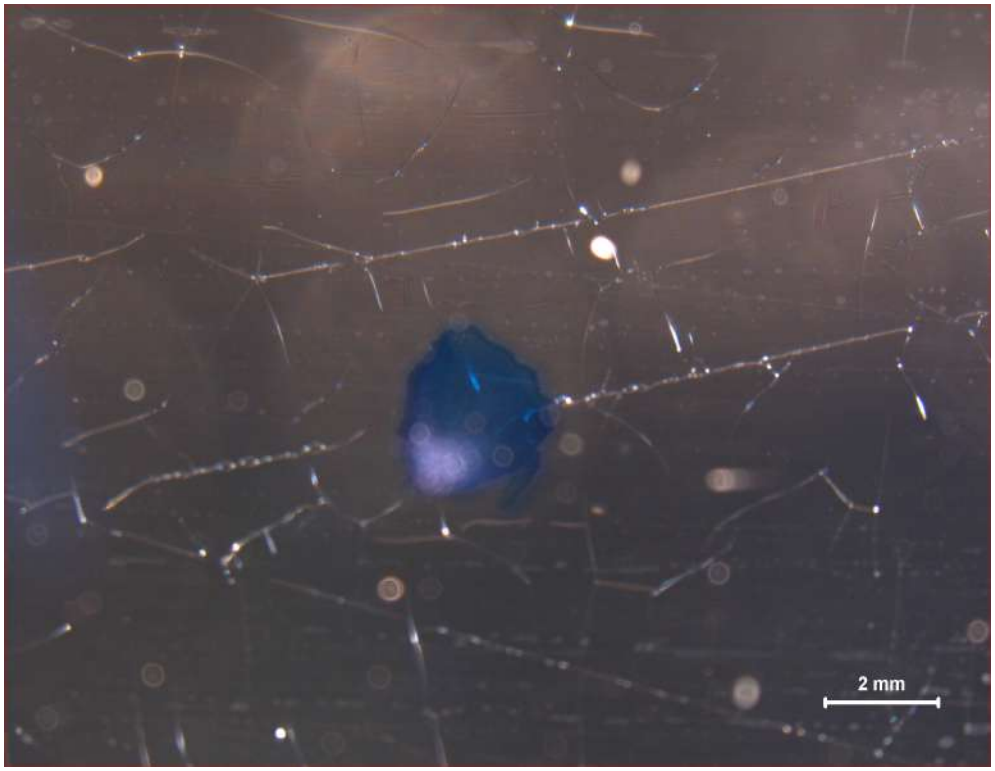


Figure 6.17: Photograph of subsurface cracks which formed in the EVT following shot 6. The blue marker was used to identify the location of cracks which were measured to identify if the crack grew following an additional shot.

6.4 Summary

Table 6.2: Summary of the make-up and results of shots 1-6.

Shot No.	Velocity	Target	Result
1	2 $\mathrm{km\,s^{-1}}$	Atmospheric tube containing air.	Catastrophic disruption of projectile.
2	1.901 $\mathrm{km\,s^{-1}}$	112 $\mathrm{kg\,m^{-3}}$ Aerogel Block.	Projectile recovered.
3	0.941 $\mathrm{km\,s^{-1}}$	2 Mylar films, aluminium stop plate.	Test inconclusive due to aluminium ejecta.
4	0.957 $\mathrm{km\,s^{-1}}$	3 Mylar foils, paper stopper, aluminium stop plate.	No sign of projectile break up.
5	2.11 $\mathrm{km\,s^{-1}}$	3 Mylar foils, paper stopper, aluminium stop plate.	Projectile breaks up after first foil
6	0.951 $\mathrm{km\,s^{-1}}$	EVT containing air.	Projectile recovered

Attempts to replicate the passage of incoming dust grains into the Earth's atmosphere using a LGG required the design and construction of a EVT capable of containing atmosphere in the evacuated target chamber of the LGG. Initial tests of the EVT showed that it was able to retain the atmosphere over the pump-down of the target chamber, and was able to survive the impact of solid projectiles into its capture medium.

Further tests involved the use of olivine peridots as MM analogues (shots 1-6). The projectiles were only able to survive passage through the chamber at speeds less than 1 $\mathrm{km\,s^{-1}}$, with the projectile undergoing catastrophic breakup upon impacting the Mylar foil at speeds exceeding this threshold.

Chapter 7
Atmospheric Flight 2: Theoretical Calculations

In order to ensure that the experiments successfully reproduce atmospheric entry and achieve the desired temperatures and pressures to initiate melting, a number of mathematical simulations were undertaken. The simulations were to firstly show that impact into the aerogel projectile stopper did not have a significant effect on the structure of the peridot, either due to the impact disrupting the projectile, or due to heating effects as it is captured; secondly, to evaluate the speeds required for the peridot to undergo melting during the atmospheric flight; and thirdly, to assist in the analysis of the results obtained.

In order to achieve these aims a number of mathematical steps were required. The momentum of the projectile at each stage of the EVT had to be calculated, requiring calculations of its speed and mass. These results were then used to calculate the temperature of the projectile during its passage through the EVT and the impact pressures it experienced. Each of these steps is described in detail in the following sections.

7.1 Atmospheric Flight

7.1.1 Atmospheric flight Background

7.1.1.1 Overview

Prior to the impact with the stopping medium, the projectile passes through, and interacts with the atmosphere, and experiences heating induced by the friction caused by the drag, and the passage of the shock-wave created by the hyper-velocity projectile

as it moves the air out of its path. These effects are discussed in more detail below. Understanding the severity of the changes prior to performing additional shots allowed for the calculation of any changes which may be needed to the experimental setup.

As the projectile passes through the atmosphere, it pushes aside the air molecules. If the projectile is moving faster than the surrounding fluid can react, a shock-wave is formed. As the projectile is travelling faster than the material can propagate, shock-waves act as a discontinuity, separating material which has no information about the incoming projectile, and material which has directly interacted with it, resulting in a plane which separates the two pressure regimes. The large increase in air pressure results in an increasing temperature of the air.

As the projectile passes through the air, it is slowed down by its interaction with the air. The amount of drag that an object generates during its passage depends on the number of collisions it experiences. Projectiles travelling with a high velocity will impact more air molecules per unit time and thus be decelerated faster than a slower travelling projectile and, as such, two identical projectiles travelling at different velocities will experience different decelerations depending on their initial velocity. The friction of the air particles on the projectile's surface also raises the temperature of the projectile.

In addition to the velocity of the projectile, the deceleration of the projectile also depends on its shape, as the angle of impact of the air molecule affects its final flight direction (i.e. an air molecule impacting on a perpendicular surface will rebound along its original route, however an air particle impacting on a surface of 15 degrees will rebound along a new path). This effect of the shape of the projectile passing through the air is taken into account by the drag coefficient, C_d, which in most cases must be found experimentally. For these calculations the peridots have been assumed to be spherical with a drag coefficient of 0.39 based on a sphere passing through a hyper velocity flow at $2\,\mathrm{km\,s^{-1}}$ *(Hodges 1957)*.

7.1.1.2 Flow Regimes

The type of interaction with the surrounding fluid experienced by an object passing through a flow, varies, depending on the Mean Free Path (MFP) of the gas, and the characteristic body length of the object *(Wilde and Ailor 2013)*. These may be combined to give the non-dimensional Knudsen number (K_n), the value of which governs the flow regime that the object is said to exist in. these can be split into roughly 4 categories:

for $K_n > 10$ the object is in the free molecular regime, for $0.1 < K_n < 10$ the object is in the transition regime, for $0.01 < K_n < 0.1$ the object is in the slip-flow regime and for $K_n < 0.01$ the object is in the continuum-flow regime *(.)* For these experiments this is situation which exists; the size of the body is much much greater than the MFP of the gas and as such continuum regime equations hold true. The gas can be described as a single, continuous entity as opposed to discrete masses with gas particles is far more likely to interact with themselves than with the object in the flow and heating is carried out by convective instead of conductive processes *(Kukkonen, Vesala, and Kulmala 1989)*. Unfortunately the modelling of this regime is difficult requiring the solution of the Navier-Stokes equations using complex computation models which was not possible in the time frame, and beyond the scope of this section.

For slightly lower Knudsen numbers, interactions occur in the slip flow regime. in this regime, equation used in the continuum regime still hold true, however additional terms are required to take into account of the temperature jump boundary and the breakdown of the no-slip condition and thus the velocity slip along the particles surface *(Colin 2012)*. The transition regime further covers the breakdown of the Navier-Stokes equation and the move from a fluid into discrete particle impacts as seen in the free molecular regime.

During true atmospheric entry, MMs generally are slowed by air inside of the Free Molecular regime. This occurs when the MFP of the air is substantially larger than the objects characteristic length, and as such any interactions between the object and gas molecules are likely to be discrete. As such interaction between air molecules in front of the projectile will not happen and no pressure change occurs around the projectile. As such aerodynamic force only depend on the collision speed between the gas molecule and the object, the objects shape and it orientation. This regime begins to break down as the MFP and the characteristic length equalise at which point the regime begin to shift into the transition regime whereby some ratio of continuum and free molecular collisions may occur. Calculations of the free molecular heating effects are described in the chapter, whilst results from these calculation will be higher than those calculated using the previous regimes, they were able to be calculated using existing equipment and they will give a estimate of the heating effects we would be expecting to see. With additional time, more complete calculation could be undertaken.

Calculating the final state of the projectile following its passage through the atmosphere contained within the EVT will enable the calculation of the peak pressure and temperature experienced by its impact with the projectile stopping medium, and allows

for the calculation of minimum firing speeds required to achieve melting, due to the atmospheric passage. It will also allow a calculation of any mass loss from the projectile prior to its impact into the aerogel.

7.1.2 Derivation of Mass Change

The mass change (m) of the projectile over time (t) as it passes through the atmosphere in the EVT can be calculated using the expression:

$$\frac{dm}{dt} = -\frac{C_h\,\rho_{air}\,A\,V^3}{2\,\zeta}\left(\frac{V^2 - V_{cr}^2}{V^2}\right) \tag{7.1}$$

$$dt = \frac{dL}{V} \tag{7.2}$$

where A is the projectile cross sectional area (m^2) and ρ_{air} is the density of the air ($\mathrm{kg\,m^{-3}}$), V is the projectile velocity ($\mathrm{m\,s^{-1}}$),V_{cr} is the projectile's critical ablation velocity; a material constant ($\mathrm{m\,s^{-1}}$), ζ is the the heat of ablation ($\mathrm{J\,kg^{-1}}$) and C_h is the heat transfer coefficient *(Melosh 1989)*. Using the definition of velocity from equation 7.2 where dL is the distance travelled by the projectile (m), the loss of mass per distance travelled can be calculated as shown in equation 7.3.

$$dm = \frac{C_h\,\rho_{air}\,A\,V^2}{2\,\zeta}\left(\frac{V^2 - V_{cr}^2}{V^2}\right)dL \tag{7.3}$$

The values of C_h of 0.02, critical ablation velocity (V_{cr}) of 3 $\mathrm{km\,s^{-1}}$ and ζ of 5×10^6 $\mathrm{J\,kg^{-1}}$ used in this solution are taken from *(Melosh 1989)*.

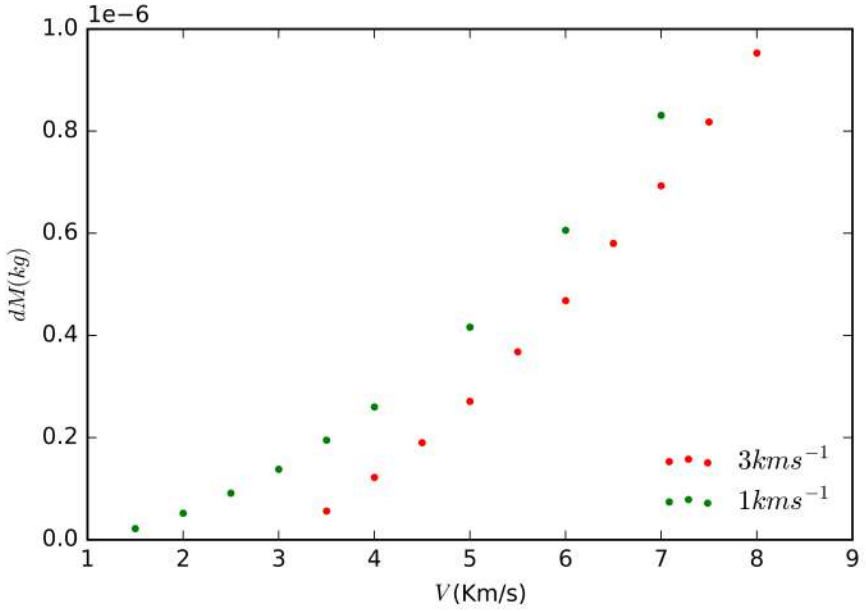


Figure 7.1: Mass lost from a 3 mm diameter olivine projectile passing through 1 metre of air under normal atmospheric conditions for two critical ablation velocities 3 $\mathrm{km\,s^{-1}}$ and 1 $\mathrm{km\,s^{-1}}$.

From these calculations it can be seen that if the critical velocity is within the estimated range of 3 $\mathrm{km\,s^{-1}}$ and 1 $\mathrm{km\,s^{-1}}$ (see Figure 7.1), the amount of mass lost is small compared to the total mass of the projectile (measured at an average mass of 2.42×10^{-5} kg) requiring shots at velocities which exceed 4 $\mathrm{km\,s^{-1}}$ for the projectile to lose 5% of its initial mass.

7.1.3 Derivation of the Impact Velocity

The velocity of the projectile upon impacting the aerogel block will be lower than that measured at the light gates due to the projectile's interaction with the gases contained in the EVT. Assuming the short Time of Flight (ToF) through the air results in little to no morphological changes to the peridot, along with no mass loss (as demonstrated in Section 7.1.2), the impact speed of the peridot into the aerogel stopping medium can be calculated as a function of the drag of the air (F_{drag}) on the particle (given in eq 7.4)

$$F_{drag} = -0.5\, C_d\, \rho_{air}\, A\, V^2 \tag{7.4}$$

where C_d is the coefficient of drag for the projectile, ρ_{air} is the density of the air ($\mathrm{kg\,m^{-3}}$), A is the cross sectional area of the projectile ($\mathrm{m^2}$) and V is its velocity ($\mathrm{m\,s^{-1}}$).

Substituting Newton's Second Law of Motion into equation 7.4 and rearranging gives

$$\frac{dV}{dt} = -\frac{C_d\,\rho_{air}\,A\,V^2}{2\,m} \tag{7.5}$$

where m is the mass of the projectile (kg), V is the instantaneous projectile velocity ($\mathrm{km\,s^{-1}}$) at time t_0 (s) and t is the TOF of the projectile through the air given by equation 7.2. If L is the length of the projectile's flight path through the air (m), substituting equation 7.2 into equation 7.5 and integrating, an expression for the change in velocity of the projectile during its flight through air along the path of length L can be found:

$$V = V_0\, e^{\frac{-A\,L\,C_d\,\rho_{air}}{2\,m}} \tag{7.6}$$

where V_0 is the firing velocity ($\mathrm{km\,s^{-1}}$) and V is the velocity of the projectile ($\mathrm{km\,s^{-1}}$) after passing through air along a path of length L (m) (the full derivation is given in Appendix H.1). The impact speed of a projectile fired at velocity V is shown in Figure 7.2.

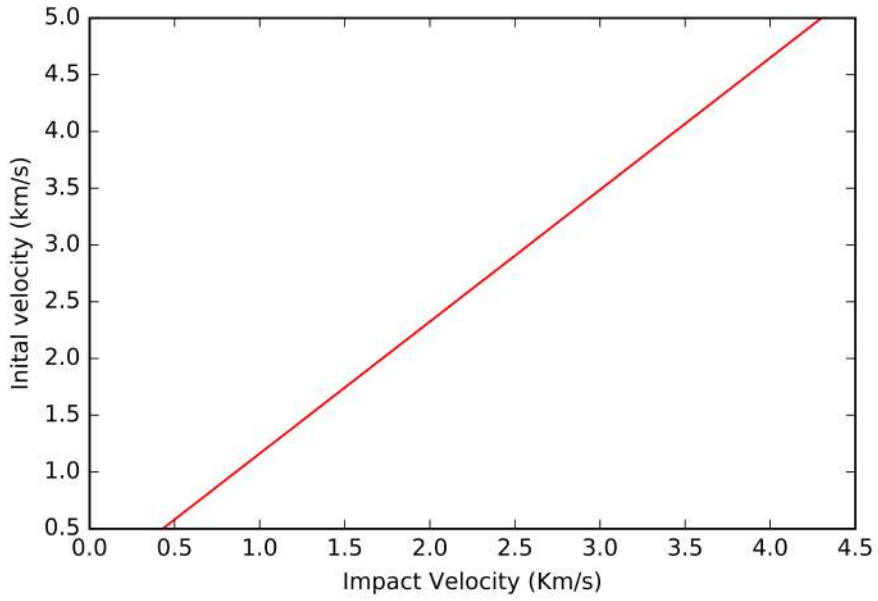


Figure 7.2: Showing the speed at which a 3 mm olivine projectiles impacts the projectile stopper after passing through 1 m of air.

From Figure 7.2 it can be seen that the difference between the initial launch velocity and impact speed is greater at higher launch speeds, implying a greater deceleration and hence greater heating of the projectile when it passes through the atmosphere at

higher velocities. This is because the change in kinetic energy is converted to heat. Consequently, during the passage through the atmosphere, the particle will already have experienced heating effects prior to its collision with the aerogel.

7.1.4 Derivation of Atmospheric Heating

As mentioned in Section 7.1.1.1 the heating effect on the projectile is due to the frictional forces applied to its surface as it passes through the air. As such the amount of heating the projectile experiences is dependant on the kinetic energy of the projectile, the amount of energy it loses to the surrounding air, and the amount of energy required to heat the projectile up. The energy required to heat the projectile is given in equation 7.7

$$Q_{in} = Q_{out} + Q_{\Delta T} \tag{7.7}$$

where Q_{in} is the heat energy received by the projectile (J), Q_{out} is the energy lost (J) and $Q_{\Delta T}$ is the energy required to heat up the projectile by a given amount (J). Q_{in} is given by:

$$Q_{in} = \frac{1}{2} M v^2 \tag{7.8}$$

Where v is the projectile velocity (ms^1), and M is the mass of the air (kg) moved by the projectile which is given by:

$$M = \rho_{air} A dL \tag{7.9}$$

where A is the projectile cross section area (m^2), dL is the distance the projectile moved (m) and ρ_{air} is the density of the air ($kg\,m^{-3}$). When the projectile is heated by air flow, it also loses heat into the surrounding environment, the amount of energy lost in this manner, Q_{out}, is given by:

$$Q_{out} = \sigma \epsilon S T^4 \tag{7.10}$$

where σ is the Boltzmann constant ($m^2\,kg\,s^{-2}\,K^{-1}$), ϵ is emissivity of the projectile, S is the surface area of the projectile (m^2) and T is the projectile's temperature (K). Finally $Q_{\Delta T}$ is given by:

$$Q_{\Delta T} = mC(T - T_0) \tag{7.11}$$

where m is the mass of the projectile (kg), C is the specific heat capacity of the projectile ($J\,kg^{-1}\,K$) and T_0 is the projectile's initial temperature (K). Substituting equations 7.8, 7.10, 7.11, into Equation 7.7 and rearranging, gives an expression for the change in temperature of the projectile as shown in equation 7.12. The derivation for this is given

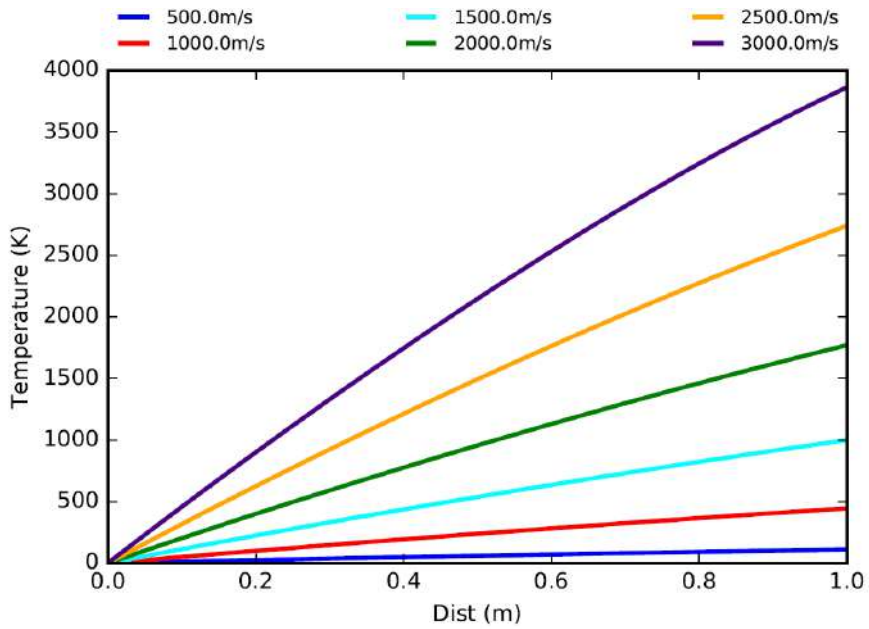


Figure 7.3: Graph showing the extent of atmospheric heating experienced by a 3 mm olivine projectile as it passes through the atmosphere contained in the EVT. These lines are curved but due to the small flight distance line curvature is difficult to see.

in Appendix H.2

$$(T - T_0) = \left(\frac{M V^2}{m C}\right) - \left(\frac{\sigma \epsilon S T^4}{M V^2}\right) \tag{7.12}$$

Substituting equation 7.9, equation 7.6 and equation 7.2 into equation 7.12 gives the temperature change of the projectile per distance travelled through air of a constant density as shown in equation 7.13.

$$(T - T_0) = \frac{\rho_{air} A \, dL \left(V_0 \, e^{\frac{-A L C_d \rho_{air}}{2m}}\right)^2}{m C} dL - \frac{\sigma \epsilon S T^4 \, e^{\left(\frac{A L C_d \rho_{air}}{2m}\right)}}{V_0 M C} dL \tag{7.13}$$

Using equation 7.13 we can iteratively calculate the maximum temperature that a projectile will reach during its passage through the atmosphere. For the 3 mm olivine projectiles that were used in the main shot program, the amount of heating experienced by the projectile fired at a range of initial velocities is displayed in Figure 7.3.

As the experiment only requires that the projectile surface begins to melt, the latent heat of fusion and evaporation are omitted. As the latent heat occurs during melting and evaporation processes respectively, the terms were not included as they were beyond the scope of the calculations, which were to find the speed required to achieve the melting point.

From Figure 7.3, it can be seen that the minimum speed needed to heat the 3 mm olivine projectile to 2000 °C (above its approx 2000 °C melting point) *(Klein Cornelis 1985),* requires that we fire the peridot at speeds exceeding 2 $\mathrm{km\,s^{-1}}$.

7.2 Impact into the Projectile Stopping Medium

7.2.1 Hypervelocity Impacts Background

Impacts of large scale hyper-velocity bodies are traditionally split into three stages: the contact and compression stage, the excavation stage and the modification stage. The contact and compression stage begins upon contact between the impactor and the target, with strong shock-waves being sent through both the target and the impacting body. The contact and compression stage ends, and the excavation stage begins, when the shock-waves propagating through the impactor dissipate, leading onto the excavation stage. During this stage the shock-waves propagate through the target followed by the slower moving stress waves. These stress waves move the material they pass through and set into motion the flow of material, which defines the final shape of the crater. The final modification stage occurs once the crater falls back into the energy realms controlled by gravity, with the crater falling back in on itself. This final stage is not applicable to these experiments, as the impacted target will not be self gravitating.

We can further subdivide the contact and compression stage into three additional substages based on the position and type of the shock-wave passing through the projectile. Firstly, the contact begins and the shock-wave propagates through the projectile. During this substage of compression, both the projectile and the target are at the same pressure and have identical particle velocities behind the shock-wave. These conditions are the same due to the lack of outlets available to the pressure build-up. The projectile cannot penetrate the target, nor can it bounce off the target due to the downwards motion of the unshocked material. Although the pressure and particle velocities of the shocked materials are identical, the internal energies and densities, and thus the shock-wave speeds, are dependant on material characteristics and as such may be different between the impactor and target *(Melosh 1989).*

The second substage of the compression stage begins at $t = t_c$, when the shock-wave which had been propagating through the impactor, reaches its rear surface. At this point the entire impactor is shocked and compressed. The time taken for the shock-wave to

pass through the projectile and reach the rear wall (T_c) is given by the equation:

$$t_c = \frac{x}{U_s} \tag{7.14}$$

where x is the initial width of the projectile (m) and U_s is the speed of the shock-wave (m/s) through the uncompressed material. This is given by equation 7.15 below:

$$U_s = S\,u_{im} + C \tag{7.15}$$

where S and C are experimentally acquired constants relating to material characteristics, and u_{im} is the particle velocity (m/s) in the impactor. Once the shock-wave has reached the rear wall, small amounts of the projectile may be ejected from the rear surface while only lightly shocked, and the pressure wave is reflected as a rarefaction wave. The rarefaction wave passes back through the compressed material releasing the material from its high pressure state *(Melosh 1989)*. During release of the compressed material, the material begins to accelerate upwards as it expands, and in situations where the temperature and pressure are sufficient, vaporisation occurs. This vapor may gain an upward velocity which lifts it out of the crater. The time taken for the rarefaction wave to reach the target/impacter boundary (t_R), and thus release the entire projectile from its compressed state is given by equation 7.16 below:

$$t_r = \frac{\rho_0\,x}{\rho_c\,C_r} \tag{7.16}$$

where ρ_0 is the initial density of the impactor ($\mathrm{kg\,m^{-3}}$), ρ_c is the compressed density of the impactor ($\mathrm{kg\,m^{-3}}$) and C_r is the speed of the rarefaction ($\mathrm{m\,s^{-1}}$) wave given by equation 7.17:

$$C_r = \left(\frac{K_0 + n\,P}{\rho_0}\right)^{0.5} \tag{7.17}$$

where K_0 is projectile bulk modulus (Pa), n is a material dependant experimentally derived unitless constant and P is the pressure (Pa).

The third substage begins once the rarefaction wave reaches the impactor/target boundary at $t = t_c + t_r$ and it passes through into the target material with only a small percentage being reflected back into the projectile. Once the rarefaction wave has passed through into the target, due to the high velocity of the rarefaction wave through the compressed materials, it is often capable of catching the shock-wave in the target, reducing its magnitude *(Melosh 1989)*.

Due to our interest only being in the projectile, we will focus solely on the initial contact and compression stages as explained above. This stage of the impact can be modelled via the planar impact approximation, where the projectile is represented by an infinitely long plate with a thickness, x, equal to the projectile's diameter (or thickness). The target is modelled as an infinitely long half-plane with the assumption that there is no reflected shock-waves rebounding onto the projectile from any external edges or internal structures. This is an approximation as even in large scale impactors, reflections of the shock wave off the walls of the impactor will play a part in the final trajectories of the main rarefaction wave. These waves also result in the lateral growth of the impactor and target, with it extending horizontally, as well as vertically. Despite this, the planar impact approximation allows the initial shock conditions, particle velocities and internal energies to be estimated *(Melosh 1989)*.

7.2.2 Derivation of u_t and v_i

7.2.2.1 Derivation of u_t

Using the planar impact approximation described above, and the initial conditions of the impact, later conditions experienced by the impactor and target can be extrapolated, which allows any alteration caused by the aerogel impact to be simulated as well. Using the conservation of momentum and the conservation of mass during the shock wave propagation, the change in pressure in both the target and impactor can be calculated using equation 7.18

$$\Delta P = U\, u_{im}\, \rho_0 \tag{7.18}$$

where ΔP is the change in pressure (Pa), U is the shock velocity (m/s), u_{im} is the impact velocity and ρ_0 is this initial destiny ($\mathrm{kg\,m^{-3}}$). For the full derivation of the equation see Appendix H.3. Substituting equation 7.15 into 7.18 gives

$$\Delta P = (C + S\, u_{im})\, \rho_0\, u_{im} \tag{7.19}$$

It is now possible to expand equation 7.19 and combine the constants as follows: $a = \rho_0 S$ and $b = \rho_0 C$. The new definitions can be substituted back into equation 7.19. If the initial pressure is set to zero, the equation for pressure becomes:

$$P = a\, u_{im}^2 + b\, u_{im} \tag{7.20}$$

Since particle velocities experienced by the target are equal to those experienced by the impactor during the contact substage, $P_t = P_{im}$, and substituting this equality into

equation 7.20 gives equation 7.21.

$$a_{im}\, u_{im}^2 \,+\, b_{im}\, u_{im} \,=\, a_t\, u_t^2 \,+\, b_t\, u_t \tag{7.21}$$

In the rest frame of the target, the unshocked material is moving downwards at a speed of v_i (ms^{-1}) which is the downwards motion of the impacting material into the target at t=0. This is given by the impacting speed of the projectile following its passage through the air contained within the EVT (see Section 7.1.3). As the shock wave is moving in the opposite direction to the projectile's initial velocity, following the interaction of the shock-wave, the shocked material within the projectile moves with velocity $u_i m$. As the particle velocity in the target and the impactor are equal, it can be stated that:

$$u_t \,=\, v_i \,-\, u_{im} \tag{7.22}$$

where u_t is the particle velocity in the target. By substituting equation 7.22 into equation 7.21, the following expression is obtained:

$$a_{im}\,(v_i \,-\, u_{im})^2 \,+\, b_{im}\,(v_i \,-\, u_{im}) \,=\, a_t\, u_t^2 \,+\, b_t\, u_t \tag{7.23}$$

which can be rearranged to give the following

$$u_t^2\,(a_t - a_{im}) \,+\, u_t\,(2\,a_{im}\,v_i \,+\, b_t \,+\, b_{im}) \,-\, a_{im}\,v_i^2 - b_{im}\,V_i = 0 \tag{7.24}$$

The equations 7.25a, 7.25b, 7.25c are created by combining the exponent multipliers in equation 7.24 and substituting them back into equation 7.24, giving the solution in simple quadratic form as shown in equation 7.26.

$$A = a_t - a_{im} \tag{7.25a}$$

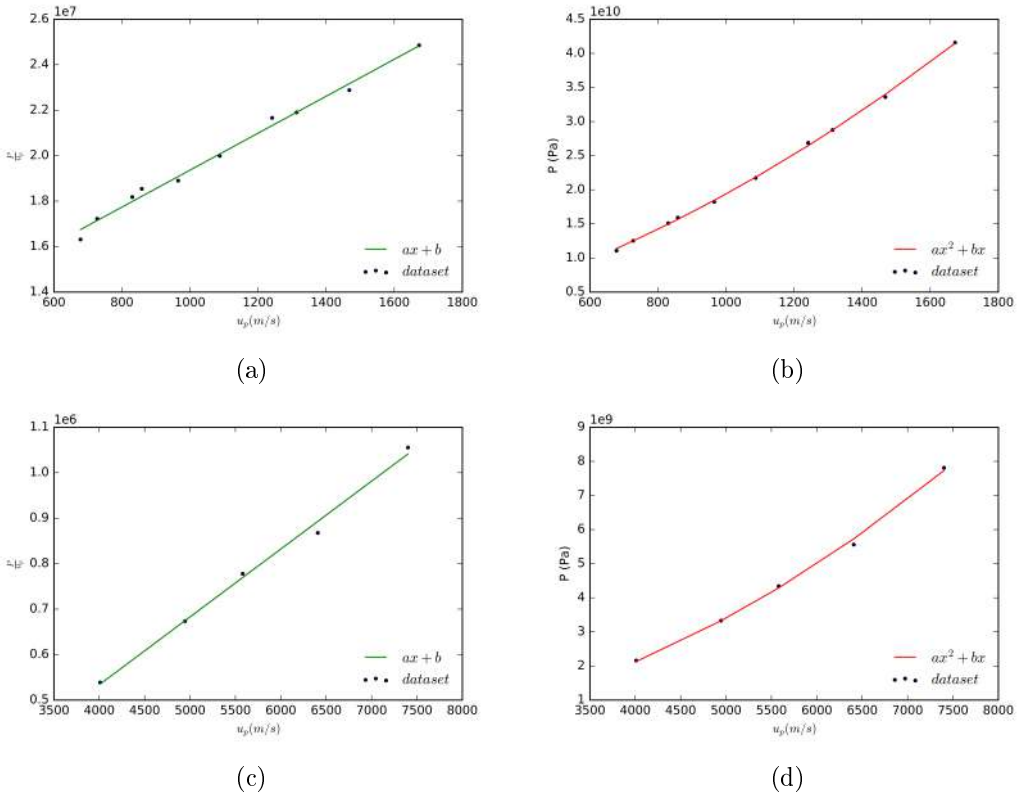
$$B = 2\,a_{im}\,v_i \,+\, b_t \,+\, b_{im} \tag{7.25b}$$

$$C = a_{im}\,v_i^2 - b_{im}\,V_i \tag{7.25c}$$

$$A\,u_t^2 \,+\, B\,u_t + C = 0 \tag{7.26}$$

From equation 7.26 it is simple to calculate the value of u_t via the quadratic formula once the values of a and b are known for the target and impactor. The full derivation can be seen in Appendix H.4.

7.2.2.2 Calculation of Peak Impact Pressure



(a) (b)

(c) (d)

Figure 7.4: Plots of pressure vs particle velocity for forsterite with different mathematical fits. Data is taken from *Huang et al. 2016* and *Holmes et al. 1984*. The lines shown in (a) and (c) are plotted using $ax + b$, The curves shown in (b) and(d) are plotted to fit the data using the quadratic $ax^2 + Bx$ function.

As the calculations for 'a' and 'b' depend on the material characteristics of the specific material, identical calculations need to be carried out for both the target material and for the impactor. Using experimental data taken from *Huang et al. 2016,* the values of a_{im} and b_{im} can be calculated by plotting the pressure (P) against the particle velocity (u_p) using the relationship shown in equation 7.20. Two methods for the calculation of 'a' and 'b' were attempted: the calculation of 'a' and 'b' relies on the fit of a line to the data set, therefore in order to improve the accuracy of the results both a linear and quadratic line were fitted. This aimed to show any bias in the fitting software due to the method of weighting individual points along the fit. The graphical representations of both the linear and quadratic fitted curves are shown in Figure 7.4.

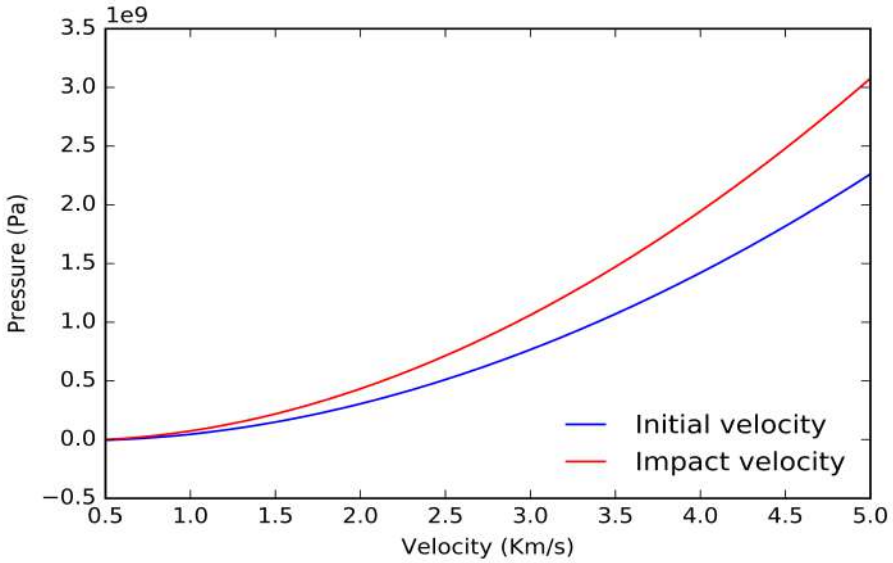


Figure 7.5: Showing the peak impact pressure achieved by an olivine projectile impacting into aerogel of density 112 $\mathrm{kg\,m^{-3}}$ against the initial (firing) velocity and its impact velocity

Table 7.1: Results for the values of 'a' and 'b' for the olivine projectile and the aerogel target.

	Projectile				Target			
	quadratic	σ	linear	σ	quadratic	σ	linear	σ
a	8036.58	240.75	8124.99	269.59	151.45	7.81	149.24	6.66
b	11344631.71	313377.01	11237589.99	304336.80	-76679.56	48670.80	-63327.50	38537.42

The results from the curve fitted lines are shown in Table 7.1. The linear and quadratic results of 'a' and 'b' are all within 1 standard deviation of each other, and show little variation. The results from the quadratic fit were used in the subsequent calculations. Using the values of 'a' and 'b' and the relationship shown in equation 7.20, it is possible to calculate the peak impact pressure achieved during impact and is shown in Figure 7.5. The initial velocity of the projectile shown in Figure 7.5 is the projectile's velocity upon passing through the light gate following the launch tube, recorded prior to the projectile's passage through the contained air, allowing peak pressures to be estimated based on the firing conditions.

From Figure 7.5, the peak impact pressure experienced by a 3 mm olivine projectile colliding with an aerogel block of density 112 $\mathrm{kg\,m^{-3}}$ can be determined. Shots under 2 $\mathrm{km\,s^{-1}}$ experience peak pressures below 500 MPa; this is below the critical threshold for damage to the projectile as measured by compression on a tensometer (UTM) in the

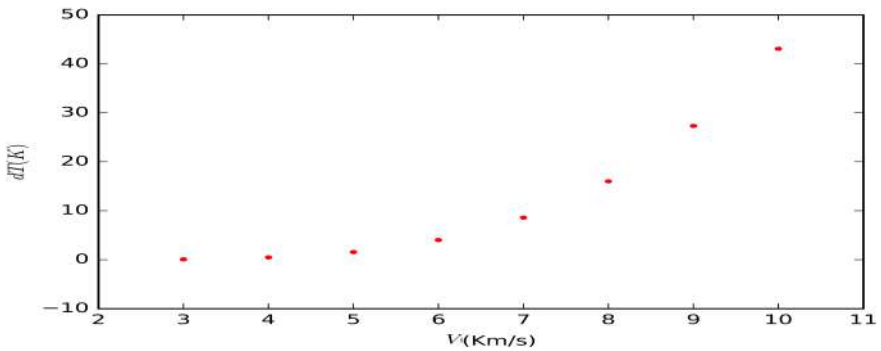


Figure 7.6: Maximum change in temperature for a 3 mm olivine projectile as it collides with a block of aerogel of density 112 kg m^{-3} following its flight through 1m of air as a function of its launch velocity.

laboratory ($\approx$ 1.2 Gpa). This agrees with the experimental results from shots 2 and 6 in the initial tests (see Section 6.3.2.1) which saw no damage. It should be noted that this is hydrostatic pressure and not shock pressure and as such the material will not behave in an identical manner. However the results give a value range which could be expected.

7.2.3 Temperature Change During Impact

The energy released during the impact of the projectile into the aerogel target can be calculated by equation 7.27

$$E_r = \frac{S}{C}\left(u_p + \frac{S}{C} ln(\frac{C}{U_{max}})\right) \tag{7.27}$$

where E_r is the energy released during the impact (J) and U_{max} is the maximum shock velocity (m/s) *(Wozniakiewicz et al. 2011)*. From the energy released E_r, the temperature change in the projectile, ΔT, upon impact can also be calculated using equation 7.28 *(Wozniakiewicz et al. 2011)*

$$\Delta T = \frac{u_p^2 - 2E_r}{2C_p} \tag{7.28}$$

where C_p is the specific heat capacity of the material (J kg^{-1} K). This assumes all energy released is given off as heat. The change in temperature experienced by the projectile upon impacting the aerogel as a function of initial launch velocity is shown in Figure 7.6

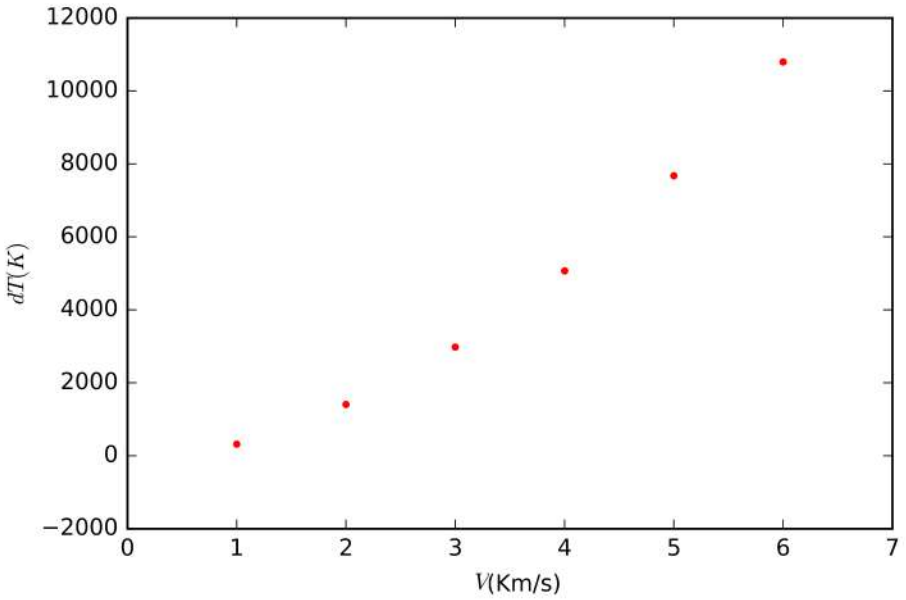


Figure 7.7: Graph showing the maximum change in temperature experienced by the block of aerogel (density 112 $\mathrm{kg\,m^{-3}}$) after impact by a 3 mm olivine projectile following its flight through 1m of air with changing launch velocities.

Using the data displayed in Figure 7.6, it can be seen that the changes in temperature experienced by the olivine projectile as a result of the impact into the aerogel block are far below the melting temperature for any of the impact speeds achievable in the LGG. As such it should be possible to ignore the thermal effects created within the olivine during its impact into the projectile stopping medium.

Figure 7.7 shows the calculated temperature change of the aerogel stopping medium due to the impact of the olivine projectile. The temperature change is plotted against launch velocity of the projectile. Here it can be seen that the temperature change of the aerogel exceeds the melting point of both the aerogel and the olivine at speeds exceeding 2.5 $\mathrm{km\,s^{-1}}$. Due to the thermal contact between the olivine and the aerogel following the collision, and olivine's higher thermal conductivity, it is likely that the olivine could be heated to equilibrium with the aerogel, and as such, it is possible that the projectile (or its surface) will be melted by the aerogel if the aerogel is superheated in this fashion. As such a launch velocity limit of 2.5 $\mathrm{km\,s^{-1}}$ was imposed.

7.3 Summary

Results from Chapter 6 demonstrate that the maximum velocity that can be achieved using the EVT is $\approx 1\,\mathrm{km\,s^{-1}}$. The theoretical calculations in this chapter show that it is unlikely that the melting of the peridots will occur before the initial firing velocity exceeds $2\,\mathrm{km\,s^{-1}}$. As such, in its current design the EVT is not able to fire the projectile at velocities that will result in melting and additional design changes would be required to achieve melting. These design changes are discussed in detail in Chapter 8.

In addition to the theoretical calculation of the atmospheric effects, the calculations for the temperature increases experienced during the impact of the projectile with the aerogel projectile stopping medium were carried out. These calculations showed that the heating and shock pressures experienced by the projectile during its deceleration were below the threshold for the onset of melting of the projectile for shot velocities below $3.5\ \mathrm{km\,s^{-1}}$. However, due to the heating experienced by the aerogel itself, and the projectile's continued thermal contact with it, the projectile can be heated above its melting point, with impact velocities of $> 2\,\mathrm{km\,s^{-1}}$ melting the aerogel and heating it to temperatures above which olivine melting occurs. Therefore any design alterations must ensure the impact velocity does not exceed this $2\,\mathrm{km\,s^{-1}}$ threshold.

Chapter 8

Atmospheric Flight 3: Thermal Alteration of Projectiles Passing Through Atmosphere

8.1 Building on Theoretical Results

8.1.1 Overview of Theoretical Results

Given that the melting temperature of Mg-rich olivine is known (around 2000 °C *(*Olivine Mineral Data *2018)*), the results from the previous chapter were used to determine the range of launch conditions able to achieve the melting of the surface of the olivine projectile. Figure 7.6 shows that a velocity of above 2 $\mathrm{km\,s^{-1}}$, through an atmosphere at 101325 Pa is needed to achieve the necessary change in temperature needed to melt the projectile. However, results from previous tests of the foils covering the EVT entry aperture (detailed in Section 6.3.3.2) showed that a launch speed at this velocity results in the catastrophic breakup of the projectile as it enters the EVT. Consequently a method for increasing the temperature experienced by the projectile without increasing its initial velocity was required.

8.1.2 EVT Design Improvement: Increasing Atmospheric Pressure

The first method investigated was increasing the pressure of the atmosphere contained within the EVT. By increasing the pressure contained within the EVT, a given temperature change can be achieved with lower velocities. For example, a projectile passing through 1 Atm of air requires a velocity greater than $2\,\mathrm{km\,s^{-1}}$, however projectiles travelling through 4 Atm only require a velocity of $1\,\mathrm{km\,s^{-1}}$ (see Figure 8.1). Accelerating

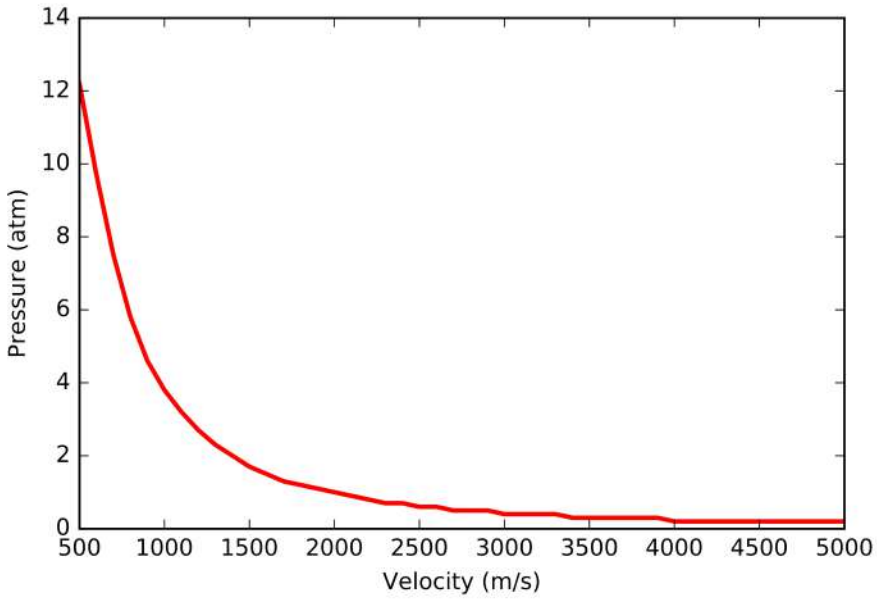


Figure 8.1: Showing the required initial velocity and pressure required to heat the olivine projectile to 2000 °C over 1 m flight distance.

the projectile to a lower velocity also has the additional benefit of reducing the shock to the projectile as it impacts the foils, as the projectile will be travelling slower per degree it is heated.

While 4 Atm is well within the structural limit of the main body of the EVT, additional design work was required to allow for safe pressurisation of the tube. Additional tests were also required to determine whether the foils covering the entry aperture were able to withstand the increased pressure and, if so, how the increased tension across their surface would affect the projectile attempting to pierce them.

8.1.2.1 Adaptations to the Environment Tube Design to Increase Contained Pressure

The EVT original design required only that an internal pressure of 1 Atm should be containable, therefore no provision was made for the transfer of pressurised gas into it. As such, in order to allow for an increase in pressure inside the EVT, a method of gas transfer and pressure measurement was required. In order to facilitate this, the breech block was modified to allow the connection of a screw thread inlet, which was done by chamfering the curved edge of the cylinder into a flat surface and drilling and tapping

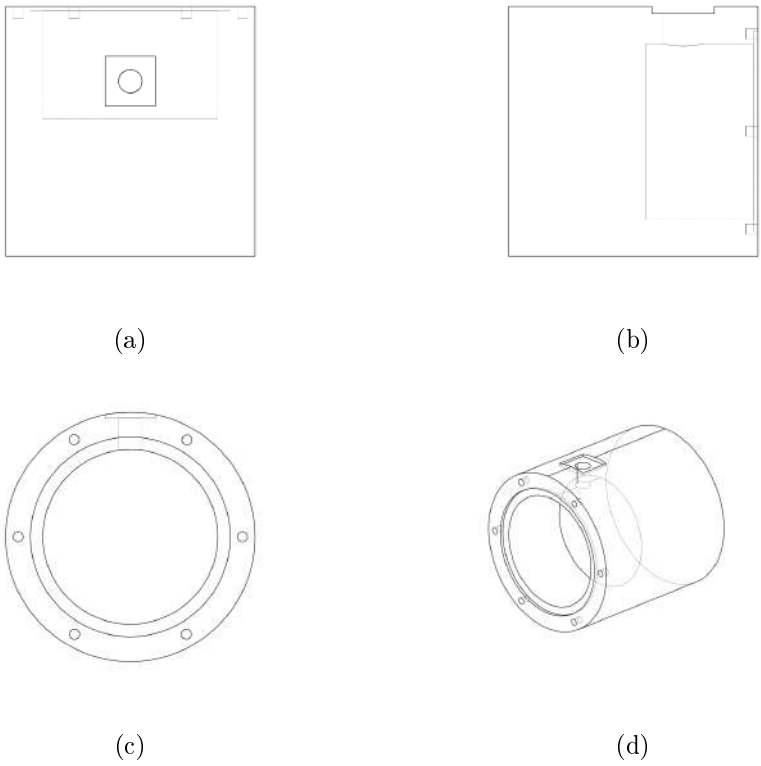


Figure 8.2: Schematics of the new breech block design to allow for the addition of gas above normal atmospheric conditions. The design is shown in a) Top down view, b) Side view, c) From the front of the breech and d) A 3D isometric view. (Dimensions removed for clarity; see Appendix G.2 for labelled diagrams).

a hole for the adapter (see Figure 8.2). A T-junction was then connected to the breech block and a pressure gauge and gas inlet attached. A non-return valve was positioned between the inlet and the tube allowing the gas supply to be disconnected so that the EVT could be placed in the target chamber without the need for piping to be exposed. This reduced the number of connectors in the setup and thus reduced the likelihood of leaking.

Prior to testing any changes to the set-up, the modified EVT was sealed at atmospheric pressure and placed inside of the target chamber. The target chamber was depressurised and the pressure inside the EVT was recorded by the pressure gauge. Following these tests a number of small changes to the connector, fastenings of the gauge inlet and aperture plates were made to improve the seal, with the results of the final test showing a pressure of 14.3 PSI (0.97 Atm) was retained with variation in the internal pressure of the tube for ten minutes following the pump shut-down.

Table 8.1: The results from pressure testing different thicknesses of Mylar foil covering the entry aperture of the EVT. Foils were tested either during the pump down of the target chamber or via the addition of high pressure nitrogen from a nearby canister. For both tests, the foils had to remain intact for ten minutes following pressurisation, with no failures for the foil to pass.

Thickness (µm)	Target chamber Pressure (mBar)(± 0.05)	Test Type
5	0.52 - 0.73	pump down
6	0.68 - 0.77	pump down
10	1.8	pressurised
15	>3	pressurised

Each foil was used to seal the EVT's entry aperture, and the tube was then either placed in the target chamber, or pressurised using compressed nitrogen from a canister once the fitting had been manufactured. Abridged results showing foil thickness versus maximum pressures are shown in Table 8.1. The tests for 5 and 6 µm thick foils showed a much larger range of failure values than the thicker foils, likely due to both material properties (i.e. amount of stretching before failure, creases etc.) and changes in pump-down rate and therefore the values shown in Table 8.1 are the minimum and maximum values for the repeated tests. The 10 and 15 µm thick foils showed a smaller spread in failure ranges.

Significant variation occurred across all foils, with rupturing occurring after different times and at different pressures during repeats, likely due to the plastic nature of the Mylar used. As such, for static tests, the foil needed to survive for 10 minutes (the time taken to fire the gun once pump down has been completed) at the maximum pressure to be considered as a pass. These results showed that the likelihood of the sub 10 µm thick Mylar surviving the pump down whilst containing a level of atmosphere required to melt the projectiles were low.

The foils were also tested to identify the limiting velocity at which the olivine projectile would break following an impact. Details of the target setup for these tests can be found in Appendix J. These tests showed that the ideal foil was 10 µm thick, with foils of a larger thickness requiring shots slow enough that no increase in heating was identified, and thinner foils requiring lower pressures which also results in a lower projectile temperature. As such simply changing the internal pressure of the EVT was unfeasible as a solution. The best ratio of foil thickness for the internal pressure proved to be the 10 µm thick foil and as such this was used in all further tests.

8.1.3 EVT Design Improvement: Reducing Foil Induced Shock

A second method for achieving higher temperatures with an intact projectile is by reducing the shock the projectile experiences on collision with the covering foil. For the previous design as described in Chapter 7, foil thickness governs both the maximum gas pressure within the EVT and the maximum launch velocity of the projectile. Hence by either removing the covering prior to impact (removing all speed limitations), or reducing its strength during the impact (allowing higher pressures to be contained by a thinner foil, resulting in the covering not disrupting the projectile), the maximum temperature achievable could be increased. Multiple methods for these outcomes were tested. It is important to note that the range in which reducing the strength of foil is viable is limited, due to the requirement that the covering be strong enough to contain the trapped atmosphere inside the EVT and therefore the experiments were limited to this range.

8.1.3.1 Adaptations to the Environment Tube Design to Reduce Foil Impact Shock

To reduce the shock experienced by the projectile when impacting into the entry aperture foil cover, and thus potentially achieve higher launch velocity survival, several adaptations were considered. One method considered for this was to remove the entry aperture foil prior to the arrival of the incoming projectile. In order for this to occur the foils would have to be removed in less than the Time of Flight (ToF) of the projectile down the gun's range (see Equation 8.1)

$$t_{tof} = \frac{L_{range}}{v_{proj}} \tag{8.1}$$

where L_{range} is the length of the gun to the entry aperture (roughly 2m) and v_{proj} is the speed of the projectile (m/s). Assuming a projectile is fired at 2 $\mathrm{km\,s^{-1}}$ as in shot 1 the foil would have to be removed, or pierced, in around 1 ms. The contact signal, however, cannot be sent from the ignition switch as a time delay of between 1 ms and 2 s exists due to the propellent burn rate, and as such would have to be sent from the signal generated at the launch barrel exit, or light gates, reducing the distance the projectile has to cover from 2 m to 1.5 m or 0.75 m. This reduces the time for a mechanism to act down to 0.75 ms and 0.375 ms respectively. Assuming a constant flow of air from the ruptured EVT, by negating the pressure change of the air inside of the EVT, the maximum percentage of air lost from the EVT to the surrounding target chamber over

the course of time, t, is given by:

$$\%loss = \frac{\pi\, r_{ap}^2\, C\, t_{tof}}{\pi\, r_t^2\, L_{tube}} \times 100 \tag{8.2}$$

where r_{ap} is the radius of the ruptured aperture (m), C is the speed of sound in the air (m/s), r_{EVT} is the radius of the EVT (m) and L_{EVT} is the length of the EVT (m). Substituting in the various values gives a maximum value of $\approx 25\%$. This loss is significantly higher than would realistically be expected, as the flow rate would not be constant, and the aperture created for the projectile would likely be less than the full diameter of the entry aperture. The calculation does however provide a maximum loss which could be compensated for by increasing the pressure contained prior to firing.

A number of ideas for removing the foil were considered: A heated wire could be placed across the the foil, which could be super-heated to melt the foil *(Hibbert et al. 2017)*. Previous experiments at the University of Kent on electronic burst discs have shown this method to be unpredictable over short periods of time. A device could be designed to pierce the foil and retract. Finally, a double projectile could be fired, using the first projectile as a sacrifice to pierce the foil before the arrival of the second. From the results of equations 8.1 and 8.2, a cycle rate of 2.66 kHz for the mechanism is required if it is triggered at the launch tube exit or 5.32 kHz if it is triggered from TOF laser. This is required to allow time for the mechanism to contact the foil and then to be removed prior to impact.

Initial design of a stationary mechanism to remove the foil from the entry aperture of the EVT showed the design to be significantly more complex than original provisioned for, due to inconsistency in timing and the need to provide a hole large enough for the projectile to pass through. Therefore, due to time constraints and simpler methods providing the same results, this idea was not carried further than the initial design phase.

A second method for removing the foil from the entry aperture used 'double stacked' projectiles (see figure 8.3) with the proceeding sabot loaded with glass spherules. The initial projectiles impact the Mylar thereby damaging it, with the glass disintegrating/vaporising on impact and hence not impacting the aerogel. The damaged film is then blown out by the air pressure contained in the EVT, allowing the closely following olivine projectile to enter the EVT intact.

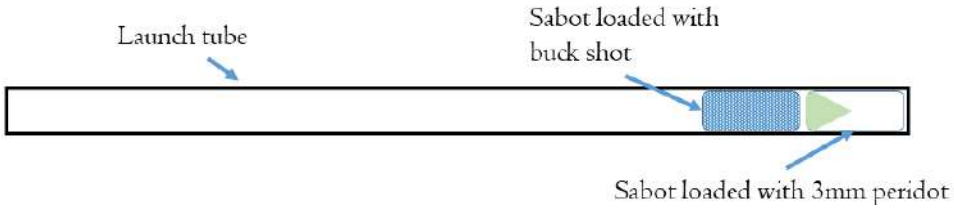


Figure 8.3: The buckshot sabot is loaded into the launch tube first so that it will reach and interact with the Mylar before the arrival of the 3mm peridot.

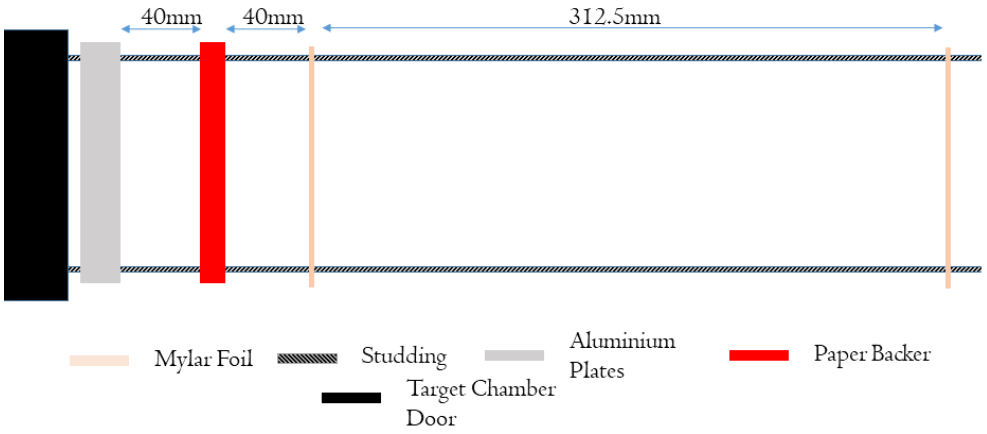


Figure 8.4: The foils set-up used in shot 8b. The set-up was to test the ability of buck shot preceeding the 3mm olivine peridot to pierce and remove the Mylar cover. The first foil is 10 µm thick with the second being thinner 5 µm Mylar.

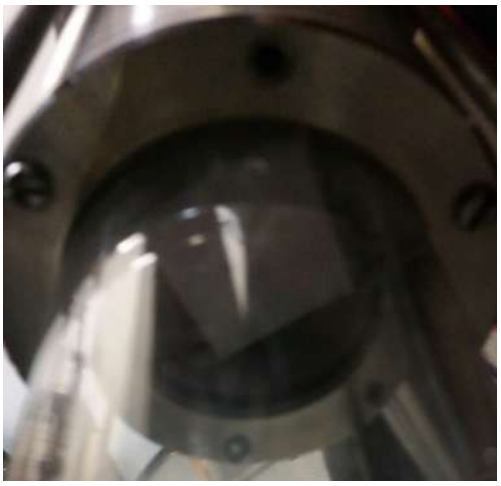
A preliminary test of this method used the foil rig with a separation as shown in Figure 8.4. For this initial shot the buck shot was comprised of 103 µm glass spheres. The two sabots were fired at 2.17 $\mathrm{km\,s^{-1}}$.

Results from the initial test were inconclusive; whilst the witness foil showed significantly less damage than shown in previous impacts of greater than 2 $\mathrm{km\,s^{-1}}$, there was more damage than would be expected from a single impact of an intact projectile. As such it is likely that whilst the buckshot did weaken the foil, it appears that the foil still retained sufficient strength to disrupt the peridot.

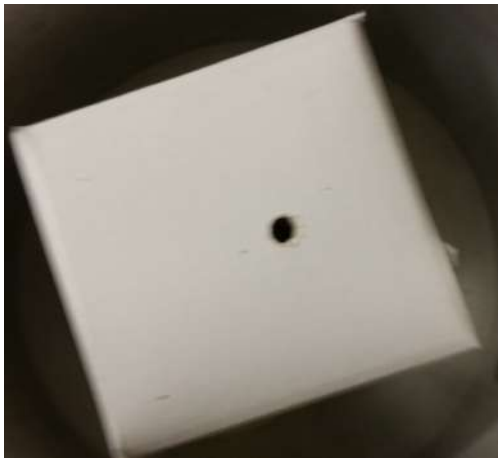
From the previous foil test (see 6.3.3.2), the 10 µm thick foils were shown to be close to their strength limit at an internal pressure of 1 Atm and, an additional shot was carried out to test if the foils would rupture and 'blow out' following the impact of the buckshot, and hence still be removed from the peridot's flight path. These required the use of the EVT as an internal air pressure was required and as such a witness foil could not be used. Instead the projectile stopper placed inside the EVT for this shot consisted

of a paper cylinder capped with a wad of paper on which impact marks would be visible. During the shot, the paper wadding became detached from the cylinder, likely as the gas escaped from the pierced foil, and was dragged up the EVT. The peridot therefore impacted with the paper at an angle, resulting in a non-circular hole. The shot was was therefore repeated, replacing the paper cylinder with a small (5 cm by 5 cm) paper box, filled with layers of paper (see Figure 8.5 a). The projectile was fired at 2.09 $\mathrm{km\,s^{-1}}$, and impacted the paper box. A single hole was formed in the outer layer (Figure 8.5 b) gradually widening through successive layers (Figures 8.5 c and d). The peridot was recovered roughly one third of the way through the stopper (Figure 8.5 e) in a damaged condition.

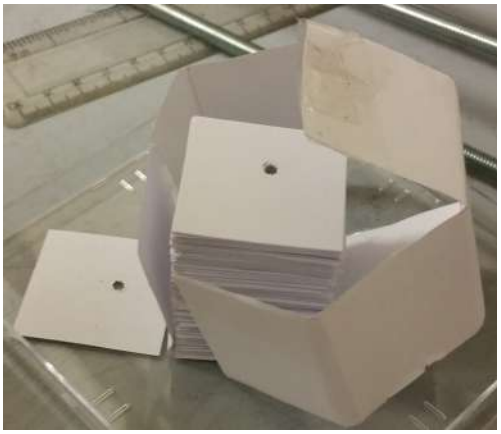
From the oscilloscope traces taken from the laser positioned along the TOF section of the gun, the relative positions of both the buckshot and the peridot as they passed along the range (see Figure 8.6) can be seen. From these data, it is possible to calculate the amount of air which escaped the EVT between the impact of the buckshot with the film and the peridot's impact with the projectile stopper. The can be calculated from the velocities of the buckshot, peridot and distance from the second lightgate to the target chamber. As the difference between the two velocities is small compared to their absolute velocities and the distance between the light gate and target chamber is also negligible, we can use the time separation recorded at the second light gate as the same as that at the target chamber.



(a)



(b)



(c)



(d)



(e)

Figure 8.5: The projectile stopping medium used in shot 10b, to test the feasibility of using buckshot to pierce the Mylar foil on the front of the EVT. Showing a) The medium in the breech prior to firing, b) The top surface after firing, c+d) The internal structure after firing, e) The crushed olivine projectile recovered in the stopping medium.

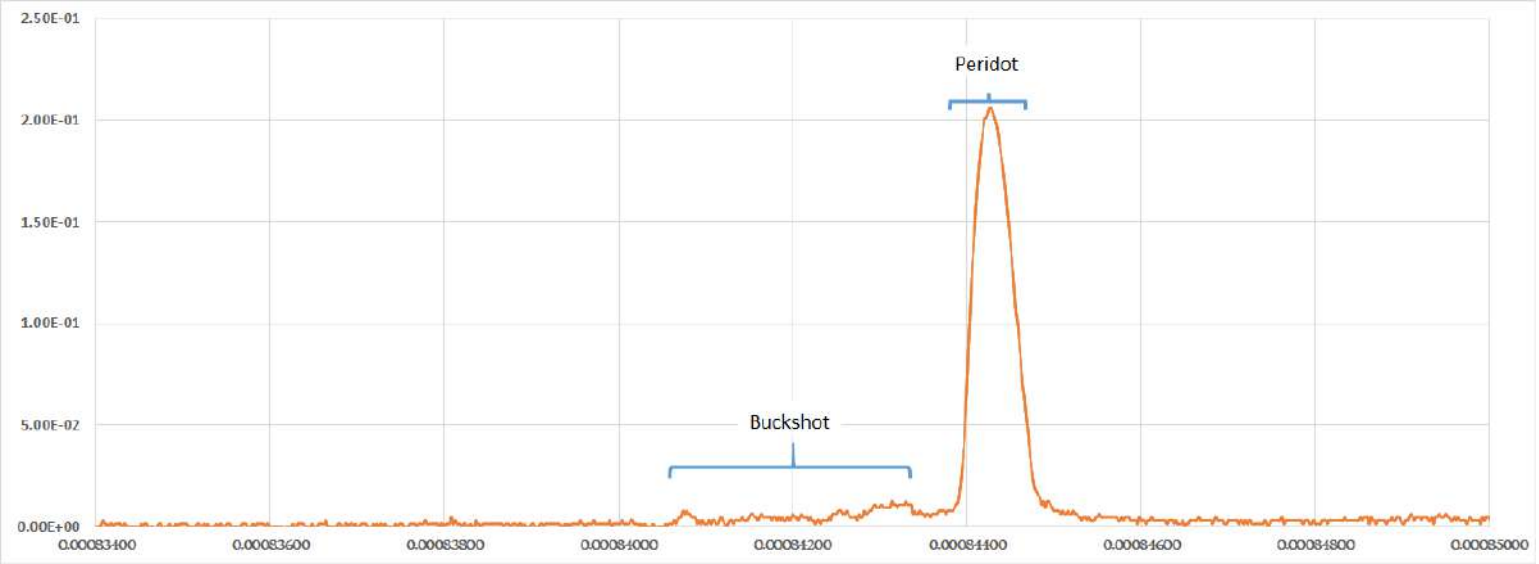


Figure 8.6: An example TOF trace (shot 16b) taken from light gate 2 showing the separation of the buckshot projectiles from the main olivine projectile.

From Figure 8.6 it can be seen that for shot 16b the peridot trailed the buckshot by 1.7×10^{-6} seconds. The amount of air which would escape the EVT in this time frame, assuming a fixed speed of sound of 330 m/s, is given by:

$$0.0625^2 \times 330 \times 1.7 \times 10^{-6} = 0.22 \times 10^{-9} \mathrm{m}^3$$

which is negligible compared to the amount of air contained within the EVT (0.12 m^3).

8.1.4 Summary of Changes Carried Forward

Following these results, it was decided to carry forward the buckshot method of removing foils from the flight-path of the projectile. This method completely removes any interaction of the projectile with the foil, simplifying the task of identifying the atmospheric effect on the projectile. In addition to the buckshot, the 10 µm thick Mylar film was to be used as a replacement for the thicker 15 µm aluminium Mylar foil for subsequent shots. Whilst this reduces the maximum amount of pressure that can be stored in the EVT during a shot (down to 1 Atm), it has no effect on the pressure during a shot and it increases the chance of the impact of the buck shot weakening and blowing out the film such that the olivine projectile can pass through unimpeded. This method allows for speeds exceeding the $2\,\mathrm{km\,s^{-1}}$ initial velocities required to melt the olivine projectile.

8.2 Shot Program 3

8.2.1 Aims

Following the successful test of the EVT using buckshot to precede the peridot, shot program 3 aimed to build upon the data obtained during the original shot program by enabling shots to be fired at higher velocities. It was intended that each shot should be duplicated and fired with and without air, with each pair of shots targeting the same aerogel batch (several batches of aerogel had been obtained although each with slightly different densities), such that meaningful comparisons could be made. Table 8.2 shows the details of each of the shots analysed, and Appendix J.2 contains all supplementary data including aerogel batch numbers for each shot.

Table 8.2: The results of the shots following changes to the firing method to include the use of buckshot prior to the peridot projectile. Details of the peridots used can be found in Appendix I. The target speed and achieved speeds for each shot are shown, with the number of major fragments (i.e. those observable by eye) displayed.

Shot No.	target Speed ($km s^{-1}$)	shot speed ($km s^{-1}$)	Atmosphere	Peridot Number	Fragments
11b	2	2.07	Yes	21	1
15b	2	1.88	no	27	1
26b	1	0.89	no	38	1
27b	1	0.64	yes	40	1
28b	2.5	2.58	No	41	1
30b	2.5	2.71	yes	44	3

8.2.2 Results

Following shooting, the peridots were retrieved from the EVT. In most cases the aerogel block had been disrupted and the peridot could simply be picked up and placed in a sample container. For shot 27b the peridot remained inside an undisrupted block at the end of the track and as such had to be cut out of the block. The peridots were positioned on an M3 nut and examined via SEM, Raman spectroscopy, and optically to identify changes to the surface morphology and chemical composition of the projectiles.

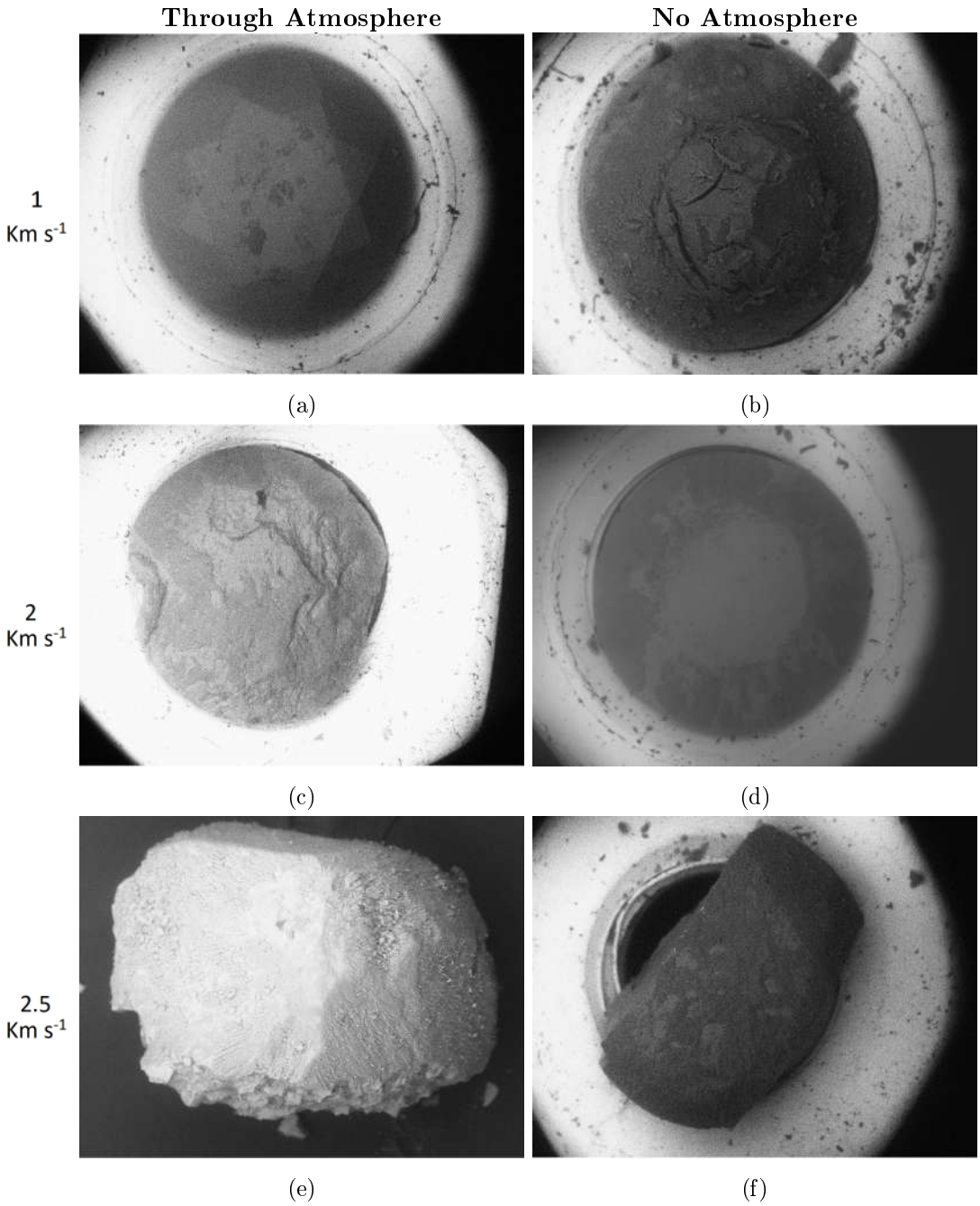


Figure 8.7: BSE images of the peridots post-shot, following their removal from the aerogel block a) peridot 40, b) peridot 38, c) peridot 21, d) peridot 27, e) peridot 44, f) peridot 41. The peridots are arranged in pairs with corresponding speeds.

From Figure 8.7 it can be seen that those projectiles that passed through atmosphere inside the EVT appear to have suffered more alteration (more surface damage, greater shape change etc.) than those travelling at similar velocities through vacuum. Com-

parisons of laser trace data taken from the TOF system during the shot shows each projectile to have been in a similar state of orientation and, neglecting peridot 41 and 44 (both shot at $2.5\,\mathrm{km\,s^{-1}}$) which appeared to have suffered damage on acceleration, show no signs of fracturing. Calculations based on the separation of the buckshot to peridot data from the TOF trace shows that in all instances it is unlikely that the peridot contacted the film as it had sufficient time to be removed from the peridot's flight path.

8.2.2.1 Surface Morphology

Comparisons of the projectile pre- and post-shooting show a number of variations on the surface of the olivine. From Figure 8.8 we can see that prior to shooting, the olivine surfaces showed only small scratches as a result of the polishing they underwent during production following cutting, however post-shooting we can see a number of changes to their surface.

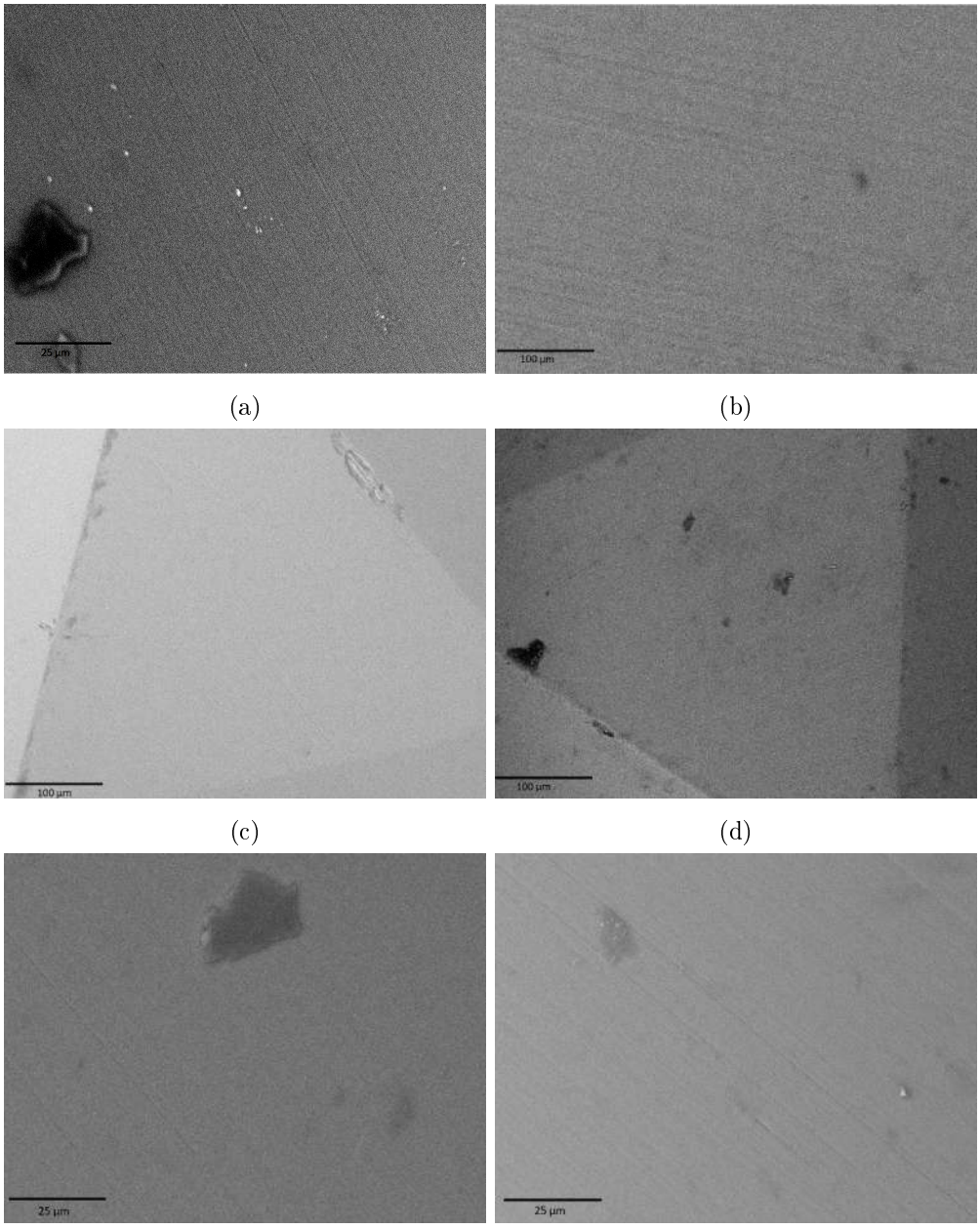


Figure 8.8: Showing example of polishing marks on the surface of each of the recovered peridots; a)21-11b b)27-15b c) 38-26b d) 40-27b e)41-28b, f) 44-30b.

Comparisons of the pre-shot images of the surface of the peridots displayed in Figure 8.8, with the post-shot images displayed in Figure 8.9 show that for slower speeds the polishing marks remain visible, however they are largely obscured by the coverage of the compacted aerogel that has welded onto the surface of the projectile. At 2 $\mathrm{km\,s^{-1}}$ however, the polishing marks cannot be seen on the surface of the projectile. More

significant surface damage is observed at 2.5 $\mathrm{km\,s^{-1}}$; large cracks appear on the surface and the projectile does not remain intact. Unfortunately due to the coverage of aerogel and the change in morphology it was not possible to re-image the same locations post-shooting and as such no direct comparison between pre- and post-shooting for a specified location could be made.

The loss of scratch marks in the shots exceeding 1 $\mathrm{km\,s^{-1}}$ implies that the surface of these projectiles has undergone a transformation which is dependant on the projectile velocity. Due to the aerogel coverage on the non-air sub 1 $\mathrm{km\,s^{-1}}$ shot, it was not possible to determine whether this surface change is due to the aerogel impact, or the atmospheric passage. However as the shock pressure experienced by the projectile impacting into the aerogel is low, and faint marks can still be seen on some of the uncovered regions, it is likely that these differences are solely due to the atmospheric passage.

It is also possible to identify significant changes to the outline of the projectile as shown in Figure 8.7. Analysis of the Mylar foils post-shot shows that the foils were blasted out of the EVT, with fragments being collected from the floor of the target chamber. Tests where the projectile has pierced the foil prior to it being removed showed that fragments of the film would be collected from the interior of the EVT. In this way we can confirm that the Mylar foil has been removed from the path of the projectile and, as such, it is unlikely that an impact with the entry film could be responsible for any damage to the projectile. As the Mylar film is not responsible for the damage to the projectile, the likely causes of damage to the projectile are either impacts into the aerogel, impacting and decelerating in the atmosphere, or during acceleration in the gun. The TOF traces were also used to identify any damage to the projectile caused by their acceleration prior to the entry into the EVT. Due to this method of identifying damage to the projectile caused during acceleration, we are able to confirm this as the reason for the major morphology changes seen in Figure 8.7 e) and f).

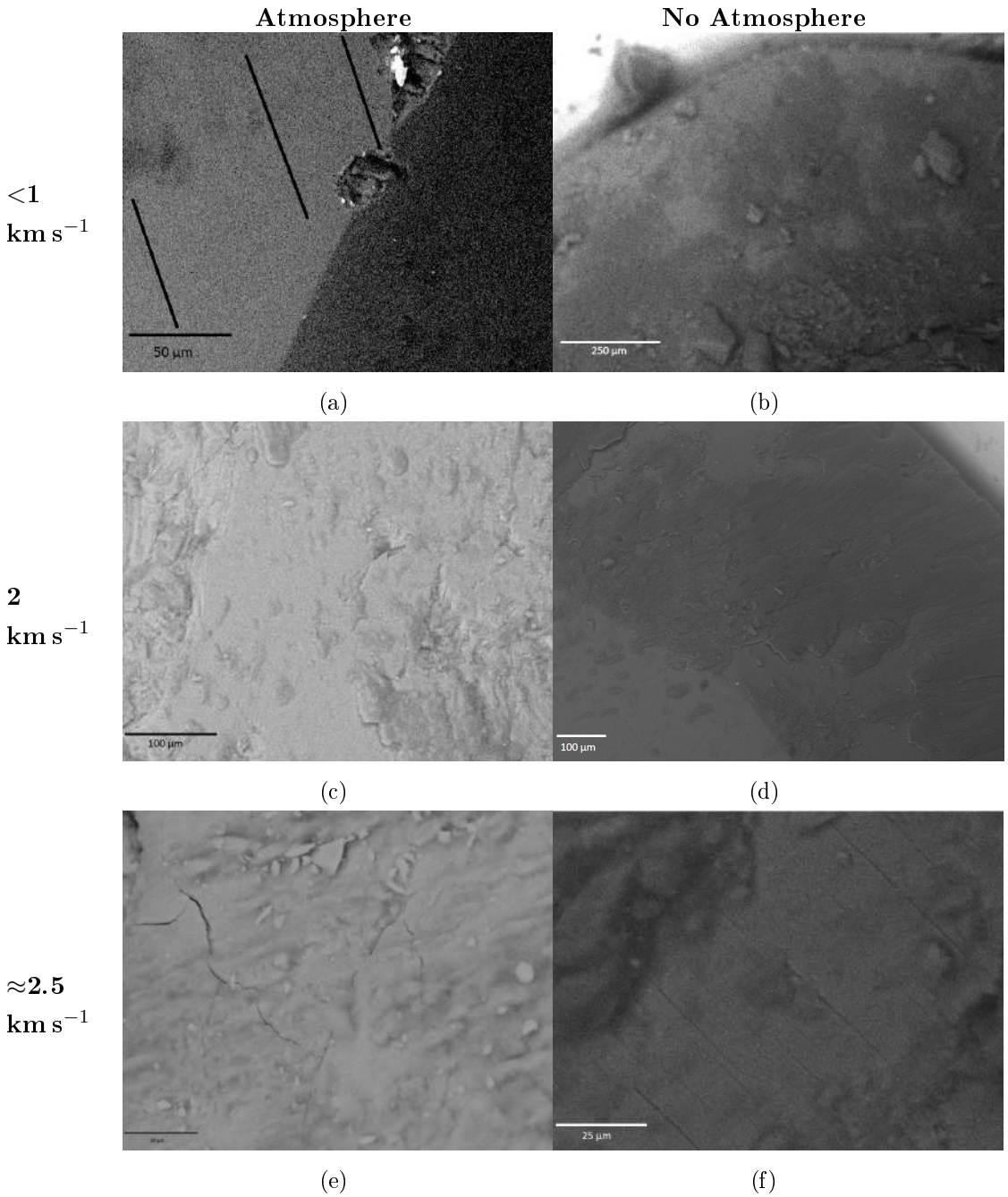


Figure 8.9: Post-shot, zoomed-in, images of the surface of the projectile. Notice small scratch marks can still be in seen in the left of image a). a) peridot 40, b) peridot 38, c) peridot 21, d) peridot 27, e) peridot 44, f) peridot 41.

Overall several morphological changes were seen on the projectile's surface. The loss of polishing marks on the peridot's surface are seen on projectile's which impacted the aerogel at speeds exceeding 1 km s^{-1}. Significant damage also appears to have occurred

to projectiles fired at speeds exceeding $2\,\mathrm{km\,s^{-1}}$ during acceleration in the launch tube and a new method is required to heat the projectiles above their melting temperature at a slower launch speed. Finally changes in the aerogel collected on the peridot's surface are seen for different velocities. Peridots fired at slower speeds have white aerogel crumbs attached to surface, whilst peridots fired at $2\,\mathrm{km\,s^{-1}}$ and above have blackened aerogel that appears to be have be molten and welded to the surface.

8.2.2.2 Chemical Composition

Following each shot the peridot was reanalysed in the SEM. Due to the aerogel coating on the surface (as seen in Figure 8.7), we were unable to directly measure the composition of the olivine without carrying out additional sample preparation. The peridots were therefore embedded positioned on the girdle so that their cross-section from front to back would be revealed when cut and polished. To ensure that they stayed in place during embedding they were held down via superglue before being embedded in Struers 'specifix' epoxy resin and left to cure. Following curing, the resin block was cut along its face plane so that the contained peridot was cut along its axis and each sample was polished using coarse to fine grit sandpapers followed by 3 µm and 1/4 µm diamond paste.

Once polished, samples were carbon coated and EDX-data was obtained via area maps in the SEM following calibration. Comparing EDX data obtained before and after shots, it appears that the Fe:Mg ratio decreases for each peridot after they have been shot as shown in Figure 8.10. This increase in Fe/Mg is likely down to a combination of factors. It is unlikely that the increase in iron is from the gun barrel, as the olivine projectiles do not contact the barrel. Comparing the two groups of data by the use of a Kolmogorov–Smirnov (KS) test on the Fe/Mg ratios gives a result of $P = 0.0766$, showing that the two groups are likely to be statistically different. However it should be noted that the use of KS tests on small datasets significantly reduces their effectiveness and reliability, and many more shots would be required to prove this difference. The peridots fired at $2\,\mathrm{km\,s^{-1}}$ showed a larger change in Fe:Mg ratio than those fired at $1\,\mathrm{km\,s^{-1}}$ with all olivine showing a reduction in the Fe:Mg ratio. Due to the break up of the $2.5\,\mathrm{km\,s^{-1}}$ projectile on launch, none of the analysable samples would have achieved a high enough temperature for vaporisation to occur and as such fractionation is unlikely to have occurred.

From these results alone however we are not able to separate out the effect of the impact with the aerogel from that of the effects of the atmospheric passage. Therefore

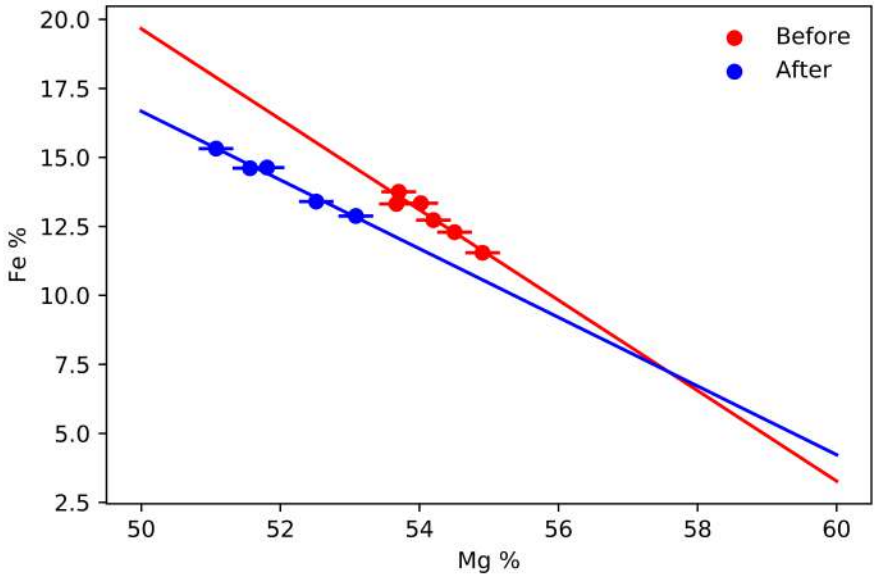


Figure 8.10: The change in iron and magnesium levels in the composition of the peridots from measurements taken prior-to and post-shot. Error bars are given as 3 sigma, taken from Aztec.

additional comparisons were made between those peridots which have passed through the atmosphere and those which did not. In Figure 8.11 it appears that those shots which have passed through an atmosphere have a greater increase in iron than shots which have only impacted the aerogel.

This implies that for velocities that should achieve melting during atmospheric passage, there is a difference between those which have passed though atmosphere contained in the EVT and those which have simply impacted into the aerogel block. These changes do not appear as morphological changes, and no evidence of the formation of a Fe-rich rim has been seen. There also appears to be a significant difference between those spectra taken prior to impact and those taken after impacting the aerogel alone and therefore the effects due to the aerogel impact, even at low speeds, cannot be ruled out. It is also possible that the aerogel impact is having an identical effect on the peridot as the atmospheric passage albeit, on a smaller scale. Without the $2.5\,\mathrm{km\,s^{-1}}$ shots to analyse it is not possible to observe any pattern that would allow this to be confirmed. A larger shot program should be performed to investigate the effects of the aerogel on the projectile and provide a method for removing this effect from the end result. With only two data sets at velocities just above, or at, the melting point of the olivine we are currently unable able to perform any method for extracting the atmospheric effects from those produced by acceleration and impact into the aerogel.

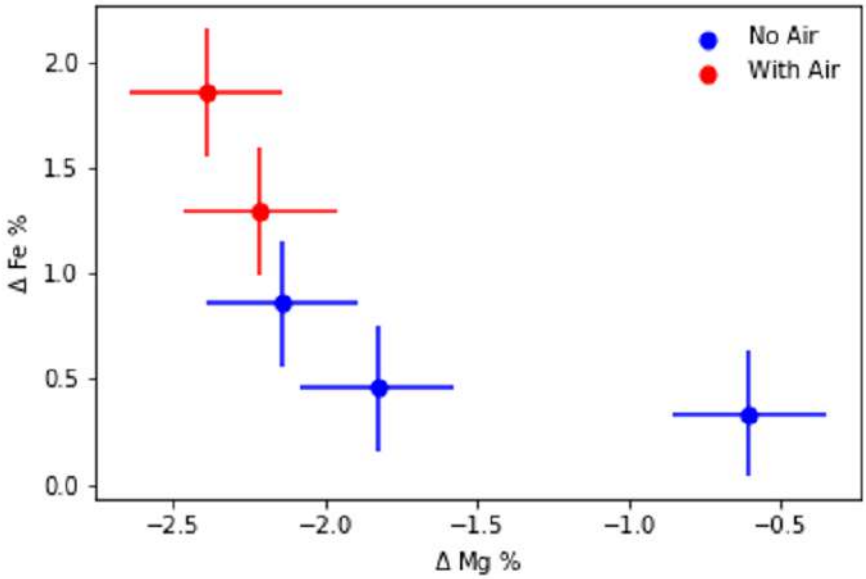


Figure 8.11: The change in iron and magnesium levels in the composition of the peridots from measurements taken as an whole body area scan prior-to and post-shot. Error bars are given as 3 sigma taken from Aztec =.

8.2.2.3 Raman Peak Locations and Structure

Unfortunately Raman analysis of the projectiles was compromised by flawed initial data taken prior to the firing of peridots. The initial analysis of the projectile mapped the surface of the peridot table, using a M3 nut to hold the irregularly shaped projectile in position, as it was not possible to use the normal method of ensuring a flat surface (e.g. embedding, polishing etc) prior to shooting. The analysis focused on peaks X (≈ 798 cm^{-1}), Y (≈ 844 cm^{-1}) and Z (≈ 918 cm^{-1}). Unfortunately following the shot program, it was found that the table surface was not horizontal (see figure 8.12) and thus two clear regimes are visible in the maps obtained and in the histogram showing the values of peak ratios of peaks X and Y, created by the focus length changing and going from over-focused to under-focused.

Although the data obtained prior to shooting were compromised, an attempt to compare the after shot peak positions was made with the compromised before data was still undertaken, the results of which can be seen in Table 8.3. Based on the previous work of *Harriss and Burchell 2016* shots into aluminium foil at speeds which result in a shock pressure below 65-85 GPa do not result in peak shifts and as such no shifts should be seen in the spectra of the shot fired directly into air. For peridots heated

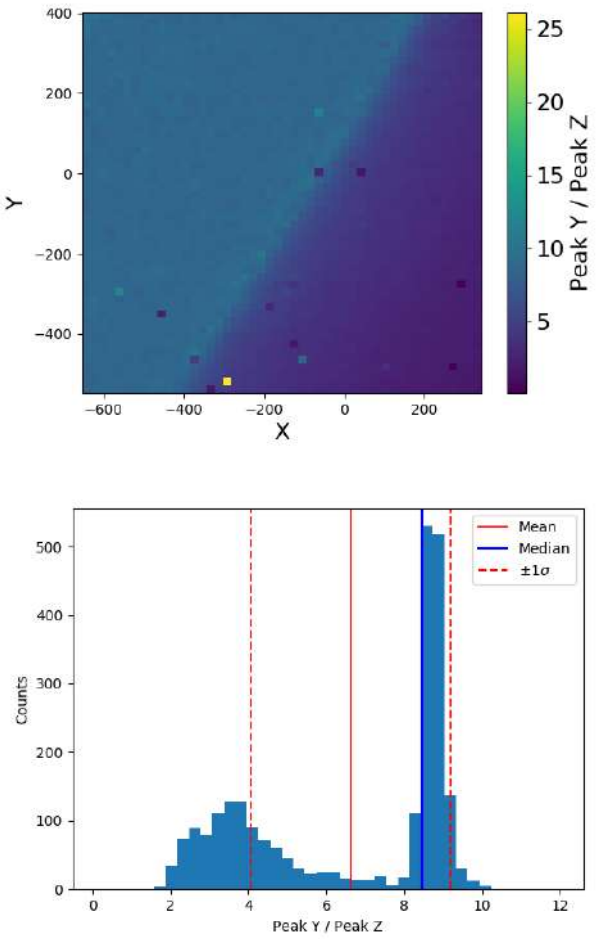


Figure 8.12: The Raman intensity map obtained from peridot '44' prior to shooting. The intensity gradient across the plot is due to the peridot not being horizontal during the analysis resulting in regions being out of focus.

during atmospheric entry, peak changes may occur due to melting, chemical changes and possibly shock due to the higher body temperature *(Harriss and Burchell 2016)*.

Table 8.3 shows the change in peak positions of each of the peridots (peridot 44 is not included as its origin location is not known). For peridots 38 and 40 ($1\,\mathrm{km\,s^{-1}}$), as expected, no change in the peak positions can be seen, as the impact shock pressure would have been well below that required for any change. For peridots 21, 27 ($2\,\mathrm{km\,s^{-1}}$) and 41 ($2.5\,\mathrm{km\,s^{-1}}$) shifts in the peak position can be seen although the peak shifts are only just above the grating limit, and in all three cases the shifts are significantly less than the spread of the data recorded prior to shooting.

Table 8.3: The Raman peak positions of the peridots taken prior to and following shooting.

Peridot No.	Velocity $km\,s^{-1}$	X peak before cm^{-1}	X peak After cm^{-1}	X peak Shift cm^{-1}	Y peak before cm^{-1}	Y peak After cm^{-1}	Y peak Shift cm^{-1}
38	1	823.47	823.37	0.10	855.24	855.35	0.11
40	1	823.53	823.47	-0.06	855.36	855.30	0.06
21	2	823.16	823.54	0.55	855.13	855.48	0.35
27	2	822.75	823.08	0.33	855.11	854.76	-0.35
41	2.5	822.88	822.92	0.03	854.56	854.99	0.439

The Raman data did show that the peridots remained crystalline at their surfaces following both the $1\,km\,s^{-1}$ and $2\,km\,s^{-1}$ shots, showing that higher temperatures are required to achieve melting. The $2.5\,km\,s^{-1}$ shot was also crystalline, however it is not known if this was an edge or interior fragment.

8.2.2.4 Line-Scans

Following sample polishing, EDX line-scan data for each of the peridots was obtained comparing element abundances across the grain boundary. If melting has occurred it would be expected that the edges would be glassy, which, when compared to the unshot grains, would result in a difference in gradient of the elements count rate, due to changes in density as the beam transitions from the olivine to the aerogel. Five lines were taken per sample in a smooth (evenly polished with no regions exhibiting plucking or gouging) region of the peridot's leading edge (see Figure 8.13). The smooth topography was vital to ensure that surface fluctuations did not influence the element line-scan data. The two clearest lines were then analysed. Due to the severe damage peridot 44 suffered during acceleration, a smooth region for only a single line was found. For peridot 40, which had large amounts of aerogel attached to the surface prior to cutting, infilling using additional resin was required to remove the void left by the aerogel breaking away during cutting.

Once the line-scan data were collected, the abundances of iron, magnesium and silicon were fit using a logistical function, the equation used is shown below:

$$f(x) = \frac{L}{1 + e^{-k(x-x_0)}} \tag{8.3}$$

where L is the curve's maximum value, x_0 is the curve's sigmoid midpoint and k is the curve's steepness. The steepness of the curve, k, was then plotted to show the rate of change of a peridot's chemistry as the line-scan approached the interaction zone on its front face.

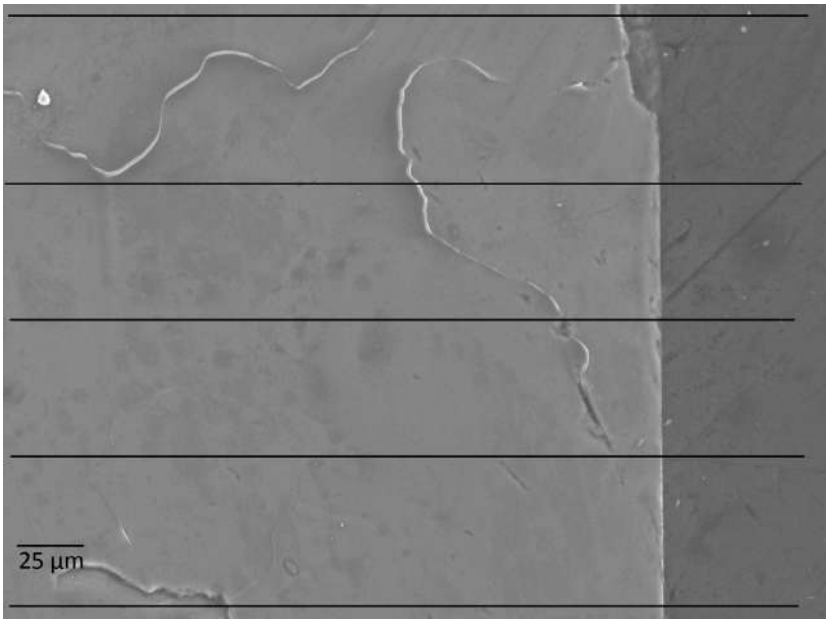
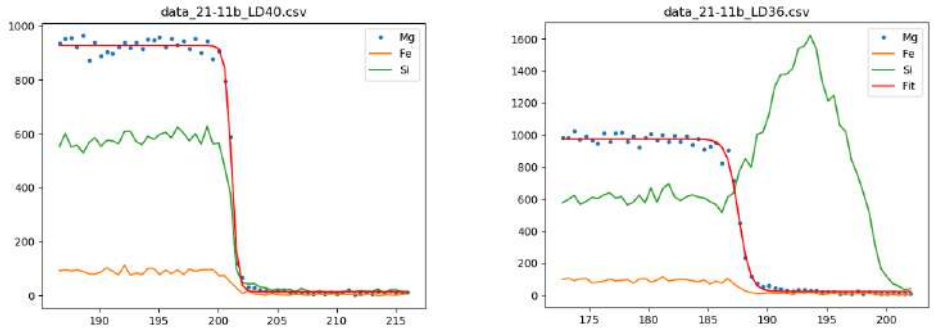


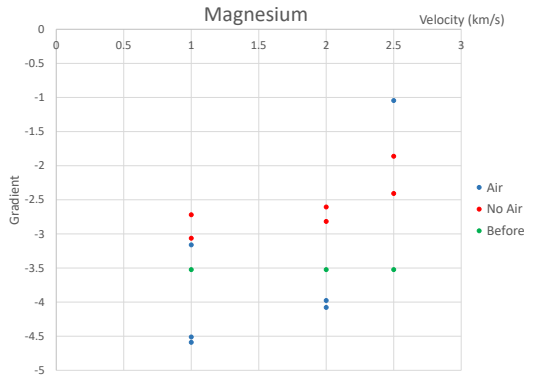
Figure 8.13: An example line-scan acquisition (peridot 21-11b) area used for the collection of line scan data. A patch of aerogel melted to the peridot surface can be seen at the top of the peridot aerogel transition.



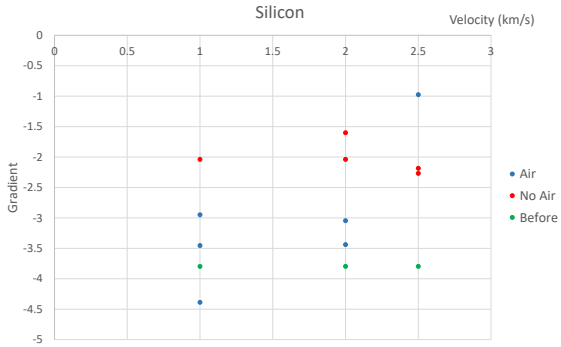
(a) (b)

Figure 8.14: Two examples of line-scan acquisition from peridot 21 plot with a fitted logistical function a) with melted aerogel on the peridot surface, b) no aerogel attached the surface

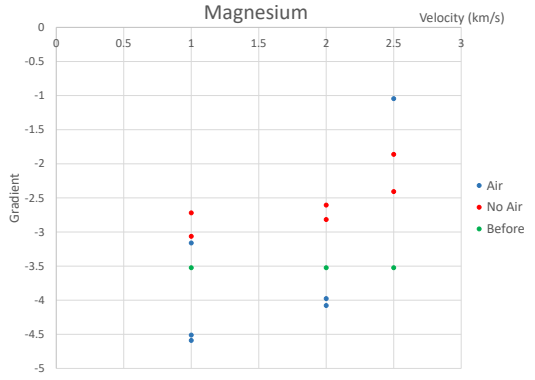
The results of the fitting function for magnesium on line-scans taken from peridot 21 can be seen in Figure 8.14. In Figure 8.14(a) a smooth transition from olivine to resin can be seen. Figure 8.14 (b) shows a spectrum obtained when the beam passes through a region of aerogel melded to the peridot's leading edge. As the aerogel is a silicate, a spike in silicon counts with a corresponding decrease in counts of magnesium and iron is seen. Following the aerogel the beam, passes into the carbon-based resin and the silicon peak fades.



(a)



(b)



(c)

Figure 8.15: The steepness of the fitted logistical function fitted to the a) Magnesium, b) Silicon and c) Iron line scan data for each peridot. Note that peridot 44 (into air at 2.5 km s^{-1}) was damaged following launch and as such the original location of the fragment is unknown.

In Figures 8.15a, 8.15b, 8.15c, the steepness of the logistic function (k) is plotted versus the firing velocity for projectiles fired into air and directly into aerogel. Figure 8.15a shows the steepness of the magnesium logistic functions and in all cases projectiles which impacted directly into aerogel show a more gradual change in counts of magnesium than those projectiles fired directly into the air and the unshot peridot, while the gradient of the fit for those projectiles which passed through the atmosphere, however, show a steeper gradient than the unshot projectile. This would suggest that the boundary is not as clear on the directly impacting projectiles or that magnesium has migrated from the edge. The reason for the increase in slope on the atmospheric projectile is currently unclear, as any changes brought about by atmospheric passage should also result in the lessening of the slope, and further work is required to identify any agency for this change.

The plots for the Si gradient changes (see Figure 8.15b) show that the samples have nearly identical silicon decay gradients, with those passing through the atmosphere having steeper gradients than those that did not. This would further suggest that the magnesium features described above are real, but may also imply that the change maybe down to the surface roughness, with the peridots which passed through the air having small surface features ablated resulting in a more defined edge.

Due to low amounts of iron contained in the peridots, the iron line-scans were unable to provide evidence of a clear pattern (see Figure 8.15c). As small changes in the iron count resulted in large percentage changes to the counts and thus had a large effect on the gradient.

8.2.2.5 FIB-TEM

TEM sections from several shot samples performed both with, and without, air were produced using the FIB at the University of Leicester. TEM analysis was scheduled at the University of Nottingham, however during transport a number of the sections were damaged (38-26b and 40-27b). The remaining sections (unshot, 21-11b ($2\,\mathrm{km\,s^{-1}}$ into air) and 27-15b ($2\,\mathrm{km\,s^{-1}}$ without air)) which were transported separately from Canterbury were analysed, however, due to equipment time constraints, it was not possible to perform lattice spacing analysis and as such only detailed imaging and EDX analyses were obtained.

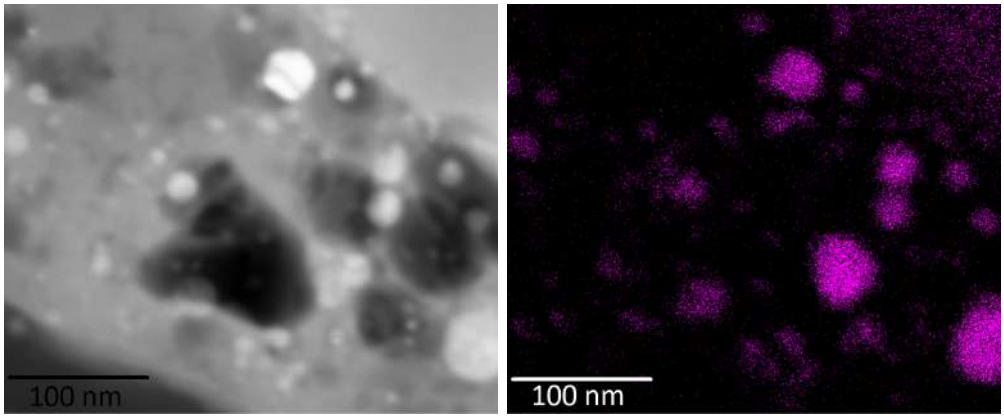


Figure 8.16: TEM image and EDX Fe intensity map of the iron beads contained inside of peridot 21.

The boundary between the peridot appears to be uniform, with no change in texture as the surface is approached, suggesting that the peridot has remained unmelted. In places the aerogel appears to be melded to the surface, with no visible gaps between the aerogel and peridot, which would suggest the aerogel was molten and flowed to cover the surface.

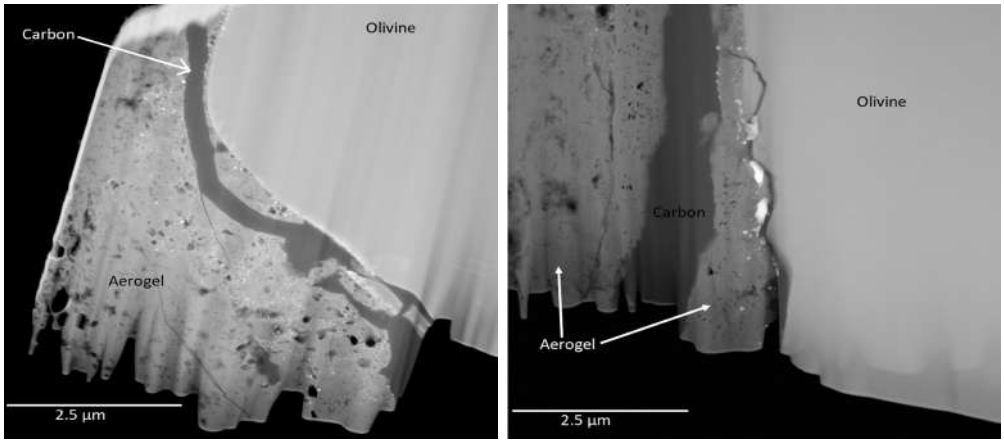
Upon imaging the aerogel peridot interface in the thin sections, nanometer scale iron beads embedded within them (see Figure 8.16) were identified. These beads could be: 1) inherent to the projectile, 2) produced by the peridot during atmospheric entry, 3) produced by the peridot during acceleration and impact into the aerogel, or 4) debris from the LGG. It is possible that they are inherent to the projectile despite none being seen during previous optical or SEM analysis. However, no section was obtained from an unshot peridot which would allow this to be proven. It is possible to rule out that they formed as solely the result of atmospheric entry as the beads can be observed on peridot 27 which was fired directly into aerogel. The production of metal beads during impact with the aerogel has previously been noted, with GEMS-like spherules (reduced metal cores with a sulphide rim) being produced during Stardust impacts *(Ishii et al. 2008)*. It is possible that the formation method of these GEMS-like beads is similar to that which formed the Fe-spherules in this experiment, however, a number of important differences occur in the morphology. The Stardust GEMS-like particles are fine grained, angular, with a sulphide rim *(Ishii 2019)*, whereas the particles seen here are more rounded and homogenous, and formed in an environment completely lacking in sulphur. There is also a significant difference in impact velocities between the two samples ($\approx 6\,\mathrm{km\,s^{-1}}$ for Stardust *(Ishii 2019)* and $\approx 2\,\mathrm{km\,s^{-1}}$ for the one shown here). As such, despite superficial similarities, it is likely that these metal beads are completely unrelated to

those seen in Stardust aerogels. It is also possible that the beads were produced during the shot, and were small pieces of metal collected by the projectile from the launch tube. Due to the peridot's large size, it is not as protected during launch as many other projectiles by the sabot, so it is feasible that material may have been collected on its surface. However most gun debris follows the projectile down the barrel and does not precede it and as such it is odd that the beads are found on the leading edge of the projectile. The metal beads are also Fe-rich and the majority of gun debris is produced from the cartridge ignition are is carbon rich and some carbon fragments might be expected. Overall, it is most likely that the beads are the result of the manufacturing or firing process, something which should be considered for future work.

Analysis of peridot 21-11b and 27-15b also showed a carbon rich layer between the silicon rich aerogel and the peridot (see Figure 8.17). It is likely that this was as a result of either the peridot collecting carbon rich debris from the inside of the gun during launch, which coated the peridot's surface prior to its impact into the aerogel or the resin. If the carbon is from the shot, the effect this 'carbon coating' would have had on the projectile prior to impact is negligible, however minor chemical changes may have resulted during the extreme heating during atmospheric passage and impact that would not have otherwise occurred during a direct aerogel impact. It should also be noted that in some areas the carbon is deposited on top of the aerogel layer. This is likely from the debris cloud, the cartridge and material removed from the barrel, which follows the projectile down the barrel. This can also be seen in higher concentrations on aerogel particles recovered from closer to the aperture of the EVT. However, the thickness of material seen makes it unlikely that the carbon is gun debris, as only a thin coating would be expected. As such it is most likely that it is resin which has seeped into cracks in the aerogel layer while liquid and solidified.

8.3 Comparison with Previous Experiments

Stationary pulse heating work by *Toppani et al. 2001* was able to demonstrate the formation of magnetite rims on MM simulants. This work has not been able to duplicate these results, likely due to insufficient heating of the projectile. Whilst iron metal beads along the projectile's surface were seen in TEM images, it is likely that these are as a result of the experimental setup and not rim formation. It is possible that this experiment would be able to produce magnetite rims on projectiles providing they are heated to a higher degree than those shot this programme. Stationary pulse experiments have succeeded in heating the MM analogues to above their melting temperature (e.g.



(a) (b)

Figure 8.17: TEM image of the thin section removed from a) the table of peridot 21 and b) the table of peridot 27.

see *Greshake, KLöCK, et al. 1998; Toppani et al. 2001*). Higher temperatures could be achieved by increasing the air pressure inside of the EVT, using the inlet attached for the pressure gauge.

Olivines have been previously fired into aerogel to simulate capture condition of particles on the Stardust spacecraft *(Foster et al. 2013)*. These results show negative shifts in fosterite content for impacted olivines. This work also demonstrates negative relationships between the Mg:fe ratios and impacts into aerogel. The shifts seen in this thesis are significantly reduced and not approaching the 20 units seen in previous experiments *(Foster et al. 2013)*. This is likely due to the significantly lower firing velocities of the experiment (max $2\,\mathrm{km\,s^{-1}}$ this work, versus $6.1\,\mathrm{km\,s^{-1}}$ for stardust intercept speed).

8.4 Summary

Building on the results of the previous shot program will give a wider data set for analysis, enabling patterns which have been postulated on to be confirmed. Repeats of the $2.5\ \mathrm{km\,s^{-1}}$ shots confirming the positions of the damaged projectiles would further corroborate, or disprove, the theories presented in this chapter. Additional shot velocities in the region of $1.5\ \mathrm{km\,s^{-1}}$ and $3.0\ \mathrm{km\,s^{-1}}$ would also provide indicators of trends which have been suggested but currently remain unproven.

The current shot program was limited by the maximum acceleration which could be withstood by the projectile and the minimum foil thickness able to withstand the internal pressure. Whilst the shot program described in Sections 6.2 and 8.2 show a dependency on velocity, temperature, and pressure to the foil thickness, and hence survivability of the projectile, the use of the buck shot method as described in Section 8.1.3 decouples the foil thickness from the maximum velocity. Unfortunately due to limited time and aerogel supplies this process was not able to be fully capitalised on during this project and it is possible to increase the maximum velocity which is achievable by the EVT for each pressure now based solely on the impact of the projectile with the air. As such future work will be able to significantly reduce the effects of the aerogel block by shooting at lower velocities for a similar heating effect and being able to use the maximum internal pressure of the EVT without damaging the projectile.

With the lowering of launch velocities needed to achieve melting temperatures and the successful conclusion of the previous shot program, future works are able to move onto increasingly complex projectiles. The previous shot programs have enabled us to test the constraints of the EVT, however the projectiles were simplified in an attempt to remove projectile composition effects from the results. We are now in a position to expand on these experiments, having gained an understanding of the behaviours of the EVT.

Final Conclusions and Future Work

Conclusions

This work has focused on two major elements of MM research; their collection and identification and recovering information lost during their passage through the atmosphere. This thesis has demonstrated that MM candidates, including an interesting candidate particle with a copper grain embedded reminiscent of that found by *Suttle and Genge 2017,* have been recovered from Kwajalein air samplers. This work has highlighted possible other compositional ratios for the identification of MMs from terrestrial debris. In particular, ratios of Fe:Si:Al show significant promise for the identification of CAI derived MMs, and ratios of Mg:Al:Ca are able to separate out most of those particles which are terrestrial from extra-terrestrial. The collections recovered show lower background levels of contamination than is observed in other locations, however, large numbers of terrestrial particles were still recovered making the identification of non-spherical particles unfeasible. Short term changes in the local particle flux were able to be identified on the basis of the collection of terrestrial particles from the nearby Pegasus rocket launch. Small scale changes in the E.T. flux were also seen which demonstrates the ability to time collections with astronomical events

Increasing the size of the database used for providing chemical details of the extra-terrestrial and terrestrial object would enable more detailed clusters to be produced and provide increasingly reliable statistics to claims of extra-terrestrial origin. Furthermore,

expanding upon the fly ash and volcanic groupings would enable comparisons to be made between subgroups in these data groups (i.e. comparisons between F and C type fly ash), allowing this work to be used in other fields of research.

Future work should also focus on obtaining more complete information on the collected particles; TEM work on the copper bearing candidate should be undertaken to confirm the grain is a constituent of the particle. Work should also be undertaken to confirm the E.T. origin of all candidates.

Due to the number of particles on the Kwajalein and BAS filter it was not possible to use machine learning as method of particle identification as simple shape models would have been insufficient due to particle overlap. However, following the identification of MMs from the filters during this project, it should now be possible to begin to build up a database for more complex AI selection, such as image recognition or source extraction. Continuing to identify MMs on the remaining filters and increasing the number of confirmed particles would allow computational selection to be increasing viable.

This thesis has also demonstrated the viability of LGG research into atmospheric entry effects on MMs and it has demonstrated the effectiveness of using a double sabot shot to protect olivine projectiles during flight allowing higher entry velocities into the EVT. This work has shown that surface variation trends can be seen with increasing launch speeds, with higher velocities removing more of the surface polishing marks. EDX line-scan data recovered from the fired projectile shows evidence of differing interactions between those projectiles fired into the atmosphere and those fired directly into aerogel, however, future work is required to provide details on what those reactions may be. Raman data taken from the peridots may imply shifting peak positions for the fastest shots, however, further work is required to reduce the errors so that small shifts can be identified. Finally, this work has not been able to reproduce melting effects and the formation of rims seen in previous work due to the limitations on the maximum

acceleration, and hence velocities, a projectile can survive.

Results from the EVT show further work is necessary to achieve temperatures more representative of those reached by MMs passing through the atmosphere. This aim could be achieved using a higher pressure inside of the EVT. The current EVT designs support internal pressures up to 6 atm which allow for temperatures of up to 5000 K to be achieved. Work could be carried out at facilities with larger target chambers allowing for the TOF of the projectile to be increased. This, again, would allow for higher and more representative temperatures to be reached and would provide an experimental setup closer to that experienced during atmospheric flight by the MMs.

Future work should also focus on the use of more representative projectiles. The peridot projectiles used in this thesis provided a simulant which balanced the needs of the engineering aspect and the science aspect of the project (i.e simple, but a relevant mineral). As the equipment has now been shown to work in a reproducible way, more complex MM simulants could now be used to proved more accurate test conditions.

Additional analysis of the projectiles could also be carried out. Due to time constraints, limited analysis was performed, and additional TEM analysis of the projectile would enable any crystal-to-glass transitions to be better identified. This could provide additional information on the patterns seen in the line-scan trace in Section 8.2.2.4, by providing more detailed chemical analysis at a smaller scale.

Bibliography

Ahmaruzzaman, M. (2010). "A review on the utilization of fly ash". In: *Progress in Energy and Combustion Science* 36.3, pp. 327–363. ISSN: 0360-1285. DOI: https://doi.org/10.1016/j.pecs.2009.11.003.

Anderson, William S. (Oct. 1983). *Solid Rocket Propellent Comprising Guignets Green Pigment*.

Barrett, R. A., M. E. Zolensky, and R. Bernhard (Mar. 1993). "Mineralogy of Chondritic Interplanetary Dust Particle Impact Residues from LDEF". In: *Lunar and Planetary Science Conference*. Vol. 24. Lunar and Planetary Science Conference, p. 65.

Beck, Andrew W. and Harry Y. McSween Jr. (2010). "Diogenites as polymict breccias composed of orthopyroxenite and harzburgite". In: *Meteoritics & Planetary Science* 45.5, pp. 850–872. DOI: 10.1111/j.1945-5100.2010.01061.x.

Berthoud, L. and K. Paul (1996). "Microparticle Impacts Observed on the Hubble Space Telescope Solar Array". In: *IAU Colloq. 150: Physics, Chemistry, and Dynamics of Interplanetary Dust*. Ed. by Bo A. S. Gustafson and Martha S. Hanner. Vol. 104. Astronomical Society of the Pacific Conference Series, p. 213.

Bischoff, A. and T. Geiger (Jan. 1995). "Meteorites from the Sahara: find locations, shock classification, degree of weathering and pairing." In: *Meteoritics* 30.1, pp. 113–122. DOI: 10.1111/j.1945-5100.1995.tb01219.x.

Blaha, U. et al. (Nov. 2008). "Micro-scale grain-size analysis and magnetic properties of coal-fired power plant fly ash and its relevance for environmental magnetic pollution

studies". In: *Atmospheric Environment* 42.36, pp. 8359–8370. DOI: http://dx.doi.org.lcproxy.shu.ac.uk/10.1016/j.atmosenv.2008.07.051.

Brearley, Adrian J (1989). "Nature and origin of matrix in the unique type 3 chondrite, Kakangari". In: *Geochimica et Cosmochimica Acta* 53.9, pp. 2395–2411. ISSN: 0016-7037. DOI: https://doi.org/10.1016/0016-7037(89)90361-X.

Brownlee, D. E., B. Bates, and L. Schramm (1997). "The Leonard Award Address Presented 1996 July 25, Berlin, Germany: The elemental composition of stony cosmic spherules". In: *Meteoritics and Planetary Science* 32.2, pp. 157–175.

Brownlee, D. E., M. B. Blanchard, et al. (1975). "Criteria for identification of ablation debris from primitive meteoric bodies". In: *Journal of Geophysical Research* 80.35, pp. 4917–4924. ISSN: 2156-2202. DOI: 10.1029/JB080i035p04917.

Brownlee, D. E., G. V. Ferry, and D. Tomandl (1976). "Stratospheric Aluminum Oxide". In: *Science* 191.4233, pp. 1270–1271.

Brownlee, D. E. and S. G. Love (1993). "A Direct Measurement of the Terrestrial Mass Accretion Rate of Cosmic Dust". In: *Science* 262.5133, pp. 550–553.

Brownlee, D. E., L. B. Pilachowski, and P. W. Hodge (Mar. 1979). "Meteorite Mining on the Ocean Floor". In: *Lunar and Planetary Science Conference*. Vol. 10. Lunar and Planetary Science Conference, pp. 157–158.

Brownlee, D. E., D. A. Tomandl, and E. Olszewski (1977). "Interplanetary dust - A new source of extraterrestrial material for laboratory studies". In: *Lunar and Planetary Science Conference Proceedings*. Ed. by R.B. Merril. Vol. 8. Lunar and Planetary Science Conference Proceedings, pp. 149–160.

Brownlee, D. E., P. Tsou, et al. (2003). "Stardust: Comet and interstellar dust sample return mission". In: *Journal of Geophysical Research: Planets* 108.E10. DOI: 10.1029/2003JE002087. eprint: https://agupubs.onlinelibrary.wiley.com/doi/pdf/10.1029/2003JE002087.

Brownlee, D.E., B. Bates, and R.H. Beauchamp (1983). "Meteor ablation spherules as chondrule analogs". In: *Chondrules and their Origins*. Ed. by King E.A. Provided by the SAO/NASA Astrophysics Data System, pp. 10–25.

Brownlee, D.E., E. Olszewski, and M. Wheelock (Mar. 1982). "A Working Taxonomy for Micrometeorites". In: *Lunar and Planetary Science Conference*. Vol. 13. Lunar and Planetary Science Conference. Provided by the SAO/NASA Astrophysics Data System, pp. 71–72.

Brownlee, Donald E. (2001). "Accretion of Extraterrestrial Matter Throughout Earth's History". In: The Origin and Properties of Dust Impacting the Earth, pp. 1–12.

Burchell, M. J. et al. (1999). *Hypervelocity impact studies using the 2 MV Van de Graaff accelerator and two-stage light gas gun of the University of Kent at Canterbury.*

Busemann, Henner et al. (2009). "Ultra-primitive interplanetary dust particles from the comet 26P/Grigg–Skjellerup dust stream collection". In: *Earth and Planetary Science Letters* 288.1, pp. 44–57. ISSN: 0012-821X. DOI: https://doi.org/10.1016/j.epsl.2009.09.007.

Carrillo-Sánchez, J. D., D. Nesvorný, et al. (2016). "Sources of cosmic dust in the Earth's atmosphere". In: *Geophysical Research Letters* 43.23, pp. 11, 979–11, 986. DOI: 10.1002/2016GL071697. eprint: https://agupubs.onlinelibrary.wiley.com/doi/pdf/10.1002/2016GL071697.

Carrillo-Sánchez, J. D., J. M. C. Plane, et al. (2015). "On the size and velocity distribution of cosmic dust particles entering the atmosphere". In: *Geophysical Research Letters* 42.15, pp. 6518–6525. DOI: 10.1002/2015GL065149. eprint: https://agupubs.onlinelibrary.wiley.com/doi/pdf/10.1002/2015GL065149.

Caswell, R. Douglas, Neil McBride, and Andrew Taylor (1995). "Olympus end of life anomaly — a perseid meteoroid impact event?" In: *International Journal of Impact Engineering* 17.1. Hypervelocity Impact, pp. 139–150. ISSN: 0734-743X. DOI: https://doi.org/10.1016/0734-743X(95)99843-G.

Clark, Donald (2018). *Gemstone Facets: Terminology and Functions.*

Colin, Stéphane (Feb. 2012). "Gas Microflows in the Slip Flow Regime: A Critical Review on Convective Heat Transfer". In: *Journal of Heat Transfer* 134, p. 020908. DOI: 10.1115/1.4005063.

Crozier, W. D. (1960). "Black, magnetic spherules in sediments". In: *Journal of Geophysical Research (1896-1977)* 65.9, pp. 2971–2977. DOI: 10.1029/JZ065i009p02971. eprint: https://agupubs.onlinelibrary.wiley.com/doi/pdf/10.1029/JZ065i009p02971.

Davidson, J. et al. (Mar. 2007). "Ancient Cosmic Dust from Triassic Halite". In: *38th Lunar and Planetary Science Conference*. Abstract #1545.

Dent, G. and E. Smith (2004). *Modern Raman Spectroscopy – A Practical Approach*. 1st ed. John Wiley and Sons ltd. ISBN: ISBN-13 978-0-471-19794-3.

Díaz-Hernández, José L. and Jesús Párraga (2008). "The nature and tropospheric formation of iberulites: Pinkish mineral microspherulites". In: *Geochimica et Cosmochimica Acta* 72.15, pp. 3883–3906. ISSN: 0016-7037. DOI: https://doi.org/10.1016/j.gca.2008.05.037.

Dobrică, E. et al. (Jan. 2012). "Transmission Electron Microscopy of CONCORDIA UltraCarbonaceous Antarctic MicroMeteorites (UCAMMs): Mineralogical properties". In: *Geochimica et Cosmochimica Acta* 76, pp. 68–82.

Dobrica., E. et al. (Mar. 2009). "Immature Carbonaceous Matter in CONCORDIA Antarctic Micrometeorites". In: *Lunar and Planetary Science Conference*. Vol. 40. Lunar and Planetary Science Conference. Provided by the SAO/NASA Astrophysics Data System, p. 1688.

Dobrica,, E. et al. (2011). "Raman characterization of carbonaceous matter in CONCORDIA Antarctic micrometeorites". In: *Meteoritics & Planetary Science* 46.9, pp. 1363–1375.

Doolan, Con (Mar. 2018). "A two-stage light gas gun for the study of high speed impact in propellants". In:

Dunne, Mike (2006). "Laser-Driven Particle Accelerators". In: *Science* 312.5772, pp. 374–376. ISSN: 0036-8075. DOI: 10.1126/science.1126051. eprint: https://science.sciencemag.org/content/312/5772/374.full.pdf.

Duprat, J., E. Dobrică, et al. (2010). "Extreme Deuterium Excesses in Ultracarbonaceous Micrometeorites from Central Antarctic Snow". In: *Science* 328.5979, pp. 742–

745. ISSN: 0036-8075. DOI: 10.1126/science.1184832. eprint: http://science.sciencemag.org/content/328/5979/742.full.pdf.

Duprat, J., C. Engrand, et al. (2007). "Micrometeorites from Central Antarctic snow: The CONCORDIA collection". In: *Advances in Space Research* 39.4, pp. 605–611.

Edmund Optics Worldwide (2018). *Understanding Microscopes and Objectives*.

EM Resolutions LTD (2014). *EM Tungsten Filaments and LaB6 cathodes*.

Engrand, C., M. Maurette, et al. (Mar. 1995). "Electron Microprobe Analyses of Antarctic Micrometeorites and Interplanetary Dust Particles Collected in the Stratosphere". In: *Lunar and Planetary Science Conference*. Vol. 26. Lunar and Planetary Inst. Technical Report.

Engrand, Cecile and Michel Maurette (1998). "Carbonaceous micrometeorites from Antarctica". In: *Meteoritics and Planetary Science* 33.4, pp. 565–580. DOI: 10.1111/j.1945-5100.1998.tb01665.x.

Flanagan, V.P.V. and P. Tayler (1967). "Tables of aerosol physics functions: Mobility and falling speed of spheres". In: *Atmospheric Environment (1967)* 1.3, pp. 327–340. ISSN: 0004-6981. DOI: https://doi.org/10.1016/0004-6981(67)90013-3.

Flynn, G. J. (2002). "Extraterrestrial Dust in the Near-Earth Environment". In: *Meteors in the Earth's Atmosphere*. Ed. by E. Murad and I. P. Williams, p. 77.

— (1989). "Atmospheric entry heating: A criterion to distinguish between asteroidal and cometary sources of interplanetary dust". In: *Icarus* 77.2, pp. 287–310. ISSN: 0019-1035. DOI: https://doi.org/10.1016/0019-1035(89)90091-2.

Flynn, George J. (1994). "Interplanetary dust particles collected from the stratosphere: physical, chemical, and mineralogical properties and implications for their sources". In: *Planetary and Space Science* 42.12, pp. 1151–1161. ISSN: 0032-0633. DOI: https://doi.org/10.1016/0032-0633(94)90014-0.

Foster, N.F. et al. (2013). "Identification by Raman spectroscopy of Mg–Fe content of olivine samples after impact at 6kms-1 onto aluminium foil and aerogel: In the laboratory and in Wild-2 cometary samples". In: *Geochimica et Cosmochimica Acta*

121, pp. 1–14. ISSN: 0016-7037. DOI: https://doi.org/10.1016/j.gca.2013.07.022.

Frimmel, F. H. (2007). *Colloidal transport in porous media*. Berlin New York: Springer. ISBN: 3540713387.

Gasso, S. et al. (2010). "A combined observational and modeling approach to study modern dust transport from the Patagonia desert to East Antarctica". In: *Atmospheric Chemistry and Physics* 10.17, pp. 8287–8303. DOI: 10.5194/acp-10-8287-2010.

Genareau, Kimberly et al. (Apr. 2015). "Lightning-induced volcanic spherules". In: *Geology* 43.4, pp. 319–322. ISSN: 0091-7613. DOI: 10.1130/G36255.1. eprint: https://pubs.geoscienceworld.org/geology/article-pdf/43/4/319/3548177/319.pdf.

Genge, M. J., C. Engrand, et al. (2008). "The classification of micrometeorites". In: *Meteoritics and Planetary Science* 43.3, pp. 497–515.

Genge, M. J., A. Gileski, and M. M. Grady (2005). "Chondrules in Antarctic micrometeorites". In: *Meteoritics and Planetary Science* 40.2, pp. 225–238.

Genge, M.J., J. Larsen, et al. (Feb. 2017). "An urban collection of modern-day large micrometeorites: Evidence for variations in the extraterrestrial dust flux through the Quaternary". In: *Geology* 45.2, pp. 119–122. ISSN: 0091-7613. DOI: 10.1130/G38352.1. eprint: https://pubs.geoscienceworld.org/geology/article-pdf/45/2/119/3549942/119.pdf.

Genge, Matthew J. (May 2006). "Igneous rims on micrometeorites". In: *Geochimica et Cosmochimica Acta* 70.10, pp. 2603–2621.

— (June 2008). "Micrometeorites and Their Implications for Meteors". In: *Earth, Moon, and Planets* 102.1. ID: Genge2008, pp. 525–535. DOI: 10.1007/s11038-007-9185-z.

— (2017). "An increased abundance of micrometeorites on Earth owing to vesicular parachutes". In: *Geophysical Research Letters* 44.4, pp. 1679–1686. DOI: 10.1002/2016GL072490. eprint: https://agupubs.onlinelibrary.wiley.com/doi/pdf/10.1002/2016GL072490.

Genge, Matthew J., Matthias van Ginneken, et al. (2018). "Accumulation mechanisms of micrometeorites in an ancient supraglacial moraine at Larkman Nunatak, Antarc-

tica". In: *Meteoritics & Planetary Science* 53.10, pp. 2051–2066. DOI: 10.1111/maps.13107. eprint: https://onlinelibrary.wiley.com/doi/pdf/10.1111/maps.13107.

Genge, Matthew J. and Monica M. Grady (1998). "Melted micrometeorites from Antarctic ice with evidence for the separation of immiscible Fe-Ni-S liquids during entry heating". In: *Meteoritics & Planetary Science* 33.3, pp. 425–434. DOI: 10.1111/j.1945-5100.1998.tb01647.x. eprint: https://onlinelibrary.wiley.com/doi/pdf/10.1111/j.1945-5100.1998.tb01647.x.

Genge, Matthew J., Monica M. Grady, and Robert Hutchison (Dec. 1997). "The textures and compositions of fine-grained Antarctic micrometeorites: Implications for comparisons with meteorites". In: *Geochimica et Cosmochimica Acta* 61.23, pp. 5149–5162.

Genge, Matthew J., Martin Suttle, and Matthias Van Ginneken (Oct. 2016). "Olivine settling in cosmic spherules during atmospheric deceleration: An indicator of the orbital eccentricity of interplanetary dust". In: *Geophysical Research Letters* 43.20. ISSN: 1944-8007. DOI: 10.1002/2016GL070874.

Genge, MJ and Monica Grady (2002). "The distribution of asteroids: evidence from Antarctic micrometeorites". In:

Ginneken, M. van, J. Gattacceca, et al. (2017). "The parent body controls on cosmic spherule texture: Evidence from the oxygen isotopic compositions of large micrometeorites". In: *Geochimica et Cosmochimica Acta* 212, pp. 196–210. ISSN: 0016-7037. DOI: https://doi.org/10.1016/j.gca.2017.05.008.

Ginneken, Matthias van, Matthew J. Genge, et al. (15 April 2016 2016). *The weathering of micrometeorites from the Transantarctic Mountains*. ID: 271865. DOI: http://dx.doi.org.chain.kent.ac.uk/10.1016/j.gca.2015.11.045.

Goodarzi, Fariborz (2006). "Characteristics and composition of fly ash from Canadian coal-fired power plants". In: *Fuel* 85.10–11, pp. 1418–1427. DOI: http://dx.doi.org.lcproxy.shu.ac.uk/10.1016/j.fuel.2005.11.022.

Goodrich, Cyrena Anne et al. (15 February 2001 2001). *Primary trapped melt inclusions in olivine in the olivine-augite-orthopyroxene ureilite Hughes 009*. ID: 271865. DOI: https://doi.org/10.1016/S0016-7037(00)00521-4.

Gounelle, Matthieu, Marc Chaussidon, et al. (2009). "A unique basaltic micrometeorite expands the inventory of solar system planetary crusts". In: *Proceedings of the National Academy of Sciences* 106.17, pp. 6904–6909. ISSN: 0027-8424. DOI: 10.1073/pnas.0900328106. eprint: https://www.pnas.org/content/106/17/6904.full.pdf.

Gounelle, Matthieu, Cécile Engrand, et al. (2005). "Small Antarctic micrometeorites: A mineralogical and in situ oxygen isotope study". In: *Meteoritics & Planetary Science* 40.6, pp. 917–932. ISSN: 1945-5100. DOI: 10.1111/j.1945-5100.2005.tb00163.x.

Greshake, Ansgar, Adolf Bischoff, and Peter Hoppe (1996). "Mineralogy, chemistry, and oxygen isotopes of refractory inclusions from stratospheric interplanetary dust particles and micrometeorites". In: *Meteoritics and Planetary Science* 31.6, pp. 739–748. DOI: 10.1111/j.1945-5100.1996.tb02109.x.

Greshake, Ansgar, WOLFGANG KLöCK, et al. (1998). "Heating experiments simulating atmospheric entry heating of micrometeorites: Clues to their parent body sources". In: *Meteoritics and Planetary Science* 33.2, pp. 267–290.

Haack, H. and T.J. McCoy (1998). "Iron and Stony-iron Meteorites." In: ed. by J. J. Papike. 1st ed. Vol. 36. Planetary Materials. Mineralogical Society of America, pp. 1.325–1.341.

Haack, Henning, K. Keil, et al. (Jan. 1996). "Meteoritic Constraints on the 500 MA Disruption of the L Chondrite Parent Body". In: *Lunar Planet. Sci* 25.

Hall, C.A. et al. (2001). "High velocity flyer plate launch capability on the Sandia Z accelerator". In: *International Journal of Impact Engineering* 26.1, pp. 275–287. ISSN: 0734-743X. DOI: https://doi.org/10.1016/S0734-743X(01)00088-4.

Hamilton, J. et al. (2017). "Development of the Space Debris Sensor (SDS)". In: 7.

Harriss, Kathryn H. and M. J. Burchell (2016). "A study of the observed shift in the peak position of olivine Raman spectra as a result of shock induced by hypervelocity

impacts". In: *Meteoritics & Planetary Science* 51.7, pp. 1289–1300. DOI: 10.1111/maps.12660. eprint: https://onlinelibrary.wiley.com/doi/pdf/10.1111/maps.12660.

Harvey, R. P. and M. Maurette (Jan. 1991). "The origin and significance of cosmic dust from the Walcott Névé, Antarctica." In: *Lunar and Planetary Science Conference Proceedings* 21, pp. 569–578.

Heiken, G. (1972). "Morphology and Petrography of Volcanic Ashes". In: *Geological Society of America Bulletin* 83, p. 1961. DOI: 10.1130/0016-7606(1972)83[1961:MAPOVA]2.0.CO;2.

Hibbert, R. et al. (2017). "The Hypervelocity Impact Facility at the University of Kent: Recent Upgrades and Specialized Capabilities." In: *Procedia Engineering* 204. 14th Hypervelocity Impact Symposium 2017, HVIS2017, 24-28 April 2017, Canterbury, Kent, UK, pp. 208–214. ISSN: 1877-7058. DOI: https://doi.org/10.1016/j.proeng.2017.09.775.

Hodges, A. J. (1957). "The Drag Coefficient of Very High Velocity Spheres". In: *Journal of the Aeronautical Sciences* 24.10, pp. 755–758. DOI: 10.2514/8.3958.

Hoerz, Friedrich et al. (Sept. 1999). "Optical Analysis of Impact Features in Aerogel From the Orbital Debris Collection Experiment on the MIR Station". In:

Holmes, N. C. et al. (1984). "Silica at ultrahigh temperature and expanded volume". In: *Applied Physics Letters* 45.6, pp. 626–628. DOI: 10.1063/1.95334. eprint: https://doi.org/10.1063/1.95334.

Hörz, F. et al. (1991). "Preliminary Analysis of LDEF Instrument AO187-1 "chemistry of Micrometeoroids Experiment"". In: *LDEF, 69 months in space : first post-retrieval symposium*. Ed. by A. S. Levine. Vol. 3134. NASA Conference Publication, p. 487.

Huang, XiaoGe et al. (Mar. 2016). "Hugoniot equation of state of olivine and its geodynamic implications". In: *Science China Earth Sciences* 59.3, pp. 619–625. ISSN: 1869-1897. DOI: 10.1007/s11430-015-5231-2.

Inc., SIVUNIQ (2010). *2010 Work Plan Site Investigation of Nine Sites at the U.S. Army Kwajalein Atoll/Reagan Test Site (USAKA/RTS) Republic of Marshall Islands*.

Inoue, Jun et al. (2014). "Chemical characteristics of Northeast Asian fly ash particles: Implications for their long-range transportation". In: *Atmospheric Environment* 95, pp. 375–382. ISSN: 1352-2310. DOI: https://doi.org/10.1016/j.atmosenv.2014.06.048.

Ishii, Hope A. (2019). "Comparison of GEMS in interplanetary dust particles and GEMS-like objects in a Stardust impact track in aerogel". In: *Meteoritics & Planetary Science* 54.1, pp. 202–219. DOI: 10.1111/maps.13182. eprint: https://onlinelibrary.wiley.com/doi/pdf/10.1111/maps.13182.

Ishii, Hope A. et al. (2008). "Comparison of Comet 81P/Wild 2 Dust with Interplanetary Dust from Comets". In: *Science* 319.5862, pp. 447–450. ISSN: 0036-8075. DOI: 10.1126/science.1150683. eprint: https://science.sciencemag.org/content/319/5862/447.full.pdf.

Kallemeyn, Gregory W. and John T. Wasson (1986). "Compositions of enstatite (EH3, EH4,5 and EL6) chondrites: Implications regarding their formation". In: *Geochimica et Cosmochimica Acta* 50.10, pp. 2153–2164. ISSN: 0016-7037. DOI: https://doi.org/10.1016/0016-7037(86)90070-0.

Kasten, Fritz (1968). "Falling Speed of Aerosol Particles". In: *Journal of Applied Meteorology* 7.5, pp. 944–947. DOI: 10.1175/1520-0450(1968)007<0944:FSOAP>2.0.CO;2. eprint: https://doi.org/10.1175/1520-0450(1968)007<0944:FSOAP>2.0.CO;2.

Keil, Klaus (Sept. 2012). "Angrites, a small but diverse suite of ancient, silica-undersaturated volcanic-plutonic mafic meteorites, and the history of their parent asteroid". In: *Chemie der Erde - Geochemistry* 72.3, pp. 191–218. DOI: http://dx.doi.org.chain.kent.ac.uk/10.1016/j.chemer.2012.06.002.

— (Oct. 2014). "Brachinite meteorites: Partial melt residues from an FeO-rich asteroid". In: *Chemie der Erde - Geochemistry* 74.3, pp. 311–329. DOI: https://doi-org.chain.kent.ac.uk/10.1016/j.chemer.2014.02.001.

Keil, Klaus et al. (2011). "A composite Fe,Ni-FeS and enstatite-forsterite-diopside-glass vitrophyre clast in the Larkman Nunatak 04316 aubrite: Origin by pyroclastic vol-

canism". In: *Meteoritics & Planetary Science* 46.11, pp. 1719–1741. DOI: 10.1111/j.1945-5100.2011.01261.x.

Klein Cornelis Hurlbut, Cornelius Jr. (1985). *Manual of Mineralogy*. Vol. 20th Edition. John Wiley and Sons ltd. ISBN: 978-0-471-80580-9.

Klöck, W. and F. J. Stadermann (1994). "Mineralogical and chemical relationships of interplanetary dust particles, micrometeorites, and meteorites". In: *AIP Conference Proceedings* 310.1, pp. 51–88.

Korotev, Randy L. (2005). "Lunar geochemistry as told by lunar meteorites". In: *Geochemistry* 65.4, pp. 297–346. ISSN: 0009-2819. DOI: https://doi.org/10.1016/j.chemer.2005.07.001.

Krot, Alexander N. et al. (Sept. 2004). "Amoeboid olivine aggregates and related objects in carbonaceous chondrites: records of nebular and asteroid processes". In: *Chemie der Erde - Geochemistry* 64.3, pp. 185–239. DOI: http://dx.doi.org/10.1016/j.chemer.2004.05.001.

Kukkonen, J., T. Vesala, and M. Kulmala (1989). "The interdependence of evaporation and settling for airborne freely falling droplets". In: *Journal of Aerosol Science* 20.7, pp. 749–763. ISSN: 0021-8502. DOI: https://doi.org/10.1016/0021-8502(89)90087-6.

Kurat, G. et al. (Sept. 1994). "Petrology and geochemistry of Antarctic micrometeorites". In: *Geochimica et Cosmochimica Acta* 58, pp. 3879–3904. DOI: 10.1016/0016-7037(94)90369-7.

Langway, Chester C. and Ursula B. Marvin (Nov. 1965). "Some Characteristics of Black Spherules". In: *Annals of the New York Academy of Sciences* 119.1, pp. 205–223. DOI: 10.1111/j.1749-6632.1965.tb47434.x.

Larkin, Peter (2018). *Infrared and Raman Spectroscopy : Principles and Spectral Interpretation*. English. Vol. Second edition. ID: Accession Number: 1543583. Amsterdam: Elsevier. ISBN: 9780128041628; 9780128042090.

Larson, Jon. (2017). *In Search of Stardust: Amazing Micrometeorites and Their Terrestrial Imposters*. Vol. 1st edition. Quarto Publishing Group. ISBN: 978-0-7603-5264-9.

Love, S. G. and D. E. Brownlee (Jan. 1991). "Heating and thermal transformation of micrometeoroids entering the earth's atmosphere". In: *Icarus* 89, pp. 26–43. DOI: 10.1016/0019-1035(91)90085-8.

— (1993). "A Direct Measurement of the Terrestrial Mass Accretion Rate of Cosmic Dust". In: *Science* 262.5133, pp. 550–553.

MacPherson, G. J. et al. (Dec. 2005). "Calcium-Aluminum-rich Inclusions: Major Unanswered Questions". In: *Chondrites and the Protoplanetary Disk*. Ed. by A. N. Krot, E. R. D. Scott, and B. Reipurth. Vol. 341. Astronomical Society of the Pacific Conference Series, p. 225.

Maurette, M., C. Hammer, D. E. Brownlee, et al. (1986). "Placers of Cosmic Dust in the Blue Ice Lakes of Greenland". In: *Science* 233.4766, pp. 869–872.

Maurette, M., C. Hammer, R. Harvey, et al. (1994). "Collection and curation of IDPs in the stratosphere and below. Part 2: The Greenland and Antarctic ice sheets". In: *Analysis of Interplanetary Dust Particles*. Ed. by M.E. Zolensky, pp. 36–40.

Maurette, M., C. Olinger, et al. (May 1991). "A collection of diverse micrometeorites recovered from 100 tonnes of Antarctic blue ice". In: *Nature* 351.6321. 10.1038/351044a0, pp. 44–47.

McDonnell, J. A. M. (Mar. 1991). "Space Debris: Orbital Microparticulates Impacting LDEF Experiments Favour a Natural Extraterrestrial Origin". In: *Lunar and Planetary Science Conference*. Vol. 22. Lunar and Planetary Science Conference.

McDonnell, J.A.M. et al. (1991). "First results of particulate impacts and foil perforations on LDEF". In: *Advances in Space Research* 11.12, pp. 109–114. ISSN: 0273-1177. DOI: https://doi.org/10.1016/0273-1177(91)90551-T.

McSween, H. Y. (1987). *Meteorites and their parent planets*.

Meeker, Gregory P. and Todd K. Hinkley (Aug. 1993). "The structure and composition of microspheres from the Kilauea Volcano, Hawaii". In: *American Mineralogist* 78.7-8, pp. 873–876. ISSN: 0003-004X. eprint: https://pubs.geoscienceworld.org/ammin/article-pdf/78/7-8/873/4218351/am78_873.pdf.

Melosh, Jay (Feb. 1989). "Impact Cratering: A Geologic Process". In: 11.

Messenger, Scott (2002). "Opportunities for the stratospheric collection of dust from short-period comets". In: *Meteoritics & Planetary Science* 37.11, pp. 1491–1505.

Messenger, Scott et al. (2015). "Pristine stratospheric collection of interplanetary dust on an oil-free polyurethane foam substrate". In: *Meteoritics & Planetary Science* 50.8, pp. 1468–1485.

Millard, H. T. and R. B. Finkelman (1970). "Chemical and mineralogical compositions of cosmic and terrestrial spherules from a marine sediment". In: *Journal of Geophysical Research* 75.11, pp. 2125–2134. ISSN: 2156-2202. DOI: 10.1029/JB075i011p02125.

Mindat.org (2019). *Antimony*. URL: https://www.mindat.org/min-262.html#autoanchor19 (visited on 03/22/2019).

Mittlefehldt, D. W., T. J. McCoy, and C. A. Goodrich (1998). "Non-chondritic meteorites from asteroidal bodies." In: ed. by J. J. Papike. 1st ed. Vol. 36. Planetary Materials. Mineralogical Society of America, pp. 4.1–4.495.

Mittlefehldt, David W., Marvin Killgore, and Michael T. Lee (2002). "Petrology and geochemistry of D'Orbigny, geochemistry of Sahara 99555, and the origin of angrites". In: *Meteoritics & Planetary Science* 37.3, pp. 345–369. DOI: 10.1111/j.1945-5100.2002.tb00821.x.

Mittlefehldt, David W. and Marilyn M. Lindstrom (May 2003). "Geochemistry of eucrites: genesis of basaltic eucrites, and Hf and Ta as petrogenetic indicators for altered antarctic eucrites". In: *Geochimica et Cosmochimica Acta* 67.10, pp. 1911–1934. DOI: http://dx.doi.org.chain.kent.ac.uk/10.1016/S0016-7037(02)01411-4.

Mouri, Takashi and Masaki Enami (2008). "Raman spectroscopic study of olivine-group minerals". In: *Journal of Mineralogical and Petrological Sciences* 103.2, pp. 100–104. DOI: 10.2465/jmps.071015.

Murr, Lawrence E. and William H. Kinard (1993). "Effects of Low Earth Orbit". In: *American Scientist* 81.2, pp. 152–165.

Murray, John and A. F. Renard (1891). "Manganese deposits from the HMS Challenger stations, supplement to: Murray, John; Renard, A F (1891): Deep-sea deposits (based on the specimens collected during the voyage of HMS Challenger in the years 1872

to 1876). Report on the scientific results of the voyage of H.M.S. Challenger during the years 1873-76; John Menzies and Co., Endinburgh, United Kingdom;" in:

Nakamura, T. et al. (Mar. 1999). "Antarctic micrometeorites collected at the Dome Fuji Station". In: *Antarctic Meteorite Research* 12. Provided by the SAO/NASA Astrophysics Data System, p. 183.

Neff, Peter D. and Nancy A. N. Bertler (2015). "Trajectory modeling of modern dust transport to the Southern Ocean and Antarctica". In: *Journal of Geophysical Research: Atmospheres* 120.18, pp. 9303–9322. DOI: 10.1002/2015JD023304. eprint: https://agupubs.onlinelibrary.wiley.com/doi/pdf/10.1002/2015JD023304.

Nesvorný, David et al. (Mar. 2010). "Cometary Origin of the Zodiacal Cloud and Carbonaceous Micrometeorites. Implications for Hot Debris Disks". In: *The Astrophysical Journal* 713, p. 816. DOI: 10.1088/0004-637X/713/2/816.

Newbury, Dale E. and Nicholas W. M. Ritchie (2013). "Is Scanning Electron Microscopy/Energy Dispersive X-ray Spectrometry (SEM/EDS) Quantitative?" In: *Scanning* 35.3, pp. 141–168. DOI: 10.1002/sca.21041. eprint: https://onlinelibrary.wiley.com/doi/pdf/10.1002/sca.21041.

Noguchi, Takaaki et al. (Jan. 2015). "Cometary dust in Antarctic ice and snow: Past and present chondritic porous micrometeorites preserved on the Earth's surface". In: *Earth and Planetary Science Letters* 410, pp. 1–11.

O'Brien, W. J. (1915). "A Study of Lithopone". In: *The Journal of Physical Chemistry* 19.2, pp. 113–144. DOI: 10.1021/j150155a002.

Office, NASA Public Affairs (2019a). *About NuSTar*. URL: https://heasarc.gsfc.nasa.gov/docs/nustar/nustar_about.html (visited on 02/22/2019).

— (2019b). *Pegasus: Countdown 101*. URL: https://www.nasa.gov/mission_pages/st-5/launch/pegasus-101.html (visited on 02/22/2019).

Office, USASMDC Public Affairs (2019c). *Missile Launch Facilities*. URL: http://www.smdc.army.mil/KWAJ/LaunchFacility.html (visited on 02/22/2019).

Oliver, John P. et al. (1994). "Long duration exposure facility (LDEF) interplanetary dust experiment (IDE) impact detector results". In: *Proc.SPIE* 2214, pp. 76–84.

Olivine Mineral Data (2018). URL: http://www.webmineral.com/data/Olivine.shtml#.WzzUbqdKiUk (visited on 07/04/2018).

Pape, J. et al. (2019). "Time and duration of chondrule formation: Constraints from 26Al-26Mg ages of individual chondrules". In: *Geochimica et Cosmochimica Acta* 244, pp. 416–436. ISSN: 0016-7037. DOI: https://doi.org/10.1016/j.gca.2018.10.017.

Parnell, John, Natalie Salter, and Peter West (June 2016). "A micrometeorite record in Ordovician Durness Group limestones, Isle of Skye". In: *Earth and Environmental Science Transactions of the Royal Society of Edinburgh* 106.2, pp. 81–87. DOI: 10.1017/S1755691016000037".

Pedersen, Søren Grube et al. (2019). "Testing accretion mechanisms of the H chondrite parent body utilizing nucleosynthetic anomalies". In: *Meteoritics & Planetary Science* 54.6, pp. 1215–1227. DOI: 10.1111/maps.13269. eprint: https://onlinelibrary.wiley.com/doi/pdf/10.1111/maps.13269.

Peng, H. and Z. Lui (1989). "Measurement of the Annual Flux of Cosmic Dust in Deep-Sea Sediments". In: *52nd Annual Meeting of the Meteoritical Society*. Vol. 712. LPI Contributions, p. 194.

Piekutowski, A.J. and K.L. Poormon (2006). "Development of a three-stage, light-gas gun at the University of Dayton Research Institute". In: *International Journal of Impact Engineering* 33.1. Hypervelocity Impact Proceedings of the 2005 Symposium, pp. 615–624. ISSN: 0734-743X. DOI: https://doi.org/10.1016/j.ijimpeng.2006.09.018.

Plane, John M. C. (2003). "Atmospheric Chemistry of Meteoric Metals". In: *Chemical Reviews* 103.12. PMID: 14664639, pp. 4963–4984. DOI: 10.1021/cr0205309. eprint: https://doi.org/10.1021/cr0205309.

— (2012). "Cosmic dust in the earth's atmosphere". In: *Chem. Soc. Rev.* 41 (19), pp. 6507–6518. DOI: 10.1039/C2CS35132C.

Prasad, M. Shyam, N. G. Rudraswami, and Dipak K. Panda (2013). "Micrometeorite flux on Earth during the last 50,000 years". In: *Journal of Geophysical Research:*

Planets 118.11. 2013JE004460, pp. 2381–2399. ISSN: 2169-9100. DOI: 10.1002/2013JE004460.

Prasad, MS (Jan. 2013). "Chondrule-like object from the Indian Ocean cosmic spherules". In: *Journal of Earth System Science* 122, p. 1161.

Reddy, K. P. J. et al. (2015). "Reddy Tube Driven Table-Top Hypersonic Shock Tunnel". In: *29th International Symposium on Shock Waves 1*. Ed. by Riccardo Bonazza and Devesh Ranjan. Cham: Springer International Publishing, pp. 403–408. ISBN: 978-3-319-16835-7.

Reed, S. J. B. (25 2008). "Scanning electron microscopy". In: Electron Microprobe Analysis and Scanning Electron Microscopy in Geology: Cambridge: Cambridge University Press, pp. 41–75. DOI: 10.1017/CBO9780511610561.005.

Rehren, Thilo et al. (Dec. 2013). *5,000 years old Egyptian iron beads made from hammered meteoritic iron*. ID: 272428. DOI: https://doi.org/10.1016/j.jas.2013.06.002.

Rochette, P. et al. (2008). "Micrometeorites from the Transantarctic Mountains". In: *Proceedings of the National Academy of Sciences of the United States of America* 105.47, pp. 18206–18211.

Rout, Surya Snata, Klaus Keil, and Addi Bischoff (Mar. 2010). "Bulk chemical compositions of Al-rich objects from Rumuruti (R) chondrites: Implications for their origin". In: *Chemie der Erde - Geochemistry* 70.1, pp. 35–53. DOI: http://dx.doi.org/10.1016/j.chemer.2009.10.002.

Rudraswami, N. G. et al. (Dec. 2016). "Ablation and Chemical Alteration of Cosmic Dust Particles during Entry into the Earth's Atmosphere". In: *Astrophysical Journal Supplement* 227, 15, p. 15. DOI: 10.3847/0067-0049/227/2/15.

Rynearson, R. J. and J. L. Rand (Sept. 1972). *Optimization of a two stage light gas gun. M.S. Thesis*. Texas A&M Univ.

Sarkar, A. et al. (Feb. 2006). "A comprehensive characterisation of fly ash from a thermal power plant in Eastern India". In: *Fuel Processing Technology* 87.3, pp. 259–277. DOI: http://dx.doi.org.lcproxy.shu.ac.uk/10.1016/j.fuproc.2005.09.005.

Scanning Electron Microscope: Training Module (15/04/2014 2014).

Schmitz, Birger, Mario Tassinari, and Bernhard Peucker-Ehrenbrink (2001). "A rain of ordinary chondritic meteorites in the early Ordovician". In: *Earth and Planetary Science Letters* 194.1, pp. 1–15. ISSN: 0012-821X. DOI: https://doi.org/10.1016/S0012-821X(01)00559-3.

Semrock Inc (2019). *Filter Types for Raman Spectroscopy Applications*. URL: https://www.semrock.com/filter-types-for-raman-spectroscopy-applications.aspx (visited on 02/25/2019).

Singerling, Sheryl A., Harry Y. McSween, and Larry A. Taylor (2013). "Glasses in howardites: Impact melts or pyroclasts?" In: *Meteoritics & Planetary Science* 48.5, pp. 715–729. DOI: 10.1111/maps.12099.

Suavet, C., J. Gattacceca, et al. (2009). "Magnetic properties of micrometeorites". In: *Journal of Geophysical Research : Solid Earth* 114, B04102. DOI: 10.1029/2008JB005831.

Suavet, Clément, Pierre Rochette, et al. (2009). "Statistical properties of the Transantarctic Mountains (TAM) micrometeorite collection". In: *Polar Science* 3.2, pp. 100–109. ISSN: 1873-9652. DOI: https://doi.org/10.1016/j.polar.2009.06.003.

Suttle, M. D., K. Twegar, et al. (Aug. 2019). "A unique CO-like micrometeorite hosting an exotic Al-Cu-Fe-bearing assemblage – close affinities with the Khatyrka meteorite". In: *Scientific Reports* 9.1. ID: Suttle2019, p. 12426. DOI: 10.1038/s41598-019-48937-0.

Suttle, Martin D. and Matthew J. Genge (2017). "Diagenetically altered fossil micrometeorites suggest cosmic dust is common in the geological record". In: *Earth and Planetary Science Letters* 476, pp. 132–142. ISSN: 0012-821X. DOI: https://doi.org/10.1016/j.epsl.2017.07.052.

T, Kyte F (Jan 1983). "Analyses of Extraterrestrial Materials in Terrestrial Sediments". PhD thesis.

Talyor, Susan, Graciela Matrajt, and Yunbin Guan (2012). "Fine-grained precursors dominate the micrometeorite flux". In: *Meteoritics and Planetary Science* 47.4, pp. 550–564.

Taylor, S., C.M.O. Alexander, and S. Wengert (Mar. 2008). "Rare Micrometeorites from the South Pole, Antarctica". In: 39. Provided by the SAO/NASA Astrophysics Data System, p. 1628.

Taylor, S. and D. E. Brownlee (Sept. 1991). "Cosmic spherules in the geologic record". In: *Meteoritics* 26, pp. 203–211.

Taylor, S., J.H. Lever, and J. Govoni (Mar. 2001). "A Second Collection of Micrometeorites from the South Pole Water Well". In: *Lunar and Planetary Science Conference*. Vol. 32. Lunar and Planetary Science Conference. Provided by the SAO/NASA Astrophysics Data System.

Taylor, S., G. Matrajt, et al. (Jan. 2007). "Size Distribution of Antarctic Micrometeorites". In: *Dust in Planetary Systems*. Ed. by H. Krueger and A. Graps. Vol. 643, pp. 145–148.

Taylor, Susan, Gregory F. Herzog, and Jeremy S. Delaney (Jan. 2007). "Crumbs from the crust of Vesta: Achondritic cosmic spherules from the South Pole water well". In: *Meteoritics and Planetary Science* 42.2, pp. 223–233. DOI: 10.1111/j.1945-5100.2007.tb00229.x.

Taylor, Susan, James H. Lever, and Ralph P. Harvey (Apr. 1998). "Accretion rate of cosmic spherules measured at the South Pole. (Cover story)". In: *Nature* 392.6679, p. 899.

— (2000). "Numbers, types, and compositions of an unbiased collection of cosmic spherules". In: *Meteoritics and Planetary Science* 35.4, pp. 651–666.

Taylor, Susan, James H. Lever, Ralph P. Harvey, and John Govoni (1997). "Collecting Micrometeorites from the South Pole Water Well". In: DIANE Publishing. ISBN: 9781428913219.

The Natural History Museum (2002). *The Meteorite Catalogue Database at the Natural History Museum.*

Thermo Fisher Scientific (2019). *SEM and TEM: what's the differnce?* URL: https://blog.phenom-world.com/sem-tem-difference (visited on 03/10/2019).

Tomkins, Andrew G. et al. (May 2016). "Ancient micrometeorites suggestive of an oxygen-rich Archaean upper atmosphere". In: *Nature* 533, p. 235.

Toppani, Alice et al. (2001). "Experimental simulation of atmospheric entry of micrometeorites". In: *Meteoritics and Planetary Science* 36.10, pp. 1377–1396. ISSN: 1945-5100. DOI: 10.1111/j.1945-5100.2001.tb01831.x.

Tupper, Andrew et al. (2004). "An evaluation of volcanic cloud detection techniques during recent significant eruptions in the western 'Ring of Fire'". In: *Remote Sensing of Environment* 91.1, pp. 27–46. ISSN: 0034-4257. DOI: https://doi.org/10.1016/j.rse.2004.02.004.

Van Ginneken, Matthias et al. (2012). "Chondritic micrometeorites from the Transantarctic Mountains". In: *Meteoritics & Planetary Science* 47.2, pp. 228–247. ISSN: 1945-5100. DOI: 10.1111/j.1945-5100.2011.01322.x.

Velbel, Michael A., Eric K. Tonui, and Michael E. Zolensky (2012). "Replacement of olivine by serpentine in the carbonaceous chondrite Nogoya (CM2)". In: *Geochimica et Cosmochimica Acta* 87, pp. 117–135. ISSN: 0016-7037. DOI: https://doi.org/10.1016/j.gca.2012.03.016.

Vernazza, Pierre et al. (2015). "The Formation and Evolution of Ordinary Chondrite Parent Bodies". In: ed. by Patrick Michel. Asteroids IV. The University of Arizona Press, p. 617.

Volkert, C. A. and A. M. Minor (2007). "Focused Ion Beam Microscopy and Micromachining". In: *MRS Bulletin* 32.5, pp. 389–399. DOI: 10.1557/mrs2007.62.

Ward, Colin R. and David French (Nov. 2006). "Determination of glass content and estimation of glass composition in fly ash using quantitative X-ray diffractometry". In: *Fuel* 85.16, pp. 2268–2277. DOI: http://dx.doi.org.lcproxy.shu.ac.uk/10.1016/j.fuel.2005.12.026.

Warren, Paul H. (Nov. 2011). "Stable isotopes and the noncarbonaceous derivation of ureilites, in common with nearly all differentiated planetary materials". In: *Geochim-*

ica et Cosmochimica Acta 75.22, pp. 6912–6926. DOI: http://dx.doi.org.chain.kent.ac.uk/10.1016/j.gca.2011.09.011.

Watt, Ian M. (1997). *The Principles and Practice of Electron Microscopy*. 2nd ed. Cambridge: Cambridge University Press. ISBN: 9780521435918 (paperback). DOI: 10.1017/CBO9781139170529.

Weisberg, M. K., T. J. McCoy, and A. N. Krot (2006). "Systematics and Evaluation of Meteorite Classification". In: *Meteorites and the Early Solar System II*. Ed. by D. S. Lauretta and H. Y. McSween, pp. 19–52.

Weisberg, Michael K., Martin Prinz, et al. (1996). "The K (Kakangari) chondrite grouplet". In: *Geochimica et Cosmochimica Acta* 60.21, pp. 4253–4263. ISSN: 0016-7037. DOI: https://doi.org/10.1016/S0016-7037(96)00233-5.

Weisberg, Michael, Harold. Jr Connolly, and Denton Ebel (Jan. 2004). "Petrology and origin of amoeboid olivine aggregates in CR chondrites". In: *Meteoritics & Planetary Science* 39, pp. 1741–1753. DOI: 10.1111/j.1945-5100.2004.tb00070.x.

Whipple, F. L. (1947). "Meteorites and space travel." In: *AJ* 52, p. 131. DOI: 10.1086/106009.

Wilde, Paul D. and William Ailor (2013). "Chapter 9 - Re-Entry Operations Safety". In: *Safety Design for Space Operations*. Ed. by Firooz A. Allahdadi, Isabelle Rongier, and Paul D. Wilde. Oxford: Butterworth-Heinemann, pp. 603–775. ISBN: 978-0-08-096921-3. DOI: https://doi.org/10.1016/B978-0-08-096921-3.00009-X.

Wozniakiewicz, Penelope. J. et al. (2011). "Investigation of iron sulfide impact crater residues: A combined analysis by scanning and transmission electron microscopy". In: *Meteoritics & Planetary Science* 46.7, pp. 1007–1024. DOI: 10.1111/j.1945-5100.2011.01206.x. eprint: https://onlinelibrary.wiley.com/doi/pdf/10.1111/j.1945-5100.2011.01206.x.

Yin, Qing-Zhu et al. (2014). "Records of the Moon-forming impact and the 470 Ma disruption of the L chondrite parent body in the asteroid belt from U-Pb apatite ages of Novato (L6)". In: *Meteoritics & Planetary Science* 49.8, pp. 1426–1439. DOI:

10.1111/maps.12340. eprint: https://onlinelibrary.wiley.com/doi/pdf/10.1111/maps.12340.

Zolensky, m., P. Bland, et al. (2006). "Flux of Extraterrestrial Materials". In: ed. by Dante S. Lauretta and Harold Y. McSween Jr. METEORITES AND THE EARLY SOLAR SYSTEM II. University of Arizona Press, p. 869.

Zolensky, M., C. Pieters, et al. (2000). "Small is beautiful: The analysis of nanogram-sized astromaterials". In: *Meteoritics and Planetary Science* 35.1, pp. 9–29.

Appendices

Appendix A

Resin Tests

Table A.1: The results of the test for embedding techniques. A number of different set-up were tested, with the set-up described by the type code. The first letter signifies the baking of adhesive; The adhesive was either baked (B) or not baked (N) to attempt to remove some of the volatiles, the second letter shows one of the two types of resin that were tested; Buehler and Struers (B or S). The second section show the adhesive method tested double sided tape (DST), carbon tape (CT) or a layered DST CT mix finally the last letter shows the application method [D] a single dab on the particle allowed to dry before the remaining resin was added, [E] resin applied to the edge of the mould, [A] mould filled all at once from the centre

Type	Ease to remove (tape) 1-easy 5-hard	LEAKED? rating	Resin Ratios	Bubbles 1- none, 2 small light... 5 large proficent	look of resin
BB DST [A]	4	N	50.0:22.7	Small bubbles along sticky edge	coloured
BB DST [E]	4	Y	50.0:22.7	Small bubbles along sticky edge	coloured
BS DST [E]	2	N	64.3:8.0	Small bubbles along sticky edge	Clear
BS DST [A]	2	N	64.3:8.0	no bubbles	Clear
NS DST [E]	2	N	35.2:5.0	Small bubbles along sticky edge	Clear
NB DST [E]	1	Y	32.01:14.6	small bubbles spread throughout resin	coloured
BS OTHER [E]	2	Y	64.3:8.0	bubbles spread through out resin	Clear
BB OTHER [E]	4	N	50.0:22.7	bubbles spread through out resin	coloured
BS CT [E]	5	N	64.3:8.0	Small bubbles along sticky edge	Clear
BB CT [E]	5	N	50.0:22.7	Small bubbles along sticky edge	coloured

Table A.1: Table A.1 continued.

Type	Ease to remove (tape) 1-easy 5-hard	LEAKED? rating	Resin Ratios	Bubbles 1- none, 2 small light... 5 large proficent	look of resin
NS CT [E]	5	N	35.2:5.0	small bubbles spread throughout resin	Clear
NB CT [E]	5	N	32.01:14.6	bubbles spread through out resin	coloured
BB DST CT [E]	5	N	50.0:22.7	small bubble spread throughout resin	coloured
BS DST CT [E]	5	N	64.3:8.0	Small bubbles along sticky edge	Clear
NB DST CT [E]	5	N	32.01:14.6	small bubbles spread throughout resin	coloured
NS DST CT [E]	5	N	35.2:5.0	large bubbles along sticky edge	Clear
BB DST [D]	2	N	50.1:22.6	Small bubbles along sticky edge	coloured
BS DST [D]	3	Y	64.3:8	small bubbles spread throughout resin	Clear
NB DST [D]	3	Y	50.1:22.6	small bubbles spread throughout resin	coloured

Table A.1: Table A.1 continued.

Type	Ease to remove (tape) 1-easy 5-hard	LEAKED? rating	Resin Ratios	Bubbles 1- none, 2 small light... 5 large proficent	look of resin
NS DST [D]	2	N	64.3:8	bubbles spread throughout resin	Clear
BB CT [D]	5	N	50.1:22.6	small bubbles spread throughout resin	coloured
BS CT [D]	5	N	64.3:8	small bubbles spread throughout resin	Clear
NB CT [D]	5	N	50.1:22.6	No real bubbles	coloured
NS CT [D]	5	N	64.3:8	bubbles spread throughout resin	Clear
BB DST CT [D]	5	Y	50.1:22.6	No real bubbles	coloured
BS DST CT [D]	5	Y	64.3:8	small bubbles spread throughout resin	Clear
NB DST CT [D]	5	N	50.1:22.6	small bubbles spread throughout resin	coloured
NS DST CT [D]	5	N	64.3:8	small bubbles spread throughout resin	Clear

Appendix B

Spherical Contamination

Table B.1: The number of collected spheres from the Kwajalein and British Antarctic Survey collections based on there dominate chemistry.

	Kwajalein				BAS			
	Filter 9	Filter 8	Filter 11	Filter 12	Filter 14	Filter 13	Filter 16	Filter 26
Type	24/05/2012	31/05/2012	21/06/2012	06/07/2012	14/04/2015	01/06/2015	15/06/2015	07/07/2015
Si Mg	4	3	14	5	3	5	7	6
FeO	15	4	18	6	4	4	11	8
Fe (Cr,Ti,Ca,S)	5	8	567	17	3	5	5	6
SiAl(Fe,Ca,Mg)	71	43	28	20	184	125	105	105
Al Rich	0	0	7	18	1	5	2	1
Other	14	6	10	12	15	10	4	9
total et	19	7	32	11	7	9	18	14
total terrestrial	90	57	612	67	203	145	116	121
total	109	64	644	78	210	154	134	135

Table B.2: The number of collected spheres from the kwajalein and British Antarctic survey MM collections which demonstrated an iron rich chemistry.

	Kwajalein				BAS			
	Filter 9	Filter 8	Filter 11	Filter 12	Filter 14	Filter 13	Filter 16	Filter 26
Type	24/05/2012	31/05/2012	21/06/2012	06/07/2012	14/04/2015	01/06/2015	15/06/2015	07/07/2015
Fe(Cr)	1	0	549	0	1	0	2	3
Fe(Ti)	3	8	7	3	1	2	1	1
Fe(S)	1	0	4	0	0	0	0	0
Fe(Ca)	0	0	1	2	0	2	0	1
FE(Si)	0	0	0	0	1	1	2	1
Fe(Ni)	0	0	0	1	0	0	0	0
total	5	8	561	6	3	5	5	6

Table B.3: The number of collected spheres from the Kwajalein and British Antarctic survey MM collections which demonstrated an aluminium rich chemistry.

	Kwajalein				BAS			
	Filter 9	Filter 8	Filter 11	Filter 12	Filter 14	Filter 13	Filter 16	Filter 26
Type	24/05/2012	31/05/2012	21/06/2012	06/07/2012	14/04/2015	01/06/2015	15/06/2015	07/07/2015
SiAl only	44	16	21	10	142	79	89	87
SiAl(Fe)	15	7	0	2	7	4	1	2
SiAl(Ca)	5	14	12	3	9	39	9	11
SiAl(Ti)	0	0	0	0	4	3	4	4
SiAl(Mg)	7	6	0	1	10	0	1	1
SiAl(CaMg)	0	0	0	0	9	0	0	0
SIAL(Ba/Sb)	0	0	0	0	3	0	1	0

Appendix C

Achondrite Meteorite subtypes

Table C.1: |Breakdown of the achondrite subtypes along with their major morphological and chemical components and a description of the likely parent body or location from which they originated

Meteorite subtype	Main Feature	Likely parent body feature
	Martian	
Shergottites	Mostly plagioclase and pyroxene Basalts show similar levels of sodium to earth basalts Shock produced glasses (maskelynite)	Similar to Martian surface rocks contains trapped Martian atmosphere Slight Magnetic field
Nakhlite	Mostly Ca rich pyroxene significantly less shocked than the shergottites	Likely Martian in origin contains trapped Martian atmosphere
Chassigny	Single sample Primarily Olivine with some pyroxene Contains Shergottite like inclusions	Likely Martian in origin Contains trapped Martian atmosphere
	Primitives	
Acapulcoites	Composition simular to E chondrites, thermally metamorphised (not fully)	S type asteroid Likely part way differentiated
Lodranites	Composition simular to E chondrites, Thermally metamorphised (not fully), coarser grained than Acapulcoites	S type asteroid Likely part way differentiated, Deeper formation depth than Acapulcoites
Winonites	fine-medium grained regions of relict chondrules related to silicate found in irons	Unknown

Weisberg, McCoy, and Krot 2006; Keil 2014; McSween 1987

Table C.1: |Breakdown of the achondrite subtypes along with their major morphological and chemical components and a description of the likely parent body or location from which they originated

Meteorite subtype	Main Feature	Likely parent body feature
Ureilites	Mostly olivine olivine and pyroxene Matrix of Graphite and Diamond Coarse grained Appear both Igneous and Primitive Oxygen isotope line similar to chondrites	possibly S or A type asteroids Requires complex history Possibly Explosive volcanism or large scale impact event
Brachinites	High in iron content Mostly unshopcked Morphologically resembles Chassigny. compositions range from near chondritic to ultra-mafic	S type asteroid Iron rich
Asteroidal		
Eucrites	mostly Ca-rich, Na poor Plagioclase Most pyroxene in the form of pigeonite almost completely dehydrated contains reduced iron mostly basaltic compositions and fine grained	thought to have originated on Vesta 4
Diogenites	Most Mg rich Ca poor orthopyroxene Large interlocking crystals	Thought to have originated on Vesta 4
Howardites	breccia containing Eucrite and Diogenite clast	Thought to have formed via impact onto Vesta 4

Weisberg, McCoy, and Krot 2006; Keil 2014; McSween 1987

Table C.1: |Breakdown of the achondrite subtypes along with their major morphological and chemical components and a description of the likely parent body or location from which they originated

Meteorite subtype	Main Feature	Likely parent body feature
Angrites		
Aubrites		
	Lunar	
Impact breccias	Contain clasts of Ca rich plagioclase may contain clasts of lunar basalt shocked, broken crystals and glasses	likely to be regolith breccia Near identical to sample found by apollo lunar Oxygen isotope ratios
Mare basalts	Consist of pyroxene and Ca-rich plagioclase	Similar in almost all respects to lunar basalt.
	Stony-Irons	
Pallasites	50-50 metal silicate mix Olivine sits at Fo 88 (most), Fo 81 (eagle rest) 5 abnormal meteorites included in the group	formed in the crust-core boundary formed in silicate layer with metal flowing in metals simular to M type asteriod compositions likely a minimum of 4 different parent bodies
Mesosiderites	Mix of silicates in metal matrix Low olivine count and high pyroxene Uniform metal composition Mix of crust silicates and core metals	Crust core boundary formation Melted metals flowing around silicates

Weisberg, McCoy, and Krot 2006; Keil 2014; McSween 1987

Appendix D

Raw Compositional Data

Table D.1: Raw data used to produce ternary diagrams showing the location of previously collected MMs

Author	Region	SiO(2)	Al(2)O(3)	FeO	CaO	MgO	SO(2)	K(2)O	Na(2)O	TiO(2)	P(2)O(5)	NiO	MnO	Cr(2)O(3)	total
Noguchi 2015	Rodderite	69.95	1.07	2.07	0.00	16.61	0.00	2.67	6.85	0.00	0.00	0.00	0.00	0.77	99.99
Noguchi 2015	Rodderite	67.66	0.66	2.34	0.30	14.83	0.00	4.28	9.29	0.00	0.00	0.00	0.40	0.24	100
Noguchi 2015	Rodderite	67.20	0.09	14.40	0.00	10.60	0.00	4.40	3.10	0.00	0.00	0.00	0.19	0.00	99.98
Genge 1997	AVG	39.87	3.01	27.09	2.07	26.71	0.04	0.01	0.02	0.13	0.10	0.49	0.38	0.28	100.2
genge 1997	AVG	35.01	4.83	32.29	1.06	19.45	0.88	0.07	0.29	0.12	0.32	0.44	0.24	0.46	95.46
Genge 1997	AVG	33.87	4.28	29.63	0.72	16.81	1.50	0.13	0.44	0.11	0.40	0.37	0.23	0.49	88.98
Genge 1997	AVG	33.89	3.09	38.32	1.59	21.64	0.10	0.01	0.04	0.12	0.25	0.58	0.27	0.40	100.3
Genge 1997	AVG	35.58	2.78	34.42	2.01	23.64	0.02	0.01	0.02	0.12	0.10	1.18	0.28	0.29	100.45
Genge 1997	AVG	40.66	2.57	21.47	2.07	32.63	0.02	0.01	0.01	0.11	0.06	0.17	0.22	0.15	100.154
Genge 1997	AVG	45.16	3.31	17.62	2.63	30.23	0.02	0.01	0.02	0.15	0.00	0.11	0.61	0.11	99.98
Genge 1997	AVG	42.57	3.62	21.64	0.39	20.55	1.73	0.14	0.40	0.11	0.22	0.57	0.18	0.63	92.75
Genge 1997	AVG	31.05	4.73	31.40	0.70	14.91	1.41	0.11	0.43	0.11	0.53	0.26	0.23	0.44	86.31
Genge 1997	AVG	33.30	4.58	31.07	0.83	17.07	1.36	0.13	0.43	0.11	0.33	0.36	0.25	0.48	90.3
Taylor 1991		47.80	2	16.69	2.51	28.04	N/M	N/M	N/M	N/M	N/M	N/M	N/M	N/M	97.04
Taylor 1991		48.30	3.27	14.64	2.27	29.13	N/M	N/M	N/M	N/M	N/M	N/M	N/M	N/M	97.61
Taylor 1991		41.98	2.91	22.77	2.09	30.25	N/M	N/M	N/M	N/M	N/M	N/M	N/M	N/M	100
Taylor 1991		42.68	2.63	24.20	1.59	27.03	N/M	N/M	N/M	N/M	N/M	N/M	N/M	N/M	98.13
Taylor 1991		37.60	2.78	29.30	2.51	25.80	N/M	N/M	N/M	N/M	N/M	N/M	N/M	N/M	97.99
Taylor 1991		35.68	2.61	36.66	2.57	20.47	N/M	N/M	N/M	N/M	N/M	N/M	N/M	N/M	97.99
Taylor 1991		14.86	0.96	75.32	0.40	8.44	N/M	N/M	N/M	N/M	N/M	N/M	N/M	N/M	99.98
Taylor 2000	18-4	52.03	3.16	9.88	1.77	33.13	N/M	N/M	N/M	0.21	N/M	0.02	0.37	0.02	100.59
Taylor 2000	18-8	56.78	2.38	9.40	3.80	27.01	N/M	N/M	N/M	0.11	N/M	0.00	0.42	0.03	99.93
Taylor 2000	18-13a	45.82	4.14	10.03	3.69	35.46	N/M	N/M	N/M	0.19	N/M	0.03	0.15	0.14	99.65
Taylor 2000	18-5	47.50	2.91	14.20	2.52	31.03	N/M	N/M	N/M	0.13	N/M	0.26	0.89	0.12	99.56
Taylor 2000	18-7	48.75	14.31	15.70	11.76	7.08	N/M	N/M	N/M	0.60	N/M	0.00	0.45	0.02	98.67
Taylor 2000	28-1	41.93	4.92	13.69	3.47	35.95	N/M	N/M	N/M	0.22	N/M	0.00	0.17	0.02	100.37
Taylor 2000	28-2	51.08	3.34	10.01	1.10	33.33	N/M	N/M	N/M	0.17	N/M	0.00	0.38	0.17	99.58
Taylor 2000	28-5	54.36	1.93	9.83	5.69	27.31	N/M	N/M	N/M	0.14	N/M	0.06	0.36	0.07	99.75
Taylor 2000	28-30	48.38	3.90	13.00	3.58	29.61	N/M	N/M	N/M	0.18	N/M	0.00	0.38	0.02	99.05
Taylor 2000	28-31	47.62	3.39	15.06	1.90	31.14	N/M	N/M	N/M	0.10	N/M	0.18	0.31	0.04	99.74
Taylor 2000	28-28	55.49	2.05	12.42	3.80	24.78	N/M	N/M	N/M	0.19	N/M	0.01	0.34	0.08	99.16
Taylor 2000	28-28	51.14	3.26	14.44	3.32	26.58	N/M	N/M	N/M	0.15	N/M	0.00	0.39	0.19	99.47
Taylor 2000	28-27	50.87	2.80	11.46	4.48	28.86	N/M	N/M	N/M	0.13	N/M	0.03	0.37	0.04	99.04

Table D.1: Raw data used to produce ternary diagrams showing the location of previously collected MMs

Author	Region	SiO(2)	Al(2)O(3)	FeO	CaO	MgO	SO(2)	K(2)O	Na(2)O	TiO(2)	P(2)O(5)	NiO	MnO	Cr(2)O(3)	total
Taylor 2000	28-24	52.32	2.79	15.94	4.31	23.14	N/M	N/M	N/M	0.24	N/M	0.00	0.33	0.19	99.26
Taylor 2000	28-23	46.21	3.75	7.27	3.83	38.51	N/M	N/M	N/M	0.16	N/M	0.08	0.23	0.00	100.04
Taylor 2000	28-22	55.96	3.52	9.99	2.97	25.81	N/M	N/M	N/M	0.18	N/M	0.03	0.36	0.35	99.17
Taylor 2000	28-15	47.22	2.71	17.41	3.27	28.42	N/M	N/M	N/M	0.07	N/M	0.00	0.34	0.04	99.48
Taylor 2000	28-12	46.81	2.54	15.87	1.85	31.61	N/M	N/M	N/M	0.13	N/M	0.08	0.41	0.20	99.5
Taylor 2000	28-11	45.55	2.62	10.95	2.77	38.09	N/M	N/M	N/M	0.08	N/M	0.01	0.38	0.00	100.45
Taylor 2000	28-9	51.94	13.68	11.00	2.81	19.28	N/M	N/M	N/M	0.47	N/M	0.00	0.20	0.00	99.38
Taylor 2000	29-1	52.72	2.49	10.09	2.12	32.32	N/M	N/M	N/M	0.13	N/M	0.02	0.46	0.01	100.36
Taylor 2000	29-2	44.35	4.62	13.05	1.77	25.25	N/M	N/M	N/M	0.19	N/M	0.02	0.19	0.01	89.45
Taylor 2000	29-3	49.91	3.11	15.39	2.04	29.02	N/M	N/M	N/M	0.15	N/M	0.04	0.37	0.02	100.05
Taylor 2000	29-44	49.25	3.44	18.68	2.10	26.39	N/M	N/M	N/M	0.11	N/M	0.24	0.40	0.02	100.63
Taylor 2000	29-45	49.08	10.1	20.94	9.27	8.45	N/M	N/M	N/M	0.69	N/M	0.01	0.65	0.32	99.51
Taylor 2000	29-6	42.25	5.45	8.61	4.05	39.66	N/M	N/M	N/M	0.23	N/M	0.00	0.13	0.00	100.38
Taylor 2000	29-7	53.11	3.06	10.12	2.12	30.93	N/M	N/M	N/M	0.11	N/M	0.00	0.41	0.20	100.06
Taylor 2000	29-48	47.17	5.23	12.44	4.54	30.11	N/M	N/M	N/M	0.25	N/M	0.00	0.20	0.05	99.99
Taylor 2000	29-49	56.68	2.29	12.52	4.78	21.92	N/M	N/M	N/M	0.11	N/M	0.14	0.44	0.12	99
Taylor 2000	29-9	50.17	3.36	17.10	1.84	26.63	N/M	N/M	N/M	0.11	N/M	0.37	0.29	0.03	99.9
Taylor 2000	29-51	47.69	0.76	29.99	5.29	14.18	N/M	N/M	N/M	1.10	N/M	0.01	1.07	0.00	100.09
Taylor 2000	29-54	46.77	2.78	6.68	5.36	37.25	N/M	N/M	N/M	0.17	N/M	0.00	0.22	0.00	99.23
Taylor 2000	29-11	48.71	5.31	8.54	4.45	32.67	N/M	N/M	N/M	0.22	N/M	0.05	0.15	0.15	100.25
Taylor 2000	29-56	40.95	3.46	24.28	3.28	28.26	N/M	N/M	N/M	0.16	N/M	0.07	0.26	0.06	100.78
Taylor 2000	29-13	51.16	3.15	15.24	3.06	27.57	N/M	N/M	N/M	0.17	N/M	0.00	0.12	0.14	100.61
Taylor 2000	29-14	50.91	3.47	11.43	4.61	28.11	N/M	N/M	N/M	0.15	N/M	0.05	0.33	0.06	99.12
Taylor 2000	29-59	53.92	2.43	10.20	1.28	32.36	N/M	N/M	N/M	0.16	N/M	0.04	0.51	0.10	101
Taylor 2000	29-68	48.25	3.48	17.44	2.33	27.82	N/M	N/M	N/M	0.14	N/M	0.08	0.37	0.26	100.17
Taylor 2000	29-67	47.98	1.82	15.87	1.42	32.44	N/M	N/M	N/M	0.06	N/M	0.03	0.50	0.18	100.3
Taylor 2000	29-60a	47.33	2.80	14.60	2.81	32.14	N/M	N/M	N/M	0.10	N/M	0.00	0.31	0.03	100.12
Taylor 2000	29-61	54.60	3.91	10.77	8.85	21.40	N/M	N/M	N/M	0.24	N/M	0.06	0.31	0.08	100.22
Taylor 2000	29-62	50.16	1.90	16.07	1.33	29.23	N/M	N/M	N/M	0.09	N/M	0.07	0.45	0.43	99.73
Taylor 2000	29-66a	49.71	3.40	10.74	2.93	32.71	N/M	N/M	N/M	0.13	N/M	0.00	0.50	0.30	100.42
Taylor 2000	29-21	43.40	3.12	16.76	2.61	33.22	N/M	N/M	N/M	0.15	N/M	0.00	0.35	0.01	99.62
Taylor 2000	29-63	47.61	3.41	14.95	2.79	30.43	N/M	N/M	N/M	0.16	N/M	0.00	0.46	0.42	100.23
Taylor 2000	29-65	47.52	2.38	15.28	1.26	33.03	N/M	N/M	N/M	0.14	N/M	0.03	0.38	0.11	100.128

Table D.1: Raw data used to produce ternary diagrams showing the location of previously collected MMs

Author	Region	SiO(2)	Al(2)O(3)	FeO	CaO	MgO	SO(2)	K(2)O	Na(2)O	TiO(2)	P(2)O(5)	NiO	MnO	Cr(2)O(3)	total
Taylor 2000	29-69	53.20	2.03	15.08	1.80	27.21	N/M	N/M	N/M	0.19	N/M	0.00	0.42	0.04	99.97
Taylor 2000	29-70	47.89	2.57	14.88	2.23	32.15	N/M	N/M	N/M	0.09	N/M	0.08	0.38	0.06	100.33
Taylor 2000	29-23	44.48	3.58	18.35	2.84	29.72	N/M	N/M	N/M	0.17	N/M	0.00	0.31	0.10	99.55
Taylor 2000	29-25	48.47	3.91	11.34	3.02	33.37	N/M	N/M	N/M	0.15	N/M	0.02	0.30	0.04	100.62
Taylor 2000	29-30	45.14	2.63	16.64	1.39	32.85	N/M	N/M	N/M	0.12	N/M	0.52	0.31	0.03	99.63
Taylor 2000	29-31	46.29	2.40	23.20	2.15	25.89	N/M	N/M	N/M	0.11	N/M	0.02	0.38	0.32	100.76
Taylor 2000	29-32	51.05	0.85	9.86	1.76	35.50	N/M	N/M	N/M	0.09	N/M	0.07	0.56	0.54	100.28
Taylor 2000	29-35	53.99	2.54	13.25	3.15	25.85	N/M	N/M	N/M	0.09	N/M	0.10	0.51	0.05	99.53
Taylor 2000	29-37	49.30	3.30	1.76	2.78	43.06	N/M	N/M	N/M	0.13	N/M	0.00	0.00	0.02	100.35
Taylor 2000	29-40	48.46	3.01	12.00	3.15	33.09	N/M	N/M	N/M	0.15	N/M	0.01	0.45	0.09	100.41
Taylor 2000	29-41	41.74	4.90	12.61	4.05	36.27	N/M	N/M	N/M	0.17	N/M	0.00	0.12	0.02	99.88
Taylor 2000	29-42	58.62	0.15	14.79	0.09	25.58	N/M	N/M	N/M	0.00	N/M	0.04	0.25	0.33	99.85
Taylor 2000	19-43	46.78	2.38	11.03	2.58	37.81	N/M	N/M	N/M	0.22	N/M	0.00	0.09	0.03	100.92
Taylor 2000	15-46	49.01	3.01	11.63	2.58	34.56	N/M	N/M	N/M	0.16	N/M	0.00	0.46	0.06	101.47
Taylor 2000	15-47	49.96	3.29	9.42	2.09	34.24	N/M	N/M	N/M	0.18	N/M	0.00	0.35	0.21	99.74
Taylor 2000	15-49	55.81	3.15	13.60	1.18	25.66	N/M	N/M	N/M	0.15	N/M	0.04	0.42	0.13	100.14
Taylor 2000	15-24	43.66	1.54	17.95	1.41	32.39	N/M	N/M	N/M	0.15	N/M	0.03	0.33	0.03	97.49
Taylor 2000	15-26	47.42	2.86	17.22	2.16	30.36	N/M	N/M	N/M	0.11	N/M	0.00	0.34	0.08	100.55
Taylor 2000	15-50	53.98	3.91	7.79	3.19	31.03	N/M	N/M	N/M	0.20	N/M	0.06	0.49	0.07	100.72
Taylor 2000	15-28	49.20	3.12	16.24	1.64	29.65	N/M	N/M	N/M	0.16	N/M	0.02	0.33	0.13	100.49
Taylor 2000	15-27	49.76	2.66	13.66	1.68	31.45	N/M	N/M	N/M	0.12	N/M	0.01	0.39	0.02	99.75
Taylor 2000	15-29	41.07	2.99	3.34	18.14	35.45	N/M	N/M	N/M	0.10	N/M	0.00	0.22	0.00	101.31
Taylor 2000	15-30	42.06	5.44	4.71	2.82	45.23	N/M	N/M	N/M	0.26	N/M	0.00	0.06	0.00	100.58
Taylor 2000	15-31	52.79	1.04	2.86	0.74	42.88	N/M	N/M	N/M	0.09	N/M	0.04	0.27	0.20	100.91
Taylor 2000	15-32	41.98	3.88	16.98	3.02	34.44	N/M	N/M	N/M	0.17	N/M	0.00	0.19	0.01	100.67
Taylor 2000	15-33	47.60	2.86	21.12	1.29	26.86	N/M	N/M	N/M	0.12	N/M	0.02	0.31	0.20	100.38
Taylor 2000	15-34	42.17	3.60	21.49	2.47	29.93	N/M	N/M	N/M	0.21	N/M	0.03	0.23	0.01	100.14
Taylor 2000	15-35	42.82	6.04	4.59	0.66	46.15	N/M	N/M	N/M	0.29	N/M	0.00	0.11	0.00	100.66
Taylor 2000	15-36	44.83	3.89	20.16	0.35	30.88	N/M	N/M	N/M	0.17	N/M	0.38	0.19	0.25	101.1
Taylor 2000	24-2	48.96	2.56	16.54	3.46	27.88	N/M	N/M	N/M	0.15	N/M	0.00	0.41	0.11	100.07
Taylor 2000	24-3	49.14	2.52	16.46	1.99	28.86	N/M	N/M	N/M	0.12	N/M	0.00	0.41	0.19	99.69
Taylor 2000	24-8	45.16	3.07	22.37	2.74	26.71	N/M	N/M	N/M	0.11	N/M	0.53	0.24	0.13	101.06
Taylor 2000	24-11	51.52	2.63	20.49	2.77	22.40	N/M	N/M	N/M	0.22	N/M	0.05	0.38	0.30	100.76

Table D.1: Raw data used to produce ternary diagrams showing the location of previously collected MMs

Author	Region	SiO(2)	Al(2)O(3)	FeO	CaO	MgO	SO(2)	K(2)O	Na(2)O	TiO(2)	P(2)O(5)	NiO	MnO	Cr(2)O(3)	total
Taylor 2000	24-16	55.25	3.33	9.52	4.87	25.74	N/M	N/M	N/M	0.14	N/M	0.01	0.38	0.24	99.48
Taylor 2000	24-26	41.69	3.48	20.80	3.10	30.33	N/M	N/M	N/M	0.16	N/M	0.02	0.36	0.00	99.94
Taylor 2000	24-33	42.60	4.10	13.80	3.84	34.78	N/M	N/M	N/M	0.20	N/M	0.15	0.26	0.00	99.73
Taylor 2000	24-47	50.38	0.16	14.64	0.09	32.35	N/M	N/M	N/M	0.01	N/M	0.05	2.39	0.20	100.27
Taylor 2000	24-43	46.03	2.51	15.18	2.07	35.13	N/M	N/M	N/M	0.12	N/M	0.01	0.34	0.35	101.74
Taylor 2000	24-45	48.69	0.85	14.51	0.62	34.42	N/M	N/M	N/M	0.05	N/M	0.01	0.62	0.19	99.96
Taylor 2000	24-52	45.23	3.03	18.67	2.73	29.79	N/M	N/M	N/M	0.11	N/M	0.14	0.52	0.39	100.61
Taylor 2000	24-56	45.20	3.24	16.34	4.19	30.79	N/M	N/M	N/M	0.15	N/M	0.00	0.30	0.03	100.24
Taylor 2000	24-68	49.47	2.50	18.98	4.39	24.30	N/M	N/M	N/M	0.19	N/M	0.01	0.30	0.25	100.39
Taylor 2000	24-73	47.76	3.72	14.01	3.27	30.42	N/M	N/M	N/M	0.18	N/M	0.00	0.36	0.39	100.107
Taylor 2000	24-79	46.81	3.87	20.86	4.87	19.11	N/M	N/M	N/M	0.19	N/M	0.36	0.53	0.14	96.74
Taylor 2000	24-59	41.09	2.77	28.83	0.71	26.68	N/M	N/M	N/M	0.10	N/M	0.03	0.17	0.68	101.06
Taylor 2000	20-90	42.32	3.73	20.13	1.02	32.74	N/M	N/M	N/M	0.19	N/M	0.00	0.26	0.00	100.39
Taylor 2000	24-114	48.18	0.93	15.71	1.15	33.40	N/M	N/M	N/M	0.09	N/M	0.18	0.27	0.03	99.94
Taylor 2000	24-115	50.35	2.27	10.84	1.25	35.88	N/M	N/M	N/M	0.19	N/M	0.11	0.18	0.11	101.18
Taylor 2000	24-121	39.56	3.15	30.67	1.38	25.62	N/M	N/M	N/M	0.13	N/M	0.03	0.24	0.05	100.83
Taylor 2000	30-0	40.18	6.18	9.82	5.25	38.63	N/M	N/M	N/M	0.25	N/M	0.00	0.12	0.02	100.45
Taylor 2000	30-1	40.44	2.92	28.30	1.52	26.70	N/M	N/M	N/M	0.11	N/M	0.08	0.38	0.61	101.06
Taylor 2000	30-2	46.50	2.49	16.17	2.02	31.95	N/M	N/M	N/M	0.09	N/M	0.02	0.46	0.39	100.09
Taylor 2000	30-3	54.08	1.54	7.43	1.36	34.17	N/M	N/M	N/M	0.09	N/M	0.04	0.52	0.08	99.31
Taylor 2000	30-4	52.86	4.13	10.61	5.67	25.82	N/M	N/M	N/M	0.07	N/M	0.05	0.56	0.52	100.29
Taylor 2000	30-12	47.10	3.11	11.46	2.76	34.55	N/M	N/M	N/M	0.14	N/M	0.17	0.37	0.02	99.68
Taylor 2000	30-14	55.37	2.72	11.88	1.76	27.41	N/M	N/M	N/M	0.13	N/M	0.00	0.54	0.23	100.04
Taylor 2000	30-24	44.08	2.86	20.24	2.90	29.16	N/M	N/M	N/M	0.16	N/M	0.02	0.29	0.15	99.86
Taylor 2000	30-27	52.31	1.70	11.24	1.46	32.21	N/M	N/M	N/M	0.12	N/M	0.03	0.38	0.79	100.24
Taylor 2000	30-33	43.94	2.77	18.12	3.70	30.44	N/M	N/M	N/M	0.05	N/M	0.12	0.36	0.00	99.5
Taylor 2000	30-34	40.80	0.58	28.27	1.48	29.99	N/M	N/M	N/M	0.01	N/M	0.02	0.47	0.03	101.65
Taylor 2000	30-36	34.93	2.31	36.00	1.76	23.97	N/M	N/M	N/M	0.12	N/M	0.59	0.23	0.33	100.24
Taylor 2000	30-38	46.92	4.53	18.47	3.65	22.68	N/M	N/M	N/M	0.10	N/M	0.77	0.31	0.11	97.54
Taylor 2000	30-40	47.50	0.28	18.12	0.27	32.86	N/M	N/M	N/M	0.00	N/M	0.05	0.40	0.08	99.56
Taylor 2000	30-53	45.92	2.45	19.12	1.53	29.67	N/M	N/M	N/M	0.12	N/M	0.02	0.43	0.10	99.36
Taylor 2000	30-54	49.76	0.69	14.37	0.55	33.72	N/M	N/M	N/M	0.06	N/M	0.00	0.55	0.29	99.99
Taylor 2000	30-60	48.51	3.06	13.62	2.32	31.05	N/M	N/M	N/M	0.13	N/M	0.00	0.35	0.03	99.07

Table D.1: Raw data used to produce ternary diagrams showing the location of previously collected MMs

Author	Region	SiO(2)	Al(2)O(3)	FeO	CaO	MgO	SO(2)	K(2)O	Na(2)O	TiO(2)	P(2)O(5)	NiO	MnO	Cr(2)O(3)	total
Taylor 2000	30-61	44.94	3.25	18.59	0.75	31.51	N/M	N/M	N/M	0.11	N/M	0.01	0.18	0.04	99.384
Taylor 2000	30-66	50.57	0.59	12.01	0.27	35.03	N/M	N/M	N/M	0.06	N/M	0.00	0.92	0.00	99.45
Taylor 2000	30-67	48.31	2.20	9.13	1.99	37.43	N/M	N/M	N/M	0.09	N/M	0.03	0.22	0.02	99.42
Taylor 2000	30-75	48.69	3.01	16.85	2.61	27.67	N/M	N/M	N/M	0.16	N/M	0.03	0.46	0.55	100.03
Taylor 2000	30-82	48.09	1.46	14.51	1.08	32.15	N/M	N/M	N/M	0.07	N/M	0.25	0.79	0.02	98.42
Taylor 2000	30-88	45.40	2.22	22.13	1.35	27.30	N/M	N/M	N/M	0.13	N/M	0.04	0.37	0.01	98.95
Taylor 2000	30-91	46.12	3.07	18.80	0.40	29.40	N/M	N/M	N/M	0.13	N/M	0.28	0.26	0.12	98.58
Taylor 2000	30-92	51.27	0.41	12.12	0.30	33.87	N/M	N/M	N/M	0.03	N/M	0.03	1.28	0.01	99.32
Taylor 2000	30-93	36.09	1.92	33.66	1.72	24.65	N/M	N/M	N/M	0.08	N/M	0.00	0.44	0.59	99.15
Taylor 2000	30-94	47.92	3.34	12.62	3.04	30.80	N/M	N/M	N/M	0.14	N/M	0.00	0.40	0.11	98.37
Taylor 2000	30-97	48.95	1.66	14.09	1.37	33.11	N/M	N/M	N/M	0.06	N/M	0.02	0.72	0.02	100
Taylor 2000	30-98	51.57	4.25	12.65	6.02	25.85	N/M	N/M	N/M	0.16	N/M	0.04	0.34	0.02	100.9
Taylor 2000	30-101	49.97	2.48	13.54	1.63	32.11	N/M	N/M	N/M	0.08	N/M	0.00	0.37	0.07	100.25
Taylor 2000	30-103	46.27	1.63	14.79	0.66	36.31	N/M	N/M	N/M	0.05	N/M	0.03	0.49	0.00	100.23
Taylor 2000	30-108	47.83	3.89	9.49	3.30	35.65	N/M	N/M	N/M	0.19	N/M	0.02	0.21	0.03	100.61
Taylor 2000	30-115	41.44	4.55	13.70	3.65	36.45	N/M	N/M	N/M	0.19	N/M	0.00	0.15	0.02	100.15
Taylor 2000	30-116	45.50	1.64	19.33	1.54	30.88	N/M	N/M	N/M	0.08	N/M	0.19	0.37	0.20	99.73
Taylor 2000	30-130	48.16	2.54	16.35	1.51	30.33	N/M	N/M	N/M	0.16	N/M	0.01	0.37	0.36	99.79
Taylor 2000	30-131	53.09	1.26	22.09	1.13	17.70	N/M	N/M	N/M	0.06	N/M	0.08	3.53	0.61	99.55
Taylor 2000	30-137	48.16	4.46	13.02	3.84	30.30	N/M	N/M	N/M	0.21	N/M	0.00	0.68	0.00	100.67
Taylor 2000	30-139	44.49	4.70	7.43	4.06	39.21	N/M	N/M	N/M	0.21	N/M	0.01	0.18	0.01	100.3
Taylor 2000	30-143	53.76	2.63	14.10	1.99	25.14	N/M	N/M	N/M	0.16	N/M	0.06	0.43	0.28	98.55
Taylor 2000	30-153	60.53	2.00	5.43	1.89	29.96	N/M	N/M	N/M	0.10	N/M	0.10	0.19	0.03	100.23
Taylor 2000	30-152	51.97	2.78	13.01	0.64	30.53	N/M	N/M	N/M	0.14	N/M	0.02	0.42	0.09	99.6
Taylor 2000	27-1	54.86	4.48	5.46	3.40	32.47	N/M	N/M	N/M	0.19	N/M	0.01	0.57	0.00	101.44
Taylor 2000	27-2	47.51	3.00	19.53	0.33	28.03	N/M	N/M	N/M	0.13	N/M	0.02	0.31	0.54	99.4
Taylor 2000	27-3	28.21	3.51	18.18	2.96	26.33	N/M	N/M	N/M	0.14	N/M	0.02	0.28	0.41	80.04
Taylor 2000	27-4	56.97	0.53	10.55	1.34	30.17	N/M	N/M	N/M	0.16	N/M	0.00	0.43	0.12	100.27
Taylor 2000	27-5	49.05	4.51	11.20	3.96	30.56	N/M	N/M	N/M	0.23	N/M	0.01	0.22	0.27	100.01
Taylor 2000	27-6	44.41	2.00	1.63	1.46	51.32	N/M	N/M	N/M	0.15	N/M	0.03	0.05	0.00	101.05
Taylor 2000	27-7	50.32	1.46	0.48	1.29	47.92	N/M	N/M	N/M	0.09	N/M	0.01	0.09	0.01	101.67
Taylor 2000	27-8	50.55	3.16	11.35	2.70	30.76	N/M	N/M	N/M	0.14	N/M	0.00	0.38	0.71	99.75
Taylor 2000	27-9	49.20	2.73	3.52	2.22	42.79	N/M	N/M	N/M	0.15	N/M	0.00	0.11	0.01	100.73

Table D.1: Raw data used to produce ternary diagrams showing the location of previously collected MMs

Author	Region	SiO(2)	Al(2)O(3)	FeO	CaO	MgO	SO(2)	K(2)O	Na(2)O	TiO(2)	P(2)O(5)	NiO	MnO	Cr(2)O(3)	total
Taylor 2000	27-10	43.86	0.38	0.49	0.35	55.66	N/M	N/M	N/M	0.02	N/M	0.02	0.00	0.01	100.79
Taylor 2000	27-11	54.91	4.59	13.37	1.66	24.95	N/M	N/M	N/M	0.16	N/M	0.02	0.29	0.00	99.95
Taylor 2000	37-12	45.10	3.87	3.26	3.27	44.43	N/M	N/M	N/M	0.18	N/M	0.09	0.18	0.10	100.48
Taylor 2000	37-13	43.30	2.75	2.97	1.63	49.51	N/M	N/M	N/M	0.07	N/M	0.03	0.04	0.00	100.3
Taylor 2000	37-14	44.94	4.68	4.50	3.84	41.52	N/M	N/M	N/M	0.21	N/M	0.00	0.27	0.00	99.96
Taylor 2000	37-15	47.95	3.81	10.10	3.21	33.43	N/M	N/M	N/M	0.17	N/M	0.02	0.40	0.03	99.12
Taylor 2000	37-16	41.38	7.26	1.29	6.91	42.55	N/M	N/M	N/M	0.33	N/M	0.00	0.02	0.01	99.75
Taylor 2000	37-17	42.13	2.90	0.01	0.54	54.21	N/M	N/M	N/M	0.00	N/M	0.01	0.00	0.02	99.82
Taylor 2000	37-18	55.11	3.49	13.61	1.61	24.57	N/M	N/M	N/M	0.15	N/M	0.16	0.40	0.11	99.21
Taylor 2000	34-13	46.34	4.33	14.34	3.67	31.01	N/M	N/M	N/M	0.19	N/M	0.00	0.33	0.64	100.85
Taylor 2000	34-15	43.87	2.93	25.06	0.22	27.03	N/M	N/M	N/M	0.14	N/M	0.00	0.22	0.69	100.16
Taylor 2000	34-12	48.50	2.92	12.24	2.53	32.03	N/M	N/M	N/M	0.15	N/M	0.01	0.61	0.20	99.19
Taylor 2000	34-21	39.94	3.20	28.71	1.06	27.04	N/M	N/M	N/M	0.14	N/M	0.05	0.25	0.17	100.56
Taylor 2000	34-25	43.39	0.80	0.07	0.79	55.01	N/M	N/M	N/M	0.07	N/M	0.06	0.01	0.00	100.2
Taylor 2000	34-30	45.88	3.22	13.66	2.62	34.33	N/M	N/M	N/M	0.18	N/M	0.00	0.34	0.01	100.24
Taylor 2000	34-42	42.14	2.38	18.48	1.57	35.33	N/M	N/M	N/M	0.08	N/M	0.39	0.43	0.08	100.88
Taylor 2000	34-43	40.00	2.14	16.61	0.36	40.87	N/M	N/M	N/M	0.09	N/M	0.32	0.22	0.27	100.88
Taylor 2000	34-57	43.34	3.40	0.01	2.08	51.71	N/M	N/M	N/M	0.14	N/M	0.00	0.00	0.00	100.68
Taylor 2000	34-56	45.48	3.37	22.25	3.29	23.99	N/M	N/M	N/M	0.15	N/M	0.69	0.31	0.13	99.66
Taylor 2000	34-65	48.87	3.39	11.68	1.32	33.86	N/M	N/M	N/M	0.18	N/M	0.00	0.18	0.21	99.69
Taylor 2000	34-86	41.09	2.64	26.49	2.29	26.66	N/M	N/M	N/M	0.12	N/M	0.10	1.27	0.11	100.77
Taylor 2000	34-85	44.95	2.13	20.12	2.49	29.82	N/M	N/M	N/M	0.15	N/M	0.55	0.32	0.34	100.87
Taylor 2000	34-84	50.97	4.00	1.17	3.27	40.45	N/M	N/M	N/M	0.19	N/M	0.00	0.31	0.00	100.36
Taylor 2000	34-83	48.91	1.06	10.88	0.79	34.13	N/M	N/M	N/M	0.08	N/M	0.02	0.93	0.72	97.52
Taylor 2000	34-0	49.92	2.65	16.25	3.54	27.24	N/M	N/M	N/M	0.15	N/M	0.01	0.35	0.11	100.22
Gournelle 2005	Bulk	46.8	1.24	8.29	0.6	38.3	N/M	0	0.07	0.1	N/M	0.17	0.16	0.5	96.23
Gournelle 2005	Bulk	54.1	0.34	1.96	0.3	34	N/M	0	0	0.07	N/M	0	0.14	0.63	91.54
Gournelle 2005	Bulk	46.4	1.09	14.6	0.76	38.6	N/M	0	0.03	0.06	N/M	0.65	0.12	0.65	102.96
Gournelle 2005	Bulk	33.4	2.49	29.6	1.26	22.9	N/M	0	0.03	0.1	N/M	0.72	0.25	0.31	91.06
Gournelle 2005	Bulk	33.2	0.98	33.2	0.49	26	N/M	0.04	0.04	0.1	N/M	0	0.23	0.61	94.89
Gournelle 2005	Bulk	12.2	5.05	53.8	0.15	9.3	N/M	0.07	0.19	0.13	N/M	0.2	0.23	2.57	83.89
Gournelle 2005	Bulk	23	3.01	30	0.36	14.6	N/M	0.1	0.21	0.07	N/M	0.21	0.23	0.31	72.1
Gournelle 2005	Bulk	56.6	3.6	1.66	0.44	31.4	N/M	0.16	0.33	0.05	N/M	0	0.09	0.26	94.59

Table D.1: Raw data used to produce ternary diagrams showing the location of previously collected MMs

Author	Region	SiO(2)	Al(2)O(3)	FeO	CaO	MgO	SO(2)	K(2)O	Na(2)O	TiO(2)	P(2)O(5)	NiO	MnO	Cr(2)O(3)	total
Gournelle 2005	Bulk	21.8	2.89	30.4	0.44	17	N/M	0.06	0.25	0.05	N/M	0.23	0.23	0.45	73.8
Gournelle 2005	Bulk	45.1	0	17.5	0	29.4	N/M	0.03	0.09	0.03	N/M	0	0.4	0.76	93.31
Gournelle 2005	Bulk	36.9	0.03	3.52	0.06	43.7	N/M	0	0.2	0	N/M	0	0.12	0.97	85.5
Gournelle 2005	Bulk	21.4	1.68	20.3	0.35	14.5	N/M	0.43	0.74	0.05	N/M	0.11	0.17	0.26	59.99
Gournelle 2005	Bulk	15.3	1.03	54.9	0.2	1.95	N/M	0.27	0.35	0	N/M	0.03	0.27	0.38	74.68
Gournelle 2005	Bulk	39.2	6.98	12	1.17	26	N/M	0	0.04	0.09	N/M	0.11	0.5	0.84	86.93
Gournelle 2005	Bulk	35	5.36	32.3	1.44	20.1	N/M	0.09	0	0.14	N/M	0	0.38	0.53	95.34
Gournelle 2005	Bulk	32.6	2.49	28.9	1.52	15.1	N/M	0.15	0.25	0.14	N/M	0.44	0.56	0.57	82.72
Gournelle 2005	Bulk	33.9	2.84	24.9	0.37	16.2	N/M	0.13	0.09	0.07	N/M	0.15	0.1	0.34	79.09
Gournelle 2005	Bulk	28.3	2.04	27.4	0.57	15.8	N/M	0.05	0.24	0.05	N/M	0.3	0.24	0.35	75.34
Gournelle 2005	Bulk	25	2.47	31.4	0.52	12.2	N/M	0.79	0.15	0.1	N/M	0.78	0.19	0.33	73.93
Gournelle 2005	Bulk	30.4	2.04	16.3	1.36	19.2	N/M	3.11	1.86	0.06	N/M	0.43	0.29	0.31	75.36
Gournelle 2005	Bulk	30	1.88	29.3	0.31	5.16	N/M	0.89	0.47	0.12	N/M	0.05	0	0.65	68.83
Gournelle 2005	Bulk	31.3	2.23	24.9	0.86	14.5	N/M	0.48	0.72	0.13	N/M	0.23	0.21	0.41	75.97
Gournelle 2005	Bulk	26.5	1.94	31.4	0.39	9.93	N/M	1.13	0.43	0.12	N/M	0.23	0.15	0.42	72.64
Gournelle 2005	Bulk	20.5	1.48	32.6	0.47	9.68	N/M	0.53	0.97	0.11	N/M	0.58	0.22	0.39	67.53
Gournelle 2005	Bulk	32.6	3.57	28.9	0.96	19.2	N/M	0.28	0.1	0.08	N/M	0.22	0.31	0.6	86.82
Gournelle 2005	Bulk	33.9	2.17	20.6	0.29	18	N/M	3.59	0.92	0.1	N/M	0.53	0.27	0.49	80.86
Gournelle 2005	Bulk	29.6	2.74	27.9	0.12	17.7	N/M	1.63	0.37	0.07	N/M	0.65	0.25	0.44	81.47
Gournelle 2005	Bulk	34.7	2.2	25.9	0.98	15.4	N/M	0.78	0.69	0.1	N/M	0.16	0.38	0.6	81.89
Gournelle 2005	Bulk	35.1	2.37	22.7	0.22	25.2	N/M	0.06	0.23	0.12	N/M	0.17	0.26	0.71	87.14
Gournelle 2005	Bulk	28.6	2.47	30.3	0.21	17.1	N/M	0.14	0.33	0.15	N/M	0.09	0.21	0.43	80.03
Gournelle 2005	Bulk	33.4	2.3	22.9	0.88	18.8	N/M	0.14	0.82	0.06	N/M	0.24	0.34	0.48	80.36
Gournelle 2005	Bulk	33.7	1.78	28.9	1	24.6	N/M	0.06	0.28	0.07	N/M	0.46	0.32	0.14	91.31
Gournelle 2005	Bulk	25.7	1.84	19.6	0.06	11.3	N/M	0.12	0.51	0.11	N/M	0.05	0.08	0.47	59.84
Gournelle 2005	Bulk	19.1	1.43	25	0.41	13.6	N/M	0.06	0.26	0.09	N/M	0.11	0.2	0.41	60.67
Gournelle 2005	Bulk	29.9	2.65	34.5	0.81	15.2	N/M	0.17	0.28	0.13	N/M	0.21	0.23	0.29	84.37
Gournelle 2005	Bulk	38.3	3.24	21.7	0.43	17.4	N/M	0.24	0.58	0.14	N/M	0.14	0.13	0.63	82.93
Gournelle 2005	Bulk	33.1	3.11	30.2	0.35	16.6	N/M	0.19	0.7	0.03	N/M	0.39	0.27	0.37	85.31
Gournelle 2005	Bulk	38.4	2.58	26.2	0.43	17.9	N/M	0.14	0.69	0.15	N/M	0.17	0.2	0.62	87.48

Table D.2: Raw data of fly ash particles used in the production of ternarys

Author	SiO(2)	Al(2)O(3)	Fe(2)O(3)	CaO	MgO	SO(3)	K(2)O	Na(2)O	TiO(2)	P(2)O(5)	NiO	MnO	Cr(2)O(3)	LOI	total
Jaarsveld 2002	61.4	33	1.1	0.6	0.3	0	0.1	0.1	2	N/M	N/M	N/M	N/M	1.4	100
Jaarsveld 2002	59.9	21.6	4.7	2.9	1.4	0.2	2.3	0.4	0.8	N/M	N/M	N/M	N/M	5.8	100
Blaha 2008	39.28	21.41	16.64	11.66	3.13	1.94	2.2	1.23	0.82	0.11	N/M	0.25	N/M	1.48	100.15
Blaha 2008	38.94	21.16	16.12	11.42	3.12	2.34	2.19	1.22	0.82	0.26	N/M	0.25	N/M	1.38	99.22
Goodzari 2006a	56.42	20.62	4.91	9.43	1.2	0	1.51	4.25	0.58	0.47	0	0.03	0.01	0	100
Goodzari 2006a	51.1	22.2	6	10.6	2.5	0	1.8	2.3	0.8	0.3	0	0	0	0.5	98.1
Goodzari 2006a	55.1	18.7	3.11	9.27	1.5	3.43	0.83	0.65	0.57	0.07	0	0.06	0	0	93.69
Goodzari 2006a	56	22.7	3.6	2.57	1.11	0.49	2.31	0.5	0.92	0.46	0.01	0.03	0.04	8.62	99.98
Goodzari 2006a	57.82	19.29	4.26	2.9	1.15	0.48	1.95	0.41	0.74	0.23	0.01	0.04	0.03	10.4	99.95
Goodzari 2006a	40	20.8	29.3	3.4	1.3	0.3	2.1	1.3	0.92	0.25	0	0.11	0.02	0	99.9
Goodzari 2006a	11.11	4.92	14.73	56.2	1.01	10.23	0.91	0.41	0.2	0.03	0	0.28	0	0	100.03
Ward + french	56.8	26.3	9.5	1.4	0.8	0.3	0.7	0.2	1.7	1.9	N/M	N/M	N/M	N/M	100
Ward + french	57	25	9.9	1.5	0.7	0.5	0.5	0.2	1.5	2.7	N/M	N/M	N/M	N/M	100
Ward + french	58.3	22.2	13.6	1.3	0.8	0.1	0.4	0.2	1.7	1	N/M	N/M	N/M	N/M	100
Ward + french	44.5	30.7	14.4	4.2	1.6	0.3	0.9	0.4	1.9	1	N/M	N/M	N/M	N/M	100
Ward + french	62.9	29.3	1.8	1.3	1.1	0.2	0.5	0.8	1.8	0.1	N/M	N/M	N/M	N/M	99.9
Ward + french	67	24.8	3.1	1	0.6	0.1	1.6	0.6	1	0.2	N/M	N/M	N/M	N/M	100
Ward + french	61.5	22.4	7.6	3.3	1.1	0.1	1.9	0.9	0.9	0.2	N/M	N/M	N/M	N/M	100
Ward + french	57.5	28.2	5.6	3.8	1.2	0.2	1.1	0.2	1.6	0.5	N/M	N/M	N/M	N/M	100
Ward + french	65.9	27.6	1.1	0.4	0.3	0.1	2.9	0.2	1.3	0.2	N/M	N/M	N/M	N/M	100
Vassilev 1995	59.7	27.6	5.8	0.9	2.5	0	2.9	0	0.7	N/M	N/M	N/M	N/M	N/M	100.1
Vassilev 1995	54.2	29.6	6.2	2.8	0.3	5.1	1.8	0	0.3	N/M	N/M	N/M	N/M	N/M	100.3
Vassilev 1995	51.7	27.1	6.5	6.4	3.5	1.8	1.3	1.7	0.4	N/M	N/M	N/M	N/M	N/M	100.4
Vassilev 1995	51.5	25.1	9	8.3	3.7	0.2	1.5	0.7	0.6	N/M	N/M	N/M	N/M	N/M	100.6
Vassilev 1995	51.2	28.2	9.1	0.8	6.2	0	1.8	2.8	0.6	N/M	N/M	N/M	N/M	N/M	100.7
Vassilev 1995	46.6	26.6	9.3	8.5	2.3	3.8	1.7	1.2	0.5	N/M	N/M	N/M	N/M	N/M	100.5
Vassilev 1995	38.1	20.7	39.6	0.1	0	0	1.6	0	0	N/M	N/M	N/M	N/M	N/M	100.1
Vassilev 1995	27.7	17.2	34.9	10.7	5.6	1.4	0.4	1.4	1.9	N/M	N/M	N/M	N/M	N/M	101.2
Vassilev 1995	14.8	10.8	60.9	7	3.7	2.8	0	0	0	N/M	N/M	N/M	N/M	N/M	100
Vassilev 1995	14	7.8	69.5	2.1	3	1.6	0.4	1.6	0.5	N/M	N/M	N/M	N/M	N/M	100.5
Vassilev 1995	10.9	8.5	74.9	2.4	3.2	0	0	0	0	N/M	N/M	N/M	N/M	N/M	99.9
Massazza book	52.56	26.33	6.81	5.96	2.21	1.02	1.14	0.24	1	N/M	N/M	N/M	N/M	3.46	100.73
Massazza book	50.09	28.1	11.7	1.62	1.54	0	0.62	0.28	1	N/M	N/M	N/M	N/M	1.27	96.22

Table D.2: Raw data of fly ash particles used in the production of ternarys

Author	SiO(2)	Al(2)O(3)	Fe(2)O(3)	CaO	MgO	SO(3)	K(2)O	Na(2)O	TiO(2)	P(2)O(5)	NiO	MnO	Cr(2)O(3)	LOI	total
Massazza book	52.24	19.01	15.71	4.48	0.89	1.34	2.05	0.82	1	N/M	N/M	N/M	N/M	0.92	98.46
Massazza book	50.46	25.74	6.53	4.32	2.24	0	4.43	2.04	1	N/M	N/M	N/M	N/M	3.95	100.71
Massazza book	57.5	26.1	4	5.1	1.3	0.4	1.35	1.5	1	N/M	N/M	N/M	N/M	1.6	99.85
Massazza book	48.75	23.21	4.15	3.93	1	0	1.1	0.24	1	N/M	N/M	N/M	N/M	10.39	93.77
Massazza book	50.8	23.9	8.6	3.6	2.8	0.8	2.9	0.8	1	N/M	N/M	N/M	N/M	2.9	98.1
Ilic 2002	52.3	25.2	4.6	10	2.2	0.6	0	0	0	N/M	N/M	N/M	N/M	0.4	95.3
Ilic 2002	49.8	17.3	8.7	24.9	1.9	4.3	1.7	0.3	0	N/M	N/M	N/M	N/M	2.3	111.2
Ilic 2002	26	10.6	6.59	42.1	1.48	5.57	0.8	0.17	0	N/M	N/M	N/M	N/M	4.55	97.86
Ilic 2002	27.4	12.8	5.5	47	2.5	6.2	0.2	0.2	0	N/M	N/M	N/M	N/M	2.4	104.2
Massazza book	51.68	27.01	6.25	1.72	1.88	0	4.49	0.54	1	N/M	N/M	N/M	N/M	4.7	99.27
Massazza book	48.1	24.68	6.5	1.41	1.82	0	4.06	0.56	1	N/M	N/M	N/M	N/M	11.7	99.83
Massazza book	55.74	24.14	6.02	2.47	2.22	1.04	0	0	1	N/M	N/M	N/M	N/M	2.74	95.37
Massazza book	53.98	22.27	11.6	3.95	1.97	0.73	0	2.71	1	N/M	N/M	N/M	N/M	2.13	100.34
Massazza book	47	17.7	25.3	2.1	1	0.3	2.3	0.7	1	N/M	N/M	N/M	N/M	2.4	99.8
Massazza book	48	38.2	4.5	3.3	1.5	0.37	1.75	0.3	1	N/M	N/M	N/M	N/M	2.3	101.22
Massazza book	53.53	23.55	6.23	5.85	1.6	0	1.75	2.2	1	N/M	N/M	N/M	N/M	3.44	99.15
Massazza book	43.8	22.1	16.2	3.5	0.8	1.1	0	4.4	1	N/M	N/M	N/M	N/M	5	97.9
Massazza book	51.2	29.6	6.8	3.4	1.2	0.5	3.1	0.6	1	N/M	N/M	N/M	N/M	3.3	100.7
dai 2010	39.84	50.84	0.93	1.75	0.15	0	0.47	0.12	0.69	0.09	N/M	N/M	N/M	0	94.88
dai 2010	39.92	51.87	0.82	1.33	0.19	0	0.52	0.2	0.67	0.12	N/M	N/M	N/M	0	95.64
Shehata 2000	41.96	19.64	20.07	5.57	1.19	0.95	2.44	0.69	0.84	0.15	N/M	N/M	N/M	3.71	97.21
Shehata 2000	47.34	22.34	15.08	6.38	0.82	1.43	1.23	0.6	1.1	0.32	N/M	N/M	N/M	2.73	99.37
Shehata 2000	61.5	20.52	4.29	8.68	1.7	0.19	0.6	0.17	1.38	0.05	N/M	N/M	N/M	0.08	99.16
Shehata 2000	50.92	23.64	4.62	13.63	0.86	0.23	0.59	3.38	0.14	0.73	N/M	N/M	N/M	0.42	99.16
Shehata 2000	45.66	21.42	5.53	12.34	2.76	0.84	0.96	7.82	0.65	0.14	N/M	N/M	N/M	0.35	98.47
Shehata 2000	51.56	22.9	4.58	15.15	1.16	0.28	0.3	2.6	0.66	0.12	N/M	N/M	N/M	0.35	99.66
Shehata 2000	40.68	21.19	4.5	15.87	3.54	2.18	0.49	8.14	0.96	0.65	N/M	N/M	N/M	0.53	98.73
Shehata 2000	44.29	20.96	5.23	17.51	4.21	2.23	0.84	1.13	1.12	0.77	N/M	N/M	N/M	1.14	99.43
Shehata 2000	39.77	21.46	5.69	18.46	3.77	1.86	0.66	3.71	1.04	0.54	N/M	N/M	N/M	1.06	98.02
Shehata 2000	32.71	19.02	5.76	18.85	4.3	4.81	0.68	8.28	1.24	0.52	N/M	N/M	N/M	1.18	97.35
Shehata 2000	38.42	20.57	5.64	20.5	4.39	1.76	0.62	2.64	1	0.52	N/M	N/M	N/M	2.01	98.07
Shehata 2000	39.83	19.56	5.54	21.53	4.62	2.14	0.6	1.55	1.2	0.71	N/M	N/M	N/M	1.68	98.96
Shehata 2000	38.22	18.43	5.72	24.61	4.72	1.55	0.44	1.39	1.42	1.04	N/M	N/M	N/M	0.18	97.72

Table D.2: Raw data of fly ash particles used in the production of ternarys

Author	SiO(2)	Al(2)O(3)	Fe(2)O(3)	CaO	MgO	SO(3)	K(2)O	Na(2)O	TiO(2)	P(2)O(5)	NiO	MnO	Cr(2)O(3)	LOI	total
Shehata 2000	35.2	18.72	6.06	26.61	5.12	2.49	0.36	1.59	1.5	1.19	N/M	N/M	N/M	0.39	99.23
Shehata 2000	36.12	18.64	6.07	26.62	5.41	1.8	0.4	1.34	1.48	1.12	N/M	N/M	N/M	0.16	99.16
Shehata 2000	34.6	16.45	7.13	27.71	5.89	2.71	0.21	1.51	1.3	0.71	N/M	N/M	N/M	0.28	98.5
Shehata 2000	31.65	16.65	7.28	29.1	6.57	3.17	0.2	1.72	1.33	0.74	N/M	N/M	N/M	0.36	98.77
Shehata 2000	41.12	11.24	5.93	30	4.4	2.13	1.76	1.1	0.47	0.1	N/M	N/M	N/M	0.78	99.03
scheetz 1998	52.5	22.8	7.5	4.9	1.3	1	1.3	0.6	N/M	N/M	N/M	N/M	N/M	2.6	94.5
scheetz 1998	36.9	17.6	6.2	25.2	5.1	1.7	0.6	2.9	N/M	N/M	N/M	N/M	N/M	0.33	96.53
Y MA	48.36	31.36	4.44	7.14	1.35	1.18	1.64	0.72	1.24	1.9	N/M	N/M	N/M	0	99.33
Massazza 1993	41.49	22.14	9.74	9.48	4.98	1.24	2.12	0.94	0.84	N/M	N/M	N/M	N/M	7.6	100.57
Massazza 1993	45.09	29.01	5.37	5.55	0.68	1.1	1.99	0.3	1.44	N/M	N/M	N/M	N/M	7.34	97.87
Massazza 1993	48.59	28.21	5.94	1.15	2.15	0.34	2.33	0.71	4.44	N/M	N/M	N/M	N/M	7.44	101.3
Massazza 1993	41.94	18.44	9.47	14.2	2.27	2.63	0	0	1.53	N/M	N/M	N/M	N/M	0	90.48
chancy	55.11	20.42	8.18	9.9	0.72	0.54	N/M	0.46	N/M	N/M	N/M	0.1	N/M	0.11	95.54
0 font 2010	52	23	4.7	3.5	1.7	1.1	3.3	0.5	0.9	0.3	N/M	0.1	N/M	0	91.1
0 font 2010	50	18	4.5	7.5	1.6	1.8	2.3	0.4	0.7	0.3	N/M	0.1	N/M	0	87.2
0 font 2010	52	10	12	8.1	1.3	1.7	2	0.9	0.7	9.6	N/M	0.1	N/M	0	98.4
0 font 2010	59	6.8	7	10.4	1.1	1	1.8	0.7	0.3	7.7	N/M	0.1	N/M	0	95.9
0 font 2010	51	20	5.2	4.1	2.1	1.4	2.6	0.4	0.8	0.2	N/M	0.1	N/M	0	87.9
0 font 2010	58	23	6.1	3.5	1.8	0.2	1.6	0.6	1.1	0.5	N/M	0.1	N/M	0	96.5
0 font 2010	54	23	8.5	3.5	2	0.4	3.2	0.9	1	0.8	N/M	0.1	N/M	0	97.4
0 font 2010	43	26	19	5.3	1.2	0.9	1.2	0.1	0.9	0.5	N/M	0.04	N/M	0	98.14
0 font 2010	52	25	7	3	1.8	0.5	3.6	0.7	1	0.6	N/M	0.1	N/M	0	95.3
0 font 2010	51	26	6.9	2.9	1.8	0.5	3.6	0.7	1	0.5	N/M	0.1	N/M	0	95
0 font 2010	49	28	4.3	6.4	1.7	0.4	0.8	0.3	1.8	1.1	N/M	0.1	N/M	0	93.9
0 font 2010	50	21	8	4.5	1.9	0.9	4.3	0.6	0.5	0.8	N/M	0.1	N/M	0	92.6
0 font 2010	57	25	9.3	6.9	3.8	1	1.9	1.2	0.9	0.7	N/M	0.1	N/M	0	107.8
0 font 2010	53	27	7.4	3.1	0.6	0.5	0.5	0.1	1.8	1.6	N/M	0.1	N/M	0	95.7
0 font 2010	52	29	8.3	1.7	1	0.4	2.3	0.5	1.5	0.2	N/M	0.03	N/M	0	96.93
TENNAKOON 2014	51.1	25.6	12.5	4.3	1.45	0.24	0.7	0.77	1.32	0.89	N/M	0.15	N/M	0.57	99.59
TENNAKOON 2014	60	24.6	8.56	0.15	0.99	0.18	0.36	0.36	1.53	0.22	N/M	0.04	N/M	1.49	98.48
TENNAKOON 2014	65.8	26.7	1.32	0.05	0.25	0.11	2.69	0.32	1.11	0.14	N/M	0.02	N/M	1.44	99.95
TENNAKOON 2014	63.2	25.2	3.36	0.07	0.57	0.18	1.81	0.72	0.99	0.25	N/M	0.07	N/M	1.31	97.73
TENNAKOON 2014	73.1	23.2	0.89	0.07	0.14	0.06	0.52	0.06	1.31	0.05	N/M	0.02	N/M	0.75	100.17

Table D.2: Raw data of fly ash particles used in the production of ternarys

Author	SiO(2)	Al(2)O(3)	Fe(2)O(3)	CaO	MgO	SO(3)	K(2)O	Na(2)O	TiO(2)	P(2)O(5)	NiO	MnO	Cr(2)O(3)	LOI	total
TENNAKOON 2014	80.4	14	3.57	0.04	0.31	0.08	0.85	0.1	0.49	0.09	N/M	0.04	N/M	0.54	100.51
Eun Oh et al 2014	65.2	23.9	4.2	2	0.7	0.3	1.4	0.1	1	0.4	N/M	0	N/M	0	99.5
Eun Oh et al 2015	51.8	20	10.3	10.1	2	0.9	1	0.6	1.2	1.4	N/M	0.1	N/M	0	99.7
JUN ET AL 2014	63.2	19.1	8.3	4	1.2	0.7	1.2	0.4	1.1	0.3	N/M	N/M	N/M	0	99.5
JUN ET AL 2014	56	23.9	7.7	4.9	1.3	0.7	1.8	0.8	1.3	0.6	N/M	N/M	N/M	0	99
JUN ET AL 2014	62.2	22.8	6	3.1	1	0.6	1.6	0.6	1.3	0.3	N/M	N/M	N/M	0	99.5
JUN ET AL 2014	54.1	23.3	9.7	4.6	1.6	0.6	3	1.3	1	0.2	N/M	N/M	N/M	0	99.4
Gledhil et al 2011	29.7	14.7	14.8	25.4	3.6	1.8	0.8	0.6	1.1	0.2	0.9	5.1	N/M	0	99.7
Luo et al 2011	27.85	14.38	8.36	18.69	4.43	2.93	0.73	1.85	1.08	1.28	N/M	0.02	N/M	17.52	100
Luo et al 2011	35.31	20.24	7.43	24.11	4.96	1.43	0.56	1.78	1.43	1.3	N/M	0.03	N/M	0.32	100.02
Luo et al 2011	33.5	19.74	7.35	24.39	5.78	1.47	0.57	2.05	1.36	1.74	N/M	0.02	N/M	0.73	100
Luo et al 2011	39.43	19.07	7.44	21.48	4.41	1.05	0.68	1.39	1.37	1.11	N/M	0.02	N/M	1.57	99.99
Luo et al 2011	36.02	18.15	6.16	25.67	5.93	1.31	0.42	1.43	1.39	1.74	N/M	0.01	N/M	0.37	100
Brown et al 2011	44.72	24.3	6.1	1.57	1	0	2.38	0.8	0.85	0.72	N/M	0.07	N/M	N/M	82.51
Brown et al 2011	51.07	22.11	6.06	2.66	1.04	0	1.67	0.95	0.91	0.51	N/M	0.12	N/M	N/M	87.1
Brown et al 2011	44.27	26.14	6.29	1.54	1.31	0	2.62	0.77	1.02	1.03	N/M	0.09	N/M	N/M	85.08
Brown et al 2011	47.16	24.14	5.54	2.8	1.02	0	1.75	0.97	1.02	0.88	N/M	0.12	N/M	N/M	85.4
Brown et al 2011	52.31	25.31	6.96	3.63	2.43	0	2.78	1.02	1.07	0.43	N/M	0.11	N/M	N/M	96.05
Brown et al 2011	43.18	25.45	8.86	5.54	3.31	0	3.36	1.95	1.23	1.98	N/M	0.14	N/M	N/M	95
Brown et al 2011	45.07	22.54	7.42	5.34	3.31	0	2.99	1.91	1.21	1.81	N/M	0.17	N/M	N/M	91.77
Brown et al 2011	58.49	20.55	8.28	3.46	1.39	0	1.06	0.33	0.93	0.24	N/M	0.06	N/M	N/M	94.79
Brown et al 2011	54.59	25.26	7.35	4.93	0.82	0	0.34	0.11	1.06	0.14	N/M	0.06	N/M	N/M	94.66
Brown et al 2011	54.15	25.15	3.16	11.41	0.73	0	0.32	0.16	1.19	0.34	N/M	0.09	N/M	N/M	96.7
Moreano et al 2005	55.2	23.3	6.9	4	2.5	0.4	3.8	0.7	0.9	0.3	N/M	0.1	N/M	1.9	100
Moreano et al 2005	42.6	35.6	2.6	8.4	2.1	0.6	0.6	0.3	1.6	1.7	N/M	0.1	N/M	3.8	100
Moreano et al 2005	49.5	26.7	12.3	2.3	0.9	0.3	1.9	0.3	0.9	0.2	N/M	0.03	N/M	4.7	100.03
Moreano et al 2005	49.2	17.6	10.4	11.8	2	2.2	0.4	0.4	0.5	0.2	N/M	0.1	N/M	5.2	100
Moreano et al 2005	48.3	23.9	16	5.4	1	0.8	1.4	0.2	0.8	0.2	N/M	0.03	N/M	2	100.03
Moreano et al 2005	52.3	28.5	5.9	2	1.5	0.1	4	0.5	1	0.4	N/M	0.1	N/M	3.7	100
Moreano et al 2005	51.2	25.5	7.5	2.8	2	0.6	3.9	0.8	0.9	0.4	N/M	0.1	N/M	4.3	100
Moreano et al 2005	44.1	23.2	14.3	8.9	1.8	1.1	2.6	0.3	0.9	0.8	N/M	0.1	N/M	1.9	100
Moreano et al 2005	41.5	30.1	12.6	5.6	1.6	1.4	1.9	0.6	0.6	0.2	N/M	0.1	N/M	3.8	100
Moreano et al 2005	48.9	30.6	7.2	3	1.6	0.3	3.9	0.6	0.8	0.1	N/M	0.03	N/M	3	100.03

Table D.2: Raw data of fly ash particles used in the production of ternarys

Author	SiO(2)	Al(2)O(3)	Fe(2)O(3)	CaO	MgO	SO(3)	K(2)O	Na(2)O	TiO(2)	P(2)O(5)	NiO	MnO	Cr(2)O(3)	LOI	total
Moreano et al 2005	58.6	27.4	7.3	0.8	1	0.2	2.4	0.3	0.7	0.1	N/M	0.1	N/M	1.1	100
Moreano et al 2005	46.8	24.8	9	6.8	3.7	1	2	1.2	0.9	0.7	N/M	0.1	N/M	3	100
Moreano et al 2005	45.3	25	8.8	6.4	1.4	1.3	1.1	0.8	1.3	1	N/M	0.03	N/M	7.5	99.93
Moreano et al 2005	53.3	26.1	7.4	3.1	0.6	0.5	0.6	0.1	1.8	1.5	N/M	0.1	N/M	4.8	99.9
Moreano et al 2005	59.6	27	3.3	0.5	0.9	0.2	2.9	0.3	1.4	0.1	N/M	0.03	N/M	3.7	99.93
Moreano et al 2005	51.3	28.9	8.4	1.8	1	0.5	2.5	0.5	1.5	0.2	N/M	0.03	N/M	3.3	99.93
Moreano et al 2005	45.2	26.5	7.1	6.1	1.6	1.1	1.2	0.8	1.3	1.1	N/M	0.03	N/M	8.1	100.13
Moreano et al 2005	52.4	25.8	7	5.6	1.6	0.6	1.4	0.7	1.3	0.9	N/M	0.1	N/M	2.8	100.2
Moreano et al 2005	53.2	26	8.6	2.4	1.6	0.6	2.7	0.5	1.3	0.3	N/M	0.1	N/M	2.7	100
Moreano et al 2005	28.5	17.9	8.4	27.3	3.8	8.6	1	0.2	1	0.3	N/M	0.03	N/M	3	100.03
Moreano et al 2005	48.2	25.9	8.8	2.3	1.5	0.6	2.6	0.5	1.3	0.3	N/M	0.1	N/M	7.9	100
Moreano et al 2005	50.8	33.4	6.4	2.4	0.8	0.3	0.7	0.4	2.6	0.3	N/M	0.03	N/M	1.9	100.03
Moreano et al 2005	41.7	29	3.8	10	2.4	0.9	0.8	0.5	1.7	1.5	N/M	0.1	N/M	7.6	100
Moreano et al 2005	48	24	7	1.8	1.2	0.3	2.3	0.8	0.9	0	N/M	0	N/M	3.2	89.5
Moreano et al 2005	52	32	15	5.3	2.1	1.7	4.5	1.8	1.1	0	N/M	0	N/M	0	115.5
Moreano et al 2005	51.2	27	10.5	2	0.8	0.5	2.4	0.3	1.2	0.5	N/M	0	N/M	0	96.4
Moreano et al 2005	49.2	28.4	11.1	2.1	0.8	0.5	2.5	0.3	1.3	0.5	N/M	0.02	N/M	0	96.72
Medina et al 2010	59.6	22.82	5.57	3.11	0.87	0.4	1.28	0.45	0.94	0.04	N/M	N/M	N/M	0	95.08
Medina et al 2010	49.24	26.75	10.96	2.04	0.76	0.51	2.32	0.27	0.34	0.54	N/M	N/M	N/M	0	93.73
Vassilev et al 2003	51.8	25.9	8.3	3.8	2.7	2.1	3.7	0.9	0.9	0	N/M	N/M	N/M	0	100.1
Vassilev et al 2003	52.9	25.7	6.3	3.9	3.2	2.1	4	0.9	1	0	N/M	N/M	N/M	0	100
Vassilev et al 2003	50.5	30.7	6	4.3	1.8	2.1	1.7	1.3	1.6	0	N/M	N/M	N/M	0	100
Vassilev et al 2003	52.3	26.6	6.9	3.4	3	1.7	4	1.1	1	0	N/M	N/M	N/M	0	100
Vassilev et al 2003	53.6	25.6	7.3	4.1	2.5	1.4	3.5	1	0.9	0	N/M	N/M	N/M	0	99.9
Vassilev et al 2003	55.1	22	7.9	5.1	3	2.6	2.2	1.2	0.8	0	N/M	N/M	N/M	0	99.9
Vassilev et al 2003	52.8	26	8.5	4.2	2.7	0.5	3.6	0.8	0.9	0.4	N/M	N/M	N/M	0	100.4
Vassilev et al 2003	54.9	25.2	6.6	3.8	3.2	0.3	4	0.9	1.1	0.8	N/M	N/M	N/M	0	100.8
Vassilev et al 2003	52.8	27.5	6.6	4.4	2.9	0.7	2.7	1.1	1.2	0.8	N/M	N/M	N/M	0	100.7
Vassilev et al 2003	52.9	27.4	6.8	3.4	3	0.3	4	1.1	0.9	0.7	N/M	N/M	N/M	0	100.5
Vassilev et al 2003	52.1	27.8	7.3	4.2	2.7	0.5	3.5	0.8	1	0.8	N/M	N/M	N/M	0	100.7
Vassilev et al 2003 (b)	53.7	31.5	5.5	2	2.6	0.6	2.4	0.8	0.7	0.3	N/M	N/M	N/M		100.1
Vassilev et al 2003 (b)	53.5	29.9	3.2	6.3	2.4	0.3	3	0.6	0.7	0.1	N/M	N/M	N/M		100
Vassilev et al 2003 (b)	50.1	30.8	2.2	10.9	1.6	0.4	2.7	0.6	0.7	0.2	N/M	N/M	N/M		100.2

Table D.2: Raw data of fly ash particles used in the production of ternarys

Author	SiO(2)	Al(2)O(3)	Fe(2)O(3)	CaO	MgO	SO(3)	K(2)O	Na(2)O	TiO(2)	P(2)O(5)	NiO	MnO	Cr(2)O(3)	LOI	total
Vassilev et al 2003 (b)	56.4	31.6	3.4	0.7	2.5	0.7	2.7	1	0.7	0.3	N/M	N/M	N/M		100
Vassilev et al 2003 (b)	52.9	33.4	5.1	1.5	2.4	0.5	2.3	0.8	0.8	0.1	N/M	N/M	N/M		99.8
Vassilev et al 2003 (b)	51	29.8	4.7	6	3.2	1.1	2.3	0.8	0.7	0.6	N/M	N/M	N/M		100.2
Vassilev et al 2003 (b)	37.1	57	2.4	0.7	1	0.4	0.2	0.3	0.6	0.4	N/M	N/M	N/M		100.1
Vassilev et al 2003 (b)	55.6	25.4	7.2	3.4	3.6	1.1	1.7	1.1	0.8	0.2	N/M	N/M	N/M		100.1
Vassilev et al 2003 (c)	31.9	16.3	41	4	3.4	0.4	1.7	0.5	0.6	0.2	N/M	N/M	N/M		100
Vassilev et al 2003 (c)	32.2	16	41	3.4	3.8	0.2	1.8	0.5	0.6	0.4	N/M	N/M	N/M		99.9
Vassilev et al 2003 (c)	31.1	16.6	42.4	3.3	3.1	0.3	1.4	0.7	0.8	0.8	N/M	N/M	N/M		100.5
Vassilev et al 2003 (c)	39.7	20.6	28.7	3.2	3.2	0.2	2.6	0.8	0.7	0.8	N/M	N/M	N/M		100.5
Vassilev et al 2003 (c)	37	17.2	31.6	4.1	3.2	0.4	2.2	0.6	0.7	0.6	N/M	N/M	N/M		97.6
Vassilev et al 2003 (c)	50.2	30.5	6.2	3.3	2.6	2.3	2.3	1.1	0.8	0.6	N/M	N/M	N/M		99.9
Vassilev et al 2003 (c)	55.1	29.5	4.6	2.7	2.9	0.9	2.4	0.7	0.9	0.3	N/M	N/M	N/M		100
Vassilev et al 2003 (c)	49.4	29.7	4.8	5.2	2.7	3.3	1.8	0.9	1.2	0.9	N/M	N/M	N/M		99.9
Vassilev et al 2003 (c)	52.8	30.6	5.2	2.1	3.1	1.3	2.5	1	0.8	0.5	N/M	N/M	N/M		99.9
Vassilev et al 2003 (c)	50.9	31.9	6	2.9	2.7	1.1	2.2	0.9	0.9	0.6	N/M	N/M	N/M		100.1
Vassilev et al 2003 (d)	34.7	19	15.2	18.6	9.1	0.7	1.2	0.6	0.7	0.2	N/M	N/M	N/M		100
Vassilev et al 2003 (d)	45.1	22.1	14.2	7.5	6.5	0.4	1.9	0.8	1	0.6	N/M	N/M	N/M		100.1
Vassilev et al 2003 (d)	38.3	25.6	19.7	5.1	3.9	1	1.3	0.8	3.1	1.1	N/M	N/M	N/M		99.9
Vassilev et al 2003 (d)	42.1	22.2	12.7	10.6	7.4	0.5	1.8	0.8	0.9	1	N/M	N/M	N/M		100
Vassilev et al 2003 (d)	47.1	27.8	8.9	7	3.5	1.2	2.2	0.7	0.9	0.7	N/M	N/M	N/M		100
Vassilev et al 2003 (d)	53.3	26.3	7.2	4.5	2.4	0.3	4.1	0.8	1.1	0.3	N/M	N/M	N/M		100.3
Vassilev et al 2003 (d)	55.9	25.4	5.7	3.6	3.2	0.3	3.9	0.9	1.1	0.6	N/M	N/M	N/M		100.6
Vassilev et al 2003 (d)	53.4	27.5	6.4	4.2	3	0.4	2.6	1.1	1.3	1.1	N/M	N/M	N/M		101
Vassilev et al 2003 (d)	53.4	27.9	5.9	3.3	3.1	0.3	4	1.2	1	1	N/M	N/M	N/M		101.1
Vassilev et al 2003 (d)	54.3	26.1	7.1	4.3	2.4	0.4	3.5	0.7	1.1	1.1	N/M	N/M	N/M		101
Vassilev et al 2007	51.4	28.9	8.4	1.8	1	0.5	2.5	0.5	1.5	0.2	N/M	0.03	N/M	3.3	100.03
Vassilev et al 2007	46.8	24.8	9	6.8	3.7	1	2	1.2	0.9	0.7	N/M	0.1	N/M	3	100
Vassilev et al 2007	45.1	26.5	7.1	6.1	1.6	1.1	1.2	0.8	1.3	1.1	N/M	0.03	N/M	8.1	100.03
Vassilev et al 2007	52.2	25.8	7	5.6	1.6	0.6	1.4	0.7	1.3	0.9	N/M	0.1	N/M	2.8	100
Vassilev et al 2007	28.5	17.9	8.4	27.3	3.8	8.6	1	0.2	1	0.3	N/M	0.03	N/M	3	100.03
Vassilev et al 2007	51.1	26.4	6.5	3.3	2.9	0.3	3.9	1.1	0.9	0.7	N/M	0.04	N/M	2.9	100.04
Vassilev et al 2007	41.5	30.1	12.6	5.6	1.6	1.4	1.9	0.6	0.6	0.2	N/M	0.1	N/M	3.8	100
Vassilev et al 2007	57.3	24.8	7.6	1.9	2.1	0.4	2.5	1.4	1	0.1	N/M	0.06	N/M	0.8	99.96

Table D.2: Raw data of fly ash particles used in the production of ternarys

Author	SiO(2)	Al(2)O(3)	Fe(2)O(3)	CaO	MgO	SO(3)	K(2)O	Na(2)O	TiO(2)	P(2)O(5)	NiO	MnO	Cr(2)O(3)	LOI	total
Vassilev et al 2007	59.7	27	3.3	0.5	0.9	0.2	2.9	0.3	1.4	0.1	N/M	0.03	N/M	3.7	100.03
Vassilev et al 2007	51.2	25.5	7.5	2.8	2	0.6	3.9	0.8	0.9	0.4	N/M	0.1	N/M	4.3	100
Vassilev et al 2007	37	20.9	15.9	2.5	1.2	1.1	2.3	0.9	0.9	0.3	N/M	0.07	N/M	16.9	99.97
Vassilev et al 2007	49.5	26.7	12.3	2.3	0.9	0.3	1.9	0.3	0.9	0.2	N/M	0.03	N/M	4.7	100.03
Vassilev et al 2007	52.3	28.5	5.9	2	1.5	0.1	4	0.5	1	0.4	N/M	0.1	N/M	3.7	100
Vassilev et al 2007	48.2	25.9	8.8	2.3	1.5	0.6	2.6	0.5	1.3	0.3	N/M	0.1	N/M	7.9	100
Vassilev et al 2007	53.2	26	8.6	2.4	1.6	0.6	2.7	0.5	1.3	0.3	N/M	0.1	N/M	2.7	100
Vassilev et al 2007	36.1	12.5	5.1	28.9	2.4	8.4	1.1	0.4	0.6	0.2	N/M	0.16	N/M	4.1	99.96
Vassilev et al 2007	49.3	24.3	7.9	3.9	2.5	0.5	3.4	0.8	0.8	0.4	N/M	0.04	N/M	6.2	100.04
Vassilev et al 2007	44.1	23.2	14.3	8.9	1.8	1.1	2.6	0.3	0.9	0.8	N/M	0.1	N/M	1.9	100
Vassilev et al 2007	42.6	35.6	2.6	8.4	2.1	0.6	0.6	0.3	1.6	1.7	N/M	0.1	N/M	3.8	100
Vassilev et al 2007	30.1	12.6	11	24.8	2	12.7	0.8	0.9	0.6	0.4	N/M	0.23	N/M	3.9	100.03
Vassilev et al 2007	45.3	22.8	13.8	8.2	2.8	2.6	0.9	1.1	0.6	0.1	N/M	0.11	N/M	1.7	100.01
Vassilev et al 2007	38.4	18.9	21.2	7.2	2.9	4.9	1	1.9	1	0.1	N/M	0.08	N/M	2.4	99.98
Vassilev et al 2007	44.4	22.9	12.4	9	2.6	3.3	0.9	0.8	0.9	0.1	N/M	0.07	N/M	2.6	99.97
Vassilev et al 2007	49.2	17.6	10.4	11.8	2	2.2	0.4	0.4	0.5	0.2	N/M	0.1	N/M	5.2	100
Vassilev et al 2007	50.8	33.4	6.4	2.4	0.8	0.3	0.7	0.4	2.6	0.3	N/M	0.03	N/M	1.9	100.03
Vassilev et al 2007	53.6	24.7	6.4	3.8	3.2	0.3	3.9	0.9	1.1	0.8	N/M	0.05	N/M	1.2	99.95
Vassilev et al 2007	47.3	24.6	5.9	4	2.6	0.6	2.4	1	1.1	0.7	N/M	0.05	N/M	9.7	99.95
Vassilev et al 2007	55.2	23.3	6.9	4	2.5	0.4	3.8	0.7	0.9	0.3	N/M	0.1	N/M	1.9	100
Vassilev et al 2007	53.3	26.2	7.4	3.1	0.6	0.5	0.6	0.1	1.8	1.5	N/M	0.1	N/M	4.8	100
Vassilev et al 2007	45.4	25	8.8	6.4	1.4	1.3	1.1	0.8	1.3	1	N/M	0.03	N/M	7.5	100.03
Vassilev et al 2007	58.6	27.4	7.3	0.8	1	0.2	2.4	0.3	0.7	0.1	N/M	0.1	N/M	1.1	100
Vassilev et al 2007	57.4	25.4	6	1.5	1.8	0.9	2.3	0.5	0.6	0.1	N/M	0.04	N/M	3.5	100.04
Vassilev et al 2007	35.6	18.3	13.3	2.7	1.1	0.8	2.2	0.7	0.9	0.1	N/M	0.06	N/M	24.2	99.96
Vassilev et al 2007	41.7	29	3.8	10	2.4	0.9	0.8	0.5	1.7	1.5	N/M	0.1	N/M	7.6	100
Vassilev et al 2007	37.9	20.5	4.7	27.9	1.8	1.9	1.3	0.3	0.7	0.3	N/M	0.04	N/M	2.7	100.04
Vassilev et al 2007	44.1	23.8	4.1	19.1	1.4	3	1.3	0.4	0.8	0.2	N/M	0.03	N/M	1.8	100.03
Vassilev et al 2007	49.5	26.4	6.9	3.9	2.6	0.5	3.3	0.8	1	0.8	N/M	0.04	N/M	4.3	100.04
Vassilev et al 2007	48.9	30.6	7.2	3	1.6	0.3	3.9	0.6	0.8	0.1	N/M	0.03	N/M	3	100.03
Vassilev et al 2007	46.7	19.7	15.7	3.9	1.2	1.5	2.8	0.9	1	0.1	N/M	0.06	N/M	6.4	99.96
Vassilev et al 2007	48.3	23.9	16	5.4	1	0.8	1.4	0.2	0.8	0.2	N/M	0.03	N/M	2	100.03
Vassilev et al 2007	33.3	16.6	7.8	2.2	1.6	1.3	2.6	0.8	0.7	0.2	N/M	0.09	N/M	32.8	99.99

Table D.2: Raw data of fly ash particles used in the production of ternarys

Author	SiO(2)	Al(2)O(3)	Fe(2)O(3)	CaO	MgO	SO(3)	K(2)O	Na(2)O	TiO(2)	P(2)O(5)	NiO	MnO	Cr(2)O(3)	LOI	total
Saker et al 2005	39.57	22.13	3.21	0.42	0.19	1.45	0.93	0.13	2.08	0.24	N/M	N/M	N/M	29.8	100.15
Saker et al 2005	43.61	23.97	4.56	0.43	0.23	0.93	1	0.14	2.06	0.23	N/M	N/M	N/M	21.3	98.46
Saker et al 2005	50.37	25.91	5.32	0.49	0.26	0.55	0.96	0.14	2.08	0.27	N/M	N/M	N/M	14.63	100.98
Saker et al 2005	51.94	26.41	5.21	0.49	0.27	0.5	0.95	0.16	2.09	0.28	N/M	N/M	N/M	9.67	97.97
Saker et al 2005	55.4	26.77	5.03	0.54	0.29	0.39	0.97	0.15	2.24	0.32	N/M	N/M	N/M	6.88	98.98
Kiattikamol et al 2001	46.25	26.43	10.71	7.61	2.21	1.85	3.07	1.11	N/M	N/M	N/M	N/M	N/M	0.23	99.47
Kiattikamol et al 2001	45.02	36.21	4.09	3.64	0.54	0.48	0.31	0.44	N/M	N/M	N/M	N/M	N/M	5.32	96.05
Kiattikamol et al 2001	43.92	36.62	3.97	3.05	0.55	0.64	0.44	0.38	N/M	N/M	N/M	N/M	N/M	7.52	97.09
Kiattikamol et al 2001	47.39	22.73	6.29	8.36	2.64	3.38	2.95	0.63	N/M	N/M	N/M	N/M	N/M	3.12	97.49
Kiattikamol et al 2001	49.04	37.91	2.75	1.03	0.39	0.18	0.52	0.38	N/M	N/M	N/M	N/M	N/M	4.7	96.9

Table D.3: Raw data of volcanic ash particles used in the production of ternarys

	SiO(2)	Al(2)O(3)	Fe(2)O(3)	CaO	MgO	SO(3)	K(2)O	Na(2)O	TiO(2)	P(2)O(5)	NiO	MnO	Cr(2)O(3)	LOI	total
Schipper 2011	46.3	8.66	11.4	8.13	18.7	0	0.52	1.24	1.97	0.06		0.17		0.06	97.21
Schipper 2011	45.7	8.15	11.7	7.64	20.6	0	0.48	1.09	1.85	0.06		0.17		? 0.21	97.44
Schipper 2011	45.3	7.95	11.8	7.48	21.4	0	0.48	1.07	1.81	0.2		0.17		? 0.17	97.66
Schipper 2011	45.2	7.49	11.7	7.02	22.6	0	0.45	0.94	1.7	0.07		0.17		? 0.29	97.34
Lautze 2006	44.79	15.83	14.42	8.59	2.55	1.6	2.62	5.99	1.66	1.26		0			99.31
Lautze 2006	42.51	14.66	16.38	10.62	3.63	1.09	2.25	4.96	1.95	0.95		0			99
Lautze 2006	39.01	13	20.46	10.96	4.44	1.79	2.66	3.59	2.02	0.81		0			98.74
Lautze 2006	44.07	14.73	14.68	10.3	3.72	1.58	2.56	5.06	2.47	0.29		0			99.46
Lautze 2006	44.19	14.45	14.43	10.63	3.8	0.93	3.02	5.12	1.89	0.94		0			99.4
Lautze 2006	44.84	14.58	13.94	10.87	4.01	1.28	3.09	4.79	2	0.48		0			99.88
Lautze 2006	43.75	15.68	15.49	10.21	3.24	0.73	3.08	4.55	1.92	1.19		0			99.84
Lautze 2006	43.04	14.94	15.23	10.31	3.72	0.78	3.23	5.1	1.89	1.21		0			99.45
Lautze 2006	36.81	12.07	24.32	9.59	3.23	1.74	2.87	4.32	3.36	0.71		0			99.02
Lautze 2006	39.64	13.12	21.54	9.09	3.9	1.48	2.68	4.03	2.89	0.66		0			99.03
Lautze 2006	41.53	14.05	18.17	9.47	3.95	0.63	2.84	4.7	2.89	0.95		0			99.18
Lautze 2006	39.62	14.46	20.91	9.36	3.45	0.91	2.56	4.66	2.31	0.67		0			98.91
Lautze 2006	45.14	18.67	12.46	9.15	2.5	1.26	2.67	4.88	1.58	0.86		0			99.17
Lautze 2006	43.85	16.41	13.62	10.45	2.91	1	2.64	5.06	1.99	1.15		0			99.08
Lautze 2006	43.59	15.75	14.05	10.89	3.01	1.38	2.98	4.99	1.7	1.15		0			99.49
Lautze 2006	43.43	16.8	13.77	10.46	2.62	1.04	2.67	5.44	1.93	1.13		0			99.29
Lautze 2006	47.85	15.93	11.45	9.25	3.31	0.35	3.49	5.12	1.79	1.16		0			99.7
Lautze 2006	48.13	16.24	10.46	9	3.56	0.6	2.8	5.69	1.53	1.25		0			99.26
Lautze 2006	45.64	16.37	12.15	9.42	3.57	0.84	2.66	5.13	2.39	1.05		0			99.22
Lautze 2006	45.53	15.75	13.26	9.45	2.79	1.14	3.5	4.92	2.03	1.47		0			99.84
Bedia 2004	62.48	16.14	0.55	5.2	3.25	0	1.68	4.99	0.65	0		0		1.68	96.62
Hopper 1980	64.21	17.2	4.74	5.07	1.85	0	1.52	4.47	0.7	0.19		0.07			100.02
Hopper 1980	66.98	16.41	3.95	4.12	1.41	0	1.75	4.59	0.59	0.17		0.06			100.03
Hopper 1980	68.2	16.15	3.56	3.7	1.22	0	1.85	4.57	0.53	0.15		0.05			99.98
Hopper 1980	76.15	13.5	1.43	1.22	0	0	3.02	4.05	0	0		0			99.37
Hopper 1980	72.2	15.4	2.51	2.48	0.98	0	1.99	3.88	0.45	0		0.04			99.93
Fruchter 1980	64.6	18	5.24	5.14	2.7	0	1.31	4.57	0.7	0.23		0.093		0.51	103.093
Fruchter 1980	59.4	17.4	6.64	6.57	4.1	0	0.88	4.35	0.88	0.27		0.12		0.56	101.17
Fruchter 1980	63.3	17.4	5.59	5.74	2.8	0	1.25	4.49	1.25	0.33		0.092		0.62	102.862

Table D.3: Raw data of volcanic ash particles used in the production of ternarys

	SiO(2)	Al(2)O(3)	Fe(2)O(3)	CaO	MgO	SO(3)	K(2)O	Na(2)O	TiO(2)	P(2)O(5)	NiO	MnO	Cr(2)O(3)	LOI	total
Fruchter 1980	60.3	16.4	5.61	5.55	2.77	0	1.56	4.83	1.56	0.46		0.087		0.56	99.687
Fruchter 1980	66.9	17.1	4.99	4.74	1.84	0	1.55	4.56	1.55	0.32		0.077		0.35	103.977
Fruchter 1980	68.2	17.2	4.22	4.77	1.61	0	1.6	4.42	1.6	0.37		0.067		0.56	104.617
Fruchter 1980	66.9	16.1	3.69	3.71	1.28	0	1.75	4.85	1.75	0.39		0.063		0.55	101.033
Fruchter 1980	68.2	16.2	3.56	4	1.33	0	1.69	4.52	1.69	0.48		0.063		0.56	102.293
Fruchter 1980	67.2	16.3	3.76	4.2	1.48	0	1.66	4.52	1.66	0.37		0.064		0.78	101.994
Quanshu 2008	62.1	15.6	6.21	5.96	1.39	0	2.45	4.54	0.78	0.98		0			100.01
Quanshu 2008	60.86	15.65	7.86	5.85	2.4	0	2.19	3.88	0.7	0.6		0			99.99
Quanshu 2008	78.78	13.15	1.84	1.07	0.32	0	2.63	2.19	0.02	0		0			100
Quanshu 2008	56.74	15.45	8.98	7.62	3.86	0	1.38	4.21	1.04	0.72		0			100
Quanshu 2008	74.87	13.73	3.25	2.01	0.55	0	2.61	2.19	0.61	0.18		0			100
Quanshu 2008	67.63	16.38	4.12	3.76	0	0	2.61	4.06	1.09	0.33		0			99.98
Quanshu 2008	59.32	15.8	7.77	6.22	2.92	0	1.93	5.01	0.78	0.22		0			99.97
Quanshu 2008	79.94	11.93	1.08	1.09	0	0	3.16	2.71	0.1	0		0			100.01
Quanshu 2008	57.3	20.45	7.66	3.04	1.2	0	4.2	4.25	1.71	0		0.18			99.99
Wallrabe-adams 2002	71.25	13.97	3.83	1.32	0.22	0	3.69	2.9	0.31	0.05		0.17			97.71
Wallrabe-adams 2002	70.66	13.72	4.44	1.6	0.29	0	3.25	5.56	0.48	0		0.18			100.18
Wallrabe-adams 2002	75.63	11.89	2.79	1.55	0.03	0	1.28	1.97	0.22	0.03		0.12			95.51
Wallrabe-adams 2002	74.09	10.9	2.56	1.59	0.03	0	1.79	3.56	0.22	0.03		0.17			94.94
Wallrabe-adams 2002	75.39	11.78	2.81	1.46	0.02	0	1.28	1.98	0.21	0.04		0.12			95.09
Wallrabe-adams 2002	75.13	11.59	2.74	1.53	0.02	0	1.41	2.39	0.22	0.03		0.13			95.19
Wallrabe-adams 2002	71.05	10.88	3.49	0.41	0.04	0	3.66	4.28	0.3	0.02		0.25			94.38
Wallrabe-adams 2002	71.05	10.92	3.46	0.52	0.03	0	3.57	4.27	0.32	0.02		0.26			94.42
Wallrabe-adams 2002	71.88	11.63	2.77	1.31	0.1	0	2.65	3.67	0.19	0.03		0.16			94.39
Wallrabe-adams 2002	71.01	11.92	3.14	1.78	0.1	0	2.18	3.65	0.23	0.03		0.22			94.26
Wallrabe-adams 2002	71.28	11.33	3.2	0.99	0.07	0	3.03	3.96	0.26	0.02		0.22			94.36
Wallrabe-adams 2002	72.04	11.44	2.84	1.23	0.08	0	2.71	3.74	0.2	0.03		0.21			94.52
Wallrabe-adams 2002	71.98	11.63	2.72	1.3	0.09	0	2.61	3.58	0.21	0.04		0.17			94.33
Wallrabe-adams 2002	72.52	12.26	2.95	1.22	0.07	0	1.9	2.17	0.21	0.03		0.11			93.44
Wallrabe-adams 2002	72.25	11.92	2.81	1.26	0.08	0	2.28	2.93	0.21	0.03		0.15			93.92
Lackschewitz 1996	51.07	14.03	11.79	11.71	6.8	0	0.09	2.16	1.52	0		0.21			99.38
Lackschewitz 1996	50.58	13.91	11.95	11.45	7.33	0	0.08	2.21	1.42	0		0.21			99.14
Lackschewitz 1996	71.72	13.84	3.71	1.35	0.19	0.06	3.45	4.57	0.26	0		0.15			99.3

Table D.3: Raw data of volcanic ash particles used in the production of ternarys

	SiO(2)	Al(2)O(3)	Fe(2)O(3)	CaO	MgO	SO(3)	K(2)O	Na(2)O	TiO(2)	P(2)O(5)	NiO	MnO	Cr(2)O(3)	LOI	total
Lackschewitz 1996	49.58	14.62	11.65	11.6	6.8	0.17	0.29	2.3	1.94	0.14		0.21			99.3
Lackschewitz 1996	74.42	12.51	2.76	0.51	0.01	0.02	3.78	4.4	0.19	0		0.07			98.67
Lackschewitz 1996	49.01	13.83	13.02	10.48	5.89	0.2	0.46	2.59	2.93	0.65		0.25			99.31
Lackschewitz 1996	49.72	12.81	13.58	9.24	4.52	0.2	0.55	2.85	3.39	0.29		0.25			97.4
Lackschewitz 1996	49.85	13.88	12.39	10.66	5.96	0.19	0.4	2.49	2.51	0.26		0.22			98.81
Lackschewitz 1996	49.83	13.92	12.1	11.1	6.24	0.18	0.33	2.42	2.33	0		0.23			98.68
Lackschewitz 1996	50.34	14.12	11.78	11.1	6.41	0.17	0.33	2.37	2.13	0		0.22			98.97
Lackschewitz 1996	49.7	14.43	11.5	11.9	7.36	0.12	0.23	2.08	1.75	0.19		0.22			99.48
Lackschewitz 1996	49.47	13.68	12.49	10.65	5.84	0.19	0.39	2.61	2.65	0.13		0.21			98.31
Leike 2013	62.3	17.7	9.9	0.7	3	0	3.3	2.2	1.1	0		0			100.2
Leike 2013	48.8	13.5	15.2	8.9	5.7	0	0.5	4.1	3.4	0		0			100.1
Leike 2013	48.3	14.4	14.6	9.1	6.5	0	0.4	3.8	2.8	0		0			99.9
Leike 2013	45.5	31.9	5.1	1.8	1.5	0	6.9	6.8	0.5	0		0			100
Leike 2013	38.4	16.7	22.1	0.2	13.2	0	5.9	0.8	2.8	0		0			100.1
Olawuyi	41.13	18.36	11.5	6.57	4.24	0.13	1.12	1.29	3.56	1		0.29		8.3	97.49
Gislason 2011	57.98	14.87	9.75	5.5	2.3	0	1.79	5.01	1.8	0.53		0.24			99.77
Gislason 2011	56.73	14.65	9.93	6.11	3.15	0	1.64	5.04	1.88	0.43		0.24			99.8
Mascarenhas-Pereira 2006	78	12	0.8	0.71	0.04	0	5.03	3.18	0.06	0		0			99.82
Mascarenhas-Pereira 2006	51	15	11	7.65	3.76	0	1.86	4.32	3.35	0		0			97.94
Mascarenhas-Pereira 2006	73	14	2.42	0.47	0.28	0	5.23	3.92	0.53	0		0			99.85
Mascarenhas-Pereira 2006	77	12	2.27	0.21	0.13	0	4.77	3.54	0.38	0		0			100.3
Mascarenhas-Pereira 2006	49	14	11	12.2	7.66	0	0.18	2.1	1.6	0.13		0			97.87
Mascarenhas-Pereira 2006	51	17	7.8	10	8.73	0	0.25	3.91	1.08	0		0			99.77
Mascarenhas-Pereira 2006	50.1	13	14.6	9.14	4.67	0	0.89	2.32	3.52	0.42		0			98.66
Mascarenhas-Pereira 2006	69.6	14.2	2.9	2.5	1.4	0	2.3	4.7	0.49	0.12		0			98.21
Mascarenhas-Pereira 2006	69.7	13.8	2.7	1.8	1.3	0	2.2	4.7	0.45	0.12		0			96.77
Mascarenhas-Pereira 2006	71.8	14.7	3.03	2.47	0.66	0	2.5	4.22	0.41	0		0			99.79
Mascarenhas-Pereira 2006	75.3	12.3	0.9	0.64	0	0	4.47	4.45	0.07	0		0			98.13
Mascarenhas-Pereira 2006	75.4	12.7	0.65	0.55	0	0	3.9	5.55	0.09	0		0			98.84
Mascarenhas-Pereira 2006	76	12	0.93	0.68	0	0	4.76	3.86	0.07	0		0			98.3
Mascarenhas-Pereira 2006	76.3	12.2	0.91	0.66	0	0	4.61	3.37	0.05	0		0			98.1
Mascarenhas-Pereira 2006	75.3	12.5	0.7	0.57	0	0	4.33	4.76	0	0		0			98.16
Mascarenhas-Pereira 2006	76.3	11.8	0.8	0.6	0	0	4.7	3.7	0.1	0		0			98

Table D.3: Raw data of volcanic ash particles used in the production of ternarys

	SiO(2)	Al(2)O(3)	Fe(2)O(3)	CaO	MgO	SO(3)	K(2)O	Na(2)O	TiO(2)	P(2)O(5)	NiO	MnO	Cr(2)O(3)	LOI	total
Mascarenhas-Pereira 2006	74.7	11.8	0.85	0.53	0	0	4.46	5.75	0.1	0		0			98.19
Mascarenhas-Pereira 2006	73.9	12.4	0.72	0.62	0	0	4.17	6.35	0.04	0		0			98.2
Mascarenhas-Pereira 2006	75.6	11.2	1.26	0.78	0	0	6	2.36	0.13	0		0			97.33
Mascarenhas-Pereira 2006	74.8	12.1	0.9	0.74	0	0	4.52	5.01	0.07	0		0			98.14
Mascarenhas-Pereira 2006	75.1	11.6	0.89	0.64	0	0	5.01	4.63	0.05	0		0			97.92
Mascarenhas-Pereira 2006	74.8	12	0.81	0.55	0	0	4.6	5.57	0.07	0		0			98.4
Mascarenhas-Pereira 2006	75	11.1	1.2	0.8	0	0	5.6	3.6	0	0		0			97.3
Mascarenhas-Pereira 2006	74.3	12.3	0.7	0.62	0	0	4.38	6.13	0.12	0		0			98.55
Mastin 2004	49.41	12.39	11.67	10.26	9.54	0.078	0.41	1.99	2.20	0.20		0.17			98.314
Mastin 2004	50.65	13.56	11.03	10.92	7.26	0.101	0.43	2.17	2.48	0.22		0.16			98.98033333
Mastin 2004	50.98	13.45	11.15	11.14	7.82	0.111	0.44	2.02	2.51	0.27		0.14			100.011
Mastin 2004	50.72	13.15	11.26	10.54	9.45	0.093	0.47	1.78	2.45	0.25		0.16			100.315
Mastin 2004	50.22	12.76	11.48	10.34	9.84	0.084	0.47	1.78	2.38	0.25		0.16			99.76875
Mastin 2004	50.28	12.80	11.62	10.51	9.43	0.079	0.44	1.60	2.37	0.23		0.16			99.53
Mastin 2004	50.22	12.68	11.26	10.40	9.47	0.098	0.45	2.10	2.29	0.22		0.16			99.34775
Mastin 2004	50.70	12.83	11.27	10.46	9.43	0.081	0.46	2.15	2.36	0.23		0.17			100.14075
Mastin 2004	50.71	12.79	11.35	10.65	9.31	0.085	0.45	2.12	2.31	0.25		0.19			100.2105
Mastin 2004	50.58	13.02	11.45	10.74	9.29	0.087	0.47	2.18	2.40	0.23		0.14			100.5905
Mastin 2004	51.01	13.43	11.34	11.22	8.01	0.066	0.46	2.22	2.49	0.24		0.15			100.6345
Mastin 2004	50.63	12.76	11.34	10.57	9.58	0.085	0.45	2.19	2.38	0.24		0.16			100.381
Mastin 2004	56.65	12.15	15.40	7.11	2.46	0.073	1.38	2.99	2.80	0.83		0.20			102.04
Mastin 2004	50.77	12.80	11.65	10.77	9.22	0.075	0.41	2.11	2.25	0.22		0.15			100.4225
Mastin 2004	51.33	13.59	12.09	10.68	5.59	0.055	0.53	2.38	2.88	0.28		0.18			99.56675
Mastin 2004	51.40	13.38	12.06	10.68	5.69	0.052	0.51	2.36	2.88	0.26		0.17			99.449
Mastin 2004	51.07	13.41	11.04	10.78	7.78	0.079	0.42	2.17	2.43	0.24		0.16			99.569
Mastin 2004	50.14	13.16	10.78	10.71	7.69	0.127	0.46	2.23	2.32	0.21		0.17			97.98825
Mastin 2004	51.22	13.28	11.46	10.81	8.18	0.08	0.44	2.13	2.40	0.21		0.14			100.345
Mastin 2004	51.22	13.42	11.43	10.83	8.09	0.086	0.45	2.16	2.32	0.22		0.17			100.39225
Mastin 2004	50.58	12.50	11.58	10.28	10.11	0.061	0.39	2.05	2.21	0.22		0.18			100.1445
Mastin 2004	50.71	12.55	11.69	10.31	10.27	0.060	0.38	2.06	2.22	0.21		0.17			100.61675
Mastin 2004	50.72	12.85	11.69	10.59	9.36	0.040	0.43	2.05	2.18	0.22		0.15			100.274
Mastin 2004	51.20	13.35	11.35	10.81	8.33	0.050	0.42	2.13	2.42	0.22		0.17			100.4535
Mastin 2004	51.30	13.45	11.08	11.07	7.99	0.067	0.42	2.16	2.39	0.22		0.17			100.31025

Table D.3: Raw data of volcanic ash particles used in the production of ternarys

	SiO(2)	Al(2)O(3)	Fe(2)O(3)	CaO	MgO	SO(3)	K(2)O	Na(2)O	TiO(2)	P(2)O(5)	NiO	MnO	Cr(2)O(3)	LOI	total
Mastin 2004	50.36	12.71	11.56	10.48	9.51	0.078	0.43	2.09	2.23	0.21		0.16			99.81075
Mastin 2004	50.80	13.43	11.45	10.83	7.87	0.128	0.37	2.28	2.21	0.21		0.18			99.76275
Mastin 2004	51.29	13.62	11.11	10.95	7.65	0.120	0.50	2.17	2.45	0.24		0.17			100.26075
Mastin 2004	50.99	13.63	11.23	11.00	7.42	0.085	0.45	2.24	2.41	0.23		0.17			99.8605
Mastin 2004	50.86	13.63	11.13	10.97	7.40	0.084	0.44	2.20	2.40	0.21		0.15			99.47725
Mastin 2004	51.17	13.34	11.35	10.75	8.15	0.069	0.45	2.20	2.29	0.21		0.17			100.1545
Mastin 2004	51.08	13.44	11.45	10.92	7.79	0.158	0.44	2.20	2.38	0.21		0.16			100.2375
Mastin 2004	50.37	12.82	11.89	10.59	8.06	0.296	0.42	2.10	2.29	0.26		0.15			99.2525
Mastin 2004	50.45	12.46	12.11	10.52	10.32	0.079	0.42	2.02	2.18	0.20		0.16			100.9
Mastin 2004	50.97	13.28	11.29	10.81	8.21	0.076	0.42	2.13	2.52	0.23		0.13			100.05
Mastin 2004	50.76	13.39	11.43	10.90	8.04	0.088	0.43	2.12	2.36	0.23		0.15			99.8975
Mastin 2004	51.40	13.45	11.41	10.87	8.13	0.095	0.43	1.86	2.34	0.24		0.16			100.375
Mastin 2004	51.18	13.42	11.45	10.79	8.16	0.108	0.41	1.81	2.38	0.24		0.15			100.1055
Mastin 2004	50.81	13.07	11.73	10.64	8.84	0.110	0.40	1.78	2.29	0.21		0.15			100.045
Mastin 2004	50.76	13.28	11.50	10.76	8.26	0.085	0.41	1.98	2.37	0.23		0.16			99.786
Mastin 2004	50.38	13.23	11.11	11.21	8.75	0.027	0.53	2.00	2.61	0.28		0.17			100.281
Mastin 2004	50.63	13.60	11.07	11.44	8.10	0.012	0.57	2.10	2.65	0.26		0.15			100.582
Mastin 2004	50.46	13.72	11.25	11.57	7.22	0.038	0.58	1.91	2.72	0.30		0.17			99.92866667
Mastin 2004	49.87	12.54	11.50	11.37	9.31	0.037	0.48	1.84	2.47	0.25		0.17			99.83266667
Mastin 2004	51.28	13.67	11.00	11.25	7.29	0.060	0.47	2.20	2.46	0.24		0.15			100.051
Mastin 2004	51.39	13.71	11.08	11.34	7.18	0.053	0.47	2.09	2.47	0.24		0.16			100.178
Mastin 2004	51.44	13.71	11.07	11.37	7.32	0.063	0.48	2.11	2.47	0.25		0.18			100.46
Mastin 2004	50.01	12.54	11.32	11.32	9.45	0.042	0.51	1.92	2.49	0.25		0.16			100.0236667
Mastin 2004	51.54	13.69	10.93	11.26	7.19	0.037	0.49	2.25	2.49	0.25		0.16			100.29625
Mastin 2004	49.4	14.2	13	10.4	8.2		0.37	1.82	2.51	0.25		0			100.15
Mastin 2004	50.6	13.8	12.5	11	7.55		0.38	2.04	2.47	0.24		0			100.58
Mastin 2004	50.7	12.9	12.6	10.6	9.65		0.38	2.02	2.36	0.22		0			101.43
Mastin 2004	48	14.7	13	10.2	7.85		0.36	1.44	2.51	0.24		0			98.3
Mastin 2004	48.6	12.8	12.9	10.5	8.16		0.46	2.07	2.75	0.3		0			98.54
Mastin 2004	48.9	13.4	12.9	10.7	7.91		0.44	2.13	2.7	0.3		0			99.38
Mastin 2004	49.2	12	13.2	9.71	11.5		0.33	1.94	2.17	0.21		0			100.26
Mastin 2004	49.2	12.3	14.1	10.2	10.2		0.4	2.1	2.26	0.23		0			100.99
Mastin 2004	50.1	12.8	13.7	10.7	9.34		0.42	2.16	2.38	0.23		0			101.83

Table D.3: Raw data of volcanic ash particles used in the production of ternarys

	SiO(2)	Al(2)O(3)	Fe(2)O(3)	CaO	MgO	SO(3)	K(2)O	Na(2)O	TiO(2)	P(2)O(5)	NiO	MnO	Cr(2)O(3)	LOI	total
Mastin 2004	51.1	13.8	13	10.7	7.3		0.48	1.66	2.65	0.28		0			100.97
Mastin 2004	50.1	12.8	12.6	10.5	9.99		0.41	2.09	2.34	0.22		0			101.05
Mastin 2004	50.4	12.9	12.6	10.8	8.89		0.41	2.12	2.45	0.23		0			100.8
Mastin 2004	50.3	12.8	12.7	10.6	9.61		0.4	2.14	2.38	0.23		0			101.16
Mastin 2004	50.4	13	12.6	10.8	8.81		0.42	2.15	2.46	0.24		0			100.88
Mastin 2004	50.3	12.6	12.8	10.6	9.75		0.39	2.01	2.36	0.22		0			101.03
Mastin 2004	48.6	13.8	12.8	11.2	6.63		0.71	2.45	3.2	0.39		0			99.78
Mastin 2004	49.4	12.7	12.8	11.5	6.82		0.72	2.53	3.16	0.35		0			99.98
Mastin 2004	49.8	13	11.4	10.1	9.29		0.37	2.02	2.22	0.22		0			98.42
Mastin 2004	49.3	11.9	11.4	9.31	12.5		0.35	1.77	2.03	0.2		0			98.76
Mastin 2004	50.2	13	10.6	9.85	9.95		0.38	2.01	2.34	0.26		0			98.59
Mastin 2004	48.3	10.9	11.8	8.6	14.8		0.32	1.62	1.88	0.19		0			98.41
Mastin 2004	49.6	12.5	11	9.89	10.7		0.36	1.95	2.15	0.24		0			98.39
Mastin 2004	49.3	12.3	11.3	9.46	11.8		0.34	1.81	2.14	0.23		0			98.68
Mastin 2004	49.1	11.4	11.2	9.08	12.9		0.3	1.75	1.94	0.19		0			97.86
Mastin 2004	48.4	11	11.1	8.67	14.7		0.32	1.71	1.95	0.18		0			98.03
Mastin 2004	49	11.9	11.3	8.91	13		0.28	1.92	1.91	0.18		0			98.4
Mastin 2004	49.3	11.9	11.4	8.97	12.5		0.3	1.93	1.94	0.18		0			98.42
Mastin 2004	48.5	11	11.3	9.11	14.7		0.32	1.77	1.94	0.18		0			98.82
Mastin 2004	49	11.4	11.2	9.53	13		0.33	1.82	2.06	0.19		0			98.53
Mastin 2004	51.3	14.2	9.36	11.1	7.05		0.44	2.28	2.66	0.29		0			98.68
Mastin 2004	50.4	12.4	10.8	10	11		0.36	1.86	2.25	0.2		0			99.27
Mastin 2004	49.5	12	11.2	9.44	12.5		0.33	1.77	2.09	0.21		0			99.04
Mastin 2004	49.3	12	11.1	9.98	11.5		0.34	1.85	2.13	0.21		0			98.41
Mastin 2004	48.2	11.3	12.3	9.47	12.3		0.31	1.78	2.05	0.21		0			97.92
Mastin 2004	49	12.2	12.3	9.98	10.8		0.35	1.96	2.3	0.23		0			99.12
Mastin 2004	48.9	12.1	11.1	9.88	11.5		0.35	1.89	2.21	0.21		0			98.14
Mastin 2004	49.1	11.7	11.2	9.78	12.7		0.33	1.77	2.06	0.19		0			98.83
Mastin 2004	49.6	11.9	11.2	9.42	12.5		0.34	1.79	2.16	0.19		0			99.1
Mastin 2004	48.8	11.4	11.1	8.85	14.6		0.31	1.71	1.97	0.19		0			98.93
Mastin 2004	48.9	10.8	11.2	8.91	15		0.31	1.71	1.96	0.18		0			98.97
Mastin 2004	48.7	11.4	11.1	8.85	14.6		0.31	1.73	2.01	0.2		0			98.9
Mastin 2004	51.5	13.4	8.85	10.6	9.7		0.36	2.03	2.27	0.23		0			98.94

Table D.3: Raw data of volcanic ash particles used in the production of ternarys

	SiO(2)	Al(2)O(3)	Fe(2)O(3)	CaO	MgO	SO(3)	K(2)O	Na(2)O	TiO(2)	P(2)O(5)	NiO	MnO	Cr(2)O(3)	LOI	total
Mastin 2004	48.5	11.3	12.6	8.94	13.2		0.3	1.65	1.91	0.2		0			98.6
Mastin 2004	51.3	13.3	12.8	9.4	5.44		0.54	2.55	3.27	0.29		0			98.89
Mastin 2004	59.2	11.3	14	5.65	0.98		2.2	2.11	1.5	1.47		0			98.41
Mastin 2004	49.1	11.7	11.2	9.53	12.8		0.33	1.82	2.02	0.18		0			98.68
Mastin 2004	48.7	13.6	11.8	11	7.7		0.55	2.26	2.93	0.28		0			98.82
Ukskins 2003	67.72	15.88	3.83	1.27	0.76		4.61	4.81	0.88			0.24			100
Ukskins 2003	70.42	14.75	3.03	0.84	0.53		5.04	4.47	0.73			0.21			100.02
Ukskins 2003	71.74	14.31	2.46	0.51	0.32		6.15	3.82	0.53			0.16			100
Ukskins 2003	73.23	13.74	2.42	0.47	0.28		5.23	3.92	0.53			0.18			100
Ukskins 2003	70.93	12.92	4.23	1.49	0.8		4.91	3.61	0.97			0.14			100
Ukskins 2003	71.26	13.04	4.03	1.14	0.65		5.11	3.75	0.88			0.14			100
Ukskins 2003	76.08	11.7	2.52	0.29	0.18		5.48	3.17	0.44			0.14			100
Ukskins 2003	77.02	11.57	2.27	0.21	0.13		4.77	3.54	0.38			0.11			100
Westgate 1998	77.68	12.27	0.84	0.79	0.05		4.88	3.16	0.08			0.08			99.83
Westgate 1998	77.57	12.24	1.02	0.63	0.04		4.73	3.55	0.06			0.04			99.88
Westgate 1998	76.05	12.94	1.23	0.89	0.14		4.17	4.07	0.15			0.09			99.73
Westgate 1998	77.7	12.21	0.83	0.71	0.04		5.03	3.18	0.06			0.09			99.85
Westgate 1998	77.71	12.16	0.89	0.74	0.05		4.93	3.24	0.06			0.07			99.85
Westgate 1998	77.78	12.26	0.86	0.8	0.04		4.94	3.08	0.05			0.05			99.86
Westgate 1998	77.63	12.21	0.87	0.8	0.06		5.05	3.13	0.05			0.06			99.86
Westgate 1998	77.81	12.02	0.86	0.75	0.05		5.03	3.24	0.05			0.03			99.84
Westgate 1998	77.76	12.06	0.88	0.76	0.05		5.02	3.21	0.06			0.06			99.86
Westgate 1998	77.76	12.1	0.87	0.8	0.05		5.12	3.08	0.03			0.06			99.87
Westgate 1998	77.68	12.12	0.88	0.83	0.06		4.96	3.22	0.05			0.05			99.85
Westgate 1998	77.69	12.09	0.88	0.82	0.06		5.04	3.14	0.09			0.05			99.86
Westgate 1998	77.67	12.14	0.89	0.75	0.05		4.98	3.24	0.07			0.06			99.85
Westgate 1998	77.64	12.14	0.87	0.77	0.04		5.09	3.22	0.05			0.05			99.87
Westgate 1998	77.57	12.16	0.92	0.83	0.05		5.06	3.17	0.05			0.07			99.88
Westgate 1998	77.58	12.12	0.9	0.78	0.06		5.18	3.1	0.07			0.06			99.85
Westgate 1998	77.71	12.04	0.85	0.74	0.05		5.17	3.14	0.08			0.07			99.85
Westgate 1998	77.62	12.2	0.9	0.79	0.05		5	3.17	0.07			0.07			99.87
Kiipli 2008	49.54	30.11	3.71	0.16	1.1		3.95	0.24	0.88	0.08		0.002		10.8	100.572
Kiipli 2009	49.85	26.28	4.57	2.05	1.81		4.25	0.41	0.87	0.15		0.02		8.75	99.01

Table D.3: Raw data of volcanic ash particles used in the production of ternarys

	SiO(2)	Al(2)O(3)	Fe(2)O(3)	CaO	MgO	SO(3)	K(2)O	Na(2)O	TiO(2)	P(2)O(5)	NiO	MnO	Cr(2)O(3)	LOI	total
Kiipli 2010	35.6	13.01	19.74	0.35	1.52		4.85	0.92	2.1	0.49		0.01		13.7	92.29
Kiipli 2011	49.8	32.9	1.37	0.43	1.7		2.53	0.9	0.53	0.07		0.015		10.9	101.145
Kiipli 2012	50	33	1.3	0.39	1.68		2.46	1.1	0.53	0.06		0.013		10.7	101.233
Kiipli 2013	48.37	24.76	8.35	0.29	0.62		4.93	0.46	1.57	0.28		0.01		12.1	101.74
Kiipli 2014	48.2	29.6	2.21	1.22	2.15		2.68	0.5	0.5	0.25		0.018		10.9	98.228
Kiipli 2015	55.06	24.47	1.68	0.4	3.56		6.33	0.72	0.34	0.14		0.013		7.3	100.013
Kiipli 2016	57.4	21.4	1	0.7	4.4		8.1	0.6	0.3	0.1		0.008		7.3	101.308
Kiipli 2017	55.47	23.94	2.11	1.57	4.29		4.29	0.39	0.5	0.23		0.022		7.92	100.732
Kiipli 2018	47.81	25.25	1.7	4.13	3.26		4.11	0.58	0.37	0.12		0.013		14.05	101.393
Kiipli 2019	50.75	26.7	1.97	0.91	3.17		5.37	0.52	0.42	0.25		0.01		10.5	100.57

Table D.4

author	M type	SiO(2)	Al(2)O(3)	FeO	CaO	MgO	SO(2)	K(2)O	Na(2)O	TiO(2)	P(2)O	NiO	MnO	Cr(2)O(3)	total
Krot et al 2001	CB	52.9	0.04	1.4	0.04	45	0	0	0.05	0.03	0	0	0.07	0.68	100.21
Krot et al 2001	CB	54.7	0.04	0.73	0.04	43.8	0	0	0.05	0.03	0	0	0.07	0.64	100.1
Krot et al 2001	CB	55	0.04	1.1	0.04	43.1	0	0	0.05	0.03	0	0	0.07	0.69	100.12
Krot et al 2001	CB	54.9	0.22	0.71	0.16	43.2	0	0	0.05	0.03	0	0	0.07	0.71	100.05
Krot et al 2001	CB	52.2	0.67	1.4	0.7	44.5	0	0	0.05	0.05	0	0	0.07	0.44	100.08
Krot et al 2001	CB	53.9	0.77	1	0.69	42.8	0	0	0.05	0.06	0	0	0.07	0.73	100.07
Krot et al 2001	CB	53.6	1.4	1.2	1.2	41.9	0	0	0.05	0.09	0	0	0.07	0.58	100.09
Krot et al 2001	CB	53.3	1.7	0.94	1.3	41.9	0	0	0.05	0.08	0	0	0.08	0.66	100.01
Krot et al 2001	CB	53	1.9	2.5	1.6	39.9	0	0	0.05	0.1	0	0	0.22	0.77	100.04
Krot et al 2001	CB	52.2	3.7	3.8	2.9	36	0	0	0.1	0.17	0	0	0.27	0.77	99.91
Krot et al 2001	CB	51.4	3.8	2.4	3.5	37.6	0	0	0.08	0.18	0	0	0.11	0.92	99.99
Krot et al 2001	CB	52.4	4.2	0.8	3.4	38.2	0	0	0.07	0.18	0	0	0.07	0.74	100.06
Krot et al 2001	CB	52.2	4.6	2.2	3.3	36.1	0	0	0.28	0.2	0	0	0.38	0.77	100.03
Krot et al 2001	CB	52.1	5.8	2.8	4.7	33.4	0	0	0.05	0.27	0	0	0.07	0.84	100.03
Krot et al 2001	CB	48.7	7	2.9	4.4	35.9	0	0	0.06	0.19	0	0	0.25	0.58	99.98
Krot et al 2001	CB	45.9	9.3	5.4	7	31.5	0	0	0.05	0.37	0	0	0.07	0.44	100.03
Krot et al 2001	CB	46.3	10.1	4.3	7.7	30.4	0	0	0.09	0.42	0	0	0.07	0.6	99.98
Krot et al 2001	CB	47.8	10.5	2.6	7.4	30.8	0	0	0.05	0.4	0	0	0.07	0.41	100.03
Krot et al 2001	CB	46.3	10.6	3.9	7.6	30.6	0	0	0.06	0.44	0	0	0.07	0.45	100.02
Krot et al 2001	CB	46.3	10.8	3.6	8	30.4	0	0	0.05	0.44	0	0	0.07	0.47	100.13
Krot et al 2001	CB	47.7	11	2.2	70.6	30.5	0	0	0.06	0.41	0	0	0.07	0.43	162.97
Krot et al 2001	CB	47.6	11.1	3.5	7.5	29.4	0	0	0.05	0.4	0	0	0.07	0.48	100.1
Krot et al 2001	CB	44.8	12.2	2.4	7.2	32.5	0	0	0.09	0.48	0	0	0.07	0.28	100.02
Krot et al 2001	CB	44.8	12.2	2.4	7.2	32.5	0	0	0.09	0.48	0	0	0.07	0.28	100.02
Krot et al 2001	CB	48.8	12.3	1.6	9.2	28.5	0	0	0.05	0.47	0	0	0.07	0.33	101.32
Krot et al 2001	CB	44.7	14	4.9	8.8	26.6	0	0	0.09	0.54	0	0	0.07	0.32	100.02
Krot et al 2001	CB	49.3	12.8	1.6	11.7	24.3	0	0	0.21	0.77	0	0	0.07	0.12	100.87
Krot et al 2001	CB	48.1	13.8	1.6	15.2	20.5	0	0	0.08	0.78	0	0	0.07	0.08	100.21
Krot et al 2001	CB	46.2	16.7	2.3	18.6	14.9	0	0	0.05	1.1	0	0	0.07	0.1	100.02
Ivanova et al 2008	CB	45.3	5.91	3.35	4.52	40.1	0	0.03	0.11	0.27	0	0.08	0.01	0.43	100.11
Ivanova et al 2008	CB	44.1	3.45	23	2.33	24	0	0.19	1.51	0.13	0	0.11	0.46	0.74	100.02
Ivanova et al 2008	CB	53.1	0.67	1.64	0.56	43.24	0	0	0.01	0.04	0	0	0.09	0.78	100.13
Ivanova et al 2008	CB	45.1	0.97	20.3	0.7	30.4	0	0.08	0.28	0.06	0	0.08	0.2	0.64	98.81

Table D.4

author	M type	SiO(2)	Al(2)O(3)	FeO	CaO	MgO	SO(2)	K(2)O	Na(2)O	TiO(2)	P(2)O	NiO	MnO	Cr(2)O(3)	total
Ivanova et al 2008	CB	48.9	8.45	4.57	6.17	31.6	0	0	0.07	0.35	0	0	0.12	0.56	100.79
Ivanova et al 2008	CB	44.5	12.1	3.18	10.7	28.2	0	0.01	0.03	0.53	0	0.04	0.03	0.3	99.62
Ivanova et al 2008	CB	38.5	2.79	26.2	1.58	29.7	0	0.05	0.47	0.13	0	0.08	0.26	0.66	100.42
Ivanova et al 2008	CB	7.71	56.4	0.84	10	20	0	0	0	3.9	0	0	0.02	0.05	98.92
Ivanova et al 2008	CB	19.2	51	2.04	23.3	1.08	0	0	0	2.38	0	0	0.02	0.09	99.11
Ivanova et al 2008	CB	5.96	62.1	0.44	24.4	0.6	0	0	0	5.67	0	0	0.02	0.02	99.21
Ivanova et al 2008	CB	18.9	42.4	1.3	33.2	1.96	0	0	0	1.03	0	0	0.02	0.04	98.85
Ivanova et al 2008	CB	13	49.6	2.8	29.7	1.08	0	0	0	1.91	0	0	0.02	0.05	98.16
Ivanova et al 2008	CB	17	46.4	2.03	15.3	19.6	0	0	0	0.18	0	0	0.02	0.12	100.65
Ivanova et al 2008	CB	12.8	49.9	0.99	32.8	0.1	0	0	0	2.45	0	0	0.02	0.02	99.08
Ivanova et al 2008	CB	20.9	34.9	5.29	34.9	2.01	0	0	0	0.85	0	0	0.03	0.02	98.9
Ivanova et al 2008	CB	1.3	71.1	0.31	21.7	1.98	0	0	0	2.22	0	0	0.02	0.04	98.67
Ivanova et al 2008	CB	0.05	66.9	2.98	23	0.89	0	0	0	5.3	0	0	0.02	0.02	99.16
Ivanova et al 2008	CB	18.1	41.5	2.54	27.8	9.26	0	0	0	0.65	0	0	0.02	0.04	99.91
Ivanova et al 2008	CB	0.07	71.5	0.46	23	0.43	0	0	0	4.95	0	0	0.02	0.02	100.45
Ivanova et al 2008	CB	19.8	31.2	0.54	40.4	1.27	0	0	0	4.95	0	0	0.02	0.02	98.2
Ivanova et al 2008	CB	17.4	57.3	0.6	18.7	4.02	0	0	0	3.31	0	0	0.02	0.07	101.42
Ivanova et al 2008	CB	14.7	45	0.63	34.3	1.62	0	0	0	3.42	0	0	0.02	0.02	99.71
Ivanova et al 2008	CB	15.1	48.4	2.08	30.1	2.15	0	0	0	1.42	0	0	0.03	0.06	99.34
Ivanova et al 2008	CB	7.56	59.6	2.25	21.8	4.74	0	0	0	2.86	0	0	0.02	0.03	98.86
Ivanova et al 2008	CB	44.6	18	1.69	15.4	17.3	0	0	0	0.91	0	0	0.06	0.13	98.09
Ivanova et al 2008	CB	42.4	15.9	2.05	12.7	25.9	0	0	0	0.58	0	0	0.02	0.24	99.79
Rubin et al 2002	CB	42.3	0.17	1.5	0.22	54.8	0	0	0.04	0.05	0	0	0.04	0.26	99.38
Rubin et al 2002	CB	57.9	0.83	1.4	0.54	37.3	0	0	0.04	0.17	0	0	0.09	0.54	98.81
Rubin et al 2002	CB	53.7	3.3	1	16.2	23.3	0	0	0.06	0.54	0	0	0.22	0.96	99.28
Weisberg et al 2001	CB	50.7	4.6	3.5	3.3	36.9	0	0.1	0.1	0.17	0	0	0.3	0.6	100.27
Weisberg et al 2001	CB	49.8	5.5	4.7	3.7	35.1	0	0.1	0.1	0.21	0	0	0.2	0.6	100.01
Weisberg et al 2001	CB	48.2	4.9	5	3.4	35.7	0	0.1	0.1	0.19	0	0	0.1	0.6	98.29
Weisberg et al 2001	CB	49.2	5.9	2.6	5.2	34.3	0	0.1	0.1	0.31	0	0	0.1	0.5	98.31
Weisberg et al 2001	CB	50.3	3.7	4.4	2.3	35.8	0	0.1	0.5	0.14	0	0	0.2	0.3	97.74
Weisberg et al 2001	CB	42.04	0	3.47	0.2	54.1	0	0	0	0	0	0	0.16	0.58	100.55
Weisberg et al 2001	CB	42.04	0	2.26	0.24	54.72	0	0	0	0	0	0	0.09	0.43	99.78
Weisberg et al 2001	CB	41.24	0	4.08	0.23	52.97	0	0	0	0	0	0	0.1	0.44	99.06

Table D.4

author	M type	SiO(2)	Al(2)O(3)	FeO	CaO	MgO	SO(2)	K(2)O	Na(2)O	TiO(2)	P(2)O	NiO	MnO	Cr(2)O(3)	total
Weisberg et al 2001	CB	42.1	0	2.48	0.22	54.86	0	0	0	0	0	0	0.1	0.34	100.1
Weisberg et al 2001	CB	42.24	0	1.46	0.1	55.38	0	0	0	0	0	0	0.17	0.1	99.45
gournelle et al 2007	CB	0.29	70.87	0.15	0.38	27.42	0	0	0	0.53	0	0	0	0.5	100.14
gournelle et al 2007	CB	42.58	34.68	1.58	19	0.63	0	0	0	0.05	0	0	0	0.01	98.53
gournelle et al 2007	CB	35.77	22.18	0.49	24.45	7.44	0	0	0	10.2	0	0.02	0	0.09	100.64
gournelle et al 2007	CB	27.31	29.14	0.2	40.18	3.13	0	0	0	0.07	0	0	0	0.03	100.06
gournelle et al 2007	CB	30.68	23.59	0.76	36.19	5.74	0	0	0	1.56	0	0	0	0.02	98.54
gournelle et al 2007	CB	43.42	13.37	4.04	23.44	13.42	0	0	0.15	0.37	0	0.12	0.05	0.11	98.49
gournelle et al 2007	CB	50.86	1.36	4.28	22.03	20.12	0	0	0.11	0.06	0	0.13	0	0.09	99.04
gournelle et al 2007	CB	32.5	18.64	0.41	40.02	6.86	0	0	0.16	0	0	0.04	0	0	98.63
gournelle et al 2007	CB	27.65	27.21	0.52	40.43	4.14	0	0	0	0.07	0	0	0	0	100.02
gournelle et al 2007	CB	31.41	19.77	0.52	40.72	6.48	0	0	0.21	0	0	0	0	0	99.11
gournelle et al 2007	CB	0.06	71.42	0.54	0.04	28.51	0	0	0	0.4	0	0	0.06	0.38	101.41
gournelle et al 2007	CB	27.68	19.96	2.21	25.16	11.75	0.08	0	0.25	2.49	0.06	0.06	0	0.19	89.89
gournelle et al 2007	CB	0.28	70.05	1.76	0.14	27.73	0	0	0	0.25	0	0.1	0.03	0.53	100.87
Bonal et al 2010	CB	41.1	0.07	2.2	0.29	55.6	0	0.04	0.03	0.04	0	0	0.12	0.52	100.01
Bonal et al 2010	CB	40.6	0.09	2.9	0.24	55.2	0	0.04	0.03	0.04	0	0	0.05	0.35	99.54
Bonal et al 2010	CB	41.5	0.03	4.4	0.15	55.1	0	0.04	0.03	0.04	0	0	0.08	0.62	101.99
Bonal et al 2010	CB	33.3	0.03	45.7	0.11	19.5	0	0.04	0.04	0.04	0	0	0.41	0.07	99.24
Bonal et al 2010	CB	55.7	0.03	1.3	0.04	42.8	0	0.04	0.16	0.04	0	0	0.23	0.31	100.65
Bonal et al 2010	CB	58.3	0.16	2.5	0.05	40.1	0	0.04	0.21	0.04	0	0	0.19	0.31	101.9
Bonal et al 2010	CB	46.6	1.62	15.4	1.09	32.7	0	0.07	0.31	0.08	0	0	0.44	0.79	99.1
Bonal et al 2010	CB	48.1	0.04	30.3	0.15	19.3	0	0.04	0.15	0.04	0	0	0.43	0.12	98.67
Bonal et al 2010	CB	49.8	3.09	1.1	2.24	40.4	0	0.04	0.03	0.12	0	0	0.08	0.57	97.47
Bonal et al 2010	CB	51.5	3.51	0.9	1.67	39.8	0	0.04	0.03	0.16	0	0	0.04	0.83	98.48
Bonal et al 2010	CB	39.8	0.14	4.4	0.21	55.1	0	0.04	0.03	0.04	0	0	0.16	0.34	100.26
Bonal et al 2010	CB	50.6	0.03	12.6	0.29	31.6	0	0.04	0.05	0.05	0	0	0.26	0.66	96.18
Bonal et al 2010	CB	50.7	4.89	3.3	2.03	35.3	0	0.04	0.03	0.25	0	0	0.02	0.94	97.5
Bonal et al 2010	CB	21.9	34.92	1.3	40.2	1.1	0	0.04	0.03	0.05	0	0	0.07	0	99.61
Bonal et al 2010	CB	0.19	70.5	0.9	0.24	28.2	0	0.04	0.03	0.46	0	0	0.03	0.08	100.67
Bonal et al 2010	CB	43.8	1.33	2.9	0.83	51.8	0	0.04	0.03	0.04	0	0	0.29	0.52	101.58
Bonal et al 2010	CB	54.9	0.03	9.99	0.05	32.4	0	0.04	0.03	0.04	0	0	0.19	0.83	98.5
Bonal et al 2010	CB	52.2	7.97	3	2.58	33.8	0	0.04	0.03	0.49	0	0	0.02	0.92	101.05

Table D.4

author	M type	SiO(2)	Al(2)O(3)	FeO	CaO	MgO	SO(2)	K(2)O	Na(2)O	TiO(2)	P(2)O	NiO	MnO	Cr(2)O(3)	total
Bonal et al 2010	CB	52	4.61	1.49	3.64	36.1	0	0.04	0.03	0.2	0	0	1.36	0.56	100.03
Bonal et al 2010	CB	58.2	1.5	1.53	1.58	37.2	0	0.04	0.03	0.15	0	0	0.12	0.68	101.03
Bonal et al 2010	CB	59.1	0.04	1.34	0.07	38.46	0	0.04	0.03	0.04	0	0	0.17	0.04	99.33
Bonal et al 2010	CB	49.75	0.69	5.67	2.48	40.8	0	0.04	0.03	0.18	0	0	0.19	0.69	100.52
Macpherson et al 2013	CV	58.21	0.82	1.02	0.54	39.74	0	0	0	0.16	0	0.31	0.09	0	100.89
Macpherson et al 2013	CV	41.94	0.24	0.47	0.61	56.5	0	0	0	0.08	0	0.11	0.02	0	99.97
Macpherson et al 2013	CV	35.13	0.14	39.69	0.18	24.16	0	0	0	0.05	0	0.14	0.25	0	99.74
Macpherson et al 2013	CV	0.21	69	2.67	0.29	26.49	0	0	0	0.02	0	0	0.02	0	98.7
Macpherson et al 2013	CV	0	65.96	15.03	0.12	18.39	0	0	0	0.11	0	0	0.03	0	99.64
Ruzicka et al 2012	CV	38.6	6.11	3.43	3.67	39.3	0	0	0.07	0	0	0	0.09	0.22	91.49
Ruzicka et al 2012	CV	40.3	6.17	3.71	4.14	41	0	0	0.1	0	0	0	0.16	0.29	95.87
Ruzicka et al 2012	CV	39.5	6.87	2.18	4.65	39.2	0	0	0.11	0	0	0	0.08	0.23	92.82
Ruzicka et al 2012	CV	35.8	8.98	7.72	5.04	32.7	0	0	0.8	0	0	0	0.09	0.2	91.33
Ruzicka et al 2012	CV	39.3	19	3.68	11.9	24	0	0	0.15	0	0	0	0.04	0.19	98.26
Ruzicka et al 2012	CV	11.9	53.7	4.34	6.38	18.7	0	0	0.46	0	0	0	0.03	0.39	95.9
Ruzicka et al 2012	CV	40.4	25.2	1.39	17.8	13.1	0	0	0.14	0	0	0	0.02	0.14	98.19
Ruzicka et al 2012	CV	49	1.83	3.11	1.27	49.6	0	0	0.06	0	0	0	0.11	0.26	105.24
Ruzicka et al 2012	CV	15.8	48.4	0.37	18.4	14	0	0	0.06	0	0	0	0.01	0.13	97.17
Ruzicka et al 2012	CV	39.6	3.15	0.41	1.32	43.4	0	0	0.01	0	0	0	0.04	0.27	88.2
Ruzicka et al 2012	CV	38.7	12.7	3.4	8.74	30.9	0	0	0.18	0	0	0	0.19	0.27	95.08
Ruzicka et al 2012	CV	41.3	4.76	4.75	2.76	41.3	0	0	0.13	0	0	0	0.14	0.29	95.43
Ruzicka et al 2012	CV	39.9	4.53	5.11	2.94	41.1	0	0	0.05	0	0	0	0.62	0.37	94.62
Ruzicka et al 2012	CV	42.4	0.14	0.58	0.17	55.8	0	0	0.01	0.03	0	0.03	0.05	0.14	99.35
Ruzicka et al 2012	CV	41.5	0.22	3.85	0.18	53.2	0	0	0.01	0.03	0	0.09	0.14	0.11	99.33
Ruzicka et al 2012	CV	38.1	0.27	20.5	0.22	39.8	0	0	0.04	0.05	0	0.1	0.21	0.17	99.46
Ruzicka et al 2012	CV	40.9	0.23	7.44	0.2	49.6	0	0	0.01	0.01	0	0.08	1.05	0.14	99.66
Maruyama et al 2011	CV	0.02	59.5	39.5	1.07	0.03	0	0	0	0.03	0	0	0.14	0	100.29
Maruyama et al 2011	CV	0.04	58.9	40.2	0.79	0.04	0	0	0	0.06	0	0.02	0.15	0	100.2
Maruyama et al 2011	CV	0.19	56.6	40.7	0.23	0.64	0	0	0	0.15	0	0.17	0.015	0	98.695
Maruyama et al 2011	CV	0.83	58	32	4.75	0.18	0	0	0.04	0.01	0	0.02	0.12	0	95.95
Maruyama et al 2011	CV	0.07	60.7	35.6	2.88	0.1	0	0	0	0.04	0	0.02	0.13	0	99.54
Maruyama et al 2011	CV	0.18	58.8	37.4	0.29	3.04	0	0	0	0.08	0	0.22	0.15	0	100.16
Maruyama et al 2011	CV	0.12	73.5	0.7	21.7	0	0	0	0	0	0	0	0	0	96.02

Table D.4

author	M type	SiO(2)	Al(2)O(3)	FeO	CaO	MgO	SO(2)	K(2)O	Na(2)O	TiO(2)	P(2)O	NiO	MnO	Cr(2)O(3)	total
Maruyama et al 2011	CV	0.23	74.3	1.79	20.8	0.02	0	0	0.02	0.01	0	0	0	0	97.17
Maruyama et al 2011	CV	0.05	74.8	0.29	20.9	0	0	0	0	0.03	0	0	0	0	96.07
Maruyama et al 2011	CV	0.02	64.2	0.09	36.5	0.02	0	0	0	0.03	0	0	0	0	100.86
Maruyama et al 2011	CV	0.41	77	1.78	2.26	0.25	0	0	0	0.11	0	0.07	0.01	0	81.89
Maruyama et al 2011	CV	18.4	39.1	3.53	37.4	0.02	0	0	0	0.62	0	0.01	0.02	0	99.1
Maruyama et al 2011	CV	0.1	55.3	30.1	11.1	0	0	0	0	2.1	0	0	0	0	98.7
Hezel and palme 2010	CV	52.32	2.44	1.37	2.61	41.24	0	0	0.3	0.16	0	0	0.09	0.44	100.97
Hezel and palme 2010	CV	44.57	1.22	1.05	1.18	52.47	0	0	0.15	0.07	0	0	0.04	0.2	100.95
Hezel and palme 2010	CV	47.93	5.68	1.17	5.38	39.22	0	0	0.66	0.34	0	0	0.09	0.29	100.76
Hezel and palme 2010	CV	46.14	3.58	2.18	2.8	45.12	0	0	0.56	0.16	0	0	0.04	0.27	100.85
Hezel and palme 2010	CV	48.5	2.63	1.61	2.35	44.81	0	0	0.27	0.17	0	0	0.08	0.35	100.77
Hezel and palme 2010	CV	49.9	0.65	2.33	0.99	47.3	0	0	0.01	0.07	0	0	0.09	0.31	101.65
Hezel and palme 2010	CV	51.32	3.94	2.02	3.11	39.73	0	0	0.24	0.21	0	0	0.06	0.28	100.91
Hezel and palme 2010	CV	56.53	3.3	2.59	2.99	34.09	0	0	0.27	0.15	0	0	0.23	0.82	100.97
Hezel and palme 2010	CR	48.54	2.37	2.37	1.61	43.7	0	0	0.16	0.1	0	0	0.13	0.65	99.63
Hezel and palme 2010	CR	53.1	1.89	1.91	2.61	39.15	0	0	0.07	0.2	0	0	0.26	0.95	100.14
Hezel and palme 2010	CR	52.22	1.83	3.53	1.84	39.15	0	0	0.08	0.11	0	0	0.5	0.87	100.13
Hezel and palme 2010	CR	48.33	5.14	2.64	4.49	37.96	0	0	0.2	0.34	0	0	0.1	0.76	99.96
Hezel and palme 2010	CR	49.66	3.73	2.58	3.59	39.76	0	0	0.03	0.18	0	0	0.14	0.71	100.38
Hezel and palme 2010	CR	47.26	4.46	4.1	3.63	38.83	0	0	0.08	0.2	0	0	0.14	0.52	99.22
Hezel and palme 2010	CR	52.64	3.45	2.84	4.06	36.01	0	0	0.06	0.21	0	0	0.19	0.83	100.29
Hezel and palme 2010	CR	56.23	2.94	1.47	3.18	35.37	0	0	0.05	0.21	0	0	0.17	0.64	100.26
Hezel and palme 2010	CR	51.36	2.26	2.16	2.43	38.58	0	0	0.14	0.16	0	0	0.25	0.65	97.99
Hezel and palme 2010	CO	51.58	6.29	6.17	12.34	22.22	0	0	0.89	0.43	0	0	0.23	0.43	100.58
Hezel and palme 2010	CO	55.17	5.24	1.32	4.52	33.89	0	0	0.26	0.23	0	0	0.08	0.38	101.09
Hezel and palme 2010	CO	48.54	2.44	3.95	2.19	43.09	0	0	0.13	0.14	0	0	0.11	0.37	100.96
Hezel and palme 2010	CO	44.61	6.28	1.13	4.8	42.5	0	0	0.58	0.34	0	0	0.05	0.23	100.52
Hezel and palme 2010	CO	48.96	5.01	4.47	3.51	37.26	0	0	0.41	0.12	0	0	0.14	0.47	100.35
Hezel and palme 2010	CO	33.84	1.04	23.45	2.04	38.01	0	0	1.54	0.13	0	0	0.23	0.27	100.55
Hezel and palme 2010	CO	49.81	1.54	1.12	1.29	45.73	0	0	0.23	0.14	0	0	0.09	0.36	100.31
Hezel and palme 2010	CO	45.23	0.46	1.87	0.74	51.01	0	0	0.01	0.11	0	0	0.06	0.3	99.79
Hezel and palme 2010	CO	41.6	2.33	4	3.19	46.02	0	0	1.34	0.24	0	0	0.18	0.5	99.4
Hezel and palme 2010	CO	37.41	1.75	40.03	1.86	18.32	0	0	1.01	0.09	0	0	0.35	0.36	101.18

Table D.4

author	M type	SiO(2)	Al(2)O(3)	FeO	CaO	MgO	SO(2)	K(2)O	Na(2)O	TiO(2)	P(2)O	NiO	MnO	Cr(2)O(3)	total
Hezel and palme 2010	CM	46.43	0.53	0.49	0.61	50.75	0	0	0	0.1	0	0	0.02	0.21	99.14
Hezel and palme 2010	CM	54.49	1.13	1.69	1.27	39.62	0	0	0.02	0.13	0	0	0.1	0.61	99.06
Hezel and palme 2010	CM	48.61	5.17	10.75	1.58	33.22	0	0	0.2	0.56	0	0	0.23	0.73	101.05
Hezel and palme 2010	CM	48.25	0.95	0.71	1.43	47.99	0	0	0.01	0.18	0	0	0.06	0.29	99.87
Hezel and palme 2010	CM	46.62	2.23	0.85	1.86	46.74	0	0	0.01	0.34	0	0	0.13	0.56	99.34
Hezel and palme 2010	CM	53.61	0.77	0.93	1.43	42.67	0	0	0	0.2	0	0	0.13	0.59	100.33
Hezel and palme 2010	CM	48.58	0.44	0.79	0.65	49.73	0	0	0	0.11	0	0	0.13	0.4	100.83
Hezel and palme 2010	CM	53.79	1.39	1.01	6.76	35.51	0	0	0.01	0.19	0	0	0.21	0.56	99.43
Hezel and palme 2010	CM	50.58	0.94	0.94	0.42	46.09	0	0	0	0.13	0	0	0.08	0.47	99.65
Hezel and palme 2010	CM	52.25	1.15	1.35	4.03	40.4	0	0	0.01	0.39	0	0	0.2	0.58	100.36
Hezel and palme 2010	CM	51.02	1.23	3.21	2.41	41.33	0	0	0	0.19	0	0	0.17	0.8	100.36
Hezel and palme 2010	CV	36.45	1.78	34.43	5.28	17.72	0	0	0.32	0.07	0	0	0.33	0.38	96.76
Hezel and palme 2010	CV	36.21	1.53	33.73	3.23	21.37	0	0	0.13	0.04	0	0	0.27	0.49	97
Hezel and palme 2010	CV	35.32	2.25	35.04	0.74	21.94	0	0	0.32	0.09	0	0	0.27	0.61	96.58
Hezel and palme 2010	CV	34.72	1.7	37.09	3.67	20.06	0	0	0.34	0.03	0	0	0.25	0.72	98.58
Hezel and palme 2010	CV	33.4	2.83	38.95	0.6	20.36	0	0	0.1	0.08	0	0	0.34	0.27	96.93
Hezel and palme 2010	CV	32.38	2.28	37.62	2.33	20.27	0	0	0.38	0.16	0	0	0.33	0.52	96.27
Hezel and palme 2010	CV	32.33	1.76	39.38	0.51	20.39	0	0	0.21	0	0	0	0.35	0.47	95.4
Hezel and palme 2010	CV	32.14	1.55	47.99	0.44	14.01	0	0	0.64	0.01	0	0	0.49	0.21	97.48
Hezel and palme 2010	CV	30.65	2.31	39.85	0.51	20.13	0	0	0.44	0.07	0	0	0.31	0.46	94.73
Hezel and palme 2010	CV	29.96	3.07	38.22	0.64	18.28	0	0	0.34	0.08	0	0	0.37	0.47	91.43
Hezel and palme 2010	CR	34.44	2.72	22.41	0.52	17.3	0	0	1.23	0.09	0	0	0.25	0.27	79.23
Hezel and palme 2010	CR	33.28	2.48	23.48	0.9	17.81	0	0	1.41	0.01	0	0	0.24	0.43	80.04
Hezel and palme 2010	CR	32.94	2.91	23.11	0.8	15.33	0	0	1.58	0.03	0	0	0.21	0.38	77.29
Hezel and palme 2010	CR	32.19	2.86	25.5	0.6	16.37	0	0	0.96	0	0	0	0.22	0.31	79.01
Hezel and palme 2010	CR	31.22	2.42	24.24	1.27	16.23	0	0	1.6	0.05	0	0	0.3	0.34	77.67
Hezel and palme 2010	CR	33.79	2.44	23.76	0.59	14.92	0	0	1.5	0.05	0	0	0.35	0.29	77.69
Hezel and palme 2010	CR	32.25	2.13	24.14	1.13	15.81	0	0	1.54	0.05	0	0	0.18	0.4	77.63
Hezel and palme 2010	CR	32.47	2.6	26.45	0.25	14.89	0	0	1.23	0.05	0	0	0.21	0.22	78.37
Hezel and palme 2010	CR	33.05	2.64	23.57	0.36	15.86	0	0	1.35	0.03	0	0	0.21	0.33	77.4
Hezel and palme 2010	CR	31.04	1.62	22.04	0.89	20.34	0	0	0.98	0.03	0	0	0.21	0.39	77.54
Hezel and palme 2010	CO	29.82	2.3	29.31	0.86	18.87	0	0	0.57	0.08	0	0	0.27	0.45	82.53
Hezel and palme 2010	CO	26.94	2.13	36.37	0.83	15.66	0	0	0.64	0.04	0	0	0.31	0.28	83.2

Table D.4

author	M type	SiO(2)	Al(2)O(3)	FeO	CaO	MgO	SO(2)	K(2)O	Na(2)O	TiO(2)	P(2)O	NiO	MnO	Cr(2)O(3)	total
Hezel and palme 2010	CO	27.15	2.36	38.44	1.4	15.3	0	0	0.69	0.06	0	0	0.37	0.27	86.04
Hezel and palme 2010	CO	29.86	2.73	27	0.87	18.98	0	0	0.79	0.07	0	0	0.32	0.4	81.02
Hezel and palme 2010	CO	29.26	1.56	39.23	0.5	18.53	0	0	0.38	0.05	0	0	0.4	0.36	90.27
Hezel and palme 2010	CO	27.53	2.77	27.97	0.53	18.58	0	0	0.79	0.06	0	0	0.31	0.37	78.91
Hezel and palme 2010	CO	27.76	3.12	29.93	1.28	18.27	0	0	0.34	0.07	0	0	0.29	0.39	81.45
Hezel and palme 2010	CO	27.21	7.04	23.65	1.19	16.25	0	0	2.71	0.08	0	0	0.22	0.34	78.69
Hezel and palme 2010	CO	27.87	2.44	29.65	0.62	18.92	0	0	0.52	0.07	0	0	0.37	0.43	80.89
Hezel and palme 2010	CO	30.4	2.52	31.33	0.54	17.77	0	0	0.88	0.06	0	0	0.38	0.34	84.22
Hezel and palme 2010	CM	25.91	2.63	37.26	1.5	11.97	0	0	0.78	0.07	0	0	0.19	0.32	80.63
Hezel and palme 2010	CM	26	3.3	34.01	2.36	13.51	0	0	0.79	0.02	0	0	0.23	0.43	80.65
Hezel and palme 2010	CM	23.32	2.3	33.99	7.67	11.69	0	0	0.72	0.08	0	0	0.26	0.34	80.37
Hezel and palme 2010	CM	25.55	3.32	35.95	1.73	14.2	0	0	0.78	0.1	0	0	0.23	0.5	82.36
Hezel and palme 2010	CM	26.82	6.25	36.74	3.62	13.27	0	0	0.88	0.18	0	0	0.21	0.19	88.16
Hezel and palme 2010	CM	25.07	2.51	36.6	1.65	14.43	0	0	0.82	0.09	0	0	0.31	0.41	81.89
Hezel and palme 2010	CM	25.49	2.69	33.07	3.31	14.22	0	0	0.73	0.07	0	0	0.24	0.34	80.16
Hezel and palme 2010	CM	26.93	2.66	33.45	1.96	14.99	0	0	0.8	0.06	0	0	0.2	0.3	81.35
Hezel and palme 2010	CM	28.47	2.89	37.04	2.15	14.64	0	0	0.57	0.11	0	0	0.21	0.31	86.39
Hezel and palme 2010	CM	24.46	2.62	40.8	1.81	11.72	0	0	0.65	0.05	0	0	0.22	0.29	82.62
Hezel +palme 2007	CV	55.69	1.6	1.47	4.65	36.97	0	0	0.01	0.26	0	0.02	0.15	0.58	101.4
Hezel +palme 2007	CV	43.45	1.3	13.34	0.47	42	0	0	0.19	0.13	0	0.01	0.11	0.25	101.25
Hezel +palme 2007	CV	51.4	3.51	5.69	6.59	30.3	0	0	0.28	0.5	0	0.42	0.42	0.76	99.87
Hezel +palme 2007	CV	47.39	0.82	3.74	2.31	46.2	0	0	0.01	0.2	0	0.08	0.1	0.38	101.23
Hezel +palme 2007	CV	55.07	3.68	0.96	2.28	37.85	0	0	0.08	0.18	0	0.08	0.1	0.49	100.77
Hezel +palme 2007	CV	55.38	4.99	1.06	2.8	37.16	0	0	0.39	0.23	0	0.07	0.09	0.4	102.57
Hezel +palme 2007	CV	53.2	1.13	2.38	1.4	43.05	0	0	0.04	0.23	0	0.05	0.1	0.3	101.88
Hezel +palme 2007	CV	49.67	0.4	1.23	0.42	49.48	0	0	0	0.08	0	0.02	0.04	0.29	101.63
Hezel +palme 2007	CV	51.81	1.74	1.84	2.9	43.01	0	0	0.02	0.22	0	0.01	0.12	0.53	102.2
Hezel +palme 2007	CV	46.89	2.69	1.08	3.11	46.48	0	0	0.19	0.22	0	0.03	0.04	0.26	100.99
Hezel +palme 2007	CV	35.77	0.94	32.48	0.52	27.91	0	0	0.01	0.06	0	0.08	0.32	0.42	98.51
Hezel +palme 2007	CV	22.52	4.03	45.2	1.07	12.32	0	0	0.28	0.03	0	2.47	0.2	0.29	88.41
Hezel +palme 2007	CV	30.51	5.37	34.68	3.84	14.11	0	0	0.67	0.4	0	2.56	0.18	0.34	92.66
Hezel +palme 2007	CV	29.76	4.35	33.18	2.7	17.24	0	0	0.98	0.07	0	2.93	0.23	0.35	91.79
Hezel +palme 2007	CV	27.69	2.46	41.28	0.66	16.2	0	0	0.33	0.02	0	2.26	0.31	0.31	91.52

Table D.4

author	M type	SiO(2)	Al(2)O(3)	FeO	CaO	MgO	SO(2)	K(2)O	Na(2)O	TiO(2)	P(2)O	NiO	MnO	Cr(2)O(3)	total
Hezel +palme 2007	CV	28.22	3.64	40.38	0.97	15.24	0	0	0.42	0.05	0	1.75	0.28	0.32	91.27
Hezel +palme 2007	CV	30.01	5.46	29.77	2.45	17.35	0	0	0.78	0.03	0	2.62	0.29	0.3	89.06
Hezel +palme 2007	CV	29.97	4.56	37.24	0.42	17.41	0	0	1.9	0.08	0	1.61	0.3	0.34	93.83
Hezel +palme 2007	CV	33.46	4.19	29.13	1.8	21.37	0	0	0.68	0.09	0	2.25	0.22	0.43	93.62
Hezel +palme 2007	CV	27.83	3.94	36.81	1.99	16.66	0	0	0.64	0.07	0	2.19	0.31	0.46	90.9
Hezel +palme 2007	CV	30.04	4.38	35.36	1.1	18.59	0	0	0.57	0.06	0	2.48	0.3	0.47	93.35
Hezel +palme 2007	CV	29.23	5.63	35.59	0.87	19.75	0	0	1.75	0.11	0	1.78	0.19	0.42	95.32
Hezel +palme 2007	CV	30.24	3.93	30.75	1.58	19.45	0	0	1.13	0.1	0	2.13	0.35	0.45	90.11
Hezel +palme 2007	CV	31.84	4.85	34.25	0.31	19.87	0	0	1.34	0.05	0	0.43	0.33	0.54	93.81
Hezel +palme 2007	CV	30.99	4.52	32.66	1.16	18.53	0	0	1.54	0.1	0	1.3	0.19	0.39	91.38
Hezel +palme 2007	CV	26.14	4.47	37.91	1	16.56	0	0	0.58	0.06	0	3.54	0.13	0.42	90.81
Tomeoka et al 2011	CV	29.5	3	17.6	1.25	21.5	1.82	0.09	0.44	0	0.27	1.77	0.17	0.44	77.85
Tomeoka et al 2011	CV	32.1	4.02	17.1	0.15	22.5	1.23	0.3	0.78	0.05	0.09	1.5	0.1	0.36	80.28
Tomeoka et al 2011	CV	26.5	2.95	30.5	1.17	17.3	1.37	0.08	0.56	0.06	0.15	1.31	0.19	0.37	82.51
Tomeoka et al 2011	CL	29.7	2.31	18.1	0.16	19.3	2.91	0.15	0.35	0.03	0	1.64	0.16	0.42	75.23
Tomeoka et al 2011	CM	22.3	3.33	33.4	0.85	14	3.41	0.13	0.31	0.04	0	2.05	0.18	0.31	80.31
Tomeoka et al 2011	CR	31.4	2.66	24.3	0.87	15.8	3.18	0.16	1.16	0.07	0	1.48	0.33	0.35	81.76
Tomeoka et al 2011	CR	35.99	2.77	19.18	0.86	25.72	1.15	0.11	0.51	0.04	0.47	1.13	0.23	0.38	88.54
Tomeoka et al 2011	Ungrouped	22.4	1.9	16.3	0.97	15.2	3.9	0.06	0.22	0.07	0	1.5	0.2	0.32	63.04
Kereszuti et al 2015	CV	43.6	32.77	0.33	21.36	1.95	0	0	0	0	0	0	0	0	100.01
Kereszuti et al 2015	CV	44.01	33.06	0	20.72	2.2	0	0	0	0	0	0	0	0	99.99
Kereszuti et al 2015	CV	47.05	29.25	1.05	18.48	1.7	0	0	2.48	0	0	0	0	0	100.01
Kereszuti et al 2015	CV	48.89	26.4	1.87	16.65	3.21	0	0	2.99	0	0	0	0	0	100.01
Kereszuti et al 2015	CV	46.68	29.59	0.42	18.4	2.48	0	0	2.44	0	0	0	0	0	100.01
Kereszuti et al 2015	CV	48.33	26.88	1.6	19.12	2.2	0	0	1.87	0	0	0	0	0	100
Kereszuti et al 2015	CV	49.48	26.3	1.79	16.04	3.16	0	0	3.23	0	0	0	0	0	100
Kereszuti et al 2015	CV	49.23	24.99	2.13	16.69	3.9	0	0	3.05	0	0	0	0	0	99.99
Kereszuti et al 2015	CV	47.16	28.66	1.31	18.43	2.6	0	0	2.68	0	0	0	0	0	100.84
Krot et al 2004	Ungrouped	42.2	0.07	0.3	0.18	57	0	0.04	0.06	0.09	0	0	0.07	0.14	100.15
Krot et al 2004	Ungrouped	43.8	0.03	0.48	0.06	56.5	0	0.04	0.06	0.09	0	0	0.29	0.31	101.66
Krot et al 2004	Ungrouped	42.7	0.04	1.2	0.44	55.5	0	0.04	0.06	0.13	0	0	0.54	0.31	100.96
Krot et al 2004	Ungrouped	43	0.03	0.95	0.16	56.4	0	0.04	0.06	0.12	0	0	0.64	0.28	101.68
Krot et al 2004	Ungrouped	42.8	0.03	1	0.14	55.4	0	0.04	0.06	0.08	0	0	1.3	0.38	101.23

Table D.4

author	M type	SiO(2)	Al(2)O(3)	FeO	CaO	MgO	SO(2)	K(2)O	Na(2)O	TiO(2)	P(2)O	NiO	MnO	Cr(2)O(3)	total
Krot et al 2004	Ungrouped	42.4	0.03	1.4	0.32	55.1	0	0.04	0.06	0.09	0	0	0.18	0.22	99.84
Krot et al 2004	Ungrouped	41.7	0.03	3.5	0.18	53.4	0	0.04	0.06	0.09	0	0	0.29	0.51	99.8
Krot et al 2004	CR	42.5	0.05	1.2	0.22	56.2	0	0.04	0.06	0.09	0	0	0.32	0.52	101.2
Krot et al 2004	CR	42.3	0.16	0.35	0.19	56.5	0	0.04	0.06	0.12	0	0	0.07	0.17	99.96
Krot et al 2004	CV	42.7	0.07	0.85	0.1	56.5	0	0.04	0.06	0.09	0	0	0.07	0.07	100.55
Krot et al 2004	Ungrouped	43.1	37.2	0.27	20.1	0.09	0	0.04	0.06	0.09	0	0	0.07	0.07	101.09
Krot et al 2004	Ungrouped	40.8	36.6	0.71	19.5	0.42	0	0.04	0.06	0.09	0	0	0.07	0.07	98.36
Krot et al 2004	CR	40.1	39	0.11	18.6	1.6	0	0.04	0.06	0.09	0	0	0.07	0.07	99.74
Krot et al 2004	CR	42.8	34.6	0.28	19.7	1.5	0	0.04	0.06	0.25	0	0	0.07	0.07	99.37
Krot et al 2004	CR	40.1	39	0.11	18.6	1.6	0	0.04	0.06	0.09	0	0	0.07	0.07	99.74
Krot et al 2004	CR	42.1	36.4	0.3	20	0.86	0	0.04	0.07	0.2	0	0	0.07	0.07	100.11
Krot et al 2004	CR	41.1	38	0.46	19.5	0.86	0	0.04	0.07	0.09	0	0	0.07	0.07	100.26
Krot et al 2004	Ungrouped	24.1	32.8	0.34	40.3	1.8	0	0.05	0.06	0.09	0	0	0.07	0.07	99.68
Krot et al 2004	Ungrouped	25	32.7	0.25	40.4	1.9	0	0.04	0.06	0.09	0	0	0.07	0.07	100.58
Krot et al 2004	Ungrouped	0.08	72.1	0.16	0.06	27.8	0	0.04	0.06	0.24	0	0	0.07	0.16	100.77
Krot et al 2004	CR	0.08	72	0.45	0.11	27.8	0	0.04	0.06	0.1	0	0	0.09	0.15	100.88
Krot et al 2004	CR	0.14	70.8	0.14	0.15	27.8	0	0.04	0.06	0.19	0	0	0.07	0.54	99.93
Krot et al 2004	CR	0.08	72.1	0.16	0.06	27.8	0	0.04	0.06	0.24	0	0	0.07	0.16	100.77
Krot et al 2004	CR	0.17	71	0.21	0.15	28.2	0	0.04	0.06	0.19	0	0	0.07	0.41	100.5
Krot et al 2004	CR	0.04	71.1	0.13	0.04	27.4	0	0.04	0.06	0.37	0	0	0.07	0.18	99.43
Krot et al 2004	CR	0.08	70.4	0.26	0.06	27.3	0	0.04	0.06	0.74	0	0	0.07	0.55	99.56
Krot et al 2004	CR	0.09	72.5	0.13	0.08	27.4	0	0.04	0.06	0.33	0	0	0.07	0.46	101.16
Krot et al 2004	CR	58.5	0.85	1.5	1.9	36.2	0	0.04	0.06	0.3	0	0	0.32	0.75	100.42
Krot et al 2004	CR	57.9	0.21	0.74	0.26	39.8	0	0.04	0.06	0.09	0	0	0.12	0.33	99.55
Krot et al 2004	Ungrouped	57.5	1.1	3	2.9	34.8	0	0.04	0.06	0.39	0	0	0.48	1	101.27
Krot et al 2004	CR	57.5	2	1.8	2.6	35.6	0	0.04	0.06	0.17	0	0	0.37	0.84	100.98
Krot et al 2004	CR	59.4	0.58	0.81	0.6	39.6	0	0.04	0.06	0.09	0	0	0.09	0.27	101.54
Krot et al 2004	fuck knows	52.2	2.8	0.93	22.9	18.8	0	0.04	0.06	1.5	0	0	0.07	0.13	99.43
Krot et al 2004	fuck knows	49.5	7.5	0.27	24.5	15.9	0	0.04	0.06	2.4	0	0	0.07	0.07	100.31
Krot et al 2004	Ungrouped	53.4	3.4	0.27	24.7	18.3	0	0.04	0.06	0.09	0	0	0.07	0.11	100.44
Krot et al 2004	Ungrouped	52.4	2.8	0.5	24	18	0	0.04	0.06	0.26	0	0	0.07	0.07	98.2
Krot et al 2004	Ungrouped	42.3	15.7	1.2	23.4	13	0	0.04	0.06	2.3	0	0	0.07	0.23	98.3
Krot et al 2004	Ungrouped	52.8	4.8	0.9	22.1	18.4	0	0.04	0.06	0.87	0	0	0.11	0.53	100.61

Table D.4

author	M type	SiO(2)	Al(2)O(3)	FeO	CaO	MgO	SO(2)	K(2)O	Na(2)O	TiO(2)	P(2)O	NiO	MnO	Cr(2)O(3)	total
Krot et al 2004	CR	32.2	27.8	0.15	23.6	9.4	0	0.04	0.06	6.7	0	0	0.07	0.07	100.09
Krot et al 2004	CR	49.5	9.3	0.09	24.1	16.7	0	0.04	0.06	0.31	0	0	0.07	0.09	100.26
Krot et al 2004	CR	54.5	1.3	0.07	23.9	19.5	0	0.04	0.06	0.09	0	0	0.07	0.07	99.6
Krot et al 2002	CR	58.6	1.1	0.85	0.45	38.5	0	0.04	0.06	0.1	0	0	0.07	0.67	100.44
Krot et al 2002	CR	58.5	1.3	0.46	0.55	38.5	0	0.04	0.06	0.33	0	0	0.07	0.54	100.35
Krot et al 2002	CH	57.4	1.3	1.6	2.7	35.5	0	0.04	0.06	0.54	0	0	0.29	1	100.43
Krot et al 2002	CR	57.5	2.2	0.72	4.4	34.8	0	0.04	0.06	0.47	0	0	0.16	0.81	101.16
Krot et al 2002	CR	53.6	2.2	1.1	17.2	22.4	0	0.04	0.06	1.1	0	0	0.43	1.5	99.63
Krot et al 2002	?	53.5	2.9	0.45	20.5	20.6	0	0.04	0.06	1.4	0	0	0.22	0.67	100.34
Krot et al 2002	CH	52.1	3	1.1	18.9	20	0	0.04	0.06	2.3	0	0	0.56	1.4	99.46
Krot et al 2002	CR	48.1	5.5	1.1	19.1	17.5	0	0.04	0.06	4.7	0	0	0.66	2.7	99.46
Krot et al 2002	?	49.1	5.2	0.64	20.5	17.1	0	0.04	0.06	5.2	0	0	0.34	1.9	100.08
Krot et al 2002	CR	42.4	0.04	1	0.23	56.2	0	0.04	0.06	0.04	0	0	0.21	0.6	100.82
Krot et al 2002	CR	41.9	0.03	1.5	0.18	55.6	0	0.04	0.06	0.04	0	0	0.16	0.6	100.11
Krot et al 2002	CR	42.7	0.04	0.78	0.26	56.3	0	0.04	0.06	0.04	0	0	0.09	0.43	100.74
Krot et al 2002	CR	42.5	0.23	0.76	0.57	56.2	0	0.04	0.06	0.08	0	0	0.07	0.19	100.7
Krot et al 2002	CR	42.5	0.09	0.59	0.25	56	0	0.04	0.06	0.13	0	0	0.11	0.31	100.08
Krot et al 2002	CR	42.1	0.11	2.2	0.32	54.5	0	0.04	0.06	0.08	0	0	0.08	0.49	99.98
Krot et al 2002	CR	44.9	34.8	0.28	19.5	0.62	0	0.04	0.06	0.04	0	0	0.07	0.06	100.37
Krot et al 2002	CR	47.2	33.1	0.33	18.1	0.69	0	0.04	0.06	0.09	0	0	0.07	0.06	99.74
Krot et al 2002	CH	51	30.5	0.95	14.7	0.59	0	0.06	0.06	0.05	0	0	0.1	0.06	98.07
Krot et al 2002	CH	47.5	32	0.25	18.2	0.96	0	0.04	0.06	0.05	0	0	0.07	0.06	99.19
Krot et al 2002	CR	47.5	32.6	0.23	18.7	0.99	0	0.04	0.06	0.04	0	0	0.07	0.06	100.29
Krot et al 2002	CR	47.7	32.6	0.23	18.5	0.89	0	0.04	0.06	0.05	0	0	0.07	0.06	100.2
Krot et al 2002	CR	45.7	33.7	0.12	19.5	1	0	0.04	0.06	0.04	0	0	0.07	0.06	100.29
Krot et al 2002	CR	46.4	33.2	0.26	19.1	1.1	0	0.04	0.06	0.04	0	0	0.06	0.06	100.32
Krot et al 2002	CH	42.6	36.4	0.29	19.9	0.27	0	0.04	0.06	0.15	0	0	0.07	0.06	99.84
Krot et al 2002	CH	45.6	37.4	0.33	18.9	0.61	0	0.04	0.06	0.12	0	0	0.07	0.06	103.19
Krot et al 2002	CR	43.8	35.7	0.21	19.9	0.52	0	0.04	0.06	0.05	0	0	0.07	0.06	100.41
Krot et al 2002	CR	44.5	35.1	0.66	19.5	0.61	0	0.04	0.06	0.04	0	0	0.07	0.06	100.64
Krot et al 2002	CR	0.07	72.2	0.71	0.05	27.3	0	0.04	0.06	0.4	0	0	0.07	0.15	101.05
Krot et al 2002	CR	0.12	66.7	0.69	0.09	26.6	0	0.04	0.06	0.54	0	0	0.07	0.1	100.01
Krot et al 2002	CR	0.06	71.5	0.28	0.05	27.3	0	0.04	0.06	0.69	0	0	0.09	0.72	100.79

Table D.4

author	M type	SiO(2)	Al(2)O(3)	FeO	CaO	MgO	SO(2)	K(2)O	Na(2)O	TiO(2)	P(2)O	NiO	MnO	Cr(2)O(3)	total
Krot et al 2002	CR	0.12	71.6	0.48	0.04	27.8	0	0.04	0.06	0.2	0	0	0.08	0.44	100.86
Krot et al 2002	CR	0.25	70.8	0.51	0.03	27.7	0	0.04	0.06	0.22	0	0	0.07	1.1	100.78
Krot et al 2002	CR	0.07	63.7	1.7	0.03	25.3	0	0.04	0.06	0.18	0	0	0.07	8.7	99.85
Krot et al 2002	CH	0.09	69.5	1.6	0.09	26.8	0	0.04	0.06	1.1	0	0	0.2	0.61	100.09
Krot et al 2000	CH	51.1	0.03	21.3	0.04	26	0	0	0.46	0.04	0	0	0.41	0.56	99.94
Krot et al 2000	CH	51.9	0.03	20.4	0.04	25.2	0	0	0.73	0.04	0	0	0.44	0.69	99.47
Krot et al 2000	CH	50.7	0.03	19.9	0.04	26.7	0	0	0.33	0.04	0	0	0.37	0.76	98.87
Krot et al 2000	CH	49.9	0.03	20.6	0.04	29.1	0	0	0.17	0.04	0	0	0.51	0.61	101
Krot et al 2000	CH	51.7	0.03	18.3	0.04	27.4	0	0	0.64	0.04	0	0	0.35	0.86	99.36
Krot et al 2000	CH	54.2	0.03	17	0.04	28.9	0	0	0.226	0.04	0	0	0.45	0.8	101.686
Krot et al 2000	CH	51.8	0.03	16.5	0.04	29.4	0	0	0.65	0.04	0	0	0.37	0.73	99.56
Krot et al 2000	CH	51.6	0.03	15.8	0.07	29.2	0	0	0.54	0.04	0	0	0.44	0.81	98.53
Krot et al 2000	CH	53.3	0.03	15.5	0.07	29.1	0	0	0.67	0.04	0	0	0.27	0.78	99.76
Krot et al 2000	CH	49.6	0.04	16.1	0.08	31.2	0	0	0.17	0.04	0	0	1.2	1.1	99.53
Krot et al 2000	CH	53.7	0.03	14.5	0.04	30	0	0	0.24	0.04	0	0	0.57	0.87	99.99
Krot et al 2000	CH	54.1	0.03	13.3	0.15	28.4	0	0	3.1	0.04	0	0	0.23	0.65	100
Krot et al 2000	CH	53.9	0.03	13.6	0.04	31.6	0	0	0.15	0.04	0	0	0.34	0.72	100.42
Krot et al 2000	CH	52.7	0.03	13.6	0.05	31.1	0	0	0.37	0.04	0	0	0.39	0.78	99.06
Krot et al 2000	CH	54	0.03	11.5	0.24	32.5	0	0	0.19	0.04	0	0	0.47	0.72	99.69
Krot et al 2000	CH	54	0.03	10.4	0.04	34.1	0	0	0.26	0.04	0	0	0.26	0.9	100.03
Krot et al 2000	CH	54.8	0.03	10.1	0.04	34.4	0	0	0.03	0.04	0	0	0.2	0.78	100.42
Krot et al 2000	CH	53.8	0.03	10	0.08	34.8	0	0	0.29	0.04	0	0	0.17	0.83	100.04
Krot et al 2000	CH	55	0.03	7.7	0.07	35.5	0	0	0.44	0.04	0	0	0.57	1.1	100.45
Krot et al 2000	CH	51.8	0.18	22.9	0.17	23.5	0	0	0.24	0.04	0	0	0.94	0.93	100.7
Krot et al 2000	CH	51.1	0.03	20.6	0.04	26.3	0	0	0.7	0.04	0	0	0.34	0.75	99.9
Krot et al 2000	CH	49.2	0.03	21.1	0.04	27.3	0	0	0.19	0.04	0	0	0.41	0.79	99.1
Krot et al 2000	CH	52.7	0.03	17.3	0.04	27.9	0	0	0.19	0.04	0	0	0.47	0.81	99.48
Krot et al 2000	CH	52.3	0.03	17.3	0.04	29.4	0	0	0.35	0.04	0	0	0.32	0.81	100.59
Krot et al 2000	CH	52.5	0.03	16.5	0.05	29.3	0	0	0.03	0.04	0	0	0.31	0.69	99.45
Krot et al 2000	CH	52.8	0.03	16.1	0.04	29.3	0	0	0.43	0.04	0	0	0.28	0.96	99.98
Krot et al 2000	CH	51.8	0.03	16	0.04	31.4	0	0	0.5	0.04	0	0	0.25	0.73	100.79
Krot et al 2000	CH	53.8	0.03	13.9	0.05	30.2	0	0	0.1	0.04	0	0	0.33	0.87	99.32
Krot et al 2000	CH	54.7	0.03	11.8	0.1	31.5	0	0	0.1	0.04	0	0	1.1	1.3	100.67

Table D.4

author	M type	SiO(2)	Al(2)O(3)	FeO	CaO	MgO	SO(2)	K(2)O	Na(2)O	TiO(2)	P(2)O	NiO	MnO	Cr(2)O(3)	total
Krot et al 2000	CH	51.2	0.03	21.3	0.04	26.1	0	0	0.46	0.04	0	0	0.41	0.56	100.14
Krot et al 2000	CH	64.5	0.03	15.3	0.04	18.7	0	0	0.55	0.04	0	0	0.33	0.52	100.01
Krot et al 2000	CH	51.3	0.03	20.2	0.04	27	0	0	0.34	0.04	0	0	0.37	0.77	100.09
Krot et al 2000	CH	49.4	0.03	20.4	0.04	28.8	0	0	0.17	0.04	0	0	0.51	0.6	99.99
Krot et al 2000	CH	51.4	0.03	19.3	0.04	27.5	0	0	0.54	0.04	0	0	0.33	0.88	100.06
Krot et al 2000	CH	56.4	0.03	17	0.04	25	0	0	0.58	0.04	0	0	0.32	0.78	100.19
Krot et al 2000	CH	53.3	0.03	16.7	0.04	28.4	0	0	0.26	0.04	0	0	0.45	0.79	100.01
Krot et al 2000	CH	55.1	0.03	15.6	0.04	27.6	0	0	0.62	0.04	0	0	0.35	0.69	100.07
Krot et al 2000	CH	52.3	0.03	16.1	0.047	29.7	0	0	0.55	0.04	0	0	0.44	0.82	100.027
Krot et al 2000	CH	59.3	0.04	13.7	0.06	25.3	0	0	0.58	0.04	0	0	0.24	0.68	99.94
Krot et al 2000	CH	49.8	0.03	16.2	0.08	31.3	0	0	0.17	0.07	0	0	1.2	1.1	99.95
Krot et al 2000	CH	53.7	0.03	14.5	0.04	30	0	0	0.24	0.04	0	0	0.57	0.87	99.99
Krot et al 2000	CH	54.1	0.03	13.3	0.15	28.4	0	0	3.1	0.04	0	0	0.23	0.65	100
Krot et al 2000	CH	59.7	0.03	12	0.04	27.5	0	0	0.14	0.04	0	0	0.3	0.63	100.38
Krot et al 2000	CH	53.2	0.03	13.7	0.04	31.4	0	0	0.37	0.04	0	0	0.39	0.79	99.96
Krot et al 2000	CH	59.8	0.03	10.2	0.21	28.5	0	0	0.17	0.06	0	0	0.42	0.64	100.03
Krot et al 2000	CH	54	0.03	10.4	0.04	34.1	0	0	0.26	0.04	0	0	0.26	0.9	100.03
Krot et al 2000	CH	55.5	0.03	9.9	0.04	33.5	0	0	0.03	0.04	0	0	0.2	0.76	100
Krot et al 2000	CH	53.8	0.03	10	0.08	34.8	0	0	0.29	0.04	0	0	0.18	0.83	100.05
Krot et al 2000	CH	54.8	0.03	7.7	0.07	35.3	0	0	0.44	0.04	0	0	0.56	1.1	100.04
Krot et al 2000	CH	51.4	0.17	22.7	0.17	23.4	0	0	0.274	0.03	0	0	0.93	0.93	100.004
Krot et al 2000	CH	49.7	0	21.3	0.04	27.5	0	0	0.19	0.04	0	0	0.41	0.8	99.98
Krot et al 2000	CH	53	0	17.4	0.03	28.1	0	0	0.19	0.01	0	0	0.48	0.82	100.03
Krot et al 2000	CH	52.1	0	17.52	0.01	29.2	0	0	0.35	0	0	0	0.32	0.81	100.31
Krot et al 2000	CH	52.8	0	16.6	0.05	29.5	0	0	0.02	0.02	0	0	0.31	0.69	99.99
Krot et al 2000	CH	52.8	0	16.1	0.01	29.3	0	0	0.43	0.02	0	0	0.28	0.96	99.9
Krot et al 2000	CH	51.4	0	15.8	0.02	31.2	0	0	0.5	0.01	0	0	0.25	0.72	99.9
Krot et al 2000	CH	54.2	0	14	0.05	30.4	0	0	0.1	0.02	0	0	0.34	0.87	99.98
Krot et al 2000	CH	54.3	0	11.7	0.1	31.3	0	0	0.1	0.05	0	0	1.1	1.3	99.95
Krot et al 2000	CH	95.2	0.04	2.4	0.04	0.83	0	0	0.03	0.04	0	0	0.07	0.03	98.68
Krot et al 2000	CH	93.8	0.04	2.3	0.04	1.1	0	0	0.03	0.04	0	0	0.07	0.03	97.45
Krot et al 2000	CH	98.8	0.04	0.83	0.04	0.04	0	0	0.03	0.04	0	0	0.07	0.03	99.92
Krot et al 2000	CH	95.7	0.04	1.4	0.04	0.36	0	0	0.03	0.04	0	0	0.07	0.03	97.71

Table D.4

author	M type	SiO(2)	Al(2)O(3)	FeO	CaO	MgO	SO(2)	K(2)O	Na(2)O	TiO(2)	P(2)O	NiO	MnO	Cr(2)O(3)	total
Krot et al 2006	CB	41.4	0.26	2.9	0.24	53.9		0.06	0.06	0.04	0	0	0.06	0.37	99.29
Krot et al 2006	CB	42	0.03	0.94	0.29	55.9		0.06	0.06	0.05	0	0	0.06	0.36	99.75
Krot et al 2006	CB	42	0.06	1.9	0.21	55.1		0.06	0.06	0.04	0	0	0.06	0.12	99.61
Krot et al 2006	CB	41.9	0.11	2.4	0.28	54.9		0.06	0.06	0.04	0	0	0.06	0.42	100.23
Krot et al 2006	CB	41.6	0.11	4	0.23	53.7		0.06	0.06	0.04	0	0	0.08	0.19	100.07
Krot et al 2006	CB	42.1	0.04	0.33	0.16	56.3		0.06	0.06	0.04	0	0	0.11	0.23	99.43
Krot et al 2006	CB	42	0.03	0.67	0.2	56		0.06	0.06	0.04	0	0	0.15	0.45	99.66
Krot et al 2006	CB	41.7	0.09	0.92	0.38	55.4		0.06	0.06	0.08	0	0	0.07	0.47	99.23
Krot et al 2006	CB	41.7	0.14	1.6	0.41	55.6		0.06	0.06	0.04	0	0	0.06	0.41	100.08
Krot et al 2006	CB	41.5	0.03	2.6	0.27	54.5		0.06	0.06	0.04	0	0	0.32	0.7	100.08
Krot et al 2006	CB	41	0.04	3	0.27	54.2		0.06	0.06	0.05	0	0	0.26	0.71	99.65
Krot et al 2006	CB	42.3	0.03	2.2	0.29	55		0.06	0.06	0.04	0	0	0.1	0.55	100.63
Krot et al 2006	CB	40.7	0.43	4.5	0.24	52.4		0.06	0.06	0.04	0	0	0.12	0.59	99.14
Krot et al 2006	CB	41.6	0.06	2.4	0.22	54.8		0.06	0.06	0.04	0	0	0.07	0.51	99.82
Krot et al 2006	CB	38.9	0.03	16.4	0.19	43.3		0.06	0.06	0.04	0	0	0.5	0.35	99.83
Krot et al 2006	CB	38	0.05	19.6	0.31	39.7		0.06	0.06	0.04	0	0	0.55	0.29	98.66
Krot et al 2006	CB	41.7	0.13	1.3	0.43	56.2		0.06	0.06	0.05	0	0	0.06	0.2	100.19
Krot et al 2006	CB	34.7	0.1	35.8	0.52	26.7		0.06	0.06	0.04	0	0	0.35	0.27	98.6
Krot et al 2006	CB	40	0.05	11.4	0.21	46.7		0.06	0.06	0.04	0	0	0.49	0.56	99.57
Krot et al 2006	CB	34.4	0.21	37	0.25	25.2		0.06	0.06	0.04	0	0	0.53	0.48	98.23
Krot et al 2006	CB	57.5	1.1	3	0.91	36.1	0	0.06	0.06	0.08	0	0	0.33	0.8	99.94
Krot et al 2006	CB	55.7	3.9	1.5	2.4	35.1	0	0.06	0.06	0.39	0	0	0.06	0.77	99.94
Krot et al 2006	CB	54.7	5.2	1.5	4.6	33.3	0	0.06	0.06	0.48	0	0	0.07	0.75	100.72
Krot et al 2006	CB	51.7	10.2	1.9	1.9	33.2	0	0.06	0.06	0.47	0	0	0.06	0.83	100.38
Krot et al 2006	CB	49.3	10.9	1.1	17.9	19.6	0	0.06	0.06	0.52	0	0	0.06	0.61	100.11
Krot et al 2006	CB	45.1	16.7	1.6	20.7	15.1	0	0.06	0.06	0.3	0	0	0.06	0.36	100.04
Krot et al 2006	CB	56.3	2.9	2	2.3	35.4	0	0.06	0.06	0.21	0	0	0.06	0.76	100.05
Krot et al 2006	CB	54.4	4.7	2.4	5.9	30.9	0	0.06	0.06	0.53	0	0	0.06	0.89	99.9
Krot et al 2006	CB	45.8	13.3	2.5	19.3	15	0	0.06	0.06	1.6	0	0	0.06	1	98.68
Krot et al 2006	CB	50.4	7.7	1.5	15.8	21.5	0	0.06	0.06	1.2	0	0	0.06	1.1	99.38
Krot et al 2006	CB	51.4	10.8	1.9	2	32.3	0	0.06	0.06	0.6	0	0	0.06	0.8	99.98
Krot et al 2006	CB	50	14.4	2	2.2	30.5	0	0.06	0.06	0.32	0	0	0.06	0.55	100.15
Krot et al 2006	CB	48.2	14.2	2	5	28.9	0	0.06	0.06	0.64	0	0	0.06	0.34	99.46

Table D.4

author	M type	SiO(2)	Al(2)O(3)	FeO	CaO	MgO	SO(2)	K(2)O	Na(2)O	TiO(2)	P(2)O	NiO	MnO	Cr(2)O(3)	total
Krot et al 2006	CB	47	15.3	2.3	11.2	23.2	0	0.06	0.06	0.43	0	0	0.06	0.27	99.88
Krot et al 2006	CB	50.3	13.3	1.1	1.8	32.9	0	0.06	0.06	0.63	0	0	0.07	0.36	100.58
Krot et al 2006	CB	43.1	19.7	1.4	23	12	0	0.06	0.06	0.81	0	0	0.06	0.31	100.5
Krot et al 2006	CB	53	0.03	0.85	0.03	45.7	0	0.06	0.06	0.04	0	0	0.06	0.5	100.33
Krot et al 2006	CB	54	0.05	1.1	0.07	43.4	0	0.06	0.06	0.04	0	0	0.18	0.7	99.66
Krot et al 2006	CB	54.2	0.08	5	0.06	40.8	0	0.06	0.08	0.04	0	0	0.45	0.66	101.43
Krot et al 2006	CB	55.2	0.13	0.81	0.13	42.6	0	0.06	0.06	0.04	0	0	0.19	0.88	100.1
Krot et al 2006	CB	52.2	0.89	2.5	0.74	42.8	0	0.06	0.06	0.07	0	0	0.07	0.85	100.24
Krot et al 2006	CB	54.5	0.93	2.2	0.73	40.9	0	0.06	0.06	0.04	0	0	0.14	0.67	100.23
Krot et al 2006	CB	53.2	1	2.2	0.77	41.7	0	0.06	0.06	0.05	0	0	0.12	0.75	99.91
Krot et al 2006	CB	56.2	1.5	0.66	1.1	39.8	0	0.06	0.06	0.09	0	0	0.1	0.9	100.47
Krot et al 2006	CB	53.4	0	0.7	0.03	46	0	0.06	0.06	0.04	0	0	0.06	0.59	100.94
Krot et al 2006	CB	54.2	0.05	1.4	0.03	43.5	0	0.06	0.06	0.04	0	0	0.06	0.66	100.06
Krot et al 2006	CB	54.9	0.18	1.3	0.13	42.7	0	0.06	0.06	0.04	0	0	0.11	0.78	100.26
Krot et al 2006	CB	54.8	0.22	0.73	0.16	44	0	0.06	0.06	0.04	0	0	0.11	0.62	100.8
Krot et al 2006	CB	54.1	0.37	0.62	0.32	43.6	0	0.06	0.06	0.04	0	0	0.15	0.75	100.07
Krot et al 2006	CB	54.1	0.52	0.26	0.4	44.2	0	0.06	0.06	0.04	0	0	0.06	0.47	100.17
Krot et al 2006	CB	53.7	0.64	1.2	0.69	42.7	0	0.06	0.06	0.04	0	0	0.11	0.8	100
Hezel et al 2003	CH	59.22	5	1.4	4.17	30.24	0	0	0.15	0.19	0	0.03	0.02	0.29	100.71
Hezel et al 2003	CH	96.87	0.61	0.3	0.12	0.58	0	0	0.07	0.02	0	0.02	0.02	0.01	98.62
Hezel et al 2003	CH	97.09	0.29	0.34	0.09	0.35	0	0	0.074	0.01	0	0.01	0	0.01	98.264
Hezel et al 2003	CH	85.2	1.77	0.67	1.37	9.74	0	0	0.08	0.07	0	0.02	0.01	0.1	99.03
Hezel et al 2003	CH	59.48	5.26	0.93	3.71	30.78	0	0	0.01	0.18	0	0	0	0.32	100.67
Hezel et al 2003	CH	99.3	0.32	0.14	0.11	0.35	0	0	0.02	0.03	0	0	0.02	0	100.29
Hezel et al 2003	CH	84.48	2.16	0.43	1.45	11.66	0	0	0.02	0.09	0	0	0.01	0.12	100.42
Hezel et al 2003	CH	52.39	0.48	27.09	0.18	18.67	0	0	0.1	0.01	0	0.32	0.06	0.43	99.73
Hezel et al 2003	CH	98.53	0.17	1.48	0.05	0.3	0	0	0.11	0.01	0	0.03	0.01	0.01	100.7
Hezel et al 2003	CH	69.46	0.36	17.61	0.13	11.87	0	0	0.11	0.01	0	11.87	0.04	0.28	111.74
Hezel et al 2003	CH	97.01	0.02	0.54	0.01	0.02	0	0	0	0.04	0	0.02	0	0.01	97.67
Hezel et al 2003	CH	52.36	0.15	27.39	0.18	16.95	0	0.04	0.28	0.03	0	0.22	0.18	0.47	98.25
Hezel et al 2003	CH	90.91	0.17	5.25	0.02	2.63	0	0	0.47	0	0	0.04	0.05	0.08	99.62
Hezel et al 2003	CH	73.95	0.16	14.99	0.09	8.93	0	0	0.38	0.01	0	0.12	0.11	0.25	98.99
Hezel et al 2003	CH	56.81	0.19	24.29	0.15	15.44	0	0	0.03	0	0	0.33	0.11	0.23	98.58

Table D.4

author	M type	SiO(2)	Al(2)O(3)	FeO	CaO	MgO	SO(2)	K(2)O	Na(2)O	TiO(2)	P(2)O	NiO	MnO	Cr(2)O(3)	total
Hezel et al 2003	CH	95.79	0.07	1.38	0.02	0.27	0	0.02	0.05	0.02	0	0.03	0.01	0.04	97.7
Hezel et al 2003	CH	79.81	0.11	10.77	0.07	6.49	0	0.04	0.04	0.01	0	0.15	0.06	0.52	98.07
Hezel et al 2003	CH	51.87	2.77	8.38	13.07	16.09	0	0.03	0.16	0.41	0	0.01	6.27	1.46	100.52
Hezel et al 2003	CH	69.04	18.13	1.16	4.63	0.47	0	0.47	5.42	0.32	0	0.04	0.35	0.03	100.06
Hezel et al 2003	CH	99.2	0.24	0.32	0.04	0.02	0	0.02	0.09	0.03	0	0.03	0.05	0.01	100.05
Hezel et al 2003	CH	72.34	6.05	3.74	6.43	6.51	0	0.14	1.55	0.26	0	0.02	2.59	0.59	100.22
Hezel et al 2003	CH	56.54	5.7	2.56	7.47	22.34	0	0.03	0.67	0.34	0	0.032	3.09	2.27	101.042
Hezel et al 2003	CH	62.11	17.47	0.88	9.21	6.5	0	0.1	2.63	0.29	0	0.02	0.93	0.66	100.8
Hezel et al 2003	CH	98.68	0.33	0.86	0.1	0.05	0	0	0.13	0.06	0	0.05	0.04	0.03	100.33
Hezel et al 2003	CH	65.48	7.79	1.82	6.61	14.27	0	0	1.08	0.28	0	0.03	1.99	1.46	100.81
Hezel et al 2003	CH	59.01	4.1	0.91	3.54	30.41	0	0.06	0.15	0.11	0	0.03	0.01	0.72	99.05
Hezel et al 2003	CH	95.98	0.46	0.28	0.11	0.6	0	0	0.4	0.01	0	0.01	0.01	0.01	97.87
Hezel et al 2003	CH	97.14	0.08	0.4	0.35	0.19	0	0	0.03	0	0	0.04	0.01	0.01	98.25
Hezel et al 2003	CH	57.84	0.67	3.65	0.92	35.82	0	0	0.09	0.04	0	0.04	0.52	0.94	100.53
Hezel et al 2003	CH	95.52	1.39	0.85	0.17	2.33	0	0	0.67	0.03	0	0.07	0.11	0.07	101.21
Hezel et al 2003	CH	71.97	0.94	2.6	0.64	23.26	0	0	0.31	0.04	0	0.05	0.37	0.61	100.79
Hezel et al 2003	CH	55.34	0.04	7.79	0.15	34.42	0	0.01	0	0.09	0	0.05	0.09	0.76	98.74
Hezel et al 2003	CH	61.79	3.54	2.26	2.81	25.43	0	0	0.43	0.15	0	0.04	1.24	1.11	98.8
Hezel et al 2003	CH	58.84	7.53	0.61	7.37	24.92	0	0	0.11	0.23	0	0.01	0.01	0.14	99.77
Hezel et al 2003	CH	95.72	0.8	0.66	0.36	0.94	0	0	0.08	0.06	0	0.04	0.03	0.02	98.71
Hezel et al 2003	CH	68.25	3.19	0.75	2.69	22.96	0	0	0.22	0.08	0	0.03	0.01	0.54	98.72
Leshin et al 1996	CL	43.6	0.12	0.5	0.25	55.9	0	0	0	0	0	0	0.08	0.42	100.87
Leshin et al 1996	CL	39.8	0	23	0.29	37.6	0	0	0	0	0	0	0.4	0.32	101.41
Leshin et al 1996	CL	41.9	0	7.5	0.08	49.8	0	0	0	0	0	0	0.51	0.49	100.28
Leshin et al 1996	CL	41.7	0	8.2	0.15	50.1	0	0	0	0	0	0	0.52	0.64	101.31
Leshin et al 1996	CL	41.2	0	10	0.03	48.6	0	0	0	0	0	0	0.57	0.08	100.48
Leshin et al 1996	CL	58.6	0.44	6.4	1.1	33.1	0	0	0	0	0	0	0.51	0.61	100.76
Leshin et al 1996	CL	55	2.2	3.1	21.6	17.6	0	0	0	0	0	0	0.38	1.7	101.58
Leshin et al 1996	CL	55.6	1.7	3.2	19.6	18.7	0	0	0	0	0	0	0.35	1.4	100.55
Morlok et al 2005	CL	41.17	3.86	11.58	0.04	25.2	2.1	0.11	0.3	0.05	0.05	0.37	0.14	0.39	85.36
Morlok et al 2005	CL	33.11	2.25	18.64	0.59	20.68	6.68	0.12	0.86	0.07	0.32	1.42	0.19	0.42	85.35
Morlok et al 2005	CL	31.55	2.13	20.89	0.5	19.76	7.16	0.13	0.89	0.07	0.19	1.45	0.24	0.41	85.37
Morlok et al 2005	CL	28.25	1.95	23.74	0.83	18.87	7.99	0.15	1.15	0.06	0.27	1.51	0.21	0.37	85.35

Table D.4

author	M type	SiO(2)	Al(2)O(3)	FeO	CaO	MgO	SO(2)	K(2)O	Na(2)O	TiO(2)	P(2)O	NiO	MnO	Cr(2)O(3)	total
Morlok et al 2005	CL	26.05	1.95	25.55	0.6	16.86	10.1	0.21	1.1	0.09	0.14	2.05	0.28	0.37	85.35
Morlok et al 2005	CL	23.9	1.61	35.4	0.64	16.77	4.73	0.1	0.45	0.08	0.23	1.06	0.08	0.31	85.36
Morlok et al 2005	CL	19.64	1.17	36.64	0.26	12.22	10.29	0.1	2.14	0.06	0.22	1.89	0.31	0.42	85.36
Morlok et al 2005	CL	30.45	2.01	22.63	1.19	19.43	6.23	0.14	0.76	0.07	0.63	1.24	0.18	0.39	85.35
Morlok et al 2005	CL	29.76	2.23	23.59	0.13	16.49	9.02	0.17	1.1	0.09	0.1	1.89	0.38	0.42	85.37
Morlok et al 2005	CL	25.8	1.76	26.74	0.41	16.16	10.79	0.2	0.62	0.08	0.21	1.83	0.3	0.44	85.34
Morlok et al 2005	CL	22.96	1.75	30.62	1.06	12.53	11.6	0.16	0.65	0.1	0.21	2.77	0.43	0.5	85.34
Morlok et al 2005	CL	20.58	1.48	35.92	0.04	11.62	11.8	0.06	0.71	0.06	0.11	2.01	0.56	0.39	85.34
Morlok et al 2005	CL	31.99	2.09	21.96	0.08	17.27	7.57	0.26	0.6	0.07	0.3	2.34	0.37	0.46	85.36
Morlok et al 2005	CL	28.89	1.99	24.2	0.3	16.63	9.48	0.25	0.81	0.07	0.22	1.87	0.24	0.41	85.36
Morlok et al 2005	CL	27.42	1.9	25.58	0.33	14.99	10.43	0.22	1.23	0.07	0.22	2.17	0.34	0.46	85.36
Morlok et al 2005	CL	25.22	1.7	30.37	0.28	13.87	9.24	0.24	1.09	0.1	0.33	2.19	0.27	0.44	85.34
Morlok et al 2005	CL	18.05	1.19	36.67	0.48	11.88	12.21	0.25	1.04	0.07	0.28	2.38	0.48	0.35	85.33
Morlok et al 2005	CL	12.7	3.09	28.8	0.06	20.8	14.8	0.09	1.03	0.08	0.08	2.54	0.6	0.67	85.34
Morlok et al 2005	CL	19.43	1.21	30.32	4.29	12.7	9.82	0.06	1.12	0.1	3.46	2.09	0.37	0.39	85.36
Morlok et al 2005	CL	35.65	2.22	18.3	0.2	20.63	5.4	0.06	0.56	0.06	0.19	1.39	0.25	0.46	85.37
Morlok et al 2005	CL	30.99	2.1	21.47	0.18	18.73	8.58	0.29	0.49	0.08	0.14	1.7	0.2	0.41	85.36
Morlok et al 2005	CL	27.89	2.01	25.58	0.99	16.22	8.97	0.14	0.66	0.06	0.15	1.86	0.38	0.44	85.35
Barat et al 2011	CL	0	3.52	33.4	2.62	24.09		0.05	0.48	0.13	0.26		0.18		64.73
Huber et al 2005	CK	36.8	0.15	29.3	0.07	33.9	0	0	0.03	0.04	0	0.58	0.23	0.04	101.14
Huber et al 2005	CK	37.5	0.02	25.6	0.14	36.3	0	0	0.01	0.04	0	0.49	0.25	0.06	100.41
Huber et al 2005	CK	37.2	0.2	28.9	0.19	34.1	0	0	0.02	0.05	0	0.25	0.24	0.08	101.23
Huber et al 2005	CK	37.2	0.56	26	0.08	25.9	0	0	0.01	0.06	0	0.37	0.22	0.13	90.53
Huber et al 2005	CK	36.8	0.02	26	0.09	35.6	0	0	0.01	0.01	0	0.41	0.24	0.09	99.27
Huber et al 2005	CK	0	2.22	84.8	0.02	0.29	0	0	0.03	0.38	0	0.25	0.04	5.03	93.06
Huber et al 2005	CK	0	0.97	84.9	0.09	0.18	0	0	0.03	0.17	0	0.2	0.04	3.62	90.2
Huber et al 2005	CK	0	1.23	85.3	0.04	0.14	0	0	0	0.19	0	0.16	0	3.7	90.76
Huber et al 2005	CK	0	3.36	84	0.22	0.97	0	0	0.02	0.78	0	0.27	0.1	3.33	93.05
Huber et al 2005	CK	0	0.83	85.2	0.05	0.12	0	0	0.02	0.19	0	0.16	0.03	4.17	90.77
Greenwood et al 2009	CV	0.1	1.32	88.72	0.23	0.31	0	0	0	0.06	0	0.18	-0.02	2.26	93.16
Greenwood et al 2009	CK	0.08	0.63	88.62	0.42	0.03	0	0	0	0.22	0	0.2	0.04	3.56	93.8
Greenwood et al 2009	CK	-0.06	1.93	84.64	0.34	0.21	0	0	0	0.51	0	0.22	0.06	4.98	92.83
Greenwood et al 2009	CV	0.08	0.12	90.37	0.14	0.03	0	0	0	-0.02	0	-0.07	-0.02	1.92	92.55

Table D.4

author	M type	SiO(2)	Al(2)O(3)	FeO	CaO	MgO	SO(2)	K(2)O	Na(2)O	TiO(2)	P(2)O	NiO	MnO	Cr(2)O(3)	total
Greenwood et al 2009	CK	-0.05	1.09	87.05	0.12	0.07	0	0	0	0.31	0	0.26	0.04	3.97	92.86
Greenwood et al 2009	CK	0.21	2.95	84.6	0.6	0.57	0	0	0	0.95	0	0.33	0.09	3.02	93.32
Greenwood et al 2009	CK	0.1	1.3	88.76	0.37	0.17	0	0	0	0.17	0	0.25	-0.03	1.17	92.26
Righter et al 2007	CK	0.11	4.97	46.82	0.08	2.48	0	0	0.02	40.72	0	0.3	0.8	2.76	99.06
Righter et al 2007	CK	0.12	0.99	85.97	0.03	0.09	0	0	0.02	0.55	0	0.32	0.03	3.6	91.72
Righter et al 2007	CK	0.13	4.59	43.26	0.06	2.25	0	0	0.01	46.59	0	0.14	0.93	1.32	99.28
Righter et al 2007	CK	0.1	0.89	86.26	0.1	0.03	0	0	0.01	0.35	0	0.25	0.03	3.55	91.57
Righter et al 2007	CK	0.1	7.04	42.3	0.04	2.74	0	0	0.01	42.92	0	0.04	0.86	4.01	100.06
Righter et al 2007	CK	0.09	1.24	85.66	0.05	0.08	0	0	0.02	0.7	0	0.23	0.04	3.71	91.82
Righter et al 2007	CK	0.15	7.07	53.89	0.02	2.22	0	0	0.02	29	0	0.17	0.74	4.11	97.39
Righter et al 2007	CK	0.12	0.42	87.04	0.02	0.01	0	0	0.01	0.46	0	0.18	0.03	3.69	91.98
Righter et al 2007	CK	0.06	13.69	45.08	0.04	3.7	0	0	0.03	30.78	0	0.1	0.74	4.53	98.75
Righter et al 2007	CK	0.08	0.79	85.12	0.04	0.11	0	0	0.01	1.34	0	0.4	0.05	3.45	91.39
Righter et al 2007	CK	0.05	10.95	48.46	0.35	3.24	0	0	0.03	28.99	0	1.03	0.64	4.15	97.89
Righter et al 2007	CK	0.07	0.34	86.29	0.15	0.02	0	0	0.01	0.66	0	0.25	0.02	3.53	91.34
Righter et al 2007	CK	0.13	8.54	40.18	0.02	3.33	0	0	0.01	40.34	0	0.41	0.79	4	97.75
Righter et al 2007	CK	0.09	1.87	85.22	0.01	0.13	0	0	0.01	1.41	0	0.27	0.07	3.49	92.57
Righter et al 2007	CK	2.22	10.35	51.97	1.59	3.38	0	0	0.06	22.5	0	0.73	0.33	3.23	96.36
Righter et al 2007	CK	0.05	0.49	86.43	0.06	0.11	0	0	0.01	0.79	0	0.23	0.02	3.35	91.54
Righter et al 2007	CK	0.15	0.63	82.44	0.02	0.12	0	0	0.01	0.4	0	0.33	0	2.94	87.04
Righter et al 2007	CK	0.03	8.19	38.8	0.11	2.7	0	0	0.01	37.56	0	0.05	0.46	2.7	90.61
Righter et al 2007	CK	0.06	0.6	86.13	0.03	0.17	0	0	0.01	1.53	0	0.16	0.01	3.05	91.75
Righter et al 2007	CK	0.07	8.1	49.91	0.01	2.88	0	0	0.03	31.25	0	0.09	0.38	3.69	96.41
Righter et al 2007	CK	0.17	0.39	86.96	0.04	0.11	0	0	0	0.27	0	0.21	0	3.37	91.52
Righter et al 2007	CK	0.14	9.53	61.97	0.04	2.25	0	0	0.02	18.54	0	0.12	0.22	4.97	97.8
Righter et al 2007	CK	0.04	0.98	85.44	0.23	0.21	0	0	0.01	0.81	0	0.25	0.01	4.03	92.01
Righter et al 2007	CK	0.07	5.91	43.33	0.2	2.35	0	0	0.03	42.6	0	0.45	0.61	3	98.55
Righter et al 2007	CK	0.06	0.46	86.93	0.05	0.11	0	0	0.02	0.28	0	0.25	0	3.87	92.03
Righter et al 2007	CK	0.07	9.23	60.18	0.05	2.91	0	0	0.02	18.33	0	0.18	0.23	4.47	95.67
Righter et al 2007	CK	0.07	0.5	86.27	0.07	0.2	0	0	0	0.73	0	0.21	0	3.63	91.68
Righter et al 2007	CK	0.11	7.24	44.18	0.13	2.82	0	0	0.03	37.7	0	0.17	0.52	2.91	95.81
Righter et al 2007	R	0.2	2.28	64.56	1.21	1.63	0	0	0	1.26	0	0	0.23	18.5	89.87
Righter et al 2007	CK	0.01	0	43.82	0.04	1.89	0	0	0	53.4	0	0.02	0.66	0.12	99.96

Table D.4

author	M type	SiO(2)	Al(2)O(3)	FeO	CaO	MgO	SO(2)	K(2)O	Na(2)O	TiO(2)	P(2)O	NiO	MnO	Cr(2)O(3)	total
Righter et al 2007	CK	0.37	4.99	56.91	0.03	2.43	0	0	0	26.19	0	0.59	0.52	3.28	95.31
Righter et al 2007	CK	0.02	0.06	43.42	1.4	1.59	0	0	0.01	49.66	0	0.33	0.98	0.2	97.67
Righter et al 2007	CK	0.06	0.63	86.46	0.22	0.06	0	0	0.01	0.15	0	0.43	0.03	3.3	91.35
Righter et al 2007	CK	0.06	54.98	27.01	0.01	10.64	0	0	0.08	0.19	0	0.37	0.03	7.06	100.43
Chizmadia et al 2007	CM	23.7	2.1	42.53	0.8	10.7	13.49	0	0	0.03	0	5.86	0	0.75	99.96
Chizmadia et al 2007	CM	31.68	4.99	40.9	0.2	16.18	4.02	0.12	0	0.13	0.41	0.66	0.25	0.46	100
Chizmadia et al 2007	CM	35.42	6.31	34.22	0.3	16.81	4.86	0.15	0	0.15	0.5	0.54	0.16	0.58	100
Chizmadia et al 2007	CM	33.42	5.61	37.79	0.24	16.48	4.42	0.13	0	0.14	0.45	0.6	0.2	0.52	100
Hewin et al 2013	CM	28.72	2.07	32.05	1.61	19.83	0	0.04	0.67	0.1	0.28	0	0.22	0	85.59
Hewin et al 2013	CM	0	1.96	29.54	1.84	18.58	0	0	0.61	0.1	0.24	0	0.22	0	53.09
Hewin et al 2013	CM	0	1.95	30.54	1.06	18.43	0	0	0.57	0.1	0.24	0	0.23	0	53.12
Hewin et al 2013	CM	0	2.21	33.02	1.51	21.19	0	0	0.41	0.11	0.25	0	0.24	0	58.94
Hewin et al 2013	CM	28.84	2.19	30.6	1.79	20.13	0	0.05	0.58	0.11	0.24	0	0.22	0	84.75
Han et al 2015	CO	0.08	71.36	0.71	0.14	27.43	0	0.02	0.01	0.14	0	0	0.01	0.1	100
Han et al 2015	CO	0.14	71.2	0.67	0.16	27.45	0	0.02	0.01	0.12	0	0	0.01	0.1	99.88
Han et al 2015	CO	0.07	72.41	0.71	0.06	27.35	0	0.01	0.01	0.1	0	0	0	0.1	100.82
Han et al 2015	CO	0.05	70.87	0.7	0.06	27.35	0	0.03	0	0.19	0	0	0.01	0.1	99.36
Han et al 2015	CO	0.02	71.29	0.74	0.08	27.66	0	0.01	0.01	0.12	0	0	0	0.1	100.03
Han et al 2015	CO	0.01	71.21	0.75	0.03	27.66	0	0.01	0.01	0.09	0	0	0	0.11	99.88
Han et al 2015	CO	0.04	71.28	0.82	0.05	27.54	0	0.02	0.01	0.1	0	0	0	0.11	99.97
Han et al 2015	CO	0.08	71.34	0.72	0.12	27.45	0	0.02	0.02	0.18	0	0	0	0.11	100.04
Han et al 2015	CO	0.05	71.24	0.74	0.05	27.52	0	0.03	0.01	0.16	0	0	0.01	0.12	99.93
Han et al 2016	CO	0.12	83.97	0.82	8.28	2.7	0	0.04	0.01	4.86	0	0	0	0.05	100.85
Han et al 2017	CO	0.06	81.73	0.78	8.95	2.59	0	0.03	0.01	6.44	0	0	0	0.06	100.65
Han et al 2018	CO	0.05	82.5	0.77	8.44	2.72	0	0.03	0	5.63	0	0	0	0.047	100.187
Han et al 2019	CO	0.07	82.39	0.75	8.83	2.59	0	0.03	0.01	6.01	0	0	0	0.06	100.74
Han et al 2020	CO	0.11	82.79	0.8	8.34	2.8	0	0.04	0.02	5.58	0	0	0	0.05	100.53
Han et al 2021	CO	0.12	82.95	0.76	8.34	2.86	0	0.02	0.01	5.62	0	0	0.01	0.05	100.74
Han et al 2022	CO	0.07	82.65	0.84	8.34	3.04	0	0.03	0.01	5.64	0	0	0	0.04	100.66
Misawa et al 1988	CO	45	7.5	7.5	6	33.1	0	0	0.3	0	0	0	0.1	0.6	100.1
Misawa et al 1988	CO	52.5	13.8	2.8	6.5	18.9	0	0.2	3.8	0.3	0	0	0.3	0.8	99.9
Misawa et al 1988	CO	52.4	7.65	7.45	7.26	23	0	0.8	1.81	0.28	0	0	0.24	0.54	101.43
Makade et al 2008 (S1)	CR	0.05	89.6	0.41	8.4	0.62	0	0.04	0.08	2.3	0	0	0.09	0.07	101.6

Table D.4

author	M type	SiO(2)	Al(2)O(3)	FeO	CaO	MgO	SO(2)	K(2)O	Na(2)O	TiO(2)	P(2)O	NiO	MnO	Cr(2)O(3)	total
Makade et al 2008 (S1)	CR	0.03	78.5	0.14	21.6	0.06	0	0.04	0.08	0.21	0	0	0.09	0.07	100.9
Makade et al 2008 (S1)	CR	0.12	0.87	0.18	40.3	0.06	0	0.04	0.08	57.8	0	0	0.09	0.07	99.6
Makade et al 2008 (S1)	CR	0.03	70.5	0.30	0.04	28.3	0	0.04	0.08	0.43	0	0	0.09	0.32	100.2
Makade et al 2008 (S1)	CR	43.3	36.6	0.09	20.4	0.06	0	0.04	0.08	0.08	0	0	0.09	0.07	100.8
Makade et al 2008 (S2)	CR	24.6	33.0	0.04	40.9	1.8	0	0.04	0.08	0.08	0	0	0.09	0.07	100.7
Makade et al 2008 (S2)	CR	23.3	34.1	0.85	37.4	1.4	0	0.04	0.08	0.46	0	0	0.09	0.07	97.8
Makade et al 2008 (S2)	CR	23.2	35.2	0.11	40.9	0.76	0	0.04	0.08	0.08	0	0	0.09	0.07	100.6
Makade et al 2008 (S2)	CR	24.4	33.0	0.03	40.9	1.6	0	0.04	0.08	0.08	0	0	0.09	0.07	100.4
Makade et al 2008 (S2)	CR	22.9	35.3	0.09	41.0	0.74	0	0.04	0.08	0.08	0	0	0.09	0.07	100.3
Makade et al 2008 (S2)	CR	21.4	36.9	0.9	39.7	0.37	0	0.04	0.08	0.08	0	0	0.09	0.07	99.6
Makade et al 2008 (S3)	CR	36.5	18.2	0.09	25.1	9.6	0	0.04	0.08	9.5	0	0	0.09	0.19	99.5
Makade et al 2008 (S3)	CR	54.4	1.2	1.4	24.7	18.0	0	0.04	0.08	0.10	0	0	0.09	0.07	100.1
Makade et al 2008 (S3)	CR	0.12	0.87	0.18	40.3	0.00	0	0.04	0.08	57.8	0	0	0.09	0.07	99.6
Makade et al 2008 (S3)	CR	55.7	1.4	0.37	25.5	18.1	0	0.04	0.08	0.08	0	0	0.09	0.07	101.6
Makade et al 2008 (S3)	CR	42.0	13.4	5.6	23.1	11.4	0	0.04	0.08	2.6	0	0	0.09	0.09	98.4
Wasson et al 2008	CR	27.9	1.95	31	0.5	15.6	4.17	0.15	1.25	0	0	0	0.18	0.37	83.07
Wasson et al 2008	CR	27.9	1.75	31.4	0.65	16.5	3.56	0.14	0.93	0	0	0	0.22	0.36	83.41
Wasson et al 2008	CR	23.2	1.89	32.13	1.42	16.29	3.69	0.09	0.73	0	0	0	0.22	0.3	79.96
Wasson et al 2008	CR	24.85	1.92	31.08	1.38	17.48	2.49	0.11	0.82	0	0	0	0.24	0.29	80.66
Wasson et al 2008	CR	17.63	1.35	26.03	10.23	15.09	1.78	0.08	0.74	0	0	0	0.51	0.2	73.64
Wasson et al 2008	CR	28.01	1.99	33.69	0.65	15.54	3.37	0.11	0.67	0	0	0	0.24	0.31	84.58
Wasson et al 2008	CR	28.74	2.01	33.41	0.57	15.99	3.46	0.11	0.67	0	0	0	0.2	0.32	85.48
Wasson et al 2008	CR	26.35	1.88	30.5	1.36	16.32	2.67	0.08	0.9	0	0	0	0.24	0.33	80.63
Wasson et al 2008	CR	27.49	1.86	30.42	1.08	17.13	3	0.09	0.94	0	0	0	0.24	0.36	82.61
Wasson et al 2008	CR	28.71	1.93	28.72	0.95	17.63	3.25	0.13	0.73	0	0	0	0.2	0.33	82.58
Wasson et al 2008	CR	29.58	1.99	28.8	0.78	17.7	3.14	0.13	0.79	0	0	0	0.19	0.36	83.46
Wasson et al 2008	CR	34.12	1.46	32.02	0.35	14.94	2.48	0.13	0.65	0	0	0	0.18	0.29	86.62
Wasson et al 2008	CR	35.08	1.53	31.79	0.37	15.37	2.56	0.13	0.72	0	0	0	0.18	0.3	88.03
Wasson et al 2008	CR	27.99	2.26	31.25	0.67	15.06	3.62	0.17	0.92	0	0	0	0.16	0.42	82.52
Wasson et al 2008	CR	26.84	2.27	32.08	0.61	14.67	3.85	0.17	0.97	0	0	0	0.15	0.39	82
Wasson et al 2008	CR	29.24	1.66	32.81	0.53	16.67	4.03	0.07	0.49	0	0	0	0.2	0.36	86.06
Wasson et al 2008	CR	26.32	1.62	33.82	0.83	16.1	4.4	0.09	0.58	0	0	0	0.22	0.36	84.34
Wasson et al 2008	CR	24.72	1.53	36.82	0.74	15.79	6.6	0.08	0.52	0	0	0	0.18	0.4	87.38

Table D.4

author	M type	SiO(2)	Al(2)O(3)	FeO	CaO	MgO	SO(2)	K(2)O	Na(2)O	TiO(2)	P(2)O	NiO	MnO	Cr(2)O(3)	total
Wasson et al 2008	CR	31.1	4.9	29.6	0.05	20	0	0.04	0.32	0.04	0	0	0.08	0.06	86.19
Wasson et al 2008	CR	32.6	3.4	22.5	0.21	23.6	0	0.04	0.36	0.07	0	0	0.23	0.52	83.53
Wasson et al 2008	CR	24.3	1.4	43.3	0.34	12.3	0	0.07	1	0.08	0	0	0.21	0.35	83.35
Wasson et al 2008	CR	32.7	2.8	30.8	0.06	21.6	0	0.04	0.33	0.12	0	0	0.38	0.33	89.16
Krot et al 2002 b	CR	41.7	0.17	3.3	0.3	53.8	0	0.04	0.05	0.06	0	0	0.07	0.55	100.04
Krot et al 2002 b	CR	55.9	3.1	0.67	2.4	36.3	0	0.04	0.05	0.42	0	0	0.07	0.47	99.42
Krot et al 2002 b	CR	53.5	4.6	1.9	1.9	37.5	0	0.04	0.05	0.32	0	0	0.07	0.78	100.66
Krot et al 2002 b	CR	51.6	6.6	2.7	3.6	34.1	0	0.04	0.05	0.37	0	0	0.07	0.73	99.86
Krot et al 2002 b	CR	54	8.3	2.1	2	33.9	0	0.04	0.05	0.28	0	0	0.07	0.51	101.25
Krot et al 2002 b	CR	52.7	10	1.7	2.1	33.7	0	0.04	0.05	0.39	0	0	0.07	0.74	101.49
Krot et al 2002 b	CR	48.4	10.9	1.5	19.2	18.3	0	0.04	0.05	1.1	0	0	0.07	0.88	100.44
Krot et al 2002 b	CR	48.6	11	1.2	20.3	17.5	0	0.04	0.05	1.4	0	0	0.07	1.2	101.36
Krot et al 2002 b	CR	43.9	17.1	0.54	21.8	14.5	0	0.04	0.05	0.85	0	0	0.07	0.59	99.44
Krot et al 2002 b	CR	50.3	25.7	1	15.6	6.7	0	0.04	0.05	0.27	0	0	0.07	0.09*	99.73
Krot et al 2002 b	CR	51.9	21	1	17.1	8	0	0.04	0.05	1.33	0	0	0.07	0.45	100.94
Krot et al 2002 b	CR	55.1	0.04	1	0.04	44.3	0	0.04	0.05	0.04	0	0	0.07	0.77	101.45
Krot et al 2002 b	CR	54.9	0.11	0.56	0.08	44.7	0	0.04	0.05	0.04	0	0	0.07	0.76	101.31
Krot et al 2002 b	CR	55.5	0.15	0.58	0.11	44.3	0	0.04	0.05	0.04	0	0	0.07	0.65	101.49
Krot et al 2002 b	CR	55.2	1.1	1	0.95	42	0	0.04	0.05	0.05	0	0	0.12	0.85	101.36
Krot et al 2002 b	CR	54.5	1.3	0.66	0.98	42.9	0	0.04	0.05	0.07	0	0	0.12	0.8	101.42
Krot et al 2002 b	CR	59.9	3.7	3.4	2.7	38.3	0	0.04	0.05	0.17	0	0	0.14	0.78	109.18
Krot et al 2002 b	CR	50.3	5.5	3.5	4	36.7	0	0.04	0.05	0.24	0	0	0.16	0.75	101.24
Krot et al 2002 b	CR	47.8	7.7	3.3	5.6	35.3	0	0.04	0.05	0.3	0	0	0.07	0.62	100.78
Krot et al 2002 b	CR	47.4	9.3	3.2	7	33.1	0	0.04	0.05	0.36	0	0	0.07	0.44	100.96
Krot et al 2002 b	CR	48.3	10.4	2.2	7.6	32.5	0	0.04	0.05	0.42	0	0	0.07	0.48	102.06
Krot et al 2002 b	CR	46.5	13.8	2.6	9.4	28	0	0.04	0.05	0.46	0	0	0.07	0.35	101.27
Krot et al 2002 b	CR	42	0.05	2.5	0.1	54.9	0	0.03	0.05	0.03	0	0	0.44	0.76	100.86
Krot et al 2002 b	CR	59	0.26	1.4	0.14	38.8	0	0.03	0.05	0.05	0	0	0.03	0.61	100.37
Krot et al 2002 b	CR	51.6	3.6	1.5	18.1	18.5	0	0.04	0.05	0.72	0	0	2	3.3	99.41
Krot et al 2002 b	CR	58.5	0.41	2.1	0.41	36.1	0	0.03	0.05	0.07	0	0	0.86	1.6	100.13
Krot et al 2002 b	CR	56.9	0.91	2.1	1.5	33.5	0	0.03	0.05	0.18	0	0	2.9	2.7	100.77
Krot et al 2002 b	CR	55.3	1.3	2.4	4.5	29.2	0	0.03	0.05	0.22	0	0	4.2	2.9	100.1
Krot et al 2002 b	CR	53.4	2.1	2.3	9.4	24.3	0	0.063	0.08	0.33	0	0	4.4	4.4	99.773

Table D.4

author	M type	SiO(2)	Al(2)O(3)	FeO	CaO	MgO	SO(2)	K(2)O	Na(2)O	TiO(2)	P(2)O	NiO	MnO	Cr(2)O(3)	total
Krot et al 2002 b	CR	51.5	3.3	1.5	16.9	18.3	0	0.03	0.22	0.58	0	0	4.1	3.2	99.63
Lehner et al 2012	EH	59.2	0.4	2.1	0.5	36.3	0	0	0.6	0	0	0	0.2	0	99.3
Lehner et al 2012	EH	59.3	0.3	0.3	0.1	39.1	0	0	0.1	0	0	0	0.1	0	99.3
Lehner et al 2012	EH	50.7	8.3	1.5	15	21.6	0	0	0.3	0	0	0	0.3	0	97.7
Lehner et al 2012	EH	70.6	20.2	0.9	0.3	1.7	0	0	4.7	0	0	0	0.1	0	98.5
Lehner et al 2012	EH	41.9	0.04	3	0.1	54.9	0	0	0.01	0	0	0	0.1	0	100.05
Lehner et al 2012	EH	96.3	0.7	0.4	0.1	0.4	0	0	0.3	0	0	0	0.05	0	98.25
Lehner et al 2012	EH	78.3	2.3	1.1	0.1	0.4	0	0	1.9	0	0	0	0.1	0	84.2
Lehner et al 2012	EH	70.1	0.2	0.7	4.2	0.2	0	0	0.5	0	0	0	0.1	0	76
Lehner et al 2012	EH	79.6	2.2	5	0.1	2.3	0	0	0.4	0	0	0	0.05	0	89.65
Rubin et al 2011	EH	59.2	0.23	0.06	0.72	39	0	0.04	0.04	0.04	0	0	0.04	0	99.37
Rubin et al 2011	EH	60	0.09	0.04	0.49	39.2	0	0.04	0.04	0	0	0	0.04	0	99.94
Rubin et al 2011	EH	59	0.3	0.82	0.27	38.8	0	0.04	0.04	0.08	0	0	0.04	0	99.39
Rubin et al 2011	EH	60.5	0.08	0.16	0.19	39.7	0	0.04	0.05	0	0	0	0.04	0	100.76
Rubin et al 2011	EH	59.2	0.1	0.57	0.27	40	0	0.04	0.04	0.04	0	0	0.04	0	100.3
Rubin et al 2011	EH	59.7	0.09	0.55	0.28	40	0	0.04	0.04	0.04	0	0	0.04	0	100.78
Rubin et al 2011	EH	60	0.22	0.22	0.79	39.7	0	0.04	0.04	0.04	0	0	0.04	0	101.09
Rubin et al 2011	EH	59.3	0.2	0.32	0.82	39.2	0	0.04	0.04	0.04	0	0	0.04	0	100
Rubin et al 2011	EH	65.3	21	0.26	2.8	0.05	0	0.9	9.3	0.04	0	0	0.04	0	99.69
Rubin et al 2011	EH	66	20.9	0.04	2.3	0.04	0	0.79	9.5	0	0	0	0.04	0	99.61
Rubin et al 2011	EH	70.2	18.6	0.04	0.04	0.04	0	1.1	11.1	0	0	0	0.04	0	101.16
Rubin et al 2011	EH	66.5	21.7	0.11	3.2	0.04	0	0.8	8.9	0.04	0	0	0.04	0	101.33
Rubin et al 2011	EH	66.8	21.4	0.21	3	0.04	0	0.77	9.3	0.04	0	0	0.04	0	101.6
Rubin et al 2011	EH	98.6	0.77	0.16	0.04	0.04	0	0.11	0.36	0.04	0	0	0.04	0	100.16
Neikerk et al 2014	EH	58.9	0.12	0.34	0.21	40.8	0	0	0	0	0	0	0	0	100.37
Neikerk et al 2014	EH	59.3	0.14	0.14	0.2	40.7	0	0	0	0	0	0	0	0	100.48
Neikerk et al 2014	EH	58.9	0.08	0.29	0.23	40.4	0	0	0	0	0	0	0	0	99.9
Neikerk et al 2014	EH	59.5	0.06	0.15	0.21	40	0	0	0	0	0	0	0	0	99.92
Neikerk et al 2014	EH	59.5	0.08	0.13	0.24	41	0	0	0	0	0	0	0	0	100.95
Neikerk et al 2014	EH	59.9	0.07	0.09	0.2	40.9	0	0	0	0	0	0	0	0	101.16
Neikerk et al 2014	EH	60.1	0.09	0.31	0.27	40	0	0	0	0	0	0	0	0	100.77
Neikerk et al 2014	EH	62	23.2	0.1	4.34	0	0	0.47	8.8	0	0	0	0	0	98.91
Neikerk et al 2014	EH	61.3	24.1	0.2	4.98	0	0	0.37	8.37	0	0	0	0	0	99.32

Table D.4

author	M type	SiO(2)	Al(2)O(3)	FeO	CaO	MgO	SO(2)	K(2)O	Na(2)O	TiO(2)	P(2)O	NiO	MnO	Cr(2)O(3)	total
Neikerk et al 2014	EH	61.3	23.9	0.3	5.01	0	0	0.39	8.24	0	0	0	0	0	99.14
Neikerk et al 2014	EH	61.7	24.3	0.1	5.05	0	0	0.38	8.4	0	0	0	0	0	99.93
Neikerk et al 2014	EH	63.7	22.8	0.2	3.33	0	0	0.52	9.16	0	0	0	0	0	99.71
Neikerk et al 2014	EH	62.1	23.5	0.2	4.76	0	0	0.46	8.53	0	0	0	0	0	99.55
Leroux et al 1997	EL	59.4	0.32	0.5	0.61	39	0	0.02	0.09	0	0	0	0	0	99.94
Leroux et al 1997	EL	64.5	21.9	0.03	5.2	0	0	0.23	8.2	0	0	0	0	0	100.06
Leroux et al 1997	EL	81	10.3	0.59	0.27	0.12	0	6.1	1.61	0	0	0	0	0	99.99
Leroux et al 1997	EL	86.6	10.6	0.85	0.14	0.68	0	0.65	0.52	0	0	0	0	0	100.04
Leroux et al 1997	EL	65	21	0.21	3.31	0	0	0.85	9.7	0	0	0	0	0	100.07
Leroux et al 1997	EL	82.2	10.1	0.14	0.35	0.47	0	6.08	0.68	0	0	0	0	0	100.02
Leroux et al 1997	EL	78.9	10	0.14	0.27	6.3	0	3.64	0.76	0	0	0	0	0	100.01
McCoy et al 1993	EL	60.6	0.24	0.13	0.89	37.9	0	0	0	0	0	0	0	0	99.76
McCoy et al 1993	EL	64.8	21.3	0.11	4.27	0	0	0.54	9.27	0	0	0	0	0	100.29
McCoy et al 1993	EL	59.7	0.15	0.37	0.33	39.4	0	0	0	0	0	0	0	0	99.95
McCoy et al 1993	EL	56.4	0.71	0.83	23.2	20.2	0	0	0	0	0	0	0	0	101.34
McCoy et al 1993	EL	62.3	23	1.13	5.44	0.07	0	0.4	8.58	0	0	0	0	0	100.92
McCoy et al 1993	EL	60.4	0.11	0.29	0.37	39.9	0	0	0	0	0	0	0	0	101.07
McCoy et al 1993	EL	65.9	20.9	0.75	3.11	0.04	0	0.64	9.8	0	0	0	0	0	101.14
McCoy et al 1993	EL	97.3	2.2	0.71	0	0	0	0	1.27	0	0	0	0	0	101.48
McCoy et al 1993	EL	77.1	12.2	0.37	0.53	0.48	0	2.77	5.64	0	0	0	0	0	99.09
McCoy et al 1993	EL	60.4	0.18	0.15	0.93	39.6	0	0	0	0	0	0	0	0	101.26
Mittlefehldt et al 2001	L (OC)	38.1	0	23.1	0.15	38.5	0	0	0	0	0	0	0.44	0.08	100.37
Mittlefehldt et al 2001	L (OC)	38	0	24.6	0.13	37.7	0	0	0	0	0	0	0.44	0.09	100.96
Mittlefehldt et al 2001	L (OC)	38.5	0	22	0.08	40	0	0	0	0	0	0	0.39	0.14	101.11
Mittlefehldt et al 2001	L (OC)	38	0	23.6	0.05	38.3	0	0	0	0	0	0	0.43	0.04	100.42
Mittlefehldt et al 2001	L (OC)	38.1	0	24	0.21	38.3	0	0	0	0	0	0	0.42	0.11	101.14
Mittlefehldt et al 2001	L (OC)	39.2	0	22	0.01	40.2	0	0	0	0	0	0	0.42	0.01	101.84
Mittlefehldt et al 2001	L (OC)	38.3	0	22.5	0.02	38.7	0	0	0	0	0	0	0.42	0.01	99.95
Bevan et al 1991	L (OC)	38.5	0	22.8	0	38.6	0	0	0	0	0	0	0.44	0	100.34
Bevan et al 1991	L (OC)	55.9	0.19	13.5	0.62	29.1	0	0	0	0	0	0	0.41	0.14	99.86
Bevan et al 1991	L (OC)	66.2	21.2	0.23	2.1	0	0	1.23	8.81	0	0	0	0	0	99.77
Bevan et al 1991	L (OC)	54.6	0.29	6.78	16.5	19.9	0	0	0	0.24	0	0	0.21	0.6	99.12
Bevan et al 1991	L (OC)	0	6.5	31.3	0	2.28	0	0	0	2.68	0	0	0.76	5.8	99.32

Table D.4

author	M type	SiO(2)	Al(2)O(3)	FeO	CaO	MgO	SO(2)	K(2)O	Na(2)O	TiO(2)	P(2)O	NiO	MnO	Cr(2)O(3)	total
Kessle et al 2006	H4	39.8	0	16.9	0	43.3	0	0	0	0	0	0	0.45	0.04	100.49
Kessle et al 2006	H4	38.7	0	17.2	0	42.2	0	0	0	0	0	0	0.46	0.018	98.578
Kessle et al 2006	H5	39.7	0	16.1	0	43.7	0	0	0	0	0	0	0.47	0.11	100.08
Kessle et al 2006	H6	39.2	0	17	0	42.5	0	0	0	0	0	0	0.45	0.31	99.46
Kessle et al 2006	L4	38.5	0	21.3	0	39.2	0	0	0	0	0	0	0.46	0.17	99.63
Kessle et al 2006	L5	37.8	0	22.5	0	38	0	0	0	0	0	0	0.46	0.13	98.89
Kessle et al 2006	L6	39.2	0	21.6	0	40.2	0	0	0	0	0	0	0.49	0.19	101.68
Kessle et al 2006	LL4	37.8	0	25.4	0	35.5	0	0	0	0	0	0	0.45	0.19	99.34
Kessle et al 2006	LL5	37.3	0	23.3	0	37.2	0	0	0	0	0	0	0.46	0	98.26
Kessle et al 2006	LL5	37.1	0	26.5	0	34.5	0	0	0	0	0	0	0.46	0.27	98.83
Kessle et al 2006	LL6	37.1	0	26	0	34.9	0	0	0	0	0	0	0.42	0.12	98.54
Kessle et al 2006	H4	56.6	0.16	11.1	0.69	31.1	0	0	0	0.15	0	0	0.56	0.26	100.62
Kessle et al 2006	H4	56.4	0.17	11.3	0.59	30.6	0	0	0	0.13	0	0	0.49	0.25	99.93
Kessle et al 2006	H5	56.4	0.18	10.5	0.7	31.1	0	0	0	0.19	0	0	0.48	0.36	99.91
Kessle et al 2006	H6	56.1	0.17	11.2	0.68	30.3	0	0	0	0.19	0	0	0.5	0.36	99.5
Kessle et al 2006	L4	56	0.14	12.5	0.39	30.1	0	0	0	0.07	0	0	0.42	0.3	99.92
Kessle et al 2006	L5	55.8	0.21	13.8	0.87	28.2	0	0	0	0.2	0	0	0.49	23	122.57
Kessle et al 2006	L6	56.8	0.14	13.6	0.82	29.6	0	0	0	0.19	0	0	0.5	0.32	101.97
Kessle et al 2006	LL4	55.1	0.3	15.4	0.58	27.4	0	0	0	0.17	0	0	0.46	0.16	99.57
Kessle et al 2006	LL5	59.4	0.17	14.3	0.7	28	0	0	0	0.12	0	0	0.48	0.16	103.33
Kessle et al 2006	LL5	54.4	0.13	16.1	0.73	26.7	0	0	0	0.19	0	0	0.45	0.36	99.06
Kessle et al 2006	LL6	54.9	0.16	15.9	0.85	26.7	0	0	0	0.2	0	0	0.45	0.35	99.51
Kessle et al 2006	H4	65.1	21.4	0	2.6	0	0	1.01	10.9	0	0	0	0	0	101.01
Kessle et al 2006	H5	65.1	21.1	0	2.4	0	0	1.14	11.1	0	0	0	0	0	100.84
Kessle et al 2006	H6	65.2	21.3	0	2.58	0	0	1.05	10. 9	0	0	0	0	0	90.13
Kessle et al 2006	L4	67.5	20.4	0	0.3	0	0	0.81	11.2	0	0	0	0	0	100.21
Kessle et al 2006	L6	64.8	21.2	0	2.09	0	0	1.97	10.2	0	0	0	0	0	100.26
Kessle et al 2006	LL4	65.7	21.1	0	1.9	0	0	0.67	11	0	0	0	0	0	100.37
Kessle et al 2006	LL5	65.7	20.7	0	2.09	0	0	0.83	11.3	0	0	0	0	0	100.62
Kessle et al 2006	LL6	65.3	21.2	0	2.27	0	0	0.75	11.3	0	0	0	0	0	100.82
Kessle et al 2006	H4	0	6.65	28.5	0	3.2	0	0	0	1.53	0	0	0.96	56.9	97.74
Kessle et al 2006	H4	0	6.71	29.1	0	3.01	0	0	0	1.51	0	0	0.97	56.2	97.5
Kessle et al 2006	H5	0	7.2	27.8	0	3.21	0	0	0	1.86	0	0	0.99	56.6	97.66

Table D.4

author	M type	SiO(2)	Al(2)O(3)	FeO	CaO	MgO	SO(2)	K(2)O	Na(2)O	TiO(2)	P(2)O	NiO	MnO	Cr(2)O(3)	total
Kessle et al 2006	H6	0	6.59	28.4	0	3.24	0	0	0	2.02	0	0	0.91	56.9	98.06
Kessle et al 2006	L4	0	3.71	30.4	0	1.83	0	0	0	1.58	0	0	0.79	58.3	96.61
Kessle et al 2006	L5	0	6.11	30.4	0	2.44	0	0	0	1.95	0	0	0.72	55.9	97.52
Kessle et al 2006	L6	0	6.1	29.9	0	2.29	0	0	0	2.31	0	0	0.76	56.4	97.76
Kessle et al 2006	LL4	0	6.06	30.9	0	1.76	0	0	0	1.86	0	0	0.62	56	97.2
Kessle et al 2006	LL5	0	6.12	30.5	0	2.17	0	0	0	2.03	0	0	0.73	55. 7	41.55
Kessle et al 2006	LL5	0	6.03	31.9	0	2.12	0	0	0	3.09	0	0	0.57	53.5	97.21
Kessle et al 2006	LL6	0	5.29	32.2	0	2.1	0	0	0	3.91	0	0	0.62	53.3	97.42
Gastineau-Lyon et al 2002	L	38.3	0.03	22.9	0.03	38.9	0	0	0.03	0.03	0	0	0.44	0.03	100.69
Gastineau-Lyon et al 2002	L	37.9	0.03	21.5	0.03	39.5	0	0	0.03	0.03	0	0	0.45	0.03	99.5
Gastineau-Lyon et al 2002	L	38.2	0.03	21.2	0.03	40.1	0	0	0.03	0.03	0	0	0.46	0.03	100.11
Gastineau-Lyon et al 2002	LL	37.6	0.03	26.1	0.04	35.5	0	0	0.03	0.03	0	0	0.44	0.03	99.8
Gastineau-Lyon et al 2002	LL	37.1	0.03	26.8	0.04	35.2	0	0	0.03	0.03	0	0	0.44	0.03	99.7
Gastineau-Lyon et al 2002	LL	37.2	0.03	27.5	0.03	35	0	0	0.03	0.03	0	0	0.44	0.03	100.29
Gastineau-Lyon et al 2002	LL	36.8	0.03	25.6	0.03	36.5	0	0	0.03	0.03	0	0	0.46	0.03	99.51
Gastineau-Lyon et al 2002	L	55.3	0.16	13.9	0.81	29.1	0	0	0.03	0.19	0	0	0.47	0.12	100.08
Gastineau-Lyon et al 2002	L	55.2	0.23	13.3	0.65	29.5	0	0	0.03	0.13	0	0	0.46	0.19	99.69
Gastineau-Lyon et al 2002	L	55.9	0.15	13	0.43	30	0	0	0.03	0.12	0	0	0.46	0.12	100.21
Gastineau-Lyon et al 2002	LL	55.1	0.17	15.8	0.88	27.2	0	0	0.03	0.2	0	0	0.44	0.15	99.97
Gastineau-Lyon et al 2002	LL	54.5	0.18	15.8	0.8	27.3	0	0	0.03	0.15	0	0	0.44	0.14	99.34
Gastineau-Lyon et al 2002	LL	54.7	0.11	16.4	0.72	27.2	0	0	0.03	0.14	0	0	0.45	0.07	99.82
Gastineau-Lyon et al 2002	LL	54.9	0.2	15.4	0.51	28	0	0	0.03	0.11	0	0	0.44	0.17	99.76
Gastineau-Lyon et al 2002	L	53.9	0.49	4.79	21.7	16.7	0	0	0.54	0.46	0	0	0.23	0.79	99.6
Gastineau-Lyon et al 2002	L	53.8	0.46	4.19	22.1	16.8	0	0	0.56	0.29	0	0	0.2	0.8	99.2
Gastineau-Lyon et al 2002	L	53.9	0.53	4.8	20.1	17.6	0	0	0.65	0.33	0	0	0.3	1.18	99.39
Gastineau-Lyon et al 2002	LL	53.2	0.49	6.03	21.4	16.1	0	0	0.51	0.43	0	0	0.23	0.78	99.17
Gastineau-Lyon et al 2002	LL	53.6	0.47	5.65	21.4	16.4	0	0	0.49	0.38	0	0	0.22	0.7	99.31
Gastineau-Lyon et al 2002	LL	53.7	0.4	5.56	22	16.2	0	0	0.46	0.35	0	0	0.2	0.69	99.56
Gastineau-Lyon et al 2002	LL	53.2	0.97	5.53	20.4	16.9	0	0	0.5	0.41	0	0	0.24	0.97	99.12
Niihara et al 2010	LL	39	0	16.8	0.05	43.5	0	0	0	0.01	0.02	0	0.45	0.17	100
Niihara et al 2010	LL	37.7	0	19.3	0.2	41.1	0	0	0.01	0.03	0.95	0	0.38	0.37	100.04
Niihara et al 2010	LL	39	0.01	16.7	0.22	43.3	0	0	0.02	0.03	0	0	0.43	0.31	100.02
Niihara et al 2010	LL	38.7	0.01	18.9	0.25	40.9	0	0	0	0.02	0.03	0	0.5	0.74	100.05

Table D.4

author	M type	SiO(2)	Al(2)O(3)	FeO	CaO	MgO	SO(2)	K(2)O	Na(2)O	TiO(2)	P(2)O	NiO	MnO	Cr(2)O(3)	total
Niihara et al 2010	LL	39.3	0	17.5	0.04	42.8	0	0	0	0.09	0.02	0	0.6	0	100.35
Niihara et al 2010	LL	39.3	0.01	17	0.1	42.8	0	0	0	0.05	0	0	0.46	0.06	99.78
Niihara et al 2010	LL	39.2	0	17	0.04	43.3	0	0	0	0	0	0	0.37	0.08	99.99
Niihara et al 2010	LL	39.5	0.01	17.3	0.03	42.5	0	0.01	0.03	0.06	0	0	0.56	0.02	100.02
Niihara et al 2010	LL	56	0.34	10.9	0.86	31.1	0	0.01	0.03	0.1	0.03	0	0.27	0.36	100
Niihara et al 2010	LL	52.6	1.64	7.5	14.9	19.9	0	0	0.4	0.41	0	0	0.45	1.45	99.25
Niihara et al 2010	LL	56.3	0.17	10.3	0.8	31.6	0	0	0.04	0.04	0.04	0	0.46	0.36	100.11
Niihara et al 2010	LL	55.7	0.41	10.9	0.73	31.2	0	0.02	0.02	0.27	0	0	0.47	0.38	100.1
Niihara et al 2010	LL	52.4	2.37	7.2	14.11	19.4	0	0.03	0.49	0.41	0.05	0	0.48	1.77	98.71
Niihara et al 2010	LL	55.8	0.29	10.5	0.71	31.7	0	0	0.04	0.19	0.02	0	0.55	0.3	100.1
Niihara et al 2010	LL	55.4	0.4	10.8	2.66	29.2	0	0.02	0.22	0.1	0	0	0.4	1.51	100.71
Niihara et al 2010	LL	56.7	0.12	10.6	0.64	30.9	0	0	0.04	0.2	0	0	0.43	0.14	99.77
Niihara et al 2010	LL	55	1.17	11	1.32	29.9	0	0	0.03	0.28	0.04	0	0.33	1.04	100.11
Niihara et al 2010	LL	65.5	19.7	1.4	3.23	0.36	0	0.07	9	0.41	0.4	0	0	0	100.07
Niihara et al 2010	LL	67.8	17	1.5	1.66	0.5	0	1.85	7.9	0.48	1.1	0	0	0.1	99.89
Niihara et al 2010	LL	65.2	21.3	1.5	2.92	0.49	0	0.1	10.4	0.02	0.2	0	0	0	102.13
Jurewicz et al 1994	LL	40.6	2.37	25.9	1.92	25.2	0	0	1	0.11	0.22	1.34	0.32	0.58	99.56
Jurewicz et al 1994	LL	36.5	2.08	35.6	1.72	23.7	0	0	0.89	0.12	0.33	2.1	0.29	0.53	103.86
Jones et al 1995	LL	57	0.37	6.4	0.19	33.9	0	0	0	0.03	0	0	0.43	0.62	98.94
Jones et al 1995	LL	57.4	0.28	4.6	0.19	35.1	0	0	0	0.03	0	0	0.06	0.62	98.28
Jones et al 1995	LL	54.6	0.23	13.2	0.5	29.3	0	0	0	0.05	0	0	0.5	0.8	99.18
Jones et al 1995	LL	56.4	0.22	7.3	0.33	33.1	0	0	0	0.05	0	0	0.56	0.88	98.84
Jones et al 1995	LL	57	0.2	6.7	0.17	33.4	0	0	0	0.03	0	0	0.39	0.62	98.51
Jones et al 1995	LL	56.1	0.12	12.6	0.12	29.4	0	0	0	0.04	0	0	0.36	0.57	99.31
Jones et al 1995	LL	56.9	0.08	11.4	0.11	30.3	0	0	0	0.02	0	0	0.4	0.54	99.75
Jones et al 1995	LL	56.7	0.18	9.5	0.14	31.5	0	0	0	0.02	0	0	0.33	0.64	99.01
Jones et al 1995	LL	54.1	0.2	15.1	0.74	27.2	0	0	0	0.03	0	0	0.52	0.87	98.76
Jones et al 1995	LL	56.4	0.14	7.1	0.26	32.8	0	0	0	0.02	0	0	0.48	0.74	97.94
Jones et al 1995	LL	57.2	0.08	9.8	0.1	32.1	0	0	0	0	0	0	0.38	0.38	100.04
Jones et al 1995	LL	54.4	0.1	16.9	0.2	27	0	0	0	0	0	0	0.47	0.47	99.54
Jones et al 1995	LL	55.5	0.56	10.9	0.63	30.7	0	0	0	0.07	0	0	0.18	0.85	99.39
Jones et al 1995	LL	57.8	0.27	7.1	0.55	32	0	0	0	0.05	0	0	0.57	0.77	99.11
Jones et al 1995	LL	55.5	0.21	15.3	0.35	27.4	0	0	0	0.04	0	0	0.5	0.75	100.05

Table D.4

author	M type	SiO(2)	Al(2)O(3)	FeO	CaO	MgO	SO(2)	K(2)O	Na(2)O	TiO(2)	P(2)O	NiO	MnO	Cr(2)O(3)	total
Jones et al 1995	LL	55.8	0.17	13.6	0.29	28.4	0	0	0	0.03	0	0	0.57	0.73	99.59
Jones et al 1995	LL	56.2	0.4	12.3	0.56	29.1	0	0	0	0.05	0	0	0.5	0.86	99.97
Jones et al 1995	LL	56.7	0.2	11.1	0.34	30.5	0	0	0	0.02	0	0	0.54	0.7	100.1
Jones et al 1995	LL	55.4	0.24	14.1	0.55	27.4	0	0	0	0	0	0	0.77	0.74	99.2
Jones et al 1995	LL	52.7	0.24	21.2	0.54	23.2	0	0	0	0	0	0	0.68	0.63	99.19
Jones et al 1995	LL	55.5	0.47	10.6	3.8	27.4	0	0	0	0.08	0	0	1.31	1.5	100.66
Jones et al 1995	LL	50.1	2.13	23.6	6.6	16.2	0	0	0	0.21	0	0	0.59	0.8	100.23
Jones et al 1995	LL	56.1	0.22	9.2	6.6	26.3	0	0	0	0.13	0	0	1.1	1.5	101.15
Jones et al 1995	LL	54.5	1.26	10.1	4.1	27.2	0	0	0	0.1	0	0	1.05	1.6	99.91
Jones et al 1995	LL	51.4	0.69	21.5	5.6	18.3	0	0	0	0.09	0	0	0.98	1.5	100.06
Jones et al 1995	LL	53.1	0.66	19.1	4.1	20.3	0	0	0	0.09	0	0	0.92	1	99.27
Jones et al 1995	LL	53.1	0.4	9.1	5.4	27.8	0	0	0	0.12	0	0	0.86	1.6	98.38
Jones et al 1995	LL	52.6	0.87	18.4	5.6	18.8	0	0	0	0.14	0	0	1.19	1.4	99
Jones et al 1995	LL	51.7	0.78	23.8	3.8	17.5	0	0	0	0.11	0	0	0.86	0.9	99.45
Jones et al 1995	LL	53.1	1.5	7.8	15.9	17.1	0	0	0	0.31	0	0	1.11	2.6	99.42
Jones et al 1995	LL	49.1	4.7	21.2	10.2	13.6	0	0	0	0.41	0	0	0.55	1.2	100.96
Jones et al 1995	LL	52.2	0.6	15.9	12.4	15.7	0	0	0	0.2	0	0	0.88	1.9	99.78
Jones et al 1995	LL	54.1	0.8	7.3	13.3	21	0	0	0	0.23	0	0	0.93	1.9	99.56
Jones et al 1995	LL	53.3	2.9	8	12.9	18.6	0	0	0	0.34	0	0	0.95	2.4	99.39
Jones et al 1995	LL	51.8	1.7	18.4	12.7	13.1	0	0	0	0.24	0	0	0.83	1	99.77
Jones et al 1995	LL	21.7	1	19.1	11.4	14	0	0	0	0.19	0	0	1.12	1.8	70.31
Jones et al 1995	LL	50.5	4.4	13.7	15.2	13.8	0	0	0	0.68	0	0	0.6	1	99.88
Jones et al 1995	LL	51.3	0.9	14.9	15.2	14.3	0	0	0	0.28	0	0	0.67	1.2	98.75
Jones et al 1995	LL	52.4	1.2	6.9	16.4	17.9	0	0	0	0.33	0	0	0.89	2.1	98.12
Jones et al 1995	LL	52.4	1.1	11	13.3	17.2	0	0	0	0.21	0	0	1.03	2	98.24
Jones et al 1995	LL	52.2	1.2	14.6	11.2	16.6	0	0	0	0.17	0	0	1.19	1.7	98.86
Jones et al 1995	LL	50.7	1.3	22.8	9.1	13.6	0	0	0	0.24	0	0	0.89	1.1	99.73
Nagashima et al 2014	K	42.4	0.02	3.39	0.04	54.6	0	0.01	0.03	0.03	0	0	0.41	0.03	100.96
Nagashima et al 2014	K	59.3	0.27	3.11	0.32	37.2	0	0.01	0.02	0.03	0	0	0.36	0.4	101.02
Nagashima et al 2014	K	53.9	2.69	2.9	17.3	20.9	0	0.01	0.37	0.46	0	0	0.63	1.56	100.72
Nagashima et al 2014	K	42.1	0.02	3.54	0.03	54.9	0	0.01	0.02	0.03	0	0	0.43	0.03	101.11
Nagashima et al 2014	K	57	0.5	6.34	2.12	32.4	0	0.01	0.19	0.03	0	0	0.57	0.87	100.03
Nagashima et al 2014	K	66.9	17.3	1.29	2.84	3.07	0	1.78	4.84	0.49	0	0	0.04	0.65	99.2

Table D.4

author	M type	SiO(2)	Al(2)O(3)	FeO	CaO	MgO	SO(2)	K(2)O	Na(2)O	TiO(2)	P(2)O	NiO	MnO	Cr(2)O(3)	total
Nagashima et al 2014	K	41.8	0.02	3.71	0.04	54.5	0	0.01	0.02	0.03	0	0	0.43	0.03	100.59
Nagashima et al 2014	K	54.9	0.58	1.58	22.7	17.3	0	0.03	1.02	0.12	0	0	0.26	1.79	100.28
Nagashima et al 2014	K	41.7	0.02	3.4	0.05	54.7	0	0.01	0.02	0.03	0	0	0.42	0.03	100.38
Nagashima et al 2014	K	54.2	0.67	7.47	17.2	16.7	0	0.02	0.89	0.3	0	0	0.82	1.73	100
Nagashima et al 2014	K	42.2	0.02	3.68	0.05	54.7	0	0.01	0.02	0.03	0	0	0.43	0.03	101.17
Nagashima et al 2014	K	59.5	0.41	3.33	0.58	36.7	0	0.01	0.02	0.03	0	0	0.47	0.49	101.54
Nagashima et al 2014	K	54.4	2.98	3	16.9	21	0	0.01	0.23	0.58	0	0	0.89	1.23	101.22
Nagashima et al 2014	K	55.2	29.8	0.46	10.6	0.3	0	0.08	4.81	0.03	0	0	0.04	0.03	101.35
Nagashima et al 2014	K	57	0.66	3.84	0.82	35.7	0	0.01	0.05	0.06	0	0	0.52	0.6	99.26
Nagashima et al 2014	K	52.1	3.53	3.46	15.6	20.6	0	0.04	0.57	0.51	0	0	0.87	1.88	99.16
Nagashima et al 2014	K	98.1	0.17	0.26	0.05	0.23	0	0.02	0.05	0.03	0	0	0.04	0.03	98.98
Nagashima et al 2014	K	41.3	0.05	3.33	0.06	54.5	0	0.01	0.02	0.03	0	0	0.42	0.03	99.75
Nagashima et al 2014	K	56.8	0.46	3.62	0.54	36.3	0	0.01	0.03	0.04	0	0	0.45	0.53	98.78
Nagashima et al 2014	K	51.2	4.17	3.12	16.8	20.1	0	0.01	0.27	0.61	0	0	0.89	1.86	99.03
Nagashima et al 2014	K	53.1	29.3	0.34	10.6	0.37	0	0.1	5.21	0.03	0	0	0.04	0.04	99.13
Nagashima et al 2014	K	40.2	0.02	6.76	0.03	51.2	0	0.01	0.02	0.03	0	0	0.32	0.03	98.62
Nagashima et al 2014	K	40	0.02	3.25	0.04	55.3	0	0.01	0.02	0.03	0	0	0.36	0.03	99.06
Nagashima et al 2014	K	52.1	0.99	14.3	1.36	26.9	0	0.01	0.14	0.08	0	0	0.41	1.2	97.49
Nagashima et al 2014	K	55.9	0.83	3.16	1	36.8	0	0.01	0.08	0.1	0	0	0.64	0.72	99.24
Nagashima et al 2014	K	47.4	33.1	0.62	15.1	0.42	0	0.06	2.77	0.04	0	0	0.04	0.03	99.58
Nagashima et al 2014	K	39.6	0.09	6.36	0.04	52.8	0	0.01	0.02	0.03	0	0	0.38	0.33	99.66
Nagashima et al 2014	K	41.1	0.1	2.73	0.06	55.1	0	0.01	0.03	0.03	0	0	0.37	0.03	99.56
Nagashima et al 2014	K	56.5	0.59	7.32	1.47	32.4	0	0.01	0.06	0.06	0	0	0.69	0.67	99.77
Nagashima et al 2014	K	58	0.14	4.49	0.46	36.6	0	0.01	0.02	0.03	0	0	0.46	0.25	100.46
Nagashima et al 2014	K	66	22	1.21	2.04	1.09	0	0.21	7.43	0.46	0	0	0.06	0.03	100.53
McCanta et al 2008	R	36.87	2.04	30.31	1.66	23.09	0	0.08	0.84	0.12	0.22	1.77	0.33	0.8	98.13
McCanta et al 2008	R	39.12	1.93	31.47	1.54	20.66	0	0.09	0.92	0	0	1.44	0.29	0.54	98
McCanta et al 2008	R	39.94	1.93	32.04	1.54	20.1	0	0.12	0.93	0.15	0	0.41	0.28	0.56	98
McCanta et al 2008	R	36.98	2.08	31.01	2.71	22.06	0	0.09	0.86	0	0	1.38	0.3	0.53	98
McCanta et al 2008	R	38.78	2.08	30.49	1.9	21.56	0	0.07	0.87	0	0	1.44	0.29	0.52	98
McCanta et al 2008	R	37.48	2.1	31.01	1.75	22.55	0	0.07	0.86	0	0	1.38	0.3	0.5	98
Rout et al 2010	R	29.4	26.3	13	9.4	12.6	0.28	0.16	0.54	1.31	0.09	3.4	0.08	0.55	97.11
Rout et al 2010	R	14	42.9	17.2	5.4	10	0.23	0.09	0.38	3.31	0.08	1.39	0.1	0.63	95.71

Table D.4

author	M type	SiO(2)	Al(2)O(3)	FeO	CaO	MgO	SO(2)	K(2)O	Na(2)O	TiO(2)	P(2)O	NiO	MnO	Cr(2)O(3)	total
Rout et al 2010	R	15	52.1	1.67	6.3	20.6	0.01	0.16	0.71	1.04	0.01	0.02	0.02	0.22	97.86
Rout et al 2010	R	18	43	10.8	9.7	14.4	0.2	0.03	0.07	2.09	n.d.	0.06	0.08	0.23	98.66
Rout et al 2010	R	3.2	56.3	21.1	0.12	10.3	0.1	0.05	0.28	1.17	0.09	0.9	0.13	0.23	93.97
Rout et al 2010	R	16.3	46	16.3	7.9	10.2	0.05	0.05	0.1	2.1	0.03	0.13	0.07	0.03	99.26
Rout et al 2010	R	10.1	49.2	20.1	3.4	12.7	0.01	0.03	0.17	1.22	0.01	0.22	0.12	0.81	98.09
Rout et al 2010	R	12.3	46.6	16.8	1.16	7.6	0.1	0.49	2.95	4.5	0.11	0.69	0.12	0.09	93.51
Rout et al 2010	R	12	49.3	18.4	1.8	9.1	0.06	0.13	1.48	3.5	0.01	0.17	0.1	1.8	97.85
Rout et al 2010	R	2.8	57.2	21.4	0.66	10.8	0.12	0.09	0.1	0.61	0.02	0.4	0.08	0.2	94.48
Rout et al 2010	R	5.7	50.8	20.6	0.24	14.1	0.04	0.04	0.08	5.7	0.03	0.43	0.15	0.15	98.06
Rout et al 2010	R	21.1	21.1	36.2	1.59	12.2	0.34	0.09	0.32	1.75	0.09	4.1	0.14	0.17	99.19
Rout et al 2010	R	8.6	53.9	16	1.29	6.9	0.02	0.31	3.81	4.3	0	0.09	0.08	0.19	95.49
Rout et al 2010	R	21	33.1	16.4	5.9	9.2	0.17	0.18	0.32	7.4	0.11	0.62	0.17	0.7	95.27
Rout et al 2010	R	6	52.3	22.7	2.9	6.2	2.5	0.36	0.76	3.5	0.65	0.36	0.06	0.1	98.39
Rout et al 2010	R	26.4	37	17.8	6.9	4.4	0.72	0.36	0.39	3.5	0.38	1.12	0.07	0.07	99.11
Rout et al 2010	R	6.5	71.7	5.5	6.7	2.6	0.04	0.08	0.48	0.3	1	0.06	0.36	0.05	95.37
Rout et al 2010	R	18.5	42.2	3	9.8	18.7	0.55	0.39	0.09	3.6	0.01	0.44	0.02	0.26	97.56
Rout et al 2010	R	17.7	46.1	4.6	8.7	19.4	0.04	0.05	0.07	1.53	0.14	0.04	0.03	0.25	98.65
Rout et al 2010	R	12.1	52.1	5.1	5.9	19.4	0.07	0.06	0.09	2.5	0.02	0.07	0.03	0.16	97.6
Rout et al 2010	R	15.6	35.4	22	4.7	13.6	0.01	0.03	0.26	6.8	0.02	0.16	0.18	0.19	98.95
Rout et al 2010	R	31.5	27.4	7.9	16.7	11.1	0.26	0.05	0.13	2.03	0.03	0.28	0.06	0.34	97.78
Rout et al 2010	R	11.2	45.4	13.3	2.5	19.7	0.02	0.02	0.03	2.8	0.06	0.29	0.05	0.09	95.46
Rout et al 2010	R	11.8	47.1	3.8	17.2	17.3	0.04	0.01	0.09	2.24	0.08	0.04	0.04	0.01	99.75
Rout et al 2010	R	23	36.9	12.1	11.6	11.2	0.07	0.07	0.38	2.8	0.02	0.74	0.06	0.15	99.09
Rout et al 2010	R	21.6	39.8	1.97	11.3	19.3	0.01	0.06	0.21	2.9	0.02	0.01	0.01	0.18	97.37
Rout et al 2010	R	17.2	44.8	9.4	6.1	12.7	0.62	0.3	0.71	2.6	0.02	0.8	0.02	0.15	95.42
Rout et al 2010	R	14.1	50.1	17.3	3	8.2	1.3	0.33	0.41	1.48	0.11	1.25	0.07	0.11	97.76
Rout et al 2010	R	18.8	39.5	18	7	10.6	0.23	0.09	0.23	3	0.21	0.29	0.01	0.13	98.09
Rout et al 2010	R	36.3	23.4	18.1	7.3	7.1	0.3	0.64	0.48	0.93	0.33	4.5	0.05	0.06	99.49
Rout et al 2010	R	18.3	45.9	10.9	1.15	5.2	0.04	0.14	9.2	1.84	0.02	0.22	0.04	0.26	93.21
Rout et al 2010	R	13.5	46.4	18.4	2.3	9.6	0.28	0.3	2.5	1.42	0.03	0.74	0.1	0.22	95.79
Rout et al 2010	R	24.5	40	13.7	4.3	7.8	0.92	0.79	3.1	0.77	0.13	2.3	0.08	0.32	98.71
Rout et al 2010	R	23.5	33.3	13.7	7.2	11.4	0.16	0.17	3	3.2	0.02	0.06	0.1	0.17	95.98
Rout et al 2010	R	24.4	41.3	14.9	0.81	6.6	0.13	0.34	6.7	1.29	0.03	0.24	0.07	0.52	97.33

Table D.4

author	M type	SiO(2)	Al(2)O(3)	FeO	CaO	MgO	SO(2)	K(2)O	Na(2)O	TiO(2)	P(2)O	NiO	MnO	Cr(2)O(3)	total
Rout et al 2010	R	26.4	34.2	15	0.88	5.9	2.09	0.15	3.9	0.9	0.06	5.6	0.11	1.15	96.34
Rout et al 2010	R	27.8	33.8	8.7	1.38	3.8	0.9	0.19	12.5	0.87	0.08	2.48	0.04	1.05	93.59
Rout et al 2010	R	37.4	20.7	12.9	2.18	10	0.3	1.04	8.2	1	0.06	1.9	0.11	0.12	95.91
Rout et al 2010	R	32.8	27.5	4.2	15	3.6	4	1.77	6.4	1.69	0.31	1.62	0	0.17	99.06
Rout et al 2010	R	4.6	54.3	19.5	0.46	10.3	0.69	0.06	1.22	1.32	0.01	0.59	0.11	1.19	94.35
Rout et al 2010	R	21.6	34.1	15.8	2.6	16.5	0.18	0.04	1.73	1.6	0.13	1.2	0.09	0.04	95.61
Rout et al 2010	R	34.3	25.2	5.8	13.3	16	0.03	0.02	0.06	1.1	0.03	0.23	0.04	0.2	96.31
Rout et al 2010	R	32.8	33.9	0.42	23.3	5.9	0.01	0.01	0.01	2.6	0.03	0.04	0.03	0.04	99.09
Rout et al 2010	R	41.5	15.2	5.7	20.3	14.1	0.01	0.02	0.06	0.9	0.02	0.08	0.04	0.15	98.08
Rout et al 2010	R	12	54.7	16	1.25	6.9	0.34	0.31	1	3.1	0.07	1.77	0.07	0.04	97.55
Rout et al 2010	R	25.7	34.6	16	7.9	7.6	2.6	0.65	1	0.76	0.06	1.05	0.04	0.09	98.05
Rout et al 2010	R	38.9	19.3	7.1	17.7	14.3	0.39	0.07	0.4	1.39	0.02	0.69	0.01	0.21	100.48
Rout et al 2010	R	27.5	26.3	15.3	11.3	12	0.35	0.06	0.2	3.9	0.17	0.94	0.07	0.09	98.18
Rout et al 2010	R	27.3	32.9	9.9	12.6	11.3	0.13	0.11	0.65	1.78	0.03	1.51	0.06	0.2	98.47
Rout et al 2010	R	37.7	21.6	6.1	17	13.5	0.05	0.06	0.17	1.5	0.21	0.08	0.05	0.15	98.17
Rout et al 2010	R	32.5	36.6	4.5	9.4	4.4	0.4	1.18	5.4	1.67	0.12	3.5	0.02	0.05	99.74
Rout et al 2010	R	21	41.3	6.9	6.9	8.4	0.43	0.87	3.1	3.4	0.02	2.7	0.03	0.04	95.09
Rout et al 2010	R	37.1	23.6	7.1	10.5	10	0.38	0.24	6.3	1.58	0.09	1.26	0.05	0.16	98.36
Rout et al 2010	R	41.4	15.9	4.3	17.4	15.5	0.15	0.17	0.25	1.21	0.07	1.04	0	0.21	97.6
Rout et al 2010	R	40.4	18.6	6.7	15.5	11.4	0.08	0.17	2.07	0.77	0.05	1.41	0.02	0.1	97.27
Rout et al 2010	R	31	28	11.6	14.1	7.4	2.22	0.32	1.69	0.55	0.81	1.18	0.09	0.22	99.18
Rout et al 2010	R	27.6	26.6	17.8	10	13.3	0.31	0.06	0.06	1.19	0.05	0.22	0.08	0.18	97.45
Rout et al 2010	R	40	17.6	4.1	17.8	15.2	0.02	0.09	0.1	1.02	0.01	0.08	0.04	0.2	96.26
Rout et al 2010	R	10.1	39.6	11.6	23.2	12.6	0.58	0.06	0.1	0.54	0.12	0.16	0.06	0.22	98.94
Rout et al 2010	R	34.3	26.8	2.5	15.6	17.8	0.04	0.02	0.06	0.99	0.02	1.02	0.03	0.14	99.32
Rout et al 2010	R	18.6	40.7	20.9	2.09	7.7	0.43	0.24	0.52	5.3	0.2	1.19	0.08	0.04	97.99
Rout et al 2010	R	29.3	25.4	16.4	8.1	12.3	1.1	0.1	0.86	2.03	0.01	3.1	0.14	0.08	98.92
Rout et al 2010	R	4.9	57.6	20.8	1.92	10.4	0.13	0.07	0.36	0.98	0.02	0.22	0.09	0.12	97.61
Rout et al 2010	R	34.6	22.4	18	1.07	6.8	0.39	0.34	4.3	2.7	0.12	1.1	0.15	3.4	95.37
Rout et al 2010	R	42.2	22.2	16.4	1.43	5.2	0.16	0.33	5.7	0.79	0.17	1.27	0.06	1.88	97.79
Rout et al 2010	R	53.2	19	9.7	2.5	3.5	0.92	0.47	7.6	0.12	0.11	1.27	0.04	0.45	98.88
Rout et al 2010	R	48.8	18.7	10	3.1	3.6	0.34	0.35	6.3	1.56	0.1	2.13	0.09	0.44	96.51
Rout et al 2010	R	43.8	22.5	9.8	3.4	3.6	0.41	0.39	5.5	1.9	0.51	2.7	0.03	0.88	95.42

Table D.4

author	M type	SiO(2)	Al(2)O(3)	FeO	CaO	MgO	SO(2)	K(2)O	Na(2)O	TiO(2)	P(2)O	NiO	MnO	Cr(2)O(3)	total
Rout et al 2010	R	17.8	40.7	21.4	1.07	9.3	0.26	0.17	1.73	2.36	0.17	2.19	0.18	1.05	98.38
Rout et al 2010	R	36.3	20.2	11.5	11.3	10.2	1.02	0.14	0.44	1.04	0.29	6.8	0.08	0.5	99.81
Rout et al 2010	R	44.8	16.7	15	2	7.1	0.42	0.43	5	3.1	0.19	3	0.15	1.93	99.82
Rout et al 2010	R	48.3	22.1	11.1	5.8	4.3	0.43	0.19	5.4	0.96	0.2	0.2	0.05	0.71	99.74
Rout et al 2010	R	59.1	18.3	3.8	2.7	1.8	0.29	0.47	8.8	0.04	0.05	0.92	0.04	0.08	96.39
Rout et al 2010	R	44	24.5	7.7	7.7	5	0.55	0.13	5.1	0.13	1.17	0.51	0.03	0.45	96.97
Rout et al 2010	R	40.1	32.1	10.2	2.37	4.5	0.11	0.25	6	1.85	0.03	0.2	0.05	1.56	99.32
Rout et al 2010	R	34	32.8	12.6	1.02	4.2	1.16	0.71	3.7	2.34	0.02	3.1	0.06	2.9	98.61
Rout et al 2010	R	43.4	27.5	11.5	3.3	3.8	0.57	0.45	6	0.6	0.09	1.2	0.09	0.88	99.38
Rout et al 2010	R	30.5	37.3	13.5	3.1	5.6	0.75	0.36	3.6	0.65	0.42	1.76	0.1	1.13	98.77
Rout et al 2010	R	20.3	40	20.2	1.12	9.2	0.31	0.14	2.3	0.79	0.06	0.53	0.11	1.36	96.42
Rout et al 2010	R	37.8	27.8	14.3	4.5	5.4	0.21	0.42	5	0.89	0.22	2.24	0.09	0.34	99.21
Rout et al 2010	R	32.8	19.1	6.9	23.9	3	1.5	0.38	4.3	0.8	4.2	1.44	0.18	0.7	99.2
Rout et al 2010	R	42.3	22.4	8.4	7.5	5.5	0.39	0.29	4.5	2.6	0.07	0.9	0.06	0.87	95.78
Rout et al 2010	R	30.2	29.2	12.6	11.8	11.1	0.13	0.06	0.35	1.34	0.11	0.99	0.05	0.14	98.07
Rout et al 2010	R	33.8	33.4	9	8.5	3.3	0.45	0.14	2.7	0.86	0.3	1.75	0.08	0.36	94.64
Rout et al 2010	R	40.9	23.3	6.9	15.7	7.8	0.19	0.35	0.87	2.06	0.49	0.97	0	0.14	99.67
Rout et al 2010	R	35	19.2	9.3	11	8.9	0.79	0.06	0.2	1.25	0.15	9.2	0.08	0.11	95.24
Rout et al 2010	R	22.4	26.7	15.3	23	4.6	0.22	0.31	3.4	1.33	0.52	0.56	0.07	0.79	99.2
Rout et al 2010	R	28.3	34.1	10.2	2.9	3.8	0.01	2.3	10.2	6.3	0.01	0.08	0.08	0.62	98.9
Rout et al 2010	R	29.6	39	12.6	5.2	7.5	0.45	0.27	0.65	1.88	0.12	1.26	0.05	0.12	98.7
Rout et al 2010	R	25.4	39	10.2	1.13	5.1	0.14	0.56	11.1	0.26	0.02	0.12	0.05	0.59	93.67
Rout et al 2010	R	14.3	47.8	16.3	1.13	6.8	0.01	0.37	6.1	2.7	0.03	0.33	0.11	0.29	96.27
Rout et al 2010	R	22.9	40	11.6	9	8.1	0.01	0.54	3.4	2.6	0.03	0.11	0.05	0.12	98.46
Rout et al 2010	R	33.7	36.9	6.7	6.7	4.8	1.18	0.83	3.3	2.28	0.11	2.9	0.05	0.05	99.5
Rout et al 2010	R	43.6	10.6	5.7	20.2	12.8	0.26	0.09	0.13	1.43	0.05	0.45	0.03	0.11	95.45
Rout et al 2010	R	42.2	21.7	7.9	14.1	8.8	0.5	0.27	0.23	2	0.17	1.5	0.07	0.14	99.58
Rout et al 2010	R	43	18.3	6.3	15.1	9.8	2.08	0.47	1.8	1.2	0.07	1.21	0.03	0.09	99.45
Rout et al 2010	R	57.5	15.6	3.3	7.7	3.6	0.2	0.42	7	0.16	0.12	0.07	0.05	0.19	95.91
Rout et al 2010	R	48.2	17.7	0.59	17.7	10.9	0.1	0.08	1.3	1.24	0.02	0.07	0.04	0.15	98.09
Rout et al 2010	R	53.4	12.5	14	1.28	12.4	0.01	0.34	6.1	0.06	0.03	0.08	0.16	0.03	100.39
Rout et al 2010	R	28.9	19.8	23.4	4.8	20.5	0.03	0.02	0.06	0.36	0.02	0.22	0.22	0.06	98.39
Rout et al 2010	R	55.9	19.1	3.3	6.9	2.23	0.06	0.53	7.3	0.43	0.07	0.35	0.03	0.14	96.34

Table D.4

author	M type	SiO(2)	Al(2)O(3)	FeO	CaO	MgO	SO(2)	K(2)O	Na(2)O	TiO(2)	P(2)O	NiO	MnO	Cr(2)O(3)	total
Rout et al 2010	R	46	22.6	4.2	10	3.9	0.2	0.53	4.6	1.15	0.09	2.28	0.02	0.15	95.72
Rout et al 2010	R	37.3	14.4	17.1	6.8	15.7	0.3	0.18	3.1	0.34	0.09	0.34	0.13	0.28	96.06
Rout et al 2010	R	41.9	12.5	1.62	8.2	30	0.03	0.42	2.8	0.56	0.01	0.03	0.02	0.22	98.31
Rout et al 2010	R	51.8	23.8	4.1	11.3	1.8	0.03	0.03	5.1	1.7	0.03	0.05	0.02	0.15	99.91
Rout et al 2010	R	49.5	20.9	4.6	10.8	4.3	0.04	0.09	4.3	0.48	0.04	0.05	0.03	0.16	95.29
Rout et al 2010	R	41.1	12.2	8.3	0.9	26	0.16	2.5	4	0.8	0.03	2.25	0.15	0.56	98.95
Rout et al 2010	R	53.1	21.6	4.8	6.2	2.5	0.04	0.28	6.5	1.58	0.02	0.1	0.05	0.2	96.97
Rout et al 2010	R	42.1	12.8	7	2.26	25.1	0.62	0.38	6.6	0.58	0.02	0.14	0.04	0.23	97.87
Rout et al 2010	R	43.9	13.2	9.4	15.8	11.6	2	0.04	1.64	1.15	0.03	0.52	0.11	0.26	
Rout et al 2010	R	43.4	14.3	3.6	9.1	25.8	0.04	0.28	1.82	0.6	0.01	0.05	0.03	0.2	99.23
Rout et al 2010	R	52	19.6	9.9	6	3.8	0.57	0.32	6	0.97	0.04	0.32	0.06	0.27	99.85
Rout et al 2010	R	49.1	20	7.3	6.6	4.5	0.5	0.12	6.1	1.08	0.04	0.24	0.07	0.21	95.86
Rout et al 2010	R	43.5	15.6	8.9	10	15.8	0.23	0.09	2.1	0.64	0.03	0.59	0.08	0.12	97.68
Bischoff et al 2010	R	35.6	0	33.2	0.04	28.8	0	0	0	0	0	0.25	0.36	0.04	98.29
Bischoff et al 2010	R	36.6	0	33.4	0.06	29.4	0	0	0	0	0	0.24	0.43	0.11	100.24
Bischoff et al 2010	R	35.7	0.02	33.4	0.02	28.8	0	0	0	0.04	0	0.22	0.37	0.08	98.65
Bischoff et al 2010	R	36	0.02	33.8	0.03	29	0	0	0	0.03	0	0.26	0.41	0.02	99.57
Bischoff et al 2010	R	35.1	0	35.1	0.11	28.6	0	0.01	0.03	0.02	0	0.15	0.48	0.02	99.62
Bischoff et al 2010	R	35.5	0	33.7	0.06	29.1	0	0.02	0	0.03	0	0.14	0.43	0.05	99.03
Bischoff et al 2010	R	36.02	0.02	32.98	0.04	29.56	0	0	0.01	0.02	0	0.36	0.43	0.02	99.46
Bischoff et al 2010	R	37.1	0.04	30.3	0.07	32.5	0	0	0	0.04	0	0.17	0.35	0.04	100.61
Bischoff et al 2010	R	42.1	0.02	4.41	0.04	53	0	0	0	0.02	0	0.02	0.24	0.38	100.23
Bischoff et al 2010	R	39.3	0	15.2	0.05	45.7	0	0	0	0	0	0.07	0.28	0.19	100.79
Bischoff et al 2010	R	42.3	0.22	0.38	0.6	57	0	0	0	0	0	0	0	0.08	100.58
Bischoff et al 2010	R	53.9	0.11	19.7	0.69	24.2	0	0	0.02	0.08	0	0.08	0.32	0.03	99.13
Bischoff et al 2010	R	54	0.12	16.6	0.38	26.6	0	0	0.05	0	0	0	0.56	0.22	98.53
Bischoff et al 2010	R	58.6	0.17	4.1	0.18	37	0	0	0.06	0	0	0	0.39	0.49	100.99
Bischoff et al 2010	R	53.2	7	3.8	2.03	32.8	0	0	0	0.42	0	0	0.1	1.14	100.49
Bischoff et al 2010	R	53.96	0.14	19.4	0.48	24.72	0	0	0.02	0.02	0	0.13	0.42	0.05	99.34
Bischoff et al 2010	R	56.7	0.44	10.2	0.5	31.9	0	0	0	0.06	0	0.04	0.26	0.3	100.4
Bischoff et al 2010	R	53.2	0.15	6.4	23.4	15.5	0	0	0.38	0.02	0	0.02	0.19	0.21	99.47
Bischoff et al 2010	R	52.7	0.62	6.3	23.5	15.2	0	0	0.61	0.06	0	0	0.21	0.41	99.61
Bischoff et al 2010	R	52	0.54	9	19.6	15.2	0	0	0.81	0.41	0	0	0.27	0.97	98.8

Table D.4

author	M type	SiO(2)	Al(2)O(3)	FeO	CaO	MgO	SO(2)	K(2)O	Na(2)O	TiO(2)	P(2)O	NiO	MnO	Cr(2)O(3)	total
Bischoff et al 2010	R	52.2	0.72	10.6	17.2	16.1	0	0	0.69	0.32	0	0	0.28	0.83	98.94
Bischoff et al 2010	R	52.2	0.92	0.28	16.1	18.8	0	0	0.56	0.22	0	0.12	0.37	0.65	90.22
Bischoff et al 2010	R	65.2	21.5	0.31	1.89	0.11	0	0.56	10.3	0	0	0	0	0	99.87
Bischoff et al 2010	R	65.94	20.83	0.62	1.56	0	0	0.41	8.69	0	0	0	0	0	98.05
Bischoff et al 2010	R	65.5	21.5	0.91	2.27	0.11	0	0.52	9.2	0	0	0	0	0	100.01
Bischoff et al 2010	R	66.3	20.9	0.68	1.58	0	0	0.98	10.4	0	0	0	0	0	100.84
Bischoff et al 2010	R	66.23	22.12	0.32	1.55	0		0.41	9.89	0	0	0	0	0	100.52
Bischoff et al 2010	R	65.8	20.5	0.56	1.9	0	0	0.69	10	0	0	0	0	0	99.45
Bischoff et al 2010	R	49.5	32	0.33	14.1	0.05	0	0.04	3.5	0	0	0	0	0	99.52
Bischoff et al 2010	R	65.1	20	0.45	1.52	0.04	0	7.4	4.8	0	0	0	0	0	99.31
Bischoff et al 2010	R	63.8	18	1.09	0.87	0	0	15.2	0.98	0	0	0	0	0	99.94
Hazel and palme 2015	CO	50.96	0.51	0.91	0.33	46.92	0	0	0.01	0.09	0	0.01	0.15	0.61	100.5
Hazel and palme 2016	CO	46.68	1.71	0.61	2.22	48.2	0	0	0.1	0.14	0	0.02	0.09	0.34	100.11
Hazel and palme 2017	CO	47.58	1.87	3.12	1.79	44.95	0	0	0.05	0.12	0	0.09	0.11	0.65	100.33
Hazel and palme 2018	CO	52.39	2.32	1.92	2.75	39.9	0	0	0.18	0.18	0	0.08	0.15	0.56	100.43
Hazel and palme 2019	CO	56.45	2.87	1.17	3.34	35.52	0	0	0.37	0.26	0	0.07	0.09	0.4	100.54
Hazel and palme 2020	CO	48.51	1.12	0.99	1.91	47.14	0	0	0.04	0.15	0	0.05	0.11	0.43	100.45
Hazel and palme 2021	CO	55.85	4	1.11	5.24	32.52	0	0	0.33	0.21	0	0.04	0.39	0.63	100.32
Hazel and palme 2022	CO	51.81	2.2	1.79	2.56	41.21	0	0	0.1	0.14	0	0.22	0.14	0.51	100.68
Hazel and palme 2023	CO	48.66	3.51	2.24	4.27	39.78	0	0	0.31	0.24	0	0.05	0.13	0.73	99.92
Hazel and palme 2024	CO	48.71	2.71	1.84	4.16	41.47	0	0	0.01	0.28	0	0.02	0.19	0.62	100.01
Hazel and palme 2025	CO	48.26	2.56	0.56	3.07	44.89	0	0	0.08	0.1	0	0.02	0.09	0.31	99.94
Hazel and palme 2026	CO	52.86	0.61	1.51	0.5	43.76	0	0	0.01	0.08	0	0.06	0.17	0.48	100.04
Hazel and palme 2027	CO	52.44	1.91	2.54	2.71	39.86	0	0	0.12	0.17	0	0.03	0.22	0.71	100.71
Hazel and palme 2028	CO	49.12	1.2	1.19	0.98	46.99	0	0	0.01	0.09	0	0.04	0.13	0.5	100.25
Hazel and palme 2029	CO	54.32	2.66	1.47	2.89	37.43	0	0	0.22	0.15	0	0.04	0.19	0.53	99.9
Hazel and palme 2030	CO	51.11	2.45	1.62	2.13	41.51	0	0	0.04	0.14	0	0.06	0.12	0.48	99.66
Hazel and palme 2031	CO	44.09	0.22	0.5	0.24	54.42	0	0	0	0.04	0	0.03	0.04	0.18	99.76
Hazel and palme 2032	CO	48.99	0.87	2.64	0.64	45.35	0	0	0.04	0.1	0	0.1	0.25	0.44	99.42
Hazel and palme 2033	CO	55.73	1.2	0.9	1.23	39.99	0	0	0.04	0.14	0	0.04	0.06	0.35	99.68
Hazel and palme 2034	CO	53.44	1.95	0.78	1.77	40.97	0	0	0.03	0.13	0	0.04	0.09	0.46	99.66
Hazel and palme 2035	CO	55.08	2.93	1.83	4.37	35.1	0	0	0.09	0.2	0	0.09	0.27	0.55	100.51
Hazel and palme 2036	CO	50.06	2.79	1.55	2.19	43.13	0	0	0.05	0.19	0	0.05	0.1	0.38	100.49

Table D.4

author	M type	SiO(2)	Al(2)O(3)	FeO	CaO	MgO	SO(2)	K(2)O	Na(2)O	TiO(2)	P(2)O	NiO	MnO	Cr(2)O(3)	total
Hazel and palme 2037	CO	53.93	2.08	4.3	1.66	37.52	0	0	0.03	0.1	0	0.04	0.3	0.73	100.69
Hazel and palme 2038	CO	50.9	4.88	1.89	4.58	37.36	0	0	0.43	0.2	0	0.08	0.1	0.21	100.63
Hazel and palme 2039	CO	47.83	1.51	3.1	2.03	44.84	0	0	0.3	0.16	0	0.07	0.1	0.27	100.21
Hazel and palme 2040	CO	52.32	3.94	1.44	2.36	39.74	0	0	0.12	0.11	0	0.06	0.13	0.41	100.63
Hazel and palme 2041	CO	50.11	2.31	0.46	3.26	43.74	0	0	0.19	0.17	0	0.03	0.12	0.15	100.54
Hazel and palme 2042	CO	51.7	3.25	1.94	3.18	38.75	0	0	0.07	0.31	0	0.06	0.16	0.58	100
Hazel and palme 2043	CO	51.99	2.07	0.76	2.76	42.16	0	0	0.01	0.22	0	0.02	0.08	0.38	100.45
Hazel and palme 2044	CO	49.62	3.25	0.71	3.63	41.33	0	0	0.74	0.16	0	0.04	0.08	0.26	99.82
Hazel and palme 2045	CO	50.57	2.09	1.51	3.08	41.34	0	0	0.04	0.18	0	0.05	0.24	0.68	99.78
Hazel and palme 2046	CO	52.13	3.12	2.7	2.8	38.11	0	0	0.16	0.17	0	0.15	0.2	0.56	100.1
Hazel and palme 2047	CO	57.48	2.63	2.37	4.99	31.81	0	0	0.2	0.2	0	0.07	0.15	0.43	100.33
Hazel and palme 2048	CO	53.41	1.99	3.63	2.1	37.28	0	0	0.63	0.15	0	0.02	0.12	0.58	99.91
Hazel and palme 2049	CO	52.06	2.28	1.68	2.96	40.31	0	0	0.09	0.13	0	0.06	0.22	0.59	100.38
Hazel and palme 2050	CO	55.33	2.47	0.89	3.01	36.8	0	0	0.51	0.13	0	0.06	0.27	0.6	100.07
Hazel and palme 2051	CO	54.69	3.38	6.04	3.28	31.26	0	0	0.66	0.14	0	0.13	0.14	0.47	100.19
Hazel and palme 2052	CO	55.43	3.44	3.27	3.74	33.27	0	0	0.41	0.21	0	0.06	0.2	0.5	100.53
Hazel and palme 2053	CO	55	1.36	0.99	1.89	40.19	0	0	0.08	0.18	0	0.02	0.12	0.48	100.31
Hazel and palme 2054	CO	47.26	1.4	8.76	1.44	40.8	0	0	0.03	0.12	0	0.06	0.34	0.64	100.85
Hazel and palme 2055	CO	51.56	3.58	0.98	3.74	39.55	0	0	0.02	0.21	0	0.05	0.23	0.5	100.42
Hazel and palme 2056	CO	49.69	1.35	1.23	1.32	45.79	0	0	0.04	0.11	0	0.05	0.13	0.43	100.14
Hazel and palme 2057	CO	41.83	0.02	3.31	0.2	53.95	0	0	0	0.02	0	0.02	0.1	0.51	99.96
Hazel and palme 2058	CO	42	0.25	0.51	0.51	56.34	0	0	0	0.09	0	0	0.06	0.24	100
Hazel and palme 2059	CO	41.56	0.02	3.2	0.2	54.23	0	0	0	0.05	0	0	0.12	0.53	99.91
Hazel and palme 2060	CO	42.03	0.04	1.16	0.2	56.12	0	0	0	0.07	0	0.02	0.07	0.25	99.96
Hazel and palme 2061	CV	42.11	0.15	0.51	0.42	56.17	0	0	0.03	0.09	0	0.03	0.07	0.26	99.84
Hazel and palme 2062	CV	42.14	0.03	4.79	0.2	52.68	0	0	0.02	0	0	0	0.13	0.09	100.08
Hazel and palme 2063	CV	42.23	0.13	1.06	0.25	55.43	0	0	0	0.12	0	0	0.17	0.49	99.88
Hazel and palme 2064	CV	42.14	0.05	1.08	0.26	55.87	0	0	0.02	0.03	0	0	0.06	0.32	99.83
Hazel and palme 2065	CV	41.59	0.14	3.39	0.32	53.93	0	0	0.05	0.03	0	0.02	0.33	0.24	100.04
Hazel and palme 2066	CV	40.73	0.03	6.52	0.21	52.09	0	0	0.02	0.01	0	0.05	0.1	0.09	99.85
Hazel and palme 2067	CO	58.1	1.47	0.83	0.63	38.31	0	0	0	0.2	0	0.09	0.09	0.38	100.1
Hazel and palme 2068	CO	58.07	1.32	1.84	0.53	37.14	0	0	0	0.19	0	0	0.07	0.83	99.99
Hazel and palme 2069	CO	58.83	0.96	0.46	0.5	38.6	0	0	0.02	0.18	0	0	0.11	0.34	100

Table D.4

author	M type	SiO(2)	Al(2)O(3)	FeO	CaO	MgO	SO(2)	K(2)O	Na(2)O	TiO(2)	P(2)O	NiO	MnO	Cr(2)O(3)	total
Hazel and palme 2070	CO	57.78	1.19	1.85	0.46	37.55	0	0	0	0.2	0	0.04	0.07	0.69	99.83
Hazel and palme 2071	CV	58.97	0.5	1.4	0.37	37.47	0	0	0.05	0.06	0	0.02	0.27	0.77	99.88
Hazel and palme 2072	CV	57.99	1.47	1.77	0.6	36.98	0	0	0	0.2	0	0.04	0.09	0.88	100.02
Hazel and palme 2073	CV	58.23	0.76	2.36	0.5	37.7	0	0	0.03	0.07	0	0.02	0.23	0	99.9
Hazel and palme 2074	CV	58.24	0.9	2.22	0.47	37.83	0	0	0	0.12	0	0	0.23	0	100.01
Hazel and palme 2075	CV	58.63	0.97	0.5	0.45	38.67	0	0	0	0.22	0	0	0.04	0.38	99.86
Hazel and palme 2076	CV	58.7	0.92	0.7	0.46	38.7	0	0	0	0.18	0	0.04	0.02	0.38	100.1
Dunn et al 2010	H	39.1	0	16.5	0.03	43.5	0	0	0	0	0	0	0.45	0.03	99.61
Dunn et al 2010	H	39.1	0	17.1	0.03	43	0	0	0	0	0	0	0.47	0.03	99.73
Dunn et al 2010	H	38.8	0	17.6	0.04	42.5	0	0	0	0	0	0	0.5	0.03	99.47
Dunn et al 2010	H	39.1	0	16.7	0.08	43.3	0	0	0	0	0	0	0.48	0.03	99.69
Dunn et al 2010	H	38.5	0	18	0.03	42.1	0	0	0	0	0	0	0.46	0.03	99.12
Dunn et al 2010	H	39	0	17.4	0.03	43.4	0	0	0	0	0	0	0.47	0.03	100.33
Dunn et al 2010	H	39	0	17.6	0.03	43	0	0	0	0	0	0	0.47	0.03	100.13
Dunn et al 2010	H	38.6	0	17.4	0.03	43	0	0	0	0	0	0	0.46	0.08	99.57
Dunn et al 2010	H	38.5	0	17.7	0.03	42.5	0	0	0	0	0	0	0.45	0.04	99.22
Dunn et al 2010	H	39.6	0	18	0.03	42.2	0	0	0	0	0	0	0.47	0.03	100.33
Dunn et al 2010	H	39.6	0	17.7	0.04	42.1	0	0	0	0	0	0	0.45	0.09	99.98
Dunn et al 2010	H	39.9	0	17.8	0.03	42.1	0	0	0	0	0	0	0.46	0.02	100.31
Dunn et al 2010	H	40	0	18.1	0.03	42.7	0	0	0	0	0	0	0.47	0.03	101.33
Dunn et al 2010	H	39.8	0	17.7	0.03	43	0	0	0	0	0	0	0.46	0.03	101.02
Dunn et al 2010	L	38.2	0	21.4	0.03	39.7	0	0	0	0	0	0	0.46	0.11	99.9
Dunn et al 2010	L	38.2	0	21.3	0.03	40.1	0	0	0	0	0	0	0.46	0.09	100.18
Dunn et al 2010	L	38.3	0	22.5	0.04	38.9	0	0	0	0	0	0	0.46	0.03	100.23
Dunn et al 2010	L	38.1	0	22.4	0.05	38.9	0	0	0	0	0	0	0.46	0.03	99.94
Dunn et al 2010	L	38.3	0	22.1	0.03	39.2	0	0	0	0	0	0	0.45	0.04	100.12
Dunn et al 2010	L	37.9	0	22.7	0.03	38.8	0	0	0	0	0	0	0.49	0.03	99.95
Dunn et al 2010	L	37.2	0	22.8	0.03	38.8	0	0	0	0	0	0	0.48	0.04	99.35
Dunn et al 2010	L	37.9	0	22.6	0.04	39	0	0	0	0	0	0	0.48	0.03	100.05
Dunn et al 2010	L	37.9	0	22.9	0.03	38.4	0	0	0	0	0	0	0.44	0.03	99.7
Dunn et al 2010	L	37.9	0	22.4	0.03	38.9	0	0	0	0	0	0	0.46	0.03	99.72
Dunn et al 2010	L	37.8	0	22.7	0.04	38.6	0	0	0	0	0	0	0.45	0.03	99.62
Dunn et al 2010	L	38.3	0	22.8	0.12	39.2	0	0	0	0	0	0	0.47	0.03	100.92

Table D.4

author	M type	SiO(2)	Al(2)O(3)	FeO	CaO	MgO	SO(2)	K(2)O	Na(2)O	TiO(2)	P(2)O	NiO	MnO	Cr(2)O(3)	total
Dunn et al 2010	L	37.9	0	22.4	0.03	38.8	0	0	0	0	0	0	0.47	0.03	99.63
Dunn et al 2010	L	37.7	0	22.2	0.06	38.6	0	0	0	0	0	0	0.49	0.03	99.08
Dunn et al 2010	LL	37.3	0	26	0.05	35.9	0	0	0	0	0	0	0.51	0.07	99.83
Dunn et al 2010	LL	37.4	0	25.3	0.04	38.6	0	0	0	0	0	0	0.46	0.03	101.83
Dunn et al 2010	LL	37.2	0	25.4	0.04	36.3	0	0	0	0	0	0	0.47	0.17	99.58
Dunn et al 2010	LL	37.2	0	27.1	0.04	35.4	0	0	0	0	0	0	0.44	0.03	100.21
Dunn et al 2010	LL	37.8	0	25.2	0.08	36.8	0	0	0	0	0	0	0.46	0.08	100.42
Dunn et al 2010	LL	36.9	0	27.1	0.05	34.9	0	0	0	0	0	0	0.44	0.03	99.42
Dunn et al 2010	LL	37.2	0	27.6	0.05	35.3	0	0	0	0	0	0	0.44	0.03	100.62
Dunn et al 2010	LL	37.6	0	25.8	0.04	36.7	0	0	0	0	0	0	0.45	0.04	100.63
Dunn et al 2010	LL	37.1	0	28.1	0.04	34.9	0	0	0	0	0	0	0.45	0.03	100.62
Dunn et al 2010	LL	37.6	0	27	0.06	35.8	0	0	0	0	0	0	0.45	0.01	100.92
Dunn et al 2010	H	55.6	0.16	13.2	0.41	29.9	0	0	0.03	0.14	0	0	0.45	0.15	100.04
Dunn et al 2010	H	55.5	0.18	13	0.8	29.8	0	0	0.03	0.13	0	0	0.49	0.19	100.12
Dunn et al 2010	H	55.4	0.36	13.4	0.7	29.4	0	0	0.05	0.15	0	0	0.46	0.4	100.32
Dunn et al 2010	H	55.4	0.23	13.4	1.02	2	0	0	0.03	0.18	0	0	0.46	0.21	72.93
Dunn et al 2010	H	55	0.13	13.7	0.72	29	0	0	0.03	0.14	0	0	0.48	0.11	99.31
Dunn et al 2010	H	55.4	0.17	13.7	0.64	29.5	0	0	0.03	0.17	0	0	0.46	0.21	100.28
Dunn et al 2010	H	54.7	0.33	13.9	0.79	28.8	0	0	0.08	0.2	0	0	0.47	0.17	99.44
Dunn et al 2010	H	55.1	0.18	13.8	0.84	29.1	0	0	0.03	0.19	0	0	0.48	0.12	99.84
Dunn et al 2010	H	54.9	0.19	14.3	0.77	28.5	0	0	0.03	0.18	0	0	0.47	0.1	99.44
Dunn et al 2010	H	54.9	0.16	13.9	0.74	28.9	0	0	0.03	0.19	0	0	0.48	0.11	99.41
Dunn et al 2010	H	54.7	0.24	14.2	1.11	28.6	0	0	0.04	0.19	0	0	0.49	0.19	99.76
Dunn et al 2010	H	55.3	0.24	13.8	1.04	29.2	0	0	0.04	0.21	0	0	0.49	0.18	100.5
Dunn et al 2010	H	55.2	0.2	13.6	0.85	28.9	0	0	0.03	0.18	0	0	0.48	0.11	99.55
Dunn et al 2010	H	55	0.22	13.5	0.91	28.8	0	0	0.03	0.18	0	0	0.48	0.11	99.23
Dunn et al 2010	L	55.6	0.16	13.2	0.41	29.9	0	0	0.03	0.14	0	0	0.45	0.15	100.04
Dunn et al 2010	L	55.5	0.18	13	0.8	29.8	0	0	0.03	0.13	0	0	0.49	0.19	100.12
Dunn et al 2010	L	55.4	0.36	13.4	0.7	29.4	0	0	0.05	0.15	0	0	0.46	0.4	100.32
Dunn et al 2010	L	55.4	0.23	13.4	1.02	29	0	0	0.03	0.18	0	0	0.46	0.21	99.93
Dunn et al 2010	L	55	0.13	13.7	0.72	29	0	0	0.03	0.14	0	0	0.48	0.11	99.31
Dunn et al 2010	L	55.4	0.17	13.7	0.64	29.2	0	0	0.03	0.17	0	0	0.46	0.21	99.98
Dunn et al 2010	L	54.7	0.33	13.9	0.79	28.8	0	0	0.08	0.2	0	0	0.47	0.17	99.44

Table D.4

author	M type	SiO(2)	Al(2)O(3)	FeO	CaO	MgO	SO(2)	K(2)O	Na(2)O	TiO(2)	P(2)O	NiO	MnO	Cr(2)O(3)	total
Dunn et al 2010	L	55.1	0.18	13.8	0.84	29.1	0	0	0.03	0.19	0	0	0.48	0.12	99.84
Dunn et al 2010	L	54.9	0.19	14.3	0.77	28.5	0	0	0.03	0.18	0	0	0.47	0.1	99.44
Dunn et al 2010	L	54.9	0.16	13.9	0.74	28.9	0	0	0.03	0.19	0	0	0.48	0.11	99.41
Dunn et al 2010	L	54.7	0.24	14.2	1.11	28.6	0	0	0.04	0.19	0	0	0.49	0.19	99.76
Dunn et al 2010	L	55.3	0.24	13.8	1.04	29.2	0	0	0.04	0.21	0	0	0.49	0.18	100.5
Dunn et al 2010	L	55.2	0.2	13.6	0.85	28.9	0	0	0.03	0.18	0	0	0.48	0.11	99.55
Dunn et al 2010	L	55	0.22	13.5	0.91	28.8	0	0	0.03	0.18	0	0	0.48	0.11	99.23
Dunn et al 2010	LL	54.3	0.42	15.1	1.2	27.2	0	0	0.08	0.15	0	0	0.44	0.31	99.2
Dunn et al 2010	LL	54.7	0.7	14.5	0.98	28	0	0	0.06	0.09	0	0	0.44	0.46	99.93
Dunn et al 2010	LL	54.6	0.3	15.3	0.81	27.9	0	0	0.04	0.12	0	0	0.44	0.21	99.72
Dunn et al 2010	LL	54.7	0.13	16.1	0.79	27.4	0	0	0.03	0.15	0	0	0.44	0.11	99.85
Dunn et al 2010	LL	55.2	0.16	15.4	0.87	27.9	0	0	0.03	0.14	0	0	0.45	0.17	100.32
Dunn et al 2010	LL	54.5	0.17	16.3	0.73	27.2	0	0	0.03	0.19	0	0	0.45	0.1	99.67
Dunn et al 2010	LL	54.6	0.23	16.5	1.04	27.3	0	0	0.03	0.2	0	0	0.43	0.17	100.5
Dunn et al 2010	LL	55.1	0.16	15.4	0.87	28.1	0	0	0.03	0.19	0	0	0.46	0.1	100.41
Dunn et al 2010	LL	54.5	0.22	17	1.12	26.9	0	0	0.06	0.21	0	0	0.44	0.15	100.6
Dunn et al 2010	LL	54.8	0.18	16	0.89	27.7	0	0	0.03	0.2	0	0	0.45	0.16	100.41
Dunn et al 2010	H	54.6	1.32	4.44	21.6	16.5	0	0	0.64	0.44	0	0	0.24	0.75	100.53
Dunn et al 2010	H	54.8	0.5	3.42	23	17.2	0	0	0.54	0.51	0	0	0.18	0.8	100.95
Dunn et al 2010	L	53.4	0.51	5.05	21.9	16.7	0	0	0.59	0.49	0	0	0.24	0.88	99.76
Dunn et al 2010	L	54	0.5	5.14	21.1	16.9	0	0	0.6	0.47	0	0	0.24	0.91	99.86
Dunn et al 2010	L	53.4	0.52	4.97	21.7	16.7	0	0	0.57	0.51	0	0	0.23	0.98	99.58
Dunn et al 2010	LL	53.1	0.9	6.51	20.7	16.3	0	0	0.61	0.49	0	0	0.29	0.91	99.81
Dunn et al 2010	LL	53.7	0.53	4.96	22.1	16.6	0	0	0.53	0.44	0	0	0.21	0.66	99.73
Dunn et al 2010	LL	53.5	0.56	6.76	21	16.3	0	0	0.55	0.46	0	0	0.24	0.82	100.19
Dunn et al 2010	LL	53.4	0.5	6.47	21.3	16.4	0	0	0.5	0.43	0	0	0.22	0.79	100.01
Lodders and Fegley (book)	CI	22.76243974	1.634353736	26.02116035	1.295656021	16.08511829	13.50930661	0	0	0	0	1.39984666	0	0	82.70788
Lodders and Fegley (book)	CM	27.16945344	2.135051701	30.45333602	1.804963571	19.0699856	6.74216781	0	0	0	0	1.565283083	0	0	88.94024
Lodders and Fegley (book)	CV	33.58743457	3.174236157	33.59875101	2.574521683	23.71311253	5.493618216	0	0	0	0	1.679815992	0	0	103.8214
Lodders and Fegley (book)	CO	33.80136728	2.645196798	35.74335214	2.210730575	24.04476445	5.493618216	0	0	0	0	1.807074779	0	0	105.7461
Lodders and Fegley (book)	CK	33.80136728	2.777456638	32.88388396	2.378634163	24.37641638	4.245068621	0	0	0	0	1.667090113	0	0	102.1299
Lodders and Fegley (book)	CR	32.08990564	2.172840227	34.02767123	1.804963571	2.81904135	4.744488459	0	0	0	0	1.667090113	0	0	79.32600
Lodders and Fegley (book)	CH	28.88091508	1.983897598	54.32989525	1.818955537	18.73833368	0.873984716	0	0	0	0	3.270550832	0	0	109.8965

Table D.4

author	M type	SiO(2)	Al(2)O(3)	FeO	CaO	MgO	SO(2)	K(2)O	Na(2)O	TiO(2)	P(2)O	NiO	MnO	Cr(2)O(3)	total
Lodders and Fegley (book)	H	36.58249243	2.002791861	38.88876712	1.707019811	23.3814606	4.994198378	0	0	0	0	2.176125262	0	0	109.7328
Lodders and Fegley (book)	L	39.791483	2.19173449	31.09671636	1.860931434	24.7080683	5.493618216	0	0	0	0	1.578008962	0	0	106.7205
Lodders and Fegley (book)	LL	40.43328111	2.229523015	28.30873489	1.846939468	25.37137215	5.243908297	0	0	0	0	1.348943145	0	0	104.7827
Lodders and Fegley (book)	r	38.50788677	2.002791861	34.88551168	1.278865662	21.39154906	10.1631937	0	0	0	0	1.832526536	0	0	110.0623
Lodders and Fegley (book)	Acap	37.86608866	2.267311541	33.59875101	1.539116223	25.86885003	6.74216781	0	0	0	0	1.908881809	0	0	109.7911
Lodders and Fegley (book)	K	36.15462703	2.456254169	35.31443191	1.707019811	25.53719811	13.73404554	0	0	0	0	1.857978294	0	0	116.7615
Lodders and Fegley (book)	eh	35.51282891	1.549329553	43.60688961	1.189317082	17.79312569	13.98375546	0	0	0	0	2.341561685	0	0	115.9768
Lodders and Fegley (book)	EL	40.21934841	1.889426284	35.45740532	1.427180498	22.80106974	7.741007486	0	0	0	0	1.870704173	0	0	111.4061

author	M type	SiO(2)	Al(2)O(3)	FeO	CaO	MgO	SO(2)	K(2)O	Na(2)O	TiO(2)	P(2)O	NiO	MnO	Cr(2)O(3)	total
Jambon 2008	Angrite	42.18	11.70	18.52	11.62	14.60	0.00	0.03	0.01	0.67	0.12	0.00	0.22	0.14	99.81
Jambon 2008	Angrite	40.40	9.19	16.00	10.80	19.40	0.00	0.00	0.02	0.73	0.08	0.00	0.24	0.02	96.88
Jambon 2008	Angrite	37.30	10.10	24.00	12.50	14.80	0.00	0.00	0.02	0.88	0.17	0.00	0.20	0.01	99.98
Jambon 2008	Angrite	39.54	12.18	25.00	14.65	6.71	0.00	0.03	0.03	0.93	0.17	0.00	0.28	0.07	99.59
Jambon 2008	Angrite	39.60	14.10	15.50	17.50	7.00	0.00	0.00	0.02	1.15	0.13	0.00	0.20	0.01	95.21
Jambon 2008	Angrite	38.40	12.40	24.70	15.00	6.59	0.00	0.01	0.02	0.89	0.16	0.00	0.28	0.05	98.50
Jambon 2008	Angrite	43.70	9.35	9.40	22.90	10.80	0.00	0.00	0.03	2.05	0.13	0.00	0.10	0.02	98.48
Keil 2012	Angrite	43.50	9.80	9.30	23.70	11.20	0.00	0.00	0.04	2.90	0.00	0.00	0.08	0.28	100.80
Keil 2012	Angrite	43.22	8.92	8.67	23.66	10.54	0.00	0.00	0.06	2.33	0.09	0.00	0.13	0.20	97.82
Keil 2012	Angrite	40.32	14.09	18.24	18.20	7.14	0.00	0.00	0.00	1.10	0.21	0.00	0.20	0.12	99.62
Keil 2012	Angrite	43.30	12.10	15.90	15.20	9.40	0.00	0.00	0.01	0.42	0.00	0.00	0.30	0.37	97.00
Keil 2012	Angrite	43.00	12.00	18.00	18.00	8.70	0.00	0.00	0.00	0.90	0.00	0.00	0.20	0.23	101.03
Keil 2012	Angrite	39.60	14.10	18.50	17.50	7.00	0.00	0.00	0.00	1.15	0.13	0.00	0.20	0.11	98.29
Keil 2012	Angrite	38.00	14.20	20.20	18.50	7.10	0.00	0.00	0.03	1.59	0.00	0.00	0.22	0.13	99.97
Keil 2012	Angrite	33.40	4.71	31.20	7.37	19.00	0.00	0.00	0.00	0.42	0.01	0.00	0.24	0.00	96.35
Keil 2012	Angrite	37.49	8.50	27.16	6.80	17.84	0.00	0.00	0.11	1.46	0.18	0.00	0.31	0.00	99.85
Keil 2012	Angrite	37.30	10.07	23.43	12.51	14.81	0.00	0.00	0.03	0.88	0.17	0.00	0.20	0.13	99.53
Keil 2012	Angrite	38.40	12.40	24.70	15.00	6.49	0.00	0.00	0.02	0.89	0.16	0.00	0.28	0.04	98.38
Keil 2012	Angrite	36.90	12.30	24.90	15.20	6.45	0.00	0.00	0.00	0.85	0.17	0.00	0.25	0.00	97.02
Keil 2012	Angrite	38.90	11.30	22.10	12.70	13.10	0.00	0.00	0.10	0.60	0.50	0.00	0.30	0.10	99.70
Keil 2012	Angrite	40.40	9.19	19.00	10.80	19.40	0.00	0.00	0.00	0.73	0.08	0.00	0.24	0.17	100.01
Keil 2012	Angrite	41.10	10.80	17.90	12.00	14.90	0.00	0.00	0.03	0.00	0.00	0.00	0.25	0.16	97.14
Keil 2012	Angrite	39.00	12.18	25.00	14.65	6.71	0.00	0.00	0.03	0.93	0.17	0.00	0.28	0.07	99.02
Keil 2012	Angrite	42.18	11.70	18.52	11.95	14.60	0.00	0.00	0.01	0.67	0.12	0.00	0.22	0.14	100.11
Keil 2012	Angrite	38.60	12.50	23.10	15.10	7.04	0.00	0.00	0.02	0.91	0.15	0.00	0.26	0.05	97.72
Keil 2012	Angrite	38.60	12.90	25.60	15.40	6.79	0.00	0.00	0.00	0.88	0.18	0.00	0.27	0.00	100.62
Fogel 2003	Aubrite	62.58	4.82	0.22	1.48	26.32	0.37	1.07	2.99	0.11	0.00	0.00	0.04	0.00	100.00
Fogel 2003	Aubrite	61.90	3.63	0.15	1.28	30.67	0.63	0.20	1.47	0.04	0.00	0.00	0.04	0.00	100.01
Fogel 2003	Aubrite	60.61	1.69	0.55	1.15	34.88	0.01	0.10	0.77	0.04	0.00	0.00	0.04	0.01	99.85
Keil 2011	Aubrite	56.10	1.80	3.48	1.70	35.40	0.00	0.10	0.50	0.08	0.01	0.00	0.33	0.19	99.69
Keil 2011	Aubrite	62.58	4.82	0.22	1.48	26.32	0.37	1.07	2.99	0.11	0.00	0.00	0.04	0.00	100.00
Keil 2011	Aubrite	61.90	3.63	0.15	1.28	30.67	0.63	0.80	1.47	0.04	0.00	0.00	0.01	0.00	100.58
Keil 2011	Aubrite	60.61	1.69	0.55	1.15	34.88	0.01	0.10	0.77	0.04	0.00	0.00	0.18	0.00	99.98
Keil 2011	Aubrite	76.20	8.30	2.76	5.70	4.90	0.19	0.36	2.14	0.22	0.00	0.00	0.41	0.00	101.18
Keil 2011	Aubrite	69.78	14.41	0.16	3.15	5.52	0.84	2.42	6.67	0.02	0.00	0.00	0.00	0.00	102.97

author	M type	SiO(2)	Al(2)O(3)	FeO	CaO	MgO	SO(2)	K(2)O	Na(2)O	TiO(2)	P(2)O	NiO	MnO	Cr(2)O(3)	total
Keil 2011	Aubrite	67.79	14.41	0.26	4.56	3.96	2.56	0.80	5.84	0.16	0.00	0.00	0.00	0.00	100.34
Keil 2011	Aubrite	74.13	16.61	0.15	0.20	0.26	0.08	0.98	7.76	0.24	0.00	0.00	0.00	0.00	100.41
watters and prinz 1979	Aubrite	59.65	0.23	0.02	0.48	38.90	0.00	0.00	0.13	0.20	0.00	0.00	0.07	0.02	99.70
watters and prinz 1979	Aubrite	59.10	2.72	0.07	1.03	34.80	0.00	0.00	1.53	0.03	0.00	0.00	0.01	0.02	99.31
watters and prinz 1979	Aubrite	57.30	0.61	0.05	2.29	37.90	0.00	0.00	0.30	0.04	0.00	0.00	0.09	0.02	98.60
watters and prinz 1979	Aubrite	57.20	0.21	0.08	0.63	38.50	0.00	0.00	0.08	0.02	0.00	0.00	0.08	0.05	96.85
watters and prinz 1979	Aubrite	59.10	1.25	0.01	0.75	37.80	0.00	0.00	0.59	0.05	0.00	0.00	0.04	0.01	99.60
watters and prinz 1979	Aubrite	59.50	0.18	0.03	0.64	39.30	0.00	0.00	0.08	0.03	0.00	0.00	0.02	0.02	99.80
watters and prinz 1979	Aubrite	59.30	2.30	0.25	0.75	34.20	0.00	0.00	1.19	0.07	0.12	0.00	0.08	0.06	98.32
watters and prinz 1979	Aubrite	56.50	0.25	0.06	1.16	39.80	0.00	0.00	0.11	0.01	0.00	0.00	0.00	0.01	97.90
watters and prinz 1979	Aubrite	59.30	0.46	0.07	0.83	38.50	0.00	0.00	0.24	0.01	0.01	0.00	0.06	0.03	99.51
watters and prinz 1979	Aubrite	59.10	1.27	0.05	0.62	37.50	0.00	0.00	0.61	0.03	0.03	0.00	0.03	0.03	99.27
watters and prinz 1979	Aubrite	48.90	0.55	0.04	0.15	32.80	0.00	0.00	0.26	0.02	0.02	0.00	0.00	0.00	82.74
Yanai 1992	Aubrite	56.41	2.20	0.10	1.72	35.53	0.00	0.11	0.96	0.00	0.07	0.32	0.18	0.03	97.63
Yanai 1992	Aubrite	57.16	0.18	0.97	0.62	39.25	0.00	0.02	0.15	0.02	0.00	0.06	0.17	0.06	98.66
Yanai 1992	EH3	36.31	2.93	0.96	1.29	19.59	0.00	0.07	0.83	0.08	0.46	1.71	0.24	0.45	64.92
Day 2012	Brachinite	52.20	14.80	11.00	8.20	4.00	0.34	0.16	5.43	0.09	4.00	0.00	0.10	0.07	100.39
Day 2012	Brachinite	56.90	17.10	8.00	6.60	2.80	0.29	0.25	5.41	0.06	2.40	0.00	0.10	0.03	99.94
Day 2012	Brachinite	56.10	14.90	10.00	5.40	4.60	0.14	0.22	6.81	0.10	1.60	0.00	0.16	0.06	100.09
Day 2012	Brachinite	57.00	17.90	8.50	5.80	2.00	0.22	0.23	5.80	0.15	2.10	0.00	0.06	0.16	99.92
Day 2012	Brachinite	57.80	18.00	9.00	5.40	2.00	0.26	0.25	5.41	0.21	1.40	0.00	0.08	0.12	99.93
Day 2012	Brachinite	55.00	14.80	11.80	4.90	4.20	1.49	0.22	6.74	0.12	1.20	0.00	0.14	0.08	100.69
Keil 2014	Brachinite	36.40	0.17	32.20	2.52	30.50	0.00	0.01	0.07	0.27	0.00	0.51	0.33	0.58	103.55
Keil 2014	Brachinite	38.06	2.03	26.75	2.10	27.27	0.52	0.05	0.67	0.12	0.30	0.13	0.34	0.65	98.99
Keil 2014	Brachinite	38.95	0.74	31.48	0.77	26.73	0.00	0.05	0.05	0.18	0.00	0.22	0.39	0.41	99.97
Keil 2014	Brachinite	37.59	1.68	28.98	1.38	28.23	0.00	0.00	0.39	0.00	0.00	0.07	0.00	0.56	98.88
Keil 2014	Brachinite	38.08	0.25	29.70	0.80	29.50	0.00	0.01	0.03	0.12	0.00	0.34	0.38	0.77	99.98
Keil 2014	Brachinite	36.43	2.45	30.86	1.85	25.37	0.00	0.07	0.80	0.32	0.00	0.89	0.33	0.58	99.95
Keil 2014	Brachinite	38.64	0.43	30.90	0.85	27.60	0.00	0.01	0.09	0.17	0.00	0.26	0.37	0.66	99.98
Barrat 2003	Eucrite	0.00	18.42	12.64	11.66	8.63	0.00	0.00	0.44	0.10	0.00	0.00	0.41	0.00	52.30
Barrat 2003	Eucrite	0.00	12.77	21.14	10.67	6.47	0.00	0.00	0.55	0.60	0.00	0.00	0.50	0.00	52.70
Barrat 2003	Eucrite	0.00	12.00	20.36	10.33	6.50	0.00	0.00	0.62	1.15	0.00	0.00	0.48	0.00	51.44
Barrat 2003	Eucrite	0.00	12.28	19.55	10.42	7.19	0.00	0.00	0.54	0.75	0.00	0.00	0.50	0.00	51.23
Barrat 2003	Eucrite	0.00	13.23	18.48	10.95	6.52	0.00	0.00	0.53	0.68	0.00	0.00	0.48	0.00	50.87
Barrat 2003	Eucrite	0.00	13.61	20.21	11.27	7.40	0.00	0.00	0.52	0.65	0.00	0.00	0.48	0.00	54.14

author	M type	SiO(2)	Al(2)O(3)	FeO	CaO	MgO	SO(2)	K(2)O	Na(2)O	TiO(2)	P(2)O	NiO	MnO	Cr(2)O(3)	total
Barrat 2003	Eucrite	0.00	12.88	18.57	10.28	7.44	0.00	0.00	0.46	0.63	0.00	0.00	0.50	0.00	50.76
Barrat 2003	Eucrite	0.00	12.48	19.88	10.33	6.74	0.00	0.00	0.48	0.77	0.00	0.00	0.50	0.00	51.18
Barrat 2003	Eucrite	0.00	12.91	19.46	10.54	7.17	0.00	0.00	0.48	0.69	0.00	0.00	0.50	0.00	51.75
Barrat 2003	Eucrite	0.00	13.14	17.84	11.40	7.77	0.00	0.00	0.00	0.62	0.00	0.00	0.56	0.00	51.33
Barrat 2003	Eucrite	0.00	12.74	18.07	10.52	6.93	0.00	0.00	0.00	0.63	0.00	0.00	0.57	0.00	49.46
Barrat 2003	Eucrite	0.00	11.81	20.55	11.76	5.53	0.00	0.00	0.00	0.93	0.00	0.00	0.57	0.00	51.15
Barrat 2003	Eucrite	0.00	12.23	20.57	10.44	7.07	0.00	0.00	0.00	0.65	0.00	0.00	0.62	0.00	51.58
Barrat 2003	Eucrite	0.00	12.56	20.26	10.97	7.14	0.00	0.00	0.00	0.71	0.00	0.00	0.62	0.00	52.26
Barrat 2003	Eucrite	0.00	12.65	19.79	10.60	6.77	0.00	0.00	0.00	0.74	0.00	0.00	0.59	0.00	51.14
Barrat 2003	Eucrite	0.00	11.74	18.23	10.09	7.05	0.00	0.00	0.00	0.67	0.00	0.00	0.58	0.00	48.36
Barrat 2003	Eucrite	0.00	12.28	17.46	10.89	8.13	0.00	0.00	0.00	0.67	0.00	0.00	0.58	0.00	50.01
Barrat 2003	Eucrite	0.00	12.19	17.14	11.40	6.92	0.00	0.00	0.00	0.79	0.00	0.00	0.62	0.00	49.06
Barrat 2003	Eucrite	0.00	12.30	18.46	10.51	6.82	0.00	0.00	0.00	0.85	0.00	0.00	0.61	0.00	49.55
Barrat 2003	Eucrite	0.00	11.18	18.86	12.31	7.29	0.00	0.00	0.00	0.85	0.00	0.00	0.58	0.00	51.07
Barrat 2003	Eucrite	0.00	10.47	17.57	12.39	7.21	0.00	0.00	0.00	0.82	0.00	0.00	0.53	0.00	48.99
Barrat 2007	Eucrite	0.00	12.26	17.18	11.27	6.04	0.00	0.15	0.60	1.35	0.09	0.00	0.43	0.33	49.70
Barrat 2007	Eucrite	0.00	12.75	18.58	10.99	6.98	0.00	0.09	0.56	1.08	0.10	0.00	0.55	0.33	52.01
Barrat 2007	Eucrite	0.00	11.60	20.07	10.40	6.26	0.00	0.10	0.56	1.06	0.14	0.00	0.50	0.33	51.02
Barrat 2007	Eucrite	0.00	12.36	20.91	10.90	5.70	0.00	0.06	0.48	0.94	0.09	0.00	0.63	0.30	52.37
Barrat 2007	Eucrite	0.00	12.93	18.71	10.39	7.18	0.00	0.05	0.42	0.63	0.08	0.00	0.53	0.35	51.27
Barrat 2010	Eucrite	53.50	1.37	18.80	2.49	23.20	0.00	0.01	0.03	0.09	0.01	0.00	0.67	0.73	100.90
Barrat 2010	Eucrite	49.70	1.06	30.90	4.83	12.00	0.00	0.01	0.03	0.29	0.01	0.00	1.04	0.49	100.36
Barrat 2010	Eucrite	51.30	0.26	16.40	21.30	9.94	0.00	0.01	0.03	0.09	0.01	0.00	0.49	0.07	99.90
Barrat 2010	Eucrite	50.70	1.22	29.60	1.82	15.90	0.00	0.01	0.03	0.12	0.01	0.00	0.82	0.42	100.65
Barrat 2010	Eucrite	52.70	1.35	20.90	2.61	21.50	0.00	0.01	0.03	0.12	0.00	0.00	0.71	0.71	100.64
Barrat 2010	Eucrite	49.90	1.19	31.60	2.32	13.90	0.00	0.01	0.03	0.12	0.00	0.00	0.95	0.49	100.51
Barrat 2010	Eucrite	50.40	0.18	34.30	1.52	12.90	0.00	0.01	0.03	0.11	0.00	0.00	1.08	0.17	100.70
Barrat 2010	Eucrite	53.40	1.51	19.00	2.48	23.20	0.00	0.01	0.03	0.17	0.00	0.00	0.65	0.95	101.40
Barrat 2010	Eucrite	48.10	1.17	32.30	11.30	6.13	0.00	0.01	0.03	0.88	0.00	0.00	1.09	0.24	101.25
Barrat 2010	Eucrite	49.60	1.26	33.40	1.59	13.30	0.00	0.02	0.03	0.20	0.01	0.00	1.06	0.50	100.97
Barrat 2010	Eucrite	54.20	1.04	17.50	2.17	24.30	0.00	0.00	0.00	0.13	0.00	0.00	0.59	0.72	100.65
Barrat 2010	Eucrite	47.60	1.04	34.20	10.90	4.31	0.00	0.00	0.00	0.92	0.00	0.00	1.03	0.10	100.10
Barrat 2010	Eucrite	50.50	1.13	32.10	2.56	14.00	0.00	0.00	0.00	0.18	0.00	0.00	0.93	0.42	101.82
Barrat 2010	Eucrite	51.10	2.75	20.40	3.57	20.30	0.00	0.01	0.03	0.26	0.00	0.00	0.75	1.06	100.23
Barrat 2010	Eucrite	47.20	1.65	30.60	14.70	4.35	0.00	0.01	0.03	1.25	0.00	0.00	0.93	0.12	100.84

author	M type	SiO(2)	Al(2)O(3)	FeO	CaO	MgO	SO(2)	K(2)O	Na(2)O	TiO(2)	P(2)O	NiO	MnO	Cr(2)O(3)	total
Barrat 2010	Eucrite	48.90	1.69	22.00	20.60	5.89	0.00	0.01	0.04	1.51	0.00	0.00	0.61	0.26	101.51
Barrat 2010	Eucrite	49.60	1.27	33.50	2.11	13.10	0.00	0.01	0.05	0.09	0.00	0.00	1.02	0.59	101.34
Barrat 2010	Eucrite	49.40	0.08	34.80	0.68	13.70	0.00	0.01	0.03	0.08	0.00	0.00	1.06	0.03	99.87
Barrat 2010	Eucrite	51.60	0.46	14.50	21.10	11.50	0.00	0.01	0.04	0.21	0.00	0.00	0.54	0.19	100.15
Barrat 2010	Eucrite	49.80	0.28	35.80	4.24	9.92	0.00	0.01	0.06	0.18	0.00	0.00	1.13	0.13	101.55
Barrat 2010	Eucrite	50.90	0.52	17.70	20.50	9.21	0.00	0.01	0.05	0.22	0.00	0.00	0.56	0.20	99.87
Barrat 2010	Eucrite	49.80	0.11	37.40	1.61	10.30	0.00	0.01	0.03	0.07	0.00	0.00	1.28	0.06	100.67
Barrat 2010	Eucrite	32.90	0.03	51.50	0.06	14.40	0.00	0.01	0.03	0.03	0.04	0.00	1.05	0.11	100.16
Barrat 2010	Eucrite	31.50	0.06	59.10	0.13	8.32	0.00	0.01	0.03	0.03	0.00	0.00	1.38	0.11	100.67
Barrat 2010	Eucrite	31.30	0.08	59.50	0.14	7.75	0.00	0.01	0.03	0.03	0.03	0.00	1.41	0.21	100.49
Barrat 2010	Eucrite	32.60	0.03	55.50	0.10	11.40	0.00	0.00	0.00	0.03	0.00	0.00	1.21	0.07	100.94
Barrat 2010	Eucrite	30.70	0.10	60.30	0.21	6.23	0.00	0.02	0.03	0.06	0.00	0.00	1.48	0.08	99.21
Barrat 2010	Eucrite	32.40	0.03	57.80	0.15	9.53	0.00	0.01	0.03	0.03	0.00	0.00	1.32	0.04	101.34
Barrat 2010	Eucrite	45.30	34.80	0.37	18.80	0.03	0.00	0.05	0.99	0.03	0.00	0.00	0.01	0.03	100.41
Barrat 2010	Eucrite	44.40	34.90	0.50	19.20	0.03	0.00	0.04	0.71	0.03	0.00	0.00	0.01	0.03	99.85
Barrat 2010	Eucrite	48.00	33.50	0.44	16.80	0.01	0.00	0.14	1.97	0.03	0.00	0.00	0.01	0.14	101.04
Barrat 2010	Eucrite	43.30	35.90	1.08	19.90	0.04	0.00	0.02	0.25	0.03	0.00	0.00	0.02	0.06	100.60
Barrat 2010	Eucrite	49.50	31.70	0.97	16.50	0.11	0.00	0.17	1.86	0.03	0.00	0.00	0.02	0.03	100.89
Barrat 2010	Eucrite	48.40	32.90	0.79	17.40	0.07	0.00	0.11	1.57	0.03	0.00	0.00	0.03	0.03	101.33
Barrat 2010	Eucrite	50.90	31.60	0.58	15.60	0.05	0.00	0.24	2.32	0.03	0.00	0.00	0.01	0.03	101.36
Barrat 2010	Eucrite	42.20	35.60	1.30	19.40	0.03	0.00	0.01	0.14	0.04	0.00	0.00	0.01	0.00	98.73
Barrat 2010	Eucrite	48.40	32.30	0.73	16.80	0.10	0.00	0.16	1.62	0.03	0.00	0.00	0.02	0.03	100.19
Barrat 2010	Eucrite	46.70	33.50	0.58	17.70	0.08	0.00	0.08	1.14	0.02	0.00	0.00	0.03	0.03	99.86
Barrat 2010	Eucrite	49.70	31.30	0.77	15.70	0.09	0.00	0.25	2.02	0.04	0.00	0.00	0.04	0.03	99.94
Barrat 2010	Eucrite	43.80	35.80	1.08	19.50	0.03	0.00	0.02	0.24	0.01	0.00	0.00	0.05	0.03	100.56
Barrat 2010	Eucrite	44.70	34.80	0.25	18.80	0.01	0.00	0.04	0.69	0.01	0.00	0.00	0.02	0.03	99.35
Barrat 2010	Eucrite	50.30	31.10	0.23	14.50	0.01	0.00	0.67	2.68	0.02	0.00	0.00	0.01	0.03	99.55
Barrat 2010	Eucrite	43.60	35.20	0.71	19.40	0.01	0.00	0.01	0.36	0.01	0.00	0.00	0.02	0.01	99.33
Barrat 2010	Eucrite	45.50	34.20	0.80	18.20	0.01	0.00	0.05	1.04	0.01	0.00	0.00	0.02	0.02	99.85
Buchanan 1996	Eucrite	51.50	12.10	16.20	10.30	8.65	0.00	0.07	0.52	0.63	0.00	0.00	0.52	0.37	100.86
Hsu 1996	Eucrite	48.40	15.70	19.10	10.40	5.00	0.00	0.07	0.00	0.62	0.00	0.00	0.52	0.30	100.11
Hsu 1996	Eucrite	48.59	12.70	19.58	10.25	6.77	0.00	0.05	0.45	0.65	0.00	0.00	0.56	0.33	99.93
Hsu 1996	Eucrite	45.40	12.40	22.10	8.80	6.80	0.00	0.03	0.16	0.70	0.00	0.00	0.60	0.36	97.35
Hsu 1996	Eucrite	48.50	12.40	20.10	9.50	7.50	0.00	0.00	0.48	0.55	0.00	0.00	0.00	0.00	99.03
Yamaguchi 2009	Eucrite	48.00	11.70	20.90	10.70	7.10	0.00	0.01	0.53	0.76	0.00	0.00	0.54	0.32	100.56

author	M type	SiO(2)	Al(2)O(3)	FeO	CaO	MgO	SO(2)	K(2)O	Na(2)O	TiO(2)	P(2)O	NiO	MnO	Cr(2)O(3)	total
Yamaguchi 2009	Eucrite	48.10	12.80	20.20	10.40	7.48	0.00	0.05	0.51	0.68	0.00	0.00	0.52	0.31	101.05
Yamaguchi 2009	Eucrite	48.60	12.10	20.10	11.50	6.40	0.00	0.03	0.50	0.70	0.00	0.00	0.52	0.31	100.75
Yamaguchi 2009	Eucrite	48.60	12.80	19.20	10.60	7.50	0.00	0.04	0.47	0.62	0.00	0.00	0.51	0.30	100.65
Yamaguchi 2009	Eucrite	0.00	13.14	17.84	11.40	7.77	0.00	0.00	0.00	0.62	0.00	0.00	0.56	0.00	51.33
Yamaguchi 2009	Eucrite	0.00	13.23	21.16	11.03	7.20	0.00	0.04	0.41	0.68	0.07	0.00	0.64	0.36	54.82
Yamaguchi 2009	Eucrite	49.10	12.90	20.20	9.80	7.20	0.00	0.00	0.40	0.51	0.00	0.00	0.59	0.33	101.03
Yamaguchi 2009	Eucrite	47.90	13.40	20.00	10.70	7.37	0.00	0.03	0.40	0.48	0.00	0.00	0.56	0.32	101.15
Yamaguchi 2009	Eucrite	0.00	13.70	19.36	10.36	7.08	0.00	0.04	0.38	0.51	0.08	0.00	0.59	0.30	52.40
Yamaguchi 2009	Eucrite	50.80	11.80	20.20	9.34	6.59	0.00	0.04	0.44	0.62	0.00	0.00	0.57	0.32	100.72
Yamaguchi 2009	Eucrite	0.00	0.00	20.07	10.80	7.40	0.00	0.06	0.46	0.65	0.07	0.00	0.60	0.32	40.43
Yamaguchi 2009	Eucrite	50.90	12.30	20.00	9.96	7.32	0.00	0.03	0.37	0.48	0.00	0.00	0.57	0.33	102.26
Yamaguchi 2009	Eucrite	0.00	13.68	20.07	11.02	7.60	0.00	0.04	0.39	0.51	0.07	0.00	0.63	0.32	54.33
NASA HED D.B.	Eucrite	49.92	13.00	18.16	10.34	6.00	0.00	0.04	0.46	0.73	0.00	0.00	0.53	0.30	99.48
NASA HED D.B.	Eucrite	49.20	12.20	18.10	10.60	7.00	0.00	0.08	0.54	0.98	0.13	0.00	0.51	0.30	99.64
NASA HED D.B.	Eucrite	48.22	14.81	14.45	10.42	8.76	0.00	0.05	0.45	0.38	0.32	0.00	0.42	0.39	98.67
NASA HED D.B.	Diogenite	50.19	0.67	16.78	0.93	29.15	0.00	0.01	0.02	0.08	0.00	0.00	0.49	0.84	99.16
NASA HED D.B.	Diogenite	52.65	1.53	16.15	1.64	26.08	0.87	0.03	0.12	0.14	0.01	0.00	0.49	0.91	100.62
Mittlefehldt 1997	Howardite	49.20	11.50	18.50	9.18	8.40	0.00	0.06	0.43	0.81	0.11	0.00	0.53	0.48	99.20
Mittlefehldt 1997	Howardite	49.50	13.40	18.80	10.30	7.20	0.00	0.04	0.41	0.60	0.13	0.00	0.55	0.32	101.25
Mittlefehldt 1997	Howardite	49.80	10.40	16.50	7.90	12.10	0.00	0.00	0.28	0.47	0.00	0.00	0.50	0.54	98.49
Mittlefehldt 1997	Howardite	49.47	9.66	16.77	9.34	10.10	0.00	0.04	0.47	0.78	0.09	0.00	0.54	0.90	98.16
Mittlefehldt 1997	Howardite	48.37	10.54	19.33	8.52	11.44	0.00	0.03	0.35	0.44	0.00	0.00	0.00	0.49	99.51
Dymek 1976	Howardite	50.26	14.53	16.65	10.94	6.48	0.00	0.03	0.49	0.37	0.00	0.00	0.53	0.11	100.39
Dymek 1977	Howardite	49.16	11.94	18.61	9.85	8.89	0.00	0.04	0.33	0.31	0.05	0.00	0.62	0.31	100.11
Nasa HED D.B.	Howardite	24.60	2.74	36.50	0.72	13.90	11.10	0.03	0.26	0.08	0.14	1.66	0.20	0.30	92.23
Nasa HED D.B.	Howardite	0.00	2.67	30.00	2.30	22.00	0.00	0.03	0.26	0.00	0.00	1.72	0.23	0.51	59.72
Gross 2013	Shergottite	44.60	5.17	21.30	6.77	17.10	0.00	0.08	1.04	0.82	0.81	0.00	0.56	0.64	98.89
Gross 2013	Shergottite	44.54	4.86	23.77	6.15	17.08	0.00	0.07	0.90	1.13	0.82	0.00	0.58	1.04	100.94
Shirai 2009	Shergottite	42.20	2.80	20.00	3.30	27.70	0.00	0.03	0.49	0.42	0.00	0.00	0.46	0.98	98.38
Shirai 2009	Shergottite	46.20	3.31	19.70	4.30	24.90	0.00	0.03	0.53	0.39	0.00	0.00	0.49	0.88	100.73
Shirai 2009	Shergottite	45.40	2.50	19.30	3.96	26.20	0.00	0.03	0.28	0.27	0.00	0.00	0.50	1.04	99.47
Warren 2011	Ureilite	42.02	0.27	15.53	0.10	40.68	0.00	0.01	0.04	0.07	0.08	0.00	0.39	0.80	99.99
Warren 2011	Ureilite	42.04	0.52	15.97	0.84	39.01	0.00	0.04	0.19	0.14	0.10	0.00	0.42	0.73	100.00
Warren 2011	Ureilite	44.87	0.34	9.85	1.45	41.69	0.00	0.00	0.09	0.20	0.07	0.00	0.44	1.00	100.00
Warren 2011	Ureilite	44.14	0.96	13.20	0.47	39.52	0.00	0.00	0.07	0.13	0.07	0.00	0.43	1.01	100.00

author	M type	SiO(2)	Al(2)O(3)	FeO	CaO	MgO	SO(2)	K(2)O	Na(2)O	TiO(2)	P(2)O	NiO	MnO	Cr(2)O(3)	total
Warren 2011	Ureilite	39.60	0.09	21.50	0.59	36.62	0.00	0.00	0.00	0.01	0.04	0.00	0.39	1.15	99.99
Warren 2011	Ureilite	41.77	0.97	18.50	1.25	36.29	0.00	0.04	0.05	0.07	0.13	0.00	0.27	0.65	99.99
Warren 2011	Ureilite	42.53	0.05	14.03	1.11	41.02	0.00	0.01	0.03	0.04	0.06	0.00	0.39	0.72	99.99
Warren 2011	Ureilite	47.15	0.30	6.91	2.54	41.80	0.00	0.00	0.05	0.10	0.09	0.00	0.45	0.60	99.99
Warren 2011	Ureilite	43.00	0.05	17.41	1.02	37.14	0.00	0.00	0.03	0.04	0.04	0.00	0.42	0.84	99.99
Warren 2011	Ureilite	39.60	0.54	20.38	1.41	37.04	0.00	0.02	0.22	0.03	0.21	0.00	0.34	0.21	100.00
Warren 2011	Ureilite	41.71	0.21	12.07	0.89	43.81	0.00	0.02	0.02	0.06	0.06	0.00	0.41	0.75	100.01
Warren 2011	Ureilite	40.62	0.89	16.68	0.85	39.48	0.00	0.01	0.09	0.08	0.05	0.00	0.50	0.75	100.00
Warren 2011	Ureilite	40.47	0.81	17.99	3.32	35.74	0.00	0.01	0.21	0.15	0.24	0.00	0.41	0.64	99.99
Warren 2011	Ureilite	35.28	0.96	21.60	0.58	39.62	0.00	0.02	0.03	0.08	0.65	0.00	0.39	0.78	99.99
Warren 2011	Ureilite	37.06	0.20	21.54	1.07	38.60	0.00	0.05	0.15	0.09	0.09	0.00	0.43	0.72	100.00
Warren 2011	Ureilite	43.93	0.87	17.83	2.06	33.73	0.00	0.02	0.21	0.13	0.08	0.00	0.37	0.78	100.01
Warren 2011	Ureilite	44.67	1.11	10.57	1.78	40.37	0.00	0.02	0.07	0.15	0.15	0.00	0.44	0.67	100.00
Warren 2011	Ureilite	39.89	0.57	19.55	1.08	37.57	0.00	0.02	0.08	0.12	0.10	0.00	0.38	0.64	100.00
Warren 2011	Ureilite	45.64	1.14	9.60	1.97	40.16	0.00	0.04	0.11	0.08	0.16	0.00	0.41	0.67	99.98
Sossi 2016	Shergottite	42.40	2.87	20.10	3.16	28.20	0.00	0.03	0.47	0.39	0.40	0.00	0.45	0.00	98.47
Sossi 2016	Shergottite	47.60	3.32	20.60	5.66	21.60	0.00	0.08	0.59	0.43	0.39	0.00	0.53	0.00	100.80
Sossi 2016	Shergottite	49.90	5.91	18.40	7.26	16.10	0.00	0.04	0.86	0.70	0.60	0.00	0.48	0.00	100.25
Sossi 2016	Nakhlite	49.20	3.59	19.23	15.00	9.33	0.00	0.29	1.01	0.07	0.27	0.00	0.45	0.00	98.44
Sossi 2016	Shergottite	46.7	3.6	20.4	6.46	15.8	0.00	0.14	1.14	0.68	0.61	0.00	0.48	0.00	96.01
Sossi 2016	Shergottite	51.30	6.88	19.40	9.60	9.30	0.00	0.17	1.39	0.82	0.67	0.00	0.52	0.00	100.05
Sossi 2016	Shergottite	50.50	6.05	18.10	10.50	11.30	0.00	0.14	1.23	0.79	0.50	0.00	0.50	0.00	99.61
Sossi 2016	Shergottite	48.60	10.40	21.40	9.89	3.74	0.00	0.24	2.22	1.43	0.66	0.00	0.47	0.00	99.05
Sossi 2016	Shergottite	49.90	5.17	17.30	6.83	18.70	0.00	0.02	0.65	0.53	0.00	0.00	0.48	0.00	99.58
Sossi 2016	Shergottite	47.72	4.19	16.52	7.83	19.36	0.00	0.03	0.55	0.35	0.49	0.00	0.39	0.00	97.44
Sossi 2016	Shergottite	47.20	4.53	18.34	5.74	20.49	0.00	0.02	0.60	0.42	0.31	0.00	0.46	0.00	98.11
Sossi 2016	Nakhlite	48.60	1.68	20.60	14.70	12.10	0.00	0.13	0.46	0.34	0.13	0.00	0.49	0.00	99.23
Sossi 2016	Nakhlite	49.50	1.74	19.70	12.90	10.90	0.00	0.18	0.82	0.35	0.00	0.00	0.67	0.00	96.76
Sossi 2016	Nakhlite	47.57	1.88	19.67	14.27	10.39	0.00	0.14	0.58	0.29	0.00	0.00	0.51	0.00	95.30
Sossi 2016	Nakhlite	46.90	2.47	21.60	13.40	12.90	0.00	0.11	0.40	0.42	0.45	0.00	0.50	0.00	99.15
Sossi 2016	Chassigny	37.40	0.72	27.30	0.66	31.80	0.00	0.04	0.12	0.08	0.07	0.00	0.53	0.00	98.72
Sossi 2016	Shergottite	47.90	11.00	18.50	11.40	6.25	0.00	0.05	1.58	1.84	0.00	0.00	0.45	0.00	98.97
Sossi 2016	ALH84001	52.80	1.29	17.50	1.82	25.00	0.00	0.02	0.14	0.21	0.01	0.00	0.46	0.00	99.25
Sossi 2016	Shergottite	45.40	2.32	19.70	4.06	26.20	0.00	0.03	0.36	0.35	0.00	0.00	0.48	0.00	98.90

Appendix E

Ternary diagrams

E.1 Titanium Oxide

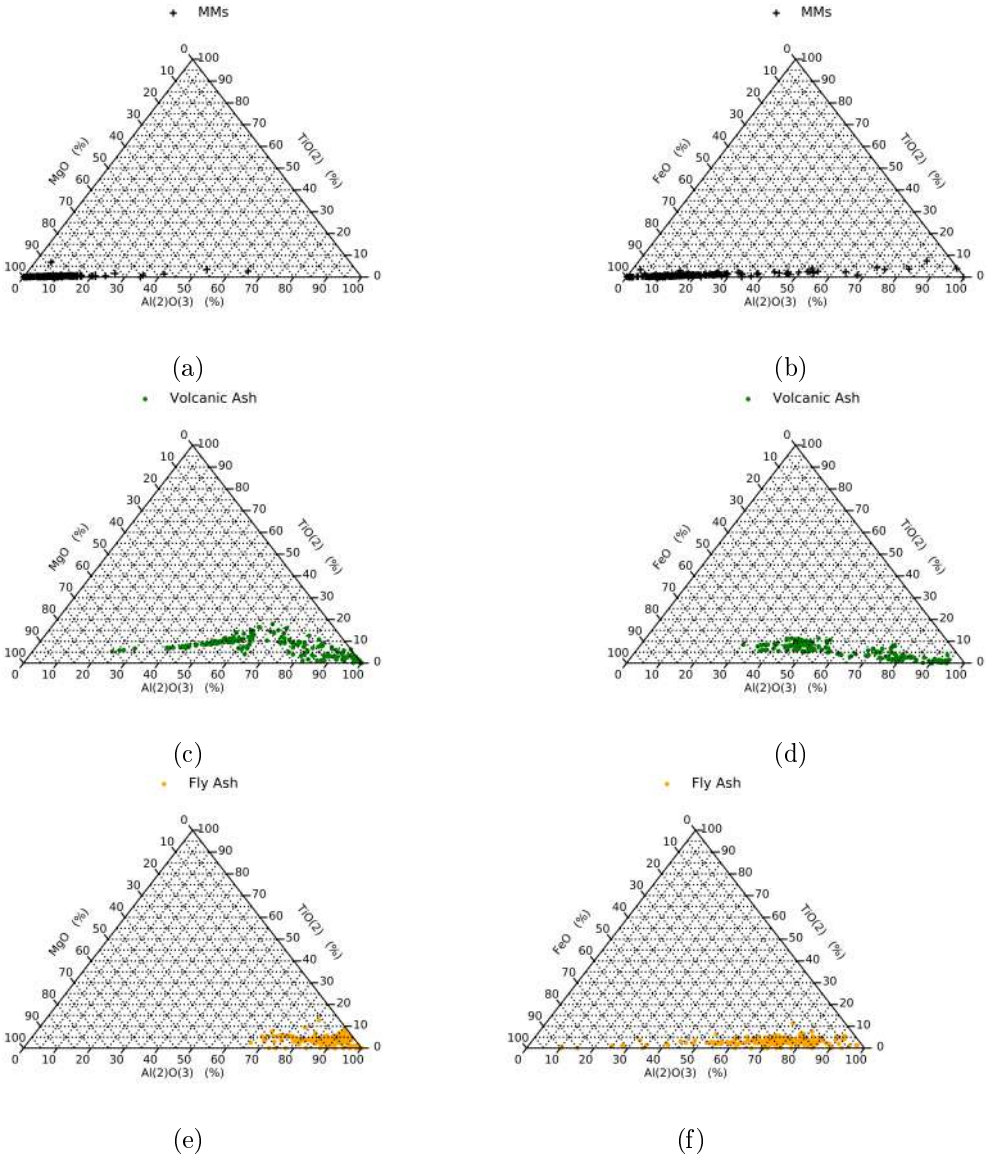


Figure E.1: Ternary diagrams showing the effects of using titanium to separate out terrestrial and E.T. material. The low relative abundance of titanium, means that it is swamped by the abundances of the more common elements.

E.2 Compositional ternary diagrams

E.2.1 Terrestrial Spheres

E.2.1.1 Fly Ash

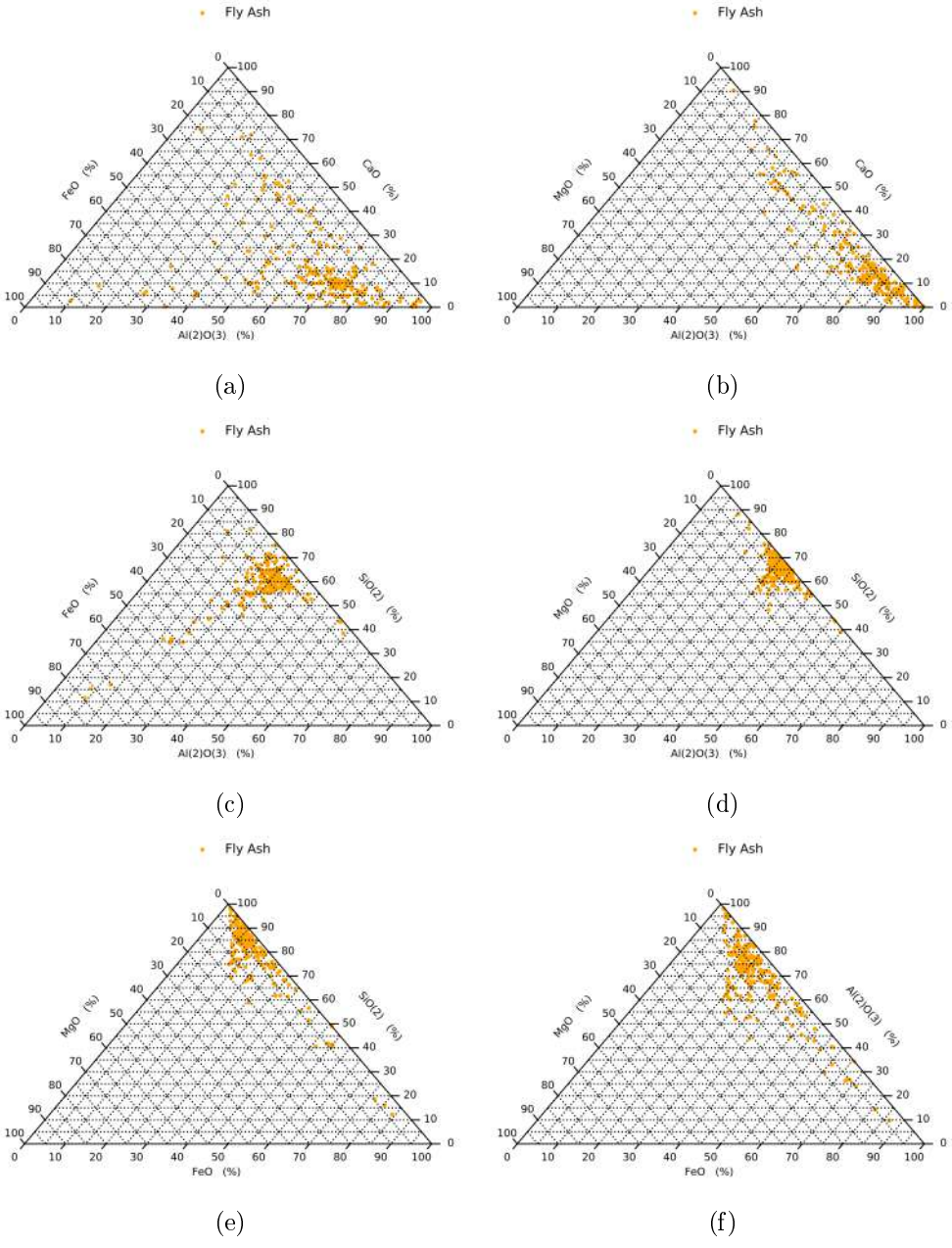


Figure E.2: Showing the ratio of oxide abundances contained in fly ash particles. References can be seen in appendix D

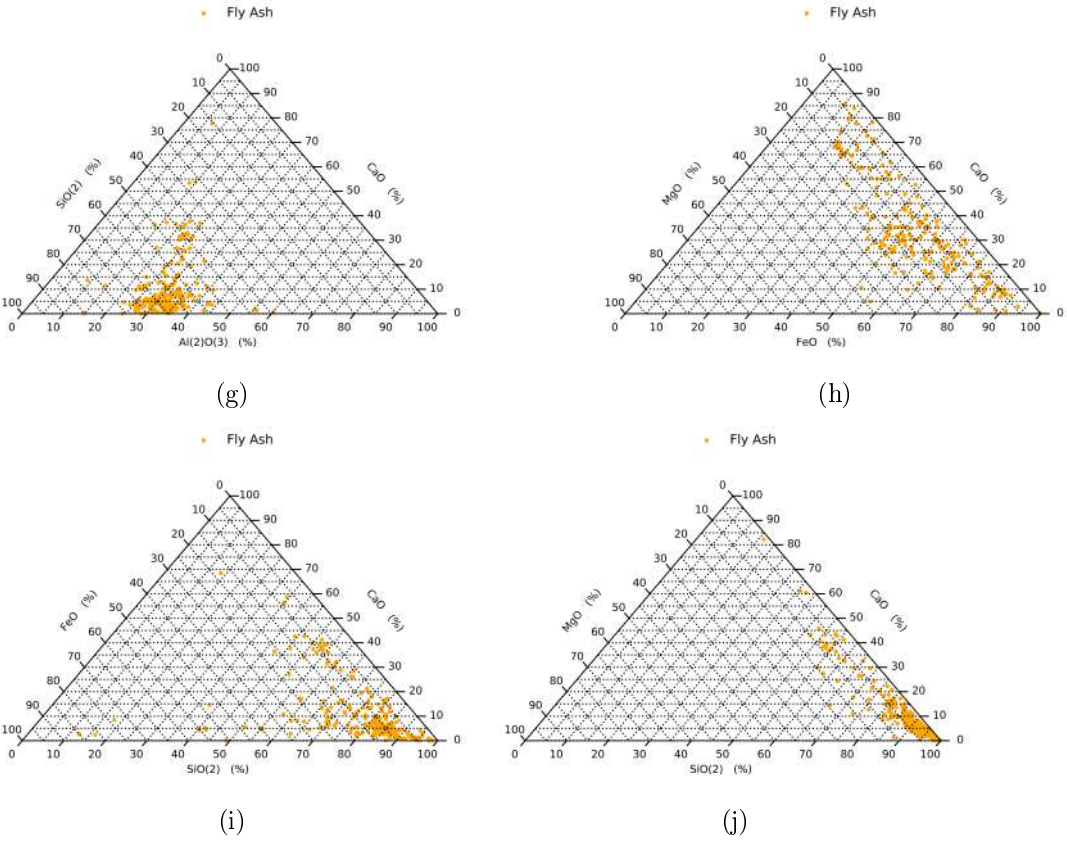


Figure E.2: Showing the ratio of oxide abundances contained in fly ash particles. References can be seen in appendix D

E.2.1.2 Volcanic Ash

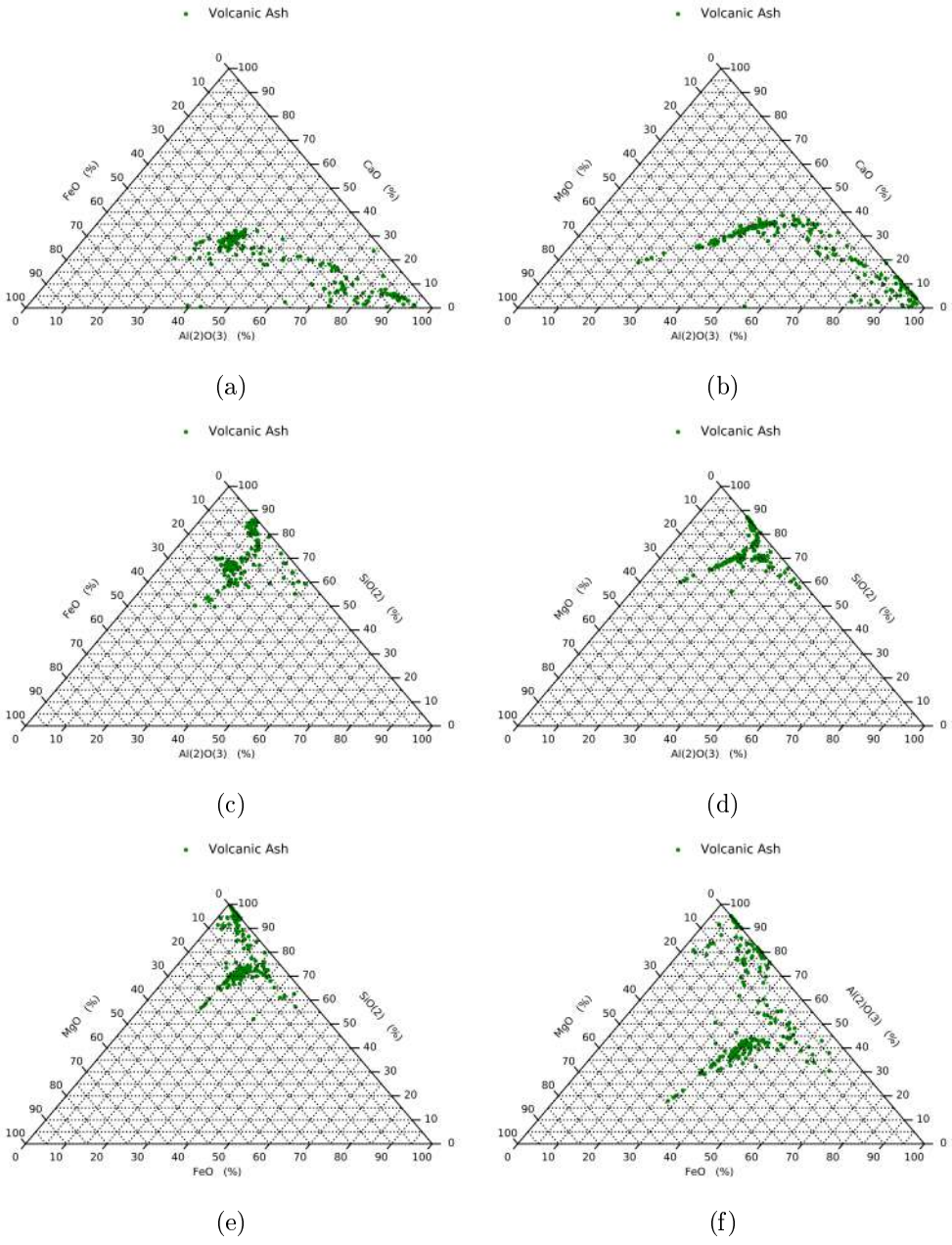


Figure E.3: Showing the ratio of oxide abundances contained in volcanic ash particles from a verity of sources. References can be seen in appendix D

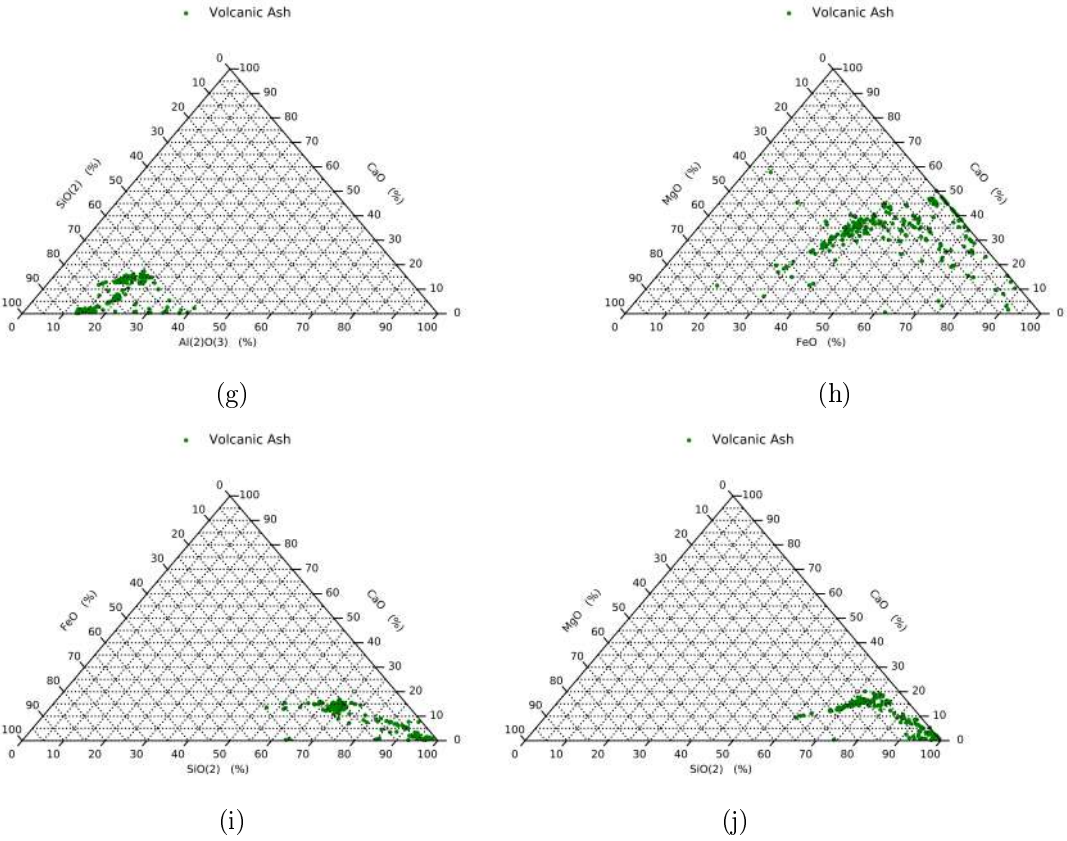


Figure E.3: Showing the ratio of oxide abundances contained in volcanic ash particles. References can be seen in appendix D

E.2.2 Chondrites

E.2.2.1 Bulk

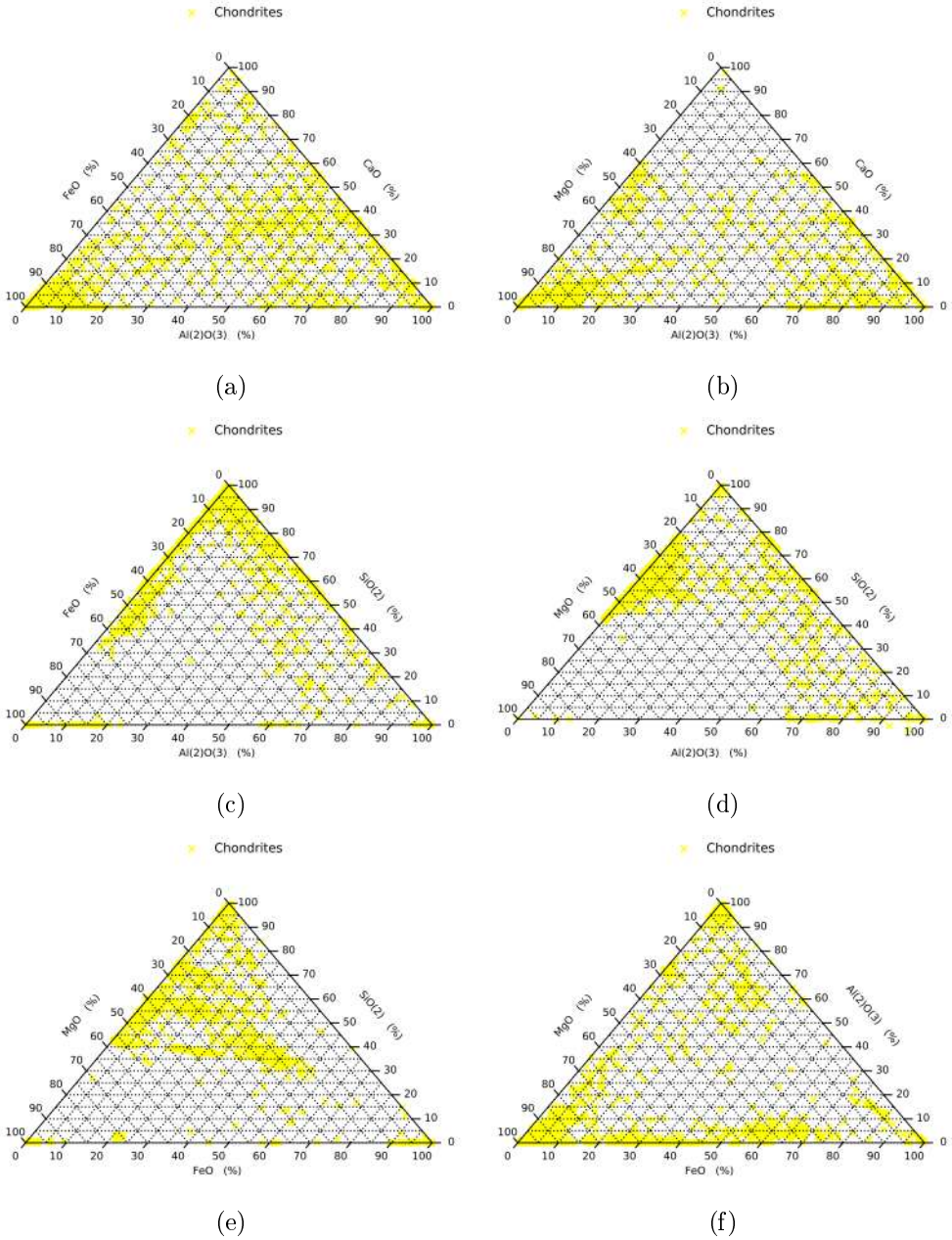
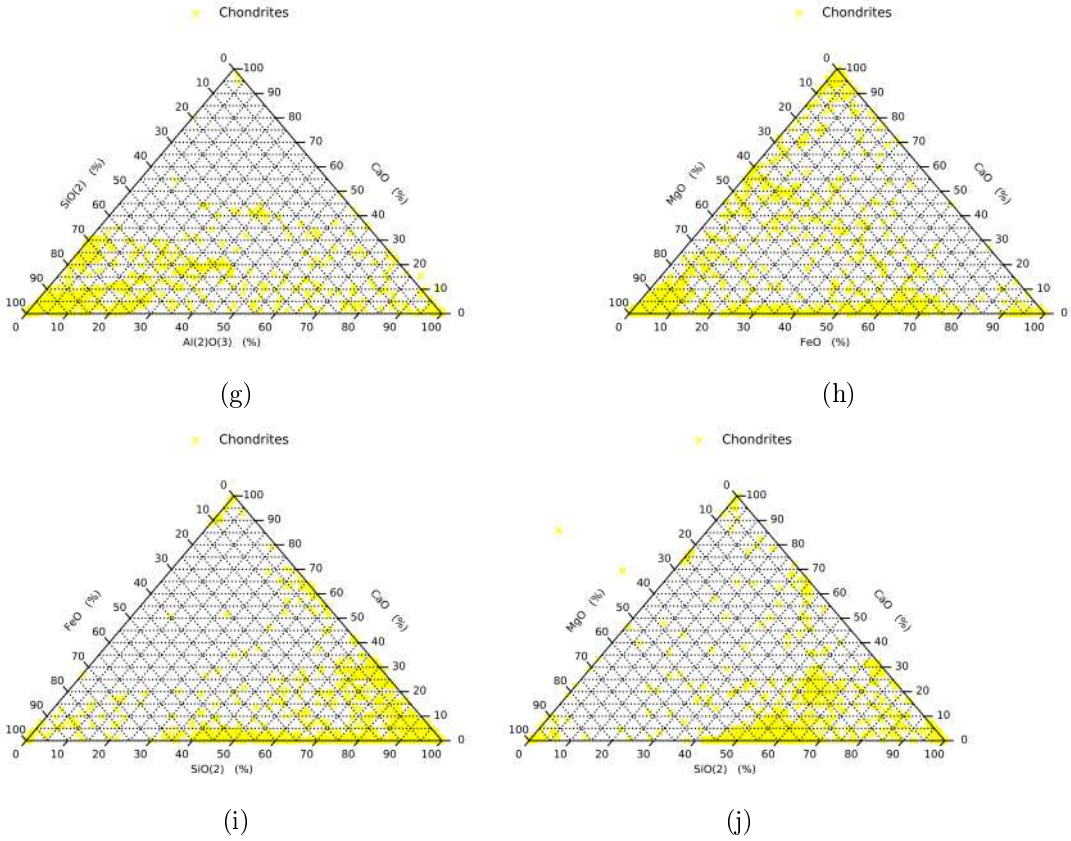


Figure E.4: Showing the ratio of oxide abundances contained in previously examined chondrites from a verity of sources. References can be seen in appendix D



(g) (h)

(i) (j)

Figure E.4: Showing the ratio of oxide abundances contained in previously examined chondrites. References can be seen in appendix D

E.2.2.2 Chondritic areas

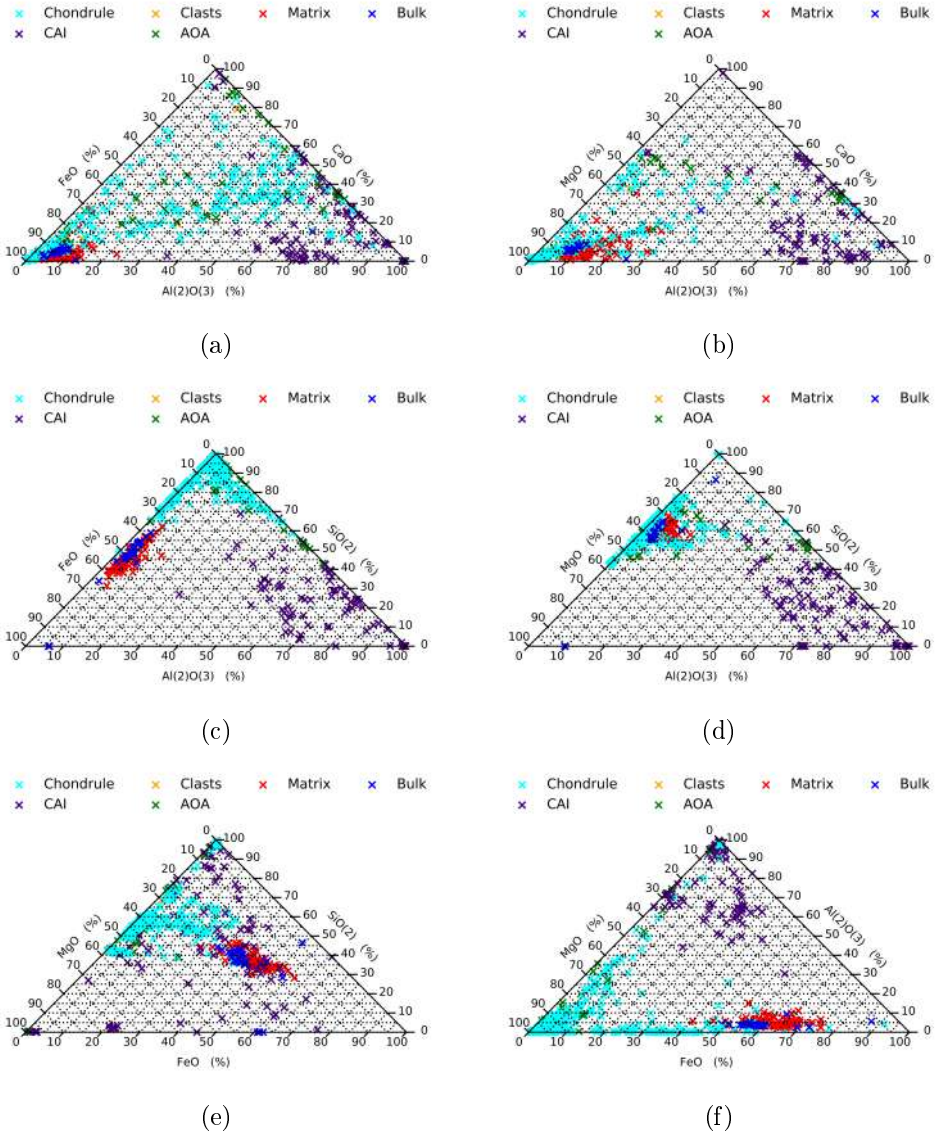


Figure E.5: Showing the ratio of oxide abundances contained in previously examined chondritic areas from a verity of sources. References can be seen in appendix D

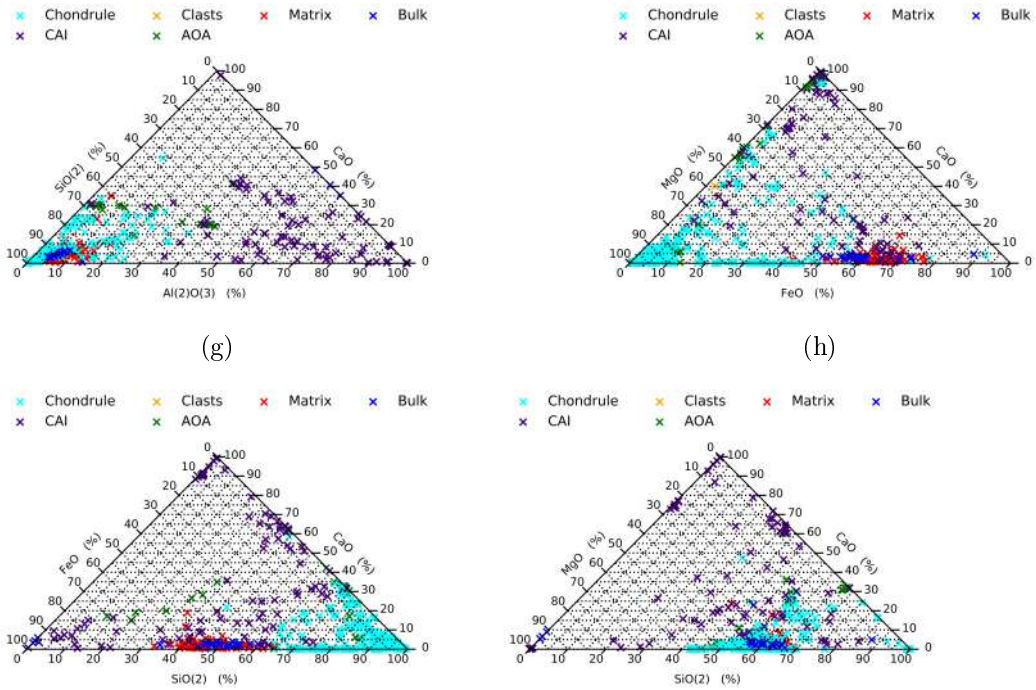


Figure E.5: Showing the ratio of oxide abundances contained in previously examined chondritic components from a verity of sources. References can be seen in appendix D

E.2.3 Achondrites

E.2.3.1 Bulk

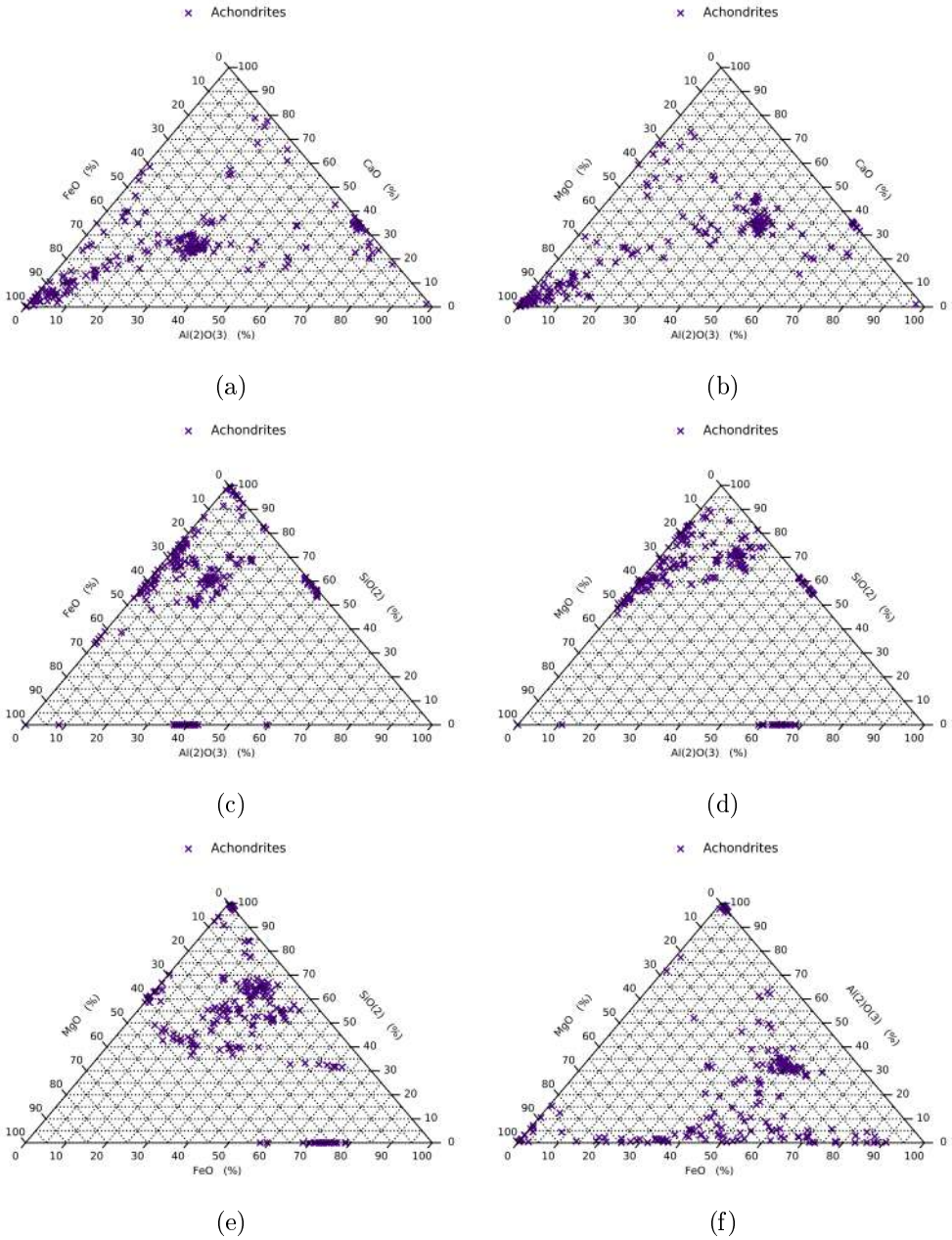


Figure E.6: Showing the ratio of oxide abundances contained in previously examined chondritic areas from a verity of sources. References can be seen in appendix D

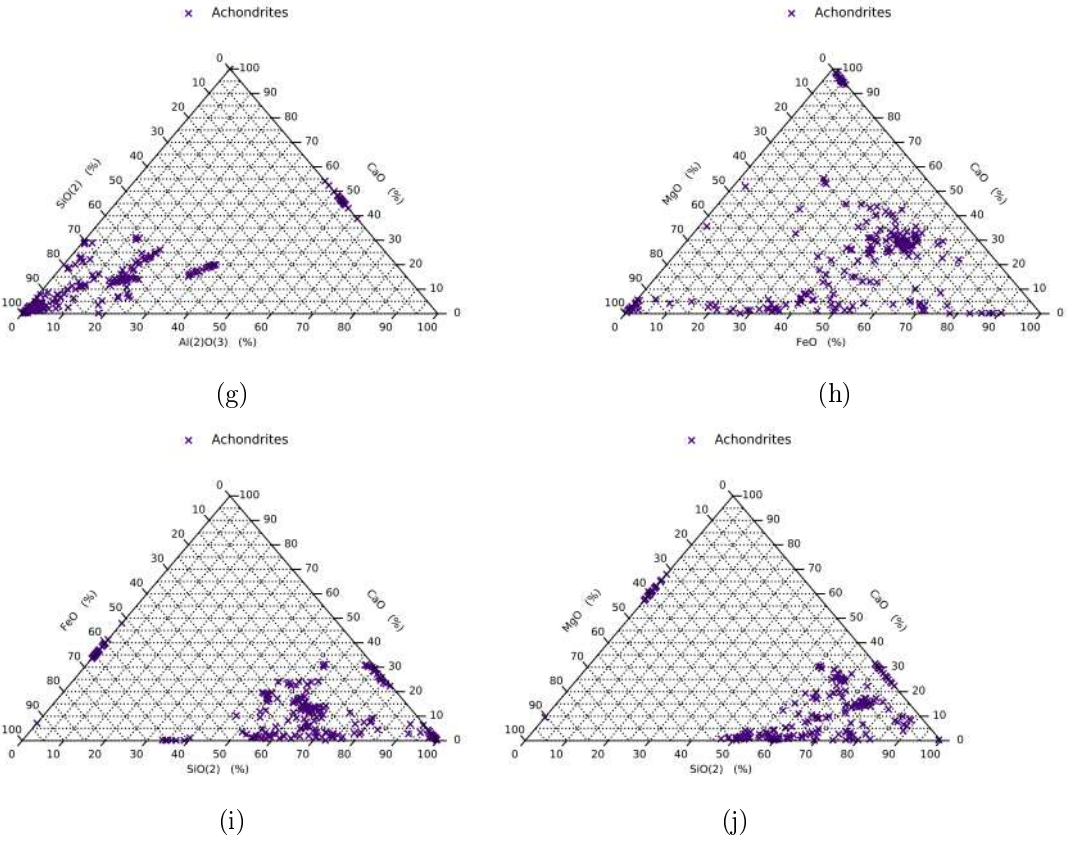
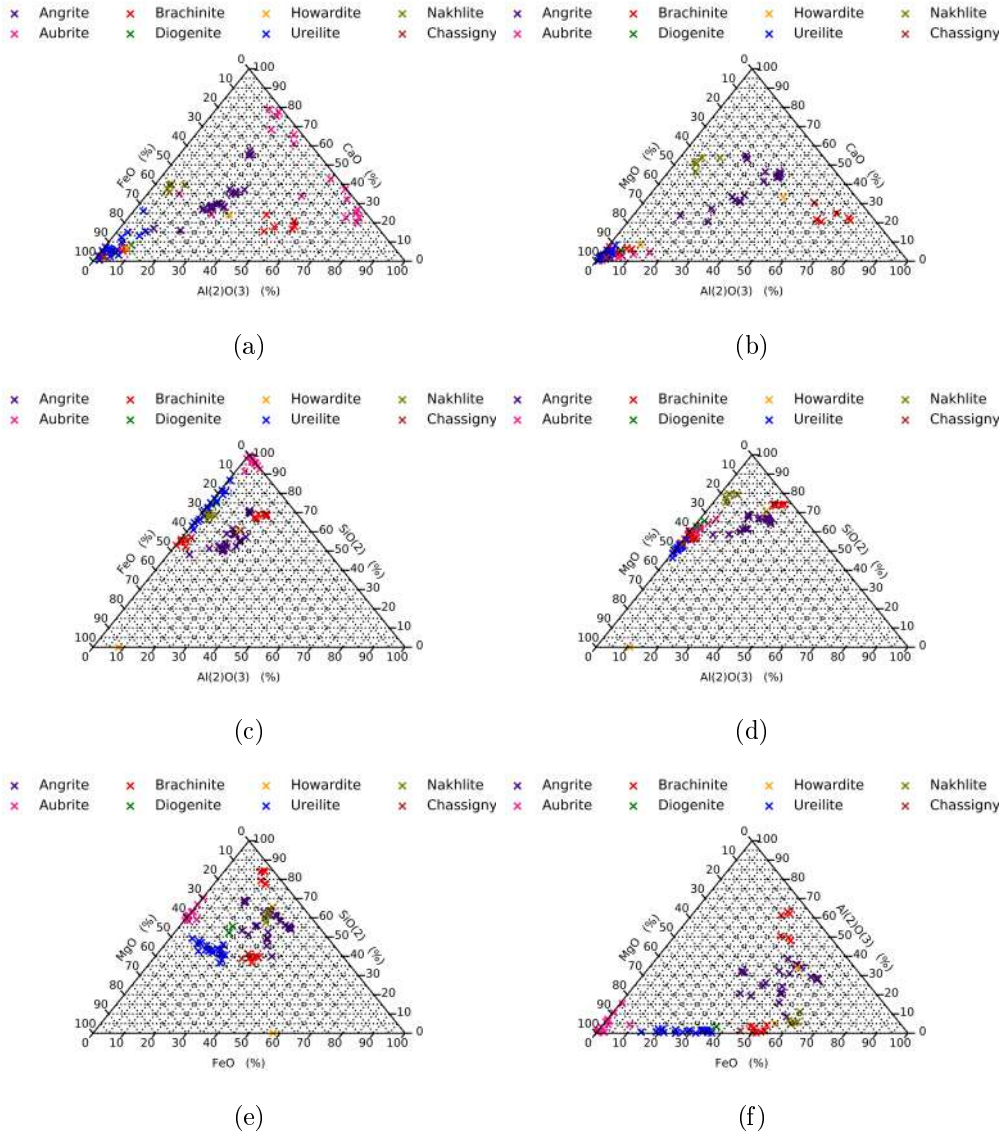


Figure E.6: Showing the ratio of oxide abundances contained in previously examined chondritic components from a verity of sources. References can be seen in appendix D

E.2.3.2 Achondrite subtypes



(a) (b) (c) (d) (e) (f)

Figure E.7: Showing the ratio of oxide abundances contained in previously examined chondritic areas from a verity of sources. References can be seen in appendix D

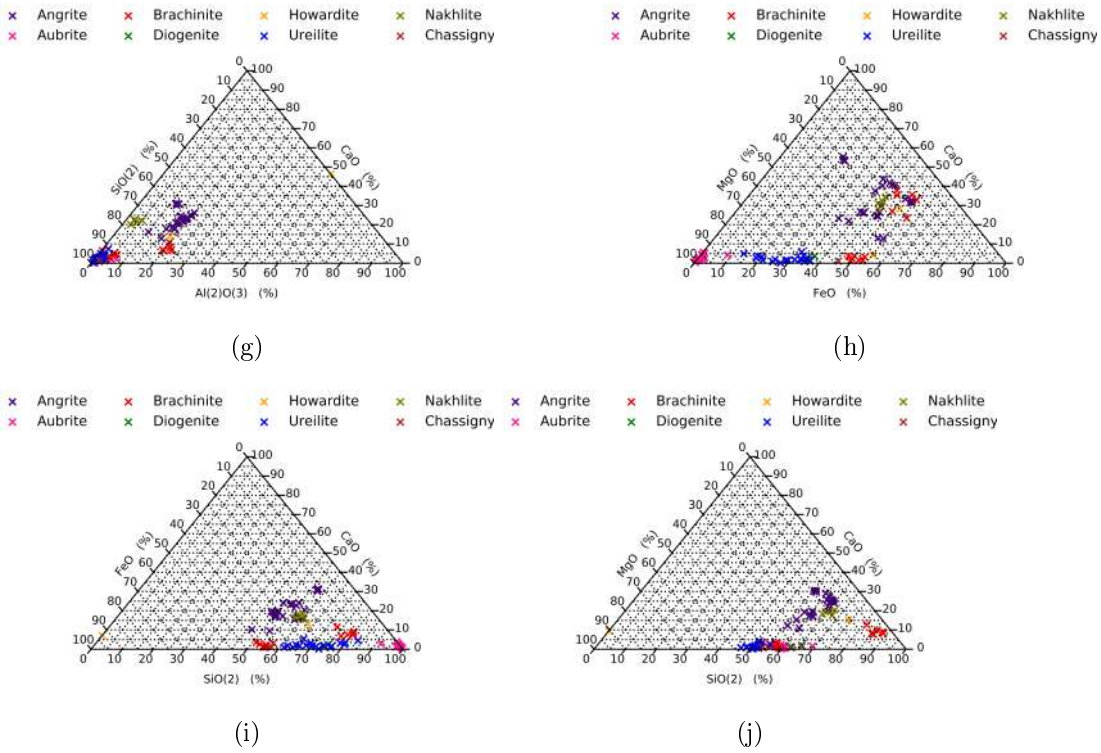


Figure E.7: Showing the ratio of oxide abundances contained in previously examined chondritic components from a verity of sources. References can be seen in appendix D

E.3 Volcanic ash composition versus Micrometeorite composition

E.3.1 Volcanic Ash

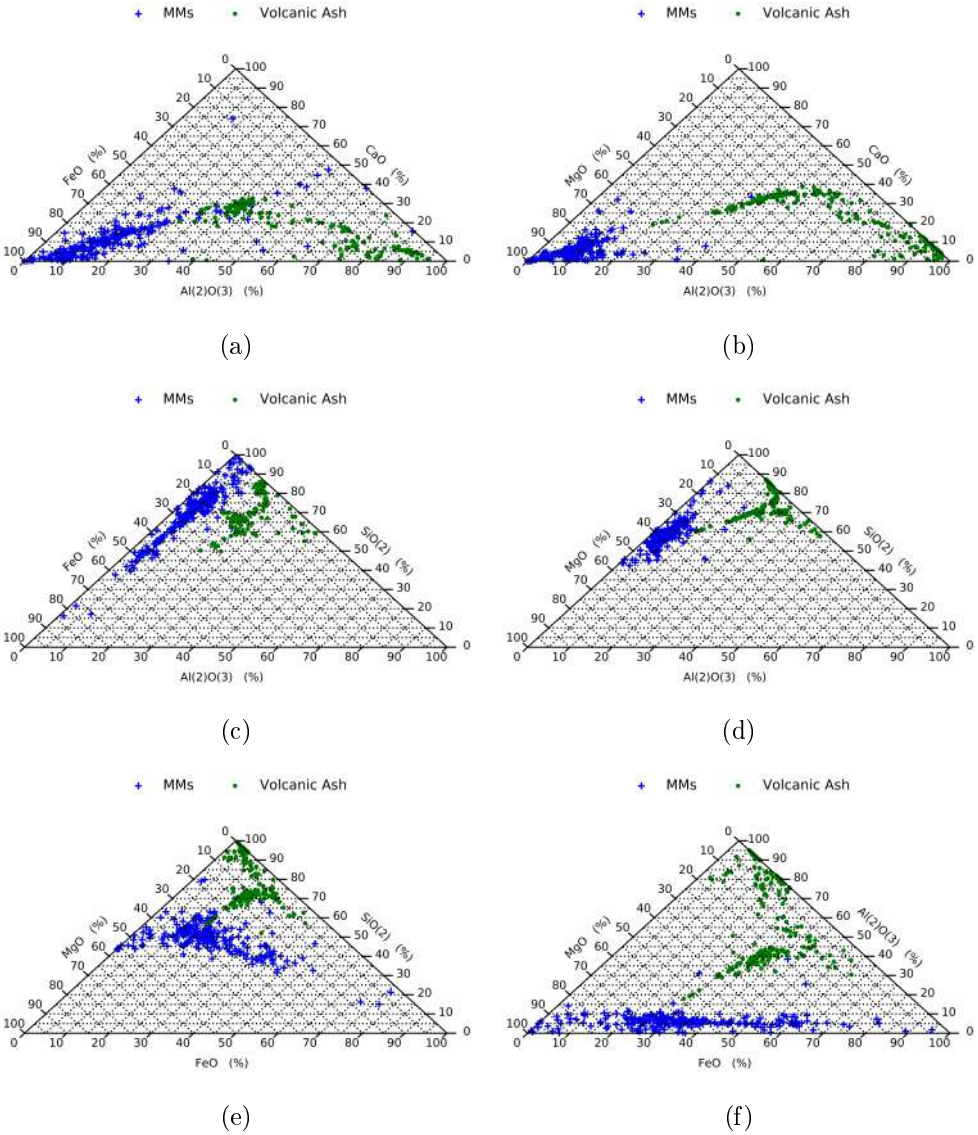


Figure E.8: Showing the ratio of oxide abundances contained in volcanic ash particles compared to that contained in micrometeorites. References can be seen in appendix D

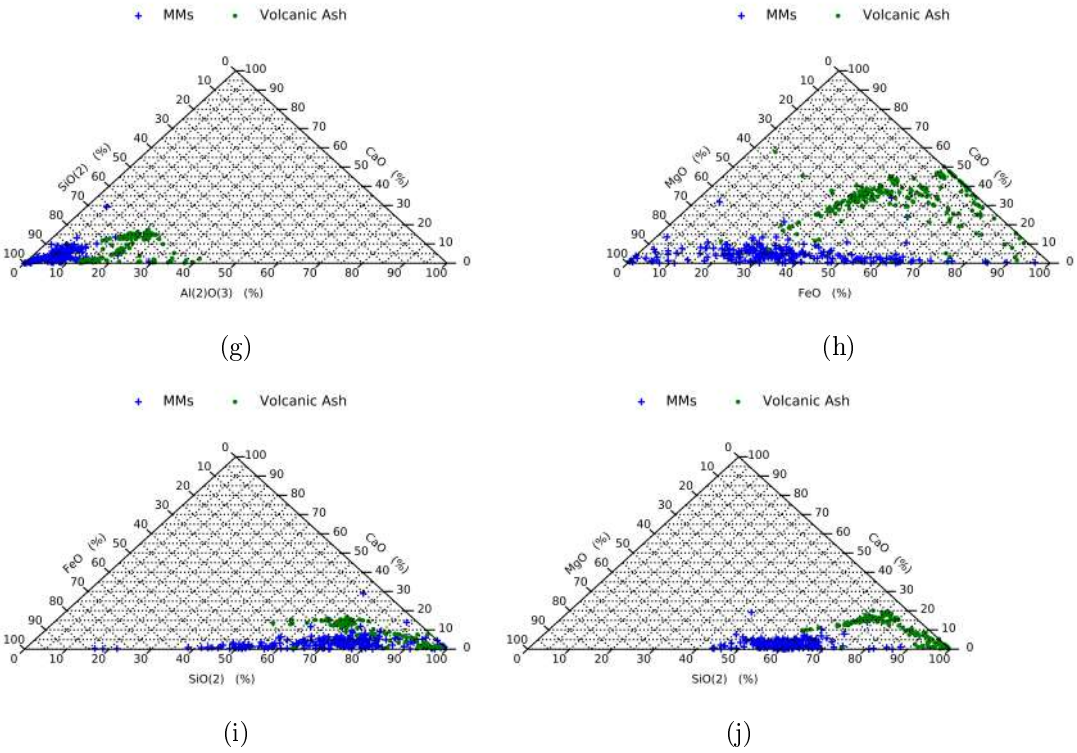


Figure E.8: Showing the ratio of oxide abundances contained in volcanic ash particles compared to that contained in micrometeorites. References can be seen in appendix D

E.4 Terrestrial Debris versus CAIs

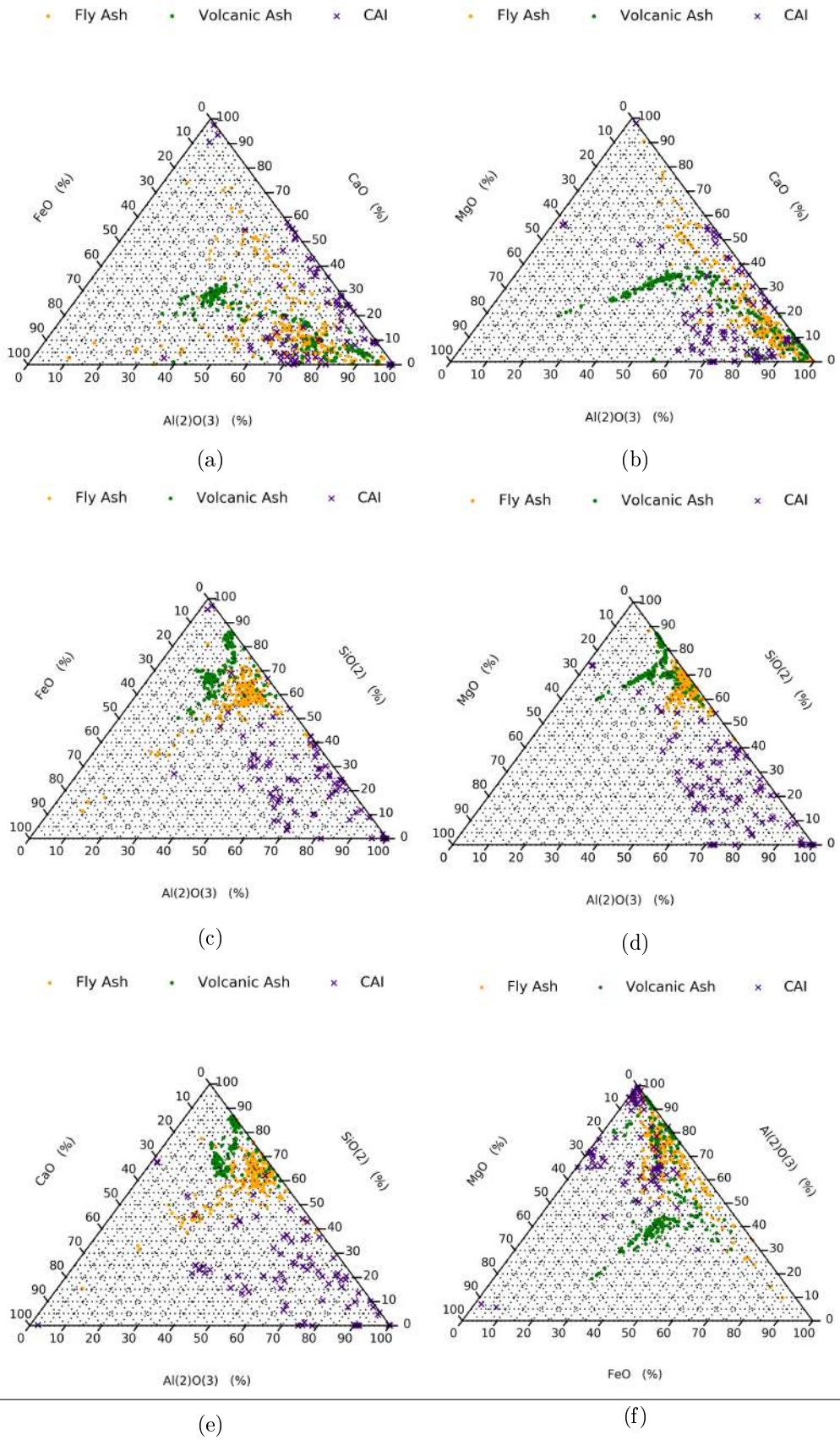
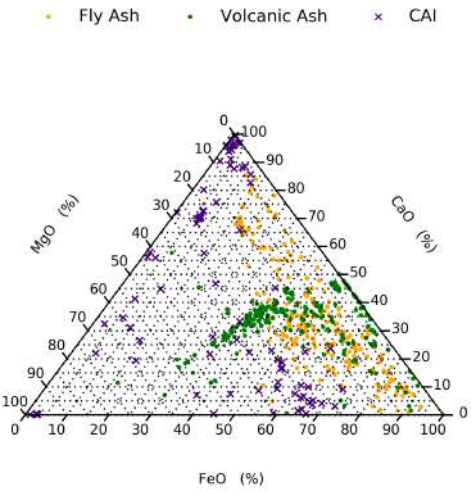
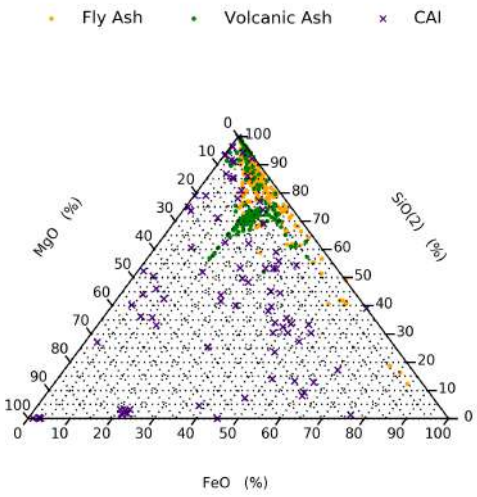


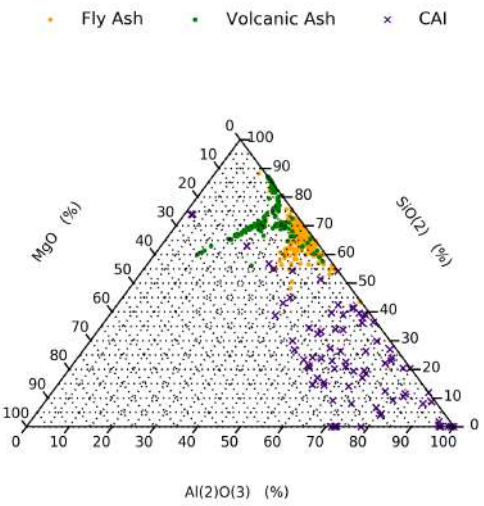
Figure E.9: A number of different element ratios used in an attempt to separate out the extra-terrestrial CAIs whose Ca-Al-Mg ratios are similar to terrestrial materials. Abundances are shown in wt%



(g)



(h)



(i)

Figure E.9: A number of different element ratios used in an attempt to separate out the extra-terrestrial CAIs whose Ca-Al-Mg ratios are similar to terrestrial materials. Abundances are shown in wt%

E.5 Chondrite Minerals versus Terrestrial Debris and MMs

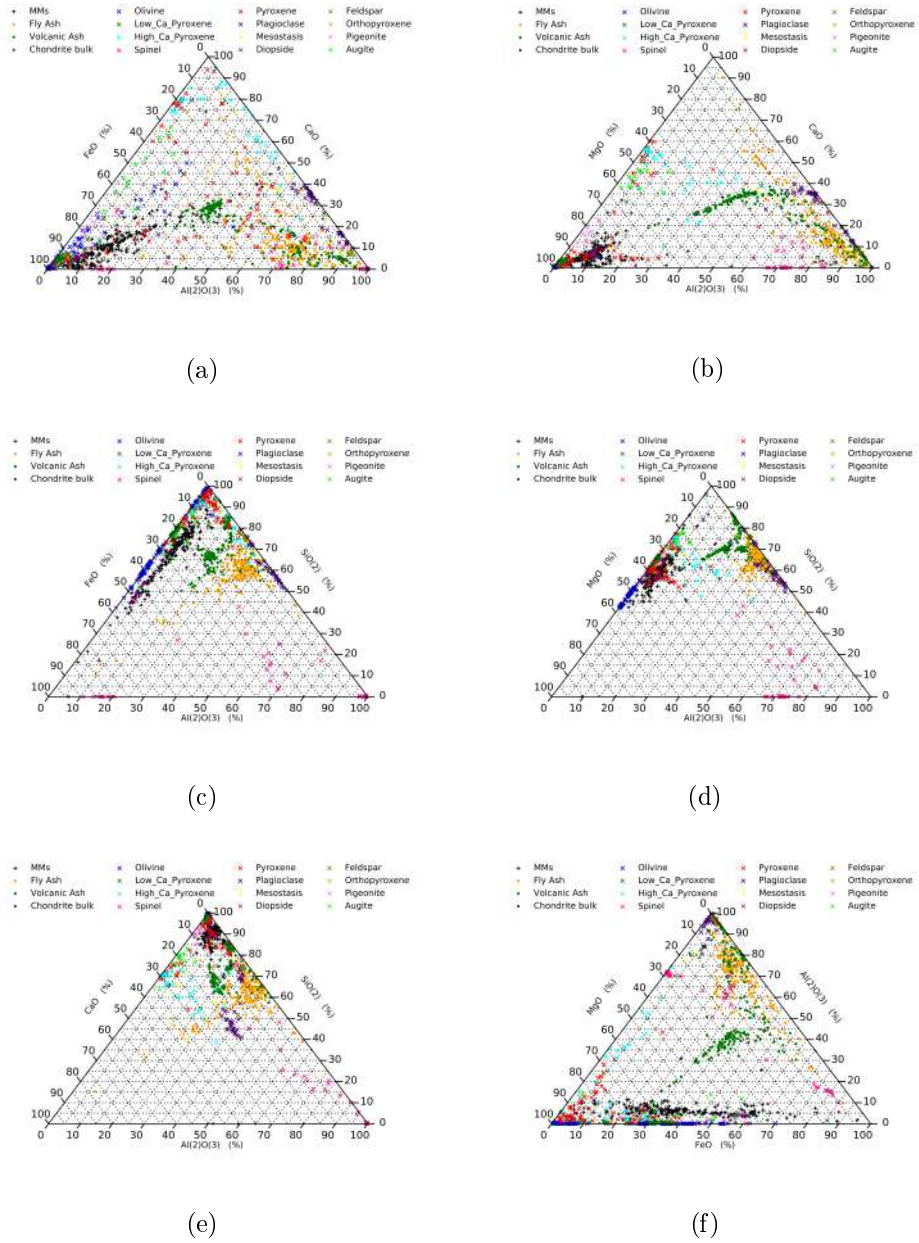
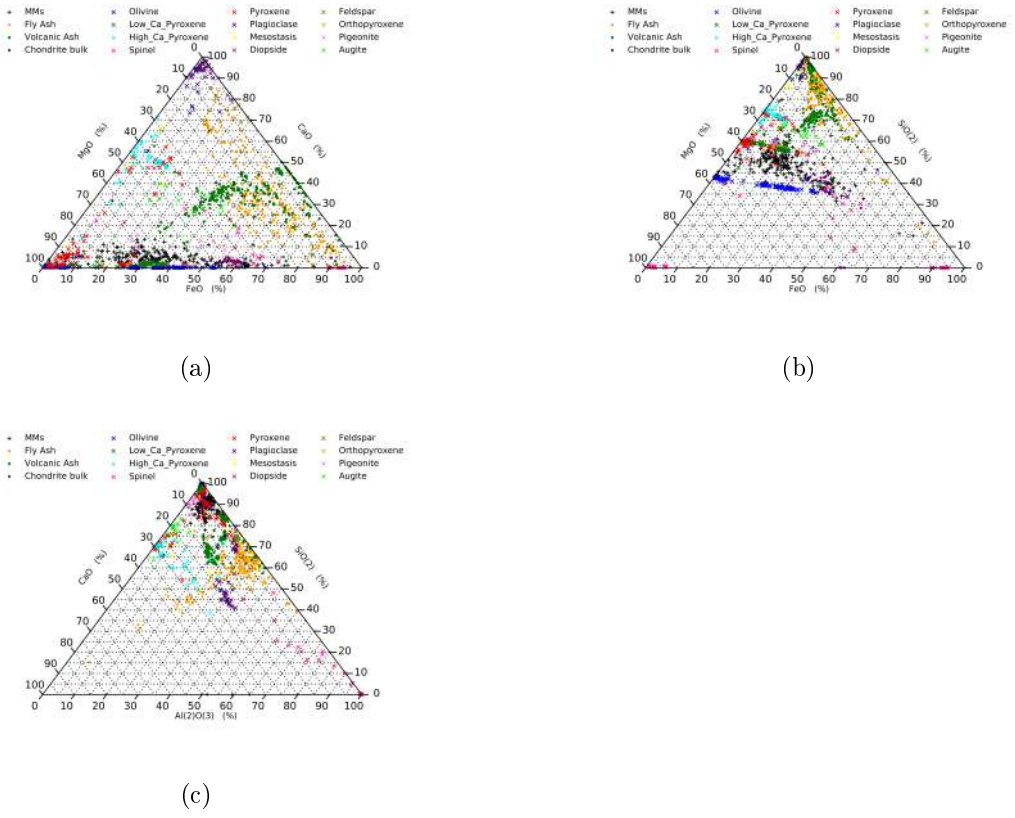


Figure E.10: Bulk compositions of different particle types commonly found during micrometeorite collections and the single point analysis chemistry of minerals commonly found in chondrites. Abundances are shown in wt%



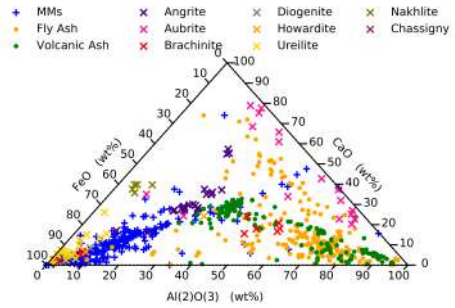
(a)

(b)

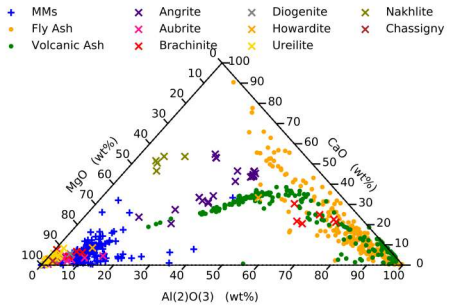
(c)

Figure E.11: Bulk compositions of different particle types commonly found during micrometeorite collections and the single point analysis chemistry of minerals commonly found in chondrites. Abundances are shown in wt%

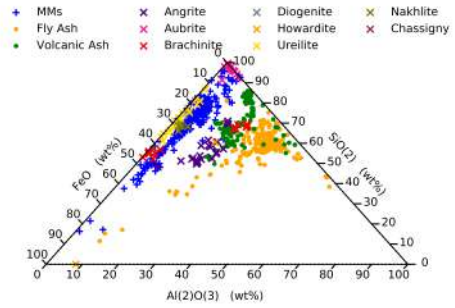
E.6 Achondrite Plots



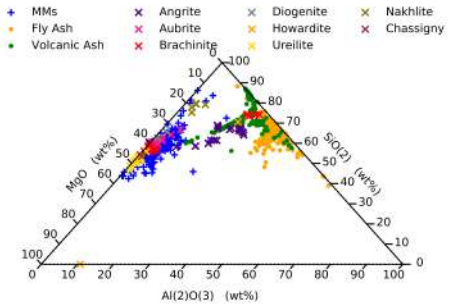
(a)



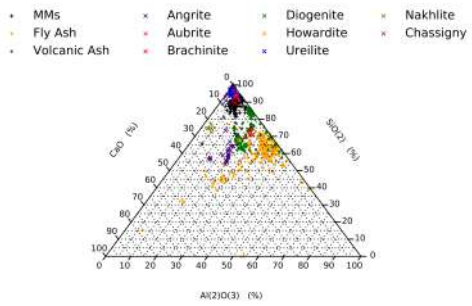
(b)



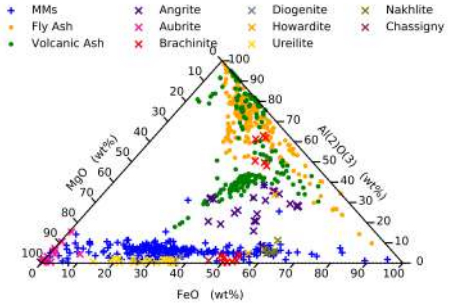
(c)



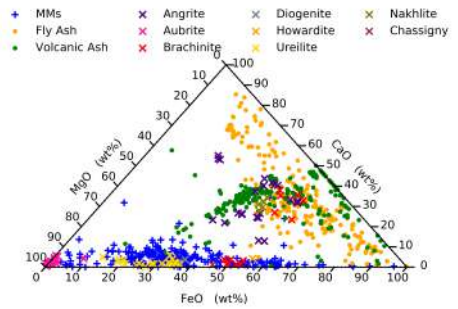
(d)



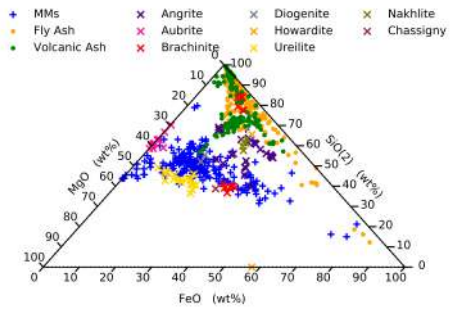
(e)



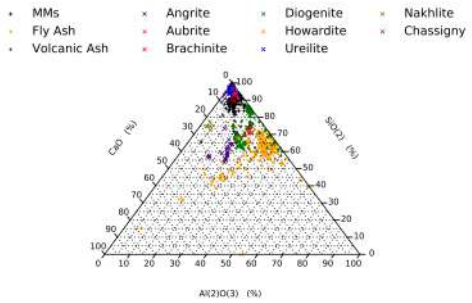
(f)



(g)



(h)



(i)

Figure E.12: Bulk compositions of different particle types commonly found during micrometeorite collections and the and the bulk analysis of the achondrite subtypes. Abundances are shown in wt%

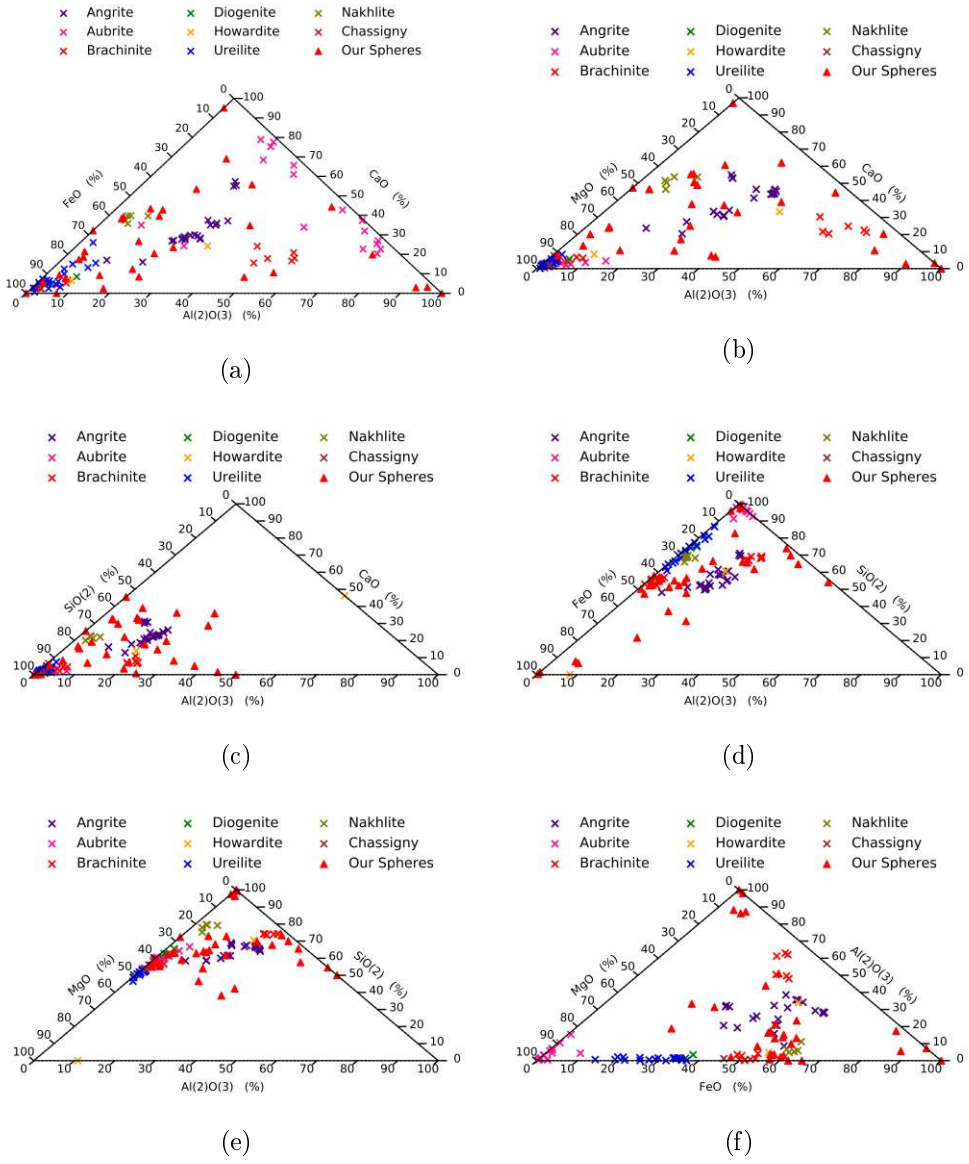
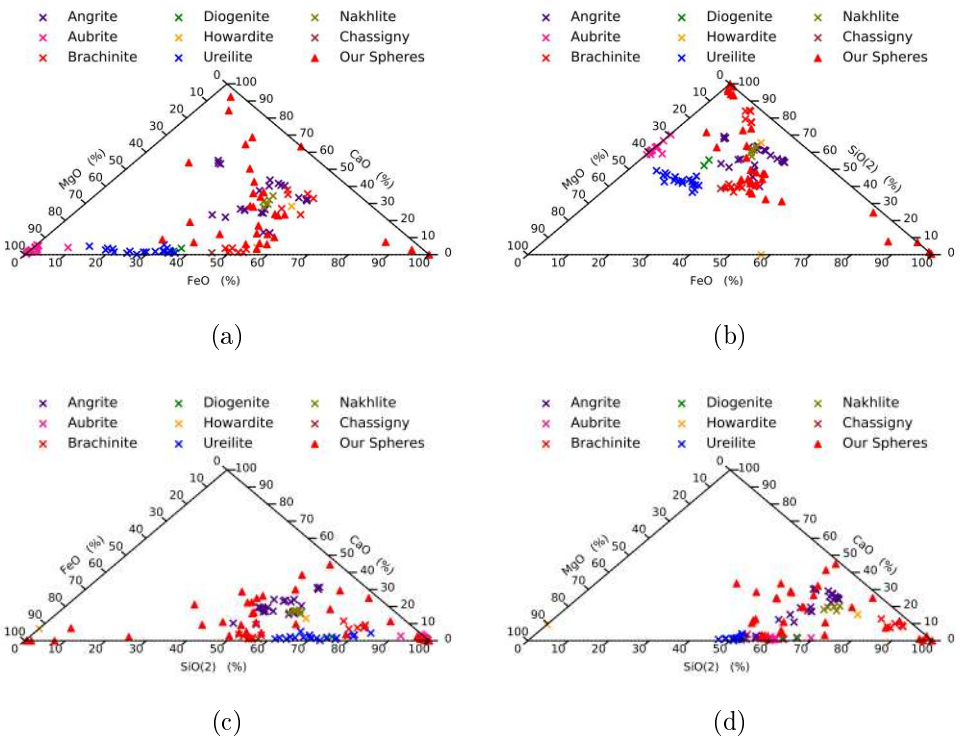


Figure E.13: Comparisons of elemental ratios of the candidate MMs versus the ratios found achondritic subtypes

E.7 Candidate MMs versus Achondrites



(a) (b)

(c) (d)

Figure E.14: Comparisons of elemental ratios of the candidate MMs versus the ratios found achondritic subtypes

Appendix F

Picked Particle details

F.1 Analysed Spheres

F.2 SEM Conditions for Picked Particle Analysis

Table F.1: List of cut and polished Extra-terrestrial candidates from filters K08, K09, K11 and K12. SEM details for analysis are given in F

Sphere	Analysed	Notes
8-2-38	?	
8-2-36	?	
8-4-2	Yes	
9-9-7	Yes	
9-7-32	?	
11-2-16	No	Lost During Picking
11-3-20	No	Lost During Picking
11-5-29	Yes	
11-7-12	?	
11-8-46	Yes	
11-9-40	Yes	
12-1-56	Yes	
12-2-10	Yes	
12-7-25	Yes	
12-8-24	Yes	

Table F.2: SEM Conditions for the quantitative analysis of the picked particles from the Kwajalein MMs collection. All work was carried out a constant voltage of 20 KV

Particle No.	Date	Time	W.D. (mm)	Current (µA)
9-9-7	07/09/18	01:55	9.8	92
8-4-2	07/09/18	02:15	10.1	92
11-9-40	07/09/18	02:35	10.0	89
12-1-56	07/09/18	03:05	10.0	88
12-8-24	07/09/18	03:26	10.1	?
11-5-29	07/09/18	03:40	9.8	88
11-8-16	26/09/18	13:00	10.1	92
12-2-10	26/09/18	13:38	10.1	87
12-7-25	26/09/18	13:55	10.0	86

Appendix G

Diagrams

G.1 Collector Casing Schematic

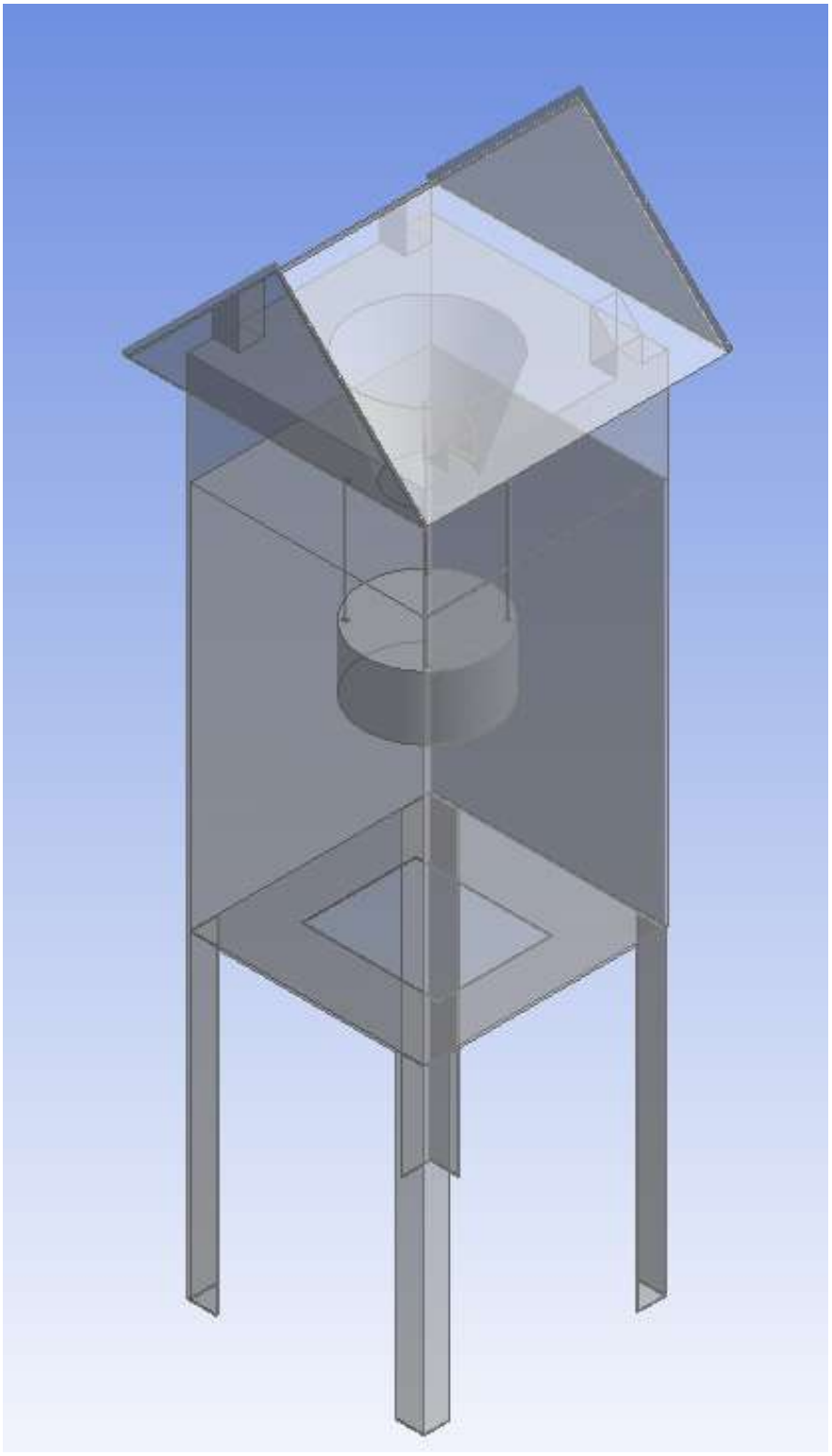


Figure G.1: simplified schematic of the casing used on the Kwajelein MM collector

G.2 Environment Tube diagrams

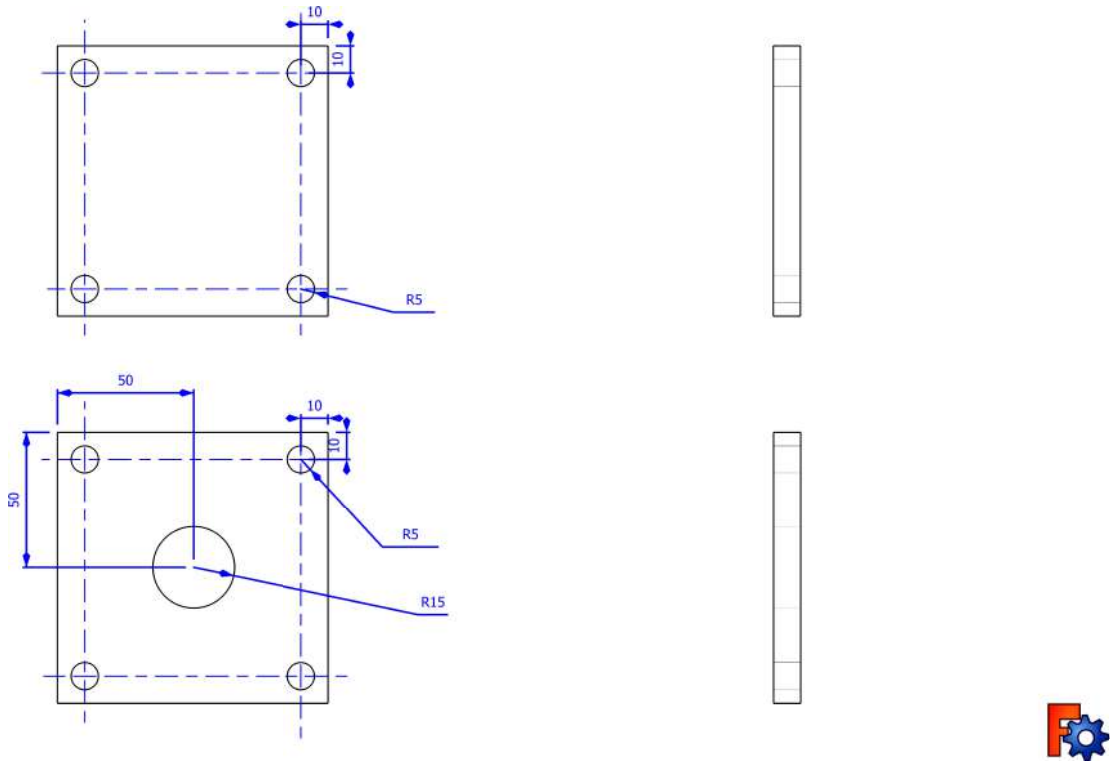


Figure G.2

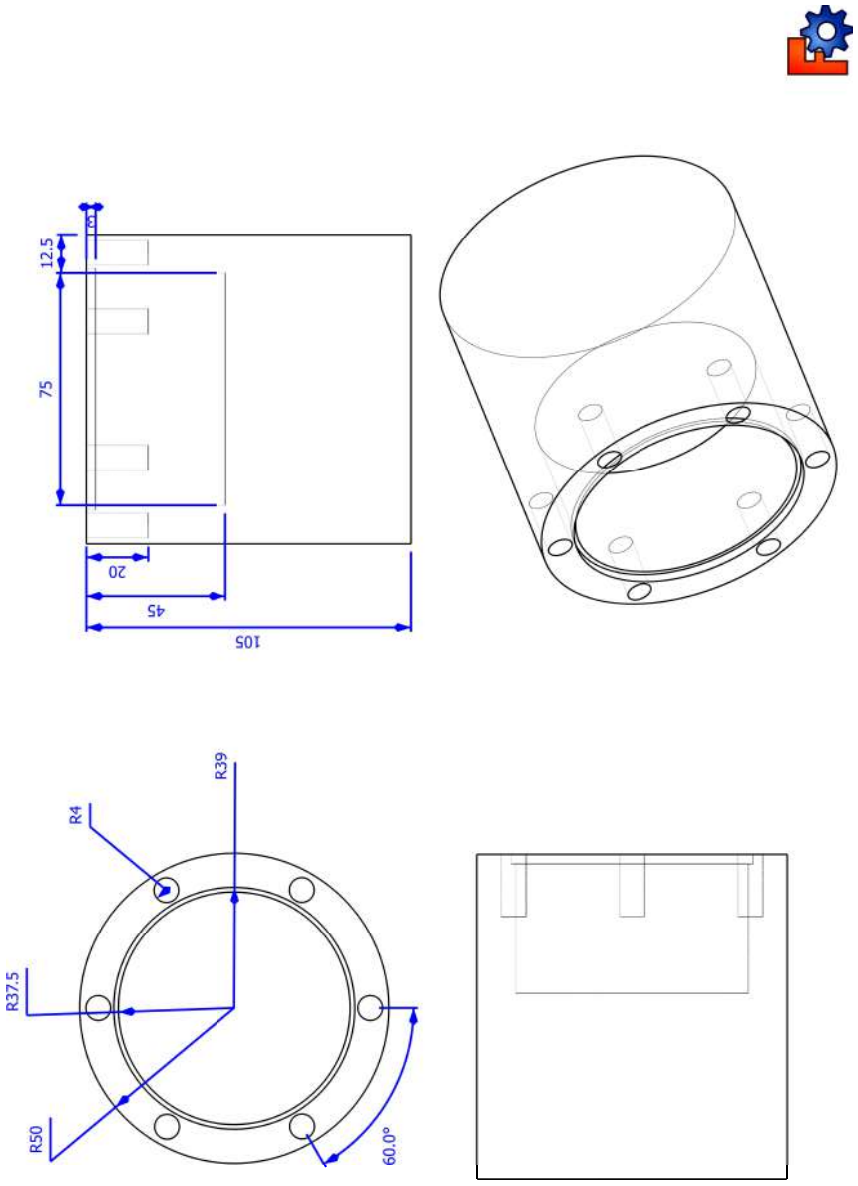


Figure G.3

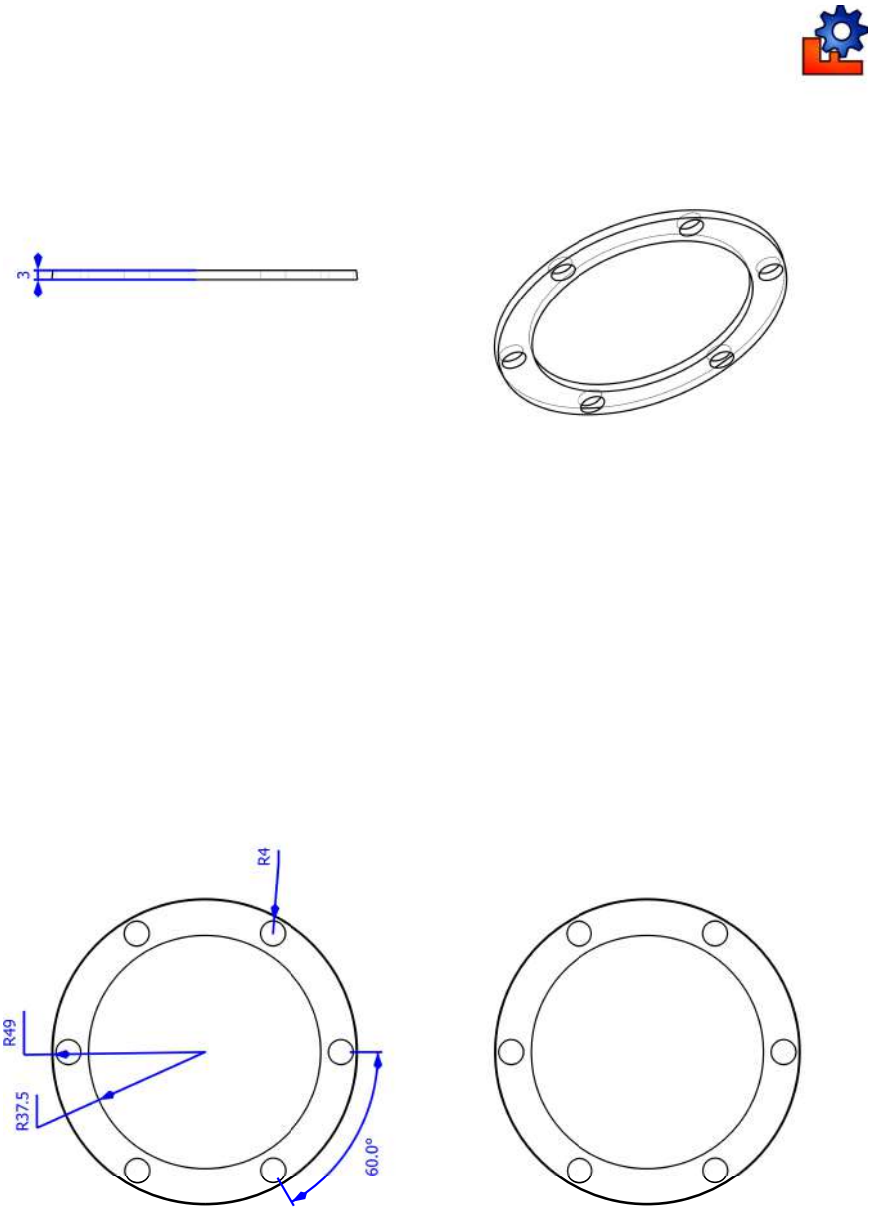


Figure G.4

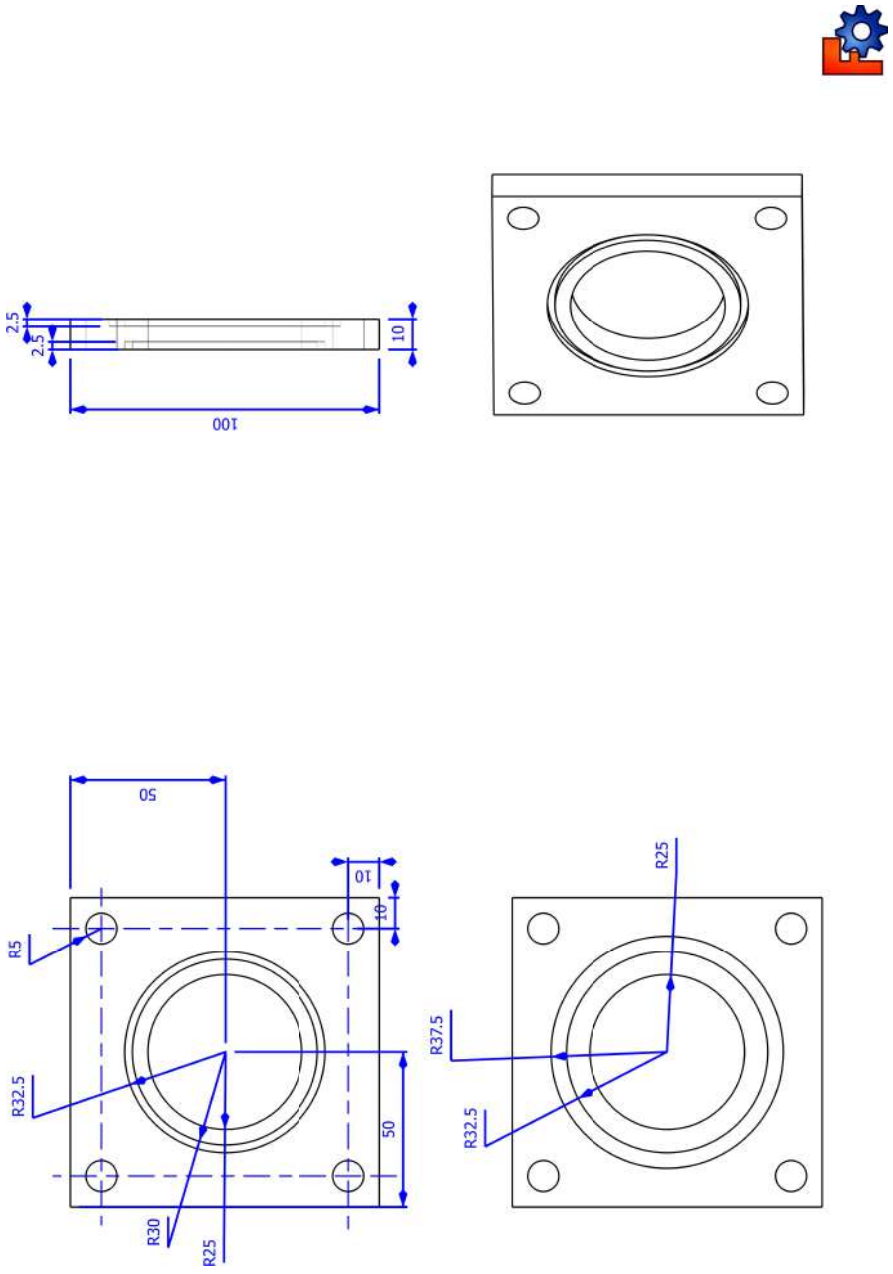


Figure G.5

Figure G.6: Engineering drawing of the edited breech block design used to attach the pressure gauge to the environment tube in shot program 2

Appendix H

Derivations

H.1 Impact Velocity

$$(1a)\ \frac{dV}{dt} = -\frac{C_d \rho A V^2}{2m} \qquad\qquad (2a)\ V \cdot dt = dL$$

Subbing (2) into (1) gives:

$$\frac{dV}{dL} = -\frac{C_d \rho A V^2}{2m} \cdot \frac{1}{V} => dV = -\frac{C_d \rho A V}{2m} \cdot dL$$

$$\int \frac{1}{V} dV = \int -\frac{C_d \rho A}{2m} dL$$

$$\ln(V) - \ln(V_0) = -\frac{C_d \rho A L}{2m}$$

$$\ln(\frac{V}{V_0}) = \frac{C_d \rho A L}{2m}$$

$$(3a)\ V = V_0 \cdot e^{-\cdot \frac{C_d \rho A L}{2m}}$$

H.2 Atmospheric Heating

$$(1b)\ Q_{in} = Q_{out} + Q_{\Delta T} \qquad (2b)\ Q_{in} = \frac{1}{2}MV^2$$

$$(3b)\ Q_{out} = \sigma\epsilon ST^4 \qquad (4b)\ Q_{\Delta T} = mC(T - T_0)$$

$$(5b)\ M = \rho_{air} AdL$$

Substitute in eq's (2b), (3b), (4b) and (5b) into eq (1b) gives eq (6b)

$$\begin{aligned}
\frac{1}{2}MV^2 &= \sigma\epsilon ST^4 + mC(T - T_0) \\
(T - T_0) &= \frac{MV^2}{2mC} - \frac{\sigma\epsilon ST^4}{mC} \\
(T - T_0) &= \frac{(rho_{air}A)V^2}{2mC} \cdot dL - \frac{\sigma\epsilon ST^4}{mC} \\
\frac{dT}{dt} &= \frac{(rho_{air}A)V^2}{2mC} \cdot dL - \frac{\sigma\epsilon ST^4}{mC} \\
V \cdot \frac{dT}{dL} &= \frac{(rho_{air}A)V^2}{2mC} \cdot dL - \frac{\sigma\epsilon ST^4}{mC} \\
\frac{dT}{dL} &= \frac{(rho_{air}A)V}{2mC} \cdot dL - \frac{\sigma\epsilon ST^4}{VmC}
\end{aligned}$$

Subsitute the equation of velocity from (3a)

$$\frac{dT}{dL} = \frac{(rho_{air}A)V_0 \cdot e^{-\cdot\frac{C_d\rho AL}{2m}}}{2mC} \cdot dL - \frac{\sigma\epsilon ST^4}{V_0 \cdot e^{-\cdot\frac{C_d\rho AL}{2m}} mC}$$

$$(6b) \qquad \frac{dT}{dL} = \frac{(rho_{air}A)V_0 \cdot e^{-\cdot\frac{C_d\rho AL}{2m}}}{2mC} \cdot dL - \frac{\sigma\epsilon ST^4 \cdot e^{-\cdot\frac{C_d\rho AL}{2m}}}{V_0 mC}$$

H.3 Derivation of Equation 7.18

A force is exerted on the shocked end of the projectile equal to:

$$F = (P - P_0) \cdot A$$

Where P_0 is the inital pressure of the shock end and hence the pressure of the unshocked end of the projectile. As F act upwards towards the central axis of the impacter perpendicular to the target plane, the momentum at time t:

$$p = \rho A L_{shocked} \cdot u_p$$

and the momentum at time t':

$$p' = \rho L'_{shocked} \cdot u_p$$

as the total momentum change is equal to the force applied to the projectile from the target over time (t - t'):

$$F(t - t') = \rho A L_{shocked} \cdot u_p - \rho L'_{shocked} \cdot u_p$$

$$(P - p_0)A \cdot (t - t') = \rho A L_{shocked} \cdot u_p - \rho L'_{shocked} \cdot u_p \tag{1c}$$

As the length of the unshocked region at time t' is equal to the original length minus the region which has encountered the shock-wave:

$$L'_{unshocked} = L_{unshocked} - U(t' - t) \tag{2c}$$

where U is the spped of the shock-wave. As such the the length of the shocked region is equal to the length of shocked region at time t, the length of the region covered by the shock-wave minus the uncompression of the shocked region:

$$(3c) \qquad L'_{shocked} = L_{shocked} + U(t' - t) - u_p(t' - t)$$

subsituting in (2c) into (1c) give:

$$(P - P_0)A \cdot (t - t') = \rho A u_p(L_s + U(t' - t) - u_p(t' - t)) - \rho u_p(L_s - U(t' - t) - u_p)(t' - t)$$

$$(P - P_0)A \cdot (t - t') = \rho A u_p(L_s - L_s + U(t' - t) - u_p(t' - t))$$

$$(P - P_0)(t - t') = \rho u_p(U(t' - t) - u_p(t' - t))$$

$$(4c) \qquad (P - P_0) = \rho u_p(U - u_p)$$

As mass must be conserved, the mass of the shocked and unshocked areas at time t and t' must equal, thus:

$$\rho L_{shocked} A + \rho_0 L_{unshocked} A = \rho L'_{shocked} A + \rho_0 L'_{unshocked} A$$

$$\rho L_{shocked} + \rho_0 L_{unshocked} = \rho L'_{shocked} + \rho_0 L'_{unshocked}$$

Subsituting (2c) and (3c) into this expression:

$$\rho L_{shocked} + \rho_0 L_{unshocked} = \rho(L_{shocked} + U(t' - t) - u_p(t' - t)) + \rho_0(L - U(t' - t))$$

$$\rho L_{shocked} - \rho_{L_s}hocked + \rho_0 L_{unshocked} - \rho_{L_u}nshocked = \rho(U(t' - t) - u_p(t' - t)) + \rho_0 U(t' - t)$$

$$0 = \rho(U(t' - t) - u_p(t' - t)) + \rho_0 U(t' - t)$$

$$(5c) \qquad \rho(U - U_p) = \rho_0 U$$

We can subsitute (5c) back into (4c) to get (6c) as given in eq 7.18:

$$(6c) \qquad (\Delta P) = (\rho_0 U)u_p)$$

H.4 Derivation of 7.26

The speed of the shockwave passing through a material is given by

$$U = Su_p + C \tag{1d}$$

where S and C are material related constants which must be found experimentally

We can now subsitute (1d) in (6c):

$$\Delta P = (\rho_0 * (Su_p + C) * u_p)$$
$$\Delta P = (\rho_0 S u_p + \rho_0 C) * u_p$$
$$\Delta P = (\rho_0 S u_p^2 + \rho_0 C u_p))$$
$$\Delta P = a u_p^2 + b u_p$$

where $a = \rho_0 S$ and $b = \rho_0 C$

As during the intial phase of contact $P_{target} = P_{impactor}$

$$a_{target} u_{target}^2 + b_{target} u_{target} = a_{impactor} u_{impactor}^2 + b_{impactor} u_{impactor} \tag{2d}$$

as the velocity of the target is equal to the impact velocity minus the impactor velocity

$$u_{impactor} = v_i - u_{target}$$

we can rearrange (2d) as follows

$$(a_{target}\ u_{target}^2) + (b_{target}\ u_{target}) =$$
$$a_{impactor} * (v_i - u_{target})^2 + b_{impactor} * (v_i - u_{target})$$
$$(a_{target}\ u_{target}^2) + (b_{target}\ u_{target}) =$$
$$a_{impactor} * (-2v_i\ u_{target} + v_i^2 + u_{target}^2)$$
$$+ b_{impactor} * (v_i - u_{target})$$
$$(a_{target}\ u_{target}^2) - (a_{impactor}\ u_{target}^2) =$$
$$(-2v_i\ a_{impactor}\ u_{target}) - (b_{target}\ u_{target})$$
$$- (b_{impactor}\ u_{target}) + (b_{impactor}\ v_i) + (a_{impactor}\ v_i^2)$$
$$u_{target}^2(a_{target} - a_{impactor}) =$$
$$u_{target}(-2v_i\ a_{impactor} - b_{target} - b_{impactor}) + b_{impactor}\ v_i$$
$$+ a_{impactor}\ v_i^2$$

We are now able to collect the terms for each coeficcent into a single constant and re-arrange into a standard quadratic formula

$$A * u_{target}^2 + B * u_{target} + C = 0$$

where :

$$A = a_{target} - a_{impactor}$$

$$= \rho_{(0,target)} S_{target} - \rho_{(0,impactor)} S_{impactor}$$

$$B = 2v_i \; a_{impactor} + b_{target} + b_{impactor}$$

$$= 2\rho_{(0,impactor)} S_{impactor} v_i + C_{target} \rho_{(0,impactor)} + \rho_{0,impactor} C_{impactor}$$

$$C = a_{impactor} V_i^2 + b_{impactor} v_i$$

$$= \rho_{(0,impactor)} S_{impactor} v_i^2 - \rho_{(0,impactor)} C_{impactor} v_i$$

Appendix I

Peridot data

Table I.1: The preliminary analysis of the peridots prior to shooting along with the shot number that this peridot was fired in and the UoK shot code cosponsoring the that shot

Peridot no.	SEM	Fa (%)	Raman	Optically	OBSERVATIONS	Shot no.	Shot Code
1	Y		Y	Y		1	
2	y		Y	y		6	
3	Y		N	Y	Chipped on girdle	N/A	
4	N		N	Y		2	
5	N		N	Y	Internal fracture, chipped girdle	N/A	
6	N		N	Y		3	

Table I.1: The preliminary analysis of the peridots prior to shooting along with the shot number that this peridot was fired in and the UoK shot code cosponsoring the that shot

Peridot no.	SEM	Fa (%)	Raman	Optically	OBSERVATIONS	Shot no.	Shot Code
7	N		N	Y		4	
8	N		N	Y		5	
9	Y		Y	Y		7	
10	Y		Y	Y	Internal fracture	N/A	
11	y	91.4	n	y		3b	
12	y	90.9	n	y	Chipped on girdle and table	N/A	
13	y	91.6	n	y	cracked	N/A	
14	y	84.5	n	y		1b	
15	y	90.4	n	y	slight chip between facet and table	2b	
16	y	89.4	n	y		10b	
17	y	81.6	n	y		4b	
18	y		n	y		5b	
19	y		n	y		6b	
20	y		n	y	Lost prior to charictorisation	N/A	
21	y	82.3	y	y		11b	

Table I.1: The preliminary analysis of the peridots prior to shooting along with the shot number that this peridot was fired in and the UoK shot code cosponsoring the that shot

Peridot no.	SEM	Fa (%)	Raman	Optically	OBSERVATIONS	Shot no.	Shot Code
22	y	81.6	n	y		7b	
23	y	83.9	n	y		12b	
24	y	79.4	n	y		8b	
25	y	79.5	n	y		9b	
26	y	80.3	y	y		13b	
27	y	76.6	y	y		15b	
28	y	80.0	y	y		17b	
29	y	80.6	y	y		16b	
30	y	77.5	y	y		18b	
31	y	79.9	y	y		19b	
32	y	82.4	y	y		20b	
33	y	81.1	y	y		21b	
34	y	82.4	y	y		23b	
35	y	79.0	y	y		22b	
36	y	81.7	y	y		24b	

Table I.1: The preliminary analysis of the peridots prior to shooting along with the shot number that this peridot was fired in and the UoK shot code cosponsoring the that shot

Peridot no.	SEM	Fa (%)	Raman	Optically	OBSERVATIONS	Shot no.	Shot Code
37	y	81.2	y	y		25b	
38	y	81.0	y	y		26b	
39	y	81.4	y	y	Crack and inclusion	N/A	
40	y	76.6	y	y		27b	
41	y	80.6	y	y		28b	
42	y	80.8	y	y		29b	
43	y	82.1	y	y	Cracked	N/A	
44	y	79.9	y	y		30b	

Appendix J

Shot Program

J.1 Shot Program 1

shot number	shot code	velocity	projectile	target	result
1		2.000	peridot	E.T. no air, 15µm mylar,aerogel	projectile destroyed
2		1.901	Peridot	E.T. no air or mylar film, aerogel(112kg m^{-3})	projectile survived
3		0.941	Peridot	Foil rig	something
4		0.957	Peridot	Foil rig	something
5		2.110	Peridot	Foil rig	Something
6		0.951	Peridot	E.T. with atmosphere and 15µm mylar,aerogel	Peridot recovered

shot number	shot code	velocity	projectile	target	result
7		0.991	Peridot	E.T. no atmosphere but with 15µm mylar and aerogel	peridot recovered

J.2 Shot Program 2

shot number	shot code	velocity	projectile	target	result
1b		0.99	Peridot	Duplicate of shot 4 target setup	
2b		1.54	Peridot	Duplicate of shot 4 target setup	
3b		1.59	Peridot	Foil rig	
4b		1.61	Peridot	Foil rig	
5b		1.33	Peridot	Foil rig	
6b		2.07	Peridot	Foil rig	
7b		1.52	Peridot	E.T. with paper stopper	
8b		2.17	Buckshot/Peridot	Foil rig	
9b		2.08	buckshot/Peridot	E.T. with 10µm mylar, atmosphere and paper stopper	
10b		2.09	buckshot/Peridot	E.T. with 10µm mylar, atmosphere and paper stopper	
11b		2.07	buckshot/Peridot	E.T. with 10µm mylar, atmosphere, HDS2-7A Aerogel	
12b		1.70	buckshot/Peridot	E.T., HDS2-7A Aerogel	

shot number	shot code	velocity	projectile	target	result
13b		1.57	buckshot/Peridot	E.T. Aerogel from shot 12b	
14b		2.12	buckshot/Peridot	E.T. no atmosphere, no foil, paper stopper	
15b		1.88	buckshot/Peridot	E.T., HDS2-7A Aerogel	
16b		3.03	buckshot/Peridot	E.T. with 10µm mylar, atmosphere, LLH2-5B Aerogel	
17b		2.09	buckshot/Peridot	E.T.LLH2-5B Aerogel	
18b		2.09	buckshot/Peridot	E.T. LLH2-5B Aerogel	
19b		2.09	buckshot/Peridot	E.T. with Aerogel reused from shot 19b	
20b		2.09	buckshot/Peridot	E.T. with LLH2-5B Aerogel	
21b		2.09	buckshot/Peridot	E.T. with 10µm mylar, atmosphere and paper stopper	

J.3 foil rig setups

Table J.3: The targets used in the foil rig during the shot programs describe in Chapters 6 and 8 , the gap is listed between the target and the preceding target foil. The 15µm Mylar film had an aluminium coating, the 10µm film is uncoated.

Shot no.	Target 1	Gap	Target 2	Gap	Target 3	gap	Target 4	gap
3	15 µm mylar	0	15 µm mylar	115mm	aluminium stopper	40	n/a	n/a
4	15 µm mylar	0	15 µm mylar	115mm	15 µm mylar	115mm	Paper	115mm
5	15 µm mylar	0	15 µm mylar	115mm	15 µm mylar	115mm	Paper	115mm
3b	10 µm mylar	0	5 µm mylar	312.8mm	Paper	73.6mm	n/a	n/a
4b	10 µm mylar	0	n/a	n/a	n/a	n/a	n/a	n/a
5b	10 µm mylar	0	5 µm mylar	312.8mm	Paper	73.6mm	n/a	n/a
6b	10 µm mylar	0	10 µm mylar	115	10 µm mylar	115	paper	115
8b	10 µm mylar	0	15 µm mylar	275	paper	115	n/a	n/a